

Advanced theory for colloidal detachment of
detrital and authigenic fines in rocks

Abolfazl Hashemi

A thesis submitted for the degree of
Doctor of Philosophy (Ph.D.)

School of Chemical Engineering
Faculty of Engineering, Computer & Mathematical Sciences
The University of Adelaide



February 2024

Table of Contents

Abstract.....	iii
Declaration.....	v
Aknowledgement.....	vi
Thesis by Publication.....	viii
1 Contextual Statement	1
1.1. Significance of the project	1
1.2. State of the art.....	4
1.3 Scope of the work	6
1.4. Thesis structure	7
1.5. Aims of the study and how the Publications are related to the Thesis	11
1.6. References.....	15
2 Critical Literature Review	17
2.1. Introduction: Migration of Authigenic and detrital fines	17
2.2. Fines detachment against electrostatic-state of the art	19
2.3. Fines detachment by breakage.....	33
2.3.1. SEM-images proofs for authigenic fines detachment by breakage.....	34
2.3. 2. Cleat-scale numerical modelling of fines detachment by breakage	36
2.3.3. Using Timoshenko and Goodier's beam theory for analytical modelling of particle deformation.....	37
2.4. Summary and conclusions from the literature review	41
2.5. References.....	43
3. Colloidal detachment in porous media: stochastic model and upscaling	48
4. Formation damage by fines breakage and migration.....	77
5. Geo-mechanical aspects for breakage detachment of rock fines by Darcys flow	78
6. Particle detachment in reservoir flows by breakage due to induced stresses and drag	93

7. Rock fines breakage by flow-induced stresses against drag: geo-energy applications.....	128
8. Fines migration and production in CSG reservoirs: laboratory & modelling study detailed coreflood treatment coal cases	169
9. Fines migration during Coal Bed Methane production: mathematical and laboratory modelling, field cases	170
10. Discussion.....	178
11. Future works.....	180
11. Conclusions.....	178

Abstract

Hereby I present a PhD thesis by publications. The thesis includes two published journal papers, one submitted journal paper, one archived paper at Cornell University (USA), and three peer-reviewed conference papers. The journals include high-impact-factor ones: Chemical Engineering Journal, International Journal of Rock Mechanics and Mining Sciences, and Geo-mechanics and Geophysics for Geo-energy and Geo-Resources.

The thesis develops a novel advanced theory for colloidal detachment of detrital and authigenic fines in natural porous reservoirs. Detrital fines are attracted to the surface by DLVO electrostatic forces, while authigenic particles form a mechanical bond with a substrate. The essence of the process is fines detachment, mobilization with further migration and recapture by the porous media. The capture of mobilized particles yields a decrease in suspension concentration and rock permeability. Significant permeability decline occurs due to straining or size exclusion. SEM images widely show open pores before the flow and image of the same pore plugged by strained particles after the flow.

Regarding detrital particles, we discuss colloidal-suspension-nano transport in porous media with particle detachment and further capture by the rock. Previous works formulate particle-scale detachment conditions and porous-media scale transport equations with empirical coefficients, which are determined from the flow tests and are not predicted from the microscale. The present thesis establishes the upscaled procedure by stochastic distribution of torque and force balance on the attached particle and derivation of macro-scale equation for maximum retained concentration of attached

particles as a function of velocity, PH, salinity, and temperature. Exact solution for 1D flow problem is used to determine Maximum Retention Function (MRF) from laboratory test and match it with the stochastic microscale model for detachment. High match obtained for four colloidal coreflood experiments validates the stochastic model and upscaling procedure.

While micro and macro scale models for detrital fines detachment are available, and only upscaling procedure must be performed, none of models is available for authigenic particles. In this thesis, integrating the 3D version of Timoshenko and Goodier's beam theory of elastic cylinder deformation with a CFD-based model for viscous flow around the attached particle and with strength failure criteria for particle-rock bond, we derived an explicit criterium for fines detachment by breakage at the pore scale. This leads to an explicit formula for the breakage flow velocity. Its upscaling yields a mathematical model for fines detachment by breakage, expressed in the form of the maximum retained concentration of attached fines versus flow velocity – MRF for breakage. We performed corefloods with piecewise constant increasing flow rates, measuring breakthrough concentration and pressure drop across the core. The behaviour of the measured data is consistent with two-population colloidal transport, attributed to detrital and authigenic fines migration. Indeed, the laboratory data show high match with the analytical model for two-population colloidal transport, which validates the proposed mathematical model for fines detachment by breakage.

This thesis developed an advanced mathematical model for colloidal-suspension-nano transport in porous reservoirs. Forthcoming research works will apply this model in several areas of chemical, environmental, petroleum, geological, and civil engineering.

Declaration

I certify that this work contains no material which has been accepted for the award of any other degree or diploma in my name, in any university or other tertiary institution and, to the best of my knowledge and belief, contains no material previously published or written by another person, except where due reference has been made in the text. In addition, I certify that no part of this work will, in the future, be used in a submission in my name, for any other degree or diploma in any university or other tertiary institution without the prior approval of the University of Adelaide and where applicable, any partner institution responsible for the joint award of this degree.

The author acknowledges that copyright of published works contained within the thesis resides with the copyright holder(s) of those works.

I give permission for the digital version of my thesis to be made available on the web, via the University's digital research repository, the Library Search and also through web search engines, unless permission has been granted by the University to restrict access for a period of time.

I acknowledge the support I have received for my research through the provision of an Australian Government Research Training Program Scholarship.

Abolfazl Hashemi

25/11/2023

Acknowledgement

I want to express my deepest appreciation to Pavel Bedrikovetski, my PhD supervisor at the University of Adelaide. Pavel's indispensable guidance in mathematics and analytical solutions played a pivotal role in the success of my research, enabling me to surpass the boundaries of my prior knowledge and undertake a challenging interdisciplinary project.

A sincere debt of thanks is also owed to my co-supervisor, Themis Carageorgos, and my lab supervisor, Alex Badalyan. Their dedicated efforts were instrumental in achieving the significant milestones of my research.

Special recognition is extended to Abbas ZeiniJahromi, Sara Borazjani, and Thomas Russell. Their willingness to engage in discussions and offer assistance greatly contributed to the success of my study.

Furthermore, my heartfelt appreciation goes out to all my friends, colleagues, and coauthors at the University of Adelaide. Your unwavering support has made this journey smoother. Although it's not feasible to mention each person individually, I want to highlight a few friends who readily come to mind: Cuong Nguyen, Grace Loi, Bryant Dang-Le, Nastaran Khazali, Yutong Yang, Nassim Hemmati, Yazan Arouri, Gabriel Malgaresi, Shahdad Ghassemzadeh, Amin Shokrollahi, and many others who played instrumental roles in this journey.

Lastly, I would like to extend my heartfelt gratitude to Matthieu Vandamme, Reza Zare, and Reza Abdullahi for their invaluable assistance. They generously devoted their time to engaging in in-depth discussions with me on the fundamental principles of Solid Mechanics and Geomechanics. Although I haven't had the chance to meet Matthieu in person, I appreciate his patience and precision in responding to numerous emails, addressing my inquiries regarding elasticity and solid mechanics.

Thesis by Publication

Published Journal Papers

Hashemi, A., Nguyen, C., Loi, G., Khazali, N., Yang, Y., Dang-Le, B., Russell, T. and Bedrikovetsky, P., 2023. Colloidal detachment in porous media: Stochastic model and upscaling. *Chemical Engineering Journal*, 474, p.145436.

Hashemi, A., Borazjani, S., Nguyen, C., Loi, G., Khazali, N., Badalyan, A., Yang, Y., Dang-Le, B., Russell, T. and Bedrikovetsky, P., 2023. Particle detachment in reservoir flows by breakage due to induced stresses and drag. *International Journal of Rock Mechanics and Mining Sciences*, 172, p.105591.

Submitted Journal Papers

Sara Borazjani, **Abolfazl Hashemi**, Cuong Nguyen, Grace Loi, Thomas Russell, Nastaran Khazali, Yutong Yang, Bryant Dang-Le, Pavel Bedrikovetsky, Rock fines breakage by flow-induced stresses against drag: geo-energy applications, Submitted to *Geomechanics and Geophysics for Geo-Energy and Geo-Resources*

International conference papers and presentations

Hashemi, A., Borazjani, S., Dang-Le, B., Yin Loi, G., Nguyen Cao, C., Badalyan, A. and Bedrikovetsky, P., 2022, February. Formation damage by fines breakage and migration. In *SPE International Conference and Exhibition on Formation Damage Control* (p. D011S002R006). SPE.

Hashemi, A., Borazjani, S., Nguyen, C., Loi, G., Badalyan, A., Dang-Le, B. and Bedrikovetsky, P., 2022, October. Fines Migration and Production in CSG Reservoirs: Laboratory & Modelling Study. In *SPE Asia Pacific Oil & Gas Conference and Exhibition*. OnePetro.

Hashemi, A., Dang-Le, B., Nguyen, C., Loi, G. and Khazali, N., 2023. Fines migration during coal bed methane production: mathematical and laboratory modelling, field cases. *The APPEA Journal*, 63(2), pp.S177-S182.

1 Contextual Statement

The chapter presents a main contextual statement about the significance and novelty of this PhD study. It comprises proved of the significance of the PhD project for colloidal-suspended-nano fluid mechanics in porous media and also for multiple engineering and natural science disciplines (Section 1.1), state of the art of the colloidal transported with particles detachment in porous media and existing gaps in knowledge and tools (Section 1.2), scope of the research development to fill the gap (Section 1.3), detailed description of the thesis structure (Section 1.4), and formulations of the aims of the study and how the aims have been achieved by publications (Section 1.5).

1.1. Significance of the project

Particle detachment, re-attachment, and transport occur in numerous natural, environmental and industrial processes. Those are covered by geology, chemical, environmental, civil, and petroleum engineering. An incomplete list of examples includes industrial filtering, size-exclusion chromatography, cold water injection into geothermal reservoirs with consequent fines migration, low-salinity water injection into aquifers for freshwater storage, propagation of viruses and bacteria in underground water, chemical treatment of contaminated soils, disposal of industrial waste, and re-injection of produced water into oilfields or aquifers (Bradford et al., 2017; 2009; 2013; Chrysikopoulos et al., 2017; Chrysikopoulos and Syngouna, 2012; Civan, 2014; Molnar et al., 2015; Syngouna and Chrysikopoulos, 2011; You et al., 2019; Yuan and Moghanloo, 2017, 2018; Yuan and Shapiro, 2011a; Zeinijahromi et al., 2016). Consequently, a broad understanding of the factors that influence particle attachment

and mobilisation from solid surfaces is required to successfully plan and design a variety of operations in environmental, chemical, and petroleum engineering.

The significance of the project is defined by wide application of colloidal detachment in numerous industrial processes and natural processes.

The reservoir fines include clays (kaolinite, illite, and chlorite), silica micro particles and powders, non-clay reservoir silk. Some fines have been incorporated in the rock during gravity separation with the following sedimentation, those particles are called detrital, and the particles that are grown natural sand grains during geological period due to mineral precipitation chemical reaction are called authigenic particles. Some authigenic particles can be broken off the rock surface by shear deformation and strong underground water flux created during rock deformation and tectonic movements. Fig. 1a, shows typical authigenic particles on the rock surface, Fig. 1b shows the detrital particles.

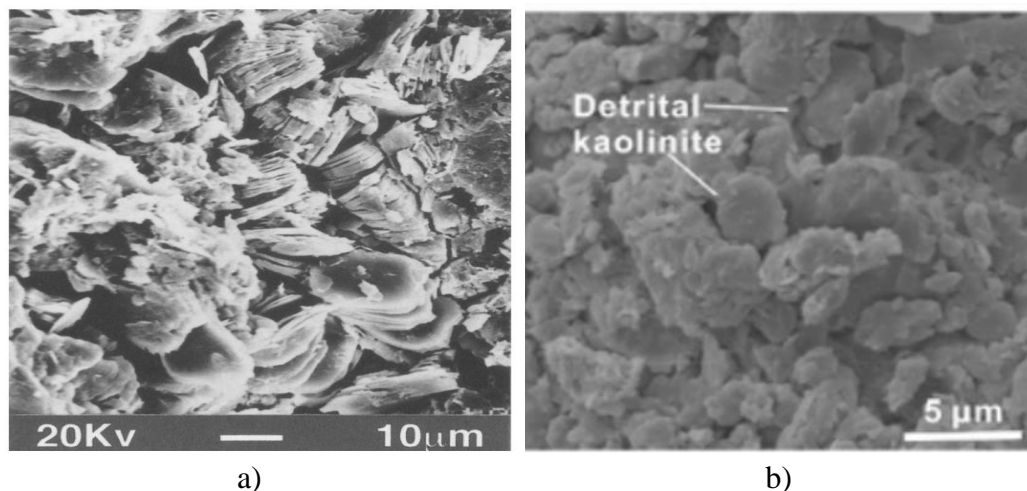


Fig. 1: SEM photos of fines attached to rock surface: a) Authigenic kaolinite (Aróstegui et al. 2000); b) Detrital kaolinite (Fang et al. 2017)

The decision making on those industrial processes is strongly relying on mathematical modelling. This mathematical model must be based on laboratory data and reflects all scales between the particle-scale and the reservoir-scale. Currently, mathematical model for detachment for the particles attached to the rock surface by electrostatic attraction is available only from tuning of the core flood data. Assuming known all microscale parameters, the model at the core and upper scale cannot be constructed. The current mathematical model for colloidal transport of detrital particles contained the detachment model in the form of maximum retention function, which by the traditional theory can be determined from coreflood only. Upscaling of the function from microscale parameters is not available. Absence of the upscaling theory yields significant restriction for prediction of colloidal transport of detrital fines in natural reservoirs.

Regarding authigenic particles, the theory for the detachment by breakage is not available. It makes impossible modelling the processes of permeability decline of geological faults and the near-fault zones by fines broken off by subterranean water flux.

Absence of a predictive model for detrital particles and absence of any models for transport of authigenic particles add to significance of the presented PhD project. The extensive industrial utilization of colloidal fines detachment, coupled with the absence of theoretical modeling, complicates the development of an advanced multiscale model for colloidal detachment in porous media. This poses a significant challenge in understanding fluid mechanics within porous media and implementing it effectively in industrial settings.

1.2. State of the art

This state of the art of the area of detachment of colloidal suspension is shown in Fig. 2. Fig. 2a shows the schematic of fines detachment from pore walls. The upper particle in left pore throat are detrital, they are detached against electrostatic DLVO attraction. The particles at the low throat wall are authigenic, they are detached by breakage the particle-rock bonded. After detachment the particles are transported by carrier water passing thick pore and strained/size excluded in thin pores.

Straining and size exclusion of fines yield significant permeability decline which constitute the main reason for study of fines migration in natural porous reservoirs. Fig. 2b, shows SEM images of a pore before flow, the pore is open. Fig. 2c, shows the same pore after flow, being blocked by the migrating fines. Fig. 2d-2f, show the schematic of detrital fines detachment. Fig. 2d, shows the SEM image of natural detrital particles attached to the rock surface. The forces asserting the attached particles submitted to viscous creeping flow in pores is presented in Fig. 2e. Viscous drag and areal dynamic lift detach particles whilst the attractive electrostatic DLVO force attaches them to the substrate. The energy potential for electrostatic force is presented in Fig. 2f where two energy minima reflect two states in attached particles for so-called favourable and unfavourable attachment conditions. The theory for electrostatic attachment is currently very well developed (Elimelech et al. 2013, Israelachvili 2015). The current detachment theory expressed by maximum retention function cannot be derived from microscale schematic in Fig. 2d-2f.

This schematic for detachment of authigenic fines is presented in Fig. 2g-2i, the placement of a single authigenic particle linked by a bond to grain, where it grew up during geological time, is presented in Fig. 2g. Fig. 2h shows the drag in the rotating moment asserting the authigenic fines from the viscous creeping flow in a single pore. This stem of the particle encompassed the induced stresses, whilst the outer particle body is almost stress-free. Fig. 2i, shows normal and shear stresses asserting the particle stem (beam). The mathematical description of bond failure due to induced stresses is not available. The model of authigenic fines detachment is absent.

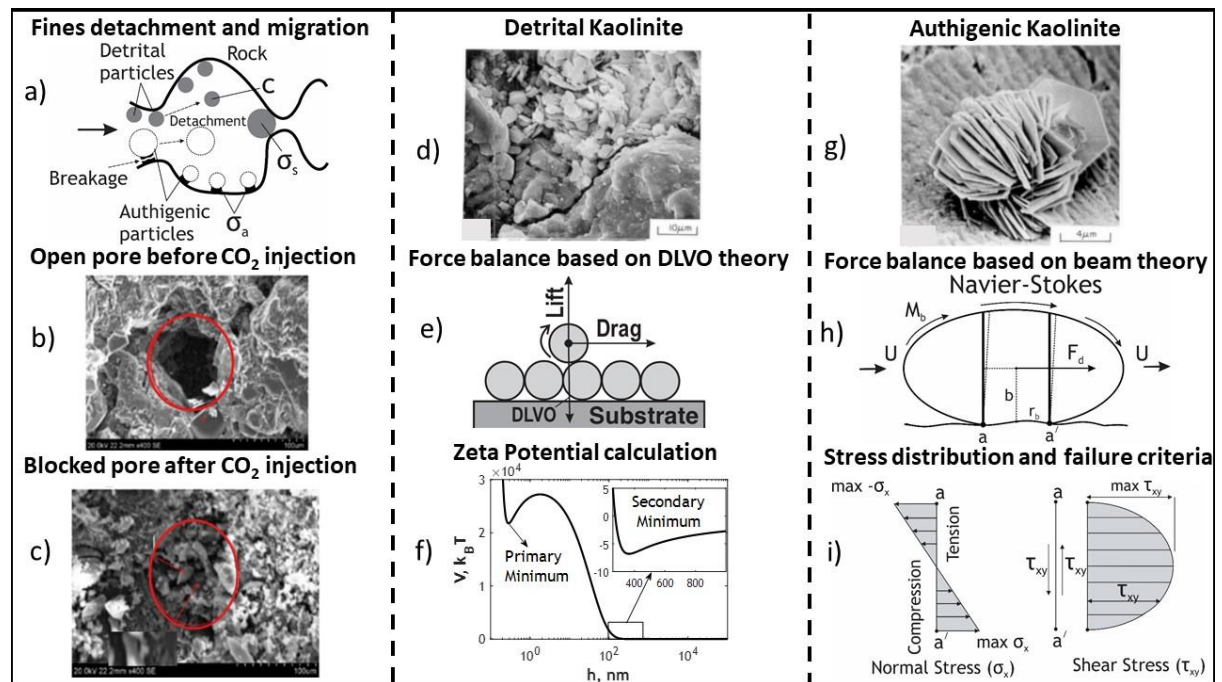


Fig. 2: Graphical abstract for modern theory of fines detachment from rock surface: a) schematic for detachment against electrostatic by breakage; b) open pore before the flow; c) the same pore plugged during the flow; d) attached detrital fines; e) attachment of detrital fines by DLVO forces; f) DLVO energy potentials; g) attached authigenic particle; h) particle and beam deformation; i) normal and shear stresses in the beam.

1.3 Scope of the work

In order to create advanced predictive multiscale mathematical model, the following steps must be undertaken:

Derivation of the upscale maximum retention function based on particle-scale mechanical equilibrium of detrital particles attached to the rock surface.;

Development of the technique for upscaling and predicting coreflood data using the upscale model

Development of the technique for downscaling, determining microscale particle parameters from the upper scale model.

Validation of the proposed model for detrital detachment by the coreflood tests.

Based on 3D beam theory, define the point of maximum of tensile and shear stresses during fines deformation by viscous flow, define dimensionless parameters determining the stress maxima. Define the geometric diagram, allowing applications of different rock failure criteria to the maxima points.

Derive upscaling technique to close system of governing equations for colloidal transport of authigenic particles.

Validation of the proposed model for authigenic detachment by the coreflood tests.

1.4. Thesis structure

This is a PhD thesis by publication. Six papers are included in the thesis of which two have been published and one has been submitted in high impact peer-reviewed journals and three full volume papers have been published in the conference proceedings and peer reviewed.

The thesis body is formed by seven chapters. The first chapter contains the context of statement of this thesis. It consists of the statement for significance of the project for theoretical fundamentals of fines detachment theory for colloidal flows (Section 1.1), formulation of the state of the art (Section 1.2), detailed description of the scope of the work (Section 1.3), the current section 1.4 describing the thesis structure, explanation how the publications solve the problem of this thesis (Section 1.5) and relevant references (Section 1.6).

The second chapter contains the literature review of colloidal detachment theory and its applications in the modern reservoir engineering. Introduction into the review (section 2.1) contains description of authigenic and detrital fines. The current theories for detrital fines detachment, including the theory of electrostatic attraction (DLVO forces), definition of maximum retention function, formulations of transport equations and their analytical solutions, the results of laboratory corefloods and determining the maximum retention function from breakthrough concentration are described in Section 2.2. Section 2.3 describes the detachment by breakage. The summary and conclusion from the critical analysis of the literature are presented in Section 2.4. Section 2.5 contains necessary literature references.

Chapter 3 “Colloidal detachment in porous media: stochastic model and upscaling” is a paper published in Chemical Engineering Journal. It develops a multiscale theory for detachment of detrital particles. The theory consists of upscaled model for mechanical equilibrium of particles, attached to the rock surface and submitted to viscous creeping flow in pores. It was found out that the upscaled conditions of mechanical equilibrium have the form of maximum retention function. The sensitivity analysis of the upscaled MRF has been performed, distinguishing more and less influential microscale parameters, affecting the MRF microscale curve. Details comparison with the results of four coreflood tests validate the model performed.

Chapter 4 “Formation Damage by Fines Breakage and Migration” is a full volume peer review paper presented at SPE conference and available from the proceeding in OnePetro as SPE-208810. Here the main idea of merging geo-mechanic with fluid mechanic in the elastic particles and Newtonian in pores flow is presented. However, stresses calculated from 2D beam theory, which limits the particle forms, where the theory can be applied. The results are compared with corefloods in sandstones.

Chapter 5 “Geo-mechanical aspects for breakage detachment of rock fines by Darcy’s flow” has been archived as an online paper by Cornell University. The chapter contains a very detailed derivation of the shear and tensile stress distributions following the analytical solutions for 3D beam theory, developed by Timoshenko and Goodier. It was found out that maxima allocated on the beam base, in particular on the base beam axis and its boundary. Based on the expression for maxima, the tensile stress diagram allows defining whether the breakage by tensile stress occurs in the middle or at the boundary of the beam base. After this, comparison of maxima of tensile stress and shear stress at

the axis of symmetry define the final breakage stress afterward the stress is compared with the corresponding strength, defining the detachment velocity. The chapter is concluded by the definition of detachment conditions based on the flow velocity which is expressed by three explicit formulae.

Chapter 6 “Particle detachment in reservoir flows by breakage due to induced stresses and drag” has been published in International Journal of Rock Mechanics and Mining Sciences. This paper presents the essence of maxima stress derivations from Chapter 6 and derives some geophysics and reservoir engineering applications. The breakage criteria are applied for 10 world documented examples for heavy oil production, polymer injection in reservoir, CO₂ injection in aquifers, water production from aquifers, well fracturing by high viscosity fracturing fluid, well fracturing by water at high injection rate, natural gas production, and flow in fractured reservoirs. It was found out that fines breakage can occurs in the majority of the cases.

Using the result of Chapter 6, Chapter 7 “Rock fines breakage by flow-induced stresses against drag: geo-energy applications” presents the analytical model for simultaneous migration of mobilised authigenic and detrital fines. The deep bed filtration model accounts for different filtration and formation damage coefficient for detached detrital and authigenic particles. The analysis of breakthrough concentration allows concluding the Constantness of the detrital filtration coefficient, and of blocked Langmuirian filtration function for authigenic fines, the paper develops the analytical model and determines MRF for authigenic and detrital fines. The method developed allows calculation of the detachable authigenic and detrital particles. This paper has been

submitted to Journal Geo-mechanic and Geophysics for Geo-energy and Geo-Resources.

Chapter 8 “Fines migration and production in CSG reservoirs: laboratory & modelling study detailed coreflood treatment coal cases” is an SPE paper (SPE-210764), presented at a SPE conference and available from proceeding at full volume peer review paper from OnePetro. The paper presents the detailed analysis of the laboratory tests on coreflooding with piecewise constant increasing rate injections. It was found out that breakage along with detachment against electrostatics occurs in 12 from 16 coreflood tests. In 4 tests, only attachment against electrostatic occurred.

Chapter 9 “Fines migration during Coal Bed Methane production: mathematical and laboratory modelling, field cases (APPEA 2023)” using the results of Chapter 8 presents the detailed analysis of one coreflood test using coal, and concludes about the results of all 8 corefloods in natural and engineered coal cores. Chapter 10 formulates general conclusion on the development of the advanced theory for detachment of colloidal-suspension-nano flows in porous media. The conclusion corresponds to detachment of both detrital and authigenic fines.

Paper	Chapter	Title	Status
1	Chapter 3	Colloidal detachment in porous media: stochastic model and upscaling	Published
2	Chapter 4	Formation Damage by Fines Breakage and Migration	Published
3	Chapter 5	Geo-mechanical aspects for breakage detachment of rock fines by Darcy's flow	Published
4	Chapter 6	Particle detachment in reservoir flows by breakage due to induced stresses and drag	Published
5	Chapter 7	Rock fines breakage by flow-induced stresses against drag: geo-energy applications	Submitted
6	Chapter 8	Fines migration and production in CSG reservoirs: laboratory & modelling study detailed coreflood treatment coal cases	Published
7	Chapter 9	Fines migration during Coal Bed Methane production: mathematical and laboratory modelling, field cases	Published

1.5. Aims of the study and how the Publications are related to the Thesis

The general aim of the thesis is the development of advanced multiscale theory for detachment of colloidal particles against electrostatic forces and by breakage. The particular aims comprise:

- (i) Upscaling of micromodel for detachment of detrital particles,
- (ii) Development of a microscale model for detachment of authigenic particles, its upscaling, and
- (iii) Derivation of analytical modelling for simultaneous detachment of authigenic and detrital fines. Let us discuss how this aim have been achieved in different publications.

The paper “Colloidal detachment in porous media: stochastic model and upscaling” presents below in Chapter 3, derives an upscaled formula for particle mechanical equilibrium and develops the explicit formula for maximum retention function at the core scale. This allows expressing micro scale detachment model in the form of MRF from probabilistic distribution of micro scale parameters of particle and pore sizes, their aspect ratios, zeta potential for particles and rock, etc. The MRF was used to close the system of governing equations for colloidal transport. This paper develops an analytical model allowing for matching the laboratory data. The obtained results show high match between the results of micro and macro modelling and the laboratory data. This development achieves the particular aim i.

The paper “Formation Damage by Fines Breakage and Migration (SPE-208810)” presents below in Chapter 4 presents a methodology for merging fluid mechanics of viscous flow in porous space around attached particles, geo-mechanics of fines deformation, and failure criteria defining breakage. The limitation of the approach is using 2D analytical beam theory of elastic body. Further in the work, the detachment equations have been improved based on 3D beam theory. However, the methodology developed contributes to aim ii.

The paper “Geo-mechanical aspects for breakage detachment of rock fines by Darcy’s flow”, presents below in Chapter 5, develops the methodology of previous paper using 3D analytical beam theory. This allows using the developed theory for spherical, spheroidal, and cylindrical particles, corresponding to conventional forms of clay and silica fines. This paper derives final explicit formula for stress maxima and breaching the failure criteria. This paper also contributes to achieving the aim ii.

The paper “Particle detachment in reservoir flows by breakage due to induced stresses and drag” presents in Chapter 6, applies the theoretical fundamental for detachment by breakage, derived in the previous paper to different cases of production and injection well exploitation in oil and gas production and in water resources management. It was found out that authigenic fines breakage can occurs in the majority of field cases this highlight the significance of the work in different area of energy production as well as in hydrology and aquifers exploitation.

The paper “Rock fines mobilisation by breakage: flow-induced stresses and electrostatic forces against drag” presents in Chapter 7, uses the exact analytical solution for stress maxima in order to close the governing system for simultaneous detachment and migration of detrital and authigenic fines. The developed theory allows to introduce MRF separately for detrital and authigenic fines, and derives analytical model for binary colloidal transport, where detrital particles filters with constant filtration coefficient, whilst the authigenic fines performs deep bed filtration by blocking Langmuir filtration function. The paper also presents the laboratory studies, undertaken to investigate separated detachment of both particle populations. The laboratory data fairly well reproduces the results of binary analytical model. High agreement between the laboratory data and upscaled model have been observed. The paper achieves aim ii.

The paper “. Fines migration and production in CSG reservoirs: laboratory & modelling study (SPE-210764)” presents in Chapter 8, develops particular case for single population transport for mobilised detrital and authigenic fines. The analysis of the available laboratory data shows that the breakthrough concentration does not show

distinguished properties reviewed by two population models. Therefore, it is more appropriate to tune the breakthrough data using a single population model, and then divides common MRF to detrital and authigenic parts. So, the model assumes equality of filtration and drift delay coefficient for detrital and authigenic fines but incorporate different condition of their detachment. Finally, 16 laboratory tests have been treated and the results have been generalised in term of fraction of detachable clays, fraction of the clays produced during coreflood and the impedance growth during the coreflood. This paper, despite presenting the results of 8 corefloods only achieves iii.

The paper “Fines migration during Coal Bed Methane production: mathematical and laboratory modelling, field cases (APPEA 2023)” presents just one coal coreflood and its matching by the analytical model, but concludes about all coreflood tests, stating close match by the mathematical model. It contributes to the conclusion of aim iii.

1.6. References

- Arostegui, J., Irabien, M.J., Nieto, F., Sangüesa, J. and Zuluaga, M.C., 2001. Microtextures and the origin of muscovite-kaolinite intergrowths in sandstones of the Utrillas Formation, Basque Cantabrian Basin, Spain. *Clays and Clay Minerals*, 49(6), pp.529-539.
- Bradford, S. A., Kim, H., Shen, C., Sasidharan, S., and Shang, J. 2017. Contributions of nanoscale roughness to anomalous colloid retention and stability behavior. *Langmuir*, 33 (38): 10094-10105. <https://doi.org/10.1021/acs.langmuir.7b02445>.
- Bradford, S. A., Kim, H. N., Haznedaroglu, B. Z., Torkzaban, S., and Walker, S. L. 2009. Coupled factors influencing concentration-dependent colloid transport and retention in saturated porous media. *Environmental Science & Technology*, 43 (18): 6996-7002. <https://doi.org/10.1021/es900840d>.
- Bradford, S. A., Torkzaban, S., and Shapiro, A. 2013. A theoretical analysis of colloid attachment and straining in chemically heterogeneous porous media. *Langmuir*, 29 (23): 6944-6952. <https://doi.org/10.1021/la4011357>.
- Chrysikopoulos, C. V., Sotirelis, N. P., and Kallithrakas-Kontos, N. G. 2017. Cotransport of graphene oxide nanoparticles and kaolinite colloids in porous media. *Transport in Porous Media*, 119 (1): 181-204. <https://doi.org/10.1007/s11242-017-0879-z>.
- Chrysikopoulos, C. V. and Syngouna, V. I. 2012. Attachment of bacteriophages MS2 and ΦX174 onto kaolinite and montmorillonite: Extended-DLVO interactions. *Colloids and Surfaces B: Biointerfaces*, 92: 74-83. <https://doi.org/10.1016/j.colsurfb.2011.11.028>.
- Civan, F. 2014. *Reservoir Formation Damage*, 3rd ed. edition. Burlington, MA, USA: Gulf Professional Publishing.
- Elimelech, M., Gregory, J. and Jia, X., 2013. *Particle deposition and aggregation: measurement, modelling and simulation*. Butterworth-Heinemann.
- Fang, Q., Hong, H., Zhao, L., Furnes, H., Lu, H., Han, W., Liu, Y., Jia, Z., Wang, C., Yin, K. and Algeo, T.J., 2017. Tectonic uplift-influenced monsoonal changes promoted hominin occupation of the Luonan Basin: insights from a loess-paleosol sequence, eastern Qinling Mountains, central China. *Quaternary Science Reviews*, 169, pp.312-329.
- Israelachvili, J.N., 2015. *Intermolecular and surface forces*. Academic press.
- Molnar, I. L., Johnson, W. P., Gerhard, J. I., Willson, C. S., and O'Carroll, D. M. 2015. Predicting colloid transport through saturated porous media: A critical review. *Water Resources Research*, 51 (9): 6804-6845. <https://doi.org/10.1002/2015WR017318>.
- Syngouna, V. I. and Chrysikopoulos, C. V. 2011. Transport of biocolloids in water saturated columns packed with sand: Effect of grain size and pore water velocity. *Journal of Contaminant Hydrology*, 126 (3): 301-314. <https://doi.org/10.1016/j.jconhyd.2012.01.010>.
- You, Z., Badalyan, A., Yang, Y., Bedrikovetsky, P., and Hand, M. 2019. Fines migration in geothermal reservoirs: Laboratory and mathematical modelling. *Geothermics*, 77: 344-367. <https://doi.org/10.1016/j.geothermics.2018.10.006>.
- Yuan, B. and Moghanloo, R. G. 2017. Analytical model of well injectivity improvement using nanofluid preflush. *Fuel*, 202: 380-394. <https://doi.org/10.1016/j.fuel.2017.04.004>.
- Yuan, B. and Moghanloo, R. G. 2018. Nanofluid pre-treatment, an effective strategy to improve the performance of low-salinity waterflooding. *Journal of Petroleum Science and Engineering*, 165: 978-991. <https://doi.org/10.1016/j.petrol.2017.11.032>.

Yuan, H. and Shapiro, A. A. 2011a. A mathematical model for non-monotonic deposition profiles in deep bed filtration systems. *Chemical Engineering Journal*, 166 (1): 105-115. <https://doi.org/10.1016/j.cej.2010.10.036>.

Zeinjahromi, A., Farajzadeh, R., Bruining, J. H., and Bedrikovetsky, P. 2016. Effect of fines migration on oil–water relative permeability during two-phase flow in porous media. *Fuel*, 176: 222-236. <https://doi.org/10.1016/j.fuel.2016.02.066>.

2 Critical Literature Review

This critical analysis of the scientific and technical literature on colloidal-suspension-nano transport in porous media and consequent formation damage comprises definition of detrital and authigenic fines (Section 2.1), state-of-the-art of the detachment theory for detrital fines (Section 2.2), state-of-the-art of the detachment theory for authigenic fines (Section 2.3), and conclusions from the literature review (Section 2.4).

2.1. Introduction: Migration of Authigenic and detrital fines

Fines migration is the wide-spread process in subterranean flow. The essence of those processes is detachment of natural reservoir fines, migration with carrier water and reattachment by the porous rocks. The attached particles as a part of the rock matrix from the point of view of detachment can be divided into two groups-authigenic and detrital fines. The authigenic particles are formed as a result of minerals or sedimentary rock deposit. They are found or observed in the same place where they have been generated. The deformation of authigenic particles is due to sedimentation of the product of chemical reaction or phase transition, causing mineral precipitation, crystallization or chemical reaction occurring directly on grain surfaces. Often the precipitation and crystallization occurred at the bottom of a sea or ocean and turned into reservoir rocks as a result of sedimentation (Marshak 2004).

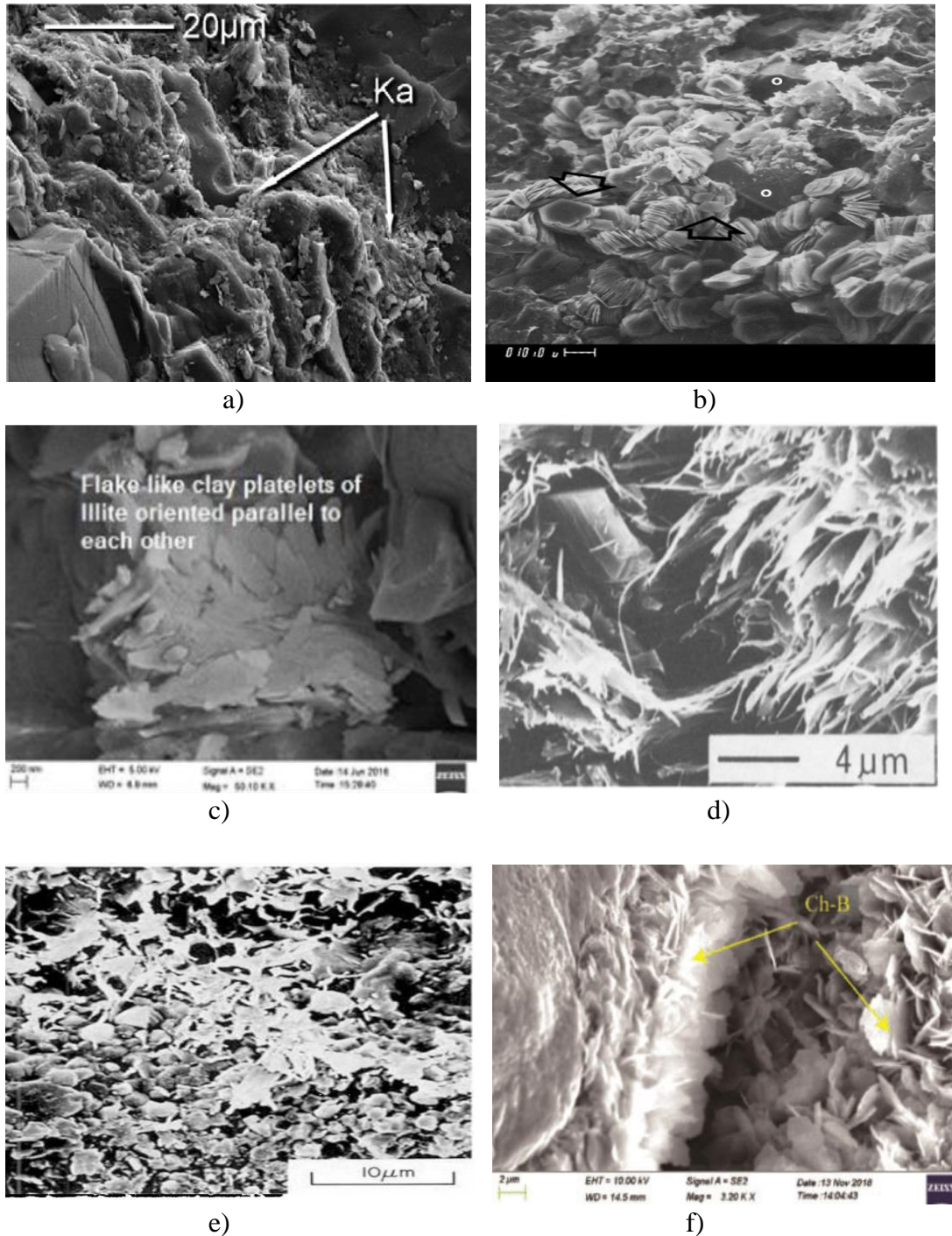


Fig. 3: SEM photos of a) Detrital kaolinite (Zou et al. 2018), b) Authigenic kaolinite (Welton, 1984), c) Detrital illite (Kar,2019), d) Authigenic illite (Burley et al. 1985), e) Detrital chlorite detrital (Wilson et al. 1977), f) Authigenic chlorite (Zhou et al., 2020).

The detrital particles are weathered by water, eroded, and transported in subterranean water to the deposition on site. Those particles are derived from existing rock matter.

Those fines consist of the particle of lithic or monomineralic fragments. During genetic processes, the detrital rocks can be weathered several times intercalated by flow within underground streams and deposited in other sites. From the point of view of mobilisation by flow in natural reservoirs, authigenic fines are detached by breakage, whilst detachment of detrital fines occurs against electrostatic attraction.

The main fines-producing clays are kaolinite, illite, and chlorite. Fig. 3a,c, and e show the detrital kaolinite, illite and chlorite. Fig. 3b,d,f show those three authigenic clays.

In the next section, we present the critical literature analysis of colloidal detachment of detrital particles.

2.2. Fines detachment against electrostatic-state of the art

Schematic of detrital fines detachment. Reliable prediction of particle detachment/mobilisation is a key step in chemical and environmental engineering applications of colloidal-suspension-nano transport modelling in porous media. The essence of those processes is detachment of particles against electrostatic DLVO attraction, mobilization with further migration and recapture by the porous media. The capture of mobilized particles yields decrease in suspension concentration and in rock permeability. Main particle capture mechanisms are size exclusion, straining, bridging, electrostatic attraction, adsorption, and Brownian diffusion into stagnant-flow zones. Fig. 4 shows the detachment of attached fines by shear stress induced by the viscous flow, migration with the carrier fluid, and size exclusion in thin pores; particle movement in large pores continues. Suspension concentration variation due to particle

Both particle capture and permeability decline are also significant for geological processes of fines mobilization during tectonic rock deformation and induced powerful water fluxes, which can significantly decrease permeabilities of faults and near fault zones (Farrell et al. 2021). These processes are important for seismic events in the geological bodies with applications to earthquake predictions.

The schematic of those processes is presented in Fig. 4. Particles are detached by shear stress induced by the viscous flux, then migrate and strain in the thin pores while the migration in thick pores continues. Fig. 5 presents SEM images for open pore prior to fines migration, and post mortem image of the same pore. The pore which was open to flow initially (Fig.5a), becomes completely plugged by mobilized and strained fines during the flow (Fig.5b).

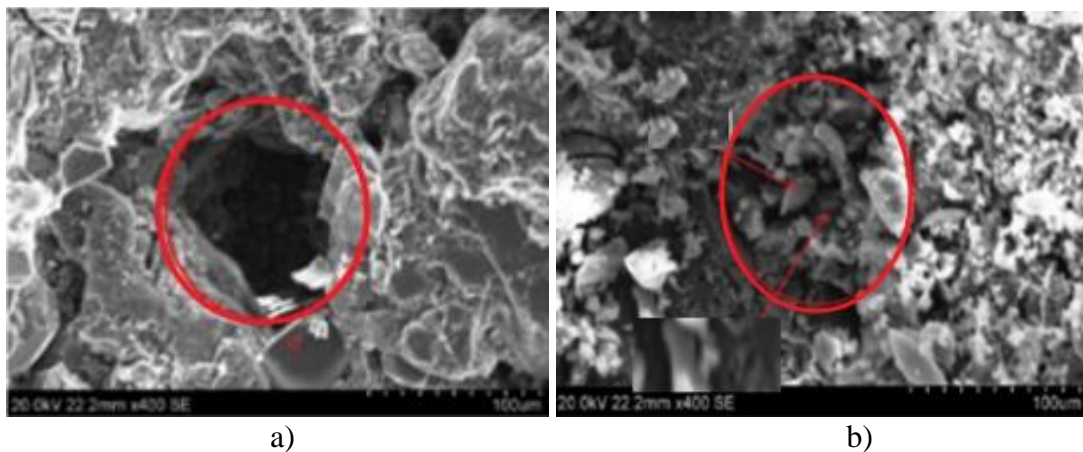


Fig. 5: Pore plugging by mobilised fine particles: a) open pore prior to flow; b) the pore blocked by released particle after the flow (Othman et al. 2018).

Traditional governing equations for colloidal transport The decision making on above mentioned technological processes strongly rely on laboratory-based mathematical modelling at the reservoir scale. The traditional mathematical model for colloidal transport with particle detachment and reattachment consists of mass balance equations

for attached, suspended, and strained particles, and detachment-reattachment rate equation.

$$\frac{\partial}{\partial t}(\phi c + \sigma_a + \sigma_s) + U_c \frac{\partial c}{\partial x} = 0 \quad (1)$$

$$\frac{\partial \sigma_s}{\partial t} = \lambda_s(\sigma_a, \sigma_s) f(c) U \quad (2)$$

$$\frac{\partial \sigma_a}{\partial t} = \lambda_a(\sigma_a, \sigma_s) f(c) U - k_{det} \sigma_a \quad (3)$$

$$U = - \frac{k}{\mu(1 + \beta_a \sigma_a)^n (1 + \beta_s \sigma_s)^m} \quad (4)$$

Where ϕ is the porosity, c is the suspended concentration, σ_a , σ_s are attached and strained concentrations, respectively, U is the flow velocity, λ is the filtration function, k_{det} is the detachment coefficient, β_a and β_s are formation damage coefficients with respect to attached and strained particles, and σ_{cr} is the stabilized strained concentration. Formation damage coefficients along with powers m and n reflect permeability variation due to fines attachment and detachment. Equation (1) assumes that particles migrate with the carrier fluid velocity. Equations (2,3) assumes simultaneous reattachment (straining) of mobilized particles with the detachment of attached particles.

This theory has several shortcomings. The filtration function $\lambda(\sigma)$ fulfils an advanced theory for deep bed filtration, including explicit formulae reflecting particle grain electrostatic interaction, Brownian diffusion, gravitational sedimentation, particle and pore sizes, etc (Bedrikovetsky 2011, 2012). The detachment coefficient is purely

empirical parameter which is determined by matching the laboratory data on breakthrough concentrations during flows in porous columns or natural reservoir rocks.

Equation (2) yields asymptotical stabilization of σ_s towards its stable value. The relaxation time in kinetics equation (3) is the ratio $1/k_{det}$, which is a reference time of stabilization provided that the attachment filtration coefficient is negligible. However, several laboratory tests show sharp permeability change due to switching (instant increase) of flow velocity (Ochi and Vernoux 1998, Guo et al. 2019, Huang et al. 2017).

Maximum retention function model for fines detachment Another approach to detachment modelling comprises the maximum (critical) attached particle concentration as a function of velocity, salinity, pH, and temperature (Bedrikovetsky et al. 2011, 2012). This function is called MRF (Maximum Retention Function). It closes the system of mass-balance equations for attached, suspended, and re-captured fines. 1D flow problem allows for exact analytical solution (Yang and Bedrikovetsky 2017). It allows determining MRF from breakthrough concentrations during coreflooding. The colloidal transport model using MRF has exhibited high match with lab data in experiments on low-salinity waterflooding (Borazjani et al. 2017), mobilisation of attached clays (Yang et al. 2022), dewatering of coal seam beds (Guo et al. 2016) and gas production from coals (Guo et al. 2018), colloidal tracers (Kianfar et al. 2022). Therefore, this model was used for simulation of nanoparticles-fines reactive transport (Yuan and Moghanloo 2017), using NPs to control fines detachment (Yuan and Moghanloo 2018), water injection into deformable rocks (Zhai and Atefi-Monfared 2020 and 2021), exploitation of coal methane reservoirs (Peng et al. 2020), water injection during waterflood (Yuan and Shapiro 2011), reservoir pressure depletion

(Tangparitkul et al. 2020), groundwater re-charge (Ye et al. 2019), filtration in ultra-filtration membranes (Nnanna et al. 2015), hot-water flooding (Ravikumar et al. 2021), water injection with proppant packing (Huang et al. 2021), and water injection with high temperature variation (Cui et al. 2019).

However, for an arbitrary porous media, MRF was calculated theoretically only for poly-layer particle attachment with constant radii of pores and particles alone (Bedrikovetsky et al. 2011, 2012); otherwise MRF is available only from coreflood data. Besides this very specific case, the predictive model for MRF is not available. The existence of MRF is a consequence of particle-scale mechanical equilibrium on the rock surface, but the theoretical link between the particle- and core scales hasn't been established, i.e., an upscaling procedure hasn't been developed. This explains the absence of predictive colloidal transport model with particle detachment in porous media.

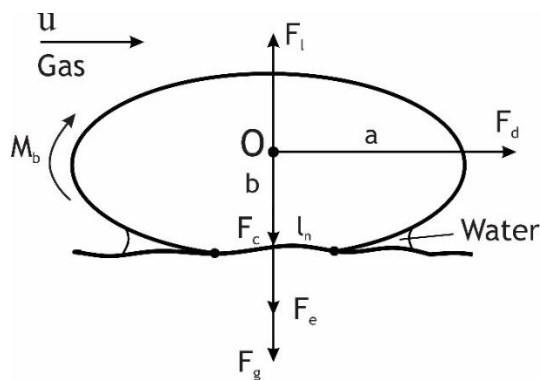


Fig. 6: Drag, lift, electrostatic, gravity and capillary forces exerting a particle from the viscous flux upon the attached fine

The MRF approach to modelling detachment has been proposed to reflect micro-scale conditions of fines detachment, which are mechanical equilibrium condition for the

attached particles submitted to viscous creeping flow. Figure (6) exhibits the forces exerting the attached particles. Here, we consider one phase flow (gas, air) with some water residing near the particle-rock contact areas. The detaching forces are drag and lift. The attaching forces are electrostatic, gravity, and capillary force in the case of water wetting area. There are three independent criteria for mechanical equilibrium of an attached particle.

Assume that the mobilized particle rotates around a centre, which is particle rock contact at the last moment before mobilization, the mechanical equilibrium is determined by torque balance.

The detaching moment of drag M_b is expressed as

$$M_b = F_d b f_M(\alpha_s) + F_l l_n = 6\pi\mu r_s u_s f_d(\alpha_s) b f_M(\alpha_s) + F_l l_n, \quad (5)$$

where μ is the fluid viscosity, r_s is the particle radius, u_s is the flow velocity at the centre of the particle, α_s is the aspect ratio for spheroidal particles, f_d and f_M are shape factors for spheroids. Here the aspect ratio is the ratio between small and large semi axis of spheroid, and r_s is the sphere with the volume equal to the volume of the spheroid:

$$\alpha_s = \frac{b}{a}, \quad \frac{4}{3}\pi a^2 b = \frac{4}{3}\pi r_s^3, \quad b = r_s \alpha_s^{2/3} \quad (6)$$

Formulae for lift, capillary force, and gravity are available from (Bedrikovetsky et al. 2011).

Mechanical equilibrium of a particle on the rock surface in the case of favourable attachment (one primary energy minimum) is determined by the following conditions:

- (i) equality of detaching and attaching torques

$$6\pi\mu r_s u_s f_d(\alpha_s) b f_M(\alpha_s) + F_l(r_s) l_n = F_e(h_m) l_n + F_c(r_s) l_n + F_g(r_s) l_n, \quad (7)$$

which can be expressed via normal force

$$F_n = F_e(h_m) + F_c(r_s) + F_g(r_s) - F_l(r_s) \quad (8)$$

$$6\pi\mu r_s u_s f_d(\alpha_s) b f_M(\alpha_s) = F_n l_n, \quad (9)$$

- (ii) equality of detaching and attaching force projections on horizontal

$$F_d = 6\pi\mu_f r_s u_c f_d(\alpha_s) = \nu_C F_n, \quad (10)$$

- (iii) equality of detaching and attaching force projections on vertical

$$F_l(u_s) = F_e(h_m) + F_g(r_s) + F_c(r_s); \quad F_n = 0 \quad (11)$$

where b and l_n are the lever arms for drag and normal forces, respectively, and ν_C is the Coulomb friction coefficient. Here in the case of attached fine particle, right sides of Eqs (9), (10), and (11), expressing the detachment by drag and lift, are lower than their left sides for $h=h_m$, that corresponds to attaching electrostatic, capillary, and gravity

forces. Breach of either equilibrium conditions (9), (10), or (11) yields fines detachment by rolling, sliding, and lifting, respectively (Chequer and Bedrikovetsky 2019, Bradford et al. 2013). In the case of two energy minima, there are two separating distances $h=h_m$ that correspond to both energy minima, and Eqs. (9), (10), and (11) are applicable to the particles that are located in primary and secondary energy minima. At low velocities, $F_l \ll F_e$, and the lifting criterium (11) can be dropped. For majority of clay fines in natural rocks, gravity is negligible. Capillary force is negligible in saturated or dry porous media.

The criterium that a particle remains attached to the rock and does not roll is:

$$\xi = \frac{6\pi\mu_f r_s u_s f_d(\alpha_s) l f_M(\alpha_s) + F_l(r_s)}{F_e(h_m) + F_c(r_s) + F_g(r_s)} < 1, \quad l = \frac{b}{l_n}, \quad (12)$$

It is implicitly assumed that the particles detached by criteria (9), (10), and (11) continue rolling over the rock surface, sliding over the surface, and move off the surface into the liquid stream, respectively. Figs. 7a and 7b show how the particle rotates around the touching “supporting” point at the detachment moment. The rotation occurs around the edge of contact particle-substrate area in Fig. 7a, and around asperity in Fig. 7b. Fig. 7c shows particle sliding over the rough surface of the rock.

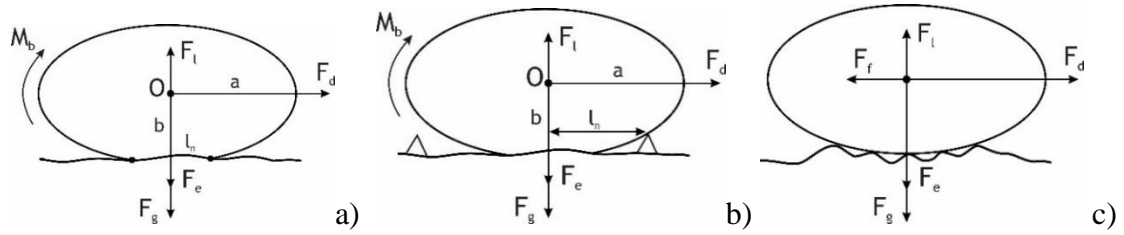


Fig. 7: Fines mobilisation by rolling and sliding: a) particle rolling around the edge of attracted particle-substrate contact area; b) particle rolling around asperity on the rock surface; c) particle sliding over rock surface.

Assume constant properties of rock and particles in equations (9), (10). In this case none of particles is detached at velocities, which is minimum of two values given by equations (9), (10). All particles are detached at any velocity that exceeds their detachment velocity. However, experimental observations contradict this stepwise detachment with flow velocity increase-each velocity increase leads to detachment of additional particles. This gradual particle detachment can be explained by multidimensional manifold of particle-rock surface contacts over the pore space. This corresponds to variation of all coefficients in equations (9), (10) over the rock surface. Increase in Darcy velocity results in the same fold increase of interstitial velocity in each point of the pore space domain. Therefore, for each attached particle there does exist Darcy velocity which would lead to breaching of either of criteria (9), (10) and its mobilization. This explains gradual fines detachment. The existing of the detaching velocity for each detrital particle follows the existence of the particle concentration retained for each given velocity. This dependency is called Maximum Retention Function (MRF). Fig. 8 shows the Maximum Retention Function, i.e. the concentration of attached fines as a function of velocity.

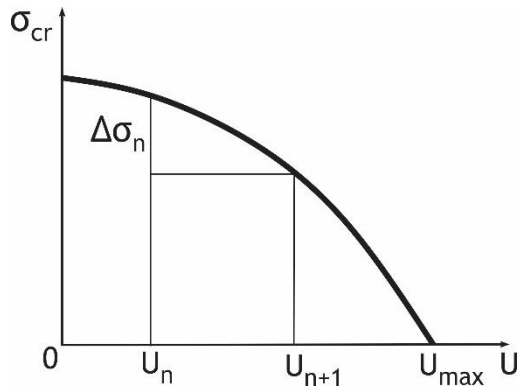


Fig. 8: Introduction of maximum retention concentration of attached fines as a function of velocity- Maximum Retention Function of Darcy's velocity

If detachment occurs due to two different physics mechanisms, MRF for each of them must be determined. The examples include detachment under unfavourable conditions where DLVO potential has two maxima, breakage, mobilisation of segregated fines, etc. Fig. 9 shows the total MRF for the case of breakage. In low fluid velocity the particles which are attracted to a substrate by electrostatic forces are detached and in high fluid velocity the particles which are mechanically bonded to a substrate are detached. The total MRF is a combination of two MRFs. When the range of fluid velocities for detachment of two types of particles are completely separated, the two MRFs do not overlap (Fig. 9a). However, sometimes the range of detachment velocities may overlap and the resulting MRF is shown in Fig. 9b.

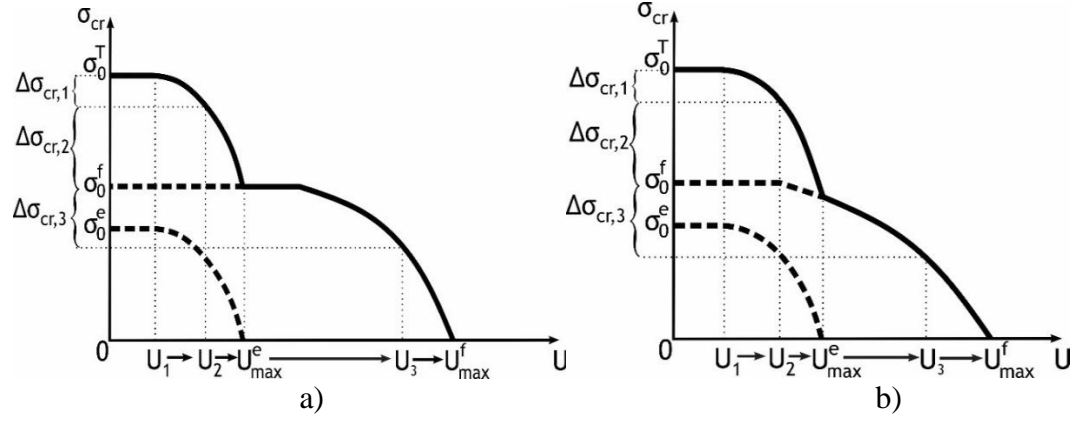


Fig. 9: Total MRF for detachment of detrital and authigenic fines: a) in the case of $U_{max}^e < U_{min}^b$, MRF has plateau; b) MRF is monotonically decreasing function of velocity in the case where $U_{max}^e > U_{min}^b$

The system of basic equations becomes:

$$\frac{\partial}{\partial t}(\phi c + \sigma_s + \sigma_a) + \bar{\nabla} \cdot (c \alpha \bar{U}) = 0 \quad (13)$$

$$\frac{\partial \sigma_{st}}{\partial t} = \lambda(\sigma_{st}) f(c) \alpha |\bar{U}| \quad (14)$$

$$\sigma_a = \sigma_{cr}(U) \quad (15)$$

To reflect permeability decline during straining Darcy's law is added to the system of (13), (14), (15).

$$\bar{U} = -\frac{k}{\mu(c)(1 + \beta \sigma_{st})} \bar{\nabla} p \quad (16)$$

Here, ϕ is the porosity, c , σ_s , and σ_a are volumetric concentrations of suspended, attached, and strained particles, α is a drift delay factor, U is flow velocity of the carrier fluid, λ is the filtration function, $f(c)$ is the suspended function, k is the permeability, β

is formation damage coefficient with respect to attached and strained particles, μ is the viscosity and p is the pressure. Drift delay coefficient α reflects the delay of sliding or rolling particles movement with respect to carrier flow velocity. Suspension function $f(c)$ reflects distribution of colloidal particles over size, zeta potential, etc.

Substituting expression for MRF (15) into mass balance equation (13), we obtain.

$$\frac{\partial}{\partial t} \left(\phi c + \sigma_s + \sigma_{cr} \left(|\bar{U}| \right) \right) + \bar{\nabla} \cdot (c \alpha \bar{U}) = 0 \quad (17)$$

System of four equations (13), (14), (15), and (16) closes the system of governing equations with respect to unknowns c, σ_s, U, p .

According to works (Bedrikovetsky et al. 2011, 2012), $\sigma_{cr}(U)$ is an empirical function describing the system rock-particles-fluid, like relative permeabilities adsorption or capillary pressure, which are material functions depending on particular rocks and fluids. Despite existence of the function $\sigma_{cr}(U)$ which is a consequence of mechanical equilibrium conditions, presented in equations (9),(10), (11), MRF does not reflect those physical effects.

For 1D corefloods, the system(13-17) simplifies and the analytical solution for is presented by explicit formulae (Yang and Bedrikovetsky 2017, Yang et al. 2022).

MRF model applications Determination of MRF from laboratory corefloods is based on exact solutions for system (9), (10), (11). These solutions have been obtained in

(Bedrikovetsky et al. 2011, 2012) for constant filtration coefficient and by Yang and Bedrikovetsky 2017 for any filtration function, $\lambda(\sigma)$. The model (Bedrikovetsky et al. 2019) have been generalized for the multicomponent colloids with distributed particle sizes, forms, zeta potentials, etc., where the exact solution also have been derived. Chequer et al. 2021 discussed initially undersaturated or over saturated system of attached particles where the exact solutions for 1D problems has also been found. Yuan and Shapiro 2011 along with Zeinijahromi et al. 2016 consider two-phase flow where the particles are detached from rock surface by one of phases, and MRF is a function of phase velocities.

Yuan and Moghanloo 2017, 2018 applied the model for fines mobilization by produced fluid to find the environment preventing fines mobilization. They also applied it for fines mobilization during low salinity water flooding. Exact solutions have been found in both cases.

Furqan Hussain and his colleagues found the solution for flow in coals (Guo et al. 2016), he also investigated fines migration during rock dissolution in the injected water, and also during CO₂ injection with rock dissolution (Othman et al. 2019). Those works include treatment of the laboratory data by the analytical model.

The above-mentioned works consider MRF as an empirical function which can be determined only from laboratory experiments. Some attempts have been made to calculate this function for simplified model system. Zeinijahromi and his colleagues in the paper Bedrikovetsky et al. 2012 assumed constant pore radius and multilayer particle attachment to rock surface. The remarkable result is the quadratic form of MRF

versus velocity. This dependency Zeinijahromi used to match field data from oil and gas wells (Zeinijahromi et al. 2012).

However, the mathematical model reflecting variation of mechanical equilibrium coefficients has not been developed. The link between MRF and particle scale model is not available. The upscaling from particle level to the core level has not been performed.

This gap has been filled in the current thesis. Publication one (“Colloidal detachment in porous media: stochastic model and upscaling”) develops stochastic model for colloidal detachment accounting for probabilistic distribution of mechanical equilibrium coefficients, which equations (9,10) contain. It allows determining Probability Distribution Function (PDF) for detaching velocity yielding direct formula for MRF. This formula reflects both detachment criteria (9), (10). The analytical expression for MRF based on particle scale mechanical equilibrium equations provides the upscaling and closes the system of transport equations for colloidal flow in porous media. Treatment of four laboratory tests have been provided by two models. Downscaling allows calculating lever arm ratio and its standard deviation.

2.3. Fines detachment by breakage

The previous section exhibits physical schematics and mathematical modeling of the detachment of detrital particles, which have been attached to the rock surface during sedimentation, transport of broken authigenic particles by the subterranean water, etc.

Despite widely spread authigenic particles in natural reservoir rocks and the intensive studies in geology, geophysics, and formation damage in petroleum engineering the similar theory for detachment of authigenic particles is currently unavailable. Below we present some visualisation evidences of authigenic particle breakage.

2.3.1. SEM-images proofs for authigenic fines detachment by breakage

Fig. 10 presents SEM images of the injection face of the Indiana limestone core Circle 1 delineates the disappearance of calcite grains, circle 2 delineates the disappearance of several small (<20 μm) calcite grains, *circle 3 delineates breakage of a grain's structure*, and circle 4 delineates pore blockage likely caused by the migration of the broken grain's structure from circle 3 (Wang et al., 2022).

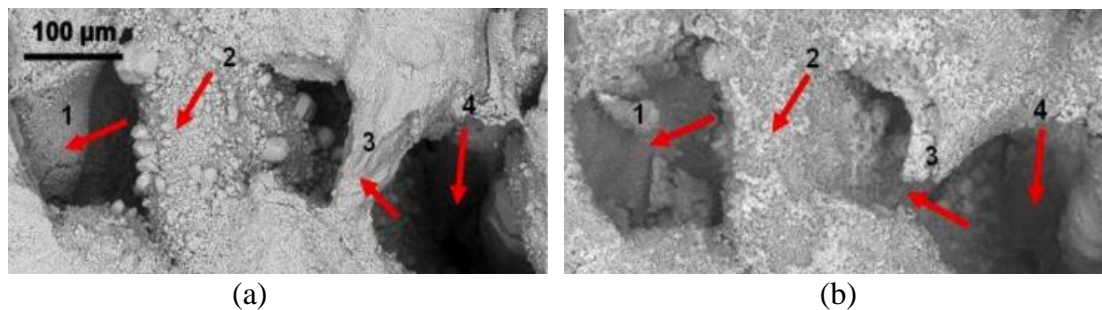


Fig. 10: SEM images of the injection face of the Indiana limestone core sample: (a) pre-injection, (b) post-injection.

The geometry of authigenic illite particles are thin long cylinders, so they are highly susceptible to breakage. Indeed, Fig. 11 shows SEM images of hairy illite broken after treatment with fracturing fluid (Liu et al., 2018).

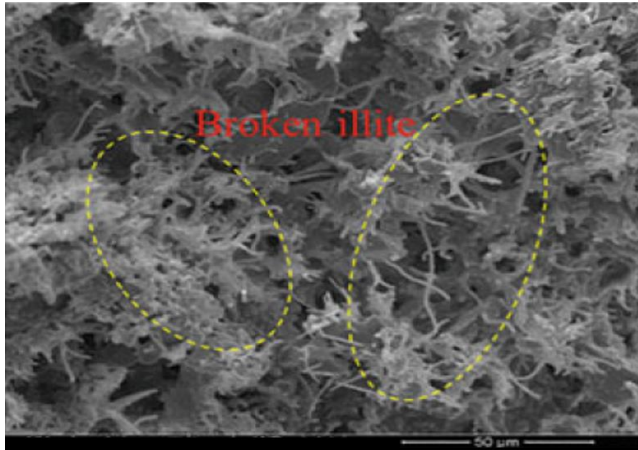


Fig. 11: SEM image of hairy illite broken by strong shear stress after treatment with high-viscosity fracturing fluid (Liu et al., 2018).

SEM images of non-damaged and broken kaolinite are shown in Fig. 12.

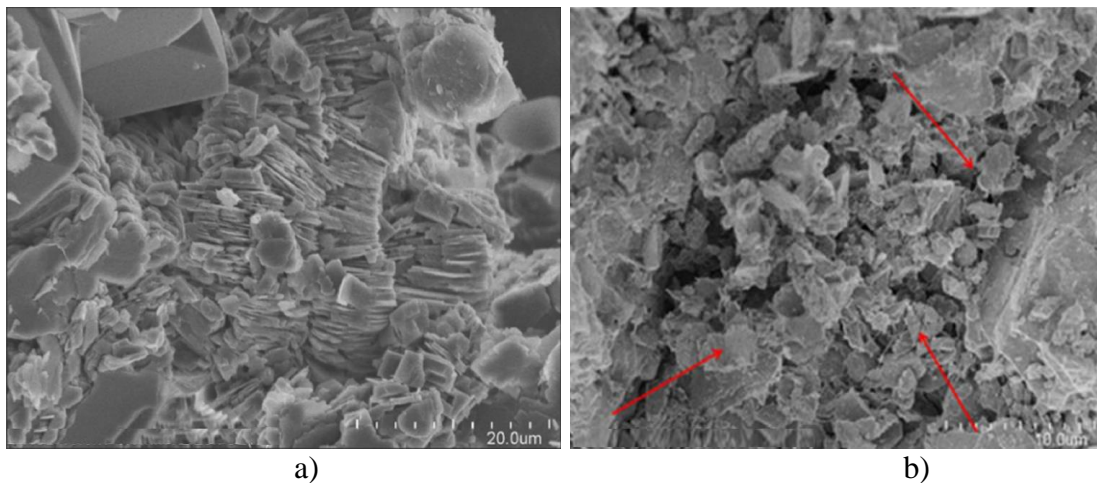


Fig. 12: SEM images of a) non-damaged kaolinite structure of Berea core, b) broken kaolinite sheets of damaged Berea core that undergone critical velocity test (Shafian et al., 2021)

CO₂ injection into water-saturated core sample results in mineral dissolution. If a kaolinite particle is attached to a surface by carbonate cement, the injected gas may react with the carbonate and reduce the cement bond (Othman et al., 2019). When the cement bond reaches a small enough value, the fluid drag force can break the remaining bond. Fig. 13 shows the kaolinite particle produced during core flooding. This particle is a kaolinite fine with attached carbonate cement. This can be explained by breakage down the cement bond between kaolinite particle and sand grain.

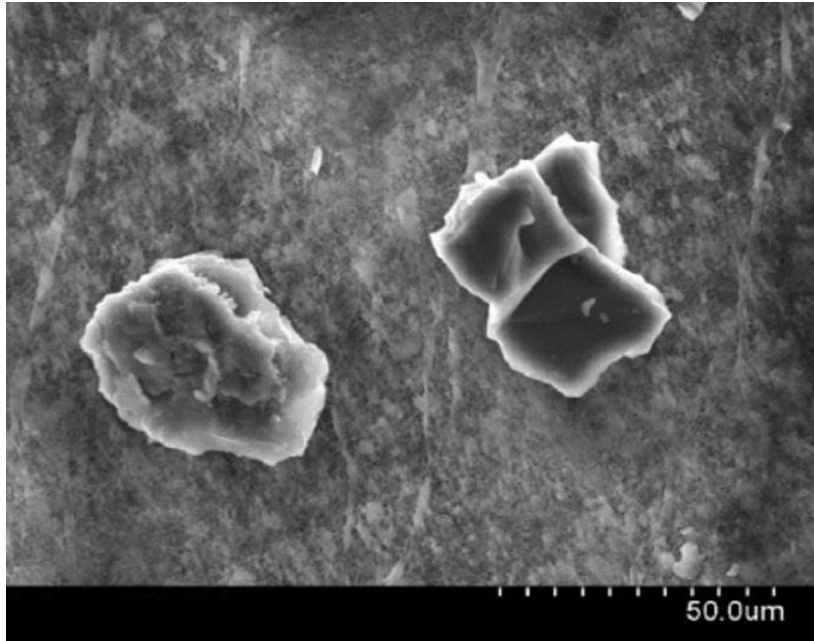


Fig. 13: SEM images a quartz fine (right) and kaolinite fine with carbonate cement (left) produced from Berea core sample during 60 g/L NaCl water-saturated super critical CO₂ injection (Othman et al., 2019).

2.3. 2. Cleat-scale numerical modelling of fines detachment by breakage

The necessity for mathematical modelling of breakage of authigenic particles has been highly recognized. Despite the absence of microscale rock failure model, which can be upscaled up to the core scale, some numerical modelling of microscale rock deformation with application of failure criteria has been performed. Fig. 14 presents three runs of microscale rock deformation model. Figs. 14a1,a2 ,a3 show SEM photos near to fracture; Figs. 14b1,b2,b3 shows digitalized images of rock, fracture, and tortuous non uniform fracture rock boundary. Figs. 14c1,c2 ,c3 show the results of numerical modelling highlighting the domains where stresses exceed strength. Figs. 14d1,d2 ,d3 zoom those failure zones. Fig. 14d1 clearly indicate breakage of particle-rock bond. The same is shown in Fig. 14d2. Fig. 14d3 shows the development of the failure zone at the advancing point of the bond contact.

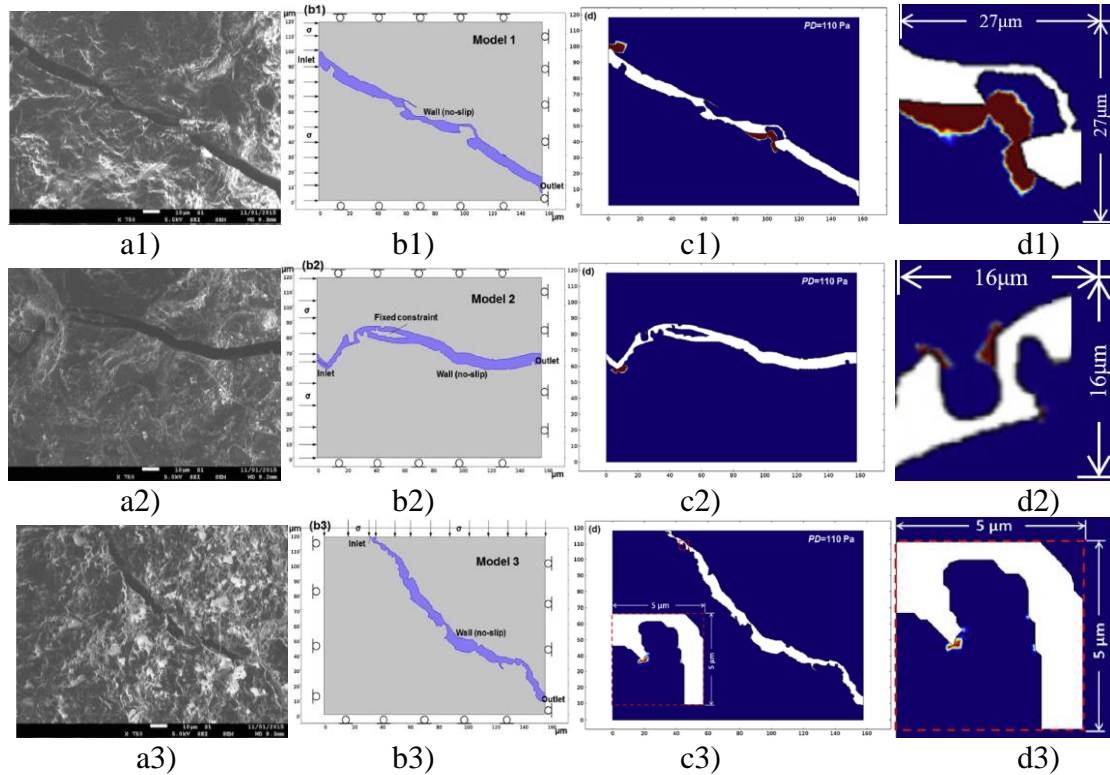


Fig. 14: SEM photos potential fine generation at different coal cleats (a1,a2,a3), cleat and asperity geometries used in numerical simulations (b1,b2,b3) and failure zones (in red) for each case as a result of numerical simulation (c1,c2,c3), and zoom for failure zones (d1,d2,d3) (Bai et al. 2015).

Similar images of stress distribution around the coal cleat, but at higher scale than in the previous work was shown by Bai et al. 2015. The figure also shows the digitalized image, the fields of stresses generated numerically, and two zooms in failure points.

2.3.3. Using Timoshenko and Goodier's beam theory for analytical modelling of particle deformation

The attached particle deformation theory suitable to detachment of authigenic fines, is 3D Timoshenko and Goodier's elastic beam theory (Timoshenko and Goodier 1951).

Under the model assumptions formulated in section 2.1, Timoshenko and Goodier's 3D solution for elastic deformation of a cylindrical beam (Fig. 15) shows that the normal stress σ_z reaches a maximum at the beam bottom, $z=0$, and the two shear stresses τ_{xz} and

τ_{yz} are independent of z . The normal and shear stresses at the beam base with applied external load F_d are:

$$\sigma_z = \frac{F_d b f_M x}{I}, \quad \sigma_x = \sigma_y = \tau_{xy} = 0 \quad (18)$$

$$\tau_{xz} = \frac{(3+2\nu)}{8(1+\nu)} \frac{F_d}{I} \left(r_b^2 - x^2 - \frac{(1-2\nu)}{(3+2\nu)} y^2 \right) \quad (19)$$

$$\tau_{yz} = -\frac{(1+2\nu)}{4(1+\nu)} \frac{F_d xy}{I} \quad (20)$$

where, σ_z is the normal bending stress at contact area, τ_{xz} is the shear stress acting on the z plane and towards the x direction, τ_{yz} is the shear stress acting on the z plane and towards the y direction, ν the is Poisson's ratio, and I is the moment of inertia, which for circular cross-section is equal to $\pi r_b^4/4$.

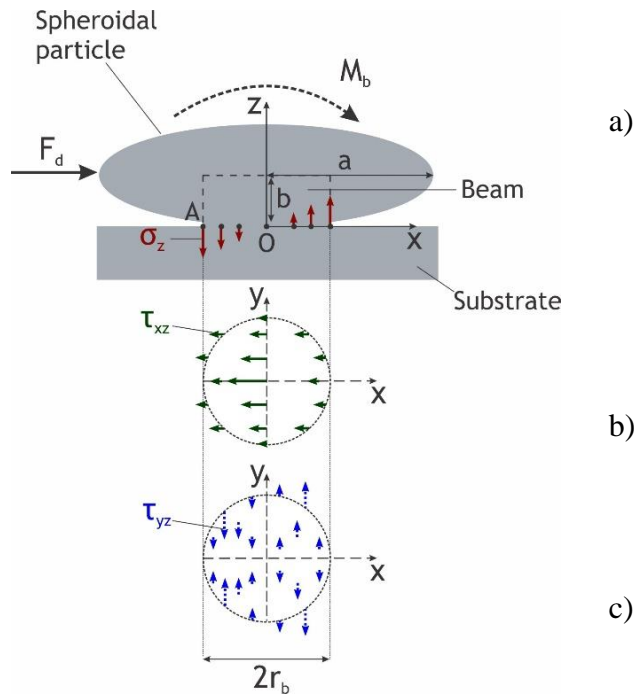


Fig. 15: Schematic of equivalent beam for attached spheroidal particle: a) loading force and moment exerting from viscous flow; b) shear in plane parallel/perpendicular by Timoshenko and Goodier's solution; c) shear in plane parallel/perpendicular by Timoshenko and Goodier's solution

As expressed by Eq. 18, the normal bending stress expands the matter at $x<0$ reaching a minimum in the advance point $x=-r_b, y=0$ (Fig. 15a) and contracts at $x>0$ reaching a maximum at the receding point $x=r_b, y=0$. Fig. 15b illustrates Eq. (19) and corresponds to shear stress that opposes the external load F_d and is equal zero only in advance and receded points. Eq. (20) is illustrated by Fig. 15c, showing the transversal shear stress.

The stress tensor, as per solution (18-20) is:

$$\begin{bmatrix} 0 & 0 & \tau_{xz} \\ 0 & 0 & \tau_{yz} \\ \tau_{xz} & \tau_{yz} & \sigma_z \end{bmatrix} \quad (21)$$

The principal stresses are eigen values of the stress tensor (21):

$$\sigma_1 = \frac{\sigma_z + \sqrt{\sigma_z^2 + 4(\tau_{xz}^2 + \tau_{yz}^2)}}{2}, \quad \sigma_2 = 0, \quad \sigma_3 = \frac{\sigma_z - \sqrt{\sigma_z^2 + 4(\tau_{xz}^2 + \tau_{yz}^2)}}{2} \quad (22)$$

where, $\sigma_1, \sigma_2, \sigma_3$ are the principal stresses in decreasing order of magnitude, and

$$\sigma_1 > \sigma_2 = 0 > \sigma_3 \quad (23)$$

Maximum tensile and shear stresses in Eqs. (22, 23) correspond to points $(\sigma_3, 0)$ and

$(\sigma_1 - \sigma_3)/2$ in plane (σ, τ) . Consequently, the maximum tensile and shear stresses are

$$\max \sigma = \sigma_3, \quad \max \tau = \frac{\sigma_1 - \sigma_3}{2}, \quad (24)$$

respectively.

It is assumed that deformation of the outer particle body does not contribute to the stem (beam) deformation (Fig. 16). The drag F_d and bending moment M_b are applied in the centre of mass of the particle; they are calculated by CFD. Stress distribution in the beam is determined from the beam theory (by Timoshenko and Goodier 1951) for known F_d and M_b

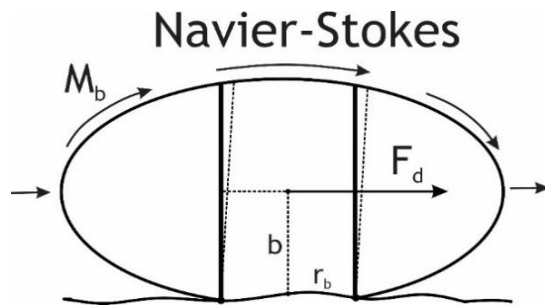


Fig. 16: Schematic for assumptions of fines deformation allowing applying 3D elastic beam theory: negligible stresses outside the stem (beam), and its small deformation.

The resulting Mohr's circles from three principal stresses presented in Eq. (22) is shown in Fig17. The biggest circles is the important one because the highest values of stress occur on this circle. The outer left value on this circle is maximum tensile stress, σ_3 and the point on the circle with the highest ordinate corresponds to maximum shear stress, $(\sigma_1 - \sigma_3)/2$.

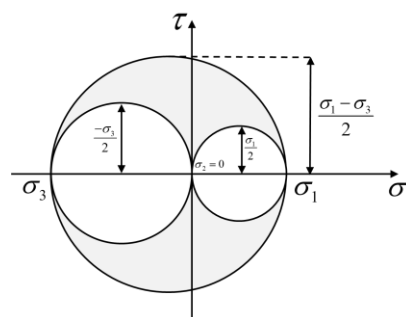


Fig. 17: Using Mohr's circles to determine maximum tensile and shear stresses and apply strength failure criteria.

In this study, a circular rock-particle contact is assumed. In future works, square or rectangular shape of rock-particle contact can be assumed. Then, it is possible to analyze the difference.

2.4. Summary and conclusions from the literature review

Detachment of natural reservoir fines from rock surface by viscous flow in those rocks has high impact on well productivity in oil and gas industry, water resources management, and the in-situ storages of CO₂ and hydrogen. Fines detachment and migration causes significant permeability decline and well impairment. This corresponds to vertical openhole, perforated, fractured, horizontal wells, and for combined cases of those completions. The detachable particles encompass detrital fines, attached to rock surface by electrostatic forces, and authigenic fines grown up on grain surfaces during geological times.

The decision making on well management significantly rely on laboratory-based predictive mathematical modelling. Those mathematical models must be available at the reservoir scale and account for fines detachment, mobilization, transport/migration, and straining/size exclusion in porous media. On the particle scale, detachment is defined by mechanical equilibrium, expressed by torque and force balance.

Both microscale mechanical equilibrium detachment model and macroscale colloidal transport with fines detachment are available for detrital particles. However, traditional kinetics detachment model contains empirical detachment coefficient which cannot be predicted from microscale. The current detachment model of maximum retention concentration also contains MRF which is not derived from microscale and is determined empirically from the laboratory tests. This allows concluding the necessity for upscaling theory for detrital particle detachment. This is one of aims of this thesis.

Regarding detachment of authigenic particles, neither particle scale nor core scale mathematical models for detachment by breakage are available. Therefore, particle scale model for bond breakage for particle rock link, its upscaling to core scale, and formulation of the transport model for authigenic particles must be developed.

Therefore, development of the particle-scale mathematical model for breakage of authigenic particles and upscaling of the micromodels for authigenic and detrital particles is a significant scientific problem of fluid mechanics in porous media with important practical applications in well management in oil/gas industry, CO₂ and hydrogen storage, and water resources. This is another of aims of this thesis.

2.5. References

- Abdi, M.R. and Mirzaeifar, H., 2016. Effects of discrete short polypropylene fibers on behavior of artificially cemented kaolinite. *International Journal of Civil Engineering*, 14(4), pp.253-262.
- Bai, T., Chen, Z., Aminossadati, S.M., Pan, Z., Liu, J. and Li, L., 2015. Characterization of coal fines generation: A micro-scale investigation. *Journal of Natural Gas Science and Engineering*, 27, pp.862-875.
- Bedrikovetsky, P., Osipov, Y., Kuzmina, L. and Malgaresi, G., 2019. Exact upscaling for transport of size-distributed colloids. *Water Resources Research*, 55(2), pp.1011-1039.
- Bedrikovetsky, P., Siqueira, F.D., Furtado, C.A. and Souza, A.L.S., 2011. Modified particle detachment model for colloidal transport in porous media. *Transport in porous media*, 86, pp.353-383.
- Bedrikovetsky, P., Zeinijahromi, A., Siqueira, F.D., Furtado, C.A. and de Souza, A.L.S., 2012. Particle detachment under velocity alternation during suspension transport in porous media. *Transport in Porous Media*, 91, pp.173-197.
- Borazjani, S., Behr, A., Genolet, L., Van Der Net, A. and Bedrikovetsky, P., 2017. Effects of fines migration on low-salinity waterflooding: analytical modelling. *Transport in Porous Media*, 116, pp.213-249.
- Bradford, S. A., Kim, H. N., Haznedaroglu, B. Z., Torkzaban, S., and Walker, S. L. 2009. Coupled factors influencing concentration-dependent colloid transport and retention in saturated porous media. *Environmental Science & Technology*, 43 (18): 6996-7002. <https://doi.org/10.1021/es900840d>.
- Bradford, S. A., Kim, H., Shen, C., Sasidharan, S., and Shang, J. 2017. Contributions of nanoscale roughness to anomalous colloid retention and stability behavior. *Langmuir*, 33 (38): 10094-10105. <https://doi.org/10.1021/acs.langmuir.7b02445>.
- Bradford, S. A., Torkzaban, S., and Shapiro, A. 2013. A theoretical analysis of colloid attachment and straining in chemically heterogeneous porous media. *Langmuir*, 29 (23): 6944-6952. <https://doi.org/10.1021/la4011357>.
- Burley, S.D., Kantorowicz, J.D. and Waugh, B., 1985. *Clastic diagenesis*. Geological Society, London, Special Publications, 18(1), pp.189-226.
- Chequer, L. and Bedrikovetsky, P., 2019. Suspension-colloidal flow accompanied by detachment of oversaturated and undersaturated fines in porous media. *Chemical Engineering Science*, 198, pp.16-32.
- Chequer, L., Carageorgos, T., Naby, M., Hussaini, M., Lee, W. and Bedrikovetsky, P., 2021. Colloidal detachment from solid surfaces: Phase diagrams to determine the detachment regime. *Chemical Engineering Science*, 229, p.116146.
- Chrysikopoulos, C. V. and Syngouna, V. I. 2012. Attachment of bacteriophages MS2 and Φ X174 onto kaolinite and montmorillonite: Extended-DLVO interactions. *Colloids and Surfaces B: Biointerfaces*, 92: 74-83. <https://doi.org/10.1016/j.colsurfb.2011.11.028>.

- Chrysikopoulos, C. V., Sotirelis, N. P., and Kallithrakas-Kontos, N. G. 2017. Cotransport of graphene oxide nanoparticles and kaolinite colloids in porous media. *Transport in Porous Media*, 119 (1): 181-204. <https://doi.org/10.1007/s11242-017-0879-z>.
- Civan, F. 2014. *Reservoir Formation Damage*, 3rd ed. edition. Burlington, MA, USA: Gulf Professional Publishing.
- Cui, Y., Zhu, J., Twaha, S., Chu, J., Bai, H., Huang, K., Chen, X., Zoras, S. and Soleimani, Z., 2019. Techno-economic assessment of the horizontal geothermal heat pump systems: A comprehensive review. *Energy Conversion and Management*, 191, pp.208-236.
- Farrell, N.J.C., Debenham, N., Wilson, L., Wilson, M.J., Healy, D., King, R.C., Holford, S.P. and Taylor, C.W., 2021. The effect of authigenic clays on fault zone permeability. *Journal of Geophysical Research: Solid Earth*, 126(10), p.e2021JB022615.
- Guo, Z., Hussain, F. and Cinar, Y., 2016. Physical and analytical modelling of permeability damage in bituminous coal caused by fines migration during water production. *Journal of Natural Gas Science and Engineering*, 35, pp.331-346.
- Guo, Z., Vu, P.N.H. and Hussain, F., 2018. A laboratory study of the effect of creep and fines migration on coal permeability during single-phase flow. *International Journal of Coal Geology*, 200, pp.61-76.
- Huang, F., Kang, Y., You, Z., You, L. and Xu, C., 2017. Critical conditions for massive fines detachment induced by single-phase flow in coalbed methane reservoirs: modeling and experiments. *Energy & Fuels*, 31(7), pp.6782-6793.
- Huang, F., Dong, C., You, Z. and Shang, X., 2021. Detachment of coal fines deposited in proppant packs induced by single-phase water flow: Theoretical and experimental analyses. *International Journal of Coal Geology*, 239, p.103728.
- Kanimozhi, B., Rajkumar, P., Kumar, R.S., Mahalingam, S., Thamizhmani, V., Selvakumar, A., Ravikumar, S., Kesavakumar, R. and Pranesh, V., 2021. Kaolinite fines colloidal-suspension transport in high temperature porous subsurface aqueous environment: Implications to the geothermal sandstone and hot sedimentary aquifer reservoirs permeability. *Geothermics*, 89, p.101975.
- Kar, R., Baruah, H. and Phukan, S., 2019. Signatures of Marine Influences in the Gondwana Sandstones of Kalijhora, Darjeeling District, West Bengal, India. *Earth Science India*, 12(1).
- Kianfar, B., Tian, J., Rozemeijer, J., van der Zaan, B., Bogaard, T.A. and Foppen, J.W., 2022. Transport characteristics of DNA-tagged silica colloids as a colloidal tracer in saturated sand columns; role of solution chemistry, flow velocity, and sand grain size. *Journal of Contaminant Hydrology*, 246, p.103954.
- Liu, J., Yuan, X., Zhang, J., Xi, W., Feng, J. and Wu, H., 2018, July. Sharp Reductions in High-Productivity Well Due to Formation Damage: Case Study in Tarim Basin, China. In *Proceedings of the International Field Exploration and Development Conference 2017* (pp. 843-857). Singapore: Springer Singapore.

- Molnar, I. L., Johnson, W. P., Gerhard, J. I., Willson, C. S., and O'Carroll, D. M. 2015. Predicting colloid transport through saturated porous media: A critical review. *Water Resources Research*, 51 (9): 6804-6845. <https://doi.org/10.1002/2015WR017318>.
- Nnanna, A.A., Sheng, C., Conrad, K. and Crowley, G., 2015, November. Performance Assessment of Pre-Filtration Strainer of an Ultrafiltration Membrane System by Particle Size Analysis. In *ASME International Mechanical Engineering Congress and Exposition* (Vol. 57465, p. V07AT09A015). American Society of Mechanical Engineers.
- Ochi, J. and Vernoux, J.F., 1998. Permeability decrease in sandstone reservoirs by fluid injection: hydrodynamic and chemical effects. *Journal of hydrology*, 208(3-4), pp.237-248.
- Othman, F., Naufaliansyah, M.A. and Hussain, F., 2019. Effect of water salinity on permeability alteration during CO₂ sequestration. *Advances in water resources*, 127, pp.237-251.
- Othman, F., Yu, M., Kamali, F. and Hussain, F., 2018. Fines migration during supercritical CO₂ injection in sandstone. *Journal of Natural Gas Science and Engineering*, 56, pp.344-357.
- Peng, F., Peng, S., Du, W. and Liu, H., 2020. Coalbed methane content prediction using deep belief network. *Interpretation*, 8(2), pp.T309-T321.
- Shafian, S.R.M., Saaid, I.M., Razali, N., Salleh, I.K. and Irawan, S., 2021. Experimental investigation of colloidal silica nanoparticles (C-SNPs) for fines migration control application. *Applied Nanoscience*, 11, pp.1993-2008.
- Syngouna, V. I. and Chrysikopoulos, C. V. 2011. Transport of biocolloids in water saturated columns packed with sand: Effect of grain size and pore water velocity. *Journal of Contaminant Hydrology*, 126 (3): 301-314. <https://doi.org/10.1016/j.jconhyd.2012.01.010>.
- Tangparitkul, S., Saul, A., Leelasukseree, C., Yusuf, M. and Kalantariasl, A., 2020. Fines migration and permeability decline during reservoir depletion coupled with clay swelling due to low-salinity water injection: An analytical study. *Journal of Petroleum Science and Engineering*, 194, p.107448.
- Timoshenko SP, Goodier JN. *Theory of Elasticity*, 3rd McGraw-Hill. New York. 1951:409.
- Wang, Y., Almutairi, A.L.Z., Bedrikovetsky, P., Timms, W.A., Privat, K.L., Bhattacharyya, S.K. and Le-Hussain, F., 2022. In-situ fines migration and grains redistribution induced by mineral reactions—Implications for clogging during water injection in carbonate aquifers. *Journal of Hydrology*, 614, p.128533.
- Welton, J.E., 1984. *SEM petrology atlas* (Vol. 4). Tulsa, Oklahoma: American Association of Petroleum Geologists.
- Wilson, M.D. and Pittman, E.D., 1977. Authigenic clays in sandstones; recognition and influence on reservoir properties and paleoenvironmental analysis. *Journal of Sedimentary Research*, 47(1), pp.3-31.

- Yang, H., Han, Z.F., Hu, J. and He, M.C., 2019b. Defect and temperature effects on the mechanical properties of kaolinite: a molecular dynamics study. *Clay Minerals*, 54(2), pp.153-159.
- Yang, S., Osipov, Y., Xu, C., Kuzmina, L., Russell, T. and Bedrikovetsky, P., 2022. Analytical solution for large-deposit non-linear reactive flows in porous media. *Chemical Engineering Journal*, 430, p.132812.
- Yang, Y. and Bedrikovetsky, P., 2017. Exact solutions for nonlinear high retention-concentration fines migration. *Transport in Porous Media*, 119, pp.351-372.
- Yang, S., Russell, T., Vaz, A. and Bedrikovetsky, P., 2022. Large-deposit non-linear chemical reactive flows in porous media: Identifiability and observability. *Journal of Natural Gas Science and Engineering*, 103, p.104611.
- Ye, X., Cui, R., Du, X., Ma, S., Zhao, J., Lu, Y. and Wan, Y., 2019. Mechanism of suspended kaolinite particle clogging in porous media during managed aquifer recharge. *Groundwater*, 57(5), pp.764-771.
- You, Z., Badalyan, A., Yang, Y., Bedrikovetsky, P., and Hand, M. 2019. Fines migration in geothermal reservoirs: Laboratory and mathematical modelling. *Geothermics*, 77: 344-367. <https://doi.org/10.1016/j.geothermics.2018.10.006>.
- Yuan, B. and Moghanloo, R. G. 2017. Analytical model of well injectivity improvement using nanofluid preflush. *Fuel*, 202: 380-394. <https://doi.org/10.1016/j.fuel.2017.04.004>.
- Yuan, B. and Moghanloo, R. G. 2018. Nanofluid pre-treatment, an effective strategy to improve the performance of low-salinity waterflooding. *Journal of Petroleum Science and Engineering*, 166: 105-115. <https://doi.org/10.1016/j.peteng.2018.04.004>.
- Yuan, H. and Shapiro, A. A. 2011. A mathematical model for non-monotonic deposition profiles in deep bed filtration systems. *Chemical Engineering Journal*, 166 (1): 105-115. <https://doi.org/10.1016/j.cej.2010.10.036>.
- Zeinijahromi, A., Farajzadeh, R., Bruining, J. H., and Bedrikovetsky, P. 2016. Effect of fines migration on oil–water relative permeability during two-phase flow in porous media. *Fuel*, 176: 222-236. <https://doi.org/10.1016/j.fuel.2016.02.066>.
- Zeinijahromi, A., Vaz, A. and Bedrikovetsky, P., 2012. Well impairment by fines migration in gas fields. *Journal of Petroleum Science and Engineering*, 88, pp.125-135.
- Zhang, G., Ranjith, P.G., Li, Z., Gao, M. and Ma, Z., 2021. Long-term effects of CO₂-water-coal interactions on structural and mechanical changes of bituminous coal. *Journal of Petroleum Science and Engineering*, 207, p.109093.
- Zhai, X. and Atefi-Monfared, K., 2020. Non-isothermal injection-induced geomechanics in a porous layer confined with flexible sealing rocks. *International Journal of Rock Mechanics and Mining Sciences*, 126, p.104173.
- Zhai, X. and Atefi-Monfared, K., 2021. Production versus injection induced poroelasticity in porous media incorporating fines migration. *Journal of Petroleum Science and Engineering*, 205, p.108953.

Zhou, Q., Lv, C., Li, C., Chen, G., Ma, X. and Li, C., 2020. Formation mechanism of authigenic chlorite in tight sandstone and its influence on tight oil adsorption, Triassic Ordos Basin, China. *Energy Exploration & Exploitation*, 38(6), pp.2667-2694.

Zou, Y., Zhao, F., Liu, D., Wang, Y. and Chen, J., 2018. Peat-accumulation models affected by the transgression-regression: a case study of mineralogy and geochemistry of the Permo-Carboniferous coals in the Lingshi Deposit, Qinshui Basin, China. *Geosciences Journal*, 22, pp.777-791.

3. Colloidal detachment in porous media: stochastic model and upscaling

Hashemi, A., Nguyen, C., Loi, G., Khazali, N., Yang, Y., Dang-Le, B., Russell, T. and Bedrikovetsky, P., 2023.

Chemical Engineering Journal, 474, p.145436.

Statement of Authorship

Title of Paper	Colloidal detachment in porous media: stochastic model and upscaling		
Publication Status	<input checked="" type="checkbox"/> Published	<input type="checkbox"/> Submitted for Publication	
	<input type="checkbox"/> Accepted for Publication	<input type="checkbox"/> Unpublished and Unsubmitted work written in manuscript style	
Publication Details	Hashemi, A., Nguyen, C., Loi, G., Khazali, N., Yang, Y., Dang-Le, B., Russell, T. and Bedrikovetsky, P., 2023. Colloidal detachment in porous media: Stochastic model and upscaling. Chemical Engineering Journal, 474, p.145436.		

Principal Author

Name of Principal Author (Candidate)	Abolfazl Hashemi		
Contribution to the Paper	Collected data, performed lab data analysis, derived some of the equations, wrote part of the manuscript.		
Overall percentage (%)	70%		
Certification:	This paper reports on original research I conducted during the period of my Higher Degree by Research candidature and is not subject to any obligations or contractual agreements with a third part that would constrain its inclusion in this thesis. I am the primary author of this paper.		
Signature		Date	15/11/2023


Co-Author Contributions

By signing the Statement of Authorship, each author certifies that:

- I. The candidate's stated contribution to the publication is accurate (as detailed above);
- II. Permission is granted to the candidate to include the publication in the thesis; and
- III. The sum of all co-author contributions is equal to 100% less the candidate's stated contribution.

Name of Co-Author	Cuong Nguyen		
Contribution to the Paper	Collecting literature data, writing code, and analysing detrital particle detachment		
Signature		Date	15/11/2023

Name of Co-Author	Grace Loi		
Contribution to the Paper	Collecting literature data, writing code, and analysing detrital particle detachment		
Signature		Date	15/11/2023

Name of Co-Author	Nastaran Khazali		
Contribution to the Paper	Deriving equations and matching lab data using two-population particle detachment mechanism.		
Signature		Date	15/11/2023

Name of Co-Author	Yutong Yang		
Contribution to the Paper	Performing sensitivity on MRF, collecting field data for fluid velocity through fracture and fault, and preparing cross plots.		
Signature		Date	15/11/2023

Name of Co-Author	Bryant Dang-Le		
Contribution to the Paper	Collecting and analysing lab data, collecting field data.		
Signature	Bryant Dang-Le	Date	15/11/2023

Name of Co-Author	Thomas Russell		
Contribution to the Paper	Co-supervising, aiding in the derivations of DLVO equations and checking the DLVO results, giving consultation on the total MRF, giving advice, and proofreading the manuscript.		
Signature		Date	15/11/2023

Name of Co-Author	Pavel Bedrikovetsky		
Contribution to the Paper	Methodology and supervision.		
Signature		Date	15/11/2023



Colloidal detachment in porous media: Stochastic model and upscaling

Abolfazl Hashemi, Cuong Nguyen, Grace Loi, Nastaran Khazali, Yutong Yang, Bryant Dang-Le, Thomas Russell, Pavel Bedrikovetsky*

School of Chemical Engineering, The University of Adelaide 5000, SA, Australia

ARTICLE INFO

Keywords:

Colloidal suspension
Transport model
Upscaling
Porous media
Particle detachment
Exact solutions

ABSTRACT

We discuss colloidal-suspension-nano transport in porous media with particle detachment and further capture by the matrix. Previous works formulate particle-scale detachment conditions and porous-media-scale transport equations with empirical coefficients, which are determined from flow tests and cannot be predicted from the particle scale. The present work derives the upscaling technique by stochastic distribution of torque and force balances on the attached particle, yielding a macro-scale equation for detachment. The upscaled detachment equation has the form of the maximum retained concentration of attached particles as a function of velocity, pH, salinity, and temperature of the carrier fluid. The upscaling procedure allows for direct calculations of the maximum retention function (MRF) from micro-scale parameters. The sensitivity analysis shows that MRF is most sensitive to the particle aspect ratio and pore size, while it is less sensitive to the standard deviations of the lever-arm ratio and particle size distributions. The exact solution for 1D flow problem is used to determine the MRF from laboratory tests and matches it with the stochastic microscale model for detachment. The high match obtained for four colloidal coreflood experiments validates the stochastic model and upscaling procedure.

1. Introduction

Reliable prediction of particle attachment and mobilisation is a key step in chemical and environmental engineering applications of colloidal-suspension-nano transport modelling (deep bed filtration) in porous media [1–3]. The essence of those processes is detachment of particles against electrostatic DLVO attraction, mobilization with further migration, and recapture by the porous media. The capture of mobilized particles yields decrease in the suspension concentration and permeability. The main particle capture mechanisms are size exclusion, straining, bridging, electrostatic attraction, adsorption, and Brownian diffusion into stagnant-flow zones. Fig. 1 shows the detachment of attached fines by shear stress induced by the viscous flow, migration with the carrier fluid, and size exclusion in thin pores, while the particle movement in large pores continues.

Changes in the suspension concentration due to particle mobilisation and capture are important in industrial filtering of liquids and gases including microfiltration, size exclusion chromatography, underground storage of CO₂ and hydrogen, disposal of industrial wastes in aquifers [4–6]. Significant permeability decline occurs due to straining or size exclusion, while electrostatic attachment, adsorption, sedimentation, or diffusion into dead-end pores do not affect the permeability. The

permeability damage can significantly affect the well rates during subterranean storage of CO₂, hydrogen, sweet or hot water, exploitation of geothermal reservoirs including enhanced processes with cold water injection, and coal bed methane production [7–9]. The SEM images of pre-flush open pores and the same pore plugged by the detached and strained particles are widely presented in the literature [9].

In the case of particle adsorption, near to the thermodynamic equilibrium, the desorption rate is proportional to the difference of chemical potentials [10]. This approach is applied for nano-colloids [11]. For detachment of particles by drag caused by viscous flow, this approach cannot be applied because flow velocity cannot be incorporated in Gibbs potential; velocity is not a thermodynamic parameter. The same corresponds to precipitation chemical reactions.

The study of particle transport in porous media is also important when considering the impact of nanoparticles on environmental systems [12]. Widespread application of nanoparticles has led to their inevitable introduction into natural systems [13]. Effective mitigation strategies rely on accurate modelling of particle transport and retention. In addition to their own impact, studies have shown that nanoparticle can influence the transport of toxic pollutants [13,14]. The transport of nanoparticles has been shown to be highly influenced by the presence of suspended colloidal particles [15,16], resulting in complex dependencies that need to be resolved to evaluate environmental impact.

* Corresponding author.

E-mail address: pavel@asp.adelaide.edu.au (P. Bedrikovetsky).

<https://doi.org/10.1016/j.cej.2023.145436>

Received 28 May 2023; Received in revised form 10 August 2023; Accepted 12 August 2023

Available online 18 August 2023

1385-8947/© 2023 Elsevier B.V. All rights reserved.

Nomenclature

a	Semi-major axis of spheroid, L
A_h	Hamaker constant, ML^2T^{-2}
b	Semi-minor axis of spheroid, L
c	Suspended particle concentration
c^{acc}	Accumulated suspended particle concentration
C_m	Molar concentration, L^{-3}
C_v	Coefficient of variation
e	Charge of an electron, TI
f(c)	Suspension function
f_{ad}	Adhesion factor
F_c	Capillary force, MLT^{-2}
f_{cr}	Detachment velocity PDF
F_d	Drag force, MLT^{-2}
f_d	Drag force shape factor
F_e	Electrostatic force, MLT^{-2}
F_g	Buoyancy force, MLT^{-2}
F_l	Lifting force, MLT^{-2}
f_M	Drag moment shape factor
F_n	Normal force, MLT^{-2}
g	Acceleration due to gravity, MT^{-2}
g_c	Conductivity, L^4
h	Particle-substrate separation distance, L
H	Distance between particle centre and substrate, L
h_c	Planck constant, ML^2T^{-1}
h_m	Electrostatic force inflection separation distance, L
J	Impedance
k	Permeability, L^2
k_B	Boltzman constant, $ML^{-2}T^{-2}\Theta^{-1}$
l	Lever arm ratio
L	System length, L
l	Pore length
l_n	Normal lever arm, L
M	Moment, ML^2T^{-2}
m	Attachment formation damage exponent
n	Straining formation damage exponent
N	Number density of R-chains withing cross-section to flow, L^{-2}
p	Pressure, $ML^{-1}T^{-2}$
P_x	xth percentile
r	Pore radius, L
R	Average distance between R-chains, L
R^2	Coefficient of determination
r_c	Critical radius (percolation threshold), L
r_e	Radial distance of each element in the SEI method, L
r_{eh}	Effective pore radius of homogeneous network, L
r_{min}	Minimum radius of conducting bonds, L
r_s	Particle radius (volume equivalent), L
r_{se}	Equivalent spheroid radius (curvature), L
T	Temperature, Θ
t	Time, T
\bar{U}	Mean of detachment velocity distribution, LT^{-1}
U	Darcy velocity, LT^{-1}
u	Average flow velocity within a pore, LT^{-1}
U_{cr}	Critical velocity, LT^{-1}
u_s	Fluid velocity at particle centre, LT^{-1}
V	Interaction energy potential between particle and substrate, ML^2T^{-2}

V_{BR}	Born interaction energy, ML^2T^{-2}
ν_e	Absorption frequency, T^{-1}
V_{EDL}	Electrostatic double layer interaction energy, ML^2T^{-2}
V_{VDW}	Van der Waals interaction energy, ML^2T^{-2}
x	Spatial coordinate, L
x_n	Rolling-sliding coefficient
z	Average coordination number
z_V	Ion valency

Greek symbols

α	Drift delay coefficient
α_s	Aspect ratio
β_a	Attached particle formation damage factor
β_s	Strained particle formation damage factor
γ	Fluid salinity, $molL^{-3}$
Γ	Sensitivity coefficient
γ_g	Reduced zeta potential of grains
γ_{GL}	Interfacial tension between gas and liquid, MT^{-2}
γ_p	Reduced zeta potential of particles
$\Delta\sigma_k$	Detached concentration during injection stage k
ϵ	Static dielectric constant
ϵ_o	Permittivity of free space, $I^2L^{-3}M^{-1}T^4$
ϵ_r	Relative permittivity of water
ζ_g	Zeta potential of grain, $ML^2T^{-3}I^{-1}$
ζ_p	Zeta potential of particle, $ML^2T^{-3}I^{-1}$
η	Refractive index
$\eta(r)$	Fraction of conducting pores
η_c	Percolation threshold
κ	Inverse Debye length, L^{-1}
$\lambda(\sigma_s)$	Filtration function, L^{-1}
μ	Fluid viscosity, $ML^{-1}T^{-1}$
ν	Correlation radius index
ν_C	Coulomb friction coefficient
ξ	Detachment probability
ρ	Density, ML^{-2}
σ^0	Detachable particle concentration
σ_a	Attached concentration
σ_c	Atomic collision coefficient, L
σ_{cr}	Critical (maximum) retention function
σ_s	Strained particle concentration
σ_U	Standard deviation of detachment velocity distribution, LT^{-1}
τ	Tortuosity
ϕ	Porosity
Ω	Microscale parameter domain
θ	Contact angle of particle
φ	Water filling angle
χ	Lift coefficient

Subscripts

o	Initial
st	Stabilised
k	During stage k
mod	Calculated from model

Abbreviations

LHS	Left-hand side
RHS	Right-hand side
MRF	Maximum retention function
PDF	Probability density function

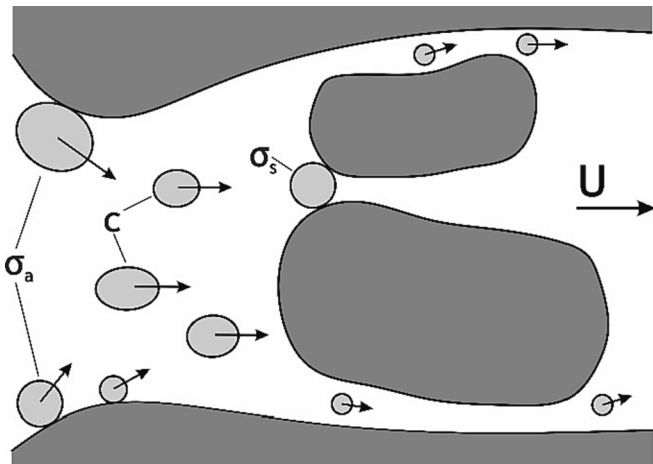


Fig. 1. Schematic for fines mobilisation, migration and straining in porous space. Here σ_a , c , and σ_s are the concentrations of attached, suspended, and strained particles, respectively; U is the velocity.

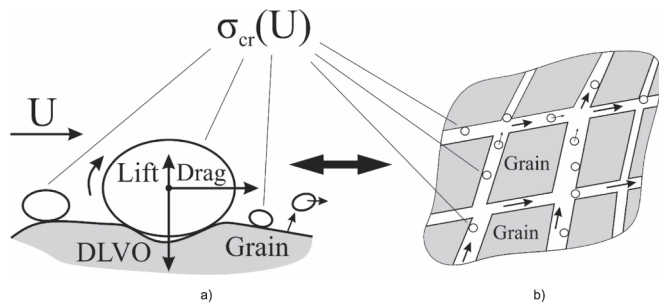


Fig. 2. Schematic for upscaling of particle detachment in colloidal transport in porous media: a) microscale model is torque balance of forces exerting the attached particles; b) macro (core, reservoir) scale model: maximum attached concentration of particle versus velocity $\sigma_{cr}(U)$.

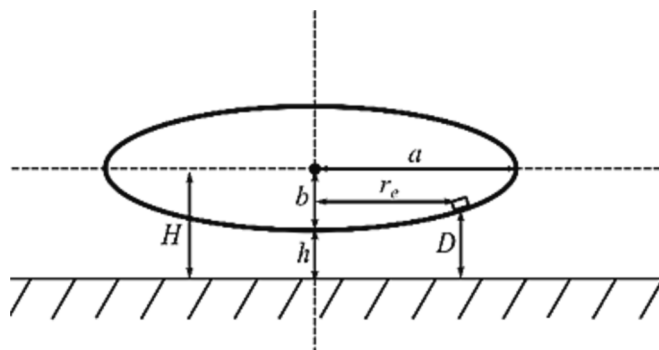


Fig. 3. Particle-substrate configuration between an oblate spheroid and an infinite flat plate for calculation of the electrostatic particle-substrate interaction by Surface Element Integration (SEI) method.

The mathematical model for the co-transport consists of population balance equations with Langmuir (blockage) filtration functions [17]. The corresponding analytical model tunes just two filtration coefficients for straining, but highly matches eight-parametric experimental data array, validating the model. The detailed review of recent achievements of nano-transport in porous media is available from recent book [18].

The state-of-the-art mathematical models for colloidal transport in porous media account for commingled reversible and irreversible attachment [19], and spatially variable colloid attachment onto the solid matrix [20]. Predictive mathematical models for nano-particle

transport in porous media have been developed for viral aggregation [21], presence of foam [22], and aggregation of nano-particles [23].

At the particle-grain scale, the attachment-detachment process is based on mechanical equilibrium of attached particles, which involves drag, lift, and electrostatic forces (Fig. 2a). Fig. 3 presents a spheroidal particle separated from the plain substrate by distance h . For irregular shape particles, drag and lift are numerically modelled by CFD, while electrostatic particle-substrate attraction is calculated by Surface Element Integration Method (SEI) [24,25]. Introduction of shape factors for drag and lift and obtaining correlations with the aspect ratio from CFD allows for a significant acceleration of attachment-detachment calculations [26].

Fig. 2b presents macroscale reference volume with multiple pores. Some particles are attached to the rock surface. Suspended particles are transported by the carrier water. Strained particles plug the pore inlets.

System of governing equations for colloidal-suspension-nano transport in porous media consists of mass balance equation for attached, suspended, and strained particles, an equation for the attachment rate, Darcy's law that accounts for permeability variation due to attachment and detachment of particles, and mass balance for incompressible carrier fluid [27,28]

$$\frac{\partial}{\partial t}(\phi c + \sigma_s + \sigma_a) + \vec{\nabla} \cdot (c\alpha \vec{U}) = 0 \quad (1)$$

$$\frac{\partial \sigma_s}{\partial t} = \lambda(\sigma_s) f(c) \alpha |\vec{U}| \quad (2)$$

$$\vec{U} = - \frac{k}{\mu(c)(1 + \beta_s \sigma_s)^n (1 + \beta_a \sigma_a)^m} \vec{\nabla} p \quad (3)$$

$$\vec{\nabla} \cdot (\vec{U}) = 0 \quad (4)$$

Here, ϕ is the porosity, c , σ_s , and σ_a are the volumetric concentrations of suspended, strained and attached particles, α is the drift delay factor, U is the flow velocity of the carrier fluid, λ is the filtration function, $f(c)$ is the suspension function, β_s and β_a are the formation damage coefficients for strained and attached fines respectively, n and m are the straining and attachment formation damage exponents, μ is the viscosity and p is the pore pressure. The drift delay coefficient α reflects the lower particle velocity with respect to the carrier fluid as a result of sliding and rolling along the pore surfaces. The suspension function $f(c)$ reflects the distribution of colloidal particles over size, zeta potential, etc [29]. The formation damage coefficient β_s and the exponent n reflect the permeability decline resulting from fines capture. The formation damage coefficient β_a and the exponent m reflect the permeability rise resulting from fines detachment. Initial permeability k_0 corresponds to the pre-flush state where all detachable fines are still attached

$$k_0 = k(1 + \beta\sigma^0)^{-m} \quad (5)$$

There are seven unknowns in system 1–4: three concentrations of suspended, strained and attached particles c , σ_s , and σ_a , three components of flow velocity U , and pressure p . However, this system comprises six equations only: three scalar Eqs. (1), (2), and (4), and one 3D vector Equation (3). To close the system, one more equation must be formulated.

The traditional closure for system 1–4 is the equation for detachment rate that assumes simultaneous particle detachment and capture; the source term (detachment rate) contains the detachment coefficient [24,25,30]. This model has proved to provide high match with numerous sets of laboratory data [31,32]. Yet, the model predicts asymptotic stabilisation of the retained concentration, which is not consistent with the abrupt change in permeability observed during laboratory tests where the flow rate is increased instantly [28]. Besides, the detachment coefficient is a purely empirical parameter which is determined by matching the laboratory data and cannot be estimated

theoretically. As a result, this model does not account for the physics of fines detachment.

Another approach to close the governing system 1–4 is the maximum (critical) attached particle concentration as a function of velocity U , salinity γ , pH, and temperature T :

$$\sigma_a = \sigma_{cr}(U, \gamma, pH, T) \quad (6)$$

where σ_a is the volumetric concentration of attached particles. Eq. (6) assumes gradual detachment during flow velocity increase, i.e., that any increase of velocity and, consequently, the drag, mobilises some attached particles. The expression for σ_{cr} is called the MRF (maximum retention function).

Substituting expression for MRF (6) into mass balance Eq. (1), we obtain

$$\frac{\partial}{\partial t} (\phi c + \sigma_s + \sigma_{cr}(|\vec{U}|)) + \vec{\nabla} \cdot (c\alpha\vec{U}) = 0 \quad (7)$$

So, Eq. (6) for the MRF closes the system of six scalar equations ((2)–(4), (7)) with respect to six scalar unknowns c , σ_s , U_x , U_y , U_z , p .

The 1D flow problem allows for an exact analytical solution [33]. The solution allows determining the MRF from breakthrough concentrations (BTCs) during coreflooding. The colloidal transport model using MRF has exhibited high match with lab data in experiments on low-salinity waterflooding [34–36], mobilisation of attached clays [9], dewatering of coal seam beds [7] and gas production from coals [8], nanoparticles-fines reactive transport [37,38], and water injection with proppant packing [39].

As of yet, there is no predictive model for colloidal detachment and MRF calculation based on micro-scale parameters, meaning that it must be determined from laboratory tests alone. Two such formulations have been presented, however they assume either poly-layer particles attachment with particles and pores of constant radii [27], or spherical particles with varying size attached to the substrate [40], making their applicability very limited. Besides these very specific cases, the predictive model for MRF is not available. The upscaling for detachment [41–43] hasn't been rigorously performed. The existence of MRF is a consequence of particle-scale mechanical equilibrium on the porous-medium surface, but the theoretical link between the particle- and core scales hasn't been established, i.e., an upscaling procedure hasn't been developed. This explains the absence of predictive colloidal transport model with particle detachment in porous media.

The directions in the arrows in Fig. 2 show the desirable upscaling and downscaling, which are missed in the current theory of colloidal-suspension transport in porous media.

The present paper fills the gap. The micro-scale detachment model becomes stochastic after introduction of probability distribution functions for all parameters / physical constants of the mechanical-equilibrium equations for the attached particles. For the first time, we upscale the particle-scale equations for mechanical equilibrium yielding the stochastic model for colloidal detachment. The upscaling of the mechanical equilibrium with probabilistically distributed coefficients allows deriving the upscaled particle-detachment equation in the form of the maximum retention concentration as a function of velocity, salinity, pH, and temperature (MRF). This permits direct calculation of the MRF from micro-scale mechanical-equilibrium parameters. We developed a mathematical procedure expressing detachment by rolling, sliding, and lifting by a single criterion. The method for predicting MRF from micro-scale parameters closes the governing system of colloidal transport in porous media. The MRF is determined from breakthrough curves during coreflooding. This leads to downscaling, i.e., determining microscale parameters from the MRF. High match between the lab and modelling data, as well as realistic values of the tuned micro-scale parameters validate the stochastic model and upscaling procedure.

The structure of the paper is as follows. Section 2 presents mechanical equilibrium of the attached fines and the detachment conditions.

Section 3 establishes the upscaling procedure and derives the stochastic model for particle detachment in the MRF equation. Section 4 incorporates the MRF into system of governing equations and presents analytical model for 1D colloidal transport that describes porous-media flow tests. Section 5 treats the laboratory coreflooding data. Section 6 discusses the limitations of the stochastic model and its promising extensions. Section 7 concludes the paper.

2. Micro-scale mechanical equilibrium of attached particles

To derive the stochastic model for colloidal particle detachment, we present the expressions for forces and torques exerting an attached particle (section 2.1), mechanical equilibrium conditions for an attached particle (section 2.2), and derive equation for flow velocity yielding particle detachment (section 2.3).

2.1. Forces exerting attached particles submitted to the viscous flow

Let us consider the forces acting on an attached particle, which is located on the plane surface (Fig. 2,3): drag force F_d acting on the particle from by-passing viscous water; electrostatic force F_e , lifting force F_l , capillary force F_c , and buoyancy F_g . The assumption that particles are significantly smaller than pores allows using the formulae for the interaction between particles and a plane surface; Fig. 3 shows the separation distance h between the particle and the plain substrate used in DLVO theory. Here we concentrate on spheroidal particles; a and b are the maximum and minimum semi-axes of the spheroid, respectively.

The electrostatic force is a potential force, where the total energy potential V depends on the particle–surface separation distance h :

$$F_e(h) = -\frac{\partial V(h)}{\partial h}, \quad V = V_{BR} + V_{EDL} + V_{VDW} \quad (8)$$

Here the total energy is a sum of Born, electric double layer, and Van der Waals energy potentials. Formulae for the three components of the electrostatic energy along with the electrostatic force exerting on a spherical particle are given in Appendix A.

An energy profile $V(h)$ which has only a primary minimum has an inflection point $h = h_m$, where the electrostatic force reaches its maximum:

$$\frac{\partial F_e(h_m)}{\partial h} = -\frac{\partial^2 V(h_m)}{\partial h^2} = 0, \quad \frac{\partial^2 F_e(h_m)}{\partial h^2} = -\frac{\partial^3 V(h_m)}{\partial h^3} < 0 \quad (9)$$

The maximum electrostatic force $F_e(h_m)$ is considered in torque and force balances for conditions of particle detachment. Following the works [44,45], maximum electrostatic force for spheroid is calculated using the SEI method, briefly described in Appendix A.

The detaching moment of drag M_b is expressed as

$$M_b = F_d b f_M(\alpha_s) + F_l l_n = 6\pi\mu r_s u_s f_d(\alpha_s) b f_M(\alpha_s) + F_l l_n \quad (10)$$

where μ is the fluid viscosity, r_s is the particle radius, u_s is the flow velocity at the centre of the particle, α_s is the aspect ratio for spheroidal particles, and f_d and f_M are shape factors for spheroids. Here the aspect ratio is the ratio between the small and large semi axes of the spheroid, and r_s is the radius of the sphere with the volume equal to the volume of the spheroid [46]:

$$\alpha_s = \frac{b}{a}, \quad \frac{4}{3}\pi a^2 b = \frac{4}{3}\pi r_s^3, \quad b = r_s \alpha_s^{2/3} \quad (11)$$

Formulae for lift, capillary force, and gravity are presented in Eqs. A (5)–A(7).

2.2. The criteria for particle detachment

Following previous works [18,47,48], this section briefly presents the detachment theory for attached fine particles. Mechanical

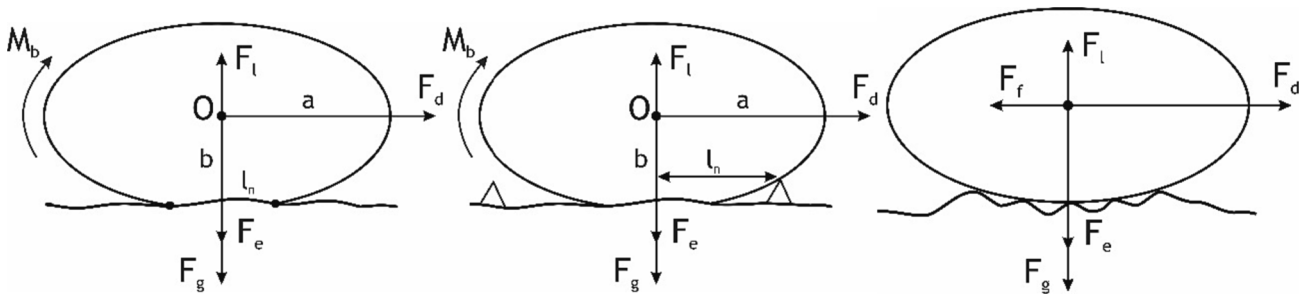


Fig. 4. Fines mobilisation by rolling and sliding: a) particle rolling around the edge of attracted particle–substrate contact area; b) particle rolling around asperity on the matrix surface; c) particle sliding over the surface.

equilibrium of a particle on the porous-media surface in the case of favourable attachment (one primary energy minimum) is determined by the following conditions.

Consider the attached particle rotation at the moment of its detachment and the rotational momentum M_b exerting on the particle from the surrounding creeping flow. Introduction of shape-factor f_d into Stokes formula for drag allows accounting for aspect ratio of the spheroidal particle attached to plain surface. The typical value for torque M_b is the product of drag and lever arm b ; introduction of shape-factor f_M makes the torque expression exact. Both factors are calculated by CFD. So, the momentum-based mechanical equilibrium criterium is:

(i) equality of detaching and attaching torques [49]

$$M_b = 6\pi\mu r_s u_s f_d(\alpha_s) b f_M(\alpha_s) + F_l(r_s) l_n = F_e(h_m) l_n + F_c(r_s) l_n + F_g(r_s) l_n \quad (12)$$

which can be expressed via the normal force F_n

$$6\pi\mu r_s u_s f_d(\alpha_s) b f_M(\alpha_s) = F_n l_n, \quad (13)$$

$$F_n = F_e(h_m) + F_c(r_s) + F_g(r_s) - F_l(r_s) \quad (14)$$

Consider dry (Coulomb) friction between the particle and substrate at the moment of detachment with further particle sliding along the surface. The friction is proportional to normal force F_n with proportionality Coulomb-friction coefficient. The corresponding mechanical equilibrium condition is:

(ii) equality of detaching and attaching force projections on the horizontal

$$F_d = 6\pi\mu_f r_s u_s f_d(\alpha_s) = \nu_c F_n \quad (15)$$

Another mechanical equilibrium condition encompasses lift, electrostatic, capillary and gravity forces and comprises the.

(iii) equality of detaching and attaching force projections on the vertical

$$F_l(u_s) = F_e(h_m) + F_g(r_s) + F_c(r_s); \quad F_n = 0 \quad (16)$$

where b and l_n are the lever arms for drag and normal forces, respectively, and ν_c is the Coulomb friction coefficient. Here in the case of an attached fine particle, the right sides of Eqs. (13), (15), and (16) are lower than their left hand sides (LHS). Breach of any of the equilibrium conditions (13), (15), or (16) yields fines detachment by rolling, sliding, and lifting, respectively. For all cases presented in this paper, there is only one energy minimum, which we confirmed by the calculations of DLVO energy profiles. In the case of two energy minima, there are two separating distances $h = h_m$ that correspond to both energy minima, and Eqs. (13), (15), and (16) are applicable to the particles that are located in primary and secondary energy minima. At low velocities, $F_l \ll F_e$, and the lifting criterium (16) can be dropped. For the majority of clay fines in natural or engineered porous media, gravity is negligible. Capillary force

is absent in fully saturated or dry porous media.

A particle remains attached to the matrix surface and does not roll if the detaching torque (LHS of Eq. (12)) does not exceed the attaching torque (right hand side (RHS)). The criterium that a particle remains attached is obtained by dividing the LHS of Eq. (12) by the RHS:

$$\xi = \frac{6\pi\mu_f r_s u_s f_d(\alpha_s) l f_M(\alpha_s) + F_l(r_s)}{F_e(h_m) + F_c(r_s) + F_g(r_s)} < 1, \quad l = \frac{b}{l_n} \quad (17)$$

It is implicitly assumed that the particles detached by criteria (13), (15), and (16) continue rolling over the porous media surface, sliding over the surface, and move off the surface into the liquid stream, respectively. Fig. 4a and b show how the particle rotates around the touching “supporting” point at the detachment moment. The rotation occurs around the edge of contact particle–substrate area in Fig. 4a, and around asperity in Fig. 4b. Fig. 4c shows particle sliding over the rough surface of the porous medium.

2.3. Detachment velocity for rolling particles

Either of torque balance (13) or horizontal and vertical force balance (15) provides the mechanical equilibrium of a fine particle on plane substrate. First, let us consider only rolling detachment condition (13). Assuming uniform particles and pores, Eq. (13) predicts a single critical velocity, below which all particles are attached, and above which all particles detach. However, all laboratory tests exhibit gradual fines detachment during velocity increase [7,8,50,51].

Gradual fines detachment is explained by the non-uniform particle and pore sizes and geometries in natural and engineered porous media. Thus, all coefficients in Eq. (13) vary over the matrix surface – particles of different sizes and shapes are attached to a rough surface. To reflect this non-uniformity, below we stochastically distribute all relevant parameters in Eq. (13). Then we calculate the probability of particles being in mechanical equilibrium.

Assume that the porous medium is a bundle of parallel capillaries. Poiseuille’s flow equation and Darcy’s law are:

$$u = -\frac{r^2}{8\mu} \nabla p, \quad U = -\frac{k}{\mu} \nabla p \quad (18)$$

allow expressing the average velocity in a pore via Darcy’s velocity

$$u = \frac{r^2 U}{8k} \quad (19)$$

We can calculate the velocity acting on the particle centre, u_s , by evaluating the Poiseuille velocity profile at the distance b from the pore wall:

$$u_s = 2 \left[1 - \left(\frac{r-b}{r} \right)^2 \right] u \approx 4 \frac{b}{r} u = \frac{rbU}{2k} \quad (20)$$

The expressions for drag F_d and rolling moment M vs U , accounting for Eq. (20), are:

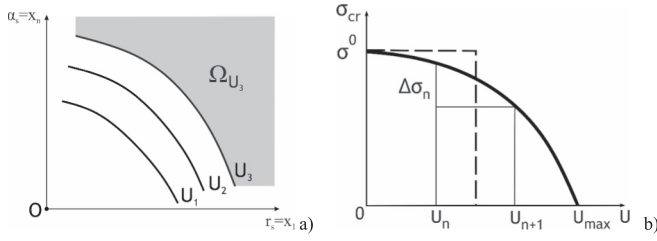


Fig. 5. Introduction of maximum retention concentration of attached fines as a function of velocity: a) detachment domain in the space of micro-scale parameters for velocity U_3 ; b) maximum retention function of Darcy's velocity.

$$F_d = 6\pi\mu r_s u_s f_d(\alpha_s) = 6\pi\mu r_s f_d(\alpha_s) \frac{rbU}{2k} \quad (21)$$

$$M = 6\pi\mu r_s u_s f_d(\alpha_s) b f_M(\alpha_s) = 6\pi\mu r_s f_d(\alpha_s) b f_M(\alpha_s) \frac{rbU}{2k}$$

Here, for solid particles, we assume small deformation, so the distance of the centre of the particle to the wall is equal to small semi-axis of the spheroid, b (Fig. 3).

The rolling condition (12) of attachment ignoring lift, capillarity and gravity becomes:

$$M = 6\pi\mu r_s f_d(\alpha_s) b f_M(\alpha_s) \frac{rbU}{2k} < F_e(r_s, \alpha_s) l_n < 1 \quad (22)$$

Expressing the small semi-axis of the spheroid, b via its effective radius r_s and aspect ratio α_s from Eq. (11), the attachment condition (17) takes the following form:

$$\xi = \frac{3\pi\mu r_s^3 \alpha_s^4 f_d(\alpha_s) f_M(\alpha_s)}{k F_e(r_s, \alpha_s) l_n} U < 1 \quad (23)$$

From Eq. (23) follows the expression for critical detachment velocity, which provides the detachment of attached particle with given properties:

$$U_{cr} = \frac{k F_e(r_s, \alpha_s) l_n}{3\pi\mu r_s^3 \alpha_s^4 f_d(\alpha_s) f_M(\alpha_s)} \quad (24)$$

In the case of a distribution of particle detachment conditions, the fraction of particles that remain attached after flow with velocity U is the probability of the event defined by Eq. (23). In other words, rather than there being a deterministic U_{cr} given by Eq. (24), it will be a probabilistic quantity with PDF $f(U_{cr})$.

If the permeability of the porous media, k , is not known, its value can be calculated by either effective medium theory (Eq. (B1)) or percolation (Eq. (B8)), presented in Appendix B. Effective medium theory is more accurate for narrow pore size distributions, $f(r)$, while percolation is more adequate for wide PDFs with high coefficient of variation. Both theories assume a regular pore network for the porous space with coordination number z . Permeability for Eq. (24) is expressed via z and PDF for pores by Eqs. (B1) or (B8). Conversely, if permeability k is known, Eqs. (B1) or (B8) determine the coordination number z , allowing us to calculate the matrix surface and pore connectivity.

3. Upscaling of the stochastic model for colloidal particle detachment

In this section, we upscale this equation assuming probabilistic distributions for mechanical equilibrium parameters (section 3.1), incorporate rolling, sliding, and lifted particles in a united MRF (section 3.2), and analyse the sensitivity of MRF with respect to micro-scale parameters and their standard deviations (section 3.3).

3.1. Upscaling of detachment particle-scale equations to MRF at core scale

In this section, we present the upscaling procedure, from mechanical equilibrium of an attached fine at the particle scale, to maximum attached concentration, expressed by right arrow in Fig. 2. Eqs. (12)–(16) represent the mathematical model for fines detachment at the particle scale. The result of its upscaling is the maximum retention function.

Appendix C Determines the MRF given by Eq. (24) from Eq. (C2) by rolling and probabilistic distributions of mechanical-equilibrium parameters contained in this equation. Axes in Fig. 5a correspond to microscale parameters from Eq. (24); the particles from the grey domain remain attached for velocities higher than U_3 . Probabilistic distribution of parameters (x_1, x_2, \dots, x_n) in RHS of Eq. (24) correspond to PDF defined over their space, shown in Fig. 5a. The continuous curves show sets of parameters with constant critical velocity; here $U_1 < U_2 < U_3$. Grey area corresponds to fraction of attached particles, which can be detached at flow velocity higher than U_3 .

The PDF for mechanical-equilibrium parameters yields distributed detachment (critical) velocity. As it follows from Eqs. (C2) and (C5) by tending the velocity U to infinity, the detachable particle concentration corresponds to zero flow velocity

$$\sigma^0 = \sigma_{cr}(0) \quad (25)$$

i.e., increase in velocity from zero to infinity detaches all detachable fines.

The normalised MRF is fully determined by the mutual PDF of the mechanical-equilibrium parameters α_s, r, l, r_s . The value of the normalised MRF for $U = U_3$ is equal to the probability of the event that the parameters belong to grey area in Fig. 5a. Eq. (24) determines the PDF for detachment velocity U . So, from Eqs. (24) and (25) it follows that.

$$\sigma_{cr}(U) = \sigma^0 \int_U^\infty f_{cr}(u) du \quad (26)$$

As it follows from Eq. (26), an increase in velocity from U_k to U_{k+1} causes detachment of particles with concentration that is equal to the difference of the MRF values for those velocities (Fig. 5b)

$$\Delta\sigma_k = \sigma_{cr}(U_k) - \sigma_{cr}(U_{k+1}) \quad (27)$$

Eq. (27) expresses the probability that critical detachment velocity is less than U_{k+1} and higher than U .

Eqs. (13), (15), (16) assume mechanical equilibrium for all attached particles. For 3D flow under isotropic detachment conditions, where U in mechanical equilibrium conditions (13), (15), and (16) is the modulus of velocity, the MRF is a function of the modulus of the flow velocity

$$\sigma_a = \sigma_{cr}(|U|) \quad (28)$$

The MRF is a function of all ion concentrations in water and temperature T via dependency of the electrostatic force of those parameters. The most influential parameters of a solute are ionic strength (total salinity) and pH, which is expressed by Eq. (6).

3.2. MRF for simultaneous DLVO detachment for rolling, sliding, and lifting particles

Let us incorporate three detachment criteria (13), (15), and (16) into the MRF using the principle of minimum detachment velocity given by Eq. (24), namely that detachment will occur at the minimum detachment velocity calculated from the three criteria. For rolling detachment, given by Eq. (13), the MRF and PDF for the detachment velocity are determined in the previous section by Eqs. (26) and (24). First, consider detachment with both rolling and sliding. In the case of flow with increasing velocity, the detachment occurs at the minimum velocity of those obtained by criteria (13) and (15). Equations (13) and (15) show

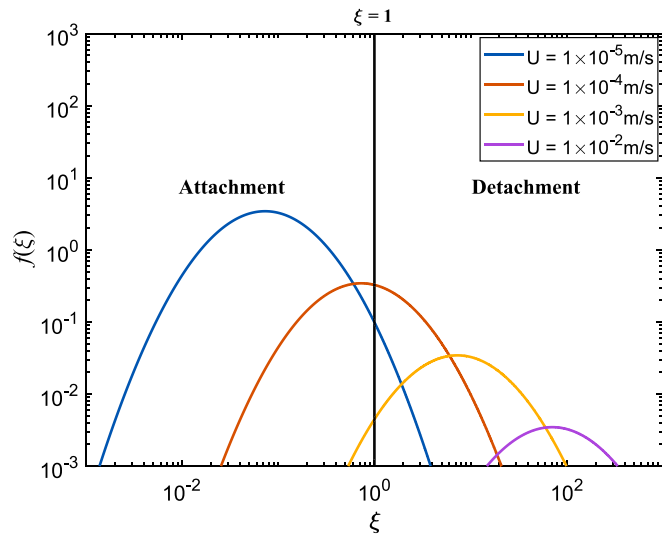


Fig. 6. PDF for detachment velocity and its dependency on Darcy's flow velocity.

that these two criteria are mathematically equivalent if the following equality holds

$$\frac{l_n}{r_s \alpha_s^{2/3} f_M(\alpha_s)} = \nu_c \tag{29}$$

Consider the general case where those two parameters are different. Let us introduce a new single parameter x_n that incorporates both parameters in Eq. (29). Assume that a particle is detached by the criterium that requires smaller velocity for breaching either of conditions (13) or (15). The detachment velocities for both rolling and sliding are proportional to both parameters (29). So, determining the minimum detachment velocity is equivalent to determining the minimum of those two parameters:

$$x_n = \min \left\{ \nu_c, \frac{l_n}{r_s \alpha_s^{2/3} f_M(\alpha_s)} \right\} \tag{30}$$

Appendix C Considers the distribution of all micro-scale mechanical-equilibrium parameters. There, \vec{x} is the vector with the components that are all those parameters. The mathematical schematic (26) accounts for both detachment criteria where the n -th component of vector \vec{x} is x_n

In particular, the expression (24) for the detachment velocity becomes

$$U_{cr} = \frac{x_n F_e(h) \phi}{6\pi\mu r_s f_d(\alpha_s)} \tag{31}$$

According to Eq. (D2) in Appendix D, if two components in the right-hand side of Eq. (26) are independent, the PDF for component x_n is

$$f(x_n) = f^l(x_n) \int_{x_n}^{\infty} f^v(y) dy + f^v(x_n) \int_{x_n}^{\infty} f^l(x) dx \tag{32}$$

where $f^v(x)$ and $f^l(y)$ are PDFs for components of the RHS of Eq. (30). Eq. (32) for the PDF of the x_n , allows accounting for both rolling and sliding in the detachment model.

If the lifting criterion (16) is fulfilled, i.e.,

$$F_l(u_s) > F_e(h_m) + F_g(r_s) + F_c(r_s) \tag{33}$$

The left-hand side of Eq. (13) exceeds the right-hand side, so the particle rolls at lower velocity. The same corresponds to Eq. (15), so the particle slides at lower velocity. In the course of increasing velocity, the particles that can be lifted, have detached by rolling or sliding. So, the micro-scale detachment model (31) automatically includes the lifting

criterion.

3.3. Sensitivity analysis for micro-scale parameters

Consider the PDF for detachment velocity and how it is affected by Darcy's velocity (Fig. 6). The attached concentration corresponds to the area below the curve and to the right of vertical line $\xi = 1$. Indeed, Eq. (23) exhibits the event of velocity lower than critical, and its probability is equal to normalised concentration of detached fines. The larger is the rate, the higher is the probability of the detachment, the less fines remain attached, so the PDF curve moves to the right with velocity increase.

For the purposes of calculations, let us assume that the four stochastically distributed parameters ($\alpha_s, r, b/l_n, r_s$) in Eq. (31) are distributed normally. To calculate the distribution of detachment velocities, a Monte Carlo procedure is used, with samples from each parameter's probability distribution used to calculate the corresponding U_{cr} value. The resulting detachment PDFs and corresponding MRFs are presented in Fig. 7.

Now let us discuss how the parameters of the mechanical equilibrium equation for the attached particles affect the PDF for detachment velocity and MRF. Consider the effect of the lever arm ratio on detachment. The lever arm measures the ratio between the extent that the drag force and electrostatic force translate into torque on the particle. A higher lever arm shifts this ratio towards the drag force, meaning that lower velocities are required for detachment. Thus, the PDF and MRF move to the left (Fig. 7a and b). The lower is the particle aspect ratio the smaller is the drag, and the higher is the maximum of electrostatic force, so the PDF and MRF move to the right (Fig. 7c and d). Decrease in zeta-potentials of both the particle and grain decreases the maximum electrostatic force, shifting both the PDF and MRF to the left.

The detachment velocity distributions, presented in Fig. 7a, c, and e, have the shape of a log-normal distribution. This has been verified by fitting the samples with such distribution. One hundred quantiles (or percentiles) of the critical velocities have been compared to the corresponding quantiles of the tuned lognormal distribution in order to evaluate the goodness of fit. Increasing the number of quantiles used for the comparison had a negligible effect on the goodness of fit.

Table 1 presents the accuracy of approximation of PDF of detachment velocity by log-normal distribution. The first column presents 9 sets of parameters that correspond to PDFs for detachment velocity shown in Fig. 7a, c, and e. The second and third columns show two parameters of the log-normal distributions. The fourth and fifth columns present mean detachment velocity and its standard deviation. High values of coefficient of determination R^2 , shown in the sixth column, allows claiming high accuracy of approximation of PDF for detachment velocity by log-normal distribution.

As it follows from Eq. (26), this defines the following properties of the MRF:

- (i) derivative of the MRF at $U = 0$ is equal to zero, i.e., the stochastic model does not account for loose fines (those which will detach under any velocity);
- (ii) derivative of the MRF is negative, i.e., any flow velocity increase yields detachment of some fines;
- (iii) derivative of the MRF decreases from zero reaching minimum at some velocity U_{km} , and then increases to zero, meaning that during incremental and constant increases in the velocity, the detached concentration during each step will increase, and then for $U > U_{km}$ begin to decrease.

Under the approximation of a lognormal detachment velocity distribution, each case can be characterised by the mean and standard deviation of PDF $f(U_{cr})$. Appendix E defines the sensitivity coefficient as a normalised variation of predicted value $\Delta y/y$ to the normalised variation of the parameter $\Delta x_k/x_k$ that causes the variation of y . Table 2

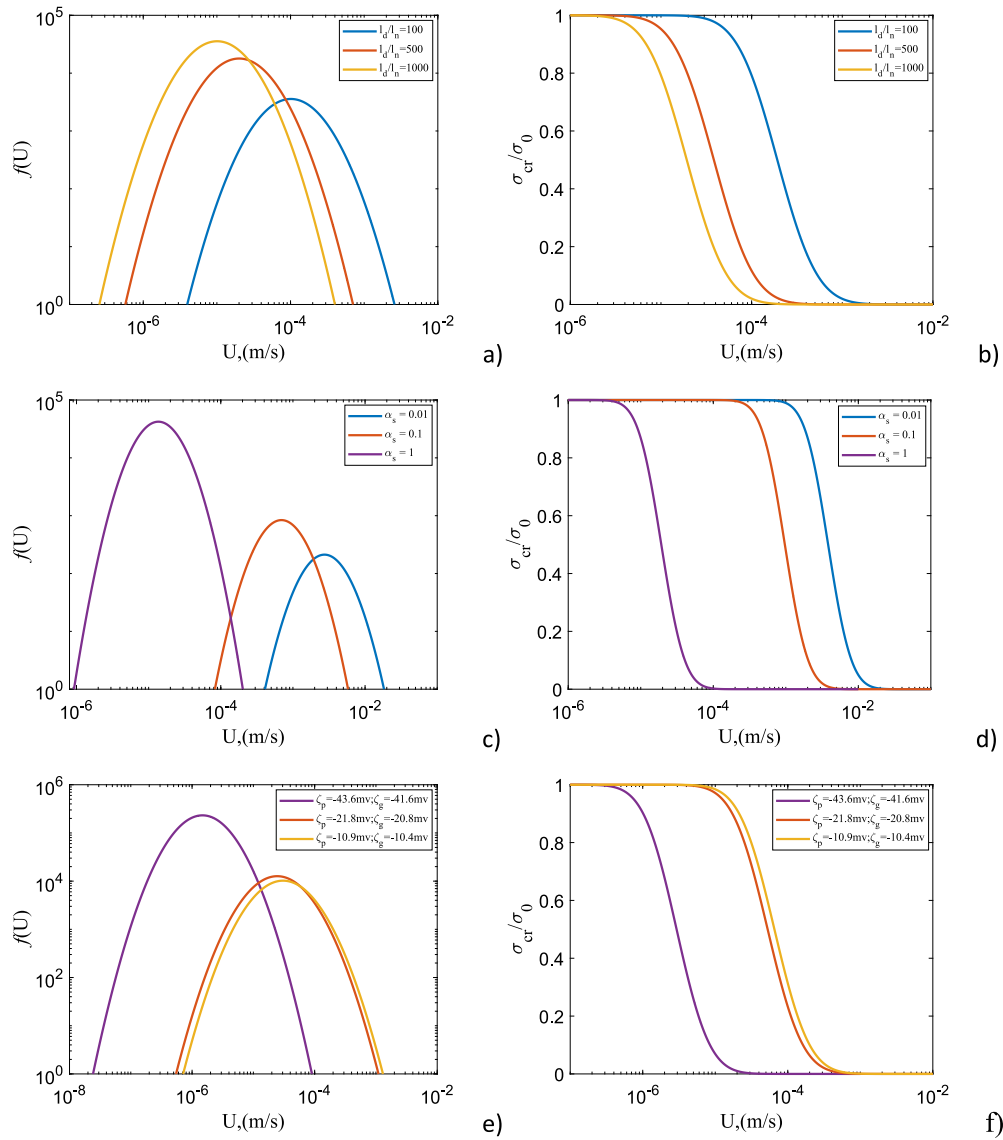


Fig. 7. Effects of lever arm ratio, aspect ratio, and zeta-potentials for particles and grain surface on probability density function (PDF) for detachment velocity and maximum retention function (MRF): a) sensitivity of PDF and b) MRF of lever arm ratio; c) sensitivity of PDF and d) MRF of aspect ratio; e,f) PDF and MRF for different zeta potentials ζ_p and ζ_g of particles and grains, respectively.

Table 1
Approximation of PDF for detachment velocity by log-normal distribution.

	$\mu(f(U))$	$\sigma(f(U))$	Mean(U), m/s	SD(U), m/s	R^2
a) $l_d/l_n = 100$	-8.495	0.972	3.279×10^{-4}	4.109×10^{-4}	0.906
$l_d/l_n = 500$	-10.115	0.962	6.425×10^{-5}	7.926×10^{-5}	0.916
$l_d/l_n = 1000$	-10.808	0.974	3.251×10^{-5}	4.089×10^{-5}	0.905
c) $\alpha_s = 0.01$	-5.535	0.593	4.706×10^{-3}	3.054×10^{-3}	0.962
$\alpha_s = 0.1$	-6.927	0.618	1.187×10^{-3}	8.089×10^{-4}	0.946
$\alpha_s = 1$	-10.832	0.620	2.394×10^{-5}	1.640×10^{-5}	0.945
e) $\zeta_p = -43.6\text{mV}$	-12.678	1.000	5.147×10^{-6}	6.754×10^{-6}	0.902
$\zeta_g = -41.6\text{mV}$					
$\zeta_p = -21.8\text{mV}$	-9.838	1.007	8.868×10^{-5}	1.176×10^{-4}	0.918
$\zeta_g = -20.8\text{mV}$					
$\zeta_p = -10.9\text{mV}$	-9.596	1.021	4.145×10^{-4}	1.551×10^{-4}	0.911
$\zeta_g = -10.4\text{mV}$					

presents the sensitivity coefficients of the mean velocity (second column) and its range ($P_{95}-P_5$) (third column) with respect to mean particle radius r_s , pore radius r , aspect ratio α_s , and lever arm ratio b/l_n (first column, rows 2, 4, 6, and 8, respectively), and their standard deviations

(rows 3, 5, 7, and 9). Fig. 8a shows the tornado plot for sensitivity of mean velocity U_{cr} ; the sensitivity of standard deviation of detachment velocity is presented in Fig. 8b.

The higher is the sensitivity coefficient Γ_i the higher is the influence

Table 2

Sensitivity for mean of detachment velocity and its standard deviation of the mechanical-equilibrium parameters and their standard deviations.

Parameters x_i , $i = 1,2,3,4$	Γ_i for mean velocity U	Γ_i for range of velocity U
$\mu(r_p)$	-1.1581	-1.2104
$\sigma(r_p)$	0.1481	0.2283
$\mu(r)$	-1.3057	-1.7419
$\sigma(r)$	0.2912	0.7014
$\mu(\alpha_s)$	-2.6512	-3.3187
$\sigma(\alpha_s)$	0.6203	1.7376
$\mu(l_d/l_n)$	-1.1844	-1.3720
$\sigma(l_d/l_n)$	0.1774	0.2738

of parameter x_i . More sensitive parameters provide higher contribution to the prediction accuracy and reliability.

Eq. (24) shows that the larger are the pore r and the lever-arm ratio b/l_n , the lower is the detachment velocity. Calculations using expressions (A3, A4) for shape factors show that the lower is the aspect ratio α_s the lower is the product $\alpha_s^{4/3} f_{dfM}$ and thus the higher is the detachment velocity. DLVO formulae show that electrostatic attraction grows with particle size increase slower than r_s^3 , thus Eq. (24) yields decrease of detachment velocity with particle radius increase. Therefore, the sensitivity coefficients for four mean parameters are negative (Fig. 8a). So, in the test with increasing of flow velocity, the particles are detached in order of decreasing of their radii, pore size, lever arm ratio and particle aspect ratio.

The higher are the standard deviations of the four parameters the higher is the mean detachment velocity, so the sensitivity coefficients are positive (Fig. 8a). For the mean detachment velocity, the most influential mechanical-equilibrium parameters as listed in the order of decreasing of their sensitivity coefficient are: aspect ratio, pore radius, level-arm ratio, particle radius, then standard deviations of aspect ratio, pore radius, lever-arm ratio, and particle radius (Table 2).

The higher are the means of the four parameters the lower is the standard deviation for detachment velocity, so the sensitivity coefficients are negative (Fig. 8b).

Eq. (24) shows that detachment velocity is monotonically decreasing function with respect to all micro-scale parameters. Therefore, the higher are variabilities of the parameters the higher is the detachment velocity variability, so the sensitivity coefficients for standard deviations are positive (Fig. 8b). For the standard deviation of detachment velocity, the most influential mechanical-equilibrium parameters as listed in the order of decreasing of their sensitivity coefficient are: aspect ratio, pore

radius, standard deviation of aspect ratio, lever arm ratio, particle radius, and standard deviations of pore radius, lever-arm ratio, and particle radius.

3.4. Downscaling

The stochastic microscale model includes the mean values of mechanical equilibrium parameters and their standard deviations. So, for n mechanical equilibrium parameters, expressed in the LHS of Eq. (23), the number of parameters in the stochastic microscale model is $2n$. Those $2n$ constants determine an upscaled MRF. The downscaling is determination of some of those parameters from MRF.

Here we consider only one detachment mechanism, which is that by drag against electrostatic attraction under favourable conditions. In this case, Eq. (23) provides an estimate of the mean detachment velocity. The variation coefficient of detachment velocity, which determines spread of MRF and gradual particle detachment during velocity increase (continuous curve in Fig. 5b) is determined by the coefficients of variation of the mechanical equilibrium parameters. For zero standard deviations of mechanical equilibrium parameters, the MRF is stepwise (traced curve in Fig. 5b). The previous section shows that for normal PDFs for microscale parameters, the normalised MRF is log-normal with high accuracy, i.e., is also two-parametric. Therefore, only two micro-scale parameters can be determined by the downscaling.

The choice of downscaling parameters is determined by the difficulty of their measurement, their availability in the specific lab work, and their sensitivity coefficients Γ_i . The less available and mostly difficult to measure are coefficients of variation of the mechanical-equilibrium parameters. In this work, the tuning micro-scale parameters – mean lever arm ratio and its coefficient of variation – have been chosen because of the difficulty of their experimental measurement and their unavailability in the original papers. The downscaling allows determining them from macro-scale laboratory measurements (Table 5).

4. Mathematical modelling at porous-media scale

To formulate the macroscale model for colloidal-suspension-nano transport in porous media, we present the model assumptions (section 4.1), 3D and 1D governing equations (section 4.2), and exact solution for 1D flow problem that corresponds to coreflood tests (section 4.3).

4.1. Assumptions of the model

The model (1–6) assumes incompressible carrier fluid and particle

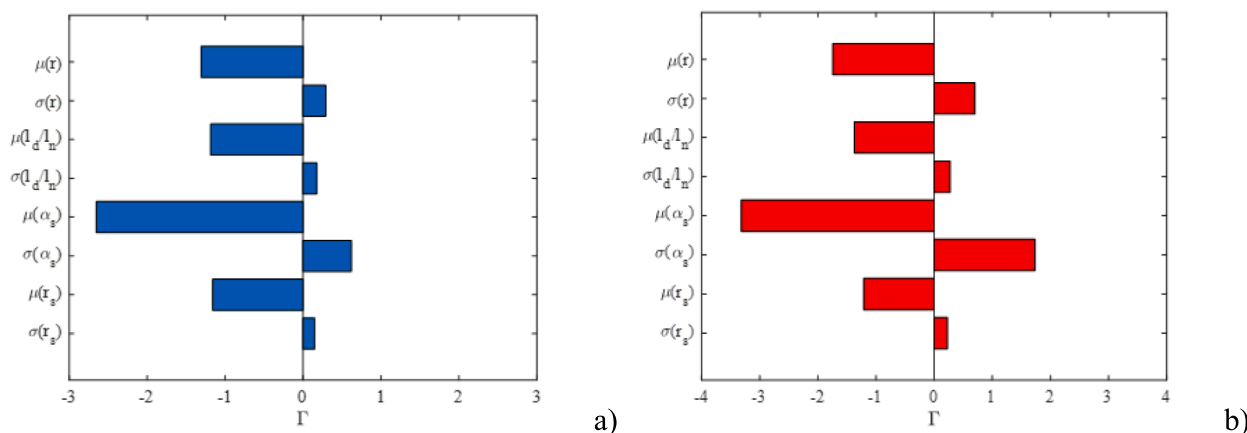


Fig. 8. Sensitivity of MRF (maximum retained concentration) with respect to mechanical-equilibrium parameters and their standard deviations: a) sensitivity of mean detachment velocity; b) sensitivity of standard deviation of the detachment velocity.

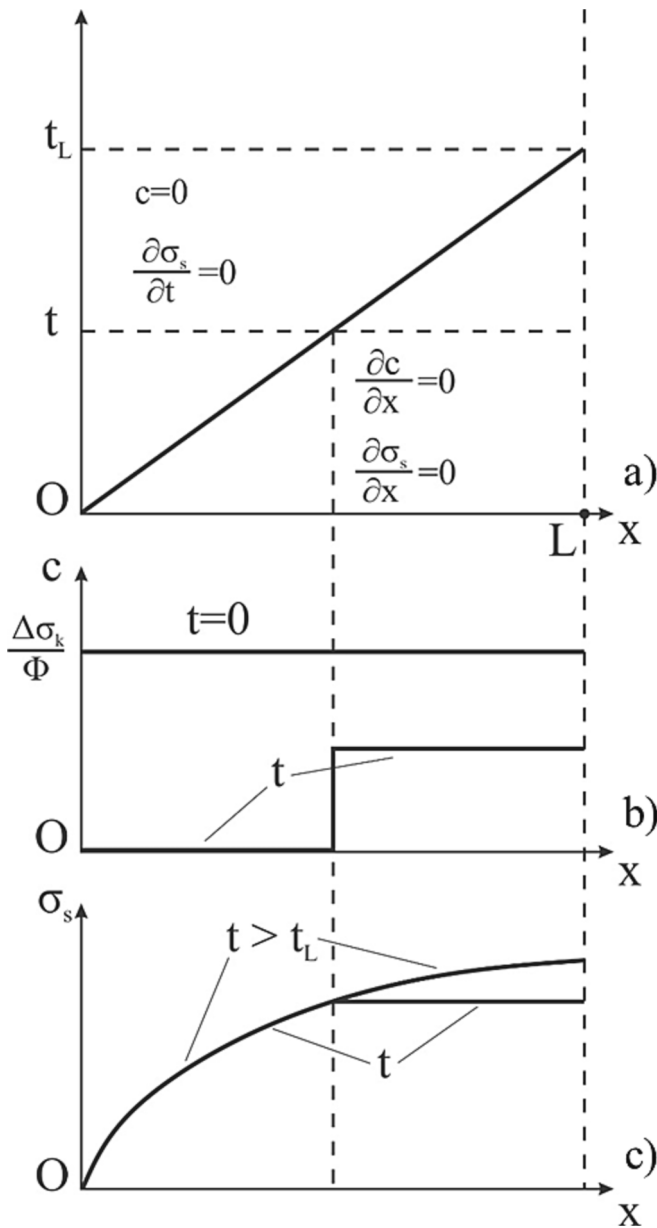


Fig. 9. Schematic of the analytical model for 1D colloidal transport with carrier water velocity U_k : a) propagation of concentration front in plane (x,t) ; b) suspension concentration profiles at the beginning of injection and at the moment before the arrival of concentration front; c) strained concentration profiles at two moments before and after the arrival of concentration front.

matter. Mass concentrations of suspended, attached, and strained particles are significantly smaller than the concentration of aqueous component in the colloidal suspension, so the particle-concentration variations do not affect the volume of the suspension. The carrier fluid is incompressible. Another assumption which does not require concentrations to be small and results in the same system of equations is the Amagat law of volume additivity with mixing: volume of the colloidal suspension is equal to the total of the carrier fluid volume and volume of the particles; in this case the concentrations are volumetric [4].

4.2. Governing system for 1D colloidal-suspension transport with particle detachment against DLVO

In following sections, we consider 1D (x,t) -flow in a reservoir core

with constant flow rate, so $U = \text{constant}$. We also consider constant filtration coefficient λ and viscosity μ , $n = 1$ in Darcy's law (3), and uniform colloids $f(c) = c$. In addition, we assume that the increase in permeability resulting from particle detachment is negligible. Under these assumptions, the system (1–3) becomes:

$$\frac{\partial}{\partial t}(\phi c + \sigma_s + \sigma_{cr}(U)) + \alpha U \frac{\partial c}{\partial x} = 0 \quad (34)$$

$$\frac{\partial \sigma_s}{\partial t} = \lambda c \alpha U \quad (35)$$

$$U = -\frac{k}{\mu(1 + \beta \sigma_s)} \frac{\partial p}{\partial x} \quad (36)$$

Eq. (36) separates from Eqs. (34) and (35), which form a 2x2 system with respect to two unknowns, c and σ_s . Pressure p is determined from Eq. (36) for known $\sigma_s(x,t)$.

4.3. Analytical model for 1D coreflood with fines mobilisation

Consider sequential injections of particle-free water with rates $U_0 = 0, U_1, U_2, \dots, U_N$ with release of concentrations $\Delta \sigma_k$ of attached particles that corresponds to suspension concentrations $\Delta \sigma_k / \phi$. The 1D analytical solution for constant rate have been presented previously [52,53]. Here we derive the solution for piecewise-constant increasing velocity U_k with accumulation of strained concentration $\sigma_k(x,t)$.

The tests are performed long enough so that $t > \phi L / \alpha U_k$, which allows all variables to stabilise. So, switching from rate U_k to rate U_{k+1} corresponds to creation of initial suspended conditions c_{ki} :

$$t = \frac{\phi L}{\alpha U_k} : c_{ki} = \frac{\sigma_{cr}(U_k) - \sigma_{cr}(U_{k+1})}{\phi} = \frac{\Delta \sigma_k}{\phi}, \quad \sigma_k = \sigma\left(x, \frac{\phi L}{\alpha U_k}\right), \quad k = 1, 2, \dots, N \quad (37)$$

where L is the core (porous column) length.

Initial conditions for strained concentration after switching from rate U_k to rate U_{k+1} corresponds to the stabilised strained concentration distribution at the moment where the injection rate is increased, when this distribution has already been stabilised.

The boundary condition corresponds to injection of particle-free water:

$$x = 0 : c = 0 \quad (38)$$

Substitution of Eq. (35) into Eq. (34) and applying the method of characteristics results in solution of problem (34,35) with respect to the suspended concentration:

$$c_{k+1}(x, t) = \begin{cases} \frac{\Delta \sigma_k}{\phi} \exp\left(-\frac{\lambda \alpha U_{k+1} t}{\phi}\right), & x > \frac{\alpha U_{k+1} t}{\phi} \\ 0, & x < \frac{\alpha U_{k+1} t}{\phi} \end{cases} \quad (39)$$

Substituting suspended concentration (39) into the rate equation (35) and integrating in t yields the solution for the strained concentration:

$$\sigma_{s,k+1}(x, t) = \begin{cases} \sigma_{s,k}\left(x, \frac{\phi L}{\alpha U_k}\right) + \Delta \sigma_k \left(1 - \exp\left(-\frac{\lambda \alpha U_{k+1} t}{\phi}\right)\right), & x > \frac{\alpha U_{k+1} t}{\phi} \\ \sigma_{s,k}\left(x, \frac{\phi L}{\alpha U_k}\right) + \Delta \sigma_k \left(1 - \exp(-\lambda x)\right), & x < \frac{\alpha U_{k+1} t}{\phi} \end{cases} \quad (40)$$

As illustrated in Fig. 9a, the concentration front of the injected particle-free water moves with velocity αU_k . Here t_L is a moment of arrival of this front to the point $x = L$. Behind the front, the suspension concentration is equal to zero and the strained concentration is steady-state (Fig. 9b and c). Ahead of the front, suspension concentration and the concentration of particle strained during velocity U_k are uniform.

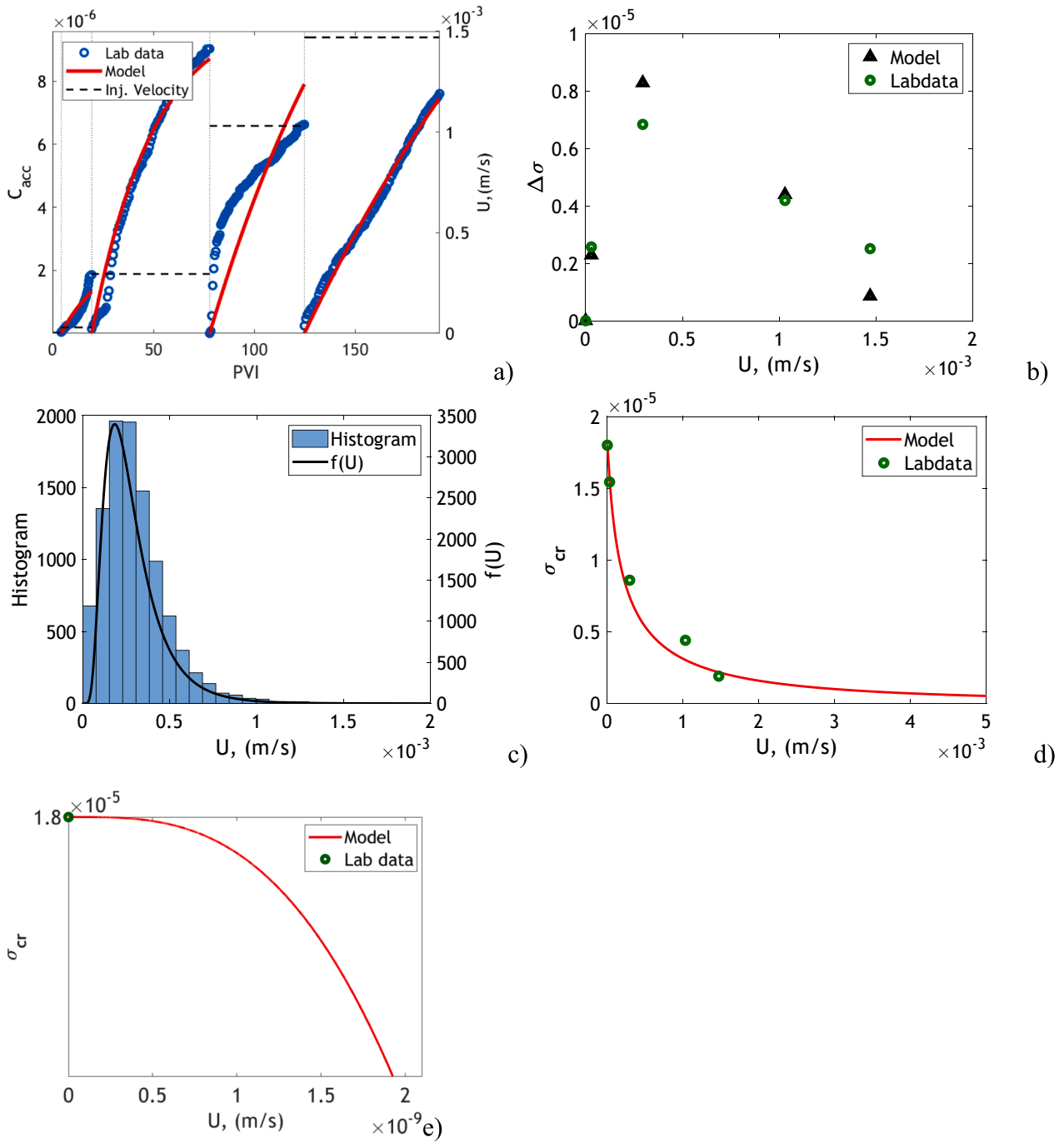


Fig. 10. Matching lab high-salinity coreflood data by Hashemi et al., 2022 using the analytical transport model and by stochastic model: a) Matched accumulated breakthrough concentrations for four flow rates; b) Tuned detached concentrations for four flow rates; c) Matching of PDF for detachment velocity by stochastic model; d) MRF; e) zoom of MRF at small velocities.

Strained concentration gradually increases at each point until the arrival of concentration front; afterwards, it remains constant.

Cumulative BTC is derived from the concentration equation at the outlet (39) by integration in t :

$$c_{k+1}^{acc}(t) = \int_0^t c_{k+1}(L, T) dT = \begin{cases} \frac{\Delta\sigma_k}{L\phi\lambda} \left(1 - \exp\left(-\frac{\lambda\alpha U_{k+1}}{\phi} t\right) \right), & t < \frac{\phi L}{\alpha U_{k+1}} \\ \frac{\Delta\sigma_k}{L\phi\lambda} (1 - \exp(-\lambda L)), & t > \frac{\phi L}{\alpha U_{k+1}} \end{cases} \quad (41)$$

Dimensionless pressure drop is called impedance

$$J_{k+1}(t) = \frac{\Delta p_{k+1}(t)}{\Delta p_1(0)} \frac{U_1}{U_{k+1}} \quad (42)$$

The expression for $J(t)$ is obtained from Darcy's Eq. (36) after substitution of the solution (40) and integration in x from zero to the reservoir length L :

where $J_{k,st}$ is the stabilised impedance from stage k .

5. Treatment of laboratory data

Using the above-derived analytical model, here we present the matching technique that uses non-linear least square method (section

Table 3

The result of matching of accumulated concentration for all cases.

Cases	U (m/s)	α	β	Λ (1/m)	$\Delta\sigma$	R^2 (Cacc)	R^2 (J)
Hashemi et al., 2022	2.95×10^{-5}	1.17×10^{-2}	–	81.12	2.57×10^{-6}	0.78	–
	2.95×10^{-4}	1.19×10^{-2}	–	54.04	6.84×10^{-6}	0.98	–
	1.03×10^{-3}	1.26×10^{-2}	–	17.54	4.19×10^{-6}	0.19	–
Torkzaban et al, 2015	1.47×10^{-3}	1.31×10^{-2}	–	8.94	2.51×10^{-6}	0.99	–
	9.26×10^{-5}	4.1×10^{-2}	0	19.52	2.87×10^{-4}	0.97	–
	3.4×10^{-4}	4.11×10^{-2}	0	19.50	1.74×10^{-4}	0.78	–
Huang et al., 2021	6.7×10^{-4}	4.11×10^{-2}	0	19.46	1.01×10^{-4}	0.96	–
	6.80×10^{-4}	3.62×10^{-2}	42.90	178	4.3×10^{-3}	0.89	0.80
	1.02×10^{-3}	3.85×10^{-2}	17.49	154.89	7.2×10^{-3}	0.91	0.85
Huang et al., 2017	1.36×10^{-3}	4.11×10^{-2}	17.60	134.77	3.8×10^{-3}	0.95	0.84
	3.97×10^{-5}	4.7×10^{-3}	0.71×10^5	647.87	3.03×10^{-6}	0.92	0.92
	5.27×10^{-5}	4.7×10^{-3}	1.94×10^5	639.15	2.97×10^{-6}	0.95	0.55
	7.34×10^{-5}	4.7×10^{-3}	1.94×10^5	625.50	2.02×10^{-6}	0.93	0.87

Table 4Input data for matching $\Delta\sigma$ and MRF by Monte-Carlo modelling for all cases.

Cases		Zeta Potential (mV)		Particle radius (μm)	Aspect ratio	Porosity
		Particles	Rock			
Hashemi et al., 2022	Mean	–20.78	–21.8	2	0.65	0.24
	C_v	0.03	0.03	0.2	0.20	–
Torkzaban et al, 2015	Mean	–44.22	–100	2	0.65	0.32
	C_v	0.03	0.03	0.2	0.2	–
Huang et al., 2021	Mean	–15.85	–7.92	9.5	0.55	0.38
	C_v	0.03	0.03	0.1	0.10	–
Huang et al., 2017	Mean	–12.17	–9.15	5	0.55	8.32×10^{-4}
	C_v	0.03	0.03	0.07	0.07	–

5.1) and show the results of matching of four lab tests (section 5.2).

Following the treatment of the BTC, the detached velocity distribution curve $f(U)$ is approximated by minimizing the squared difference

$$J_{k+1}(t) = \begin{cases} J_{k,st} + \beta\Delta\sigma_k \left(\frac{\alpha U_{k+1}}{\phi L} t + \frac{1}{\lambda L} \exp\left(-\lambda \frac{\alpha U_{k+1}}{\phi} t\right) - \frac{1}{\lambda L} + \left(1 - \frac{\alpha U_{k+1}}{\phi L} t\right) \left(1 - \exp\left(-\frac{\lambda \alpha U_{k+1}}{\phi} t\right)\right) \right), & t < \frac{L\phi}{\alpha U_{k+1}} \\ J_{k,st} + \beta\Delta\sigma_k \left(\left(1 + \frac{1}{\lambda L} \exp(-\lambda L) - \frac{1}{\lambda L}\right) \right), & t > \frac{L\phi}{\alpha U_{k+1}} \end{cases} \quad (43)$$

5.1. Methodology for lab data treatment by analytical modelling

Consider that breakthrough particle concentrations $c_1(t)$, $c_2(t)$, ..., $c_N(t)$ have been measured during coreflood until stabilization, $t_{k+1} - t_k > 1/\alpha$. During each rate increase, we can tune the filtration coefficient λ , drift delay factor α , and the concentration of detached particles $\Delta\sigma_k$ that corresponds to rate change from U_k to U_{k+1} . Matching is performed by non-linear least square method by minimizing the overall deviation between raw laboratory data and the modelling results:

$$\min_{\lambda, \alpha, \Delta\sigma_k} \sum_{k=0}^N \int_{t_k}^{t_{k+1}} [c_k(t) - c_{mod}(t)]^2 dt \quad (44)$$

We assume that the filtration coefficient λ and the drift-delay factor α are independent of rate U . So, the number of tuned parameters from the N -rates test is equal to $N + 2$.

Fig. 10a shows the cumulative BTC after each injection rate change (blue points) and modelling data (red curves). The obtained data on detached concentrations $\Delta\sigma_k$ are given in Fig. 10b. The concentration of detachable particles σ^0 is the total of all particles detached during five injections with increasing rate:

$$\sigma^0 = \sum_{k=1}^N \Delta\sigma_k \quad (45)$$

between the concentrations of detached particles $\Delta\sigma_k$ and the corresponding detached concentration calculated from the log normal $f(U)$. Here the tuning parameters are the mean velocity (\bar{U}), and its standard deviation (σ_U).

$$\min_{\bar{U}, \sigma_U} \sum_{k=1}^N \left(\frac{\Delta\sigma_k}{\sigma^0} - \int_{U_k}^{U_{k+1}} f(u) du \right)^2 \quad (46)$$

In addition to fitting directly with a lognormal $f(U)$, we also directly use the equation for the detachment velocity to fit the laboratory data. Three parameters are stochastically distributed ($b \setminus \ln$, α_s , r_s) and are assumed to be normally distributed. The properties of the distributions for α_s , and r_s are taken from available literature, while the distribution for the lever arm ratio is tuned from the data given the difficulty in measuring it *a priori*. A Monte Carlo procedure is used to calculate samples of the detachment velocity. The mean and standard deviation of these samples is then calculated to calculate the mean and standard deviation of the lognormal approximation for $f(U)$. Deviation from the laboratory data is then calculated using Eq. (46), with an optimization procedure used to tune the mean and standard deviation of the lever arm ratio to maximise the fit to the laboratory data.

In general, other parameters in the detachment velocity equation can be used for tuning depending on the availability and reliability of data.

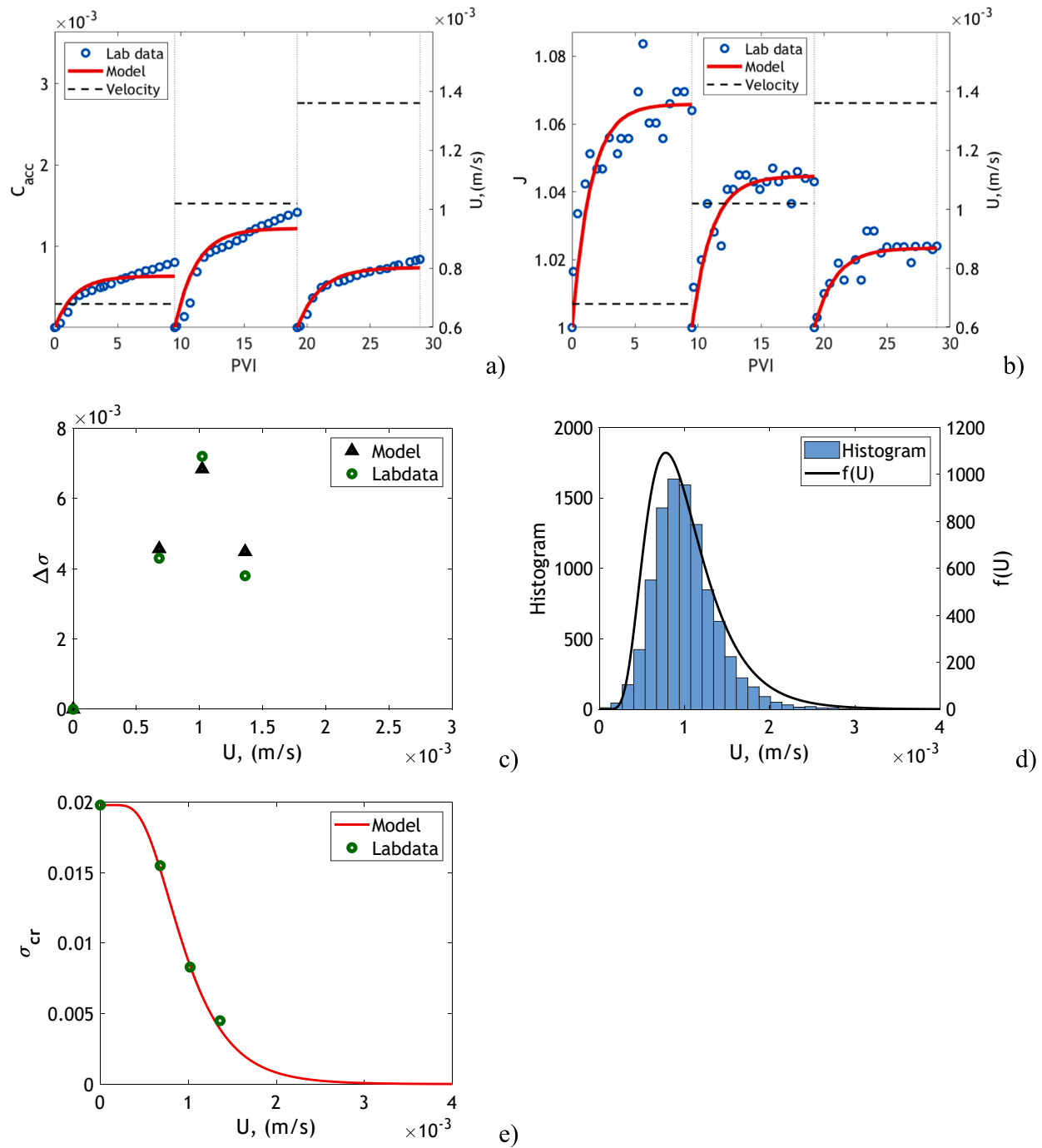


Fig. 11. Treatment of high-salinity flood of coal core by Huang et al., 2021 [39]: a) Breakthrough concentrations; b) Impedance; c) Detached concentrations at three rates; d) PDFs for detachment velocity as obtained by the stochastic model (histogram) and from three detached concentrations; e) MRF.

Table 5
Tuning parameters and the results of matching $\Delta\sigma$ and MRF for all cases.

Cases	σ^0	$\langle l_d/l_n \rangle$	$C_v (l_d/l_n)$	$R^2(\Delta\sigma)$	$R^2(\sigma_{cr})$
Hashemi et al., 2022	1.80×10^{-5}	100	0.50	0.86	0.99
Torkzaban et al, 2015	9.65×10^{-4}	111.97	0.53	0.97	0.98
Huang et al., 2021	1.98×10^{-2}	216.39	0.28	0.84	0.99
Huang et al., 2017	8.54×10^{-6}	749.17	0.08	0.99	0.99

5.2. Treatment of coreflood data

Now we will present the treatment of laboratory coreflood data. Hashemi, Borazjani, Dang-Le, Yin Loi, Nguyen Cao, Badalyan and Bedrikovetsky [54] was using Castlegate sandstone core plug of 0.038 m diameter and 0.05 m length with 2.6% of kaolinite clay. High salinity water was injected. The obtained permeability was 888 mD, porosity was 24.3%. The results of the measured data and matching are presented in Fig. 10.

The tuning data from BTCs using analytical model (41) are given in Table 3. Fig. 10a presents matching the BTCs for four different injection rates. The results of fitting of the detached concentration during each rate change are shown in Fig. 10b along with the values obtained by the log-normal approximation. Fig. 10c shows the histogram of the detachment velocity samples calculated using the Monte Carlo procedure (blue) and the corresponding lognormal $f(U)$ (black). The corresponding MRF is shown in Fig. 10d. Fig. 10e presents zoom of MRF at small velocities, which shows that MRF has zero derivative at $U = 0$. Table 4 presents the input data as taken from the original paper [54]; here PDFs for aspect ratio were taken from Cheng, Zhang, Liu and Leung [55]. Two micro-scale parameters – lever arm ratio and its standard deviation – have been tuned from normalised log-normal MRF by an optimization procedure. The downscaling results are given in Table 5. The obtained values of drift delay factor and filtration coefficient lie within commonly reported intervals [2,3,5,7,24,25,31,33,37,40,41,56,57]. The mean lever arm ratio denoted as $\langle \rangle$, also belongs to common intervals [58], while its standard deviation in porous media hasn't been reported.

The result of data treatment for low salinity water injection into sandstone core by Torkzaban, Bradford, Vanderzalm, Patterson, Harris and Prommer [59] are presented in Fig. S1 and Tables 3–5.

Huang, Dong, You and Shang [39] performed a coreflooding experiment in coal core. Besides the measurements of BTCs, like it was performed in the work [54], this study presents pressure drop across the core for each rate. The coal sample was grounded from a medium-rank bituminous coal. The rock with porosity 0.38 contains 3% fines. The core length is 0.1 m and diameter 0.025 m. Fig. 11 presents the results of matching following the methodology given in section 4.1. Fig. 11a shows the matching of cumulative BTCs. Fig. 11b, shows the matching result of the impedance, which allows determining the formation damage coefficient β . The resulting tuning parameters are presented in Table 3 along with the coefficient of determination for concentration and pressure drop matching. Table 4 presents the mean values and coefficients of variation for the input parameters available from the original paper; here PDFs for particle aspect ratio in coals were taken from Mathews, Eser, Hatcher and Scaroni [60]. Fig. 11d shows the PDF for detachment velocity. Here the two tuning parameters are the mean and coefficient of variation of the lever arm ratio. The tuning data are shown in Table 5 along with high coefficients of agreement. Fig. 11c and 11e show the matching results for three detached concentrations and MRFs.

The data matching of another coal core flooding by Huang, Kang, You, You and Xu [61] are presented in Fig. S2 and Tables 3–5.

High match between the laboratory data and those obtained by the stochastic model along with common values of the model coefficients, obtained in four tests, validate the stochastic model (Tables 3-5).

6. Discussions and summary

Stochastic nature of the model. Micro-heterogeneity of natural porous media and variability of the properties of attached particles can be expressed by PDFs of the corresponding micro-scale parameters. The stochastic model follows from the statement that gradual fines detachment from the porous media surface and consequent continuous MRF are a consequence of the micro-scale non-uniformity, i.e., the probabilistic distribution of the parameters that the equation of mechanical equilibrium for attached particle contains. Otherwise, for constant parameters, the MRF is stepwise, i.e., there does exist such a single velocity

where the overall detachment occurs.

Therefore, we consider PDFs for all model parameters and calculate the probability that the detaching torque does not exceed the attaching torque. This probability versus flow velocity is the normalised MRF. MRF is the product of this probability, that is determined by variability of the microscale parameters, and the overall concentration of detachable fines, which depends on multiple properties of the porous medium: initial clay concentration in the matrix, surface roughness, pore connectivity, etc. The independent variables of MRF are Darcy's velocity, controlling detachment via drag, and ionic strength, pH, and temperature, that affect the detachment via electrostatic forces.

The stochastic model allows us to calculate σ_{cr}/σ^0 , which describes the total capacity of the rock to hold fine particles at given conditions. The parameter σ^0 describes the actual occupancy of those possible attachment sites and cannot be determined using the proposed model. Therefore, it remains one of the primary outputs of experimental data tuning.

Upscaling and downscaling The MRF is a core-scale model for particle detachment that closes the governing system of colloidal transport Eqs. (1)–(3). The micro scale model for detachment, outlined in sections 2.1 and 2.2, is upscaled to the MRF using the stochastic parameter distributions by Eqs. (24) and (26). The microscale parameters include particle radius, pore size, aspect ratio, zeta potentials for particle and grain, lever arm ratio, and their standard deviations.

Formulation of the macro scale detachment model in terms of the actual mechanism for detachment allows for the underlying model parameters and their distributions to be measured. Particle size and aspect ratio and their PDFs can be measured from SEM images of fines, produced during corefloods, or from slices of the porous media [55,60]. PDFs for pore sizes can be determined by mercury porosimetry. Grain form and size distributions can be measured from grinding the porous media, which also allows calculating PDFs for pore size [62]. DLVO parameters can be measured from electrophoresis experiments and refractive index testing. If the lever arm caused by deformation, shown in Fig. 2a and 4a, can be determined by Hertz' theory [58] while that due to asperities (Fig. 4b) is unavailable. If the distributions for all microscale parameters are known, the normalised MRF - CDF $\sigma_{cr}(U)/\sigma^0$ - can be predicted.

The technique of tuning the BTCs using analytical modelling, presented in Section 3 allows determining σ_{cr} . The ratio $\sigma_{cr}(U)/\sigma^0$ is determined by the stochastic properties on the microscale. The downscaling procedure determines the microscale parameters, which facilitates the calculation of those microscale parameters that are not available through measurement. In this work we use a two-stage tuning – determining the MRF from breakthrough concentrations and downscaling by matching the MRF by Eqs. (24),26).

We show that for normal PDFs for microscale parameters, the normalised MRF is also two-parametric, so only two microscale parameters can be determined. In this work, the tuning micro-scale parameters – mean lever arm ratio and its coefficient of variation – have been chosen because of the difficulty of their experimental measurement and their unavailability in the original papers. The downscaling allows determining them from macro-scale laboratory measurements.

Extensions of the stochastic model The present paper predicts colloidal transport by matching the lab flow tests with varying Darcy's velocity. In the same way, the tests with varying salinity, pH, and temperature, can be investigated. The MRF is a function of physical macro-scale variables that affect the mechanical equilibrium. Those variables include ionic strength, pH, and temperature, which the electrostatic DLVO force depends on. One dimensional problems for fines migration with salinity, pH, or temperature variation allow for exact solutions [52,53]. Therefore, the technique for matching the widely available data on injection of particle-free low-salinity, high pH and temperature water, developed in sections 3-4, can be applied for those tests without modification.

Using more sophisticated microscale models for surface roughness

and heterogeneous distributions of surface charges and DLVO parameters, presented in [18], the proposed approach of “stochastization” of physics constants can incorporate those phenomena in the upscaled equations for colloidal transport.

The detachment velocity distribution can be modelled in the case of *multiple detachment mechanisms*. Some examples include detachment against electrostatic force and by mechanical breakage, detachment of particles in the primary and secondary minima of the DLVO energy profile, in pore throats and bodies, etc. In the case of two-mechanism attachment, the number of degrees of freedom of the bimodal CDF for detaching velocity is equal to 4, so 4 microscale parameters can be calculated by downscaling.

Usually, an *incomplete lab data* are available: some micro-scale parameters are uncertain; a few rates have been applied in the coreflood, so BTC information is not enough to tune macroscale model parameters. In this case, a mixed set of micro- and macroscale parameters can be tuned. For example, mean lever-arm ratio can be known from either Hertz theory or asperity distribution. In this case, the standard deviation of lever-arm ratio can be used as a tuning parameter along with macroscale parameters α , λ , and $\Delta\sigma_k$. So, the mean values and standard deviations of a microscale parameter can compensate the lack of macroscale measurements.

Measurement of *pressure drop* histories allows determining 4 more parameters: formation damage coefficients for attachment and straining, and the corresponding powers in Darcy' Eq. (3). The three-point-pressure method where pressure drop is measured along the core and its first section by drilling the port in the middle of the core provides further increase in laboratory data for tuning the model coefficients [63].

The developed approach allows extension to the cases where *lift, capillary and gravitational forces* are comparable with drag and electrostatic forces. The detachment condition (12) contains the expression for lift, which is proportional to velocity in power 3/2 [64,65]. In this case, the expression for detachment velocity follows from the solution of cubic equation. In the case of high flow rates and rough surface, turbulent flow adds quadratic term U^2 in Stokes expression for drag [66], but lift is negligible. In this case, the detachment velocity expression is obtained from solution of quadratic equation. For a non-Newtonian fluid, depending on its rheology, drag is expressed via U by a complex functional dependency, to the detachment velocity is obtained by numerical solution of transcendental equation.

Here we discuss detachment of spheroidal particles by deriving a simplified expression for DLVO attraction. Any *irregular form* colloidal or nanoparticles can be included in the upscaling procedure by the introduction of shape factors for drag and DLVO forces.

The effective upper scale transport equations for more complex mentioned above colloidal systems, can be derived using different upscaling techniques: random-walk models [67], continuous upscaling [68,69], Boltzmann's equation [70], averaging of micro-scale CFD-DEM modelling data [56,71] or numerical 3D network modelling [41]. In large-scale approximation, where dissipative and non-equilibrium fluxes are neglected if compared with the advective fluxes [4], the exact solutions are derived by non-linear modifications of method of characteristics using Riemann invariants [53,72]. The dissipative and non-equilibrium effects can be accounted for in analytical solutions by matching the asymptotic expansions [52,73].

The developed upscaling methodology can be applied for *plugging chemical reactors* by solid particles, like dust emitted during loading and packing the catalytic grains or precipitated solid reaction products. Other applications include CO₂ storage in carbonates under chemical reactions between carbonic acid and matrix, and in sandstones where low-pH reactions exterminate particle-substrate bonds.

7. Conclusions

Derivation of stochastic model for colloidal detachment in porous media and its validation by laboratory corefloods allows formulating the following conclusions:

The gradual release of fine particles during corefloods with increasing injection rates is explained by the distribution of physical parameters which determine the mechanical equilibrium of attached particles. Based on this principle, an upscaling procedure is developed which involves deriving the PDF of the detachment velocity from the PDFs of the relevant physical parameters. The CDF of the detachment velocity distribution is then combined with the detachable concentration to derive the maximum retention function. Following the development of this model, the detached concentration can be calculated directly from the distributions of the parameters which affect particle attachment. The stochastic model describes detachment by rolling, sliding, and lifting. The derived MRF can be presented in terms of velocity, salinity, pH, and temperature.

A new DLVO-based formula derived for spheroidal particle-plane substrate attraction exhibits less than 1% error across a wide range of geometric and electrostatic parameters. If compared with the traditional Surface Element Integration Method, the formula allows significant simplification of the numerical MRF calculations.

Assuming normal PDFs for all micro scale parameters, the PDF of detachment velocity can be approximated by log-normal distribution with high accuracy. Therefore, the MRF has the form of cumulative function for log-normal distribution. So, the MRF is three-parametric, which includes the mean and standard deviation the detachment velocity, and the overall detachable concentration. Only two microscale parameters can be determined by the downscaling procedure, i.e., from the normalised MRF.

Sensitivity analysis shows that the most influential parameters for mean and standard deviation of detachment velocity are aspect ratio and pore radius. The less influential are variation of lever-arm ratio and particle radius.

Increase in particle radius, pore size, aspect ratio, and lever are ratio results in decreasing of mean detachment velocity. Variations of those 4 parameters result in increase of mean detachment velocity. Increase in all 4 parameters decreases standard deviation of detachment velocity, while increase in their standard deviations results in increase of standard deviation of detachment velocity.

For four coreflood tests on detrital fines detachment, high accuracy of the agreement between the lab data and the stochastic model have been observed. The mean value of the lever-arm ratio as well as macroscale parameters vary in commonly reported intervals. This validates the stochastic model for fines detachment.

Declaration of Competing Interest

The authors declare that they have no known competing financial interests or personal relationships that could have appeared to influence the work reported in this paper.

Data availability

No data was used for the research described in the article.

Acknowledgements

Fruitful discussions with Drs. Abbas Zeinijahromi, Alex Badalyan, Themis Carageorgos, Zhao Feng Tian, Heng Zheng Ting (Uni of Adelaide) are highly appreciated. The work was sponsored by Australian Research Council Discovery Project DP190103457 and Linkage Project LP180100890.

Appendix A. Forces acting on a particle attached to substrate.

Electrostatic forces The interaction energy between an oblate spheroid (*sph*) and substrate was calculated by the Surface Element Integration (SEI) Method [26,74]. The interaction energy and total electrostatic force are given by:

$$V_{sph} = 2\pi \int_0^a \left[V \left(H - b\sqrt{1 - \frac{r_e^2}{a^2}} \right) - V \left(H + b\sqrt{1 - \frac{r_e^2}{a^2}} \right) \right] r_e dr_e, \quad F_e = -\frac{\partial V_{sph}}{\partial h} \quad (A1)$$

where H is the distance between particle centre and substrate, r_e is the radial distance of each element, and h is the closest distance between particle and substrate. $V(h)$ is the interaction energy per unit area of two infinite parallel plates separated by distance h . A schematic representation of the particle-substrate configuration is presented in Fig. 3.

Formulae for $V(h)$ for plane-plane interactions are as follows [44,47]:

$$V_{BR} = \frac{A_h \sigma_c^6}{360\pi h^8}, \quad V_{VDW} = -\frac{A_h}{12\pi h^2}, \quad V_{EDL} = 32\varepsilon_0 \varepsilon_r \kappa \gamma_p \gamma_g \left(\frac{k_B T}{z_v e} \right)^2 \exp(-\kappa h) \quad (A2)$$

The energy potential with primary minimum alone has an inflection point $h = h_m$, where the electrostatic force reaches its maximum, as expressed by Eqs. (3).

Drag Force The CFD-based expressions for drag factor f_d and moment factor f_M for spheroidal particles are [26]:

$$f_d = (0.8707\alpha_s^2 + 0.7908\alpha_s + 0.05844)(\alpha_s + 0.008453)^{-1} \quad (A3)$$

$$f_M = (1.296\alpha_s^2 + 0.1509\alpha_s + 0.03718)(\alpha_s^2 + 0.0843\alpha_s + 0.0002284)^{-1} \quad (A4)$$

Buoyancy force for spherical particles is given by:

$$F_g = (4/3)\pi r_s^3 \Delta\rho \cdot g \quad (A5)$$

where $\Delta\rho$ is the density difference between the particles and water.

Lift force for spherical particles is given by [64]:

$$F_l = \chi r_s^3 \sqrt{\frac{\rho \mu u_s}{r_s^3}} \quad (A6)$$

where r is the pore radius, ρ is density of the fluid, χ is the lift coefficient and it is equal to 89.5 [75].

Capillary force for spherical particles is given by [76]:

$$F_c = -2\pi r_s \gamma_{GL} \sin\varphi \sin(\theta + \varphi) \quad (A7)$$

where γ_{GL} is the interfacial tension between gas and liquid, φ is the water filling angle to indicate the water level surrounding particles, and θ is the contact angle of particles.

Appendix B. Percolation and effective medium theories for permeability.

Equation (19) relates the pore scale velocity with the Darcy velocity, incorporating the pore radius, r , and following averaging, the pore radii distribution, $f(r)$. The permeability in this equation is assumed to be known and hence must be determined from experiments. In reality, the permeability will be a function of the pore size distribution. Accounting for this dependency will allow for more accurately representing the influence of the pore size distribution on the distribution on critical velocities.

For relatively homogeneous porous media, such as well sorted sands or bed reactors used in chemical engineering applications, we can use an effective medium theory approximation of the porous medium such as the one used by Kirkpatrick [77]. In this model, the permeability is given by:

$$k = \frac{\phi r_{eh}^2}{8\tau} \quad (B1)$$

where r_{eh} is the effective radius of the homogenous network used to approximate the porous medium and τ is the tortuosity. The effective radius is determined by solving:

$$\int_0^\infty \frac{r_{eh}^4 - r^4}{r^4 - \left(\frac{z}{2} - 1\right)r_{eh}^4} f(r) dr = 0 \quad (B2)$$

where z is the coordination number of the lattice.

For more heterogeneous porous media, a percolation model can be more accurate. In this case we represent the porous medium as a complete lattice where the conductivity of the smallest bonds ($r < r_{min}$) vanishes. The fraction of conducting pores is given by [78]:

$$\eta(r_{min}) = \int_{r_{min}}^\infty f(r) dr \quad (B3)$$

If the value r_{min} reaches some critical value, r_c , the network will no longer be conducting. The resulting fraction $\eta_c = \eta(r_c)$ is called the percolation

threshold.

With a certain fraction, η , of conducting bonds, we approximate the network by a number of chains which extend infinitely in the direction of flow. The distance within the cross-section between each of these chains is given by:

$$R(r_{\min}) = l \left[\frac{1 - \eta_c}{\eta(r_{\min}) - \eta_c} \right]^\nu \quad (B4)$$

where l is the bond length, and ν is the correlation radius index, which for 3D networks is equal to 0.9. The number density of these chains at each cross section is then.

$$N(r_{\min}) = R(r_{\min})^{-2} \quad (B5)$$

Each chain is characterised by the minimum conducting radius within that chain. Thus we can describe a set of chains by their probability density over the variable r_{\min} :

$$F(r_{\min}) = -\frac{dN(r_{\min})}{dr_{\min}} = \frac{2\nu f(r_{\min})}{(l[1 - \eta_c]^\nu)^2} \left(\int_{r_{\min}}^{r_c} f(r) dr \right)^{(2\nu-1)} \quad (B6)$$

The conductivity of each chain is calculated from the harmonic average of the conductivity of the bonds along the chain. This is calculated from Poiseuille's equation and results in:

$$g_c(r_{\min}) = \frac{\pi}{8} \frac{\int_{r_{\min}}^{\infty} f(r) dr}{\int_{r_{\min}}^{\infty} r^{-4} f(r) dr} \quad (B7)$$

Then we can calculate the total conductivity of the porous medium by averaging these conductivities over the probability distribution $F(r_{\min})$, and dividing by the average cross-sectional area of each chain:

$$k = \frac{1}{A} \int_0^{r_c} g_c(r) F(r) dr, \quad A = \frac{\int_{r_{\min}}^{\infty} f(r) dr}{\pi \int_{r_{\min}}^{\infty} r^2 f(r) dr} \quad (B8)$$

Appendix C. Definition of stochastic model for fines detachment.

Assume probabilistic distribution of the following parameters: particle size r_s , its aspect ratio α_s , lever arm of the normal force l_n , pore radius r , and DLVO parameters ζ_p and ζ_g . Those parameters form vector \mathbf{x} in Euclidian space R^n . For each velocity U , define a domain of attached fines.

$$\Omega_U = \{ \vec{x} \in R^n : U > U_{cr}(\vec{x}) \} \quad (C1)$$

where U_{cr} is the detachment velocity. At first, we concentrate on rolling particles, so U_{cr} given by Eq. (24). The fraction of attached particles under flow with velocity U is equal to probability of the event defined by Eq. (23):

$$P(U > U_{cr}(\vec{x})) = \iiint_{\Omega_U} f_{cr}(\vec{x}) d\mathbf{x}^n \quad (C2)$$

Probability P is equal to zero at $U = 0$, meaning that there is no loose fines (those which detached under any velocity) in the system. The probability P tends to one when U tends to infinity, where all attached particles are detached. The detachable area corresponding velocity U_3 in Fig. 5a is highlighted in grey. Here $f_{cr}(\mathbf{x})$ is the probability density function (PDF) for vector \mathbf{x} . If parameters x_1, x_2, \dots, x_n are distributed independently, their mutual PDF is a product of the individual PDFs for all parameters.

$$f_{cr}(\vec{x}) = \prod_{k=1}^{k=n} f_{cr}^k(x_k) \quad (C3)$$

Equation (24) defines PDF for detachment velocity.

$$f_{cr}(U) = \frac{d}{dU} \left[\iiint_{\Omega_U} f_{cr}(\vec{x}) d\mathbf{x}^n \right] \quad (C4)$$

Concentration of particles attached under flow with velocity U , as it follows from Eq. (26) is.

$$\sigma_{cr}(U) = \sigma^0 \iiint_{\Omega_U} f_{cr}(\vec{x}) d\mathbf{x}^n \quad (C5)$$

and is called the maximum (critical) retention function (MRF). Here σ^0 is the concentration of detachable fines that corresponds to $U = 0$.

Three mechanical-equilibrium criteria (13), (15), and (16) can be incorporated in the model (C5) by defining a minimum detachment velocity for each state \mathbf{x} :

$$U_{cr}(\vec{x}) = \min \{ U_{cr}^r(\vec{x}), U_{cr}^s(\vec{x}), U_{cr}^l(\vec{x}) \} \quad (C6)$$

where the three detachment velocities U_{cr}^r , U_{cr}^s , and U_{cr}^l are determined from Eqs. (13), (15), and (16), respectively.

Appendix D. Probability distribution function for minimum of two stochastic variables.

Consider two independently distributed positive values y and z with PDFs $f(y)$ and $g(z)$, respectively. Let us calculate the PDF for their minimum x_n :

$$x_n = \min\{y, z\} \quad (D1)$$

If $y < z$, this event comprises all z varying from y to infinity. If $z < y$, value all y that vary from z to infinity.

Fig. 12 shows that if $x_n = y$, then z exceeds y : $y < z < \infty$; if $x_n = z$ then y exceeds z : $z < y < \infty$. The independence of those two events follows from the independence of variables y and z . Therefore, the probability of the sum of two events is:

$$f_n(x_n) = f(x_n) \int_{x_n}^{\infty} g(y) dy + g(x_n) \int_{x_n}^{\infty} f(x) dx \quad (D2)$$

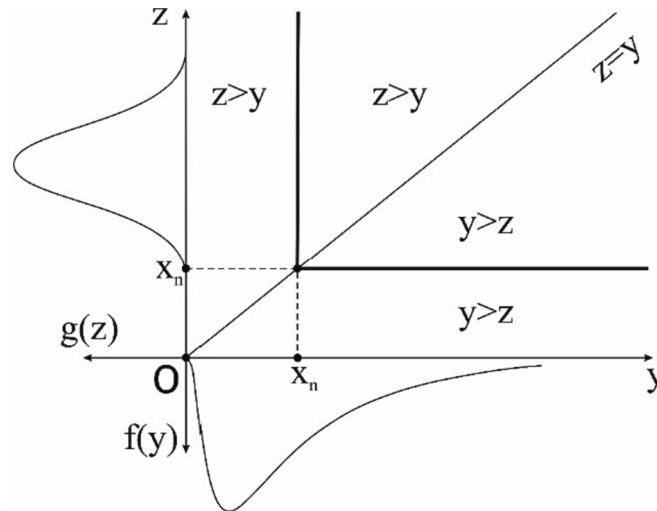


Fig. 12. Distribution for minimum of two stochastic variables x and y ; individual PDFs for x and y are $f(x)$ and $g(y)$, respectively.

Appendix E. Sensitivity coefficients with respect to multiple parameters.

Consider smooth function of n variables.

$$y = y(x_1, x_2, \dots, x_n) \quad (E1)$$

and normalised response of y to normalised perturbation of variable x_i . The limit of their ratio with perturbation of variable x_i tending to zero.

$$\Gamma_i = \lim_{\Delta x_i \rightarrow 0} \frac{\Delta y}{y} : \frac{\Delta x_i}{x_i} = \lim_{\Delta x_i \rightarrow 0} \frac{x_i}{y} \frac{\Delta y}{\Delta x_i} = \frac{x_i}{y} \frac{\partial y(x_1, x_2, \dots, x_n)}{\partial x_i}, \quad i = 1, 2, \dots, n \quad (E2)$$

is called the sensitivity coefficient of y with respect to variable x_i .

If function (E1) is given by an explicit formula, the sensitivity coefficient Γ_i is determined by calculation of the partial derivative by Eq. (E2). If dependency (E1) is provided by a numerical model, sensitivity coefficients are calculated by Eq. (E2) using finite differences.

Comparison of different sensitivity coefficients allows determining the most influential factors. During matching of experimental data by a model, the sensitivity coefficients of measured data y by the tuning parameters are calculated. The matching starts by tuning the parameter with highest sensitivity coefficient, then other parameters are considered in order of decreasing of their sensitivity coefficients.

Appendix F. Supplementary data

Supplementary data to this article can be found online at <https://doi.org/10.1016/j.cej.2023.145436>.

References

- [1] V. Gitis, I. Rubinstein, M. Livshits, G. Ziskind, Deep-bed filtration model with multistage deposition kinetics, *Chem. Eng. J.* 163 (1–2) (2010) 78–85.
- [2] H. Yuan, A.A. Shapiro, Modeling non-Fickian transport and hyperexponential deposition for deep bed filtration, *Chem. Eng. J.* 162 (3) (2010) 974–988.
- [3] H. Yuan, A.A. Shapiro, A mathematical model for non-monotonic deposition profiles in deep bed filtration systems, *Chem. Eng. J.* 166 (1) (2011) 105–115.
- [4] P. Bedrikovetsky, *Mathematical theory of oil and gas recovery (with applications to ex-USSR oil and gas fields)*, Springer Science & Business Media, London, 2013.
- [5] H. Yuan, Z. You, A. Shapiro, P. Bedrikovetsky, Improved population balance model for straining-dominant deep bed filtration using network calculations, *Chem. Eng. J.* 226 (2013) 227–237.
- [6] M. Asraf-Snir, V. Gitis, Tracer studies with fluorescent-dyed microorganisms—A new method for determination of residence time in chlorination reactors, *Chem. Eng. J.* 166 (2) (2011) 579–585.
- [7] Z. Guo, F. Hussain, Y. Cinar, Physical and analytical modelling of permeability damage in bituminous coal caused by fines migration during water production, *J. Nat. Gas Sci. Eng.* 35 (2016) 331–346.

- [8] Z. Guo, P.N.H. Vu, F. Hussain, A laboratory study of the effect of creep and fines migration on coal permeability during single-phase flow, *Int. J. Coal Geol.* 200 (2018) 61–76.
- [9] Y. Yang, W. Yuan, J. Hou, Z. You, Review on physical and chemical factors affecting fines migration in porous media, *Water Res.* 214 (2022) 118172.
- [10] H.S. Fogler, *Elements of chemical reaction engineering*, 4th ed., Prentice Hall, Upper Saddle River, NJ, 2006.
- [11] A.D. Monfared, M. Ghazanfari, M. Jamialahmadi, A. Helalizadeh, Adsorption of silica nanoparticles onto calcite: Equilibrium, kinetic, thermodynamic and DLVO analysis, *Chem. Eng. J.* 281 (2015) 334–344.
- [12] H.H. Liu, Y. Cohen, Multimedia environmental distribution of engineered nanomaterials, *Environ. Sci. Tech.* 48 (6) (2014) 3281–3292.
- [13] X. Ling, Z. Yan, Y. Liu, G. Lu, Transport of nanoparticles in porous media and its effects on the co-existing pollutants, *Environ. Pollut.* 283 (2021), 117098.
- [14] C.V. Chrysikopoulos, T.V. Fountouli, Cotransport of titanium dioxide nanoparticles and formaldehyde in saturated and unsaturated columns packed with quartz sand, *Vadose Zone J.* 22 (1) (2023) e20175.
- [15] C.V. Chrysikopoulos, N.P. Sotiropoulos, N.G. Kallithrakas-Kontos, Cotransport of graphene oxide nanoparticles and kaolinite colloids in porous media, *Transport Porous Med.* 119 (1) (2017) 181–204.
- [16] A.E. Bayat, R. Junin, R. Mohsin, M. Hokmabadi, S. Shamsirband, Influence of clay particles on Al₂O₃ and TiO₂ nanoparticles transport and retention through limestone porous media: measurements and mechanisms, *J. Nanopart. Res.* 17 (2015) 1–14.
- [17] G.V.C. Malgaresi, H. Zhang, C.V. Chrysikopoulos, P. Bedrikovetsky, Cotransport of suspended colloids and nanoparticles in porous media, *Transport Porous Med.* 128 (1) (2019) 153–177.
- [18] W.P. Johnson, E. Pazmino, *Colloid (Nano- and Micro-Particle) Transport and Surface Interaction in Groundwater The Groundwater project*, Guelph, Ontario, Canada, 2023.
- [19] V.E. Katzourakis, C.V. Chrysikopoulos, Two-site colloid transport with reversible and irreversible attachment: analytical solutions, *Adv. Water Resour.* 130 (2019) 29–36.
- [20] V.E. Katzourakis, C.V. Chrysikopoulos, Impact of spatially variable collision efficiency on the transport of biocolloids in geochemically heterogeneous porous media, *Water Resour. Res.* 54 (6) (2018) 3841–3862.
- [21] D. Zhang, Q. Li, V. Prigiobbe, Population balance modeling of homogeneous viral aggregation, *Chem. Eng. Sci.* 247 (2022), 117035.
- [22] Q. Li, V. Prigiobbe, Modeling nanoparticle transport in porous media in the presence of a foam, *Transport Porous Med.* 131 (1) (2020) 269–288.
- [23] V.E. Katzourakis, C.V. Chrysikopoulos, Modeling the transport of aggregating nanoparticles in porous media, *Water Resour. Res.* 57 (1) (2021), e2020WR027946.
- [24] Y. Du, S.A. Bradford, C. Shen, T. Li, X. Bi, D. Liu, Y. Huang, Novel analytical expressions for determining van der Waals interaction between a particle and air–water interface: Unexpected stronger van der Waals force than capillary force, *J. Colloid Interface Sci.* 610 (2022) 982–993.
- [25] T. Li, C. Shen, W.P. Johnson, H. Ma, C. Jin, C. Zhang, X. Chu, K. Ma, B. Xing, Important role of concave surfaces in deposition of colloids under favorable conditions as revealed by microscale visualization, *Environ. Sci. Tech.* 56 (7) (2022) 4121–4131.
- [26] H.Z. Ting, P. Bedrikovetsky, Z.F. Tian, T. Carageorgos, Impact of shape on particle detachment in linear shear flows, *Chem. Eng. Sci.* 241 (2021), 116658.
- [27] P. Bedrikovetsky, F.D. Siqueira, C.A. Furtado, A.L.S. Souza, Modified Particle Detachment Model for Colloidal Transport in Porous Media, *Transport Porous Med.* 86 (2) (2011) 383–413, <https://doi.org/10.1007/s11242-010-9626-4>.
- [28] P. Bedrikovetsky, A. Zeinijahromi, F.D. Siqueira, C.A. Furtado, A.L.S. de Souza, Particle Detachment Under Velocity Alternation During Suspension Transport in Porous Media, *Transport Porous Med.* 91 (1) (2012) 173–197, <https://doi.org/10.1007/s11242-011-9839-1>.
- [29] P. Bedrikovetsky, Y. Osipov, L. Kuzmina, G. Malgaresi, Exact upscaling for transport of size-distributed colloids, *Water Resour. Res.* 55 (2) (2019) 1011–1039.
- [30] S.A. Bradford, S. Torkzaban, A. Shapiro, A theoretical analysis of colloid attachment and straining in chemically heterogeneous porous media, *Langmuir: ACS J. Surf. Colloids* 29 (23) (2013) 6944–6952, <https://doi.org/10.1021/la4011357>.
- [31] B. Kianfar, J. Tian, J. Rozemeijer, B. van der Zaan, T.A. Bogaard, J.W. Foppen, Transport characteristics of DNA-tagged silica colloids as a colloidal tracer in saturated sand columns; role of solution chemistry, flow velocity, and sand grain size, *J. Contam. Hydrol.* 246 (2022), 103954.
- [32] D. Lin, L. Hu, S.A. Bradford, X. Zhang, I.M. Lo, Pore-network modeling of colloid transport and retention considering surface deposition, hydrodynamic bridging, and straining, *J. Hydrol.* 603 (2021), 127020.
- [33] Y. Yang, P. Bedrikovetsky, Exact Solutions for Nonlinear High Retention-Concentration Fines Migration, *Transport Porous Med.* 119 (2) (2017) 351–372.
- [34] M. Coronado, M.A. Díaz-Viera, Modeling fines migration and permeability loss caused by low salinity in porous media, *J. Pet. Sci. Eng.* 150 (2017) 355–365.
- [35] R. Muneer, M.R. Hashmet, P. Pourafshary, DLVO Modeling to Predict Critical Salt Concentration to Initiate Fines Migration Pre-and Post-Nanofluid Treatment in Sandstones, *Spe J.* 27(04) (2022) 1915–1929.
- [36] R. Muneer, P. Pourafshary, M.R. Hashmet, An integrated modeling approach to predict critical flow rate for fines migration initiation in sandstone reservoirs and water-bearing formations, *J. Mol. Liq.* 376 (2023), 121462.
- [37] B. Yuan, R.G. Moganloo, W. Wang, Using nanofluids to control fines migration for oil recovery: Nanofluids co-injection or nanofluids pre-flush? A comprehensive answer, *Fuel* 215 (2018) 474–483.
- [38] B. Yuan, R.G. Moganloo, Nanofluid pre-treatment, an effective strategy to improve the performance of low-salinity waterflooding, *J. Pet. Sci. Eng.* 165 (2018) 978–991.
- [39] F. Huang, C. Dong, Z. You, X. Shang, Detachment of coal fines deposited in proppant packs induced by single-phase water flow: Theoretical and experimental analyses, *Int. J. Coal Geol.* 239 (2021), 103728.
- [40] Z. You, P. Bedrikovetsky, A. Badalyan, M. Hand, Particle mobilization in porous media: Temperature effects on competing electrostatic and drag forces, *Geophys. Res. Lett.* 42 (8) (2015) 2852–2860.
- [41] H. Yuan, A. Shapiro, Z. You, A. Badalyan, Estimating filtration coefficients for straining from percolation and random walk theories, *Chem. Eng. J.* 210 (2012) 63–73.
- [42] T.V. Fountouli, C.V. Chrysikopoulos, Effect of clay colloid particles on formaldehyde transport in unsaturated porous media, *Water* 12 (12) (2020) 3541.
- [43] W.P. Johnson, Quantitative linking of nanoscale interactions to continuum-scale nanoparticle and microplastic transport in environmental granular media, *Environ. Sci. Tech.* 54 (13) (2020) 8032–8042.
- [44] T. Mahmood, A. Amirtharajah, T.W. Sturm, K.E. Dennett, A micromechanics approach for attachment and detachment of asymmetric colloidal particles, *Colloids Surf. A Physicochem. Eng. Asp.* 177 (2–3) (2001) 99–110.
- [45] S. Bhattacharjee, J.Y. Chen, M. Elimelech, DLVO interaction energy between spheroidal particles and a flat surface, *Colloids Surf. A Physicochem. Eng. Asp.* 165 (1–3) (2000) 143–156.
- [46] S. Sternberg, *Lectures on differential geometry*, American Mathematical Soc. 1999.
- [47] J.N. Israelachvili, *Intermolecular and surface forces: revised third edition*, Academic press 2011.
- [48] M. Elimelech, J. Gregory, X. Jia, *Particle deposition and aggregation: measurement, modelling and simulation*, Butterworth-Heinemann 2013.
- [49] G. Ziskind, Particle resuspension from surfaces: revisited and re-evaluated, *Rev. Chem. Eng.* 22 (1–2) (2006) 1–123.
- [50] J. Shang, M. Flury, G. Chen, J. Zhuang, Impact of flow rate, water content, and capillary forces on in situ colloid mobilization during infiltration in unsaturated sediments, *Water Resour. Res.* 44 (6) (2008).
- [51] F. Huang, Y. Kang, L. You, X. Li, Z. You, Massive fines detachment induced by moving gas-water interfaces during early stage two-phase flow in coalbed methane reservoirs, *Fuel* 222 (2018) 193–206.
- [52] A.D. Polyani, V.F. Zaitsev, A. Moussiaux, *Handbook of first-order partial differential equations*, CRC Press, 2001.
- [53] A.D. Polyani, V.F. Zaitsev, *Handbook of nonlinear partial differential equations*, Chapman & Hall/CRC, Boca Raton, FL, 2006.
- [54] A. Hashemi, S. Borazjani, B. Dang-Le, G. Yin Loi, C. Nguyen Cao, A. Badalyan, P. Bedrikovetsky, Formation damage by fines breakage and migration, SPE International Conference and Exhibition on Formation Damage Control, SPE, 2022, p. D011S002R006.
- [55] H. Cheng, Z. Zhang, Q. Liu, J. Leung, A new method for determining platy particle aspect ratio: A kaolinite case study, *Appl. Clay Sci.* 97 (2014) 125–131.
- [56] Z. Xie, S. Wang, Y. Shen, CFD-DEM modelling of the migration of fines in suspension flow through a solid packed bed, *Chem. Eng. Sci.* 231 (2021), 116261.
- [57] X. Peng, S. Zhu, Z. You, Z. Du, P. Deng, C. Wang, M. Wang, Numerical simulation study of fines migration impacts on an early water drainage period in undersaturated coal seam gas reservoirs, *Geofluids* 2019 (2019) 1–16.
- [58] A. Kalantariasi, P. Bedrikovetsky, Stabilization of external filter cake by colloidal forces in a “well-reservoir” system, *Ind. Eng. Chem. Res.* 53 (2) (2013) 930–944.
- [59] S. Torkzaban, S.A. Bradford, J.L. Vanderzalm, B.M. Patterson, B. Harris, H. Prommer, Colloid release and clogging in porous media: Effects of solution ionic strength and flow velocity, *J. Contam. Hydrol.* 181 (2015) 161–171.
- [60] J.P. Mathews, S. Eser, P.G. Hatcher, A.W. Scaroni, The shape of pulverized bituminous vitrinite coal particles, *Kona Powder Part. J.* 25 (0) (2007) 145–152.
- [61] F. Huang, Y. Kang, Z. You, L. You, C. Xu, X. You, Critical conditions for massive fines detachment induced by single-phase flow in coalbed methane reservoirs: modeling and experiments, *Energy Fuel* 31 (7) (2017) 6782–6793.
- [62] H. Safari, B.J. Balcom, A. Afrough, Characterization of pore and grain size distributions in porous geological samples—An image processing workflow, *Comput. Geosci.* 156 (2021), 104895.
- [63] P. Bedrikovetsky, D. Marchesin, F. Shecaira, A.L. Souza, P.V. Milanez, E. Rezende, Characterisation of deep bed filtration system from laboratory pressure drop measurements, *J Petrol Sci Eng* 32(2-4) (2001) 167-177. [https://doi.org/Pii/S0920-4105\(01\)00159-0](https://doi.org/Pii/S0920-4105(01)00159-0) Doi 10.1016/S0920-4105(01)00159-0.
- [64] P. Saffman, The lift on a small sphere in a slow shear flow, *J. Fluid Mech.* 22 (02) (1965) 385–400.
- [65] I. Akhatov, J. Hoey, O. Swenson, D. Schulz, Aerosol focusing in micro-capillaries: Theory and experiment, *J. Aerosol. Sci.* 39 (8) (2008) 691–709.
- [66] G. Ziskind, M. Fichman, C. Gutfinger, Resuspension of particulates from surfaces to turbulent flows—review and analysis, *J. Aerosol. Sci.* 26 (4) (1995) 613–644.
- [67] A.A. Shapiro, Elliptic equation for random walks. Application to transport in microporous media, *Phys. A: Stat. Mech. Appl.* 375 (1) (2007) 81–96.
- [68] A.A. Shapiro, Continuous upscaling and averaging, *Chem. Eng. Sci.* 234 (2021), 116454.
- [69] A.A. Shapiro, Continuous upscaling of the 3D diffusion equation in a heterogeneous medium, *Chem. Eng. Sci.* 248 (2022), 117247.
- [70] A. Shapiro, J. Wesselingh, Gas transport in tight porous media: Gas kinetic approach, *Chem. Eng. J.* 142 (1) (2008) 14–22.
- [71] Z. Xie, S. Wang, Y. Shen, A novel hybrid CFD-DEM method for high-fidelity multi-resolution modelling of cross-scale particulate flow, *Chem. Eng. J.* 455 (2023), 140731.

- [72] A.D. Polyaniin, A.M. Kutepov, D. Kazenin, A. Vyazmin, Hydrodynamics, mass and heat transfer in chemical engineering, CRC Press, 2001.
- [73] A. Polyaniin, V.V. Dilman, Methods of modeling equations and analogies in chemical engineering, CRC Press, Boca Raton, FI, 1994.
- [74] S. Bhattacharjee, M. Elimelech, Surface element integration: a novel technique for evaluation of DLVO interaction between a particle and a flat plate, *J. Colloid Interface Sci.* 193 (2) (1997) 273–285.
- [75] S.-T. Kang, A. Subramani, E.M. Hoek, M.A. Deshusses, M.R. Matsumoto, Direct observation of biofouling in cross-flow microfiltration: mechanisms of deposition and release, *J. Membr. Sci.* 244 (1) (2004) 151–165.
- [76] L. Chequer, P. Bedrikovetsky, A. Badalyan, V. Gitis, Water level and mobilisation of colloids in porous media, *Adv. Water Resour.* 143 (2020), 103670.
- [77] S. Kirkpatrick, Percolation and conduction, *Rev. Mod. Phys.* 45 (4) (1973) 574–588.
- [78] V. Selyakov, V. Kadet, Percolation models for transport in porous media: with applications to reservoir engineering, Springer Science & Business Media, 2013.

4. Formation damage by fines breakage and migration

Hashemi, A., Borazjani, S., Dang-Le, B., Yin Loi, G., Nguyen Cao, C., Badalyan, A. and Bedrikovetsky, P. 2022, February.

In SPE International Conference and Exhibition on Formation Damage Control (p. D011S002R006). SPE.

Statement of Authorship

Title of Paper	Formation damage by fines breakage and migration		
Publication Status	<input checked="" type="checkbox"/> Published	<input type="checkbox"/> Submitted for Publication	
	<input type="checkbox"/> Accepted for Publication	<input type="checkbox"/> Unpublished and Unsubmitted work written in manuscript style	
Publication Details	Hashemi, A., Borazjani, S., Dang-Le, B., Yin Loi, G., Nguyen Cao, C., Badalyan, A. and Bedrikovetsky, P., 2022, February. Formation damage by fines breakage and migration. In SPE International Conference and Exhibition on Formation Damage Control (p. D011S002R006). SPE.		

Principal Author

Name of Principal Author (Candidate)	Abolfazl Hashemi		
Contribution to the Paper	Collecting data, performing lab data analysis, deriving the equations, writing code for the authigenic particle detachment, preparing the graphs, writing part of the manuscript.		
Overall percentage (%)	80%		
Certification:	This paper reports on original research I conducted during the period of my Higher Degree by Research candidature and is not subject to any obligations or contractual agreements with a third part that would constrain its inclusion in this thesis. I am the primary author of this paper.		
Signature		Date	15/11/2023

Co-Author Contributions

By signing the Statement of Authorship, each author certifies that:

- I. The candidate's stated contribution to the publication is accurate (as detailed above);
- II. Permission is granted to the candidate to include the publication in the thesis; and
- III. The sum of all co-author contributions is equal to 100% less the candidate's stated contribution

Name of Co-Author	Sara Borazjani		
Contribution to the Paper	Co-supervising, aiding in the derivations of equations and checking the results		
Signature		Date	15/11/2023

Name of Co-Author	Bryant Dang-Le		
Contribution to the Paper	Collecting and analysing lab data, collecting field data.		
Signature	Bryant Dang-Le	Date	15/11/2023

Name of Co-Author	Grace Loi		
Contribution to the Paper	Collecting literature data, writing code, and analysing detrital particle detachment		
Signature		Date	15/11/2023

Name of Co-Author	Cuong Cao Nguyen		
Contribution to the Paper	Collecting literature data, writing code and analysing detrital particle detachment		
Signature		Date	15/11/2023

Name of Co-Author	Alex Badalyan		
Contribution to the Paper	Supervising lab design and data collection		
Signature		Date	15/11/2023

Name of Co-Author	Pavel Bedrikovetsky		
Contribution to the Paper	Methodology and supervision.		
Signature		Date	15/11/2023



Society of Petroleum Engineers

SPE-208810-MS

Formation Damage by Fines Breakage and Migration

Abolfazl Hashemi, Sara Borazjani, Bryant Dang-Le, Grace Yin Loi, Cuong Nguyen Cao, Alex Badalyan, and Pavel Bedrikovetsky, University of Adelaide

Copyright 2022, Society of Petroleum Engineers DOI [10.2118/208810-MS](https://doi.org/10.2118/208810-MS)

This paper was prepared for presentation at the SPE International Conference and Exhibition on Formation Damage Control, Lafayette, Louisiana, USA, 23 - 24 February 2022.

This paper was selected for presentation by an SPE program committee following review of information contained in an abstract submitted by the author(s). Contents of the paper have not been reviewed by the Society of Petroleum Engineers and are subject to correction by the author(s). The material does not necessarily reflect any position of the Society of Petroleum Engineers, its officers, or members. Electronic reproduction, distribution, or storage of any part of this paper without the written consent of the Society of Petroleum Engineers is prohibited. Permission to reproduce in print is restricted to an abstract of not more than 300 words; illustrations may not be copied. The abstract must contain conspicuous acknowledgment of SPE copyright.

Abstract

Fines migration is one of the most drastic causes for formation damage - the detached clays migrate and impairs well productivity. Two types of damaging clays are encountered in petroleum reservoirs: authigenic clays that grew on the grain surfaces during geological times, and detrital clays that have been broken off the grains by local stresses. Detailed laboratory and mathematical modelling have been carried out for detrital-clay formation damage. The theory for formation damage by authigenic clays is not available. The aim of this work is the development of a laboratory procedure to estimate formation damage by authigenic clays and the derivation of a mathematical model for core scale. We performed two test of corefloods using Castlegate core samples. In the first test, injection rate increased in a stepwise manner up to 100 mL/min and in the second one up to a 200mL/min to make sure both detrital and authigenic particles are detached. The pressure drop across the overall core and the concentration of the fine in the produced fluid have been measured. We have derived equations for authigenic-fines detachment using the beam theory and the von Mises failure criteria to obtain analytical solutions for linear system of equations. Matching the laboratory data by the analytical model allows determining the percentage of authigenic and detrital clays in the cores. The laboratory data exhibit a good match with the mathematical model for the two coreflood tests. The non-monotonic change of the concentration of the detached fine, with the initial and final risings, determines the type curve that evidence the mobilization of both, authigenic and detrital clays. The treatment of the measured data in test#2 shows that 82% of the initial attached particles are authigenic. The model parameters in order of decrease of their sensitivity are contact-bond radius, pore radius, particle size, lever-arm ratio, tensile strength and aspect ratio. A novel experimental procedure to determine fines-migration formation damage by authigenic and detrital clays was developed. A newly derived mathematical model allows determining the model coefficients from the laboratory tests and predict future detachment rate of authigenic and detrital particles.

Introduction

Fines migration is one of the most severe reasons for formation damage - the detached clays migrate and damages well productivity. Two types of damaging clays exist in petroleum reservoirs: authigenic clays that

grew on the grain surfaces during geological times, and detrital clays that have been broken off the grains by local stresses (Sarkisyan 1971, 1972; Dutta et al. 1986; Farrell et al. 2021). Wilson et al. 1977 inspected over 3000 sandstones of different geological ages and discovered that authigenic clays exist in most of the samples. Fig. 1 shows the typical shapes of authigenic and detrital kaolinites in porous media. In Fig. 1a the booklet shape and the growth orientation of the authigenic kaolinite is evident, while detrital kaolinite in Fig. 1b is an aggregate of particles with no specific orientation (Wilson et al. 1977).

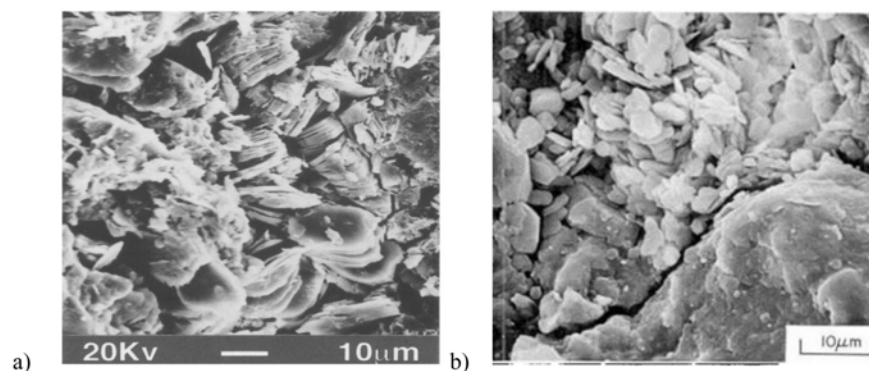


Figure 1—SEM photographs a) Authigenic kaolinite (Aróstegui et al. 2000), b) Detrital kaolinite (Wilson et al. 1977)

Detailed laboratory and mathematical modelling have been carried out for detrital-clay detachment and their consequent formation damage (Bedrikovetsky et al. 2011, 2012; Russell et al. 2017; and, Prempeh et al. 2020). Detrital particles are attached to a substrate by an electrostatic force and can be modelled using the DLVO theory. However, most of the core samples have certain amount of authigenic clay content, i.e. clay particles are bonded to rock (Wilson and Tillman, 1974; Wilson et al. 1977). To study the formation damage due to the detachment of the authigenic clay, a new formulation should be presented. The formulation should be based on failure or breakage criteria of contact bond between particle and a substrate. To the best of our knowledge, the theory for detachment of single authigenic particle is not available. The purpose of this study is the development of a laboratory-based mathematical model to estimate formation damage by authigenic clays. To be able to describe the detachment of the authigenic clays, we investigated different approaches in modelling of the bonded particles. De Josselin de Jong 1969 used photoelastic technique to show the change of stress at a particle due to a contact by neighboring particle. He observed that the effect of particle-particle contact is very local and mainly between the centre of two connecting particles. So, to model particle-particle contact or particle-wall contact, he placed a beam between two grains. Based on this finding Cundall and stark 1979 developed the theory of Discrete Element Model (DEM), where two springs are placed between two rigid particles. One resists against normal force and the other one against shear force. And later on, Potyondy and Cundall 2004 proposed the theory of Bonded Particle Model (BPM). In their theory, a parallel bond approximates the mechanical behavior of a brittle elastic cement connecting the two bonded particles. The parallel bond can be imagined as set of elastic springs uniformly distributed over cross section. There would be two sets of spring, one perpendicular to contact plane and one parallel to contact plane. The first set carries the normal stress and the later one carries shear stress. If the maximum tensile stress surpasses the tensile strength of the material or the maximum shear stress surpasses the shear strength of the material, the parallel bond breaks. Further on, Obermayr et al. 2013 and Andre et al. 2012 have developed the idea of Cohesive Beam Model (CBM) to formulate bonding cement between particles. Instead of springs, they considered the bond as a continuous beam with small deformation. In order to predict the state of stress and defamation of the beam due to the applied forces, Andre et al. 2012 used Euler-Bernoulli beam theory (Timoshenko, 1983). In this theory, the axial length of the beam is considered at least ten times more than other dimensions. Obermayr et al. 2013 used Timoshenko beam model (Timoshenko and Goodier 1971). In Euler-Bernoulli beams, the shear deformation of the beam cross sections is neglected, so that the transverse

plane remains plane and perpendicular to the axial direction. However, in Timoshenko beam theory, the shear deformation is considered and as a result is more accurate for describing the behavior of short beams (Asghari et al. 2011). A beam with one fixed end and one free end is called cantilever beam (Slaughter 2012). For slender member, because there is no transverse stresses (i.e. shear and normal stresses transverse to the beam axis) at the boundary, the transverse stresses inside the beam can be ignored.

The elastic cantilever beam theory has been applied for different materials and different sizes. Liu et al. 2008 used the theory to study the behavior of silicon micro-cantilever beam which is a brittle material. Stephens et al. 2001 and Jin et al. 2018 investigated the failure analysis of Nickel micro-post and reinforced concrete columns which have ductile behavior. Furthermore, Young et al. 2008 and Robinson 1970 extended the beam theory to investigate the detachment of cantilevered seacliffs and big pieces of sandstone rock in Zion Canyon, respectively. In their study the ratio of thickness to length is comparatively high. Therefore, they consider not only normal stress but also shear stress distribution in the structures. Normal stress and shear stress distributions have been derived by Timoshenko and Goodier (Timoshenko and Goodier 1971) for an elastic cantilever beam with narrow rectangular cross-section. The shear stress has a parabolic shape which is zero at the boundary and maximum at the centre of the beam.

In this paper, we assume the bond between the authigenic clay and rock acts as a cantilever beam. Cohesive Beam Model is applied to formulate the detachment of the particle due to the applied drag force. The stress state at the bond is governed by Timoshenko beam theory (Timoshenko and Goodier 1951). These equations are applicable for elastic limit of both brittle (elastic) and ductile (elastic-plastic) material and only different failure criteria are applied (Archer et al. 1978). Increasing the fluid drag force on a particle can change the stress state at its bond and by applying a related failure criteria, the detachment of the particle from a substrate is predicted. Kaolinite in porous media is assumed to be elastic-perfectly plastic. This denotes that for an uniaxial loading, there is an elastic region where the stress is changing linearly with strain up to a yield stress (σ_Y) and after the yield stress, the stress remains at σ_Y as the strain continues to increase. For defining the failure for this type of material, yield criteria is applied. The von Mises yield criterion is used to define failure.

For detachment of every particle, a specific drag force or a fluid velocity needs to be applied. Since, there are large number of particles with different random properties in porous media, by considering a distribution for each property, we can get a distribution for detachment velocity. By taking integral from this distribution bounding to experimental velocities, we can obtain the amount of detachment between two fluid velocities. The same procedure is done for detrital particles and authigenic particles. Total detachment concentration is the sum of authigenic and detrital particles. The total detachment is matched with laboratory data. Having obtained the matching parameters, maximum retention function curve can be plotted. This new maximum retention function takes into account the detachment of both authigenic and detrital particles.

This manuscript is structured as follows. Section 2 presents the assumptions, the mathematical modelling for detachment of detrital and authigenic particles, the formulations of maximum retention function, and the formation damage formulation. Section 3 contains laboratory study including the description of our setup, the procedure, and the data collection. Section 4 discusses the matching procedures and the results. Section 5 includes a brief summary and conclusions.

Physics of fines detachemnt in porous media

In this part we present the assumptions of our models (section 2.1), governing equation for detrital particle detachment (section 2.2), and governing equations for detachment of authigenic particle (section 2.3), finally the formation damage formulation and solutions, which are applicable for both detrital and authigenic particles, are presented in the last section (section 2.4).

Assumptions

We make the following simplifying and reasonable assumptions in order to solve the general models. The main assumptions for fines migration are: diffusive flux on particle in porous media is negligible, incompressibility for the system of particles suspended in the carrier fluid and of retained particles; Darcy's law for single phase flow of carrying suspended particle fluid; the permeability changes as a function of strained particle concentration, and linear kinetics for particle strained by the rock from the suspension, and porous media is modelled as a bundle of parallel capillary tubes with different radii. For detachment of authigenic particles, the main assumptions are: the material is homogenous and isotropic, the material of the bond and the particle is the same, deformation of the material is small and it does not change the value of fluid drag force, stress-strain curve in kaolinite is considered as elastic-perfectly plastic, in elastic-perfectly plastic material yield stress is the same as the tensile strength, and failure at any point is the same as breakage at that point.

Mechanisms of detrital particle mobilisation

Detrital particle detachment is studied using a torque balance for a particle with simple spherical shape. A representation of an attached particle with the acting forces is presented in Fig. 2. Particle detachment in porous media can occur by lifting, sliding, or rolling. However, studies have shown that rolling is the most likely detachment mechanic (Sharma et al. 1992). The effective forces on the particle are the drag force exerted on particle by fluid flow, F_d , the lifting force, F_L , the force due to gravity, F_g , and the electrostatic force, F_e . The drag and lifting forces will create detaching torques, the electrostatic force will create an attaching torque, and the gravitational force will create either a detaching or attaching torque based on the particles situation inside the pore space. Studies have shown that in general the gravitational and lifting forces are much smaller than the drag and electrostatic forces (You et al. 2015). Therefore, in this study only rolling is considered and lifting and gravity forces are ignored.

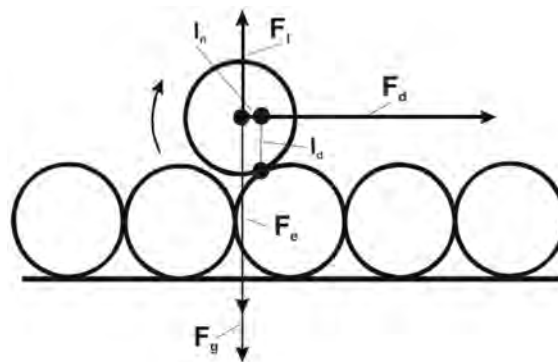


Figure 2—Forces acting on a detrital particle: drag, lift, electrostatic, and gravitational forces (by Bedrikovetsky et al. 2011).

As a result, detachment is mainly governed by the strength of the torques created by the electrostatic and hydrodynamic drag forces. The equation which dictates particle detachment is:

$$T_a - T_d = F_e l_n - F_d l_d \leq 0 \quad (1)$$

where l_d and l_n are the distance between acting lines of drag and electrostatic forces and the point of rotation, T_a and T_d are the attached and detached torques of the electrostatic and drag forces, respectively.

Drag force is the hydrodynamic force acting on the particle and mostly depends on the carrier fluid velocity. Equation for drag force is (O'Neill 1968):

$$F_d = 6\pi\mu r_s V \omega \quad (2)$$

where μ is the fluid viscosity, r_s is the particle radius, V is the interstitial fluid velocity, and ϖ is the shape factor, which for a perfect sphere is 1.7009.

Ting et al. 2021 modelled kaolinite particles having a range of shapes, changing from a perfect sphere to a flat cylinder. They derived a shape factor as follows:

$$\varpi = (0.8306\alpha_s^2 + 0.8525\alpha_s + 0.03278)(\alpha_s + 0.00294)^{-1} \quad (3)$$

where, α_s is the aspect ratio (i.e. thickness divided by length of the particle).

Each detrital particle is detached if detaching torque is more the attaching torque (i.e. Eq.1). For a constat fine geometry and brine composition, drag in Eq. (1) is a function of velocity. For a particular velocity, Eq. (1) concludes which particles are mobilised and which stay attached. Therefore, the attached concentration of particles σ_a is a function of velocity and can be presented as the following:

$$\sigma_a = \sigma_{cr}(U) \quad (4)$$

This expression is called the maximum retention function (Bedrikovetsky et al. 2011, 2012). The plot of this reation (i.e. Eq. 4) is presented in Fig. 3. At zero fluid injection rate, all the detrital particles are attached to a sand surface. Increasing the injection rate, increases the drag force and consequently the concentration of attached partilces is reduced. At maximum velocity (U_m), all detrital particles are detached, so concentration of detrital particles withen porous media is zero. Fig. 3 also displays how maximum retention function can be obtained experimentally by measurements of the amount of particle detachments $\Delta\sigma_n$ by increasing velocity from U_n to U_{n+1} where $n=1,2$.

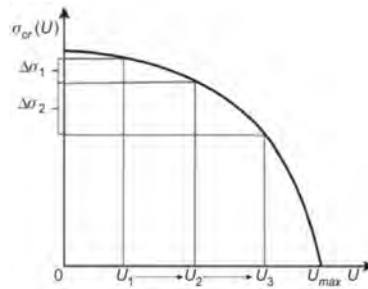


Figure 3—Maximum retention function for detrital particles as a function of flow velocity (by Bedrikovetsky et al. 2011).

The electrostatic force is computed from the extended DLVO (Derjaguin-Landau-Verwey-Overbeek) theory accounting for the interacting energies between the particles and the grain surface. The total energy is the sum of the London-Van der Waals, Electrical Double Layer, and Born Repulsive potentials (Derjaguin and Landau 1941; Elimelech et al. 2013; Gregory 1981; Hogg et al. 1966; Israelachvili 2015; Verwey et al. 1999).

$$\begin{aligned} V_{total} &= V_{LVW} + V_{EDL} + V_{BR} \\ V_{LVW} &= -\frac{A_{132}r_s}{6h} \\ V_{EDL} &= 64\pi\epsilon_m\epsilon_0r_s\left(\frac{k_B T e}{ze}\right)^2 \gamma_p \gamma_s \exp(-\kappa h) \\ V_{BR} &= \frac{A_{132}r_s\sigma_{LJ}^6}{1260h^7} \end{aligned} \quad (5)$$

where V values are different potential energies, A_{132} is the Hamaker constant, h is the particle-surface separation distance, k_B is the Boltzmann constant (4.116×10^{-21} J), T is the absolute temperature in degrees Kelvin, κ is the Debye-Huckel factor, γ_p and γ_s are the surface potentials of particles and surfaces respectively, ϵ_m is the static dielectric constant of water, ϵ_0 is the permittivity of the vacuum, and σ_{LJ} is the atomic collision diameter.

Surface potentials for particle and sand grain (γ_p , γ_s) are calculated from the zeta potentials of particle and surface using the following equations Gregory 1975:

$$\begin{aligned}\gamma_p &= \tanh\left(\frac{ze\zeta_s}{4k_B T e}\right) \\ \gamma_s &= \tanh\left(\frac{ze\zeta_p}{4k_B T e}\right)\end{aligned}\quad (6)$$

where, z is the valence of the cation in solution, e is the elementary charge ($1.602 \times 10^{-19} \text{C}$), T is the temperature in degrees Kelvin and ζ_s and ζ_p are the zeta potentials of grain surface and particle respectively in volts.

The zeta potential of sand can be calculated as:

$$\zeta_s = A(1 - e^{-(B \times pH + C)\gamma})(D \times pH + E) + (F \times pH + G) \quad (7)$$

where, pH is the measure of acidity, γ is fluid salinity, and $A=0.998$; $B=-1.8526$; $C=24.537$; $D=0.6022$; $E=21.677$; $F=-1.9666$; $G=-32.826$.

The electrostatic force is computed as the negative of the electrical potential energy gradient:

$$F_e = -\frac{\partial V_{total}}{\partial h} \quad (8)$$

Plugging Eq. (2) in the critical state of Eq. (1), the velocity is defined as following:

$$V_{cr}^{Fe} = \frac{l_n}{l_d} \times F_e \times \frac{1}{6\pi\omega r_s^2 \mu} \quad (9)$$

Here V_{cr}^{Fe} is the critical interstitial velocity for detachment of detrital particles. In order to obtain Darcy's velocity, interstitial velocity is multiplied by porosity:

$$U_{cr} = \phi V_{cr} \quad (10)$$

Assuming pore space as a bundle of parallel capillary tubes with average radius r_p , the porosity can be defined as following (Reddi et al. 2000):

$$\phi = \frac{8k_0}{r_p^2} \quad (11)$$

where k_0 is the permeability of the core sample at the start of the test. Combining Eqs. (9-11), yields:

$$U_{cr}^{Fe} = \frac{8k_0}{r_p^2} \times \frac{l_n}{l_d} \times F_e \times \frac{1}{6\pi\omega r_s^2 \mu} \quad (12)$$

where, U_{cr}^{Fe} is the critical Darcy's velocity for detachment of detrital particles.

Mechanisms of authigenic particle detachment

A schematic of a bonded particle with the primary acting forces is presented in Figure 4. Using the concepts of CBM a cantilever beam is considered between the substrate and the particle. The beam has a circular cross section. Fluid flow exerts the drag force (F_d) on the particle and as a result a bending moment (M_b) is created. Consequently, a state of stress at the contact-bond adjacent to the substrate is created. According to Timoshenko and Goodier 1951, the only significant stresses are normal stress perpendicular to fluid flow direction and a shear stress parallel to fluid flow direction. These stresses for circular cross sectional beam can be defined as:

$$\sigma_n = \frac{M_b y}{I} \quad (13)$$

$$\tau = \frac{F_d}{3I} (a^2 - y^2) \quad (14)$$

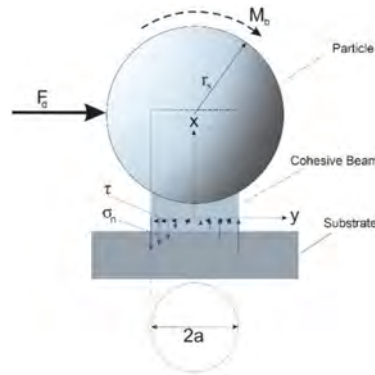


Figure 4—Schematic of spherical particle bonded on a substrate by a circular cross sectional cantilever beam.

Here σ_n and τ are normal and shear stresses at the base of the beam, M_b is the bending moment due to fluid flow, F_d is the drag force, I is the moment of inertia for the area of the contact, a is the radius of area of contact, and y is the coordinate axis which is zero at the middle of the beam. Assuming the height of the bond is negligible in comparison with the radius of the particle, the equation of bending moment and the moment of inertia for circular cross section are as follows:

$$M_b = F_d r_s \quad (15)$$

$$I = \frac{\pi}{4} a^4, \quad (16)$$

Failure happens when either of normal stress or shear stress or a combination of both in one specific orientation exceed a threshold value. Since, fluid drag force is constant, it can be assumed that if failure happens in one point, the beam will be weaker and adjacent points will fail consequently. So it is important to find out which points have critical state of stress. In order to find those points in the contact area with radius a , where stresses are critical, we need to do the following preliminary study.

Preliminary study

We study two imaginary cases. In the first case, a sphere shape particle with the properties given in Table 1. This data is from our laboratory data and tensile strength is the average of all reported values for kaolinite in literature, which is presented in section (4). In this table, Normal stress (σ_n) and shear stress (τ) are calculated by using Eqs. (13) and (14). Fig. 5 shows the results when they are plotted versus y value. In this plot, tensile stress is plotted towards the negative y -axis to show its difference with compressive stress.

Table 1—Parameters for imaginary case 1

Property	Value
Particle radius,[μm]	4.32
Aspect ratio,(thickness/length)	1
pore radius,[μm]	9.48
bond radius,[μm]	0.25
fluid viscosity,[pa.s]	0.001
permeability,[m ²]	$8.75 \cdot 10^{-13}$
Fluid velocity,[m/s]	0.01964
Tensile strength,[MPa]	4

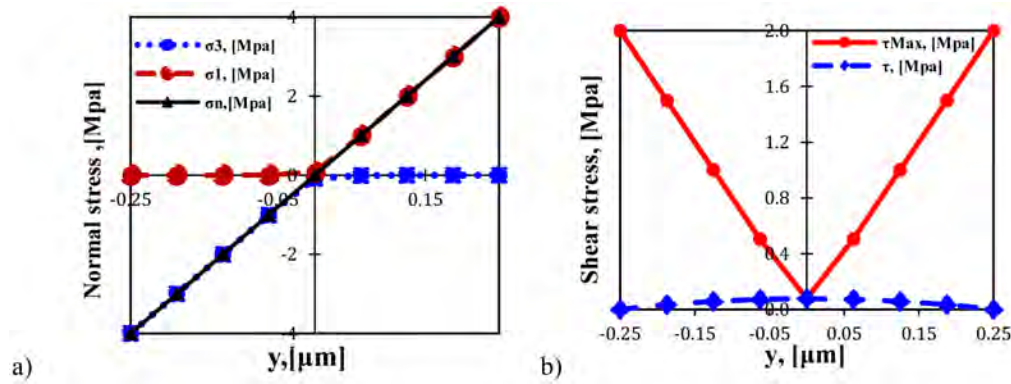


Figure 5—Stresses at contact points; a) normal stress and principal stresses, b) shear stress and maximum shear stress.

Mohr's circle is applied to find shear and normal stresses at different orientation of any given points. The normal stress and the principal stresses are shown in Fig. 5a and the shear stress and the maximum shear stress are shown in Fig. 5b. The principal stresses are maximum and equal to the calculated normal stresses at point $y = -0.2$ and $y = 0.2$. In other words, the maximum tension and compression are at $y = -0.2$ and $y = 0.2$, respectively. At these points, the values of maximum shear stress is half the absolute value of principal stresses.

Tensile strength of a rock is considerably less than its compressive strength (Hudson and Harrison 2000) and bonding material is more sensitive to tension than compression (Obermayer et al. 2013). Therefore, we consider tension as the main criteria of bond failure. This shows that the detachment of the particle due to bending can start at $y = -0.2$. After failure of this point, the same process will be repeated for the adjacent point in the contact bond. Noting that the area of contact has reduced and the values of normal stress will be higher, the breakage of the other points will follow. In this case, the breakage is due to the high bending moment. High bending moment leads to rolling, so the whole process of detachment of this particle is called rolling.

For the second case, we consider a flat-cylindrical particle with low aspect ratio shown in Fig. 6. The properties of this case is presented in Table 2. A low aspect ratio is considered to simulate the flat kaolinite particles. The fluid velocity is increased to reach failure criteria. Critical shear stress is added to the table and its values is tensile strength divided by $\sqrt{3}$, which is explained in section (2.3.2).

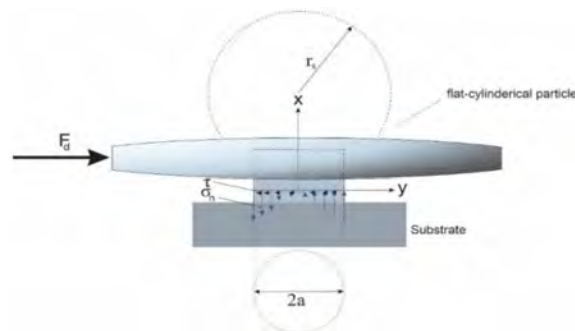


Figure 6—Schematic of flat-cylindrical particle bonded on a substrate by a circular cross sectional beam

Table 2—Parameters for imaginary case 2

Property	Value
Particle radius,[μm]	4.32
Aspect ratio,(thickness/length)	0.005
pore radius,[μm]	9.48
bond radius,[μm]	0.25
fluid viscosity,[pa.s]	0.001
permeability,[m2]	$8.75 \cdot 10^{-13}$
Injection fluid velocity,[m/s]	0.1562
Tensile strength,[MPa]	4
Critical Shear Stress, [Mpa]	2.31

Eq. (2) is used to update the drag force for the new aspect ratio (Ting et al. 2021). The major difference between this case and the previous one, is the value of bending moment (M_b). The resulting bending moment is less than the previous case, because the lever arm for drag force is much lower. To calculate the new lever arm, a cylinder with low aspect ratio and the same volume as the particle in case one is considered. The new graphs for normal and shear stresses are created and shown in Fig. 7. Mohr's circle was applied to obtain the principal stresses and maximum shear stress at each point. The normal stress and the principal stresses are shown in Fig. 7a and the shear stress and the maximum shear stress are shown in Fig. 7b. For this case, it can be observed that the maximum shear stress is at $y=0$ and is bigger than shear stresses at $y=\pm 0.2$. Furthermore, it can be detected that the tensile stress at $y=-0.2$ is less than 4 Mpa, while the shear stress at $y=0$ is equal the critical shear stress of the material. So shear failure will happen at this point at a plane parallel to the fluid flow.

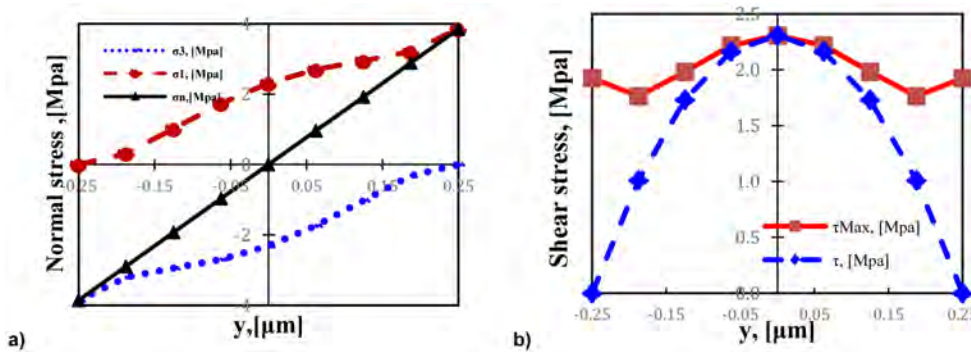


Figure 7—Stresses at contact points; a) normal stress and principal stresses, b) shear stress and maximum shear stress.

The created shear stress is due to the drag force and not the bending moment. This kind of detachment mainly due to shear force is called sliding. The sliding starts at comparatively high fluid velocity (11 times more than the first case) and for particles that have very low aspect ratio (200 times less than the first case).

Having discussed these two cases, it is concluded that the stresses at two points are important to consider. One is the outer point of the bond (i.e. $y=-0.2$) which is under the highest tensile stress and its failure leads to particle rolling. The other one is the middle point of the bond (i.e. $y=0$) which for a flat particle has the highest shear stress and its failure leads to particle sliding. So, the maximum stresses for these two conditions are presented as following:

$$\sigma_n^{\text{max}} = \frac{M_b a}{I}, \quad (17)$$

$$\tau^{\max} = \frac{F_d}{3I} a^2, \quad (18)$$

Here σ_n^{\max} and τ^{\max} are the maximum normal and shear stress.

Failure criteria

Breakage happens when either of normal stress and shear stresses or a specific combination of both of them exceed a threshold value. The type of failure criteria depends on the material at contact bond. Having studied about the elastic properties, it shows the wet kaolinite is a ductile material (Zhao et al. 2020; Maher et al. 1994). Assuming stress-strain curve for kaolinite material is elastic-perfectly plastic, yield criterion are defined. The most well-known yield criterion is von Mises stress (σ_{vM}) (Obermayr et al. 2013; Andre et al. 2012). The von Mises is the following combination of stresses at each point:

$$\sigma_{vM} = \sqrt{\sigma_n^2 + 3\tau^2} \geq \sigma_Y \quad (19)$$

The bond will fail when von Mises stress exceeds the yield stress (σ_Y) of the material. So for rolling (i.e. failure at point $y=-0.2$, where shear stress is zero), the failure occurs when normal stress surpasses the yield stress. For sliding (i.e. at point $y=0$, where normal stress is zero), failure occurs when shear stress at the plane parallel to fluid flow is equal to or higher than $\sigma_Y/\sqrt{3}$ (Jaeger et al. 2007). In this paper, it is assumed the collected tensile strength from literature is the same as yield stress for kaolinite.

Calculation of velocity distribution

Plugging in Eqs. (15) and (16) into Eq. (17) and considering tensile strength, critical fluid velocity for rolling can be obtained as:

$$V_{cr}^R = \frac{\sigma_{nc} a}{24\mu\omega} \left(\frac{a}{r_s}\right)^2 \quad (20)$$

Here V_{cr}^R is the interstitial velocity and in order to obtain the critical Darcy velocity, it is multiplied with porosity. Assuming pore space as a bundle of parallel capillary tubes with average radius r_p and applying Eq. (11) result in:

$$U_{cr}^R = \frac{\sigma_{nc} a k_0}{3\mu\omega r_p^2} \left(\frac{a}{r_s}\right)^2 \quad (21)$$

where, U_{cr}^R is the critical Darcy's velocity which causes particle rolling after failure.

Repeating the same procedure for Eq. (18), the critical injection velocity for particle sliding can be calculated like:

$$U_{cr}^S = \frac{\sigma_{nc} a k_0}{\sqrt{3}\mu\omega r_p^2} \left(\frac{a}{r_s}\right) \quad (22)$$

where, U_{cr}^S is the critical Darcy's velocity which causes particle sliding.

Comparing Eqs. (21) and (22) show that sliding happens in higher velocities. Moreover it was discussed in imaginary case 2, the sliding happens only for flat particles with very low aspect ratio. Assuming particles with these geometrical shape have small concentration inside porous media, sliding is not considered.

Creating maximum retention function

Checking Eqs. (12), (21), most of the parameters in these equations are uncertain and a distribution for each of them can be considered. Considering a distribution for each parameter and applying Monte Carlo simulation, a histogram for each velocity can be obtained. Fitting a probability distribution function to each histogram, we can find two probability distribution functions. First one is the probability distribution

function of detrital particles, $f_e(U)$ and the second one is the probability distribution function of authigenic particles, $f_f(U)$.

Assuming at each velocity increment, both detrital and authigenic particles are produced, the total concentration of detached particles can be introduced as following:

$$\Delta\sigma_n = \sigma_0^e \int_{U_{n-1}}^{U_n} f_e(U) du + \sigma_0^f \int_{U_{n-1}}^{U_n} f_f(U) du \quad (23)$$

where $\Delta\sigma_n$ is the concentration of particle detached when fluid injection velocity increases from U_{n-1} to U_n , the σ_0^e is the initial concentration of detrital particles and σ_0^f is the initial concentration of authigenic particles in the rock at $U=0$. In equation above, $\Delta\sigma_n$ from Eq. (23) and $\Delta\sigma_n$ from experiment can be matched by changing the fitting parameters. As a results, σ_0^e and σ_0^f can be obtained. Having these concentration, we can calculate the maximum retention function by applying the following equation:

$$\sigma_{cr}(U) = \sigma_0^e \int_U^{\infty} f_e(U) du + \sigma_0^f \int_U^{\infty} f_f(U) du \quad (24)$$

Formation damage formulation for single-phase high velocity fluid

The formulae in this section already derived by Russell et al. 2018 and we only briefly explain the equations and boundary/initial conditions and the solutions. Fines migration is the process encountered in porous media in which small particles detach from pore surfaces and travel through the pore space. The migration path of a detached particle is often terminated when the particle meets a pore throat smaller than its size. This is referred to as straining and reduces the permeability of the porous medium. The schematic of permeability decrease due to fines migration is shown in Figure 8. In this figure the concentration of attached (σ_a), suspended (C) and strained (σ_s) particles are displayed.

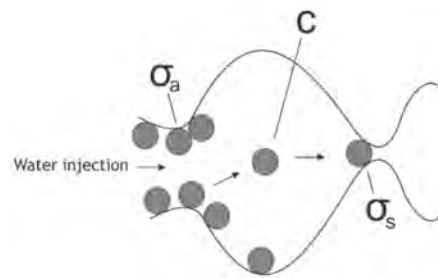


Figure 8—Graphical illustration of particle detachment from grain surface, migration in carrier fluid, and straining in thin pore.

Mathematical modeling of fines migration normally starts from a continuity equation for the suspended particle concentration. Considering the suspended particles are transported by the reduced velocity, i.e. $U_s = \alpha U$, the continuity equation can be written as:

$$\frac{\partial}{\partial t}(\phi c + \sigma_s + \sigma_a) + \alpha U \frac{\partial c}{\partial x} = 0 \quad (25)$$

Here ϕ is the porosity, c , σ_a , and σ_s are the concentrations of suspended, attached and strained particles, $\alpha \ll 1$ is the drift delay factor and U is Darcy fluid velocity.

The straining rate is assumed to be a function of particle advection flux, cU (Bedrikovetsky 2008; Herzig et al. 1970):

$$\frac{\partial \sigma_s}{\partial t} = \lambda c \alpha U \quad (26)$$

where λ is called the filtration coefficient.

Particle straining leads to permeability decline and the Darcy's law can be expressed as follows:

$$U = -\frac{k_0}{\mu(1+\beta\sigma_s)} \frac{\partial p}{\partial x} \quad (27)$$

where β is the formation damage coefficient and p is pressure.

The four Eqs. (25-27) and Eq. (4) make a system of equations with four unknowns c , σ_a , σ_s , and p , which describe the detachment, migration, and straining of particles in pore space. The initial and boundary condition for this system were written as

$$t = 0: c = \frac{\Delta\sigma}{\phi}, \sigma_a = \sigma_{cr}(U_1), \sigma_s = 0; \quad x = 0: c = 0, \sigma_s = 0 \quad (28)$$

Before solving the system of equations, the following dimensionless parameters were introduced to make dimensionless equations:

$$X = \frac{x}{L}, T = \frac{\int_0^t U(\gamma) d\gamma}{\phi L}, C = \frac{c}{\Delta\sigma}, S_s = \frac{\sigma_s}{\phi\Delta\sigma}, S_a = \frac{\sigma_a}{\phi\Delta\sigma}, \Lambda = \lambda L, P = \frac{pk_0}{U\mu L} \quad (29)$$

where L is the core length, and $\Delta\sigma = \sigma_{cr}(U_0) - \sigma_{cr}(U_1)$ is the total detached particle concentration (detrital plus authigenic) when the fluid velocity is increased from U_0 to U_1 . Plugging in these parameters into the system of Eq. (4) and Eqs. (25-27) yields:

$$\begin{aligned} S_a &= S_{cr}(U) \\ \frac{\partial}{\partial T}(C + S_s + S_a) + \alpha \frac{\partial C}{\partial X} &= 0 \\ \frac{\partial S_s}{\partial T} &= \Lambda \alpha C \\ 1 &= -\frac{1}{1 + \beta\phi\Delta\sigma S_s} \frac{\partial P}{\partial X} \end{aligned} \quad (30)$$

In dimensionless coordinates, the initial and boundary conditions become, respectively:

$$T = 0: C = 1, S_a = S_{cr}(U_1), S_s = 0, \quad X = 0: C = 0, S_s = 0$$

The dimensionless pressure drop $J(T)$, referred to as the impedance, were solved by integrating fourth equation in (30) directly using separation of variables:

$$J(T) = \int_0^1 \left(-\frac{\partial P}{\partial X} \right) dX = 1 + \beta\phi\Delta\sigma \int_0^1 S_s(X, T) dX \quad (31)$$

The one dimensional solutions for suspended and strained concentrations, and impedance ahead and behind the particle front were derived in Russell et al. 2018. Inserting the resulted expression for the strained concentration into Eq.(31) and integrating make it possible to derive the impedance as:

$$J(T) = \begin{cases} 1 + \beta\phi\Delta\sigma_{cr} \left[1 - \frac{1}{\Lambda} - \left(1 - \frac{1}{\Lambda} - \alpha T \right) e^{-\alpha\Lambda T} \right], & T < \frac{1}{\alpha} \\ 1 + \beta\phi\Delta\sigma_{cr} \left(1 - \frac{1}{\Lambda} + \frac{e^{-\Lambda}}{\Lambda} \right), & T \geq \frac{1}{\alpha} \end{cases} \quad (32)$$

The expressions for suspended concentration were used to obtain the accumulated concentration at the outlet of the core as:

$$C_{acc} = \alpha \int_0^T C(1, \gamma) d\gamma = \begin{cases} -\frac{1}{\Lambda} (\exp(-\alpha\Lambda T) - 1), & T < 1/\alpha \\ -\frac{1}{\Lambda} (\exp(-\Lambda) - 1), & T > 1/\alpha \end{cases} \quad (33)$$

Laboratory study

In this section, the rock properties of core sample, fluid preparation, our laboratory set-up and the experimental study on fines mobilization and migration are presented.

Rock and fluid properties

The rock sample is Castlegate sandstone core plug of 3.8 cm diameter and 5 cm length. Based on X-Ray diffraction (XRD) analysis, Castlegate sandstone is composed of Quartz (90.6%), Feldspar (2.1%), clay-Illite (4%), clay-Kaolinite (2.6%), and Calcite (0.8%) (Rafieepour et al. 2017). Moreover, the SEM and mineralogy study on Castlegate rock samples show that the amount of authigenic kaolinite clay is significant. Bruno et al. 1991 reported that Castlegate core has 4% authigenic clay content and Best et al. 2010 detected 5% clay, mostly authigenic kaolinite, in thin section images.

Pore volume of the core was calculated by recording the volume of brine required to saturate the dry core sample. Bulk volume of the core is the multiplication of cross sectional area and length of the core. Then, porosity was obtained by dividing pore volume by bulk volume. Initial permeability was calculated by injecting brine into the sample. The porosity and initial permeability of the core sample were 24.3% and 888 mDarcy, respectively.

Ultra-pure deaerated MilliQ™ water was used to make an injection solution for the experiment. To prepare one litre of the solution, one litre DI water and 35.1(gram) NaCl crystals were mixed to produce one litre of 0.6 M (mol/L) NaCl brine. The prepared brine had a pH of 7.2.

Laboratory set-up

A graphical illustration of the setup for injecting brine into core sample is presented in Fig. 9. In this setup, the core plug was placed inside a coreholder and an overburden pressure was applied. A piston pump was used to supply high-pressure brine to the core. The inlet and outlet pressures of the core were recorded by two absolute transmitters. To make sure fluid was injected with constant pressure, a back-pressure was applied at the outlet. After the back-pressure value, there was a sensor to record the conductivity of the fluid. All data from transmitters and sensors were transferred to a real-time data acquisition system. The data acquisition system analysed the data and delivered real-time values of differential pressure and fluid viscosity to an Excel file. In the excel sheet, the collected data at each time step were used to calculate permeability by applying Darcy's law. At the outlet, there was a centrifugal fraction collector to collect effluent suspensions into plastic tubes. The particle concentration of each plastic tube was measured using a compact particle counter/sizer.

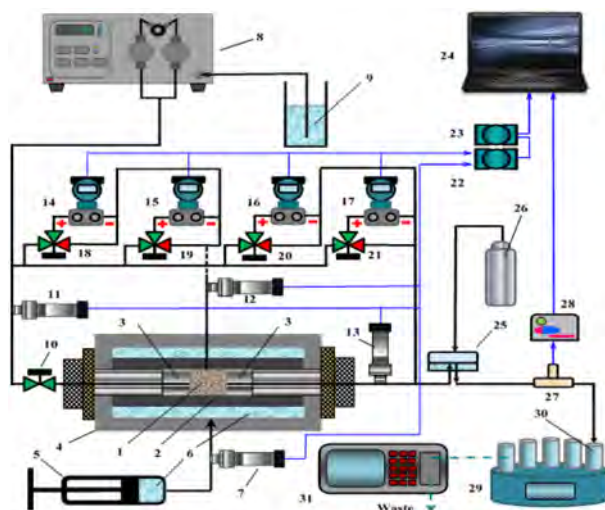


Figure 9—Laboratory set-up for particle detachment due to DLVO and breakage: 1 - core sample, 2 - Viton cover, 3 - flow distributors, 4 - core holder, 5 - manual pressure generator, 6 - distilled water, 7, 11, 12 and 13 - pressure transmitter, 8 - High-performance liquid chromatography (HPLC) pump, 9 - brine solution, 10 - control valve, 14-17 - pressure transducers, 18-21 - three-way manual valves, 22 - data acquisition module, 23 - signal converter, 24 - personal computer, 25-back-pressure regulator, 26 - gas cylinder, 27 - conductivity sensor, 28 - signal conditioning and signal transmitting conductivity isoPod, 29 - fraction collector, 30 - plastic tubes, 31-particle counter.

Experimental procedure

The core was fixed inside the coreholder and an overburden of 1000 psi and a back pressure of 300 psi were applied to the sample. The experiment is started by injecting 0.6 M NaCl solution at a superficial velocity of 2.94×10^{-6} m/s (equivalent to the volume flow rate of 0.2 mL/min). The injection continued until pressure drop was stabilized. The initial permeability of the sample is calculated at this flow rate. After stabilization, the injection rate was increased to a next value.

Two tests has been done and for test#1, the volumetric injection rates were 2, 20, 70, and 100 mL/min and for test#2, the volumetric injection rates were 2, 20, 70, 100, 120, 170, 200 mL/min. During the whole process of brine injection, the effluent samples were collected into plastic tubes. And at the end of each test, the particle counter/sizer, POLA 2000™, was used to measure the particle concentration collected in each plastic tube.

Discussion and Results

Matching the experimental data by the analytical model

Particle concentration at the outlet and the corresponding impedance ($J(T)$) were measured during the experiment. For each injection rate, the accumulated concentrations (C_{acc}) were calculated. Then least-squared curve fitting tool in MATLAB was used to simultaneously match both experimental datasets with the analytical models. The model (Eqs. 32, 33), contains four unknowns, i.e. filtration coefficient, λ , drift delay factor, α , formation damage coefficient, β , and detachment concentration, $\Delta\sigma$. These parameters were considered as fitting parameters. The experimental data was matched with the model, the fitting parameters and coefficient of determination R^2 for both are shown in Table 3.

Table 3—Tuning parameters for our lab test

Parameters	Test#	2(mL/min)	20(mL/min)	70(mL/min)	100(mL/min)	120(mL/min)	170(mL/min)	200(mL/min)
$\lambda(1/m)$	1	1.83	1.23	1.10	5.53	0.23	-	-
	2	1	1.36×10^{-8}	0.78	3.34	0.73	1.10	1.63
α	1	0.09	0.05	1.72×10^{-2}	0.02	1.43×10^{-2}	-	-
	2	0.05	0.05	1.69×10^{-2}	2.07×10^{-2}	1.45×10^{-2}	1.21×10^{-2}	1.04×10^{-2}
β	1	0	1.21×10^5	1.38×10^4	7.63×10^3	5.54×10^4	-	-
	2	2×10^5	0	-2.8×10^4	-1.66×10^3	1.95×10^4	2.64×10^3	1×10^3
$\Delta\sigma$	1	2.95×10^{-6}	2.8×10^{-6}	1.54×10^{-5}	3.29×10^{-5}	8.75×10^{-6}	-	-
	2	2.22×10^{-6}	8.02×10^{-6}	2.32×10^{-5}	1.30×10^{-5}	1.97×10^{-5}	3.66×10^{-5}	3.14×10^{-5}
$R^2(J)$	1	0.85	0.93	0.73	0.54	0.88	-	-
	2	1×10^{-3}	5×10^{-3}	0.1	0.44	0.71	0.19	0.60
$R^2(C_{acc})$	1	0.98	0.59	0.99	0.91	0.99	-	-
	2	0.97	0.99	0.98	0.82	0.98	0.99	0.92

The experimental data and the matched model for both tests are presented in Figure 10 and Figure 11. The results show good agreement between the laboratory data and the models.

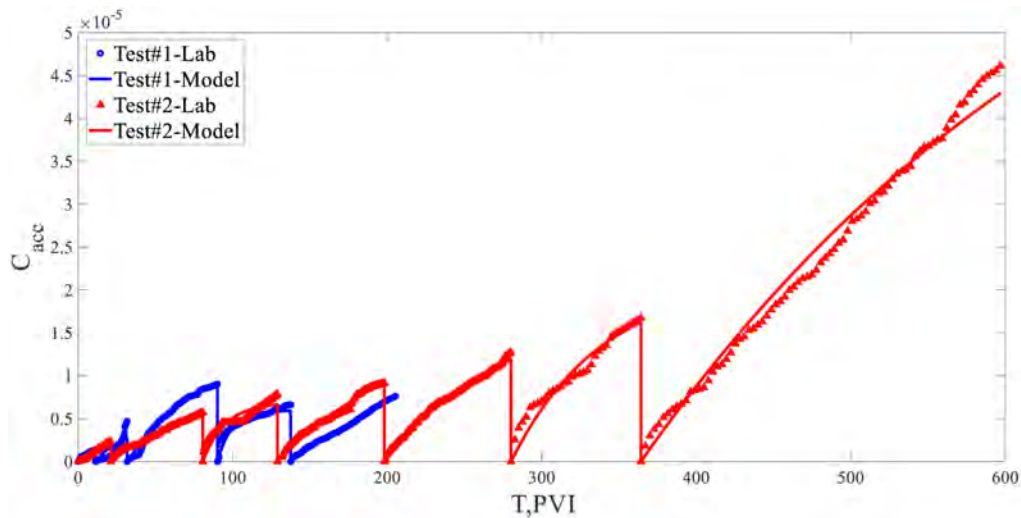


Figure 10—Experimental data for accumulated outlet concentration of suspended particles matched with the model (PVI: number of pore volumes injected.)

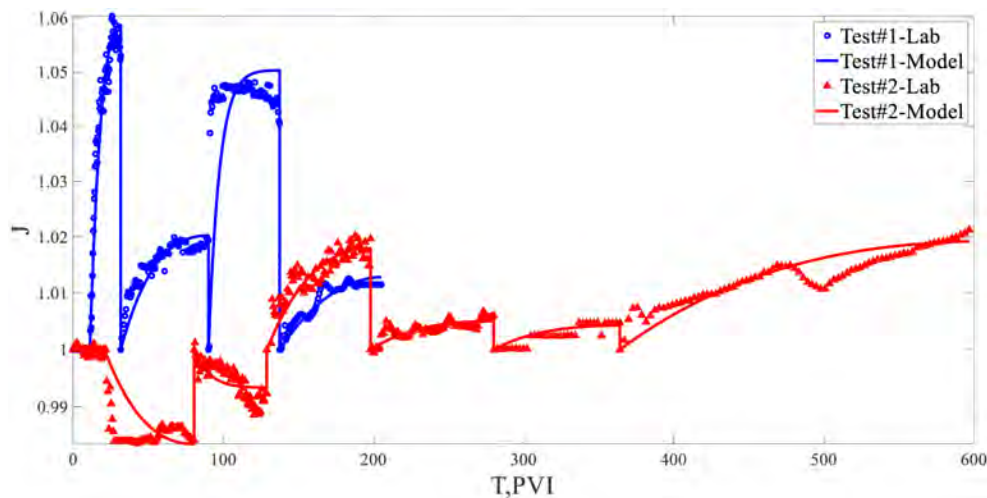


Figure 11—Experimental data for impedance matched with the model

The values of drift delay factor are much less than one. Since the drift delay factor is the ratio of particle velocity to fluid velocity, it can be concluded that the particles moved with a velocity much slower than the fluid velocity. As a result for each injection rate, the stabilization time is much higher than the time to inject a single-pore volume.

Matching detachment concentration

The detachment concentration ($\Delta\sigma$) for each injection rate is shown in Table 3. In works of Bruno et al. 1991 and Best et al. 2010 reported that Castlegate core samples have a significant amount of authigenic clay particles, therefore in our experiment the detachments of both authigenic and detrital clays are probable. To detach the detrital particle, drag force needs to overcome the attaching electrostatic forces, while for authigenic particles the drag force needs to break the existing bond between the clay and rock.

To define the initial amount of detrital and authigenic particles inside the core, a new method based on Monte Carlo simulation was developed. First, the distribution for each parameters need to be defined. The parameters like pore size, particle size, aspect ratio of particle, zeta potential, strengths of material, contact-bond radius, and lever arm ratio are not constant for particles and, they can have random values within a certain limit. Except contact-bond radius and lever arm ratio, the rest of the parameters are measurable, and

their values are reported in literature. The corresponding values were collected, and a normal probability distribution function was fitted to them. Table 4 presents mean value (M) and standard deviation (SD) for the normal probability distribution function of each parameter. Orlander et al. 2021 and M'barki et al. 2021 measured pore size distribution for Castlegate sandstone using the Mercury Injection Capillary Pressure. Examining their data, it was found out that the pore size can deviate from their mean value by 50%. The mean

value of pore size is calculated from $r_p = 5\sqrt{\frac{k_0}{\phi}}$ (Amix et al., 1964), where the values of initial permeability and porosity were already measured. Having the mean value and the range, the standard deviation was obtained. For particle size, a normal distribution is fitted to particle size measured with POLA 2000™ in our laboratory set-up. The range of values is compatible with the particle size range reported in Varzaneh et al., 2021 for Castlegate core sample.

Table 4—Distribution of parameters

Parameters	Distribution	M	SD	References
Zata potential-Particles (mV)	Normal	- 20.8	0.69	Walker et al. 2018
Zata potential-Rock (mV)		- 21.8	0.73	Walker et al. 2018
Poisson's ratio		0. 31	0.02	Horabik et al. 2021; Mikowski et al. 2007; Mondol et al. 2008
Young Modulus, [GPa]		1 5.09	4.02	Horabik et al., 2021; Mondol et al. 2008; Yang et al. 2019
Tensile strength, [MPa]		4. 00	1.07	Sang et al. 2015; Reddi et al. 1997; Charkley et al. 2019; Barzegar et al. 1995; Horabik et al. 2021
Aspect ratio, α		0. 08	0.02	Cheng et al. 2014; Zhang et al. 2017
Pore size, [μm]		9. 48	1.58	Orlander et al. 2021 Mbarki et al. 2021
Particle radius, [μm]		4. 32	1.15	Varzaneh et al., 2021

For the rest of the properties in Table 4, their values were collected from literature and a normal distribution function was matched between the minimum and maximum values. The mechanical properties of kaolinite rock is not available in literature because getting pure kaolinite sample is not possible. Therefore, kaolinite soils are collected and tested. The mechanical properties of kaolinite in Table 4 are for kaolinite soils and we assume these properties are applicable to kaolinite particle in porous media. Moreover, we need to use the yield stress of kaolinite to use it in von Mises failure criteria. The yield stress of kaolinite is not available and it is assumed it is the same as the tensile strength.

Second, two histograms for detachment velocities were created, using the Monte Carlo simulation for Eqs. (12) and (21) and the values reported in Table 4. The two histograms were separately fitted with probability distribution functions (i.e. $f_e(U)$ and $f_f(U)$). Using those obtained values and Eq. (23) we calculate the detachment concentration for the incremental injection rate intervals.

Depending on the value of contact-bond radius, the two distributions (i.e. $f_e(U)$ and $f_f(U)$) might overlap or might be completely separated. Therefore, it was logical to check the detachment concentration in experimental data and look for two separate histograms. If the obtained $\Delta\sigma$ from experimental data treatment shows one maximum (i.e. one hump), it was assumed that only one type of particles are produced, either detrital or authigenic and the matching was done with only one mechanism. If two rising trends (i.e. two humps) were detected, the first hump was matched for detrital detachment (DLVO theory) and second hump was matched for authigenic detachment (Breakage theory). Given that the average fluid velocity required to break the bond in authigenic particles is more than the average fluid velocity required to detach detrital particles.

In order to match our model with our laboratory data, we choose the most uncertain parameters as fitting parameters. Our preliminary study shows that for detrital case, initial concentration of particles, mean value and standard deviation of lever arm ratio are most uncertain parameters where for authigenic particles, initial concentration of particles and mean value and standard deviation of bond radius are uncertain. Since every histogram can be plotted by three known values (i.e. mean value, standard deviation, and number of samples), three fitting parameters for each mechanism can be obtained. If there is one histogram, the three uncertain parameters are obtained and if there are two humps, the six unknowns can be calculated.

In Figure 12 the detachment concentrations obtained in laboratory test#1 were plotted in green circles. There is only one hump in this test. Using least-squared curve fitting tool in MATLAB, laboratory data was matched with each mechanism, separately. The matching with the model accounting for detrital particle detachment was selected, as the fitting parameter are in acceptable range. The fitting parameters of this test were shown in Table 5.

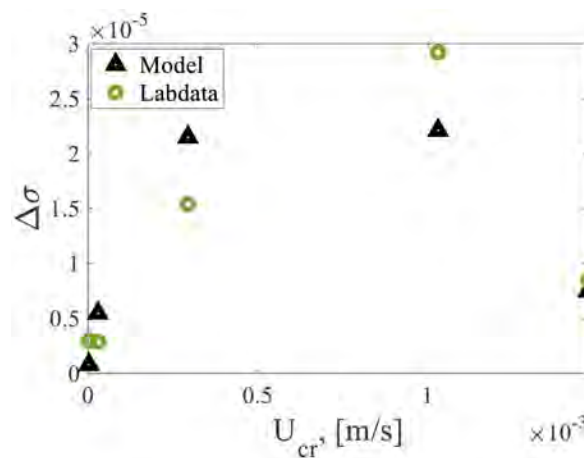


Figure 12—Matching the experimental data and the model for test#1.

Table 5—Tuning parameters to match histograms

Test#	DLVO parameter	Value	Failure parameter	Value
1	σ_0^e	1.67×10^{-4}	σ_0^f	*
2		1.51×10^{-4}		7.2×10^{-4}
1	M (Lever arm ratio)	101.49	M (Bond radius), [μm]	*
2		231.99		0.25
1	SD (Lever arm ratio)	4.25×10^{-4}	SD (Bond radius), [μm]	*
2		9.26×10^{-4}		1×10^{-5}
1	$R^2 (\Delta\sigma)$	0.83	$R^2 (\Delta\sigma)$	*
2		0.96		0.90
1	$R^2 (\sigma_{cr})$	0.98	$R^2 (\sigma_{cr})$	*
2		0.99		0.99

*Stage01 is matched only with DLVO.

In Figure 13 the detachment concentrations obtained in laboratory test#2 were plotted in green circles. Two humps are detected, so the first histogram was matched with DLVO and the second one was matched with breakage equation. As it is shown, the maximum detachment of detrital particle is at $U=1\text{e-}3$ m/s while

maximum amount of authigenic particles mobilizes at $U=2.5e-3$ m/s. The fitting parameters of this test were also reported in Table 5.

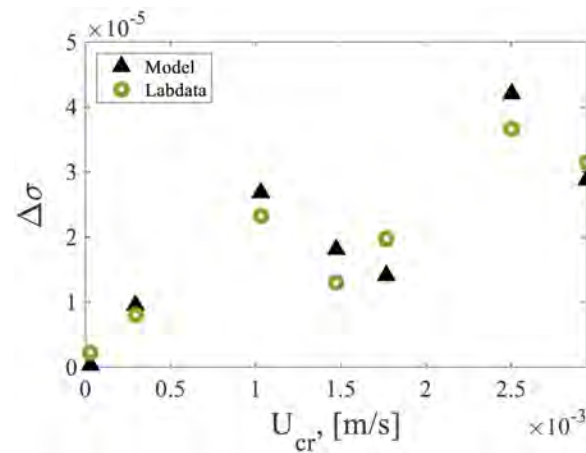


Figure 13—Matching the experimental data and the model for Stage3.

Comparing two initial concentrations (i.e. σ_0^e and σ_0^f) in Table 5, the ratio of initial authigenic particle to initial detrital particles for test#2 is 4.46 (i.e. about 82% of the particle inside porous media are authigenic). Moreover, the ratio of mean value of particle radius and contact-bond radius is about 17, which implies our assumption for narrow beam is valid.

After finding the initial concentrations of detrital and authigenic particles in porous media and finalizing the detachment velocity distributions for both mechanisms, it is possible to use Eq. (24) to obtain the maximum retention function curve for each test. The results are demonstrated in Fig. 14 and Fig. 15.

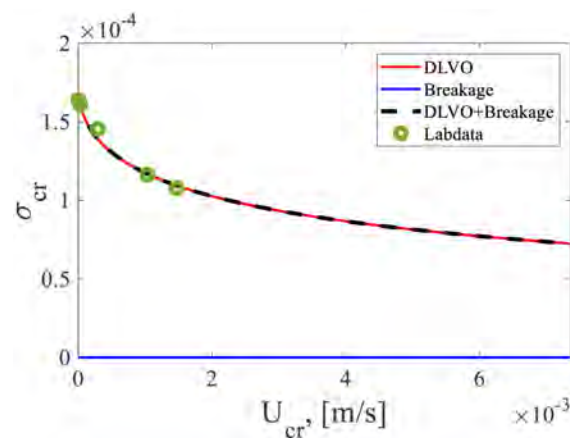


Figure 14—Maximum retention function for test#1

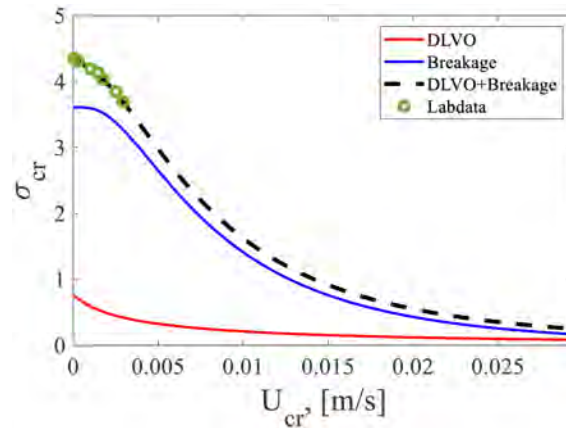


Figure 15—Maximum retention function for test#2

In test#2, both processes were involved and the total detachment model from Eq. (24) matched with laboratory data. As shown in Fig. 15, the critical retention function curve due to breakage (blue curve) is almost constant at low velocities while the DLVO curve (red curve) has a decreasing trend. At higher injection rates, no significant decrease is observed in DLVO but breakage curve starts decreasing (blue curve). Adding up these two curves, the black dashed curve is created which matches the laboratory data.

Summary and Conclusions

In this paper, we proposed a new laboratory-based model to determine the detachment of the authigenic and detrital particles. We assumed that the detrital particles are attached to the rock surface by electrostatic forces and the classical DLVO theory was used to predict their detachments. The authigenic particles are assumed to be bonded to a surface and their mechanical detachment is modelled using CBM and von Mises failure criteria. This work allows drawing the following conclusions:

- Treatment of measured breakthrough concentration and pressure drop during water flooding allows determining the amount of detached particles.
- For the first time, the Monte Carlo simulation using the variation of multiple parameters has been successfully used to create histograms for detachment velocities.
- The non-monotonic change of the concentration of the detached fine, with the initial and final risings, determines the type curve that evidence the mobilisation of both, authigenic and detrital clays.
- A mathematical model accounting only for DLVO theory cannot predict the trend of detached particle concentration measured during the experiment
- A novel technique based on the CBM and von Mises yield criteria was proposed to predict the detachment of authigenic particles due to the applied drag force
- The model parameters in order of decrease of their sensitivity are contact-bond radius, pore radius, particle size, lever-arm ratio, tensile strength, and aspect ratio.
- The laboratory data exhibit a high match with the mathematical model for the two coreflood series. test#1 was matched only with DLVO theory while DLVO and breakage theory were applied to match the test#2
- The maximum retention function for a system of detrital and authigenic particles is obtained. Having the maximum retention function, the further particle detachment by higher flow rates can be predicted.
- The results show that the ratio of initial authigenic particle to initial detrital particles for test#2 is 4.46 (i.e. 82% of the particle inside porous media are authigenic)

- For particle sizes varying from 1.72 microns to 15.56 microns in Castlegate core sample with pore size varying 9.5 to 28.5 microns, normal pH, salinity, tensile strength and level arm ratio, the maximum detachment of detrital particle is at $U=1e-3$ m/s while maximum amount of authigenic particles mobilizes at $U=2.5e-3$ m/s.

Nomenclature

English letters

A	Area of contact, L^2
A_{132}	Hamaker constant, $M L^2 T^{-2}$
a	Area of contact radius, L
C	Dimensionless particle suspension concentration
C_{acc}	Accumulated concentrations
c	Particle suspension concentration
e	Charge of electron, TA
F_d	Drag force, $M L T^{-2}$
F_e	Electrostatic force, $M L T^{-2}$
F_g	Gravity force, $M L T^{-2}$
F_l	Lifting force, $M L T^{-2}$
F_n	Normal Force, $M L T^{-2}$
F_s	Shear Force, $M L T^{-2}$
f	Probability distribution function of detaching velocity
f_e	Probability distribution function of detaching velocity by drag resisting electrostatic force
f_f	Probability distribution function of detaching velocity by breakage
I	Second moment of area or Moment of inertia, L^4
I_p	Polar moment of inertia, L^4
J	Impedance
k_0	Initial absolute permeability, L^2
k_B	Boltzmann constant
k_{det}	Detachment coefficient
L	Core length, L
l_d	Drag force lever arm, L
l_n	Electrostatic lever arm, L
M_b	Bending moment, ML^2T^{-2}
M_t	Twisting moment, ML^2T^{-2}
$n_{1,2,3}$	Refractive indices of kaolinite, sandstone and water
P	Dimensionless pressure
p	Pressure, $M L^{-1} T^{-2}$
R^2	Coefficient of determination
r	Fraction of detrital particles
r_p	Pore radius, L
r_s	Particle radius, L
S_a	Dimensionless attached particle concentration
S_s	Dimensionless strained particle concentration
T	Dimensionless time
T_a	Attached Torque, ML^2T^{-2}

T_d	Detached Torque, ML^2T^{-2}
T_e	Absolute temperature, K
h	Particle-Surface separation distance, L
t	Time, T
U	Fluid velocity, MT^{-1}
U_{cr}	Critical Darcy velocity, MT^{-1}
U_m	Maximum fluid velocity, MT^{-1}
U_s	Particle velocity, MT^{-1}
V	Interstitial fluid velocity, MT^{-1}
V_{cr}	Critical interstitial velocity, MT^{-1}
V_{LVW}	London-van der Waals, ML^2T^{-2}
V_{EDL}	Electrostatic double layer, ML^2T^{-2}
V_{BR}	Born repulsion, ML^2T^{-2}
V_{total}	Total electrostatic potential, ML^2T^{-2}
ν_e	Constant value of absorption frequency
X	Dimensionless length
x	Coordinate, L
y	Coordinate, L
z	Ion valency

Greek letters

α	Drift delay factor
α_s	Aspect Ratio
β	Formation damage coefficient
β'	Angle of breakage plane
γ	Salinity of fluid (mol/L),
γ_p	Reduced surface potential for particle
γ_s	Reduced surface potential for grain
ϵ_0	Permittivity of the vacuum, $M^{-1}A^2T^4L^{-3}$
$\epsilon_{1,2,3}$	Static dielectric constants of kaolinite, sandstone and water
ϵ_m	Static dielectric constant of water
ζ_s	Zeta potential for grain (Sandstone), L^2T^{-2}
ζ_p	Zeta potential for particle (Kaolinite), L^2T^{-2}
κ	Inverse of Debye length, L^{-1}
λ	Dimensionless filtration coefficient
λ	Filtration coefficient, L^{-1}
λ_a	Filtration coefficient for attachment, L^{-1}
μ	Fluid viscosity, $ML^{-1}T^{-1}$
σ	Retained concentration
σ_0	Initial particle concentration
σ_a	Attached particle concentration
σ_{cr}	Critical retention function
σ_{LJ}	Atomic collision constant
σ_n	Normal stress, $ML^{-1}T^{-2}$
σ_{nc}	Critical normal stress or tensile strength, $ML^{-1}T^{-2}$
σ_{nmax}	Maximum normal stress, $ML^{-1}T^{-2}$

- σ_s Strained particle concentration,
- σ_{vM} Von Mises stress, $M L^{-1} T^{-2}$
- $\Delta\sigma_n$ Concentration of detached particles
- τ Shear stress, $M L^{-1} T^{-2}$
- τ_c Critical shear stress or shear strength, $M L^{-1} T^{-2}$
- φ Porosity
- ϖ Aspect ratio or shape factor

Subscript

- exp* Experimental data
- acc* Accumulated
- n* Natural number
- 1,2,3* Indexes of Principal stresses

Superscript

- e* detrital particles
- f* authigenic particles
- r* Rolling
- s* Sliding

References

- André, D., Iordanoff, I., Charles, J.L. and Néauport, J., 2012. Discrete element method to simulate continuous material by using the cohesive beam model. *Computer methods in applied mechanics and engineering*, **213**, pp.113-125.
- Archer, R.R., Crandall, S.H., Dahl, N.C., Lardner, T.J. and Sivakumar, M.S. eds., 2012. *An introduction to mechanics of solids*. Tata McGraw-Hill Education.
- Arostegui, J., Irabien, M.J., Nieto, F., Sangüesa, J. and Zuluaga, M.C., 2001. Microtextures and the origin of muscovite-kaolinite intergrowths in sandstones of the Utrillas Formation, Basque Cantabrian Basin, Spain. *Clays and Clay Minerals*, **49**(6), pp.529-539.
- Asghari, M., Kahrobaiyan, M.H., Rahaeifard, M. and Ahmadian, M.T., 2011. Investigation of the size effects in Timoshenko beams based on the couple stress theory. *Archive of Applied Mechanics*, **81**(7), pp.863-874.
- Barzegar, A.R., Oades, J.M., Rengasamy, P. and Murray, R.S., 1995. Tensile strength of dry, remoulded soils as affected by properties of the clay fraction. *Geoderma*, **65**(1-2), pp.93-108.
- Bedrikovetsky, P., 2008. Upscaling of stochastic micro model for suspension transport in porous media. *Transport in porous media*, **75**(3), pp.335-369.
- Bedrikovetsky, P., Siqueira, F.D., Furtado, C.A. and Souza, A.L.S., 2011. Modified particle detachment model for colloidal transport in porous media. *Transport in porous media*, **86**(2), pp.353-383.
- Bedrikovetsky, P., Zeinijahromi, A., Siqueira, F.D., Furtado, C.A. and de Souza, A.L.S., 2012. Particle detachment under velocity alternation during suspension transport in porous media. *Transport in Porous Media*, **91**(1), pp.173-197.
- Best, S.T., Sears, S.O. and Willson, C.S., 2010. PS Integration of Imaging Techniques over Multiple Scales.
- Bruno, M.S., Bovberg, C.A. and Nakagawa, F.M., 1991, July. Anisotropic stress influence on the permeability of weakly-cemented sandstones. In *The 32nd US symposium on rock mechanics (USRMS)*. OnePetro.
- Charkley, F.N., Zhang, K. and Mei, G., 2019. Shear strength of compacted clays as affected by mineral content and wet-dry cycles. *Advances in Civil Engineering*, **2019**.
- Cheng, H., Zhang, Z., Liu, Q. and Leung, J., 2014. A new method for determining platy particle aspect ratio: A kaolinite case study. *Applied clay science*, **97**, pp.125-131.
- Cundall, P.A. and Strack, O.D., 1979. A discrete numerical model for granular assemblies. *geotechnique*, **29**(1), pp.47-65.
- De Josselin de Jong, G., 1969. Etude photoélastique d'un empilement de disques. *Cah. Grpe fr: Etud. Rheol.*, **2**, pp.73-86.
- Dutta, P.K. and Suttner, L.J., 1986. Alluvial sandstone composition and paleoclimate; II, Authigenic mineralogy. *Journal of Sedimentary Research*, **56**(3), pp.346-358.
- Deraguin, B.V. and Landau, L., 1941. Theory of the stability of strongly charged lyophobic sols and of the adhesion of strongly charged particles in solution of electrolytes. *Acta Physicochim: USSR*, **14**, pp.633-662.

- Elimelech, M., Gregory, J. and Jia, X., 2013. *Particle deposition and aggregation: measurement, modelling and simulation*. Butterworth-Heinemann.
- Farrell, N.J.C., Debenham, N., Wilson, L., Wilson, M.J., Healy, D., King, R.C., Holford, S.P. and Taylor, C.W., 2021. The effect of authigenic clays on fault zone permeability. *Journal of Geophysical Research: Solid Earth*, **126**(10), p.e2021JB022615.
- Gregory, J., 1981. Approximate expressions for retarded van der Waals interaction. *Journal of colloid and interface science*, **83**(1), pp.138-145.
- Herzig, J.P., Leclerc, D.M. and Goff, P.L., 1970. Flow of suspensions through porous media—application to deep filtration. *Industrial & Engineering Chemistry*, **62**(5), pp.8-35.
- Hogg, R.T.W.D.W., Healy, T.W. and Fuerstenau, D.W., 1966. Mutual coagulation of colloidal dispersions. *Transactions of the Faraday Society*, **62**, pp.1638-1651.
- Maher, M.H. and Ho, Y.C., 1994. Mechanical properties of kaolinite/fiber soil composite. *Journal of Geotechnical Engineering*, **120**(8), pp.1381-1393.
- Horabik, J. and Jozefaciuk, G., 2021. Structure and strength of kaolinite–soil silt aggregates: Measurements and modeling. *Geoderma*, **382**, p.114687.
- Hudson, J.A. and Harrison, J.P., 2000. *Engineering rock mechanics: an introduction to the principles*. Elsevier.
- Israelachvili, J.N., 2015. *Intermolecular and surface forces*. Academic press.
- Jin, L., Yu, W., Su, X., Zhang, S., Du, X., Han, J. and Li, D., 2018. Effect of cross-section size on the flexural failure behavior of RC cantilever beams under low cyclic and monotonic lateral loadings. *Engineering Structures*, **156**, pp.567-586.
- Jaeger, J.C., Cook, N.G. and Zimmerman, R., 2009. *Fundamentals of rock mechanics*. John Wiley & Sons.
- Liu, H.K., Pan, C.H. and Liu, P.P., 2008. Dimension effect on mechanical behavior of silicon micro-cantilever beams. *Measurement*, **41**(8), pp.885-895.
- Mondol, Nazmul Haque, Jahren, Jens, Bjørlykke, Knut et al. 2008. Elastic properties of clay minerals. *The Leading Edge* **27** (6): 758-770.
- Mikowski, A., Soares, P., Wypych, F., Gardolinski, J.E.F.C. and Lepienski, C.M., 2007. Mechanical properties of kaolinite ‘macro-crystals’. *Philosophical Magazine*, **87**(29), pp.4445-4459.
- M'Barki, O., Brame, S., Diaz, O.C., Katiyar, A., Crosley, M., Knight, T. and Nguyen, Q.P., 2021. The effect of rock composition and microstructure on steam foam rheology in sandstone reservoirs. *Fuel*, **287**, p.119471.
- Obermayr, M., Dressler, K., Vrettos, C. and Eberhard, P., 2013. A bonded-particle model for cemented sand. *Computers and Geotechnics*, **49**, pp.299-313.
- O'Neill, M.E., 1968. A sphere in contact with a plane wall in a slow linear shear flow. *Chemical Engineering Science*, **23**(11), pp.1293-1298.
- Orlander, T., Milsch, H. and Fabricius, I.L., 2021. Comparison of gas, Klinkenberg, and liquid permeability of sandstone: Flow regime and pore size. *AAPG Bulletin*, **105**(7), pp.1383-1403.
- Prempeh, K., Chequer, L., Badalyan, A. and Bedrikovetsky, P., 2020, February. Effects of kaolinite on fines migration and formation damage. In SPE International Conference and Exhibition on Formation Damage Control. OnePetro.
- Potyondy, D.O. and Cundall, P.A., 2004. A bonded-particle model for rock. *International journal of rock mechanics and mining sciences*, **41**(8), pp.1329-1364.
- Rafieepour, S., Miska, S.Z., Ozbayoglu, E., Yu, M., Takach, N.E., Zhang, J. and Majidi, R., 2017, June. Experimental study of reservoir stress path and hysteresis during depletion and injection under different deformational conditions. In 51st US rock mechanics/geomechanics symposium. OnePetro.
- Reddi, L.N. and Govindaraju, R.S., 1995. Particle Mobilization in Sand-Clay Mixtures and Facilitation of Contaminant Removal-Critical Shear Stress Concept. In *Geoenvironment 2000: Characterization, Containment, Remediation, and Performance in Environmental Geotechnics* (pp. 1222-1236). ASCE.
- Reddi, L.N. and Bonala, M.V., 1997. Critical shear stress and its relationship with cohesion for sand. kaolinite mixtures. *Canadian geotechnical journal*, **34**(1), pp.26-33.
- Reddi, L.N., Lee, I.M. and Bonala, M.V., 2000. Comparison of internal and surface erosion using flow pump tests on a sand-kaolinite mixture. *Geotechnical testing journal*, **23**(1), pp.116-122.
- Robinson, E.S., 1970. Mechanical disintegration of the Navajo sandstone in Zion Canyon, Utah. *Geological Society of America Bulletin*, **81**(9), pp.2799-2806.
- Russell, T., Chequer, L., Borazjani, S., You, Z., Zeinijahromi, A. and Bedrikovetsky, P., 2018. Formation damage by fines migration: Mathematical and laboratory modeling, field cases. In *Formation Damage During Improved Oil Recovery* (pp. 69-175). Gulf Professional Publishing.
- Russell, T., Pham, D., Neishaboor, M.T., Badalyan, A., Behr, A., Genolet, L., Kowollik, P., Zeinijahromi, A. and Bedrikovetsky, P., 2017. Effects of kaolinite in rocks on fines migration. *Journal of Natural Gas Science and Engineering*, **45**, pp.243-255.

- Sang, J., Allen, P., Dunbar, J. and Hanson, G., 2015. Development of semi-physically based model to predict erosion rate of kaolinite clay under different moisture content. *Canadian Geotechnical Journal*, **52**(5), pp.577-586.
- Sarkisyan, S.G., 1971. Application of the scanning electron microscope in the investigation of oil and gas reservoir rocks. *Journal of Sedimentary Research*, **41**(1), pp.289-292.
- Sarkisyan, S.G., 1972. Origin of authigenic clay minerals and their significance in petroleum geology. *Sedimentary Geology*, **7**(1), pp.1-22.
- Sharma, M.M., Chamoun, H., Sarma, D.S.R. and Schechter, R.S., 1992. Factors controlling the hydrodynamic detachment of particles from surfaces. *Journal of colloid and interface science*, **149**(1), pp.121-134.
- Slaughter, W.S., 2012. *The linearized theory of elasticity*. Springer Science & Business Media.
- Stephens, L.S., Kelly, K.W., Simhadri, S., McCandless, A.B. and Meletis, E.I., 2001. Mechanical property evaluation and failure analysis of cantilevered LIGA nickel microposts. *Journal of microelectromechanical systems*, **10**(3), pp.347-359.
- Timoshenko, S.P. and Goodier, J.N., 1951. Theory of elasticity.
- Zhao, J., Qin, X., Wang, J. and He, M., 2020. Effect of Mg (II) and Na (I) doping on the electronic structure and mechanical properties of kaolinite. *Minerals*, **10**(4), p.368.
- Timoshenko, S., 1983. History of strength of materials: with a brief account of the history of theory of elasticity and theory of structures. Courier Corporation.
- Ting, H.Z., Bedrikovetsky, P., Tian, Z.F. and Carageorgos, T., 2021. Impact of shape on particle detachment in linear shear flows. *Chemical Engineering Science*, **241**, p.116658.
- Varzaneh, Ali Asghar Safari, Ahmadi, Morteza, and Goshtasbi, Kamran. 2021. Simulation of hydraulic fracturing and Darcy fluid flow in a porous medium using a coupled Discrete Element Method with fluid flow. *Journal of Petroleum Science and Engineering* **204**: 108706.
- Verwey, E.J.W., 1947. Theory of the stability of lyophobic colloids. *The Journal of Physical Chemistry*, **51**(3), pp.631-636.
- Walker, E. and Glover, P.W.J., 2018. Measurements of the relationship between microstructure, pH, and the streaming and zeta potentials of sandstones. *Transport in porous media*, **121**(1), pp.183-206.
- Wilson, M.D. and Tillman, R.W., 1974. Diagenetic destruction of feldspar and genesis of clay: their influence on sandstone classification and grain size analysis. In *Geological Society of America Abstracts with Programs* (Vol. **5**, pp. 130-131).
- Wilson, M.D. and Pittman, E.D., 1977. Authigenic clays in sandstones; recognition and influence on reservoir properties and paleoenvironmental analysis. *Journal of Sedimentary Research*, **47**(1), pp.3-31.
- Yang, H., He, M., Lu, C. and Gong, W., 2019. Deformation and failure processes of kaolinite under tension: Insights from molecular dynamics simulations. *SCIENCE CHINA Physics, Mechanics & Astronomy*, **62**(6), p.64612.
- You, Z., Bedrikovetsky, P., Badalyan, A. and Hand, M., 2015. Particle mobilization in porous media: temperature effects on competing electrostatic and drag forces. *Geophysical Research Letters*, **42**(8), pp.2852-2860.
- Young, A.P. and Ashford, S.A., 2008. Instability investigation of cantilevered seacliffs. *Earth Surface Processes and Landforms: The Journal of the British Geomorphological Research Group*, **33**(11), pp.1661-1677.
- Zhang, S., Liu, Q., Yang, Y., Wang, D., He, J. and Sun, L., 2017. Preparation, morphology, and structure of kaolinites with various aspect ratios. *Applied Clay Science*, **147**, pp.117-122.

5. Geo-mechanical aspects for breakage detachment of rock fines by Darcys flow

Hashemi, A., Borazjani, S., Nguyen, C., Loi, G., Khazali, N., Badalyan, A., Yang, Y.,
Tian, Z.F., Ting, H.Z., Dang-Le, B. and Russell, T.,2023.

arXiv preprint arXiv:2301.01422.

Statement of Authorship

Title of Paper	Geo-mechanical aspects for breakage detachment of rock fines by Darcys flow		
Publication Status	<input checked="" type="checkbox"/> Published	<input type="checkbox"/> Submitted for Publication	
	<input type="checkbox"/> Accepted for Publication	<input type="checkbox"/> Unpublished and Unsubmitted work written in manuscript style	
Publication Details	Hashemi, A., Borazjani, S., Nguyen, C., Loi, G., Khazali, N., Badalyan, A., Yang, Y., Tian, Z.F., Ting, H.Z., Dang-Le, B. and Russell, T., 2023. Geo-mechanical aspects for breakage detachment of rock fines by Darcys flow. arXiv preprint arXiv:2301.01422.		

Principal Author

Name of Principal Author (Candidate)	Abolfazl Hashemi		
Contribution to the Paper	Collecting data, performing lab data analysis, deriving the equations, writing code for the authigenic particle detachment, preparing the graphs, writing part of the manuscript.		
Overall percentage (%)	85%		
Certification:	This paper reports on original research I conducted during the period of my Higher Degree by Research candidature and is not subject to any obligations or contractual agreements with a third part that would constrain its inclusion in this thesis. I am the primary author of this paper.		
Signature		Date	15/11/2023

Co-Author Contributions

By signing the Statement of Authorship, each author certifies that:

- I. The candidate's stated contribution to the publication is accurate (as detailed above);
- II. Permission is granted to the candidate to include the publication in the thesis; and
- III. The sum of all co-author contributions is equal to 100% less the candidate's stated contribution

Name of Co-Author	Sara Borazjani		
Contribution to the Paper	Co-supervising, aiding in the derivations of breakage equations and checking the results		
Signature		Date	15/11/2023

Name of Co-Author	Cuong Cao Nguyen		
Contribution to the Paper	Collecting literature data, writing code, and analysing detrital particle detachment		
Signature		Date	15/11/2023

Name of Co-Author	Grace Loi		
Contribution to the Paper	Collecting literature data, writing code, and analysing detrital particle detachment		
Signature		Date	15/11/2023

Name of Co-Author	Nastaran Khazali		
Contribution to the Paper	Deriving equations and matching lab data using two-population particle detachment mechanism.		
Signature		Date	15/11/2023

Name of Co-Author	Alex Badalyan		
Contribution to the Paper	Supervising lab design and data collection		
Signature		Date	15/11/2023

Name of Co-Author	Yutong Yang		
Contribution to the Paper	Performing sensitivity on MRF, collecting field data for fluid velocity through fracture and fault, and preparing cross plots.		
Signature		Date	15/11/2023

Name of Co-Author	Zhao Feng Tian		
Contribution to the Paper	Supervising the CFD modelling part.		
Signature		Date	15/11/2023

Name of Co-Author	Heng Zheng Ting		
Contribution to the Paper	Performing CFD modelling and delivering shape factor equations.		
Signature		Date	15/11/2023

Name of Co-Author	Bryant Dang-Le		
Contribution to the Paper	Collecting and analysing lab data, collecting field data.		
Signature	Bryant Dang-Le	Date	15/11/2023

Name of Co-Author	Thomas Russell		
Contribution to the Paper	Co-supervising, aiding in the derivations of DLVO equations and checking the DLVO results, giving consultation on the total MRF, giving advice, and proofreading the manuscript.		
Signature		Date	15/11/2023

Name of Co-Author	Pavel Bedrikovetsky		
Contribution to the Paper	Methodology and supervision.		
Signature		Date	15/11/2023

Geo-mechanical aspects for breakage detachment of rock fines by Darcy's flow

Abolfazl Hashemi¹, Sara Borazjani¹, Cuong Nguyen¹, Grace Loi¹, Nastaran Khazali¹, Alex Badalyan¹, Yutong Yang¹, Zhao Feng Tian², Heng Zheng Ting², Bryant Dang-Le¹, Thomas Russell¹, Pavel Bedrikovetsky¹

¹*School of Chemical Engineering, The University of Adelaide 5000, SA, Australia*

²*School of Mechanical Engineering, The University of Adelaide 5000, SA, Australia*

Keywords

Bond breakage, Failure criteria, Beam theory, Particle detachment, Fines migration, Analytical model

ABSTRACT Suspension-colloidal-nano transport in porous media encompasses the detachment of detrital fines against electrostatic attraction and authigenic fines by breakage, from the rock surface. While much is currently known about the underlying mechanisms governing detachment of detrital particles, including detachment criteria at the pore scale and its upscaling for the core scale, a critical gap exists due to absence of this knowledge for authigenic fines. Integrating 3D Timoshenko's beam theory of elastic cylinder deformation with CFD-based model for viscous flow around the attached particle and with strength failure criteria for particle-rock bond, we developed a novel theory for fines detachment by breakage at the pore scale. The breakage criterium derived includes analytical expressions for tensile and shear stress maxima along with two geometric diagrams which allow determining the breaking stress. This leads to an explicit formula for the breakage flow velocity. Its upscaling yields a mathematical model for fines detachment by breakage, expressed in the form of the maximum retained concentration of attached fines versus flow velocity – maximum retention function (MRF) for breakage. We performed corefloods with piecewise constant increasing flow rates, measuring breakthrough concentration and pressure drop across the core. The behaviour of the measured data is consistent with two-population colloidal transport, attributed to detrital and authigenic fines migration. Indeed, the laboratory data show high match with the analytical model for two-population colloidal transport, which validates the proposed mathematical model for fines detachment by breakage.

1. Introduction

Dislodgement of natural reservoir fines from rock surfaces, induced by viscous flow in porous media, with the following migration and capture by the rock is essential in numerous natural and industrial processes. These include well fracturing, production of coal bed methane, water and polymer injection in aquifers and oilfields, heavy oil production, underground storage of CO₂ in aquifers and depleted oil and gas fields, fresh and hot water storage in aquifers, radioactive nuclear waste, and enhanced geothermal projects.¹⁻⁶ Usually, the migrating fines are clays (kaolinite, illite, chlorite), silica particles, or coals.⁷⁻⁹ Fig. 1 shows SEM images of potentially migrating fines attached to rock surface. Figs. 1a and 1c show *authigenic* particles that naturally grow on rock surfaces during geological times, while Figs. 1b and 1d show *detrital* particles attached to rock surfaces by electrostatic forces. Viscous flows in porous media induce drag and lift exerting on attached particles, which can result in their detachment. Authigenic particles are dislodged by stresses that initiate breakage of the particle-substrate

bond, while detrital fines are detached by overcoming the electrostatic particle-substrate attraction.¹⁰

The detachment schematic at the pore scale is presented in Fig. 2a, where the detachment of authigenic and detrital particles occurs at the lower and upper parts of pore throat, respectively. The mobilisation of fines yields their straining in thin pore throats which consequently alters the fluid flow. The attached fines coat the rock surface, so their dislodging causes low-to-moderate permeability increase, while plugging the flow paths yields significant decline of permeability.^{5, 11} The consequent decrease of well productivity and injectivity motivates significant efforts in studying migration of natural reservoir fines in porous media.^{8, 12-14} Indeed, currently this topic is well developed for detrital fines.¹²⁻¹⁴

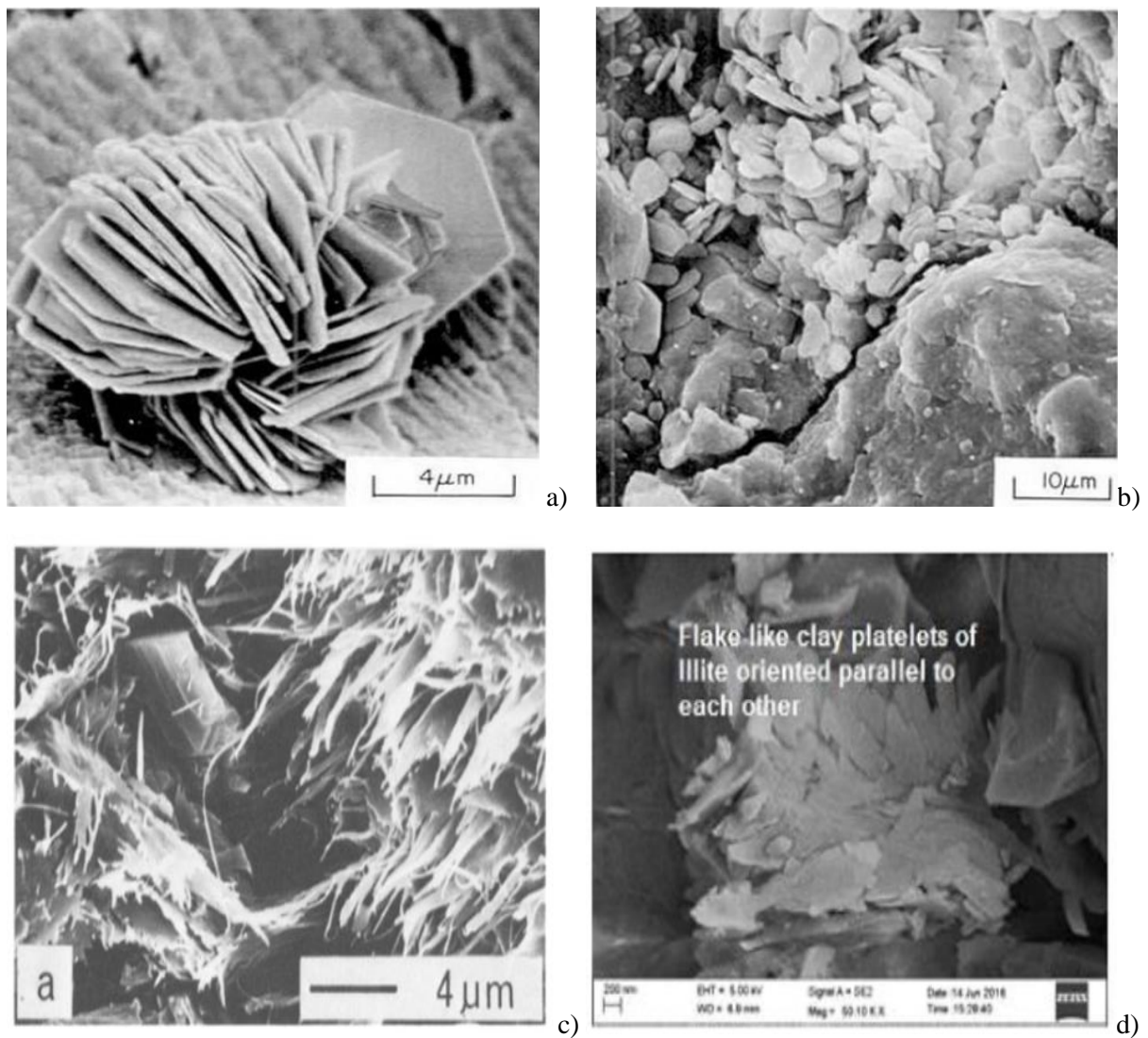


Figure 1: SEM photos of clay particles attached to the grains of sandstone rocks: a) authigenic kaolinite,¹⁵ b) detrital kaolinite,¹⁵ c) authigenic illite,¹⁶ d) detrital illite¹⁷

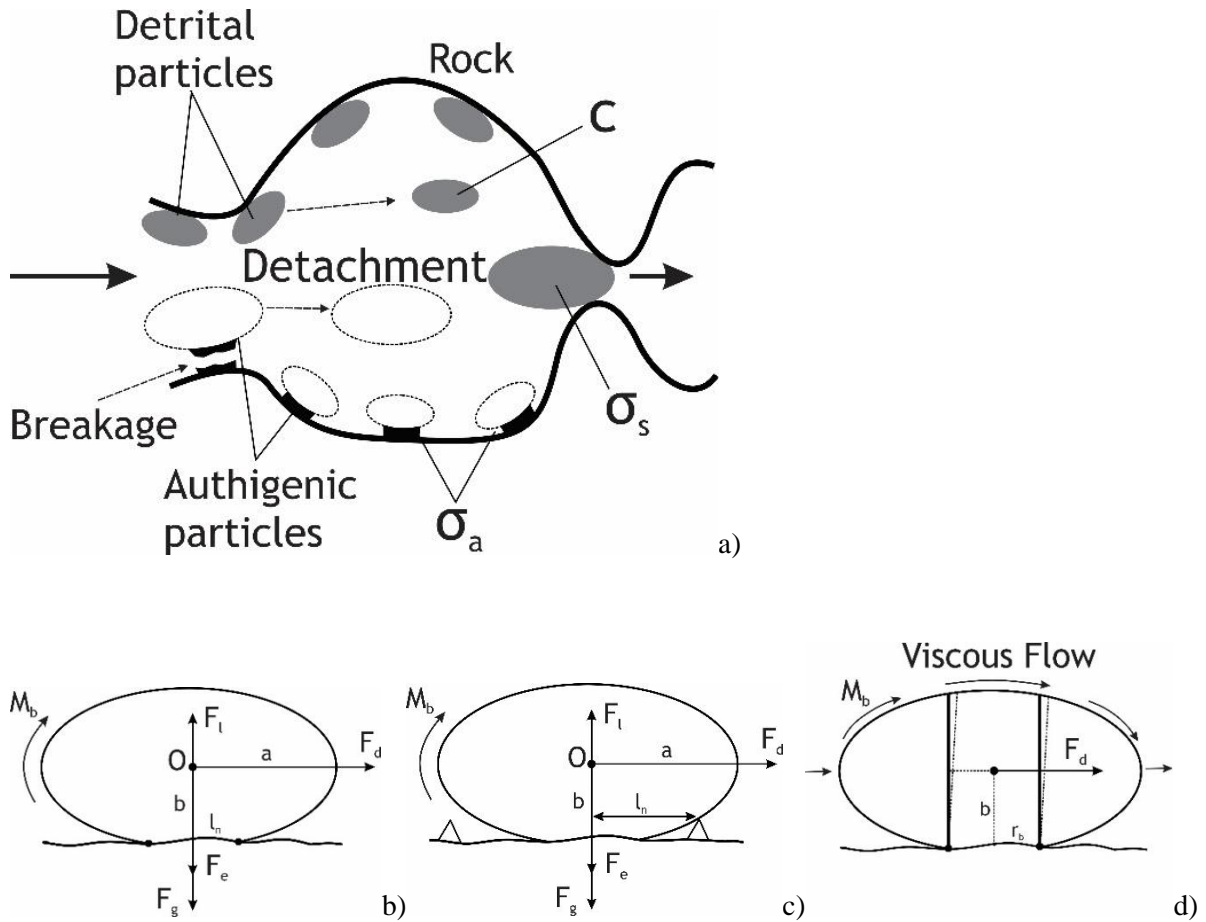


Figure 2. Detachment for detrital and authigenic clay particles: a) schematic for detachment at the pore scale; b) force (torque) balance at attached detrital fine with lever arm due to particle deformation; c) lever arm at attached detrital fine due to rock surface asperity; d) representation of attached authigenic particle by deformable beam¹⁸

Current mathematical and lab modelling for detachment of detrital fines is based on mechanical equilibrium of a particle situated on the solid substrate.^{13, 19-21} Detrital fines detachment by drag against electrostatic forces is shown at the upper part of the entrance throat in Fig. 2a. Figs. 2b and 2c show drag, electrostatic, lift, and gravity forces exerting on an isolated fine particle. At the moment of dislodging, a particle rotates around a contact point on the rock surface. The corresponding lever arm is determined by either mutual particle-rock deformation, like in Fig. 2b, or by the size of the rock surface asperity, like in Fig. 2c. The attaching electrostatic force is described by DLVO theory.²¹ The mathematical model for fines dislodging is either a linear-kinetics equation for detachment rate,^{12, 14} or a function of retained concentration of attached particles versus velocity that is derived from mechanical equilibrium.^{22, 23} Both models close the system of governing equations for colloidal-suspension-nano transport in porous media. In this work, to upscale the detachment model from pore to rock scale, we use the approach of maximum retention function (MRF). Whereas much is currently known about the underlying mechanisms governing the flow-induced detachment of detrital fines, a critical gap exists due to the absence of geomechanics-flow breakage criteria for authigenic fines.

Detachment of authigenic fines during flow in rocks, as it is shown in Figs. 2d, 3d, and 3h, occurs by breakage. Particle dislodgement by breakage under viscous flows in porous media

has been observed during sand production,²⁴ well acidizing,^{25, 26} cement dissolution in sandstones,^{27, 28} carbonate rock dissolution in water,²⁹ and illite breakage under flow during hydraulic fracturing.¹⁰ Guo et al. 2016 observed coal fines detachment by breakage during coreflood under piecewise-constant increasing velocity.³⁰ Wang et al. 2020 observed produced calcite particles from broken bonds with grains during waterflood tests.²⁶ Using SEM images, the above works clearly distinguish between detachment of detrital fines against electrostatic attraction and breakage of authigenic particles.

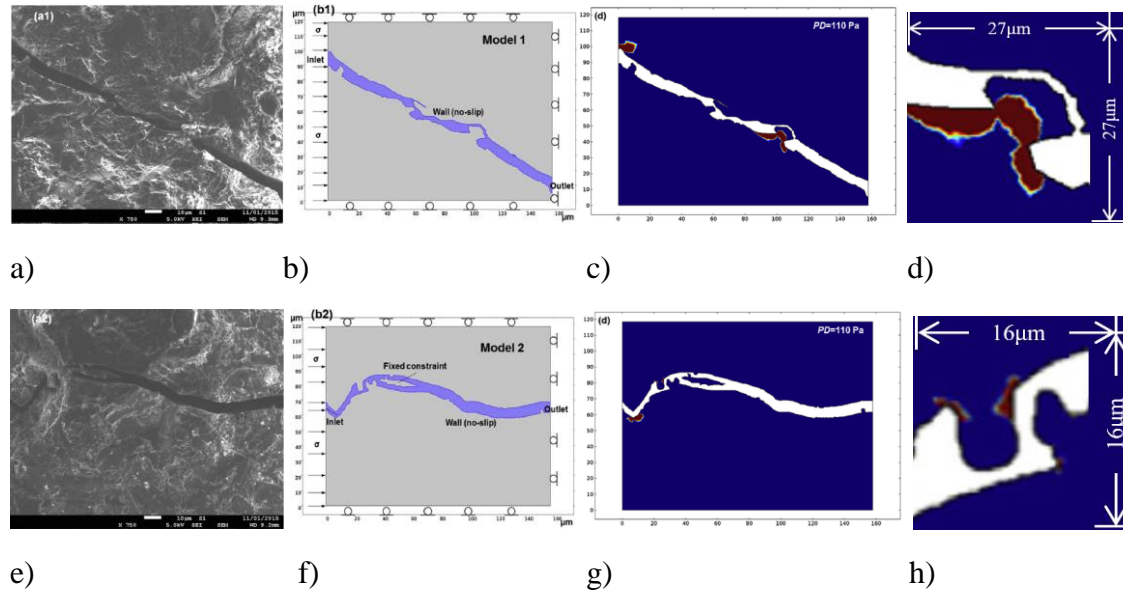


Figure 3: SEM photos of potential fine generation at different coal cleats (a and e), cleat and asperity geometries used in numerical simulations (b and f), failure zones (in red) for each case as a result of numerical simulation (c and g), and zoom for failure zones (d and h)³¹

The micro-scale numerical fines-detachment models couple flow and stress equations.^{31, 32} SEM images (Figs. 3a, 3e) allow defining the channel model geometries (Figs. 3b, 3f), where the boundary conditions on the liquid-solid interfaces are posed and setting the detailed coupled numerical model for flow in porous channels and induced stresses in the rock (Figs. 3c, 3g). The failure zones are calculated from the stress field using various failure criteria (Figs. 3d, 3h), predicting particle detachment at the pore scale (Figs. 3d, 3h). The analytical model for stresses, induced by the external load, based on beam theory³³ was used to predict rock failure in sea-cliffs and sandstone canyon cliffs,^{34, 35} and between grains consolidated by cement.^{18, 36}

Micro scale modelling of particle detachment by breakage strongly depends on the rheological behaviour of particles bonded with the rock surface, the corresponding breakage criteria, and critical stress conditions. Laboratory pore-scale bending tests for single particles bonded to solid substrate have been performed for kerogen-rich shales, and brittle behaviour has been observed.³⁷ Other tests related to non-mineral-rock materials – polymer-clay,³⁸ glass,³⁹ and silicon⁴⁰⁻⁴² – also exhibited brittle behaviour, while the tests with nickel showed ductile behaviour.⁴³ Geo-mechanical tests with partly water-saturated kaolinite powder detect brittle behaviour,⁴⁴⁻⁴⁹ while for high saturations of water, the powder becomes ductile.^{44, 50, 51} Mixing kaolinite soil with more than 1% of cement changes ductile behaviour of the stress-strain diagram into brittle.⁵² Quartz powder and its rich mixtures with kaolinite exhibit brittle behaviour.⁵³ Carbonate powders, and their rich mixtures with quartz in low water saturations show typical brittle stress-strain diagrams.^{53, 54} Moreover, sand particles bonded with calcium

carbonate powder under tensile and shear tests show shape decline after failure which is an indication of brittle behaviour.⁵⁴

Other laboratory studies also encountered either brittle or ductile failure in reservoir rocks, in particular in kaolinite-rich rocks,^{55, 56} illite-rich shales,⁵⁷⁻⁵⁹ chlorite-rich black shale rocks,⁶⁰ quartz-rich sandstone,^{61, 62} cement mortar rock,⁶³ and coal rocks.⁶⁴⁻⁶⁶

Molecular-dynamic simulation of rheological kaolinite behaviour for hydrated and defected kaolinite crystals with the typical length of 100 Angstrom shows brittle properties under stress loading at the tension case with parallel and perpendicular to layering.⁶⁷⁻⁶⁹ Zhang et al. 2021 simulate both tension and compaction loads; tension stress-strain diagrams have brittle type for load parallel and perpendicular to layering, while those for compression are brittle for parallel load and are ductile for perpendicular load.⁷⁰

The above experimental studies highlight the prevalence of mechanical failure of colloidal particles in porous media. The difference in detachment criteria for authigenic and detrital particles is important for understanding and modelling fines migration. However, this distinction hasn't been used in the analysis of coreflooding or field production data. Despite these phenomena being widely spread, a pore-scale mathematical model and its upscaling to the rock scale transport are not available.

The present paper fills the gap. This contribution integrates CFD-based modelling of viscous fluid – attached particle interaction, 3D elastic beam theory, and strength failure criteria, yielding an explicit expression for breakage detachment conditions of authigenic fines. It was found that stress maxima are reached at either the middle or boundary of the beam base. Introduction of tensile-stress and shear-tensile diagrams allows determining which stress causes the particle failure. Formulae for breakage flow velocities have been derived for all cases of particle breakage by different stresses. The expressions for breakage velocity allow determining the maximum retention concentration versus velocity (MRF), which is a mathematical model for fines mobilisation by breakage at the rock (laboratory cores and reservoirs) scale. The laboratory test undertaken comprises coreflooding with 7 rates taken in increasing order while measuring particle breakthrough concentrations and pressure drop across the core. High match between the model and the experimental data from this test, and also from 4 tests taken from the literature, validate the mathematical model for particle detachment by breakage.

2. Microscale model for particle detachment from rock surface by breakage

This section integrates Timoshenko's beam theory with creeping viscous flow around attached particles. This includes assumptions of the model (section 2.1), CFD-based expressions for drag and torque for the particles with different geometries (section 2.2), and derivations for tensile and shear stress distributions over the beam base (section 2.3).

2.1. Assumptions of the particle breakage model

The breakage detachment model for a single particle is based on Navier-Stokes equations for viscous flow around the attached particle with resulting drag force and moment exerting on the particle, elastic beam theory,³³ and the rock failure criteria by tensile or shear strength.⁷¹⁻⁷³ The main detaching force is drag (Figs. 2b, 2c). We assume small deformation for solid mineral particles and negligible effect of particle deformation on the drag force and moment.

Fig. 2d shows 3D cantilever beam for spheroidal particle; the undeformed vertical configuration is exhibited by continuous lines; the end loading by drag displaces material points to the deformed shape shown by dashed curves. The stresses in the particle outside the beam are lower than those inside, which justifies the beam approximation of an irregularly shaped particle for deformation modelling. The assumption that the particle volume around the beam stem has negligible impact on the stress maxima over the particle-substrate contact area has been used by Robinson et al. 1970, Young and Ashford 2008, Obermayer et al. 2013, Wagner et al. 2016, and Chen et al. 2022. ^{18, 34, 35, 74, 75}

Because drag is applied to the centre of mass of the particle, the beam connects the base to the centre, and the drag acts as an external load on the top cross-section of the beam. We assume that the particle shape is spheroidal, and the contact area is circular. Cylindrical shaped particles are considered too. We also assume homogenous and linear-elastic particle matter.

It is assumed that planar sections perpendicular to the neutral axis before deformations remain planar, but not necessarily perpendicular to the neutral axis after deformation, i.e., shear deformations cannot be ignored. This is particularly important for “short” kaolinite and chlorite clay particles that represent the most widely spread fines in natural reservoirs. Therefore, stress modelling for fines breakage is based on Timoshenko’s rather than Bernoulli-Euler beam theory. ⁷⁵

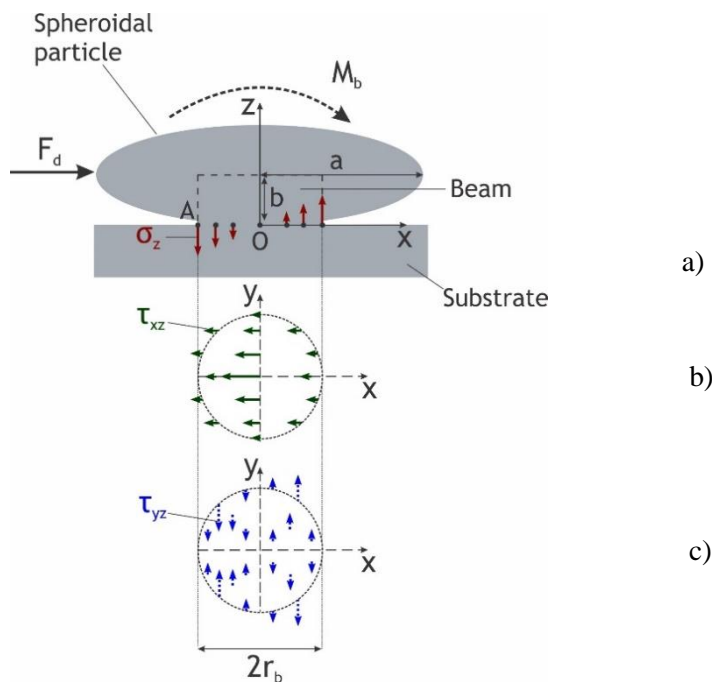


Figure 4: Schematic of equivalent beam for attached spheroidal particle: a) loading force and moment exerting from viscous flow; b) shear in plane parallel/perpendicular by Timoshenko’s solution; c) shear in plane parallel/perpendicular by Timoshenko’s solution

The present work assumes that the maximum stress in the particle-substrate contact area due to drag is determined by the deformation of the cylindrical beam with the base equal to the particle-substrate contact area. This assumption was adopted from Obermayer et al. 2013. ¹⁸ Therefore, the failure criteria for the attached particle is determined from the cylindric beam deformation from Timoshenko’s solution. The same assumption has already been used by Robinson, 1970, and Young and Ashford, 2008. ^{34, 35}

Figs. 2b, 2c show the spheroidal particle, drag exerting from the moving viscous fluid, and the induced moment. Under slow creeping flows in porous media, lift is negligibly small if compared with drag. Gravity can also be ignored. Fig. 4a shows the normal stress σ_z versus the horizontal x-coordinate at the beam base $z=0$. The advancing point of the particle is in extension as a result of the drag, and the receding point is in compression. Figs. 4b and 4c exhibit the distributions of shear stresses (τ_{xz} and τ_{yz}) over the beam cross section. Stress τ_{xz} is maximum at central point of the base, while stress τ_{yz} is zero at this point. Timoshenko's beam model assumes that normal stress over a cross section is distributed in the same manner as in the case of pure bending. The remaining three stress components i.e. σ_x , σ_y , and τ_{xy} are zero.³³ The expressions for all stresses of the beam theory are presented in Appendix A.

The particle exhibits brittle behaviour with breakage. The breakage occurs instantly according to maximum stress criteria, i.e., if either tensile or shear stress reaches strength (maximum) values.^{71, 72}

2.2. Drag force and moment

Consider Couette flow of viscous fluid over a plane substrate and around the attached particle (Figs. 2b, 2c, 2d). Drag F_d and its moment M_b for spherical, oblate spheroidal, and cylindrical particles are extensions of the Stokes formula, which is valid for spherical particles⁷⁶:

$$F_d = 6\pi\mu_f r_s V f_d(\alpha_s) \quad (1)$$

$$M_b = F_d b f_M(\alpha_s) = 6\pi\mu_f r_s V f_d(\alpha_s) b f_M(\alpha_s) \quad (2)$$

where, μ_f is the fluid viscosity, r_s is the particle radius, V is the interstitial fluid velocity, f_d is the shape factor for drag force, b is the lever arm for drag force, and f_b is the moment shape factor. Interstitial fluid velocity V is expressed via Darcy's velocity U as

$$U = \phi V \quad (3)$$

where ϕ is the porosity.

For a non-spherical particle, the effective radius, r_s is determined based on the equality of the volume of the desired shape and a sphere with radius r_s .

For a cylindrical particle, the effective radius and aspect ratio, α_s are defined as

$$2\pi a_c^2 b_c = \frac{4}{3}\pi r_s^3, \quad r_s = b_c \left(\frac{2}{3}\alpha_s^2 \right)^{-1/3}, \quad \alpha_s = b_c / a_c \quad (4)$$

where a_c and b_c are the cylinder base radius and height, respectively.

The effective radius r_s and aspect ratio for a spheroidal particle are defined similarly as:

$$\pi a^2 b = \frac{4}{3}\pi r_s^3, \quad r_s = b \alpha_s^{-2/3}, \quad \alpha_s = b / a \quad (5)$$

where a and b are semi-major and semi-minor axes of spheroid, respectively, and α_s is the aspect ratio.

Following Ting et al. 2021, we calculate the shape factors for drag force and moment using CFD package ANSYS/CFX.⁷⁷ The calculations are performed for long thin cylinders, which approximate illite clay particles (Figs. 1c, 1d). Figs. 2a, 2b, 2c show the schematic for fluid flow around the attached particle. Drag is calculated from the solution of the Navier-Stokes equations for viscous flow with no-slip conditions at the solid-fluid particle and substrate surfaces. The shape factors for drag force and moment, f_D and f_M , respectively, are calculated from the numerical solution using Eqs. (1) and (2).

For long thin cylinders, which correspond to aspect ratio $\alpha_s > 1$, the correlations for drag force and moment factors, based on multiple runs of the CFD package, are:

$$f_d = (0.9014\alpha_s^2 + 1.599\alpha_s + 2.265)(\alpha_s + 1.752)^{-1} \quad (6)$$

$$f_M = (0.0002161\alpha_s^3 + 1.34\alpha_s^2 + 44.18\alpha_s + 21.27)(\alpha_s^2 + 31.34\alpha_s + 10.38)^{-1} \quad (7)$$

respectively. We will be using these correlations further in the text to calculate maximum stresses and predict the particle-substrate bond breakage. The expressions for drag and moment factors for spheroidal and thin-cylinder particles, which model kaolinite, chlorite, and silica particles, are available from Ting et al. 2021.⁷⁷

2.3. Stress distributions at the base of the beam

Substitution of beam stress equations (A1-A3) into the expressions for principal stresses (A5), yields the equations for maximum tensile and shear stresses at the beam base:

$$\sigma_3 = \frac{1}{2} \frac{F_d}{I} r_b^2 \left(\frac{bf_M}{r_b} \frac{x}{r_b} - \sqrt{\left(\frac{bf_M}{r_b} \right)^2 \left(\frac{x}{r_b} \right)^2 + 4 \left(\left(\frac{(3+2\nu)}{8(1+\nu)} \left(1 - \left(\frac{x}{r_b} \right)^2 - \frac{(1-2\nu)}{(3+2\nu)} \left(\frac{y}{r_b} \right)^2 \right) \right)^2 + \left(-\frac{(1+2\nu)}{4(1+\nu)} \frac{x}{r_b} \frac{y}{r_b} \right)^2} \right) \quad (8)$$

$$\frac{\sigma_1 - \sigma_3}{2} = \frac{1}{2} \frac{F_d}{I} r_b^2 \left(\sqrt{\left(\frac{bf_M}{r_b} \right)^2 \left(\frac{x}{r_b} \right)^2 + 4 \left(\left(\frac{(3+2\nu)}{8(1+\nu)} \left(1 - \left(\frac{x}{r_b} \right)^2 - \frac{(1-2\nu)}{(3+2\nu)} \left(\frac{y}{r_b} \right)^2 \right) \right)^2 + \left(-\frac{(1+2\nu)}{4(1+\nu)} \frac{x}{r_b} \frac{y}{r_b} \right)^2} \right) \quad (9)$$

Axes are shown in Fig. 4.

Eqs (8) and (9) for normalised stresses can be transformed into the following dimensionless form

$$\frac{\sigma_3}{T_0} = \frac{1}{\kappa} \left(X - \sqrt{X^2 + \chi \left(1 - X^2 - \frac{(1-2\nu)}{(3+2\nu)} Y^2 \right)^2} + \chi \frac{4(1+2\nu)^2}{(3+2\nu)^2} (XY)^2 \right) \quad (10)$$

$$\frac{\sigma_1 - \sigma_3}{2S_0} = \frac{\eta}{\kappa} \sqrt{X^2 + \chi \left(1 - X^2 - \frac{(1-2\nu)}{(3+2\nu)} Y^2 \right)^2} + \chi \frac{4(1+2\nu)^2}{(3+2\nu)^2} (XY)^2 \quad (11)$$

where T_0 and S_0 are the tensile and shear strengths, respectively. Normalised stress expressions (10, 11) contain three dimensionless groups reflecting the interaction between the creeping flow around an attached particle and the induced elastic deformation of the particle – dimensionless numbers κ , χ , and η :

$$\kappa = \frac{2T_0}{F_d} \frac{I}{r_b b f_M} = \frac{2T_0}{F_d} \frac{I}{\delta \alpha_s f_M}, \quad \chi = \left[\frac{r_b}{b f_M} \frac{3+2\nu}{4(1+\nu)} \right]^2 = \left[\frac{\delta}{\alpha_s f_M} \frac{3+2\nu}{4(1+\nu)} \right]^2, \quad \eta = \frac{T_0}{S_0}, \quad \delta = \frac{r_b}{a}, \quad X = \frac{x}{r_b}, \quad Y = \frac{y}{r_b} \quad (12)$$

Dimensionless group κ is proportional to the ratio between tensile strength and fluid pressure caused by the drag exerting on the particle cross section and is called the *strength-drag number*. Dimensionless number κ also depends on bond ratio δ , aspect ratio α_s , and moment of inertia I . Dimensionless group χ depends on geometric parameters, namely the bond ratio δ and aspect ratio α_s , and on the Poisson ratio ν and is called, therefore, the *shape-Poisson number*. The *strength number* η is the ratio between tensile and shear strengths.

Common interval of parameters for rock minerals are: aspect ratio α_s varies from 0.03 to 1.0 for spheroids and flat cylinders and from 1 to 100 for long cylinders, bond ratio δ - from 10^{-3} to 1.0, and Poisson's ratio ν - from zero to 0.5. Eq. (12) along with formulae for drag and moment shape factors results in values of the shape-Poisson number χ varying from 2.4×10^{-7} to 4.8 for spheroids, from 2.4×10^{-5} to 0.3 for long cylinders, and from 0.18 to 135 for flat cylinders.

3. Derivation of maxima for tensile and shear stresses

Here we transform a graphical technique to determine the stress that meets the strength failure criteria. It includes the derivation of stress maxima at the beam base (section 3.1), calculation of tensile stress maxima over the beam base middle and boundary (section 3.2) and their comparison using the tensile stress diagram (section 3.3), calculation of shear stress maxima over the beam base middle and boundary (section 3.4) definition of the failing stress using the tensile-shear diagram (section 3.5).

The failure criteria used in this work correspond to reaching the strength values by maximum tensile and shear stresses.^{71,73} The corresponding expressions for tensile and shear failures are:

$$-\sigma_3 \geq T_0, \quad \frac{-\sigma_3}{T_0} \geq 1 \quad (13)$$

$$\frac{\sigma_1 - \sigma_3}{2} \geq S_0, \quad \frac{\sigma_1 - \sigma_3}{2S_0} \geq 1, \quad (14)$$

respectively. Here T_0 is the tensile strength, and S_0 is the shear strength.

To determine which stress causes failure, the following maxima must be compared

$$\max_{X^2+Y^2 \leq 1} \frac{-\sigma_3(X,Y)}{T_0}, \quad \max_{X^2+Y^2 \leq 1} \frac{\sigma_1(X,Y) - \sigma_3(X,Y)}{2S_0} \quad (15)$$

To apply failure criteria (13, 14) to the expressions for normalised tensile and shear stresses at the base of the beam, in the next section we calculate the maxima of those stress functions over the area $X^2+Y^2 \leq 1$.

3.1. Stress maxima at the base of the beam

Consider maxima of the tensile and shear stresses given by Eqs. (10, 11). If the maxima points (X_m, Y_m) are located inside the base circle, $X_m^2 + Y_m^2 < 1$, partial derivatives of both expressions (10) and (11) over Y must be zero. Both expressions depend on Y^2 , so the expressions for first

partial derivatives in Y contain Y as a multiplier and is zero at $Y=0$. It is possible to show that the multiplier inside the unitary circle is positive, and that second partial derivatives in Y of both expressions (10) and (11) are negative at $Y=0$. Therefore, all maxima inside the base circle $X_m^2 + Y_m^2 < 1$ are reached along the middle of the base, i.e., axis $Y=0$. Otherwise, tensile or shear stresses reaches maxima at the beam base over the boundary $X_m^2 + Y_m^2 = 1$.

Expressions for normalised tensile and shear stresses versus X in the *beam middle* $Y=0$ are obtained from Eqs. (10, 11):

$$\frac{\sigma_3}{T_0} = T^0(X, \chi) = \frac{1}{\kappa} \left(X - \sqrt{X^2 + \chi(1 - X^2)^2} \right) \quad (16)$$

$$\frac{\sigma_1 - \sigma_3}{2S_0} = S^0(X, \chi) = \frac{\eta}{\kappa} \sqrt{X^2 + \chi(1 - X^2)^2} \quad (17)$$

Expressions for normalised tensile and shear stresses versus X at the *cylinder boundary* are obtained from Eqs. (10, 11) by substituting $Y^2 = 1 - X^2$:

$$\frac{\sigma_3}{T_0} = T^1(X, \chi, \nu) = \frac{1}{\kappa} \left(X - \sqrt{X^2 + \chi \frac{4(1+2\nu)^2}{(3+2\nu)^2} (1 - X^2)} \right) \quad (18)$$

$$\frac{\sigma_1 - \sigma_3}{2S_0} = S^1(X, \chi, \nu) = \frac{\eta}{\kappa} \sqrt{X^2 + \chi \frac{4(1+2\nu)^2}{(3+2\nu)^2} (1 - X^2)} \quad (19)$$

3.2. Maxima of tensile stresses in the beam middle and boundary

In order to apply failure criteria (13, 14) to expressions for normalised tensile and shear stresses at the cylinder middle and at boundary, let us calculate maxima of the four stress functions (16-19) over the closed X -interval $[-1, 1]$. Fortunately, for all 4 cases, the maximum points X_m and the corresponding values of normalised stresses can be found explicitly. In the middle of the base, maxima of the two functions (16) and (16) inside the base circle $(-1, 1)$ are determined by conditions of zero first derivative in X at some point $X=X_m$, and negative second derivative in the same point. Then the obtained maxima are compared with stresses at the boundary $X=-1$ and $X=1$. The same procedure is applied for stress functions (18, 19) on the beam base boundary. Afterward, the detachment regime and the detachment point X_m are determined by comparison of the 4 normalised tensile and shear stresses at the boundaries $X=-1$ and $X=1$, and the open interval between them.

From now on, we call dimensionless stress the product of strength-drag number κ and normalised stress, defined in Eqs. (16-19).

The profiles for dimensionless tensile stress $\kappa T_m^0(X)$ in the middle of the cylinder base for four values of the shape-Poisson number $\chi=1, 2, \chi=\chi_l$, and $\chi=4.5$ are presented in Fig. 5a. Here $\chi=\chi_l$ is the value where κT_m^0 at the boundary $X=-1$ is equal to maximum inside the interval. As χ tends to zero, the plot of $\kappa T_m^0(X)$ tends to two straight lines corresponding to two values of square root in expressions (34, 35). At some χ there does appear a maximum inside the open interval $(-1, 1)$, which remains below $\kappa T_m^0(-1, \chi)=2$, reached in the advanced point $X_m=-1$. Inequality $\kappa T_m^0 < 2$ remains fulfilled for $\chi < \chi_l$. The threshold value χ_l and corresponding

maximum point $X=X_m$ are determined from system of two transcendental equations and one inequality:

$$\kappa T^0(X_m, \chi_1) = 2, \quad \frac{\partial \kappa T^0}{\partial X}(X_m, \chi_1) = 0, \quad \frac{\partial^2 \kappa T^0}{\partial X^2}(X_m, \chi_1) < 0 \quad (20)$$

The solution of (36) is unique; the roots are found numerically: $\chi_1=3.38, X_{m1}=-0.33$.

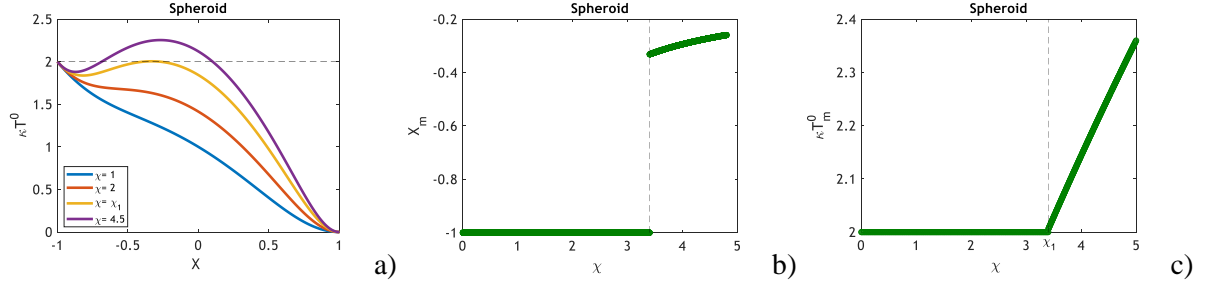


Fig. 5. Maximum tensile stress at $Y=0$: a) dimensionless tensile stress in the middle versus χ for 3 different values of aspect-Poisson number χ ; b) position of maximum tensile stress X_m at $Y=0$; c) maximum value of tensile stress at $Y=0$ versus χ

For $\chi > \chi_1$, the maximum is reached inside the open interval $-1 < X_m < 1$ (violet curve in Fig. 5a). The expression for maximum normalised tensile stress at $Y=0$ is

$$T_m^0(\chi) = \frac{1}{\kappa} \begin{cases} 2, & \chi \leq \chi_1 \\ -X_m(\chi) + \sqrt{X_m^2 + \chi(1 - X_m^2)^2}, & \chi > \chi_1 \end{cases}; \quad X_m = \begin{cases} -1, & \chi \leq \chi_1 \\ -\sqrt{\frac{\sqrt{(4\chi-1)(4\chi-9)} - 4\chi + 3}{8\chi}}, & \chi > \chi_1 \end{cases} \quad (21)$$

Substituting X_m into $T_m^0(\chi)$ in Eq. (21), we obtain

$$T_m^0(\chi) = \frac{1}{\kappa} \begin{cases} 2, & \chi \leq \chi_1 \\ \sqrt{\frac{\sqrt{(4\chi-1)(4\chi-9)} - 4\chi + 3}{8\chi}} + \sqrt{\frac{\sqrt{(4\chi-1)(4\chi-9)} - 4\chi + 3}{8\chi}} + \chi \left(1 + \frac{\sqrt{(4\chi-1)(4\chi-9)} - 4\chi + 3}{8\chi} \right)^2, & \chi > \chi_1 \end{cases} \quad (22)$$

Figs. 5b and 5c show the plot of maximum point X_m and maximum tensile stress in the middle $T_m^0(\chi)$ versus the aspect-Poisson ratio. For χ lower than χ_1 , the maximum is reached in the advance point $X_m=-1$. For higher χ -values, the point X_m jumps to X_{m1} and then continuously moves to the right towards the origin.

Eq. (34) for dimensionless tensile strength on the base boundary shows that T_m^l depends on the dimensionless group ξ which is proportional to χ . The proportionality coefficient depends on Poisson ratio:

$$\xi = \chi \frac{4(1+2\nu)^2}{(3+2\nu)^2} \quad (23)$$

Fig. 6a shows the profiles for dimensionless tensile stress on the beam boundary for different values of ξ . At $\xi < 2$, $\kappa T_m^l(X, \chi)$ monotonically decreases versus X , so the maximum is reached at the point $X_m=-1$. At $\xi=2$, the slope of profile at $X=-1$ reaches zero, and at $\xi > 2$ a maximum is reached inside the interval at $X > -1$. The expressions for maximum $T_m^l(\xi)$ and X_m are

$$T_m^1(\chi, \nu) = \frac{1}{\kappa} \begin{cases} 2, & \xi \leq 2 \\ \xi(\xi-1)^{-0.5}, & \xi > 2 \end{cases}; X_m = \begin{cases} -1, & \xi \leq 2 \\ -(\xi-1)^{-0.5}, & \xi > 2 \end{cases} \quad (24)$$

Figs. 6b and 6c show the plots for maximum point and value vs χ at three Poisson ratios. For low χ , determined by condition $\xi < 2$, the maximum is reached at the advance point $X = -1$ and is equal to 2. For higher χ , the maximum point continuously moves right from the advance point, and the maximum value monotonically increases from 2.

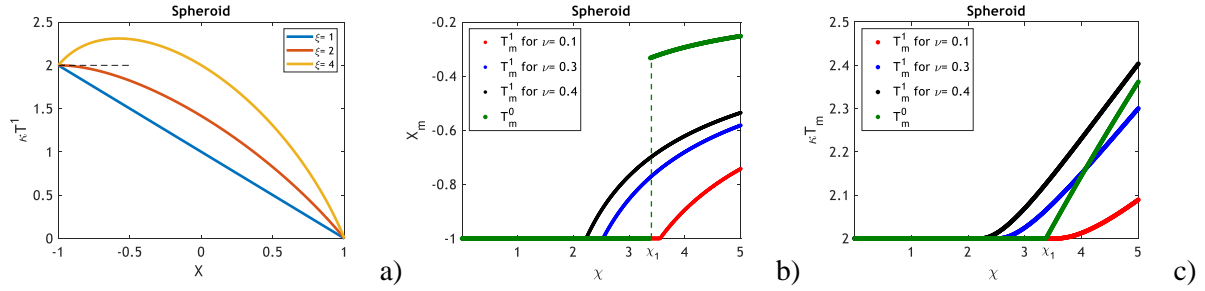


Fig. 6. Maximum tensile stress at beam boundary: a) dimensionless tensile stress on the beam boundary versus χ for 3 different values of ν ; b) position of maximum tensile stress X_m at the beam boundary; c) maximum value of tensile stress over the boundary versus χ

3.3. Comparison of maximum tensile stresses in the beam middle and boundary

Consider the stress equality, separating the domains in (χ, ν) plane where either of the stresses dominate

$$T_m^0(\chi) = T_m^1(\chi, \nu) \quad (25)$$

The black curve in Fig. 7a corresponds to $\xi = 2$; the equation for the black curve follows from the expression (23):

$$\chi = \frac{(3+2\nu)^2}{2(1+2\nu)^2}, \quad \nu = \left(1 - \sqrt{\frac{\xi}{4\chi}}\right)^{-1} - \frac{3}{2}. \quad (26)$$

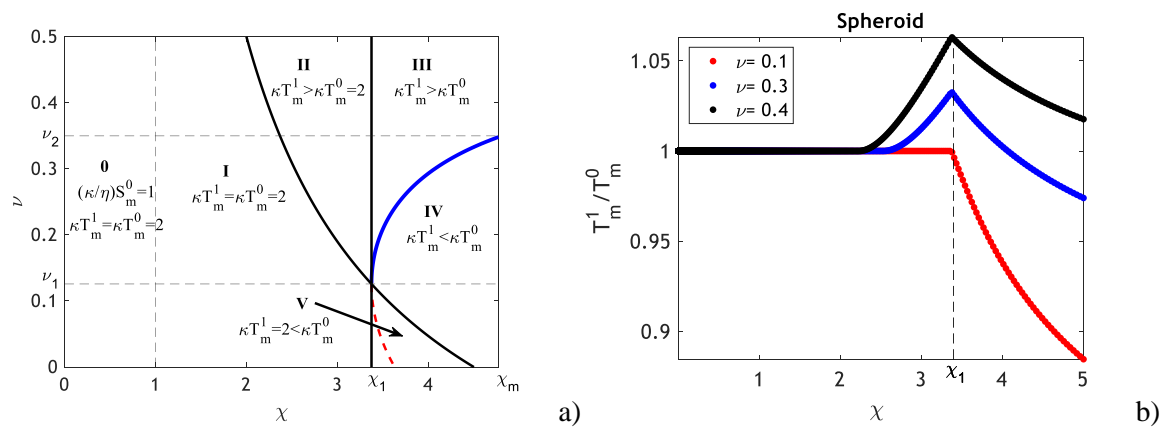


Fig. 7. Comparison between dimensionless tensile stresses in the middle and on the beam boundary: a) determination of the critical Poisson ratio whether the tensile stresses are equal; b) the ratio between tensile stresses on the boundary and in the middle

The straight line $\chi=\chi_1$ and curve (26) for $\xi=2$ separate plane (χ, v) into 4 domains that correspond to different expressions (22) and (24) for maximum tensile stresses (Fig. 7a). Three lines cross in point with $\chi=\chi_1$ and $v=v_1=0.125$.

Here the variables are limited by maximum χ -values for natural minerals: $\chi<5$.

Altogether 5 different domains that defines maxima between T_m^0 and T_m^l can be distinguished:

- I. In the case $\chi < \chi_1$ and $\xi < 2$, both tensile stresses are equal to 2.
- II. In domain $\chi < \chi_1$ and $\xi > 2$, $T_m^0=2$. Equation (25) for the boundary between regions I and II becomes: $T_m^l(\chi, v)=2$.

This equation has only one root: $\xi=2$. For $\xi > 2$, T_m^l monotonically increases. Therefore, in this domain $T_m^l > T_m^0$.

Consider the case where $\chi > \chi_1$ and $\xi > 2$. In this region, both κT_m^0 and κT_m^l are greater than 2. The region can be divided into two regions in which each stress is greater. Substituting the second line of Eq. (24) into equality (25) and expressing ξ yields

$$\xi = \frac{(\kappa T_m^0(\chi))^2 \pm \kappa T_m^0(\chi) \sqrt{(\kappa T_m^0(\chi))^2 - 4}}{2}; \chi > \chi_1 \quad (27)$$

Critical Poisson's ratios where the tensile stresses in the middle and on the boundary are equal are determined by substitution of expression (23) for ξ into Eq. (27) and solving for v :

$$v_m(\chi) = \frac{3\sqrt{(\kappa T_m^0(\chi))^2 \pm \kappa T_m^0(\chi) \sqrt{(\kappa T_m^0(\chi))^2 - 4}} - \sqrt{8\chi}}{4\sqrt{2\chi} - 2\sqrt{(\kappa T_m^0(\chi))^2 \pm \kappa T_m^0(\chi) \sqrt{(\kappa T_m^0(\chi))^2 - 4}}} \quad (28)$$

Explicit expression $v=v_m(\chi)$ is determined by equating the second lines of Eqs. (22) and (24) and is very cumbersome.

Fig. 7a shows the plot $v=v_m(\chi)$. It consists of two branches – the blue branch corresponds to the positive square root in Eq. (28), and the red branch to the negative root. Over the red branch, we have $\xi < 2$, so only the blue branch belongs to the domain $\chi > \chi_1$ and $\xi > 2$. This determines zones III and IV:

- III. In the case where $\chi > \chi_1$ and $v > v_m(\chi)$, $T_m^l > T_m^0$.
- IV. In the case where $\chi > \chi_1$ and $v < v_m(\chi)$, $\xi > 2$, $T_m^l < T_m^0$.

The blue curve (45) crosses the line $\chi=\chi_1$ at the point with ordinate v_1 .

- V. In the case $\chi > \chi_1$ and $\xi < 2$, $T_m^l=2$. As it follows from definition (20) of χ_1 , equation $T_m^0(\chi)=2$ has root $\chi = \chi_1$. No more roots exist for $\chi > \chi_1$. Therefore, in this domain $T_m^0 > T_m^l=2$.

Five domains I, II..V in the so-called tensile stress diagram (Fig. 7a) determine where maximum tensile stress is higher –at the boundary of the beam base or in the middle. Their ratio versus shape-Poisson number is presented in Fig. 7b for three value of Poisson ratio: $v < v_1$, $v_1 < v < v_2$, and $v > v_2$.

3.4. Maxima shear stresses in the beam middle and boundary

Fig. 8a shows profiles for shear stress in the middle of the beam base for different χ . For χ tending to zero, the profile tends to two straight lines. At higher χ , there does appear a maximum at $X_m=0$, which reaches unitary value at $\chi = \chi_2=1$. At $\chi < \chi_2$, the maximum remains in the advancing and receding points, for $\chi > \chi_2$ it moves to the origin. Expressions for stress maximum are obtained from Eq. (17):

$$S_m^0(\chi) = \frac{\eta}{\kappa} \begin{cases} 1, & \chi < 1 \\ \sqrt{\chi}, & \chi > 1 \end{cases}; X_m = \begin{cases} \pm 1, & \chi < 1 \\ 0, & \chi > 1 \end{cases}; \eta = \frac{T_0}{S_0} \quad (29)$$

Fig. 8b shows that the maximum points lie at the edges of the beam middle at $X_m=-1$ and $X_m=1$ for $\chi < \chi_2$, then moves to the centre point, $X=0$ for $\chi > \chi_2$. The maximum shear is equal to one for $\chi < \chi_2=1$, and monotonically increases from 1 for $\chi > \chi_2$ (Fig. 8c).

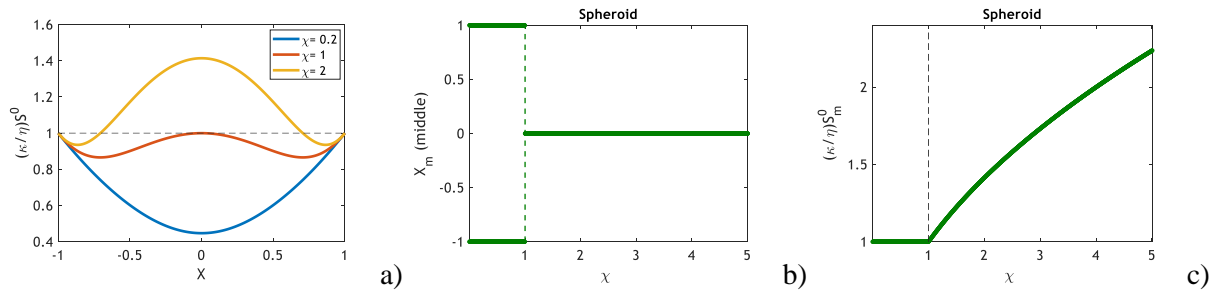


Fig. 8. Dimensionless maximum shear stress in the middle of the beam base: a) profiles for dimensionless stress in the middle of the beam base for different versus χ ; b) position of the maximum point X_m ; c) maximum dimensionless stress versus χ

The expression for maximum tensile stress along the boundary is obtained from Eq. (19):

$$S_m^1(\chi_1) = \frac{\eta}{\kappa} \begin{cases} \sqrt{\xi}, & \xi \geq 1 \\ 1, & \xi < 1 \end{cases}; X_m = \begin{cases} 0, & \xi \geq 1 \\ \pm 1, & \xi < 1 \end{cases} \quad (30)$$

Corresponding profiles and maximum plots and presented in Fig. 9.

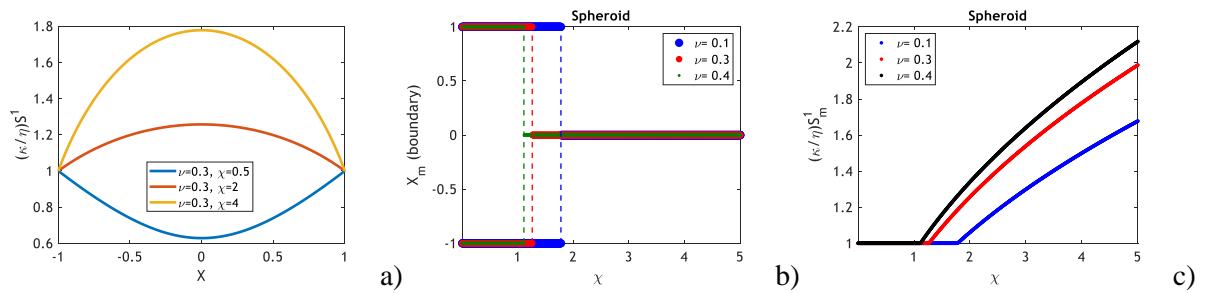


Fig. 9. Dimensionless maximum shear stress on the beam boundary: a) profiles for dimensionless stress for different ν ; b) position of the maximum point X_m ; c) maximum dimensionless stress versus χ

Fig. 10 shows the ratio S_m^1/S_m^0 versus χ for 3 values of Poisson ratio. For all parameter values, the ratio does not exceed one, i.e. $S_m^1 < S_m^0$. Therefore, further in determining the breakage regime, shear at the base boundary is not considered.

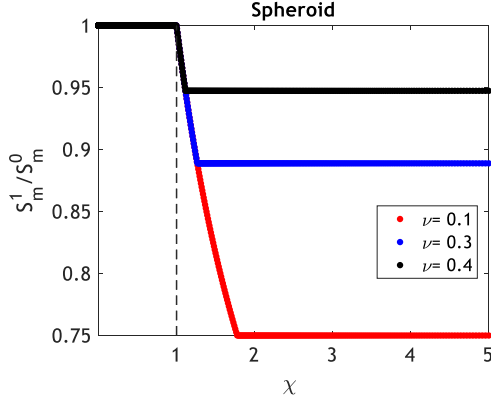


Fig. 10. Comparison between maximum shear stresses in the middle and on the boundary

Introduce region 0 in (χ, ν) -plane for $\chi < 1$ (tensile-stress diagram in Fig. 7a). According to Eq. (29), here the dimensionless shear is equal to one, while both tensile stress maxima are equal to two.

3.5. Determination of breakage regime using the breakage function

This section compares maxima of tensile and shear stresses, Eqs. (22, 24, 29). The tensile-stress diagram in Fig. 11a shows which maximum tensile stress – in the beam middle or at the boundary – is higher. Shear stress in the middle is always higher than that at the boundary. Now consider breakage by tensile stress, where equality (13) is fulfilled at some point $(X_m, 0)$ and normalised tensile stress reaches its maximum which equals one, while equality (14) is not fulfilled for any point $-1 < X < 1$. Consequently, the condition for breakage by tensile stress is

$$\frac{\max(-\sigma_3)}{T_0} \geq \frac{\max(\sigma_1 - \sigma_3)}{2S_0} \quad (31)$$

Define the breakage regime function, $g(\chi, \nu)$ as the ratio of the dimensionless tensile stress to the dimensionless shear stress. Comparing with Eq. (31), we arrive at:

$$g(\chi, \nu) = \frac{\kappa T_m(\chi, \nu)}{\left(\frac{\kappa}{\eta}\right) S_m^0(\chi)} = \frac{T_m(\chi, \nu)}{S_m^0(\chi)} \eta > \frac{T_0}{S_0} = \eta \quad (32)$$

$$T_m(\chi, \nu) = \max\{T_m^0(\chi), T_m^1(\chi, \nu)\} \quad (33)$$

Here $T_m(\chi, \nu)$ is maximum of two normalised tensile stresses $T_m^0(\chi)$ and $T_m^1(\chi, \nu)$; $S_m^0(\chi)$ is the maximum of the dimensionless shear stress in the middle of the beam. We introduce the breakage regime function $g(\chi, \nu)$, which is the ratio of the stress maxima $T_m(\chi, \nu)$ and $S_m^0(\chi)$. If a state point in plane (χ, η) is located above the curve $g(\chi, \nu)$, the breakage occurs by tensile stress; otherwise it is shear stress that causes the breakage.

To further clarify the meaning of this equality, consider a system at the point of shear failure, i.e. $S_m^0 = S_0$. If $g(\chi, \nu) < \eta$, then it follows that $T_m < I$. Thus, at the point of shear failure, the tensile stress does not exceed the tensile strength and tensile failure is not expected. Thus, in the situation of a gradually increasing load, shear failure will occur before tensile failure. Similarly,

if $g(\chi, \nu) > \eta$, then $T_m > I$ (for $S_m^0 = 1$) and thus at the onset of shear failure, the condition for tensile failure is already satisfied and therefore the particle will first experience tensile failure.

The tensile-stress diagram shows that as χ changes from zero to χ_m , different sequences of domains appear in three intervals of Poisson's ratio: $[0, \nu_1]$, $[\nu_1, \nu_2]$, and $[\nu_2, 0.5]$ (Fig. 7a). A graph of the breakage function $g(\chi)$ is presented in Figs. 11a, d, and g in those three intervals, respectively. Sharp transitions in the behaviour of the function are observed when different boundaries in the tensile-stress diagram are reached. Figs. 11b, e, and h show the plots of the numerator and denominator of expression (32) of $g(\chi, \nu)$ for three values of Poisson's ratio ν , taken from the three above-mentioned intervals, by red, black, and green curves, respectively. Points X_m where breakage occurs, are shown in Figs. 11c, f, and i.

The graph of function $g(\chi, \nu)$ allows determining whether breakage occurs by tensile or shear stress. Thus, $g(\chi, \nu)$ is called the breakage regime function, and plane (χ, ν) with different domains – the tensile-shear diagram (Figs. 11a, 11d, 11g).

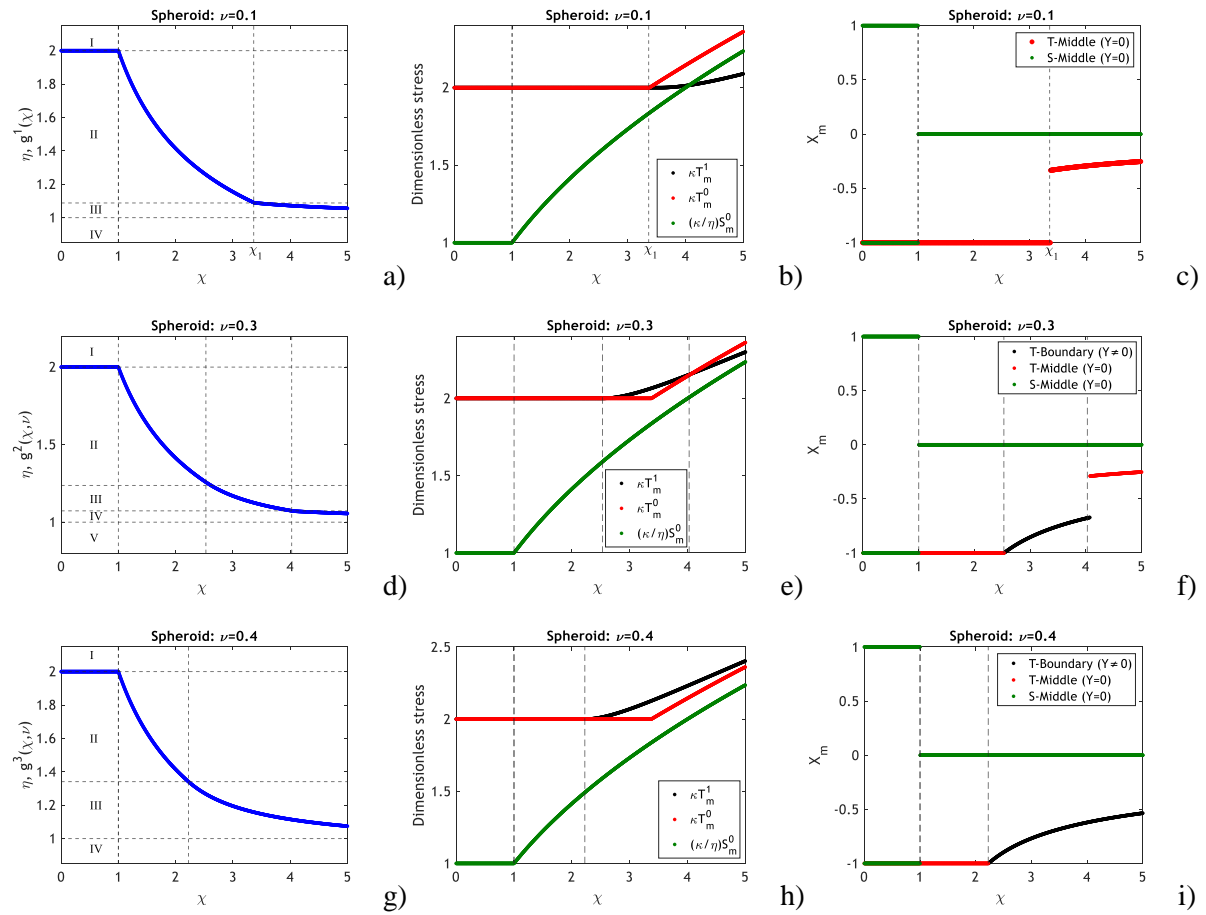


Fig. 11. Breakage regime function $g(\chi)$ for different Poisson ratios ν : a,b,c) $\nu < \nu_1$; d,e,f) $\nu_1 < \nu < \nu_2$; g,h,i) $\nu_2 < \nu < 0.5$

For values of χ less than 1, the curve $g(\chi, \nu)$ is equal to two (Figs. 11a, d, g), and both the tensile and shear stresses are constant (Figs. 11b, e, h). Breakage occurs in the advancing point, $X_m = -1$ (Figs. 11c, f, i). As χ increases, a decrease in $g(\chi, \nu)$ is observed, defined by a constant tensile stress, but increasing shear stress. Shear failure for values of $\chi > 1$ occurs in the particle centre, $X_m = 0$. Further increases to the shape-Poisson number, χ , result in an increasing tensile stress, leading to a less sharply decreasing breakage regime function. This transition occurs for only

one of the two tensile stresses, while the other begins increasing at higher χ . For intermediate Poisson's ratio ($v_1 < v < v_2$), tensile failure occurs first on the boundary, then at higher χ it occurs in the middle of the particle (Fig. 11e). In all cases, increasing tensile stress results in tensile failure occurring at an intermediate point in the advancing half of the particle ($-l < X_m < 0$, see Figs. 11e, f, i).

The value of the shape-Poisson number χ that corresponds to a given strength ratio η

$$\chi_{cr} = g^{-1}(\eta), \quad g(\chi_{cr}) = \eta \quad (34)$$

is called the critical value.

For a given value of the strength ratio, η , let us discuss the determination of the failure type. In the case where the strength ratio exceeds 2 (region I in Figs. 11a, d, g), $\eta > 2$, the breakage is by shear for all values of the shape-Poisson number χ . Similarly, if the strength ratio is less than one, $0 < \eta < 1$ (region IV, Figs. 11a, g, or region V for $v_1 < v < v_2$, Fig. 11d), the breakage is by tensile failure for all values of the shape-Poisson number χ . For values of η between 1 and 2 (regions II-III, Figs. 11a, d, g, and region IV for $v_1 < v < v_2$, Fig. 11d), breakage will occur by tensile failure for values of χ less than the critical value, χ_{cr} , and by shear failure for values larger than it.

4. Detrital fines detachment against electrostatic DLVO forces

Following Derjaguin and Landau 1941, Verwey and Overbeek, 1948, Israelachvili 2015, Bradford et al. 2013, this section briefly presents the fines detachment theory for detrital fines. [13, 21, 78, 79](#)

Detrital fines have been brought to the rock by groundwater flows after being broken-off the rock surface and attached to the rock surface by electrostatic forces. Figs. 2b, 2c show the forces exerting on an attached detrital particle: attaching electrostatic F_e and gravity F_g forces, and detaching drag F_d and lift F_l forces. Electrostatic is a potential force, where the energy potential E depends on the particle-surface separation distance, h :

$$F_e(h) = -\frac{\partial E(h)}{\partial h} \quad (35)$$

An energy profile with only a single minimum has an inflection point $h = h_m$, where the electrostatic force reaches its maximum:

$$\frac{\partial F_e(h_m)}{\partial h} = -\frac{\partial^2 E(h_m)}{\partial h^2} = 0, \quad \frac{\partial^2 F_e(h_m)}{\partial h^2} = -\frac{\partial^3 E(h_m)}{\partial h^3} < 0 \quad (36)$$

Mechanical equilibrium of a particle on the rock surface in the case of favourable attachment (one primary energy minimum) is determined by the following conditions: equality of detaching and attaching torques

$$M_b = 6\pi\mu_f r_s V f_d(\alpha_s) b f_M(\alpha_s) = F_e(h) l_n, \quad (37)$$

equality of detaching and attaching force projections on horizontal

$$F_d = 6\pi\mu_f r_s V f_d(\alpha_s) = v_c F_e(h), \quad (38)$$

and equality of detaching and attaching force projections on vertical

$$F_l(U) = F_e(h) + F_g \quad (39)$$

where l_d and l_n are the lever arms for drag and normal forces, respectively, and ν_C is the Coulomb friction coefficient. Particle detachment occurs when the left hand side of (37), (38), or (39) exceeds the right hand side when $h=h_m$ (at the maximum electrostatic force). When these terms are insufficient to detach the particle, they are equilibrated by a smaller electrostatic force, and the particle sits at some distance $h < h_m$. Breach of either equilibrium conditions (37), (38), or (39) yields fines detachment by rolling, sliding, and lifting, respectively. In the case of two energy minima, there are two separating distances $h=h_m$ that correspond to both energy minima, and the equilibrium conditions (37), (39), and (39) are applicable to the particles that are located in primary and secondary energy minima. It is implicitly assumed that the particles detached by the three criteria (37), (39), and (39) continue rolling over the rock surface, sliding over the surface, and move off the surface into the liquid stream, respectively.

Under dominance of electrostatic force in Eq. (39), lifting does not occur, and the lifting criterium can be dropped.

5. Maximum retention function as a mathematical model for fines detachment

This section develops a novel model for fines detachment by breakage that includes a derivation of breakage flow velocity (section 5.1), model for breakage detachment and its expression as a maximum retention function MRF (section 5.2), and determination of the breakage parameters from and experimentally derived MRF (section 5.3).

5.1. Determination of breakage velocity

Let us determine the breakage velocity based on either formula for normalised stresses (22, 24, 29) or the (χ, v) and (χ, η) diagrams.

First, we compare normalised tensile stresses in the middle and on the boundary, using Eqs. (22) and (24). Since both normalised stresses are proportional to κ^{-1} , the choice of maximum normalised tensile stress is determined by the values in brackets in Eqs. (22, 24) (dimensionless stresses), so the knowledge of κ^{-1} is not required at this stage. The choice between T^0 and T^l can be done using the (χ, v) diagram (Fig. 7a).

Then, we compare the maximum normalised tensile stress T_m with the normalised shear stress in the middle S_m^0 , using Eqs. (22, 24) and (29). Also, both normalised stresses are proportional to κ^{-1} , so the choice is based on the comparison between the value in brackets in Eq. (22, 24) and the value in brackets in Eq. (29) times the strength ratio. As an alternative, the choice between maximum normalised tensile stress and normalised shear can be done using breakage function $\eta = g(\chi, v)$ in (χ, η) plane (Fig. 11).

So, at this stage the breakage regime was determined. Consider the chosen maximum stress equation, either (22), (24), or (29). At the point of failure, the chosen normalised stress is equal to one, the value in bracket has already been calculated, allowing us to determine the strength-drag number κ . For cases where the maximum is tensile stress in the middle, tensile stress on the boundary, and shear stress in the middle, the formulae for strength-drag numbers κ are:

$$\kappa = \begin{cases} 2, & \chi \leq \chi_1 \\ \sqrt{\frac{\sqrt{(4\chi-1)(4\chi-9)}-4\chi+3}{8\chi}} + \sqrt{\left(\sqrt{\frac{\sqrt{(4\chi-1)(4\chi-9)}-4\chi+3}{8\chi}}\right)^2} + \chi \left(1 - \left(\sqrt{\frac{\sqrt{(4\chi-1)(4\chi-9)}-4\chi+3}{8\chi}}\right)^2\right), & \chi > \chi_1 \end{cases} \quad (40)$$

$$\kappa = \begin{cases} 2, & \xi \leq 2 \\ \xi(\xi-1)^{-0.5}, & \xi > 2 \end{cases}; \quad \xi = \chi \frac{4(1+2\nu)^2}{(3+2\nu)^2} \quad (41)$$

$$\kappa = \frac{T_0}{S_0} \begin{cases} 1, & \chi < 1 \\ \sqrt{\chi}, & \chi > 1 \end{cases}, \quad (42)$$

respectively.

Substituting expression for drag from Eq. (1) into Eq. (12), we obtain

$$\kappa^{-1} = \frac{1}{2T_0} \frac{F_d}{I} r_b^2 \frac{bf_M}{r_b} = \frac{1}{T_0} \frac{2F_d}{\pi r_b^2} \frac{\alpha_s f_M}{\delta} = \frac{12}{T_0} \frac{\pi \mu_f r_s V f_d}{\pi r_b^2} \frac{\alpha_s f_M}{\delta} = \frac{12}{T_0} \frac{\pi \mu_f r_s U f_d}{\pi r_b^2} \frac{\alpha_s f_M}{\delta \phi} = \frac{12 \alpha_s f_M f_d}{\delta \phi} \frac{\mu_f r_s U}{T_0 r_b^2} \quad (43)$$

This allows determining the breakage velocity for authigenic particles

$$U_{cr}^b = \frac{\delta \phi T_0 r_b^2}{12 \alpha_s f_M f_d \mu_f r_s} \kappa^{-1} \quad (44)$$

where κ is calculated by either of three formulae (40), (41), or (42).

Critical breakage velocity versus spheroidal particle radius for different aspect ratios is investigated in Fig. 12a. The smaller is the particle, the higher is the breakage velocity. So, in a test with piecewise constant increasing velocity, the largest particles are detached first, and further detachment is continuing in the order of decreasing particle size.

However, critical breakage velocity U_{cr}^b is non-monotonic with respect to aspect ratio – the two smallest critical velocities are exhibited by very oblate spheroids ($\alpha_s=0.025$) and for perfect spheres ($\alpha_s=1$). Fig. 12b shows that maxima of breakage velocity are reached for intermediate aspect ratios. The effect is attributed to non-monotonicity of the product of three α_s dependent functions in the denominator of the expression (44) (Fig. 12c). The overall drag is the total of surface integrals of pressure gradient and viscous shear over the particle surface. The flatter is the particle, the lower is the aspect ratio, the lower is the particle cross-section transversal to flow. This results in a lower pressure-gradient component of drag, but a higher shear viscosity component due to an increase of the contact area and the Couette flow alignment. So, the non-monotonicity of drag shown in Fig. 12d is the result of two effects of pressure gradient and shear, i.e., normal and tangential components of drag, which are competing and at odds with each other. The above also explains non-monotonicity of lift, shown in the same figure.

Fig. 12e shows that the higher is the aspect ratio, the lower are drag, moment and lift factors. Lift is significantly lower than the drag; both forces are non-monotonic α_s -functions (Fig. 12e).

For the case of long cylinders, all the dependencies, calculated above for spheroidal particles, become monotonic for long cylinders (Fig. 13). The larger the particle the lower is the breakage velocity, i.e., the long cylinders are detached in order of decreasing of their sizes; large particles are broken first during velocity increase (Fig. 13a). The higher is the aspect ratio, the lower is

the breakage velocity, i.e., it is easier to break a long thin cylinder (Fig. 13b). The aspect-ratio-dependent group that enters the expression (44) is monotonic too (Fig. 13c). The higher is the aspect ratio, the higher are the drag force (Fig. 13d) and drag factor (Fig. 13e). The lift is negligible.

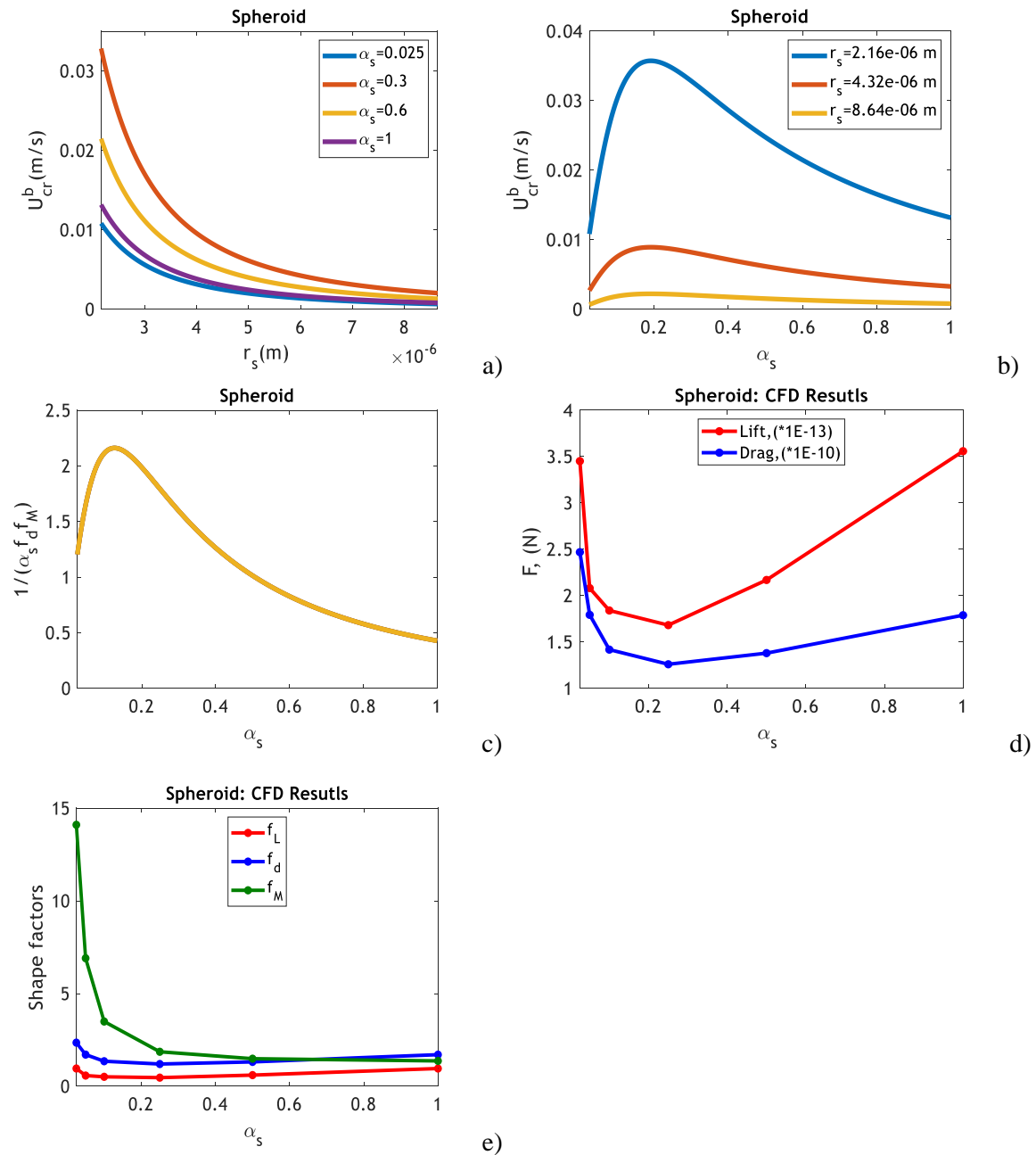


Fig. 12. Critical breakage velocity of oblate spheroids: a) Dependence of critical breakage velocity on particle radius; b) Dependence of critical breakage velocity on particle aspect ratio; c) ; d) aspect-ratio dependency for shape factor; e) aspect-ratio dependencies for drag and lift.

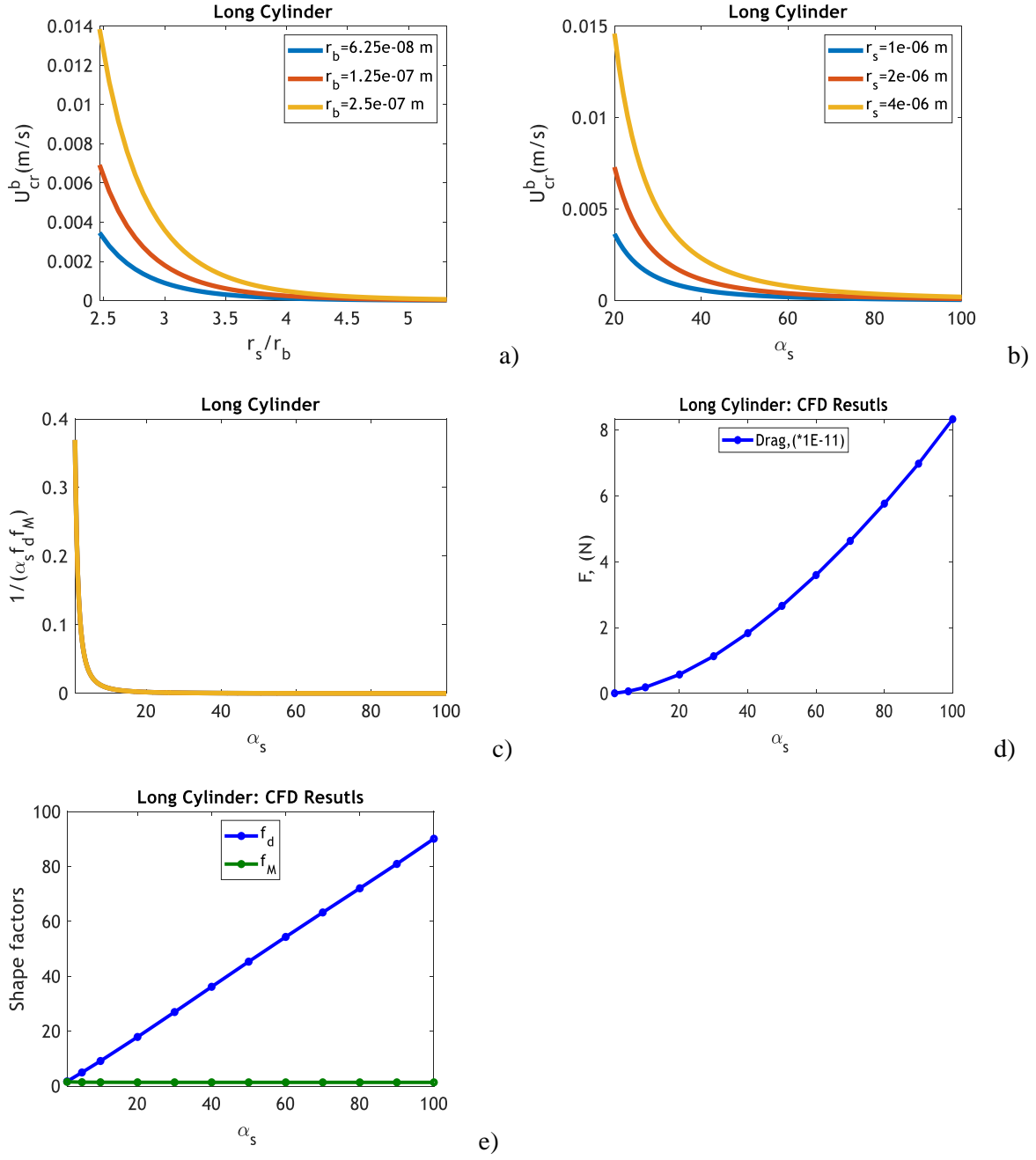


Fig. 13. Critical breakage velocity of long cylinders: a) Dependence of critical breakage velocity on particle radius; b) Dependence of critical breakage velocity on particle aspect ratio; c) c) dependency of $\alpha_s f_d f_M$ of α_s ; d) aspect-ratio dependency for shape factor; e) aspect-ratio dependencies for drag and lift.

5.2. Formulation of fines breakage model: maximum retention function

Breakage criterion (32, 33) yields the expression (44) of the breakage velocity U_{cr}^b versus particle and rock surface properties. For uniform plane substrate and the attached particles, all the particles remain attached for velocities lower than U_{cr}^b , and all become detached for any velocity above U_{cr}^b . However, fines detachment during the velocity increase occurs gradually.

Consider a multidimensional manifold of particles of different sizes and forms situated at various sites of an asperous, micro heterogeneous rock surface. Flow velocity of creeping flow

near the rock surface is probabilistically distributed over the porous space. Under the assumption of Stokes flow in the porous space, velocity distribution over the porous space is determined by the macroscale Darcy's velocity U , i.e., local microscale speeds are proportional to U .⁸⁰ The mechanical equilibrium failure conditions (32, 33) indicate whether each attached to rock surface particle is broken or remains attached under a given velocity U . It makes attached concentration a function of velocity that is called the MRF (maximum retention function). The MRF $\sigma_{cr}(U)$ is a mathematical model for particle mobilisation by breakage. For 3D flows, the MRF is a function of the modulus of velocity:

$$\sigma_a = \sigma_{cr}^b(|U|) \quad (45)$$

Eq. (44) contains coefficients reflecting properties of authigenic particles, the particle-substrate bonds, and porous medium: tensile strength T_0 , aspect ratio α_s , fluid viscosity μ_f , particle radius r_s ,

Poisson ratio ν , bond radius r_b , bond ratio δ , and porosity ϕ . These parameters determine the functional expression (45) for the MRF.

As it follows from the definition of the MRF as the total concentration of particles that remain attached under a given velocity U , the MRF monotonically decreases from zero velocity and tends to zero as velocity tends to infinity. A minimum breakage velocity, where the “first” particle is broken off, corresponds to equality of the MRF $\sigma_{cr}(U_{min})$ to the initial concentration of movable particles. Similarly, for an MRF which reaches zero at a finite velocity, this maximum breakage velocity, U_{max} , corresponds to the minimum flow velocity that yields failure for all bonds over the rock surface.

5.3. Maximum retention function for simultaneous breakage and DLVO detachment

Eqs. 1, 2, and 3 as applied with the local flow velocity around the attached particle, allow determining whether any arbitrary particle is detached for any velocity U , or remains attached. The maximum retention function for DLVO attraction, $\sigma_{cr}^e(U)$, is determined by the total particle concentration that remain attached by DLVO forces for a given velocity U .^{22, 23, 81, 82} Expressing the interstitial speed V in Eqs. (37, 38) via Darcy's velocity $U=V\phi$, we obtain two expressions for critical velocity for particle detachment against electrostatic DLVO forces for the conditions of rolling and sliding:

$$U_{cr}^e = \frac{F_e \phi l_n}{6\pi\mu_f r_s f_d(\alpha_s) b f_M(\alpha_s)} \quad (46)$$

$$U_{cr}^e = \frac{\nu_c F_e(h) \phi}{6\pi\mu_f r_s f_d(\alpha_s)} \quad (47)$$

respectively. Here U_{cr}^e is the Darcy' velocity that detaches the particles under the conditions given in right side of Eqs. (46) and (47).

Critical detachment velocity against DLVO forces is determined by the minimum critical velocity from those given by two criteria (46) and (47). Two failure criteria – by rolling and by Coulomb's friction, given by Eqs. (46) and (47), respectively, are mathematically equivalent, provided that

$$v_c = \frac{l_n}{bf_M(\alpha_s)} \quad (48)$$

Eqs. (37, 38) contain a set of parameters, which are properties of either particles or surface: particle radius r_s , its aspect ratio α_s , zeta potentials of particles ψ_{01} and rock ψ_{02} , brine salinity, pH, lever arm ratio l , temperature T , tensile strength T_0 , and beam radius r_b . Continuity of the MRF $\sigma_{cr}(U)$ – gradual fines detachment with continuous flow velocity increase – is determined by the probabilistic distributions of those parameters.⁸³

The assumption of independent detachment of particles against DLVO forces and by breakage determines the overall MRF as a sum of the two individual MRFs:

$$\sigma_{cr}(U) = \sigma_{cr}^e(U) + \sigma_{cr}^b(U) \quad (49)$$

Fig. 14 shows that the MRF is monotonically decreasing – the higher is the velocity, the lower is the attached concentration. A velocity increase from U_n to U_{n+1} yields detachment of particles with retained concentration $\Delta\sigma_n$:

$$\Delta\sigma_n = \sigma_{cr}(U_n) - \sigma_{cr}(U_{n+1}), \quad (50)$$

which are transformed into suspension concentration

$$c = \Delta\sigma / \phi \quad (51)$$

Fig. 14 presents the form of MRF for fines detachment against electrostatic force, by breakage, and the total MRF. Lower dashed curves represent the MRF for detrital particles, the combined dashed-solid curves correspond to the breakage MRF, and the solid curves show the total MRF.

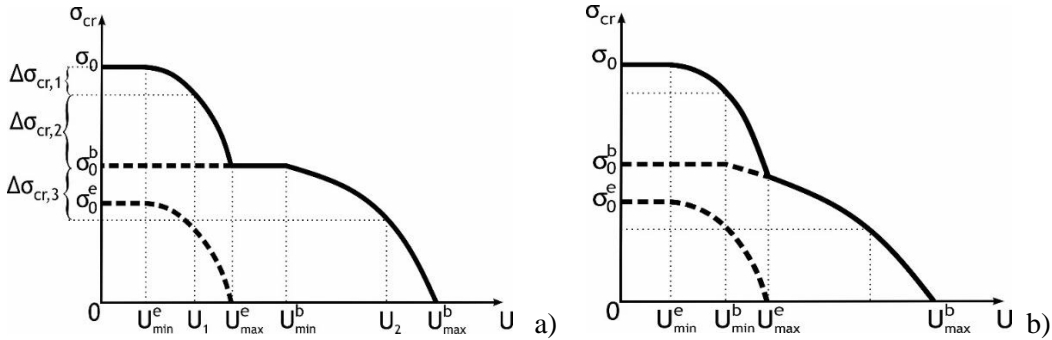


Figure 14: Total MRF for detachment of detrital and authigenic fines: a) in the case of $U_{max}^e < U_{min}^b$, MRF has plateau; b) MRF is monotonically decreasing function of velocity in the case where $U_{max}^e > U_{min}^b$

Consider piecewise-constant injection rate increase; each constant-rate stage is maintained until stabilisation. The case of Fig. 14a corresponds to weak electrostatic attraction (using low-salinity, high-pH or high-temperature water) and high particle-rock-bond strength (highly consolidated sandstones). The detrital particles start detaching at velocity U_{min}^e and continue mobilisation until velocity U_{max}^e , where all movable detrital fines are detached. At a velocity that is higher than the minimum plateau velocity, the maximum DLVO force cannot secure any detrital particle on the rock surface, i.e., all detrital particles detach. In this case, where $U_{max}^e < U_{min}^b$, no further particle detachment occurs until the velocity reaches U_{min}^b , where the first

authigenic particle experiences failure. All movable authigenic particles are detached once the velocity reaches U_{max}^b . In this case, the total MRF has a plateau, where all detrital particles are detached under velocities that are lower than the minimum plateau velocity, and authigenic fines remain attached until a velocity that is higher than the maximum plateau velocity. No detachment occurs at plateau velocities. For high electrostatic attraction and low strength, the velocity intervals for detachment by both causes overlap (Fig. 14b).

Existence of two plateaus in MRF indicates three detachment mechanisms. For example, if the DLVO energy profile has two minima in the case of unfavourable fines attachment and the particle-rock bond strength is high, the MRF can have two plateaus.

Finally, there appears the following *algorithm of fines detachment modelling*: (i) identifying the appropriate domain in plane (χ, ν) – the tensile-stress diagram – and determining which tensile stress maximum on the beam base – along the symmetry axis or the boundary of the beam base – is higher; (ii) determining whether the failure occurs by tensile or shear stress from the inequality for the breakage regime function $g(\chi, \nu) > \eta$ in the shear-tensile diagram; (iii) calculation of breakage velocity from the drag-strength number κ ; (iv) determining the probabilistic distribution of breakage velocity; (v) calculation of the MRF for breakage; (vi) adding the MRFs for breakage and detachment against electrostatic attraction.

MRF (49) in set of points $U_1 < U_2 < \dots < U_n$ is determined from a laboratory coreflood with piecewise-constant injection rate increase from breakthrough particle concentrations.

6. Laboratory study of fines detachment by breakage by coreflooding

6.1. Laboratory study

The laboratory study conducted as part of this study comprised of core drying, core saturation by water with 0.6 M of NaCl under vacuum, and injection of this water into the core. A Castlegate sandstone core with permeability 917 mD and porosity 0.24, length 5.1 cm and pore volume 13.7 cu cm was used in the test. Seven flow rates were applied in order of increasing rate. Fig. 15 presents the schematic of laboratory set-up. The essential parts of the setup are coreholder with the core placed in a Viton sleeve, four differential pressure transmitters, HPLC pump, effluent fraction collector, and particle counter. The overburden pressure was created by a manual pressure generator. A data acquisition module along with signal convertor provided results which were visualised on a PC screen in real time. Breakthrough concentration (Fig. 16a) and size distributions of produced particles along with pressure drop across the core (Fig. 16b) have been measured during each constant-rate injection step.

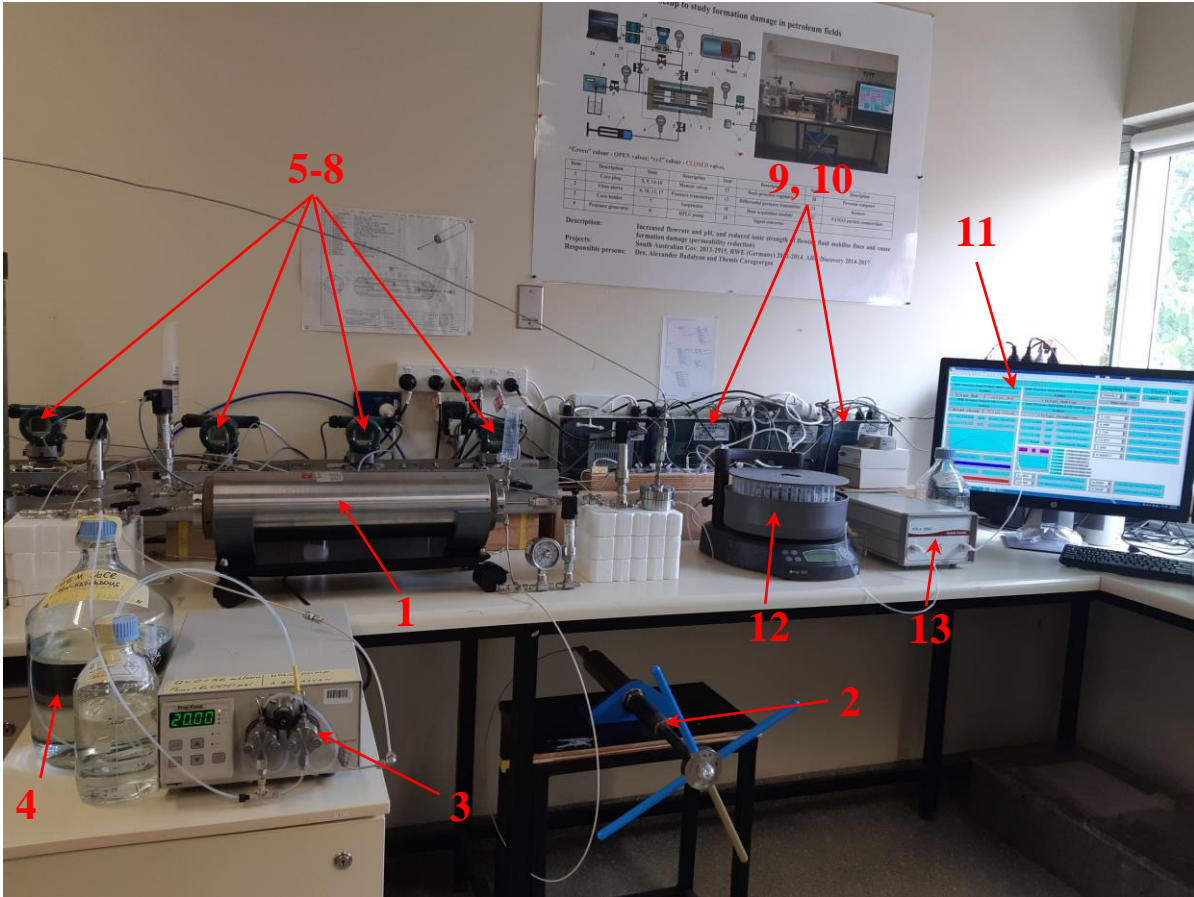


Figure 15. Laboratory set-up for particle detachment due to DLVO and breakage: 1 - core holder, 2 - manual pressure generator, 3 - high-performance liquid chromatography (HPLC) pump, 4 - brine solution, 5-8 - differential pressure transmitters, 9 – data acquisition module, 10 – signal converter, 11 - personal computer, 12 - fraction collector, 13 - particle counter.

Fig. 16a shows that at low rate, the breakthrough concentration declines exponentially, which is typical for deep bed filtration of low-concentration colloids with constant filtration coefficient.^{20, 84} At high rates, this behaviour is combined with a sharp and fast concentration decrease down to low values, indicating that particle capture intensity is decreasing, until the point where all capture vacancies are filled and no further capture occurs. Here the capture rate is described by the Langmuir filtration function.^{85, 86}

Relative change of average core permeability is captured by impedance J

$$J(t) = \frac{\Delta p(t) U(0)}{\Delta p(0) U(t)} \quad (52)$$

where Δp is the pressure drop across the core.

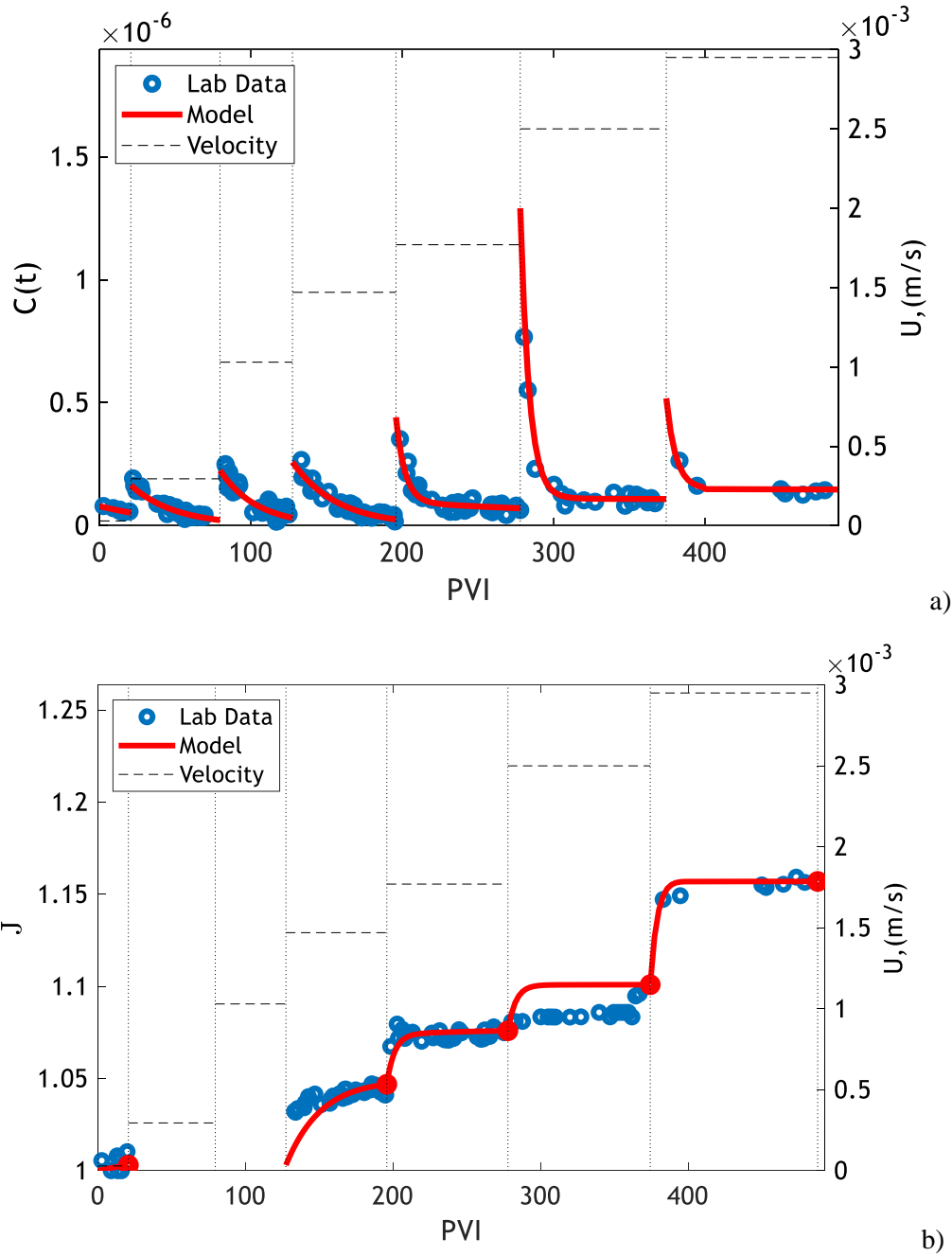


Fig. 16. Breakthrough concentrations (left axes) during the test with seven rates (right axis)

For large rates, impedance first increases sharply and then switches to slow growth (Fig. 16b). This transition occurs at approximately the same time as the suspended concentration switches from a sharp decrease to a slow decrease (Fig. 16a). Colloidal flow with a Langmuir filtration coefficient is attributed to asperous authigenic fines with rough surfaces after breakage, which are strained in the large pore throats with fast filling of all of them, while the capture of smoother detrital particles is less intensive and continues significantly longer.

The size distributions of produced particles at high rates have a clear bimodal structure, which also supports the two-population hypothesis.

The next section supports the two-population hypothesis by successful matching of experimental data with a two-population colloidal transport model.

6.2. Mathematical model for transport of detached colloids

To match the breakthrough and impedance histories, we have developed a two-population model of deep bed filtration, given by Eqs. (B1-B4) and described in Appendix B. The system contains mass conservations for both populations, Eqs. (B1) for $k=1,2$, where the delay of each particle population's velocity comparing with the carrier water velocity is expressed by drift-delay factors α_k . Particle capture rates for each particle population are proportional to the respective particle fluxes $c_k\alpha_k U$; the proportionality coefficients are λ_1 and λ_2 . The filtration coefficients λ_1 and λ_2 are equal to probabilities of the particle capture by the rock per unit length of the particle trajectory in the porous space. The first population filtrates with constant filtration coefficient λ_1 , and the filtration coefficient for the second population $\lambda_2(\sigma_2)$ has Langmuir form given by Eq. (B4). The interaction of two population fluxes is expressed by the joint contribution of the retained particles of both types to the overall rock hydraulic resistance. Dependence of permeability on both retained concentrations in Eq. (B3) is obtained by first order Taylor's expansion of the inverse to permeability as a function of the retained concentrations of two populations. Here k_0 is the initial (undamaged) permeability, and formation damage coefficients β_1 and β_2 quantify the extent of permeability decline caused by each of the particle populations.

The assumption of the independence of the model parameters of fluid pressure separates four equations (B1, B2) for $k=1,2$ from Eq. (B3). Dependence of the individual model parameters on their particular retention concentrations separates systems (B1, B2) for $k=1,2$ from each other. Initial conditions (B5) correspond to electrostatic and breakage detachment with instant particle mobilisation: the detached concentration $\Delta\sigma_{cr}$ due to change of flow rate from U_{n-1} to U_n , determined by MRF is instantly translated into suspension concentration $\Delta\sigma_{cr}/\phi$.

Initial-boundary problem (B5, B6) for 1D flow system (B1, B2) allows for an exact solution.⁸⁶⁻⁸⁸ Suspended and retained concentrations of both populations are expressed by explicit formulae (B7). This allows for the derivation of an explicit formula for the pressure gradient. Yet, the pressure drop across the core and impedance are calculated by numerical integration.

6.3. Results

Fig.16 shows the experimental data by blue dots and the matched modelling data by red curves. High match for breakthrough concentrations is supported by the coefficient of determination $R^2=0.96$. Breakthrough concentrations highly exceed the accuracy of the particle counter used in the set-up (Fig. 15). The accuracy of pressure transducers exceeds the measured pressure drops only by a factor of 2-3, so the formation damage coefficients have been tuned by the final impedance values alone, which are shown by red dots in Fig. 16b. However, the coefficient of determination for the overall impedance is also high $R^2=0.94$.

The parameters obtained from tuning – filtration coefficients $\lambda_1=98$ 1/m and $\lambda_2=87$ 1/m, formation damage coefficients $\beta_1=5300$ and $\beta_2=7300$, and delay-drift factors $\alpha_1=5\times 10^{-3}$ and $\alpha_2=23\times 10^{-3}$ – belong to commonly reported intervals.^{13,20,30,84} The tensile strength for kaolinite is determined from Eq. (44), which presents an unbiased breakage velocity estimate, and is equal to $T_0=0.15$ MPa. Although this value is lower than typical tensile strengths for minerals, significantly smaller values for coals and clays have been reported.^{31,32,48,89,90} The detached concentration $\Delta\sigma_{cr}(U)$ versus velocity increases at small rates from zero and declines at high velocities up to zero, which complies with the typical form of the maximum retention function

curve.^{22, 23, 81, 91} High match shown in Fig. 16 validates the two-population model for deep bed filtration of broken-off and DLVO-detached fines.

Close match by a single-population model has been achieved for lab data on coal flooding by Guo 2016 and Huang et al. 2017, 2021, and on sandstone floods by Ochi and Vernoux 1998, and Torkzaban et al. 2015.^{30, 73, 92-94} Here the coefficient of determination R^2 varies in the interval [0.88,0.94], exhibiting a close match. The tuned parameters have the same order of magnitude as those obtained in our test.

7. Feasibility of fines breakage during injection and production in natural reservoirs

A fines migration test is a routine laboratory experiment to prevent formation damage due to fines migration. A core is submitted to flow with piecewise-constant increasing velocity. Minimum fines migration velocity is determined by appearance of the first fine particles in the effluent. This determines maximum well rate under which fines migration does not occur. Here we predict the minimum velocity for fines migration using the stress diagram technique and conclude about the viability of fines detachment by breakage during water, oil, and gas injection and production. The results below also illustrate using the sequential techniques for tensile-stress diagram, shear-stress diagram, and equation (44) for the breakage velocity.

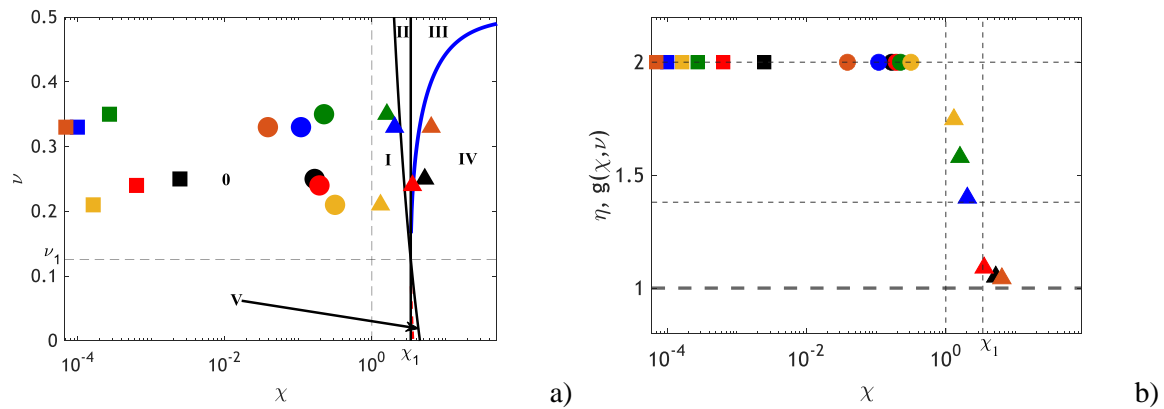


Fig. 17. Determining breakage regime for 6 examples of injection and injection in natural reservoirs: a) tensile-stress diagram, b) shear-tensile diagram

The data for the cases of production of heavy oil, polymer injection, dewatering of coal seams, CO₂ injection, well fracturing by water, and well fracturing by highly-viscous fluid, which are marked in Fig. 17 by black, red, green, yellow, blue, and orange, respectively, are taken from the corresponding papers by Ado 2021, Gao 2011, Shi et al. 2008, Spivak et al. 1989, and Prasetio et al. 2021.⁹⁵⁻⁹⁹ Circular, triangular, and square points in Fig. 17 correspond to spheroidal, flat and long cylinder particles. Volume-equivalent particle size $r_s=2 \times 10^{-6}$ m and wellbore radius $r_w=0.1$ m are assumed for all cases. Poisson's ratios ν varies in the interval 0.21 to 0.35. Fluid viscosities were taken as high as 1000, 300, and 40 cp for fracturing fluid, heavy oil, and polymer solution and as low as 0.02 cp for CO₂. For the composite particle-rock bond, a low value of tensile strength $T_0=0.2$ MPa is assumed for all cases; yet several works report lower T_0 values.^{31, 32, 45, 89} Other data are presented in the Table 1. The values of shape-Poisson numbers χ have been calculated by Eq. (12), which allows placing the corresponding state points into the tensile-stress diagram (χ, ν) in Fig. 17a. Values of χ and ν allow calculating breakage function $\eta=g(\chi, \nu)$ for the state points and determine their position in the tensile-shear diagram (χ, η) (Fig. 17b). Here the state points are located on breakage regime curves $\eta=g(\chi, \nu)$

that correspond to different Poisson's ratios. Breakage function $g(\chi, \nu)=2$ for spheroidal and long cylindrical cases. For all cases, like in papers by Gao et al. 2014, Guo et al. 2018, and Horabik and Jozefaciuk 2021, the strength ratio η is assumed to be equal to one.¹⁰⁰⁻¹⁰² As discussed earlier, for values of η lower than or equal to 1, breakage occurs by tensile failure (Fig. 11).

Table 1: Calculation of minimum fines breakage velocity of the fluid at the well / fracture wall

	α_s	δ	ν	χ	μ , (Pa.s)	U_{cr}^b , (m/s)
Heavy oil	1	0.8	0.25	0.17	0.30	4.14×10^{-4}
Polymer	0.8	0.7	0.24	0.19	0.04	2.89×10^{-3}
CBM	0.6	0.6	0.35	0.22	1×10^{-3}	0.17
CO ₂	0.4	0.5	0.21	0.32	2.28×10^{-5}	3.02
HF-W	0.2	0.4	0.33	0.11	1×10^{-3}	7.74×10^{-2}
HF	0.1	0.3	0.33	0.04	1	1.64×10^{-5}

Fig. 17a shows that for spheroidal and long cylindrical particles, all 12 cases belong to domain 0, where both tensile stresses κT_m^0 and κT_m^l are equal to two, while for short cylindrical particles some points belong to domain I, III, IV. For both cases of maximum tensile stress in the middle and the boundary of the beam base, Eqs. (40) and (41) show that the strength-drag numbers are equal, i.e. $\kappa=2$. It allows calculating minimum breakage velocities using Eq. (44). Points in Fig. 17b correspond to different Poisson's ratios and, therefore, are located on different breakage regime curves, $\eta=g(\chi, \nu)$. However, the overall curve has the same general tendency as those presented in Fig. 11.

The breakage velocities are presented in the eighth column of Table 1. The breakage velocities for heavy oil production, hydraulic fracturing by water, and dewatering of coal bed seam are untypically high, i.e., fines breakage is unlikely. The calculated breakage velocity for polymer solution is feasible during injection in a highly permeable reservoir. The calculated breakage velocity for hydraulic fracturing by a highly viscous fluid is typical. The CO₂ breakage injection velocity is too high for field cases, but it can decrease down to any arbitrarily low value during mineral dissolution of particle-rock bond in carbonic acid. The same corresponds to waterflooding of carbonate reservoirs during rock dissolution in water. The above demonstrates likelihood of particle breakage near to injection and production wells.

8. Conclusions

Integration of Timoshenko's beam theory with breakage criteria for particle-substrate bonds and CFD flow modelling allows concluding the following.

Breakage conditions where either of the tensile or shear stresses reaches the strength value, is determined by three dimensionless groups: the strength-drag number κ , the aspect-Poisson number χ , strength ratio η , as well as the Poisson's ratio ν .

Stress maxima are reached at the base of the particle, either at the central axis, $Y=0$ or at the base boundary, $X^2+Y^2=1$.

Stress maxima along the axis $Y=0$ are determined by the aspect-Poisson number χ alone, while the maxima at the beam boundary are determined by both the aspect-Poisson number χ and

Poisson's ratio ν . Equality of tensile stress maxima at the beam base axes and boundary separates the plane (χ, ν) , which is called the tensile stress diagram, into 5 domains, where one tensile maximum exceeds the other.

Shear stress maximum at the central axis of the particle base is always higher than that at the boundary.

The breakage regime – by either tensile or shear stress – is determined by breakage function $g(\chi, \nu)$, which is the ratio of stress maximum of two tensile maxima and maximum shear. The breakage regime depends on the shape-Poisson number, Poisson's ratio, and the ratio η between tensile and shear strengths. The breakage occurs by tensile failure if $g(\chi, \nu) > \eta$, i.e., where the point (χ, η) is located below the curve $g(\chi, \nu)$ in the shear-tensile diagram (χ, η) . If the strength ratio exceeds 2, particles are detached by shear stress for all values of χ and ν . For strength ratios below two and above one, the particles are detached by shear stress for shape-Poisson numbers χ such that η exceeds $g(\chi, \nu)$; for lower aspect-Poisson ratios, particles are detached by tensile stress. For strength ratios below one, the particles are detached by tensile stress for all Poisson's ratios.

The definition of the breakage regime – by either tensile or shear stress, in the base middle or at the boundary - is independent of flow velocity. For an identified breakage regime, the breakage flow velocity is determined by the strength-drag number $\kappa(\chi, \nu)$ alone. For a given particle shape, the critical breakage velocity is proportional to the strength and particle size and is inversely proportional to viscosity. These conclusions are the consequence of the assumptions of a Newtonian fluid, elastic beam deformation, and the strength failure criteria.

During bond breakage under increasing velocity, the particles of all shapes detach in order of decreasing of their radii, i.e., the large particles break first. For particles of the same volume, the breakage velocity versus aspect ratio is non-monotonic for spherical particles – very flat or almost spherical particles are detached at low flow velocities while the highest flux detaches particles with intermediate aspect ratio. However, for long cylinders, the product of drag and moment factors by the aspect ratio versus aspect ratio is a monotonically decreasing function, and the lower the aspect ratio the higher the breakage velocity.

A mathematical model for colloidal detachment by breakage is a maximum retention function (MRF), derived from the formula for breakage flow velocity.

With simultaneous detachment of authigenic and detrital fines, the MRF is the total of those obtained from mechanical equilibrium conditions for detachment against electrostatic attraction, and by breakage. For weak DLVO particle-rock attraction and high bond strength, the total MRF has a velocity plateau, where all detrital particles are already detached and authigenic particle breakage hasn't started yet. For high electrostatic attraction and low bond strength, the velocity intervals for detachment by both causes overlap, and the plateau disappears.

The breakage MRF allows closing the governing equations for migration of authigenic clays with bond failure. The total MRF for authigenic and detrital fines can be determined from breakthrough particle concentration during a coreflood with piecewise constant and increasing velocity. The determination of the MRF is based on the analytical model for fines mobilisation, migration, and straining (size exclusion). Matching the breakthrough curve allows determining the MRF along with the filtration coefficient for straining and drift-delay factor.

For an MRF with a plateau, the initial percentage of authigenic and detrital fines is calculated directly from the plateau height. For MRF without plateau, the percentage of authigenic and detrital fines is calculated by tuning the MRF coefficients.

The model for fines detachment by breakage is validated by the coreflood with 7 constant-rate injections by the two-population feature of produced particle concentrations. High match of the breakthrough concentrations and pressure drop using the two-population model, tuned coefficients within commonly reported intervals, as well as bimodal size distributions of produced fines all support the validity of the proposed formulation.

Calculations of breakage velocity shows that breakage of authigenic particles can occur during CO₂ injection for storage, polymer injection into oilfields, leak-off of highly viscous fracturing fluids during well fracturing, and waterflooding in carbonate oilfields. Fines detachment by breakage during heavy oil production, dewatering of coal seams, and well fracturing by water is unlikely.

Appendix A. Expressions for stresses in 3D elastic beam model

Under the model assumptions formulated in section 2.1, Timoshenko's 3D solution for elastic deformation of a cylindrical beam (Fig. 4) shows that the normal stress σ_z reaches a maximum at the beam bottom, $z=0$, and the two shear stresses τ_{xz} and τ_{yz} are independent of z . The normal and shear stresses at the beam base with applied external load F_d are: ³³

$$\sigma_z = \frac{F_d b f_M x}{I}, \quad \sigma_x = \sigma_y = \tau_{xy} = 0 \quad (\text{A1})$$

$$\tau_{xz} = \frac{(3+2\nu) F_d}{8(1+\nu) I} \left(r_b^2 - x^2 - \frac{(1-2\nu)}{(3+2\nu)} y^2 \right) \quad (\text{A2})$$

$$\tau_{yz} = -\frac{(1+2\nu) F_d xy}{4(1+\nu) I} \quad (\text{A3})$$

where, σ_z is the normal bending stress at contact area, τ_{xz} is the shear stress acting on the z plane and towards the x direction, τ_{yz} is the shear stress acting on the z plane and towards the y direction, ν the is Poisson's ratio, and I is the moment of inertia, which for circular cross-section is equal to $\pi r_b^4/4$.

As expressed by Eq. A1, the normal bending stress expands the matter at $x<0$ reaching a minimum in the advance point $x=-r_b$, $y=0$ (Fig. 4a) and contracts at $x>0$ reaching a maximum at the receding point $x=r_b$, $y=0$. Fig. 4b illustrates Eq. (A2) and corresponds to shear stress that opposes the external load F_d and is equal zero only in advance and receded points. Eq. (A3) is illustrated by Fig. 4c, showing the transversal shear stress.

The stress tensor, as per solution (A1-A3) is:

$$\begin{bmatrix} 0 & 0 & \tau_{xz} \\ 0 & 0 & \tau_{yz} \\ \tau_{xz} & \tau_{yz} & \sigma_z \end{bmatrix} \quad (\text{A4})$$

The principal stresses are eigen values of the stress tensor (A4):

$$\sigma_1 = \frac{\sigma_z + \sqrt{\sigma_z^2 + 4(\tau_{xz}^2 + \tau_{yz}^2)}}{2}, \quad \sigma_2 = 0, \quad \sigma_3 = \frac{\sigma_z - \sqrt{\sigma_z^2 + 4(\tau_{xz}^2 + \tau_{yz}^2)}}{2} \quad (\text{A5})$$

where, $\sigma_1, \sigma_2, \sigma_3$ are the principal stresses in decreasing order of magnitude, and

$$\sigma_1 > \sigma_2 = 0 > \sigma_3. \quad (\text{A6})$$

Maximum tensile and shear stresses in Eqs. (8, 9) correspond to points $(\sigma_3, 0)$ and $(\sigma_1 + \sigma_3)/2, (\sigma_1 - \sigma_3)/2$ in plane (σ, τ) . Consequently, the maximum tensile and shear stresses are

$$\max \sigma = \sigma_3, \quad \max \tau = \frac{\sigma_1 - \sigma_3}{2}, \quad (\text{A7})$$

respectively.

Appendix B. Two-population colloidal-suspension transport in porous media

We discuss deep bed filtration of two particle populations for detrital and authigenic fines. Mass balance and capture rate equations and Darcy's law for both populations are:^{12,13,103}

$$\frac{\partial}{\partial t}(\phi c_k + \sigma_k) + \frac{\partial}{\partial x}(c_k \alpha_k U_n) = 0 \quad (\text{B1})$$

$$\frac{\partial \sigma_k}{\partial t} = \lambda_k c_k \alpha_k U_n, \quad k = 1, 2, \quad n = 0, 1, 2, \dots \quad (\text{B2})$$

$$U_n = -\frac{k}{1 + \beta_1 \sigma_1 + \beta_2 \sigma_2} \frac{\partial p}{\partial x} \quad (\text{B3})$$

where ϕ is the porosity, c_k and σ_k are the suspended and retained concentrations for both populations, $k=1,2$, λ_k are the filtration coefficients, α_k are the drift-delay factors, U_n is the flow velocity, k_0 is the initial permeability, p is the pressure, and β_k are the formation damage coefficients. Index k corresponds to the two populations; index n is attributed to the injection velocity at the n -th step of the test. The filtration coefficient for the first population is constant. The filtration coefficient for the second population is a blocking (Langmuir) function of retained second-population concentration¹⁰³

$$\lambda_1 = \text{const}$$

$$\lambda_2(\sigma_2) = \begin{cases} \lambda_{20} \left(1 - \frac{\sigma_2}{\sigma_{20}}\right), & \sigma_2 < \sigma_{20} \\ 0, & \sigma_2 > \sigma_{20} \end{cases} \quad (\text{B4})$$

Initial retained concentrations for both populations are equal to the concentrations of mobilised fines after a velocity increase

$$t = 0: c_{k0} = \frac{\sigma_{cr}^k(U_n) - \sigma_{cr}^k(U_{n-1})}{\phi} = \frac{\Delta \sigma_{cr}^k(U)}{\phi}, \quad k = 1, 2 \quad (\text{B5})$$

Inlet boundary condition corresponds to the injection of particle-free water

$$x = 0: c_k = 0, \quad k = 1, 2 \quad (\text{B6})$$

Breakthrough concentration is a total of those for both populations. The exact solution is^{88,89}

$$c(x, t) = c_1(x, t) + c_2(x, t)$$

$$c_1 = \begin{cases} \frac{\Delta\sigma_1(U)}{\phi} \exp\left(-\frac{\lambda_1\alpha_1 U}{\phi} t\right), & x > \frac{\alpha_1 U}{\phi} t \\ 0, & x < \frac{\alpha_1 U}{\phi} t \end{cases}$$

$$c_2 = \begin{cases} 0, & x > \frac{\alpha_2 U}{\phi} t \\ c_2 = \frac{\sigma_m \left(\frac{\Delta\sigma_2}{\sigma_m} - 1 \right)}{\phi \left\{ 1 - \frac{\sigma_m}{\Delta\sigma_2(U)} \exp\left[\frac{\lambda_2\alpha_2 U}{\phi} t \left(1 - \frac{\Delta\sigma_2}{\sigma_m} \right) \right] \right\}}, & x < \frac{\alpha_2 U}{\phi} t \end{cases} \quad (\text{B7})$$

Acknowledgements

The authors are deeply grateful for fruitful discussions and support to A/Profs Giang D. Nguyen and Abbas Zeinijahromi, Drs Nouné Melkounian, Zhao Feng Tian, Themis Carageorgos and Heng Zheng Ting (University of Adelaide), Prof Leslie Banks-Sills (Tel-Aviv University) and A/Prof Hamid Roshan (University of New South Wales).

References

1. Hashemi S, Melkounian N. A strain energy criterion based on grain dislodgment at borehole wall in poorly cemented sands. *International Journal of Rock Mechanics and Mining Sciences*. 2016;87:90-103.
2. De Silva G, Ranjith P, Perera M, Dai Z, Yang S. An experimental evaluation of unique CO₂ flow behaviour in loosely held fine particles rich sandstone under deep reservoir conditions and influencing factors. *Energy*. 2017;119:121-37.
3. Jayasekara D, Ranjith P, Wanniarachchi W, Rathnaweera T. Understanding the chemico-mineralogical changes of caprock sealing in deep saline CO₂ sequestration environments: A review study. *The Journal of Supercritical Fluids*. 2020;161:104819.
4. Kong L, Ranjith PG, Li BQ. Fluid-driven micro-cracking behaviour of crystalline rock using a coupled hydro-grain-based discrete element method. *International Journal of Rock Mechanics and Mining Sciences*. 2021;144:104766.
5. Kamel KEM, Gerard P, Colliat J-B, Massart TJ. Modelling stress-induced permeability alterations in sandstones using CT scan-based representations of the pore space morphology. *International Journal of Rock Mechanics and Mining Sciences*. 2022;150:104998.
6. Song J, Xiang D, Hu D, Zhou H, Guo D, Zhang G. Creep characteristics of a fracturing fluid-softened shale investigated by microindentation. *International Journal of Rock Mechanics and Mining Sciences*. 2022;152:105067.
7. Appelo CAJ, Postma D. *Geochemistry, groundwater and pollution*: CRC press; 2004.
8. Bandara K, Ranjith P, Haque A, Wanniarachchi W, Zheng W, Rathnaweera T. An experimental investigation of the effect of long-term, time-dependent proppant embedment on fracture

- permeability and fracture aperture reduction. *International Journal of Rock Mechanics and Mining Sciences*. 2021;144:104813.
9. Castro R, Arancibia L, Gómez R. Quantifying fines migration in block caving through 3D experiments. *International Journal of Rock Mechanics and Mining Sciences*. 2022;151:105033.
 10. Liu J, Yuan X, Zhang J, Xi W, Feng J, Wu H, editors. *Sharp Reductions in High-Productivity Well Due to Formation Damage: Case Study in Tarim Basin, China*. Proceedings of the International Field Exploration and Development Conference 2017; 2019: Springer.
 11. Song Y, Ranjith P, Wu B. A study of ellipsoidal and spherical particle flow, clogging and unclogging dynamics. *Powder Technology*. 2021;392:424-37.
 12. Bradford SA, Simunek J, Bettahar M, Van Genuchten MT, Yates SR. Modeling colloid attachment, straining, and exclusion in saturated porous media. *Environmental science & technology*. 2003;37(10):2242-50.
 13. Bradford SA, Torkzaban S, Shapiro A. A theoretical analysis of colloid attachment and straining in chemically heterogeneous porous media. *Langmuir*. 2013;29(23):6944-52.
 14. Johnson WP. Quantitative linking of nanoscale interactions to continuum-scale nanoparticle and microplastic transport in environmental granular media. *Environmental Science & Technology*. 2020;54(13):8032-42.
 15. Wilson MD, Pittman ED. Authigenic clays in sandstones; recognition and influence on reservoir properties and paleoenvironmental analysis. *Journal of Sedimentary Research*. 1977;47(1):3-31.
 16. Burley S, Kantorowicz J, Waugh B. *Clastic diagenesis*. Geological Society, London, Special Publications. 1985;18(1):189-226.
 17. Kar R, Baruah H, Phukan S. Signatures of Marine Influences in the Gondwana Sandstones of Kalijhora, Darjeeling District, West Bengal, India. *Earth Science India*. 2019;12(1).
 18. Obermayr M, Dressler K, Vrettos C, Eberhard P. A bonded-particle model for cemented sand. *Computers and Geotechnics*. 2013;49:299-313.
 19. Bergendahl J, Grasso D. Prediction of colloid detachment in a model porous media: hydrodynamics. *Chemical Engineering Science*. 2000;55(9):1523-32.
 20. Chen C, Packman AI, Gaillard JF. Pore-scale analysis of permeability reduction resulting from colloid deposition. *Geophysical Research Letters*. 2008;35(7).
 21. Israelachvili JN. *Intermolecular and surface forces*: Academic press; 2011.
 22. Bedrikovetsky P, Siqueira FD, Furtado CA, Souza ALS. Modified particle detachment model for colloidal transport in porous media. *Transport in porous media*. 2011;86(2):353-83.
 23. Bedrikovetsky P, Zeinijahromi A, Siqueira FD, Furtado CA, de Souza ALS. Particle detachment under velocity alternation during suspension transport in porous media. *Transport in Porous Media*. 2012;91(1):173-97.
 24. Mishra S, Ojha K, editors. *A Novel Chemical Composition to Consolidate the Loose Sand Formation in the Oil Field*. International Petroleum Technology Conference; 2016: OnePetro.
 25. Turner LG, Steel KM. A study into the effect of cleat demineralisation by hydrochloric acid on the permeability of coal. *Journal of Natural Gas Science and Engineering*. 2016;36:931-42.
 26. Wang J, Huang Y, Zhou F, Song Z, Liang X. Study on reservoir damage during acidizing for high-temperature and ultra-deep tight sandstone. *Journal of Petroleum Science and Engineering*. 2020;191:107231.
 27. Tang Y, Lv C, Wang R, Cui M. Mineral dissolution and mobilization during CO₂ injection into the water-flooded layer of the Pucheng Oilfield, China. *Journal of Natural Gas Science and Engineering*. 2016;33:1364-73.
 28. Othman F, Yu M, Kamali F, Hussain F. Fines migration during supercritical CO₂ injection in sandstone. *Journal of Natural Gas Science and Engineering*. 2018;56:344-57.
 29. Hadi Y, Hussain F, Othman F, editors. *Low salinity water flooding in carbonate reservoirs—dissolution effect*. IOP Conference Series: Materials Science and Engineering; 2019: IOP Publishing.
 30. Guo Z, Hussain F, Cinar Y. Physical and analytical modelling of permeability damage in bituminous coal caused by fines migration during water production. *Journal of Natural Gas Science and Engineering*. 2016;35:331-46.

31. Bai T, Chen Z, Aminossadati SM, Pan Z, Liu J, Li L. Characterization of coal fines generation: A micro-scale investigation. *Journal of Natural Gas Science and Engineering*. 2015;27:862-75.
32. Bai T, Chen Z, Aminossadati SM, Li L, Liu J, Lu H. Dimensional analysis and prediction of coal fines generation under two-phase flow conditions. *Fuel*. 2017;194:460-79.
33. Timoshenko S, Goodier JN. *Theory of Elasticity*: by S. Timoshenko and JN Goodier: McGraw-Hill; 1951.
34. Robinson ES. Mechanical disintegration of the Navajo sandstone in Zion Canyon, Utah. *Geological Society of America Bulletin*. 1970;81(9):2799-806.
35. Young AP, Ashford SA. Instability investigation of cantilevered seacliffs. *Earth Surface Processes and Landforms: The Journal of the British Geomorphological Research Group*. 2008;33(11):1661-77.
36. Potyondy DO, Cundall P. A bonded-particle model for rock. *International journal of rock mechanics and mining sciences*. 2004;41(8):1329-64.
37. Abousleiman Y, Hull K, Han Y, Al-Muntasheri G, Hosemann P, Parker S, et al. The granular and polymer composite nature of kerogen-rich shale. *Acta Geotechnica*. 2016;11(3):573-94.
38. Allison PG, Moser RD, Schirer JP, Martens RL, Jordon JB, Chandler MQ. In-situ nanomechanical studies of deformation and damage mechanisms in nanocomposites monitored using scanning electron microscopy. *Materials Letters*. 2014;131:313-6.
39. Khoo HS, Liu K-K, Tseng F-G. Mechanical strength and interfacial failure analysis of cantilevered SU-8 microposts. *Journal of micromechanics and microengineering*. 2003;13(6):822.
40. Liu H-K, Pan C, Liu P-P. Dimension effect on mechanical behavior of silicon micro-cantilever beams. *Measurement*. 2008;41(8):885-95.
41. Darnbrough J, Liu D, Flewitt P. Micro-scale testing of ductile and brittle cantilever beam specimens in situ with a dual beam workstation. *Measurement Science and Technology*. 2013;24(5):055010.
42. Matoy K, Schönherr H, Detzel T, Schöberl T, Pippan R, Motz C, et al. A comparative micro-cantilever study of the mechanical behavior of silicon based passivation films. *Thin Solid Films*. 2009;518(1):247-56.
43. Stephens LS, Kelly KW, Simhadri S, McCandless AB, Meletis E. Mechanical property evaluation and failure analysis of cantilevered LIGA nickel microposts. *Journal of microelectromechanical systems*. 2001;10(3):347-59.
44. Vallejo LE. Fissure parameters in stiff clays under compression. *Journal of geotechnical engineering*. 1989;115(9):1303-17.
45. Akin ID, Likos W. Brazilian tensile strength testing of compacted clay. *Geotechnical Testing Journal*. 2017;40(4):608-17.
46. Maltman AJ. Shear zones in argillaceous sediments—an experimental study. Geological Society, London, Special Publications. 1987;29(1):77-87.
47. Vallejo L, Shettima M, Alaasmi A. Unconfined compressive strength of brittle material containing multiple cracks. *International Journal of Geotechnical Engineering*. 2013;7(3):318-21.
48. Zhang B-y, Li Q-m, Yuan H-n, Sun X. Tensile fracture characteristics of compacted soils under uniaxial tension. *Journal of Materials in Civil Engineering*. 2015;27(10):04014274.
49. Tschebatorioff F. The tensile strength of disturbed and recompacted soils. *Proc 3rd ICSMFE*, 1953. 1953;1:207-10.
50. Kalhor A, Mirabi K. Experimental Investigation of the Geotextile Effect on the Strength of Kaolinite Clay. *American Journal of Scientific Research*. 2013(89):47-59.
51. Maher M, Ho Y. Mechanical properties of kaolinite/fiber soil composite. *Journal of Geotechnical Engineering*. 1994;120(8):1381-93.
52. Abdi MR, Mirzaeifar H. Effects of discrete short polypropylene fibers on behavior of artificially cemented kaolinite. *International Journal of Civil Engineering*. 2016;14(4):253-62.
53. Feng R, Zhang Y, Rezagholilou A, Roshan H, Sarmadivaleh M. Brittleness Index: from conventional to hydraulic fracturing energy model. *Rock Mechanics and Rock Engineering*. 2020;53(2):739-53.
54. Ren J, He H, Senetakis K. A Micromechanical-based investigation on the frictional behaviour of artificially bonded analogue sedimentary rock with calcium carbonate. *Pure and Applied Geophysics*. 2021;178(11):4461-86.

55. Corkum A, Martin C. The mechanical behaviour of weak mudstone (Opalinus Clay) at low stresses. *International Journal of Rock Mechanics and Mining Sciences*. 2007;44(2):196-209.
56. Mamen B, Kolli M, Ouedraogo E, Hamidouche M, Djoudi H, Fanttozi G. Experimental characterisation and numerical simulation of the thermomechanical damage behaviour of kaolinitic refractory materials. *Journal of the Australian Ceramic Society*. 2019;55(2):555-65.
57. Josh M, Esteban L, Delle Piane C, Sarout J, Dewhurst D, Clennell M. Laboratory characterisation of shale properties. *Journal of Petroleum Science and Engineering*. 2012;88:107-24.
58. Huang T, Cao L, Cai J, Xu P. Experimental investigation on rock structure and chemical properties of hard brittle shale under different drilling fluids. *Journal of Petroleum Science and Engineering*. 2019;181:106185.
59. Zhao J, Cao Y, Wang L, Zhang H-J, He M-C. Investigation on Atomic Structure and Mechanical Property of Na-and Mg-Montmorillonite under High Pressure by First-Principles Calculations. *Minerals*. 2021;11(6):613.
60. Ding C, Hu D, Zhou H, Lu J, Lv T. Investigations of P-Wave velocity, mechanical behavior and thermal properties of anisotropic slate. *International Journal of Rock Mechanics and Mining Sciences*. 2020;127:104176.
61. Ranjith P, Viete DR, Chen BJ, Perera MSA. Transformation plasticity and the effect of temperature on the mechanical behaviour of Hawkesbury sandstone at atmospheric pressure. *Engineering Geology*. 2012;151:120-7.
62. Choens R, Bauer S, Shalev E, Lyakhovsky V. Modelling yield cap evolution in sandstone based on brittle creep experiments. *International Journal of Rock Mechanics and Mining Sciences*. 2021;141:104706.
63. Wang S, Xu W, Yang L. Experimental and elastoplastic model investigation on brittle-ductile transition and hydro-mechanical behaviors of cement mortar. *Construction and Building Materials*. 2019;224:19-28.
64. Zhang X, Ranjith P, Ranathunga A, Li D. Variation of mechanical properties of bituminous coal under CO₂ and H₂O saturation. *Journal of Natural Gas Science and Engineering*. 2019;61:158-68.
65. Zhang G, Ranjith P, Li Z, Gao M, Ma Z. Long-term effects of CO₂-water-coal interactions on structural and mechanical changes of bituminous coal. *Journal of Petroleum Science and Engineering*. 2021;207:109093.
66. Kim B-H, Larson MK. Laboratory investigation of the anisotropic confinement-dependent brittle-ductile transition of a Utah coal. *International journal of mining science and technology*. 2021;31(1):51-7.
67. Han Z, Yang H, He M. A molecular dynamics study on the structural and mechanical properties of hydrated kaolinite system under tension. *Materials Research Express*. 2019;6(8):0850c3.
68. Yang H, He M, Lu C, Gong W. Deformation and failure processes of kaolinite under tension: Insights from molecular dynamics simulations. *SCIENCE CHINA Physics, Mechanics & Astronomy*. 2019;62(6):1-9.
69. Yang H, Han Z, Hu J, He M. Defect and temperature effects on the mechanical properties of kaolinite: a molecular dynamics study. *Clay Minerals*. 2019;54(2):153-9.
70. Zhang L-L, Zheng Y-Y, Wei P-C, Diao Q-F, Yin Z-Y. Nanoscale mechanical behavior of kaolinite under uniaxial strain conditions. *Applied Clay Science*. 2021;201:105961.
71. Fjaer E, Holt RM, Horsrud P, Raaen AM. *Petroleum related rock mechanics*: Elsevier; 2008.
72. Jaeger JC, Cook NG, Zimmerman R. *Fundamentals of rock mechanics*: John Wiley & Sons; 2009.
73. Huang F, Kang Y, You Z, You L, Xu C. Critical conditions for massive fines detachment induced by single-phase flow in coalbed methane reservoirs: modeling and experiments. *Energy & Fuels*. 2017;31(7):6782-93.
74. Wagner TJ, James TD, Murray T, Vella D. On the role of buoyant flexure in glacier calving. *Geophysical Research Letters*. 2016;43(1):232-40A.
75. Chen X, Peng D, Morrissey JP, Ooi JY. A comparative assessment and unification of bond models in DEM simulations. *Granular Matter*. 2022;24(1):1-20.
76. O'Neill M. A sphere in contact with a plane wall in a slow linear shear flow. *Chemical Engineering Science*. 1968;23(11):1293-8.

77. Ting HZ, Bedrikovetsky P, Tian ZF, Carageorgos T. Impact of shape on particle detachment in linear shear flows. *Chemical Engineering Science*. 2021;241:116658.
78. Derjaguin B, Landau L. The theory of stability of highly charged lyophobic sols and coalescence of highly charged particles in electrolyte solutions. *Acta Physicochim URSS*. 1941;14(633-52):58.
79. Verwey E, Overbeek JTG, Nes Kv. Theory of the stability of lyophobic colloids: the interaction of sol particles having an electric double layer. 1948.
80. Landau LD, Lifshitz EM. *Fluid Mechanics: Landau and Lifshitz: Course of Theoretical Physics, Volume 6*: Elsevier; 2013.
81. Yuan B, Moghanloo RG. Analytical modeling nanoparticles-fines reactive transport in porous media saturated with mobile immiscible fluids. *AIChE Journal*. 2019;65(10):e16702.
82. Yuan H, Shapiro AA. Induced migration of fines during waterflooding in communicating layer-cake reservoirs. *Journal of Petroleum Science and Engineering*. 2011;78(3-4):618-26.
83. Ting HZ, Yang Y, Tian ZF, Carageorgos T, Bedrikovetsky P. Image interpretation for kaolinite detachment from solid substrate: Type curves, stochastic model. *Colloids and Surfaces A: Physicochemical and Engineering Aspects*. 2022;650:129451.
84. You Z, Bedrikovetsky P, Badalyan A, Hand M. Particle mobilization in porous media: temperature effects on competing electrostatic and drag forces. *Geophysical Research Letters*. 2015;42(8):2852-60.
85. Zhang H, Malgaresi G, Bedrikovetsky P. Exact solutions for suspension-colloidal transport with multiple capture mechanisms. *International Journal of Non-Linear Mechanics*. 2018;105:27-42.
86. Teitelbaum Y, Shimony T, Saavedra Cifuentes E, Dallmann J, Phillips CB, Packman AI, et al. A Novel Framework for Simulating Particle Deposition With Moving Bedforms. *Geophysical Research Letters*. 2022;49(4):e2021GL097223.
87. Polyanin AD. *Linear partial differential equations for Engineers and Scientists*. Chapman and Hall/CRC. 2002.
88. Polyanin AD, Zaitsev VF. *Nonlinear Partial Differential Equations*. Chapman and Hall/CRC New York; 2004.
89. Zoback MD. *Reservoir geomechanics*: Cambridge university press; 2010.
90. Cai W, Dou L, Ju Y, Cao W, Yuan S, Si G. A plastic strain-based damage model for heterogeneous coal using cohesion and dilation angle. *International Journal of Rock Mechanics and Mining Sciences*. 2018;110:151-60.
91. Yuan B, Moghanloo RG. Nanofluid precoating: an effective method to reduce fines migration in radial systems saturated with two mobile immiscible fluids. *SPE Journal*. 2018;23(03):998-1018.
92. Huang F, Dong C, You Z, Shang X. Detachment of coal fines deposited in proppant packs induced by single-phase water flow: Theoretical and experimental analyses. *International Journal of Coal Geology*. 2021;239:103728.
93. Ochi J, Vernoux J-F. Permeability decrease in sandstone reservoirs by fluid injection: hydrodynamic and chemical effects. *Journal of hydrology*. 1998;208(3-4):237-48.
94. Torkzaban S, Bradford SA, Vanderzalm JL, Patterson BM, Harris B, Prommer H. Colloid release and clogging in porous media: Effects of solution ionic strength and flow velocity. *Journal of contaminant hydrology*. 2015;181:161-71.
95. Ado MR. Improving heavy oil production rates in THAI process using wells configured in a staggered line drive (SLD) instead of in a direct line drive (DLD) configuration: detailed simulation investigations. *Journal of Petroleum Exploration and Production Technology*. 2021;11(11):4117-30.
96. Gao CH. Scientific research and field applications of polymer flooding in heavy oil recovery. *Journal of Petroleum Exploration and Production Technology*. 2011;1(2):65-70.
97. Shi J-Q, Durucan S, Fujioka M. A reservoir simulation study of CO₂ injection and N₂ flooding at the Ishikari coalfield CO₂ storage pilot project, Japan. *International Journal of Greenhouse Gas Control*. 2008;2(1):47-57.
98. Spivak A, Karaoguz D, Issever K, Nolen J, editors. Simulation of immiscible CO₂ injection in a fractured carbonate reservoir, Bati Raman Field, Turkey. *SPE California regional meeting*; 1989: OnePetro.

99. Prasetyo MH, Anggraini H, Tjahjono H, Pramadana AB, Akbari A, Madyanova M, et al., editors. Success Story of Optimizing Hydraulic Fracturing Design at Alpha Low-Permeability Reservoir. SPE/IATMI Asia Pacific Oil & Gas Conference and Exhibition; 2021: OnePetro.
100. Gao F, Stead D, Kang H. Numerical investigation of the scale effect and anisotropy in the strength and deformability of coal. *International Journal of Coal Geology*. 2014;136:25-37.
101. Guo W-Y, Tan Y-L, Yu F-H, Zhao T-B, Hu S-C, Huang D-M, et al. Mechanical behavior of rock-coal-rock specimens with different coal thicknesses. *Geomechanics and Engineering*. 2018;15(4):1017-27.
102. Horabik J, Jozefaciuk G. Structure and strength of kaolinite–soil silt aggregates: Measurements and modeling. *Geoderma*. 2021;382:114687.
103. Bedrikovetsky P. *Mathematical theory of oil and gas recovery*. Springer Science & Business Media; 2013.

6. Particle detachment in reservoir flows by breakage due to induced stresses and drag

Hashemi, A., Borazjani, S., Nguyen, C., Loi, G., Khazali, N., Badalyan, A., Yang, Y.,
Dang-Le, B., Russell, T. and Bedrikovetsky, P., 2023.

International Journal of Rock Mechanics and Mining Sciences, 172, p.105591.

Statement of Authorship

Title of Paper	Particle detachment in reservoir flows by breakage due to induced stresses and drag
Publication Status	<input checked="" type="checkbox"/> Published <input type="checkbox"/> Submitted for Publication <input type="checkbox"/> Accepted for Publication <input type="checkbox"/> Unpublished and Unsubmitted work written in manuscript style
Publication Details	Hashemi, A., Borazjani, S., Nguyen, C., Loi, G., Khazali, N., Badalyan, A., Yang, Y., Dang-Le, B., Russell, T. and Bedrikovetsky, P., 2023. Particle detachment in reservoir flows by breakage due to induced stresses and drag. International Journal of Rock Mechanics and Mining Sciences, 172, p.105591.

Principal Author

Name of Principal Author (Candidate)	Abolfazl Hashemi		
Contribution to the Paper	Collecting data, performing lab data analysis, deriving the equations, writing code for the authigenic particle detachment, preparing the graphs, writing part of the manuscript.		
Overall percentage (%)	85%		
Certification:	This paper reports on original research I conducted during the period of my Higher Degree by Research candidature and is not subject to any obligations or contractual agreements with a third part that would constrain its inclusion in this thesis. I am the primary author of this paper.		
Signature		Date	15/11/2023

Co-Author Contributions

By signing the Statement of Authorship, each author certifies that:

- I. The candidate's stated contribution to the publication is accurate (as detailed above);
- II. Permission is granted to the candidate to include the publication in the thesis; and
- III. The sum of all co-author contributions is equal to 100% less the candidate's stated contribution

Name of Co-Author	Sara Borazjani		
Contribution to the Paper	Co-supervising, aiding in the derivations of breakage equations and checking the results		
Signature		Date	15/11/2023

Name of Co-Author	Cuong Cao Nguyen		
Contribution to the Paper	Collecting literature data, writing code, and analysing detrital particle detachment		
Signature		Date	15/11/2023

Name of Co-Author	Grace Loi		
Contribution to the Paper	Collecting literature data, writing code, and analysing detrital particle detachment		
Signature		Date	15/11/2023

Name of Co-Author	Nastaran Khazali		
Contribution to the Paper	Deriving equations and matching lab data using two-population particle detachment mechanism.		
Signature		Date	15/11/2023

Name of Co-Author	Alex Badalyan		
Contribution to the Paper	Supervising lab design and data collection		
Signature		Date	15/11/2023

Name of Co-Author	Yutong Yang		
Contribution to the Paper	Performing sensitivity on MRF, collecting field data for fluid velocity through fracture and fault, and preparing cross plots.		
Signature		Date	15/11/2023

Name of Co-Author	Bryant Dang-Le		
Contribution to the Paper	Collecting and analysing lab data, collecting field data.		
Signature	Bryant Dang-Le	Date	15/11/2023

Name of Co-Author	Thomas Russell		
Contribution to the Paper	Co-supervising, aiding in the derivations of DLVO equations and checking the DLVO results, giving consultation on the total MRF, giving advice, and proofreading the manuscript.		
Signature		Date	15/11/2023

Name of Co-Author	Pavel Bedrikovetsky		
Contribution to the Paper	Methodology and supervision.		
Signature		Date	15/11/2023



Particle detachment in reservoir flows by breakage due to induced stresses and drag

Abolfazl Hashemi, Sara Borazjani, Cuong Nguyen, Grace Loi, Nastaran Khazali, Alex Badalyan, Yutong Yang, Bryant Dang-Le, Thomas Russell^{*}, Pavel Bedrikovetsky

School of Chemical Engineering, The University of Adelaide, 5000, SA, Australia

ARTICLE INFO

Keywords:

Bond breakage
Failure criteria
Beam theory
Particle detachment
Fines migration
Analytical model

ABSTRACT

Suspension-colloidal-nano transport in porous media encompasses the detachment of detrital fines against electrostatic attraction and authigenic fines by breakage, from the rock surface. While much is currently known about the underlying mechanisms governing detachment of detrital particles, including detachment criteria at the pore scale and its upscaling for the core scale, a critical gap exists due to absence of this knowledge for authigenic fines. For the first time, we integrate the 3D version of Timoshenko's beam theory of elastic cylinder deformation with a CFD-based model for viscous flow around the attached particle and with strength failure criteria for particle-rock bond. This results in a novel explicit criterium for fines detachment by breakage at the pore scale. The criterium includes analytical expressions for tensile and shear stress maxima along with two geometric diagrams which allow determining the breaking stress. This leads to an explicit formula for the flow velocity that provides the particle-rock bond breakage. Its upscaling yields a novel mathematical model for fines detachment by breakage, expressed in the form of the maximum retained concentration of attached fines versus flow velocity – maximum retention function (MRF) for breakage. We performed corefloods with piecewise constant increasing flow rates, measuring breakthrough concentration and pressure drop across the core. It was found out that the behaviour of the measured data is consistent with two-population colloidal transport, attributed to detrital and authigenic fines migration. Indeed, the laboratory data show high match with the analytical model for two-population colloidal transport, which validates the proposed mathematical model for fines detachment by breakage.

1. Introduction

Dislodgement of natural reservoir fines from rock surfaces, induced by viscous flow in porous media, with the following migration and capture by the rock is essential in numerous natural and industrial processes. These include well fracturing, production of coal bed methane, water and polymer injection in aquifers and oilfields, heavy oil production, underground storage of CO₂ in aquifers and depleted oil and gas fields, fresh and hot water storage in aquifers, radioactive nuclear waste, and enhanced geothermal projects.^{1–6} Usually, the migrating fines are clays (kaolinite, illite, chlorite), silica particles, or coals.^{7–9} Detailed SEM images of potentially migrating authigenic and detrital fines attached to rock surface are presented in Ref. 15 for kaolinite, and in^{16,17} – for illite. The images clearly show the *authigenic* particles that naturally grow on rock surfaces during geological times, as well as the *detrital* particles that are attached to rock surfaces. Viscous flows in

porous media induce drag and lift exerting on attached particles, which can result in their detachment. Authigenic particles are dislodged by stresses that initiate breakage of the particle-substrate bond, while detrital fines are detached by overcoming the electrostatic particle-rock attraction.¹⁰

The detachment schematic at the pore scale is presented in Fig. 1a, where the detachment of authigenic and detrital particles occurs at the lower and upper parts of pore throat, respectively. Here σ_a , c , and σ_s are the volumetric concentrations of attached, suspended, and strained concentrations, which are used in the governing equations for the transport of colloidal particles (Appendix B). The mobilisation of fines yields their straining in thin pore throats which consequently alters the fluid flow. The attached fines coat the rock surface, so their dislodging causes low-to-moderate permeability increase, while plugging the flow paths yields significant decline of permeability.^{5,11} The consequent decrease of well productivity and injectivity motivates significant efforts in studying migration of natural reservoir fines in porous media.^{8,12–14}

^{*} Corresponding author.

E-mail address: thomas.l.russell@adelaide.edu.au (T. Russell).

<https://doi.org/10.1016/j.ijmms.2023.105591>

Received 30 December 2022; Received in revised form 22 August 2023; Accepted 29 September 2023

Available online 23 October 2023

1365-1609/© 2023 The Authors. Published by Elsevier Ltd. This is an open access article under the CC BY license (<http://creativecommons.org/licenses/by/4.0/>).

Nomenclature		X, Y, Z	Dimensionless Euclidean coordinates
<i>English letters</i>		x, y, z	Euclidean coordinates, L
a	Semi-major axis of the spheroidal particle, L	<i>Greek letters</i>	
b	Semi-minor axis of the spheroidal particle, L	α	Drift delay factor
c	Particle suspension concentration	α_s	Aspect ratio of the particle
E	Energy Potential, $M L^{-1} T^{-2}$	β	Formation damage coefficient
F	Force, $M L T^{-2}$	$\Delta\sigma_n$	Detached concentration between two consecutive velocities U_{n-1} to U_n
F_d	Drag force, $M L T^{-2}$	δ	Bond ratio
F_e	Maximum electrostatic force, $M L T^{-2}$	η	Strength number
F_g	Gravity force, $M L T^{-2}$	κ	Strength-drag number
F_l	Lifting force, $M L T^{-2}$	λ	Filtration coefficient, L^{-1}
f_d	Shape factor for drag	μ_f	Fluid viscosity, $M L^{-1} T^{-1}$
f_l	Shape factor for lift	ν_c	Coulomb friction coefficient
f_M	Shape factor for moment	ξ	Dimensionless parameter proportional to χ and depending on v
g	Breakage regime function	σ	Tensile stress, $M L^{-1} T^{-2}$
h	Particle-surface separation distance, L	$\sigma_{1,2,3}$	Principal stresses, $M L^{-1} T^{-2}$
I	Moment of inertia, L^4	σ_a	Attached particle concentration
J	Impedance	σ_{cr}	Critical retention function MRF
k	Index that corresponds to the two populations	σ_k	Retained concentration
k_0	Initial absolute permeability, L^2	σ_m	Maximum number of vacancies in porous media
l_n	Lever arm for electrostatic force, L	σ_s	Strained particle concentration
M_b	Bending moment, $M L^2 T^{-2}$	σ_x	Normal stress in x-direction, $M L^{-1} T^{-2}$
n	Index that is attributed to the injection velocity steps	σ_y	Normal stress in y-direction, $M L^{-1} T^{-2}$
PVI	Pore volume injected	σ_z	Normal stress in z-direction, $M L^{-1} T^{-2}$
p	Pressure, $M L^{-1} T^{-2}$	τ	Shear stress, $M L^{-1} T^{-2}$
r_b	Beam radius (or bond radius), L	τ_{xy}	Shear stress at y-plane towards x-direction, $M L^{-1} T^{-2}$
r_s	Effective particle radius, L	τ_{xz}	Shear stress at z-plane towards x-direction, $M L^{-1} T^{-2}$
r_w	Well radius, L	τ_{yz}	Shear stress at z-plane towards y-direction, $M L^{-1} T^{-2}$
S^0	Normalised shear stress at the middle of the beam, $M L^{-1} T^{-2}$	ν	Poisson's ratio
S^1	Normalised shear stress at the boundary of the beam, $M L^{-1} T^{-2}$	ϕ	Porosity
S_0	Shear strength, $M L^{-1} T^{-2}$	χ	Shape-Poisson number
t	Time, T	ψ	Zeta potential of particle, V
T^0	Normalised tensile stress at the middle of the beam, $M L^{-1} T^{-2}$	<i>Subscript</i>	
T^1	Normalised tensile stress at the boundary of the beam, $M L^{-1} T^{-2}$	c	Cylinder
T_0	Tensile strength, $M L^{-1} T^{-2}$	cr	Critical
t	Time, T	m	Maximum
U	Darcy's velocity, MT^{-1}	<i>Superscript</i>	
U^b	Breakage Darcy's velocity, MT^{-1}	b	Breakage
V	Interstitial fluid velocity, MT^{-1}	e	Electrostatic or detrital particles

Indeed, currently this topic is well developed for detrital fines.¹²⁻¹⁴

Current mathematical and lab modelling for *detachment of detrital fines* is based on mechanical equilibrium of a particle situated on the solid substrate.^{13,19-21} Detrital fines detachment by drag against electrostatic forces is shown at the upper part of the entrance throat in Fig. 1a. Fig. 1b and c show drag F_d , electrostatic F_e , lift F_l , and gravity F_g forces exerting on an isolated fine particle. At the moment of dislodging, a particle rotates around a contact point on the rock surface. The corresponding lever arm for normal force l_n , which is the vertical component of lift, electrostatic, and gravity forces, is determined by either mutual particle-rock deformation, like in Fig. 1b, or by the size of the rock surface asperity, like in Fig. 1c. The attaching electrostatic force is described by DLVO theory.²¹ The mathematical model for fines dislodging is either a linear-kinetics equation for detachment rate,^{12,14} or a function of retained concentration of attached particles versus velocity that is derived from mechanical equilibrium.^{22,23} Both models close the system of governing equations for colloidal-suspension-nano transport in porous media. In this work, to upscale the detachment model from

pore to rock scale, we use the approach of maximum retention function (MRF). Whereas much is currently known about the underlying mechanisms governing the flow-induced detachment of detrital fines, a critical gap exists due to the absence of geomechanics-flow breakage criteria for authigenic fines.

Detachment of authigenic fines during flow in rocks, as it is shown in Fig. 2d occurs by breakage. Particle dislodgement by breakage under viscous flows in porous media has been observed during sand production,²⁴ well acidizing,^{25,26} cement dissolution in sandstones,^{27,28} carbonate rock dissolution in water,²⁹ and illite breakage under flow during hydraulic fracturing.¹⁰ Guo et al. (2016) observed coal fines detachment by breakage during coreflood under piecewise-constant increasing velocity.³⁰ Wang et al. (2020) observed produced calcite particles from broken bonds with grains during waterflood tests.²⁶ Othman et al. (2019) show kaolinite fine with attached carbonate cement produced during the coreflood of sandstone Berea core by super critical CO₂. The appearance of the fine with cement attached is attributed to breakage of the fine-rock cement bond.¹⁰⁶ Wang et al. (2022) exhibited the injection

face of the Indiana limestone core sample with arrows delineated breakage of a grain's structure.¹⁰⁷ Liu et al. (2019) show the images of hairy illite broken after treatment with fracturing fluid.¹⁰ Using SEM images, the above works clearly distinguish between detachment of detrital fines against electrostatic attraction and by breakage of authigenic particles.

The micro-scale numerical models for detachment of authigenic particles by breakage couple flow and stress equations.^{31,32} SEM images, presented in those works, allow defining the channel model geometries, where the boundary conditions on the liquid-solid interfaces are posed and setting the detailed coupled numerical model for flow in porous channels and induced stresses in the rock. The failure zones are calculated from the stress field using various failure criteria, predicting particle detachment at the pore scale. In the current work, the failure criteria are expressed by explicit formula, which is derived from the exact solution for the deformation-stress problem of the particle, submitted to the viscous flow through the porous medium.

The analytical model for stresses, induced by the external load, based on beam theory³³ was used to predict rock failure in sea-cliffs and sandstone canyon cliffs,^{34,35} and between grains consolidated by cement.^{18,36} The present paper uses the beam theory for detachment of individual fine particles attached to the rock surface.

Micro scale modelling of particle detachment by breakage strongly depends on the rheological behaviour of particles bonded with the rock surface, the corresponding breakage criteria, and critical stress conditions. Laboratory pore-scale bending tests for single particles bonded to solid substrate have been performed for kerogen-rich shales, and brittle behaviour has been observed.³⁷ Other tests related to non-mineral-rock

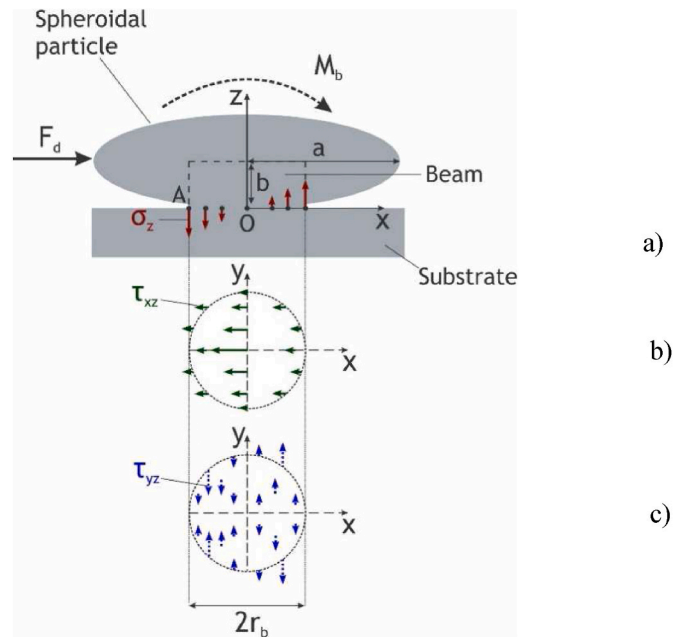


Fig. 2. Schematic of equivalent beam for attached spheroidal particle: a) loading force and moment exerting from viscous flow; b) shear in plane parallel/perpendicular by Timoshenko's solution; c) shear in plane parallel/perpendicular by Timoshenko's solution.

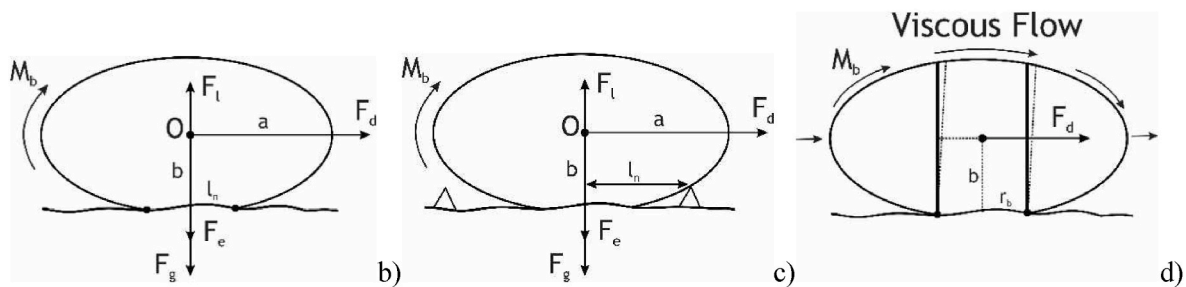
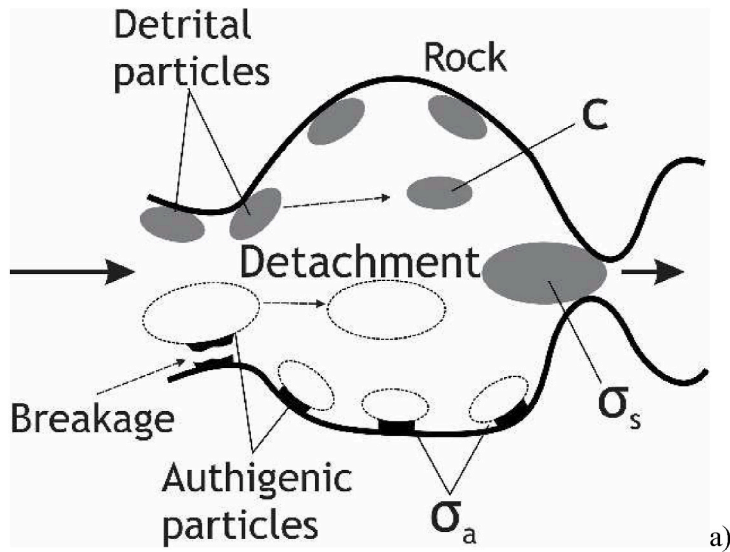


Fig. 1. Detachment of detrital and authigenic clay particles: a) schematic for detachment, migration, and plugging at the pore scale; b) force (torque) balance at attached detrital fine with normal lever arm l_n due to particle deformation; c) lever arm at attached detrital fine due to rock surface asperity; d) representation of attached authigenic particle by deformable beam.¹⁸

materials – polymer-clay,³⁸ glass,³⁹ and silicon^{40–42} – also exhibited brittle behaviour, while the tests with nickel showed ductile behaviour.⁴³ Geo-mechanical tests with partly water-saturated kaolinite powder detect brittle behaviour,^{44–49} while for high saturations of water, the powder becomes ductile.^{44,50,51} Mixing kaolinite soil with more than 1% of cement changes ductile behaviour of the stress-strain diagram into brittle.⁵² Quartz powder and its rich mixtures with kaolinite exhibit brittle behaviour.⁵³ Carbonate powders, and their rich mixtures with quartz in low water saturations show typical brittle stress-strain diagrams.^{53,54} Moreover, sand particles bonded with calcium carbonate powder under tensile and shear tests show shape decline after failure which is an indication of brittle behaviour.⁵⁴

Other laboratory studies also encountered either brittle or ductile failure in reservoir rocks, in particular in kaolinite-rich rocks,^{55,56} illite-rich shales,^{57–59} chlorite-rich black shale rocks,⁶⁰ quartz-rich sandstone,^{61,62} cement mortar rock,⁶³ and coal rocks.^{64–66}

Molecular-dynamic simulation of rheological kaolinite behaviour for hydrated and defected kaolinite crystals with the typical length of 100 Å shows brittle properties under stress loading at the tension case with parallel and perpendicular to layering.^{67–69} Zhang et al. (2021) simulate both tension and compaction loads; tension stress-strain diagrams have brittle type for load parallel and perpendicular to layering, while those for compression are brittle for parallel load and are ductile for perpendicular load.⁷⁰

The above experimental studies highlight the prevalence of mechanical failure of colloidal particles in porous media. The difference in detachment criteria for authigenic and detrital particles is important for understanding and modelling fines migration. However, this distinction hasn't been used in the analysis of coreflooding or field production data. Despite these phenomena being widely spread, a pore-scale mathematical model and its upscaling to the rock scale transport are not available.

The present paper fills the gap. For the first time, this contribution integrates CFD-based modelling of the viscous fluid flowing around an attached particle, 3D elastic beam theory, and strength failure criteria. The integrated theory yields an explicit expression for the detachment conditions for authigenic fines in the form of the breakage velocity. It was found that stress maxima are reached at either the middle or boundary of the beam base. Introduction of tensile-stress and shear-tensile diagrams allows determining which stress causes the particle failure. Formulae for breakage flow velocities have been derived for all cases of particle breakage by different stresses. The expressions for breakage velocity allow determining the maximum retention concentration versus velocity (MRF), which is a mathematical model for fines mobilisation by breakage at the rock (laboratory cores and reservoirs) scale. The laboratory test undertaken comprises coreflooding with 7 rates taken in increasing order while measuring particle breakthrough concentrations and pressure drop across the core. High match between the model and the experimental data from this test, and also from 4 tests taken from the literature, validate the novel mathematical model for particle detachment by breakage.

2. Forces and stresses in the beam

This section integrates Timoshenko's beam theory with creeping viscous flow around attached particles. This includes assumptions of the model (section 2.1), CFD-based expressions for drag and torque for the particles with different geometries (section 2.2), and derivations for tensile and shear stress distributions over the beam base (section 2.3).

2.1. Assumptions of the particle breakage model

The breakage detachment model for a single particle is based on Navier-Stokes equations for viscous flow around the attached particle with resulting drag force and moment exerting on the particle, elastic beam theory,³³ and the rock failure criteria by tensile or shear strength.^{71–73} The main detaching force is drag (Fig. 1b, c). We assume

small deformation for solid mineral particles and negligible effect of particle deformation on the drag force and moment.

Fig. 2 shows 3D cantilever beam for spheroidal particle; the undeformed vertical configuration is exhibited by continuous lines; the end loading by drag displaces material points to the deformed shape shown by dashed curves. The stresses in the particle outside the beam are lower than those inside, which justifies the beam approximation of an irregularly shaped particle for deformation modelling. The assumption that the particle volume around the beam stem has negligible impact on the stress maxima over the particle-substrate contact area has been used by Robinson et al. (1970), Young and Ashford (2008), Obermayer et al. (2013), Wagner et al. (2016), and Chen et al. (2022).^{18,34,35,74,75}

Because drag is applied to the centre of mass of the particle, the beam connects the base to the centre, and the drag acts as an external load on the top cross-section of the beam. We assume that the particle shape is spheroidal, and the contact area is circular. Cylindrical shaped particles are considered too. We also assume homogenous and linear-elastic particle matter.

It is assumed that planar sections perpendicular to the neutral axis before deformations remain planar, but not necessarily perpendicular to the neutral axis after deformation, i.e., shear deformations cannot be ignored. This is particularly important for "short" kaolinite and chlorite clay particles that represent the most widely spread fines in natural reservoirs. Therefore, stress modelling for fines breakage is based on Timoshenko's rather than Bernoulli-Euler beam theory.⁷⁵

The present work assumes that the maximum stress in the particle-substrate contact area due to drag is determined by the deformation of the cylindrical beam with the base equal to the particle-substrate contact area. This assumption was adopted from Obermayer et al. (2013).¹⁸ Therefore, the failure criteria for the attached particle is determined from the cylindrical beam deformation from Timoshenko's solution. The same assumption has already been used by Robinson (1970), and Young and Ashford (2008).^{34,35}

Fig. 1b, c show the spheroidal particle, drag exerting from the moving viscous fluid, and the induced moment. Under slow creeping flows in porous media, lift is negligibly small if compared with the drag. Gravity can also be ignored. Fig. 2a shows the normal stress σ_z versus the horizontal x-coordinate at the beam base $z = 0$. The advancing point of the particle is in extension as a result of the drag, and the receding point is in compression. Fig. 2b and c exhibit the distributions of shear stresses (τ_{xz} and τ_{yz}) over the beam cross section. Stress τ_{xz} is maximum at central point of the base, while stress τ_{yz} is zero at this point. Timoshenko's beam model assumes that normal stress over a cross section is distributed in the same manner as in the case of pure bending. The remaining three stress components i.e. σ_x , σ_y , and τ_{xy} are zero.³³ The expressions for all stresses of the beam theory are presented in Appendix A.

The particle exhibits brittle behaviour with breakage. The breakage occurs instantly according to maximum stress criteria, i.e., if either tensile or shear stress reaches strength (maximum) values.^{71,72}

2.2. Drag force and moment

Consider Couette flow of viscous fluid over a plane substrate and around the attached particle (Fig. 1b, c, 1d). Drag F_d and its moment M_b for spherical, oblate spheroidal, and cylindrical particles are extensions of the Stokes formula, which is valid for spherical particles⁷⁶:

$$F_d = 6\pi\mu_f r_s V f_d(\alpha_s) \quad (1)$$

$$M_b = F_d b f_M(\alpha_s) = 6\pi\mu_f r_s V f_d(\alpha_s) b f_M(\alpha_s) \quad (2)$$

where, μ_f is the fluid viscosity, r_s is the particle effective radius, V is the interstitial fluid velocity, f_d is the shape factor for drag force, b is the lever arm for drag force, and f_M is the moment shape factor. Interstitial fluid velocity V is expressed via Darcy's velocity U as

$$U = \phi V \quad (3)$$

where ϕ is the porosity.

To cover a wide range of minerals forming the migrating fines, we use the particle shapes of spheroids and cylinders with different aspect ratio. Kaolinite particles can be in the form of separate platelets or combined booklets, which we represent as spheroids. Platelets have low aspect ratio, while booklets can have an aspect ratio close to one. For illite particles, the shape of thin long cylinders is assumed.

For a non-spherical particle, the effective radius, r_s is determined based on the equality of the volume of the desired shape and a sphere with radius r_s .

For a cylindrical particle, the effective radius and aspect ratio, α_s are defined as

$$2\pi a_c^2 b_c = \frac{4}{3}\pi r_s^3, r_s = b_c \left(\frac{2}{3}\alpha_s^2\right)^{-1/3}, \alpha_s = b_c/a_c \quad (4)$$

where a_c and b_c are the cylinder base radius and height, respectively.

The effective radius r_s and aspect ratio for a spheroidal particle are defined similarly as:

$$\pi a^2 b = \frac{4}{3}\pi r_s^3, r_s = b\alpha_s^{-2/3}, \alpha_s = b/a \quad (5)$$

where a and b are semi-major and semi-minor axes of spheroid, respectively, and α_s is the aspect ratio.

Following Ting et al. (2021), the details of numerical CFD model and its validation are presented below. We calculate the shape factors for the drag force and moment using CFD package ANSYS/CFX.⁷⁷ Fig. 1a, b, 1c show the schematic for fluid flow around the attached particle. The calculations are performed for long thin cylinders, which approximate

normal component of the pressure drop, and the total moment, M , via an integral of the tangent shear stress over the particle-fluid surface. Deviation of the drag, moment, and lift is 0.28%, 4%, and 0.02% respectively compared to the analytical formulae for a sphere when the Reynolds number is below 0.1. A grid independence test was performed which showed that the mesh size was sufficiently refined. For non-spherical particles, the shape factors for the drag force and moment (f_D and f_M respectively) are calculated using Eqs. (1) and (2).

For long thin cylinders, which correspond to aspect ratio $\alpha_s > 1$, the correlations for drag force and moment factors, based on multiple runs of the CFD package, are:

$$f_d = (0.9014\alpha_s^2 + 1.599\alpha_s + 2.265)(\alpha_s + 1.752)^{-1} \quad (6)$$

$$f_M = (0.0002161\alpha_s^3 + 1.34\alpha_s^2 + 44.18\alpha_s + 21.27)(\alpha_s^2 + 31.34\alpha_s + 10.38)^{-1} \quad (7)$$

respectively. We will be using these correlations further in the text to calculate maximum stresses and predict the particle-substrate bond breakage. The expressions for drag and moment factors for spheroidal and thin-cylinder particles, which model kaolinite, chlorite, and silica particles, are available from Ting et al. (2021).⁷⁷

2.3. Stress distributions at the base of the beam

Substitution of beam stress equations (A1-A3) into the expressions for principal stresses (A5), yields the equations for maximum tensile and shear stresses at the beam base:

$$\sigma_3 = \frac{1}{2} \frac{F_d r_b^2}{I} \left(\frac{bf_M}{r_b} \frac{x}{r_b} - \sqrt{\left(\frac{bf_M}{r_b}\right)^2 \left(\frac{x}{r_b}\right)^2 + 4 \left(\left(\frac{(3+2v)}{8(1+v)} \left(1 - \left(\frac{x}{r_b}\right)^2 - \frac{(1-2v)}{(3+2v)} \left(\frac{y}{r_b}\right)^2 \right) \right)^2 + \left(-\frac{(1+2v)}{4(1+v)} \frac{x}{r_b} \frac{y}{r_b} \right)^2 } \right) \quad (8)$$

$$\frac{\sigma_1 - \sigma_3}{2} = \frac{1}{2} \frac{F_d r_b^2}{I} \left(\sqrt{\left(\frac{bf_M}{r_b}\right)^2 \left(\frac{x}{r_b}\right)^2 + 4 \left(\left(\frac{(3+2v)}{8(1+v)} \left(1 - \left(\frac{x}{r_b}\right)^2 - \frac{(1-2v)}{(3+2v)} \left(\frac{y}{r_b}\right)^2 \right) \right)^2 + \left(-\frac{(1+2v)}{4(1+v)} \frac{x}{r_b} \frac{y}{r_b} \right)^2 } \right) \quad (9)$$

illite clay particles. The fluid is assumed to be incompressible and Newtonian, and both the particle and substrate are assumed to be non-deformable. The flow regime is assumed to be laminar, and the corresponding solver is used.

A rectangular simulation domain is established with dimensions $72r_s \times 24r_s \times 24r_s$ (length \times width \times height). The boundary conditions at the liquid-particle and liquid-substrate for the Navier-Stokes equations correspond to the no-slip condition. With a zero-velocity condition set on the bottom surface, Couette flow is modelled with a linear shear by setting the velocity at the top surface to 0.05 m/s. In order to accurately capture the flow field near the particle, the mesh adjacent to the particle was refined. Symmetry boundary conditions were applied at the two vertical sides of the domain.

Based on the numerical solution of the 3D flow problem we can calculate the total drag acting on the particle, F_d , via an integral of the

Axes are shown in Fig. 2. Bond radius r_b is shown in Figs. 1 and 2.

Eqs. (8) and (9) for normalised stresses can be transformed into the following dimensionless form

$$\frac{\sigma_3}{T_0} = \frac{1}{\kappa} \left(X - \sqrt{X^2 + \chi \left(1 - X^2 - \frac{(1-2v)}{(3+2v)} Y^2 \right)^2} + \chi \frac{4(1+2v)^2}{(3+2v)^2} (XY)^2 \right) \quad (10)$$

$$\frac{\sigma_1 - \sigma_3}{2S_0} = \frac{\eta}{\kappa} \sqrt{X^2 + \chi \left(1 - X^2 - \frac{(1-2v)}{(3+2v)} Y^2 \right)^2} + \chi \frac{4(1+2v)^2}{(3+2v)^2} (XY)^2 \quad (11)$$

where T_0 and S_0 are the tensile and shear strengths, respectively. Normalised stress expressions (10, 11) contain three dimensionless groups

reflecting the interaction between the creeping flow around an attached particle and the induced elastic deformation of the particle – dimensionless numbers κ , χ , and η :

$$\kappa = \frac{2T_0}{F_d} \frac{I}{r_b b f_M} = \frac{2T_0}{F_d} \frac{I}{\delta \alpha_s f_M}, \chi = \left[\frac{r_b}{b f_M} \frac{3+2\nu}{4(1+\nu)} \right]^2 = \left[\frac{\delta}{\alpha_s f_M} \frac{3+2\nu}{4(1+\nu)} \right]^2, \eta = \frac{T_0}{S_0}, \delta = \frac{r_b}{a}, X = \frac{x}{r_b}, Y = \frac{y}{r_b} \quad (12)$$

Dimensionless group κ is proportional to the ratio between tensile strength and fluid pressure caused by the drag exerting on the particle cross section and is called the *strength-drag number*. Dimensionless number κ also depends on bond ratio δ , aspect ratio α_s , and moment of inertia I . Dimensionless group χ depends on geometric parameters, namely the bond ratio δ and aspect ratio α_s , and on the Poisson ratio ν and is called, therefore, the *shape-Poisson number*. The *strength number* η is the ratio between tensile and shear strengths.

Common interval of parameters for rock minerals are⁸³: aspect ratio α_s varies from 0.03 to 1.0 for spheroids and flat cylinders and from 1 to 100 for long cylinders, bond ratio δ - from 10^{-3} to 1.0, and Poisson's ratio ν - from zero to 0.5. Eq. (12) along with formulae for drag and moment shape factors results in values of the shape-Poisson number χ varying from 2.4×10^{-7} to 4.8 for spheroids, from 2.4×10^{-5} to 0.3 for long cylinders, and from 0.18 to 135 for flat cylinders.

3. Stress maxima and breakage regime

Here we create a graphical technique to determine the stress that meets the strength failure criteria. It includes the derivation of stress maxima at the beam base (section 3.1), calculation of tensile stress maxima over the beam base middle and boundary (section 3.2) and their comparison using the tensile stress diagram (section 3.3), calculation of shear stress maxima over the beam base middle and boundary (section 3.4) definition of the failing stress using the tensile-shear diagram (section 3.5).

The failure criteria used in this work correspond to reaching the strength values by maximum tensile and shear stresses.^{71,73} The corresponding expressions for tensile and shear failures are (Eq. (A8)):

$$-\sigma_3 \geq T_0, \frac{-\sigma_3}{T_0} \geq 1 \quad (13)$$

$$\frac{\sigma_1 - \sigma_3}{2} \geq S_0, \frac{\sigma_1 - \sigma_3}{2S_0} \geq 1, \quad (14)$$

respectively. Here T_0 is the tensile strength, and S_0 is the shear strength.

To determine which stress causes failure, the following maxima must be compared

$$\max_{x^2+y^2 \leq 1} \frac{-\sigma_3(X, Y)}{T_0}, \max_{x^2+y^2 \leq 1} \frac{\sigma_1(X, Y) - \sigma_3(X, Y)}{2S_0} \quad (15)$$

To apply failure criteria (13,14) to the expressions for normalised tensile and shear stresses at the base of the beam, in the next section we calculate the maxima of those stress functions over the area $X^2+Y^2 \leq 1$.

3.1. Stress maxima at the base of the beam

Consider maxima of the tensile and shear stresses given by Eqs. (10, 11). If the maxima points (X_m, Y_m) are located inside the base circle, $X_m^2+Y_m^2 < 1$, partial derivatives of both expressions (10) and (11) over Y must be zero. Both expressions depend on Y^2 , so the expressions for first partial derivatives in Y contain Y as a multiplier and is zero at $Y = 0$. It is possible to show that the multiplier inside the unitary circle is positive,

and that second partial derivatives in Y of both expressions (10) and (11) are negative at $Y = 0$. Therefore, all maxima inside the base circle $X_m^2+Y_m^2 < 1$ are reached along the middle of the base, i.e., axis $Y = 0$.

Otherwise, tensile or shear stresses reaches maxima at the beam base over the boundary $X_m^2+Y_m^2 = 1$.

Expressions for normalised tensile and shear stresses versus X in the beam middle $Y = 0$ are obtained from Eqs. (10, 11):

$$\frac{\sigma_3}{T_0} = T^0(X, \chi) = \frac{1}{\kappa} \left(X - \sqrt{X^2 + \chi(1 - X^2)^2} \right) \quad (16)$$

$$\frac{\sigma_1 - \sigma_3}{2S_0} = S^0(X, \chi) = \frac{\eta}{\kappa} \sqrt{X^2 + \chi(1 - X^2)^2} \quad (17)$$

Expressions for normalised tensile and shear stresses versus X at the cylinder boundary are obtained from Eqs. (10, 11) by substituting $Y^2 = 1 - X^2$:

$$\frac{\sigma_3}{T_0} = T^1(X, \chi, \nu) = \frac{1}{\kappa} \left(X - \sqrt{X^2 + \chi \frac{4(1+2\nu)^2}{(3+2\nu)^2} (1 - X^2)} \right) \quad (18)$$

$$\frac{\sigma_1 - \sigma_3}{2S_0} = S^1(X, \chi, \nu) = \frac{\eta}{\kappa} \sqrt{X^2 + \chi \frac{4(1+2\nu)^2}{(3+2\nu)^2} (1 - X^2)} \quad (19)$$

3.2. Maxima of tensile stresses in the beam middle and boundary

In order to apply failure criteria (13, 14) to expressions for normalised tensile and shear stresses at the cylinder middle and at boundary, let us calculate maxima of the four stress functions (16-19) over the closed X -interval $[-1, 1]$. Fortunately, for all 4 cases, the maximum points X_m and the corresponding values of normalised stresses can be found explicitly. In the middle of the base, maxima of the two functions (16) and (17) inside the base circle $(-1, 1)$ are determined by conditions of zero first derivative in X at some point $X = X_m$, and negative second derivative in the same point. Then the obtained maxima are compared with stresses at the boundary $X = -1$ and $X = 1$. The same procedure is applied for stress functions (18, 19) on the beam base boundary. Afterward, the detachment regime and the detachment point X_m are determined by comparison of the 4 normalised tensile and shear stresses at the boundaries $X = -1$ and $X = 1$, and the open interval between them.

From now on, we call dimensionless stress the product of strength-drag number κ and normalised stress, defined in Eqs. (16-19).

The profiles for dimensionless tensile stress $\kappa T_m^0(X)$ in the middle of the cylinder base for four values of the shape-Poisson number $\chi = 1, 2, \chi = \chi_1$, and $\chi = 4.5$ are presented in Fig. 3a. Here $\chi = \chi_1$ is the value where κT_m^0 at the boundary $X = -1$ is equal to maximum inside the interval. As χ tends to zero, the plot of $\kappa T_m^0(X)$ tends to two straight lines corresponding to two values of square root in expressions (34, 35). At some χ there does appear a maximum inside the open interval $(-1, 1)$, which remains below $\kappa T_m^0(-1, \chi) = 2$, reached in the advanced point $X_m = -1$. Inequality $\kappa T_m^0 < 2$ remains fulfilled for $\chi < \chi_1$. The threshold value χ_1 and corresponding maximum point $X = X_m$ are determined from system of two transcendental equations and one inequality:

$$\kappa T^0(X_m, \chi_1) = 2, \frac{\partial \kappa T^0}{\partial X}(X_m, \chi_1) = 0, \frac{\partial^2 \kappa T^0}{\partial X^2}(X_m, \chi_1) < 0 \quad (20)$$

The solution of Eq. (20) is unique; the roots are found numerically:

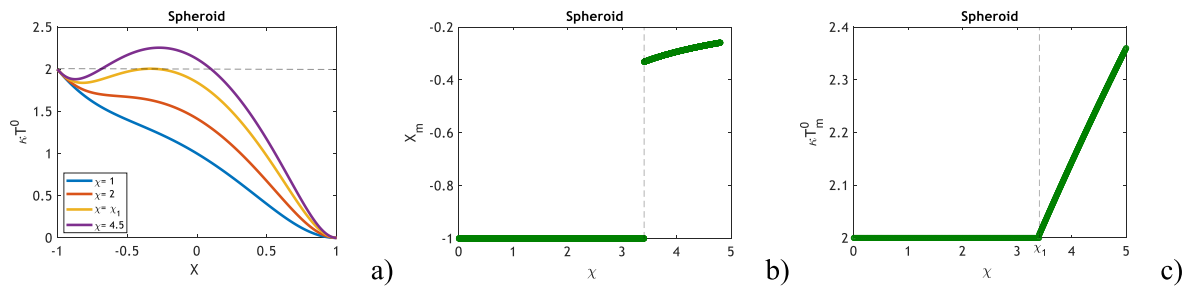


Fig. 3. Maximum tensile stress in the middle of the beam at $Y = 0$: a) dimensionless tensile stress along flow direction (versus X) for 3 different values of shape-Poisson number χ ; b) position of maximum tensile stress X_m at $Y = 0$ versus shape-Poisson number χ ; c) maximum value of tensile stress at $Y = 0$ versus χ

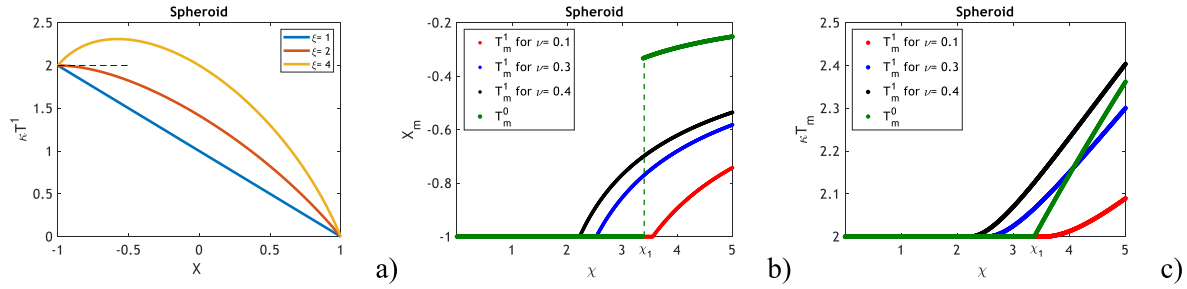


Fig. 4. Maximum tensile stress at beam boundary: a) dimensionless tensile stress on the beam boundary versus shape-Poisson number χ for 3 different values of Poisson ratio ν (or parameter ξ); b) position of maximum tensile stress X_m at the beam boundary versus χ ; c) maximum value of tensile stress over the boundary versus χ

$\chi_{l1} = 3.38, X_{m1} = -0.33$.

For $\chi > \chi_{l1}$, the maximum is reached inside the open interval $-1 < X_m < 1$ (violet curve in Fig. 3a). The expression for maximum normalised tensile stress at $Y = 0$ is

$$T_m^0(\chi) = \frac{1}{\kappa} \begin{cases} 2, & \chi \leq \chi_{l1} \\ -X_m(\chi) + \sqrt{X_m^2 + \chi(1 - X_m^2)^2}, & \chi > \chi_{l1} \end{cases}; \quad X_m = \begin{cases} -1, & \chi \leq \chi_{l1} \\ -\sqrt{\frac{\sqrt{(4\chi - 1)(4\chi - 9)} - 4\chi + 3}{8\chi}}, & \chi > \chi_{l1} \end{cases} \quad (21)$$

Substituting X_m into $T_m^0(\chi)$ in Eq. (21), we obtain

$$T_m^0(\chi) = \frac{1}{\kappa} \begin{cases} 2, & \chi \leq \chi_{l1} \\ \sqrt{\frac{\sqrt{(4\chi - 1)(4\chi - 9)} - 4\chi + 3}{8\chi}} + \sqrt{\frac{\sqrt{(4\chi - 1)(4\chi - 9)} - 4\chi + 3}{8\chi} + \chi \left(1 + \frac{\sqrt{(4\chi - 1)(4\chi - 9)} - 4\chi + 3}{8\chi} \right)^2}, & \chi > \chi_{l1} \end{cases} \quad (22)$$

Fig. 3b and c show the plot of maximum point X_m and maximum tensile stress in the middle $T_m^0(\chi)$ versus the shape-Poisson number. For χ lower than χ_{l1} , the maximum is reached in the advance point $X_m = -1$. For higher χ -values, the point X_m jumps to X_{m1} and then continuously moves to the right towards the origin.

Eq. (34) for dimensionless tensile strength on the base boundary shows that T_m^l depends on the dimensionless group ξ which is proportional to χ . The proportionality coefficient depends on Poisson ratio:

$$\xi = \chi \frac{4(1 + 2\nu)^2}{(3 + 2\nu)^2} \quad (23)$$

Fig. 4a shows the profiles for dimensionless tensile stress on the beam boundary for different values of ξ . At $\xi < 2$, $\kappa T_m^l(X, \chi)$ monotonically decreases versus X , so the maximum is reached at the point $X_m = -1$. At $\xi = 2$, the slope of profile at $X = -1$ reaches zero, and at $\xi > 2$ a maximum is reached inside the interval at $X > -1$. The expressions for maximum $T_m^l(\xi)$ and X_m are

$$T_m^l(\chi, \nu) = \frac{1}{\kappa} \begin{cases} 2, & \xi \leq 2 \\ \xi(\xi - 1)^{-0.5}, & \xi > 2 \end{cases}; \quad X_m = \begin{cases} -1, & \xi \leq 2 \\ -(\xi - 1)^{-0.5}, & \xi > 2 \end{cases} \quad (24)$$

Fig. 4b and c show the plots for maximum point and value vs χ at three Poisson ratios. For low χ , determined by condition $\xi < 2$, the maximum is reached at the advance point $X = -1$ and is equal to 2. For higher χ , the maximum point continuously moves right from the

advance point, and the maximum value monotonically increases from 2.

3.3. Comparison of maximum tensile stresses in the beam middle and boundary

Consider the stress equality, separating the domains in (χ, ν) plane where either of the stresses dominate

$$T_m^0(\chi) = T_m^l(\chi, \nu) \quad (25)$$

The black curve in Fig. 5a corresponds to $\xi = 2$; the equation for the black curve follows from the expression (23):

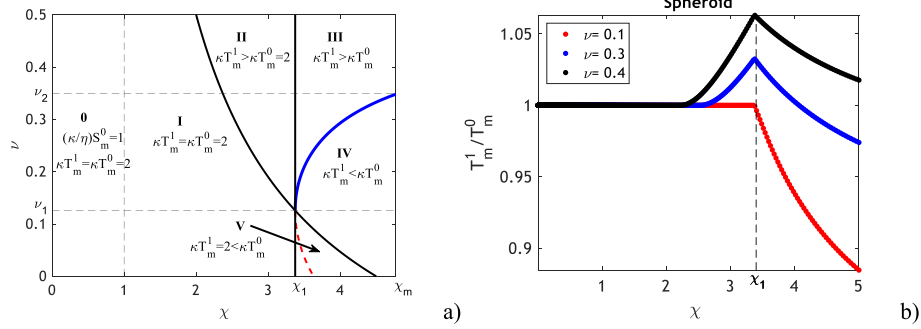


Fig. 5. Comparison between dimensionless tensile stresses in the middle and on the beam boundary: a) determination of the critical Poisson ratios ν where the tensile stresses are equal; b) the ratio between tensile stresses on the boundary and in the middle for three Poisson ratios ν

$$\chi = \frac{(3 + 2\nu)^2}{2(1 + 2\nu)^2}, \nu = \left(1 - \sqrt{\frac{\xi}{4\chi}}\right)^{-1} - \frac{3}{2}. \quad (26)$$

The straight line $\chi = \chi_1$ and curve (26) for $\xi = 2$ separate plane (χ, ν) into 4 domains that correspond to different expressions (22) and (24) for maximum tensile stresses (Fig. 5a). Three lines cross in point with $\chi = \chi_1$ and $\nu = \nu_1 = 0.125$.

Here the variables are limited by maximum χ -values for natural minerals: $\chi < 5$.

Altogether 5 different domains that defines maxima between T_m^0 and T_m^1 can be distinguished:

- I. In the case $\chi < \chi_1$ and $\xi < 2$, both tensile stresses are equal to 2.
- II. In domain $\chi < \chi_1$ and $\xi > 2$, $T_m^0 = 2$. Equation (25) for the boundary between regions I and II becomes: $T_m^1(\chi, \nu) = 2$.

This equation has only one root: $\xi = 2$. For $\xi > 2$, T_m^1 monotonically increases. Therefore, in this domain $T_m^1 > T_m^0$.

Consider the case where $\chi > \chi_1$ and $\xi > 2$. In this region, both κT_m^0 and κT_m^1 are greater than 2. The region can be divided into two regions in which each stress is greater. Substituting the second line of Eq. (24) into equality (25) and expressing ξ yields

$$\xi = \frac{(\kappa T_m^0(\chi))^2 \pm \kappa T_m^0(\chi) \sqrt{(\kappa T_m^0(\chi))^2 - 4}}{2}; \chi > \chi_1 \quad (27)$$

Critical Poisson's ratios where the tensile stresses in the middle and on the boundary are equal are determined by substitution of expression (23) for ξ into Eq. (27) and solving for ν :

$$\nu_m(\chi) = \frac{3\sqrt{(\kappa T_m^0(\chi))^2 \pm \kappa T_m^0(\chi) \sqrt{(\kappa T_m^0(\chi))^2 - 4}} - \sqrt{8\chi}}{4\sqrt{2\chi} - 2\sqrt{(\kappa T_m^0(\chi))^2 \pm \kappa T_m^0(\chi) \sqrt{(\kappa T_m^0(\chi))^2 - 4}}} \quad (28)$$

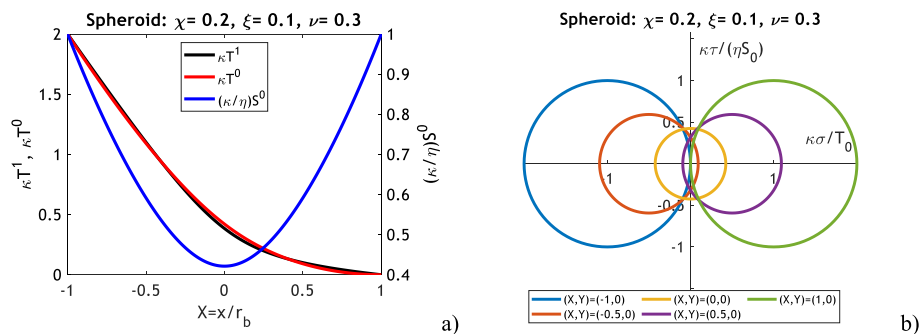


Fig. 6. Comparison between tensile and shear stresses and their maxima: a) profiles of tensile and shear stresses along the beam middle and the tensile stress over the beam boundary; b) Mohr circles in five points of the beam middle.

Explicit expression $\nu = \nu_m(\chi)$ is determined by equating the second lines of Eqs. (22) and (24) and is very cumbersome.

Fig. 5a shows the plot $\nu = \nu_m(\chi)$. It consists of two branches – the blue branch corresponds to the positive square root in Eq. (28), and the red branch to the negative root. Over the red branch, we have $\xi < 2$, so only the blue branch belongs to the domain $\chi > \chi_1$ and $\xi > 2$. This determines zones III and IV:

- III. In the case where $\chi > \chi_1$ and $\nu > \nu_m(\chi)$, $T_m^1 > T_m^0$.
- IV. In the case where $\chi > \chi_1$ and $\nu < \nu_m(\chi)$, $\xi > 2$, $T_m^1 < T_m^0$.

The blue curve (28) crosses the line $\chi = \chi_1$ at the point with ordinate ν_1 .

- V. In the case $\chi > \chi_1$ and $\xi < 2$, $T_m^1 = 2$. As it follows from definition (20) of χ_1 , equation $T_m^0(\chi) = 2$ has root $\chi = \chi_1$. No more roots exist for $\chi > \chi_1$. Therefore, in this domain $T_m^0 > T_m^1 = 2$.

Five domains I, II, ... V in the so-called tensile stress diagram (Fig. 5a) determine where maximum tensile stress is higher –at the boundary of the beam base or in the middle. Their ratio versus shape-Poisson number is presented in Fig. 5b for three value of Poisson ratio: $\nu < \nu_1$, $\nu_1 < \nu < \nu_2$, and $\nu > \nu_2$.

Let us compare the tensile and shear stresses and their maxima in zone 0 using Mohr circles. Fig. 6a shows profiles for dimensionless tensile and shear stresses, calculated by Eqs. (16-18). Fig. 6b shows Mohr circles that correspond to zone 0 and five points in the middle $(X, 0)$ where the value of X changes from -1 to 1 . Mohr circles are built based on Eqs. (A7, 8). The profiles for dimensionless tensile stresses monotonically decrease from 2 at $X = -1$ to zero at $X = 1$. This corresponds to change of position of maximum tensile stress in Fig. 8b, which corresponds to left edge point of circles $(-\sigma_3, 0)$ from -2 to zero. Maximum shear stress that is equal to circle radius, decreases from 1 to min at $X = 0$ and then increases back to one (Fig. 6a). This corresponds

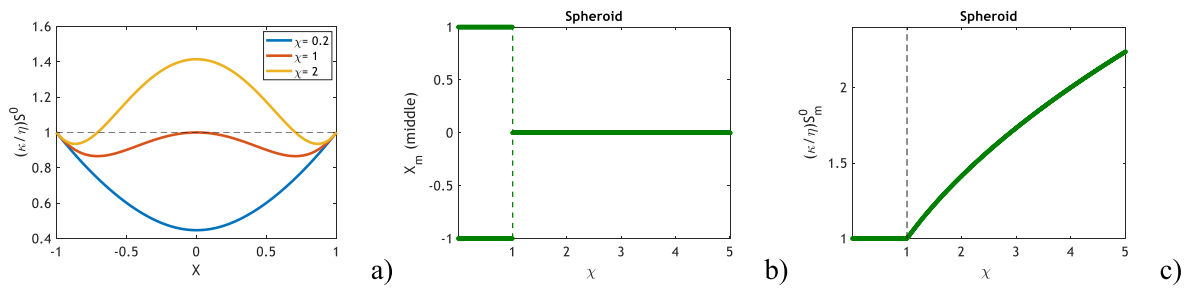


Fig. 7. Dimensionless maximum shear stress in the middle of the beam base: a) profiles for dimensionless stress in the middle of the beam base for three different shape-Poisson ratios versus X ; b) position of the maximum point X_m versus X ; c) maximum dimensionless stress versus χ

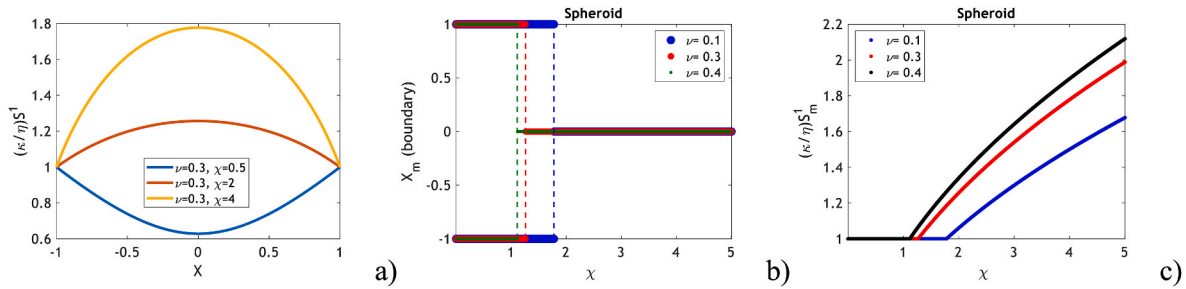


Fig. 8. Dimensionless maximum shear stress on the beam boundary: a) profiles for dimensionless stress for different Poisson ratio ν and shape-Poisson number χ ; b) position of the maximum point X_m versus χ ; c) maximum dimensionless stress versus χ

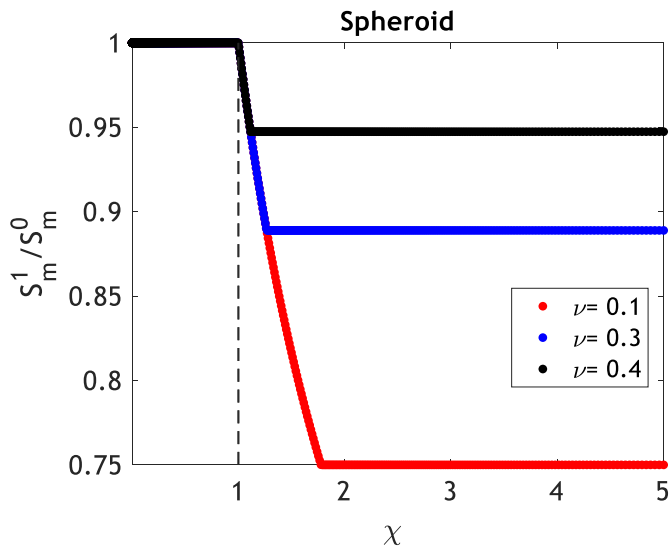


Fig. 9. Comparison between maximum shear stresses in the middle, S_m^1 , and on the boundary, S_m^0 .

to movement of the top point of circles from maximum at $X = -1$ to min at $X = 0$ and then to max in the receded point. Abscissa of the circle centre is obtained from Eq. (A7) and is proportional to σ_z , which in turn is proportional to x (Eq. (A1)). This corresponds to movement of the circle centre from -1 at advanced point to zero at the base beam centre and to one in receded point.

3.4. Maxima shear stresses in the beam middle and boundary

Fig. 7a shows profiles for shear stress in the middle of the beam base for different χ . For χ tending to zero, the profile tends to two straight lines. At higher χ , there does appear a maximum at $X_m = 0$, which reaches unitary value at $\chi = \chi_2 = 1$. At $\chi < \chi_2$, the maximum remains in

the advancing and receding points, for $\chi > \chi_2$ it moves to the origin. Expressions for stress maximum are obtained from Eq. (17):

$$S_m^0(\chi) = \frac{\eta}{\kappa} \begin{cases} 1, & \chi < 1 \\ \sqrt{\chi}, & \chi > 1 \end{cases}; \quad X_m = \begin{cases} \pm 1, & \chi < 1 \\ 0, & \chi > 1 \end{cases}; \quad \eta = \frac{T_0}{S_0} \quad (29)$$

Fig. 7b shows that the maximum points lie at the edges of the beam middle at $X_m = -1$ and $X_m = 1$ for $\chi < \chi_2$, then moves to the centre point, $X = 0$ for $\chi > \chi_2$. The maximum shear is equal to one for $\chi < \chi_2 = 1$, and monotonically increases from 1 for $\chi > \chi_2$ (Fig. 7c).

The expression for maximum tensile stress along the boundary is obtained from Eq. (19):

$$S_m^1(\chi_1) = \frac{\eta}{\kappa} \begin{cases} \sqrt{\xi}, & \xi \geq 1 \\ 1, & \xi < 1 \end{cases}; \quad X_m = \begin{cases} 0, & \xi \geq 1 \\ \pm 1, & \xi < 1 \end{cases} \quad (30)$$

Corresponding profiles and maximum plots and presented in Fig. 8.

Fig. 9 shows the ratio S_m^1/S_m^0 versus χ for 3 values of Poisson ratio. For all parameter values, the ratio does not exceed one, i.e. $S_m^1 < S_m^0$. Therefore, further in determining the breakage regime, shear at the base boundary is not considered. In particular, shear at the base boundary hasn't been considered in Fig. 6.

Introduce region 0 in (χ, ν) -plane for $\chi < 1$ (tensile-stress diagram in Fig. 5a). According to Eq. (29), here the dimensionless shear is equal to one, while both tensile stress maxima are equal to two.

3.5. Determination of breakage regime using the breakage function

This section compares maxima of tensile and shear stresses, Eqs. (22, 24, 29). The tensile-stress diagram in Fig. 10a shows which maximum tensile stress – in the beam middle or at the boundary – is higher. Shear stress in the middle is always higher than that at the boundary. Now consider breakage by tensile stress, where equality (13) is fulfilled at some point $(X_m, 0)$ and normalised tensile stress reaches its maximum which equals one, while equality (14) is not fulfilled for any point $-1 < X < 1$. Consequently, the condition for breakage by tensile stress is

$$\frac{\max(-\sigma_3)}{T_0} \geq \frac{\max(\sigma_1 - \sigma_3)}{2S_0} \quad (31)$$

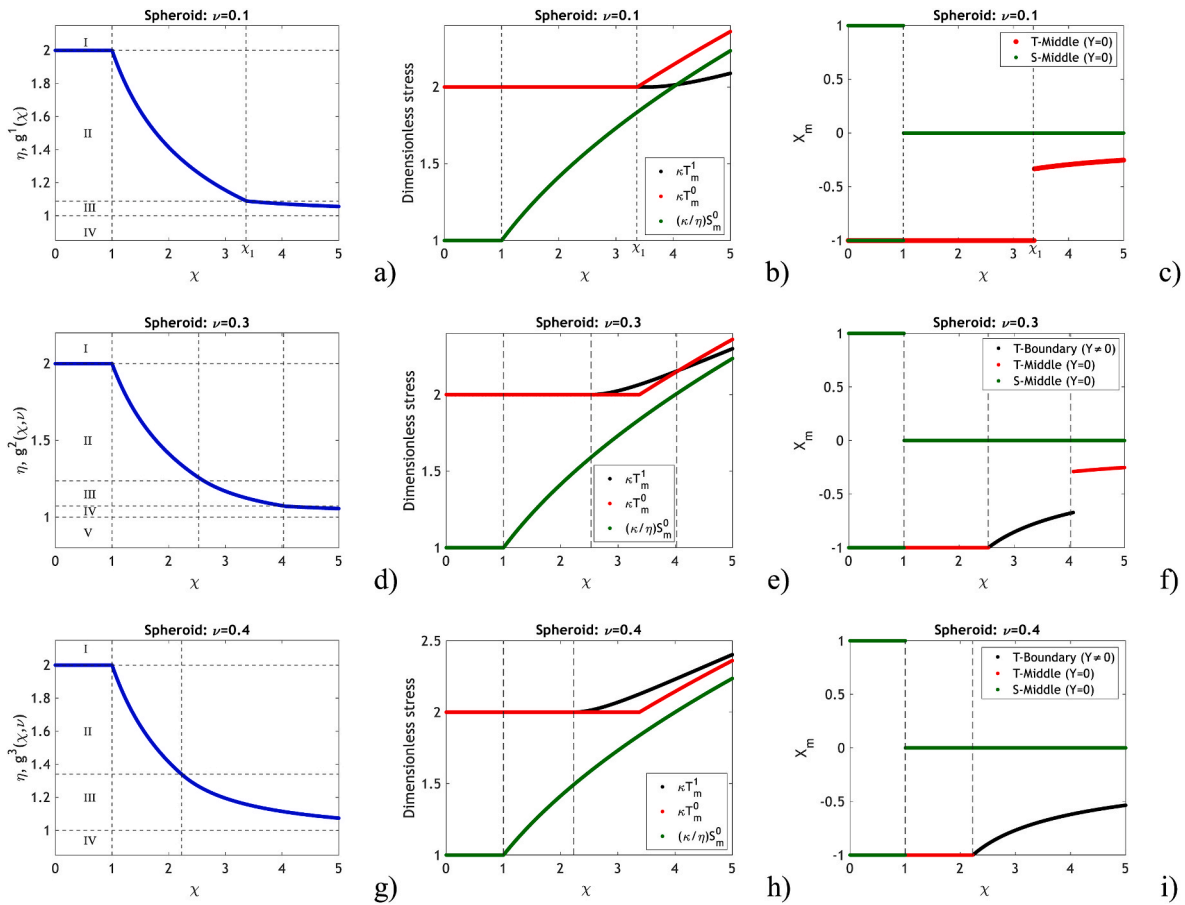


Fig. 10. Breakage regime function $g(\chi)$ for different Poisson ratios ν : a,b,c) $v < v_1$; d,e,f) $v_1 < v < v_2$; g,h,i) $v_2 < v < 0.5$.

Define the breakage regime function, $g(\chi, \nu)$ as the ratio of the dimensionless tensile stress to the dimensionless shear stress. Comparing with Eq. (31), we arrive at:

$$g(\chi, \nu) = \frac{\kappa T_m(\chi, \nu)}{\left(\frac{\kappa}{\eta}\right) S_m^0(\chi)} = \frac{T_m(\chi, \nu)}{S_m^0(\chi)} \eta > \frac{T_0}{S_0} = \eta \quad (32)$$

$$T_m(\chi, \nu) = \max\{T_m^0(\chi), T_m^1(\chi, \nu)\} \quad (33)$$

Here $T_m(\chi, \nu)$ is maximum of two normalised tensile stresses $T_m^0(\chi)$ and $T_m^1(\chi, \nu)$; $S_m^0(\chi)$ is the maximum of the dimensionless shear stress in the middle of the beam. We introduce the breakage regime function $g(\chi, \nu)$, which is the ratio of the stress maxima $T_m(\chi, \nu)$ and $S_m^0(\chi)$. If a state point in plane (χ, η) is located above the curve $g(\chi, \nu)$, the breakage occurs by tensile stress; otherwise it is shear stress that causes the breakage.

To further clarify the meaning of this equality, consider a system at the point of shear failure, i.e. $S_m^0 = S_0$. If $g(\chi, \nu) < \eta$, then it follows that $T_m < 1$. Thus, at the point of shear failure, the tensile stress does not exceed the tensile strength and tensile failure is not expected. Thus, in the situation of a gradually increasing load, shear failure will occur before tensile failure. Similarly, if $g(\chi, \nu) > \eta$, then $T_m > 1$ (for $S_m^0 = 1$) and thus at the onset of shear failure, the condition for tensile failure is already satisfied and therefore the particle will first experience tensile failure.

The tensile-stress diagram shows that as χ changes from zero to χ_m , different sequences of domains appear in three intervals of Poisson's ratio: $[0, v_1]$, $[v_1, v_2]$, and $[v_2, 0.5]$ (Fig. 5a). A graph of the breakage function $g(\chi)$ is presented in Fig. 10a, d, and g in those three intervals, respectively. Sharp transitions in the behaviour of the function are observed when different boundaries in the tensile-stress diagram are

reached. Fig. 10b, e, and h show the plots of the numerator and denominator of expression (32) of $g(\chi, \nu)$ for three values of Poisson's ratio ν , taken from the three above-mentioned intervals, by red, black, and green curves, respectively. Points X_m where breakage occurs, are shown in Fig. 10c, f, and i.

The graph of function $g(\chi, \nu)$ allows determining whether breakage occurs by tensile or shear stress. Thus, $g(\chi, \nu)$ is called the breakage regime function, and plane (χ, ν) with different domains – the tensile-shear diagram (Fig. 10a, d, and g).

For values of χ less than 1, the curve $g(\chi, \nu)$ is equal to two (Fig. 10a, d, and g), and both the tensile and shear stresses are constant (Fig. 10b, e, and h). Breakage occurs in the advancing point, $X_m = -1$ (Fig. 10c, f, and i). As χ increases, a decrease in $g(\chi, \nu)$ is observed, defined by a constant tensile stress, but increasing shear stress. Shear failure for values of $\chi > 1$ occurs in the particle centre, $X_m = 0$. Further increases to the shape-Poisson number, χ , result in an increasing tensile stress, leading to a less sharply decreasing breakage regime function. This transition occurs for only one of the two tensile stresses, while the other begins increasing at higher χ . For intermediate Poisson's ratio ($v_1 < v < v_2$), tensile failure occurs first on the boundary, then at higher χ it occurs in the middle of the particle (Fig. 10e). In all cases, increasing tensile stress results in tensile failure occurring at an intermediate point in the advancing half of the particle ($-1 < X_m < 0$, see Fig. 10e, f, and i).

The value of the shape-Poisson number χ that corresponds to a given strength ratio η

$$\chi_{cr} = g^{-1}(\eta), g(\chi_{cr}) = \eta \quad (34)$$

is called the critical value.

For a given value of the strength ratio, η , let us discuss the determination of the failure type. In the case where the strength ratio exceeds

2 (region I in Fig. 10a, d, and g), $\eta > 2$, the breakage is by shear for all values of the shape-Poisson number χ . Similarly, if the strength ratio is less than one, $0 < \eta < 1$ (region IV, Fig. 10a, g, or region V for $\nu_1 < \nu < \nu_2$, Fig. 10d), the breakage is by tensile failure for all values of the shape-Poisson number χ . For values of η between 1 and 2 (regions II-III, Fig. 10a, d, and g, and region IV for $\nu_1 < \nu < \nu_2$, Fig. 10d), breakage will occur by tensile failure for values of χ less than the critical value, χ_{cr} , and by shear failure for values larger than it.

4. Detachment of detrital fines against electrostatic forces

Following Derjaguin and Landau (1941), Verwey and Overbeek (1948), Israelachvili (2015), Bradford et al. (2013), this section briefly presents the fines detachment theory for detrital fines.^{13,21,78,79}

Detrital fines have been brought to the rock by groundwater flows after being broken-off the rock surface and attached to the rock surface by electrostatic forces. Fig. 1b, c show the forces exerting on an attached detrital particle: attaching electrostatic F_e and gravity F_g forces, and detaching drag F_d and lift F_l forces. Electrostatic is a potential force, where the energy potential E depends on the particle-surface separation distance, h :

$$F_e(h) = -\frac{\partial E(h)}{\partial h} \quad (35)$$

An energy profile with only a single minimum has an inflection point

$h = h_m$, where the electrostatic force reaches its maximum:

$$\frac{\partial F_e(h_m)}{\partial h} = -\frac{\partial^2 E(h_m)}{\partial h^2} = 0, \quad \frac{\partial^2 F_e(h_m)}{\partial h^2} = -\frac{\partial^3 E(h_m)}{\partial h^3} < 0 \quad (36)$$

Mechanical equilibrium of a particle on the rock surface in the case of favourable attachment (one primary energy minimum) is determined by the following conditions: equality of detaching and attaching torques

$$M_b = 6\pi\mu_f r_s V f_d(\alpha_s) b f_M(\alpha_s) = F_e(h) l_n, \quad (37)$$

equality of detaching and attaching force projections on horizontal

$$F_d = 6\pi\mu_f r_s V f_d(\alpha_s) = \nu_C F_e(h), \quad (38)$$

and equality of detaching and attaching force projections on vertical

$$F_l(U) = F_e(h) + F_g \quad (39)$$

where l_d and l_n are the lever arms for drag and normal forces, respectively, and ν_C is the Coulomb friction coefficient. Particle detachment occurs when the left hand side of (37), (38), or (39) exceeds the right hand side when $h = h_m$ (at the maximum electrostatic force). When these terms are insufficient to detach the particle, they are equilibrated by a smaller electrostatic force, and the particle sits at some distance $h < h_m$. Breach of either equilibrium conditions (37), (38), or (39) yields fines detachment by rolling, sliding, and lifting, respectively. In the case of two energy minima, there are two separating distances $h = h_m$ that

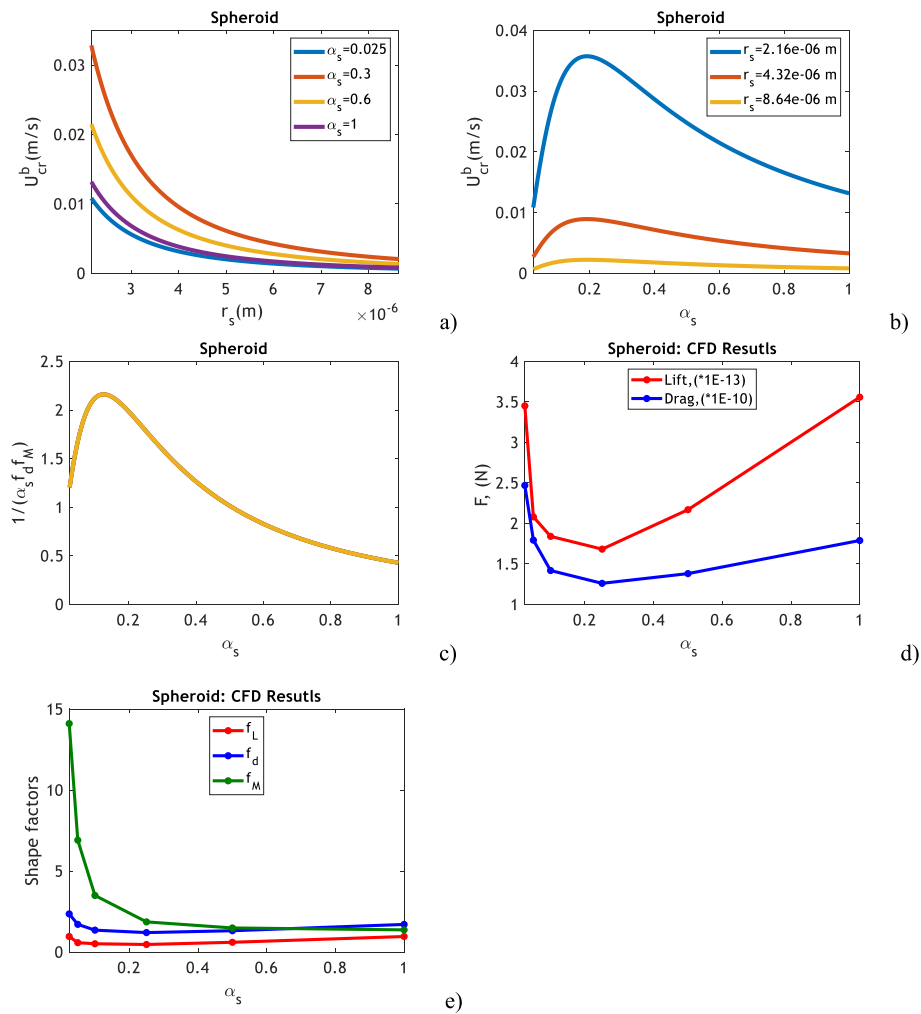


Fig. 11. Critical breakage velocity of oblate spheroids: a) Dependence of critical breakage velocity on particle radius; b) Dependence of critical breakage velocity on particle aspect ratio α_s ; c) aspect-ratio dependency for the product of shape factors and aspect ratio; d) aspect-ratio dependency for drag and lift; e) aspect-ratio dependencies for three shape factors.

correspond to both energy minima, and the equilibrium conditions (37), (38), and (39) are applicable to the particles that are located in primary and secondary energy minima. It is implicitly assumed that the particles detached by the three criteria (37), (38), and (39) continue rolling over the rock surface, sliding over the surface, and move off the surface into the liquid stream, respectively.

Under dominance of electrostatic force in Eq. (39), lifting does not occur, and the lifting criterium can be dropped.

5. Modelling fines detachment by maximum retention function

This section develops a novel model for fines detachment by breakage that includes a derivation of breakage flow velocity (section 5.1), model for breakage detachment and its expression as a maximum retention function MRF (section 5.2), and determination of the breakage parameters from and experimentally derived MRF (section 5.3).

5.1. Determination of breakage velocity

Let us determine the breakage velocity based on either formula for normalised stresses (22, 24, 29) or the (χ, ν) and (χ, η) diagrams.

First, we compare normalised tensile stresses in the middle and on the boundary, using Eqs. (22) and (24). Since both normalised stresses are proportional to κ^{-1} , the choice of maximum normalised tensile stress is determined by the values in brackets in Eqs. (22, 24) (dimensionless stresses), so the knowledge of κ^{-1} is not required at this stage. The choice between T^0 and T^1 can be done using the (χ, ν) diagram (Fig. 5a).

Then, we compare the maximum normalised tensile stress T_m with the normalised shear stress in the middle S_m^0 , using Eqs. (22, 24) and (29). Also, both normalised stresses are proportional to κ^{-1} , so the choice is based on the comparison between the value in brackets in Eq. (22, 24) and the value in brackets in Eq. (29) times the strength ratio. As an alternative, the choice between maximum normalised tensile stress and normalised shear can be done using breakage function $\eta = g(\chi, \nu)$ in (χ, η) plane (Fig. 10).

So, at this stage the breakage regime was determined. Consider the chosen maximum stress equation, either (22), (24), or (29). At the point of failure, the chosen normalised stress is equal to one, the value in bracket has already been calculated, allowing us to determine the strength-drag number κ . For cases where the maximum is tensile stress in the middle, tensile stress on the boundary, and shear stress in the middle, the formulae for strength-drag numbers κ are:

$$\kappa = \begin{cases} 2, & \chi \leq \chi_1 \\ \sqrt{\frac{\sqrt{(4\chi-1)(4\chi-9)} - 4\chi + 3}{8\chi}} + \sqrt{\left(\sqrt{\frac{\sqrt{(4\chi-1)(4\chi-9)} - 4\chi + 3}{8\chi}}\right)^2 + \chi \left(1 - \left(\sqrt{\frac{\sqrt{(4\chi-1)(4\chi-9)} - 4\chi + 3}{8\chi}}\right)^2\right)^2}, & \chi > \chi_1 \end{cases} \quad (40)$$

$$\kappa = \begin{cases} 2, & \xi \leq 2 \\ \xi(\xi - 1)^{-0.5}, & \xi > 2 \end{cases}; \quad \xi = \chi \frac{4(1+2\nu)^2}{(3+2\nu)^2} \quad (41)$$

$$\kappa = \frac{T_0}{S_0} \begin{cases} 1, & \chi < 1 \\ \sqrt{\chi}, & \chi > 1 \end{cases} \quad (42)$$

respectively.

Substituting expression for drag from Eq. (1) into Eq. (12), we obtain

$$\begin{aligned} \kappa^{-1} &= \frac{1}{2T_0} \frac{F_d}{I_b} \frac{2bf_M}{r_b} = \frac{1}{T_0} \frac{2F_d}{\pi r_b^2} \frac{\alpha_s f_M}{\delta} = \frac{12}{T_0} \frac{\pi \mu_f r_s V f_d}{\pi r_b^2} \frac{\alpha_s f_M}{\delta} = \frac{12}{T_0} \frac{\pi \mu_f r_s U f_d}{\pi r_b^2} \frac{\alpha_s f_M}{\delta \phi} \\ &= \frac{12 \alpha_s f_M f_d \mu_f r_s U}{\delta \phi T_0 r_b^2} \end{aligned} \quad (43)$$

This allows determining the breakage velocity for authigenic particles

$$U_{cr}^b = \frac{\delta \phi T_0 r_b^2}{12 \alpha_s f_M f_d \mu_f r_s} \kappa^{-1} \quad (44)$$

where κ is calculated by either of three formulae (40), (41), or (42).

Critical breakage velocity versus spheroidal particle radius for different aspect ratios is investigated in Fig. 11a. The smaller is the particle, the higher is the breakage velocity. So, in a test with piecewise constant increasing velocity, the largest particles are detached first, and further detachment is continuing in the order of decreasing particle size.

However, critical breakage velocity U_{cr}^b is non-monotonic with respect to aspect ratio – the two smallest critical velocities are exhibited by very oblate spheroids ($\alpha_s = 0.025$) and for perfect spheres ($\alpha_s = 1$). Fig. 11b shows that maxima of breakage velocity are reached for intermediate aspect ratios. The effect is attributed to non-monotonicity of the product of three α_s dependent functions in the denominator of the expression (44) (Fig. 11c). The overall drag is the total of surface integrals of pressure gradient and viscous shear over the particle surface. The flatter is the particle, the lower is the aspect ratio, the lower is the particle cross-section transversal to flow. This results in a lower pressure-gradient component of drag, but a higher shear viscosity component due to an increase of the contact area and the Couette flow alignment. So, the non-monotonicity of drag shown in Fig. 11d is the result of two effects of pressure gradient and shear, i.e., normal and tangential components of drag, which are competing and at odds with each other. The above also explains non-monotonicity of lift, shown in the same figure.

Fig. 11e shows that the higher is the aspect ratio, the lower are drag, moment and lift factors. Lift is significantly lower than the drag; both forces are non-monotonic α_s -functions (Fig. 11e).

For the case of long cylinders, all the dependencies, calculated above for spheroidal particles, become monotonic for long cylinders (Fig. 12). The larger the particle the lower is the breakage velocity, i.e., the long cylinders are detached in order of decreasing of their sizes; large parti-

cles are broken first during velocity increase (Fig. 12a). The higher is the aspect ratio, the lower is the breakage velocity, i.e., it is easier to break a long thin cylinder (Fig. 12b). The aspect-ratio-dependent group that enters the expression (44) is monotonic too (Fig. 12c). The higher is the aspect ratio, the higher are the drag force (Fig. 13d) and drag factor (Fig. 12e). The lift is negligible.

5.2. Formulation of fines breakage model: maximum retention function

Breakage criterion (32, 33) yields the expression (44) of the breakage velocity U_{cr}^b versus particle and rock surface properties. For uniform plane substrate and the attached particles, all the particles remain attached for velocities lower than U_{cr}^b , and all become detached for any

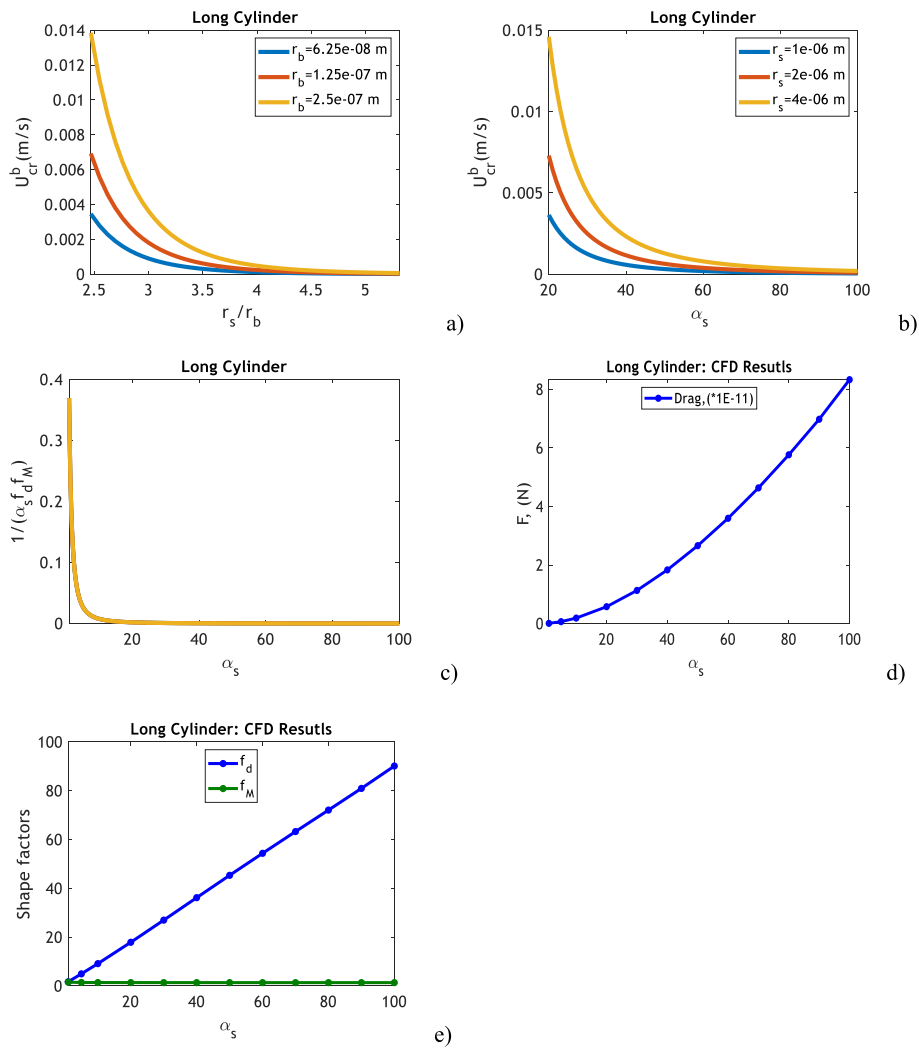


Fig. 12. Critical breakage velocity of long cylinders: a) Dependence of critical breakage velocity on particle and bond radii; b) Dependence of critical breakage velocity on particle aspect ratio; c) dependency of $\alpha_s f_d / f_M$ of α_s ; d) aspect-ratio dependency for drag; e) aspect-ratio dependencies for shape factors.

velocity above U_{cr}^b . However, fines detachment during the velocity increase occurs gradually.

Consider a multidimensional manifold of particles of different sizes and forms situated at various sites of an asperous, micro heterogeneous rock surface. Flow velocity of creeping flow near the rock surface is probabilistically distributed over the porous space. Under the assumption of Stokes flow in the porous space, velocity distribution over the porous space is determined by the macroscale Darcy's velocity U , i.e., local microscale speeds are proportional to U .⁸⁰ The mechanical equilibrium failure conditions (32, 33) indicate whether each attached to

rock surface particle is broken or remains attached under a given velocity U . It makes attached concentration a function of velocity that is called the MRF (maximum retention function). The MRF $\sigma_{cr}(U)$ is a mathematical model for particle mobilisation by breakage. For 3D flows, the MRF is a function of the modulus of velocity:

$$\sigma_a = \sigma_{cr}^b(|U|) \tag{45}$$

Here σ_a is the volumetric concentration of attached particles, and σ_{cr}^b is MRF for detachment by breakage.

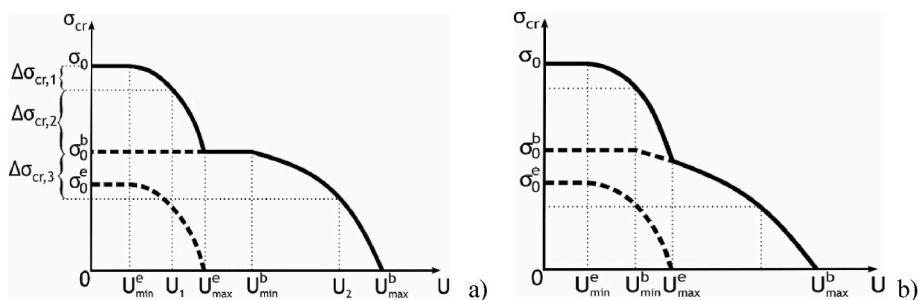


Fig. 13. Total MRF for detachment of detrital and authigenic fines: a) in the case of $U_{max}^e < U_{min}^b$, MRF has plateau; b) MRF is monotonically decreasing function of velocity in the case where $U_{max}^e > U_{min}^b$.

Eq. (44) contains coefficients reflecting properties of authigenic particles, the particle-substrate bonds, and porous medium: tensile strength T_0 , aspect ratio α_s , fluid viscosity μ_f , particle radius r_s , Poisson ratio ν , bond radius r_b , bond ratio δ , and porosity ϕ . These parameters determine the functional expression (45) for the MRF.

As it follows from the definition of the MRF as the total concentration of particles that remain attached under a given velocity U , the MRF monotonically decreases from zero velocity and tends to zero as velocity tends to infinity. A minimum breakage velocity, where the “first” particle is broken off, corresponds to equality of the MRF $\sigma_{cr}(U_{min})$ to the initial concentration of movable particles. Similarly, for an MRF which reaches zero at a finite velocity, this maximum breakage velocity, U_{max} , corresponds to the minimum flow velocity that yields failure for all bonds over the rock surface.

5.3. Maximum retention function for simultaneous breakage and DLVO detachment

Eqs. (1)–(3) as applied with the local flow velocity around the attached particle, allow determining whether any arbitrary particle is detached for any velocity U , or remains attached. The maximum retention function for DLVO attraction, $\sigma_{cr}^e(U)$, is determined by the total particle concentration that remain attached by DLVO forces for a given velocity U .^{22,23,81,82} Expressing the interstitial speed V in Eqs. (37, 38) via Darcy’s velocity $U=V\phi$, we obtain two expressions for critical velocity for particle detachment against electrostatic DLVO forces for the conditions of rolling and sliding:

$$U_{cr}^e = \frac{F_e \phi l_n}{6\pi\mu_f r_s f_d(\alpha_s) b f_M(\alpha_s)} \tag{46}$$

$$U_{cr}^e = \frac{\nu_c F_c(h)\phi}{6\pi\mu_f r_s f_d(\alpha_s)} \tag{47}$$

respectively. Here U_{cr}^e is the Darcy’ velocity that detaches the particles under the conditions given in right side of Eqs. (46) and (47).

Critical detachment velocity against DLVO forces is determined by the minimum critical velocity from those given by two criteria (46) and (47). Two failure criteria – by rolling and by Coulomb’s friction, given by Eqs. (46) and (47), respectively, are mathematically equivalent, provided that

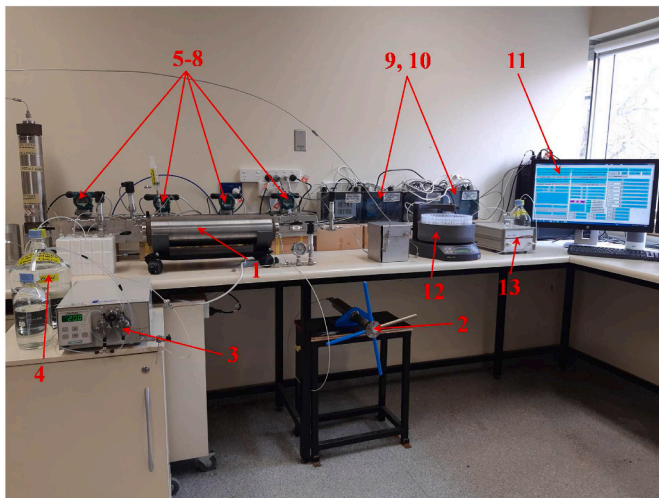


Fig. 14. Laboratory set-up for particle detachment against DLVO forces and by breakage: 1 - core holder, 2 - manual pressure generator, 3 - high-performance liquid chromatography (HPLC) pump, 4 - brine solution, 5-8 - differential pressure transmitters, 9 - data acquisition module, 10 - signal converter, 11 - personal computer, 12 - fraction collector, 13 - particle counter.

$$\nu_c = \frac{l_n}{b f_M(\alpha_s)} \tag{48}$$

Eqs. (37, 38) contain a set of parameters, which are properties of either particles or surface: particle radius r_s , its aspect ratio α_s , zeta potentials of particles ψ_{01} and rock ψ_{02} , brine salinity, pH, lever arm ratio l , temperature T , tensile strength T_0 , and beam radius r_b . Continuity of the MRF $\sigma_{cr}^e(U)$ – gradual fines detachment with continuous flow velocity increase – is determined by the probabilistic distributions of those parameters.⁸³

The assumption of independent detachment of particles against DLVO forces and by breakage determines the overall MRF as a sum of the two individual MRFs:

$$\sigma_{cr}(U) = \sigma_{cr}^e(U) + \sigma_{cr}^b(U) \tag{49}$$

Fig. 13 shows that the MRF is monotonically decreasing – the higher is the velocity, the lower is the attached concentration. A velocity increase from U_n to U_{n+1} yields detachment of particles with retained concentration $\Delta\sigma_n$:

$$\Delta\sigma_n = \sigma_{cr}(U_n) - \sigma_{cr}(U_{n+1}), \tag{50}$$

which are transformed into suspension concentration

$$c = \Delta\sigma/\phi \tag{51}$$

Fig. 13 presents the form of MRF for fines detachment against electrostatic force, by breakage, and the total MRF. Lower dashed curves represent the MRF for detrital particles, the combined dashed-solid curves correspond to the breakage MRF, and the solid curves show the total MRF.

Consider piecewise-constant injection rate increase; each constant-

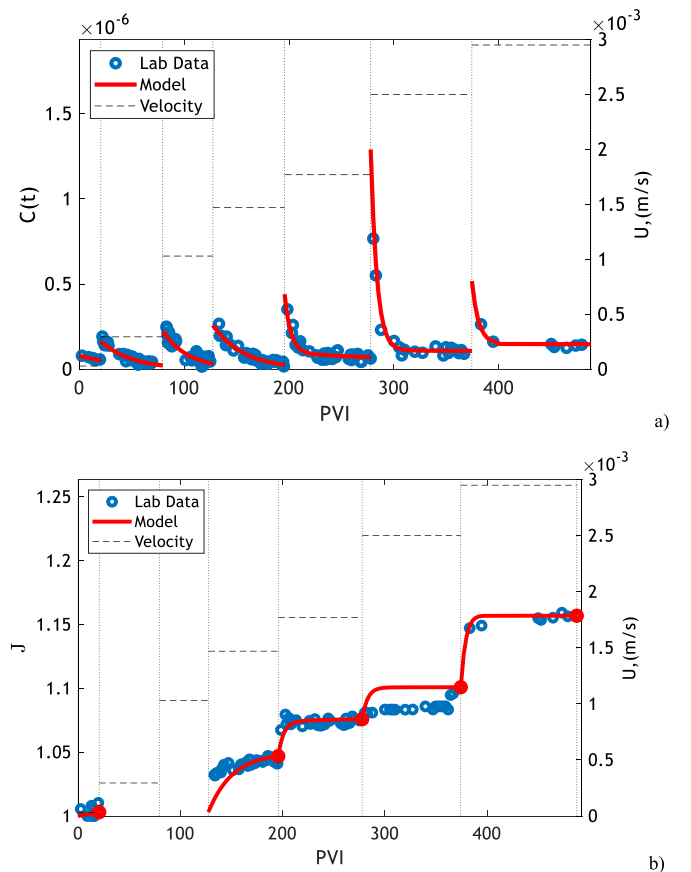


Fig. 15. Breakthrough concentrations (left axes) during the test with seven rates (right axis), a) breakthrough concentrations, C, b) impedance, J

rate stage is maintained until stabilisation. The case of Fig. 13a corresponds to weak electrostatic attraction (using low-salinity, high-pH or high-temperature water) and high particle-rock-bond strength (highly consolidated sandstones). The detrital particles start detaching at velocity U_{min}^e and continue mobilisation until velocity U_{max}^e , where all movable detrital fines are detached. At a velocity that is higher than the minimum plateau velocity, the maximum DLVO force cannot secure any detrital particle on the rock surface, i.e., all detrital particles detach. In this case, where $U_{max}^e < U_{min}^b$, no further particle detachment occurs until the velocity reaches U_{min}^b , where the first authigenic particle experiences failure. All movable authigenic particles are detached once the velocity reaches U_{max}^b . In this case, the total MRF has a plateau, where all detrital particles are detached under velocities that are lower than the minimum plateau velocity, and authigenic fines remain attached until a velocity that is higher than the maximum plateau velocity. No detachment occurs at plateau velocities. For high electrostatic attraction and low strength, the velocity intervals for detachment by both causes overlap (Fig. 13b).

Existence of two plateaus in MRF indicates three detachment mechanisms. For example, if the DLVO energy profile has two minima in the case of unfavourable fines attachment and the particle-rock bond strength is high, the MRF can have two plateaus.

Finally, there appears the following *algorithm of fines detachment modelling*: (i) identifying the appropriate domain in plane (χ, ν) – the tensile-stress diagram – and determining which tensile stress maximum on the beam base – along the symmetry axis or the boundary of the beam base – is higher; (ii) determining whether the failure occurs by tensile or shear stress from the inequality for the breakage regime function $g(\chi, \nu) > \eta$ in the shear-tensile diagram; (iii) calculation of breakage velocity from the drag-strength number κ ; (iv) determining the probabilistic distribution of breakage velocity; (v) calculation of the MRF for breakage; (vi) adding the MRFs for breakage and detachment against electrostatic attraction.

MRF (49) in set of points $U_1 < U_2 < \dots < U_n$ is determined from a laboratory coreflood with piecewise-constant injection rate increase from breakthrough particle concentrations.

6. Laboratory validation of the model for fines detachment by breakage

6.1. Laboratory study

The laboratory study conducted as part of this study comprised of core drying, core saturation by water with 0.6 M of NaCl under vacuum, and injection of this water into the core. A Castlegate sandstone core with permeability 917 mD and porosity 0.24, length 5.1 cm and pore volume 13.7 cu cm was used in the test. Seven flow rates were applied in order of increasing rate. Fig. 14 presents the schematic of laboratory set-up. The essential parts of the setup are coreholder with the core placed in a Viton sleeve, four differential pressure transmitters, HPLC pump, effluent fraction collector, and particle counter. The overburden

pressure was created by a manual pressure generator. A data acquisition module along with signal convertor provided results which were visualised on a PC screen in real time. Breakthrough concentration (Fig. 15a) and size distributions of produced particles along with pressure drop across the core (Fig. 15b) have been measured during each constant-rate injection step.

Fig. 15a shows that at low rate, the breakthrough concentration declines exponentially, which is typical for deep bed filtration of low-concentration colloids with constant filtration coefficient.^{20,84} At high rates, this behaviour is combined with a sharp and fast concentration decrease down to low values, indicating that particle capture intensity is decreasing, until the point where all capture vacancies are filled and no further capture occurs. Here the capture rate is described by the Langmuir filtration function.^{85,86}

Relative change of average core permeability is captured by impedance J

$$J(t) = \frac{\Delta p(t)}{\Delta p(0)} \frac{U(0)}{U(t)} \tag{52}$$

where Δp is the pressure drop across the core.

For large rates, impedance first increases sharply and then switches to slow growth (Fig. 15b). This transition occurs at approximately the same time as the suspended concentration switches from a sharp decrease to a slow decrease (Fig. 15a). Colloidal flow with a Langmuir filtration coefficient is attributed to asperous authigenic fines with rough surfaces after breakage, which are strained in the large pore throats with fast filling of all of them, while the capture of smoother detrital particles is less intensive and continues significantly longer.

The size distributions of produced particles at high rates have a clear bimodal structure, which also supports the two-population hypothesis.

The next section supports the two-population hypothesis by successful matching of experimental data with a two-population colloidal transport model.

6.2. Mathematical model for transport of detached colloids

To match the breakthrough and impedance histories, we have developed a two-population model of deep bed filtration, given by Eqs. (B1-B4) and described in Appendix B. The system contains mass conservations for both populations, Eq. (B1) for $k = 1, 2$, where the delay of each particle population's velocity comparing with the carrier water velocity is expressed by drift-delay factors α_k . Particle capture rates for each particle population are proportional to the respective particle fluxes $c_k \alpha_k U$; the proportionality coefficients are λ_1 and λ_2 . The filtration coefficients λ_1 and λ_2 are equal to probabilities of the particle capture by the rock per unit length of the particle trajectory in the porous space. The first population filtrates with constant filtration coefficient λ_1 , and the filtration coefficient for the second population $\lambda_2(\sigma_2)$ has Langmuir form given by Eq. (B4). The interaction of two population fluxes is expressed by the joint contribution of the retained particles of both types

Table 1
Tuned parameters of two-population model for each flow rate.

q (ml/min)	2	20	70	100	120	170	200
U (m/s)	2.95×10^{-5}	2.95×10^{-4}	1.03×10^{-3}	1.47×10^{-3}	1.77×10^{-3}	2.5×10^{-3}	2.95×10^{-3}
α_1	2×10^{-3}	4×10^{-3}	5.5×10^{-3}	7×10^{-3}	7.5×10^{-3}	7.7×10^{-3}	7.9×10^{-3}
α_2	0	0	0	0	0.02	0.02	0.04
β_1	958.98	–	–	6367.62	3663.3	3663.3	3663.3
β_2	0	0	0	0	7248	1956.64	32985.68
λ_1 (1/m)	200	170	150	98	10	0.55	0.3
λ_2 (1/m)	0	0	0	0	170	170	80
$\Delta\sigma_1$	9.68×10^{-6}	9.99×10^{-6}	9.96×10^{-6}	9.01×10^{-6}	3.11×10^{-6}	3.5×10^{-6}	4.6×10^{-6}
$\Delta\sigma_2$	0	0	0	0	4.21×10^{-6}	1.44×10^{-5}	2.25×10^{-6}
$\Delta\sigma$	9.68×10^{-6}	9.99×10^{-6}	9.96×10^{-6}	9.01×10^{-6}	7.32×10^{-6}	1.79×10^{-5}	6.85×10^{-6}
$R^2(c)$	0.81	0.91	0.81	0.90	0.87	0.94	0.90
$R^2(J)$	0.94						

to the overall rock hydraulic resistance. Dependence of permeability on both retained concentrations in Eq. (B3) is obtained by first order Taylor’s expansion of the inverse to permeability as a function of the retained concentrations of two populations. Here k_0 is the initial (undamaged) permeability, and formation damage coefficients β_1 and β_2 quantify the extent of permeability decline caused by each of the particle populations.

The assumption of the independence of the model parameters of fluid pressure separates four equations (B1, B2) for $k = 1,2$ from Eq. (B3). Dependence of the individual model parameters on their particular retention concentrations separates systems (B1, B2) for $k = 1,2$ from each other. Initial conditions (B5) correspond to electrostatic and breakage detachment with instant particle mobilisation: the detached concentration $\Delta\sigma_{cr}$ due to change of flow rate from U_{n-1} to U_n , determined by MRF is instantly translated into suspension concentration $\Delta\sigma_{cr}/\phi$.

Initial-boundary problem (B5, B6) for 1D flow system (B1, B2) allows for an exact solution.^{86–88} Suspended and retained concentrations of both populations are expressed by explicit formulae (B7). This allows for the derivation of an explicit formula for the pressure gradient. Yet, the pressure drop across the core and impedance are calculated by numerical integration.

6.3. Results

The analytical 1D model (B7) for governing equations (B1-B3) for matching the lab data. Fig. 15 shows the experimental data by blue dots and the matched modelling data by red curves. Breakthrough concentrations highly exceed the accuracy of the particle counter used in the laboratory set-up (Fig. 14). The measured pressure drops exceed the accuracy of pressure transducers only by a factor of 2–3, so the formation damage coefficients have been tuned by the final impedance values alone, which are shown by red dots in Fig. 15b. The results of tuning – filtration and formation damage coefficients and drift delay factors along with detached concentrations for each rate for both populations are presented in Table 1.

Here the first population with lower filtration and formation damage coefficients is attributed to smoother detrital particles, while broken-off rough-shaped authigenic particles are represented by second population with higher filtration and formation damage coefficients. The parameters obtained from tuning - filtration coefficients, formation damage coefficients, and delay-drift factors - belong to commonly reported intervals.^{13,20,30,84} The curves for detached concentration $\Delta\sigma_{cr}(U)$ versus velocity for both populations, obtained by extrapolation of detached concentrations at different rates in lines 9 and 10 of Table 1, increase at small velocities from zero and declines at high velocities up to zero. This complies with the typical form of the maximum retention curve.^{22,23,81,91} Extrapolation of detached concentrations for each velocity and corresponding curves $\Delta\sigma_{cr}(U)$ for both populations allow determining the concentrations of detachable authigenic and detrital fines, which are found to be $\sigma_0^b = 5.67 \times 10^{-5}$ and $\sigma_0^o = 5.5 \times 10^{-5}$,

respectively. So, the detachable concentrations of both populations are almost equal.

Let us estimate the tensile strength T_0 . The tensile strength for kaolinite as determined from Eq. (44), presents an unbiased breakage velocity estimate. The minimum breakage velocity is determined from the extrapolated curve $\Delta\sigma_{cr}(U)$ for authigenic fines (line 10 in Table 1). It corresponds to minimum value of numerator and maximum of denominator in ratio (44). We assumed a minimum bond ratio of $\delta = 0.05$. The obtained tensile strength is equal to $T_0 = 0.41$ MPa. Although this value is lower than typical tensile strengths for minerals, significantly smaller values for coals and clays have been reported.^{31,32,48,89,90}

High match for breakthrough concentrations is supported by high coefficient of determination R^2 , which varies from 0.81 to 0.94. The coefficient of determination for the overall impedance is also high $R^2 = 0.94$. High match shown in Fig. 15 and Table 1 validates the two-population model for deep bed filtration of broken-off and DLVO-detached fines.

We assume that velocity variation in the curves $\Delta\sigma_{cr}(U)$ for both populations is due to variability of two model parameters – lever arm ratio l for first population and bond radius r_b for second population. It allows determining their mean values – $l = 110$ and $r_b = 0.16 \times 10^{-6}$ m and estimating their standard deviations – $C_v(l) = 0.15$, $C_v(r_b) = 0.02$. Even using SEM images, the lever arm ratio and bond radius cannot be measured, but Eqs. (40-44) along with the coreflood data allow their estimation.

Simpler approach to large scale modelling uses a single-population model, which is the case $c_2 = 0$ in Eq. (B1-B7). The total MRF, as obtained by matching with single-population model, is decomposed into two MRFs for detrital and authigenic fines, while using two-population model (B1-B7) yields direct calculation of MRFs for each population from breakthrough concentrations. Close match by a single-population model has been also achieved for the data of 6 corefloods on coal flooding by Guo (2016) and Huang et al. (2017), (2021) and on sandstone floods by Ochi and Vernoux (1998), and Torkzaban et al. (2015)^{30,73,92–94} The coefficient of determination R^2 varies in the interval [0.88,0.94], exhibiting a close match. The tuned parameters have the same order of magnitude as those obtained in our test. The results are presented in works.^{104,105}

7. Fines breakage near to injection and production wells

A fines migration test is a routine laboratory experiment to prevent formation damage due to fines migration.^{30,89} A core is submitted to flow with piecewise-constant increasing velocity. Minimum fines migration velocity is determined by appearance of the fine particles in the effluent. This determines maximum well rate under which fines migration does not occur. In this section we predict the minimum velocity for fines migration using the stress diagram technique and conclude about the viability of fines detachment by breakage during water, oil, and gas injection and production. The results below also illustrate using the sequential techniques for tensile-stress diagram,

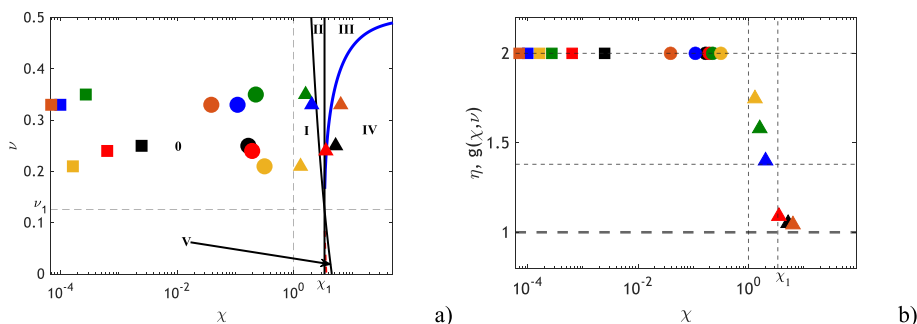


Fig. 16. Determining breakage regime for 6 examples of production and injection in natural reservoirs: a) tensile-stress diagram, b) shear-tensile diagram.

Table 2
Model parameters for three types of particles to build the diagrams in Fig. 16

	Refs.	Spheroid			Short cylinder			Long cylinder		
		α_s	δ	f_M	α_s	δ	f_M	α_s	δ	f_M
Heavy oil	95	1	0.8	1.37	0.15	1	2.04	10	1	1.41
Polymer	96	0.8	0.7	1.4	0.19	1	1.96	20	1	1.39
CBM	97	0.6	0.6	1.45	0.3	1	1.81	30	1	1.38
CO ₂	98	0.4	0.5	1.57	0.35	1	1.76	40	1	1.38
HF-W	99	0.2	0.4	2.09	0.26	1	1.85	50	1	1.38
HF	99	0.1	0.3	3.5	0.13	1	2.09	60	1	1.37

Table 3
Comparison between fines breakage velocity and fluid velocity at the well/fracture wall.

Spherical	δ	ν	χ	μ_f (Pa.s)	U_{min}^b (m/s)	U_w (m/s)
Heavy oil	0.05	0.25	6.54×10^{-4}	0.30	1.01×10^{-6}	5.67×10^{-6}
Polymer	0.05	0.24	6.57×10^{-4}	0.04	6.69×10^{-6}	8.8×10^{-5}
CBM	0.05	0.35	6.27×10^{-4}	1×10^{-3}	3.57×10^{-4}	1.14×10^{-5}
CO ₂	0.05	0.21	6.67×10^{-4}	1.49×10^{-4}	8.51×10^{-4}	4.74×10^{-5}
HF-W	0.05	0.33	6.32×10^{-4}	1×10^{-3}	8.93×10^{-4}	1.38×10^{-2}
HF	0.05	0.33	6.32×10^{-4}	1	8.93×10^{-7}	1.38×10^{-2}

shear-stress diagram, and equation (44) for the breakage of attached fine particles.

The data for the cases of production of heavy oil, polymer injection, dewatering of coal gas seams, CO₂ injection in aquifer, well fracturing by water, and well fracturing by highly-viscous fluid, which are marked in Fig. 16 by black, red, green, yellow, blue, and orange, respectively, are taken from the corresponding papers by Ado (2021), Gao (2011), Shi et al. (2008), Spivak et al. (1989), and Prasetyo et al. (2021).^{95–99} Circular, triangular, and square points in Fig. 16 correspond to spheroidal, flat and long cylinder particles. The data for those three types of particles are given in Table 2. Other data are presented in Table 3. Bond ratio for short and long cylinders are one. High shear flows with large pressure gradients for heavy oil and polymer break the grain-grain cement in low consolidated sandstones, so particle shapes are assumed close to one (Lines 3 and 4 in third column in Table 2). For kaolinite platelets detached during well fracturing, aspect ratio is small (Lines 7 and 8 in second column in Table 2). Aspect ratios for short cylinders are significantly lower than one (6th column), while for long cylinders they significantly exceed one (9th column).

Volume-equivalent particle size $r_s = 2 \times 10^{-6}$ m and wellbore radius $r_w = 0.1$ m are assumed for all cases. Poisson's ratios ν varies in the interval 0.21 to 0.35. Fluid viscosities as taken from the original papers, are as high as 1000, 300, and 40 cp for fracturing fluid, heavy oil, and polymer solution and as low as 0.02 cp for CO₂. For the composite particle-rock bond, a low value of tensile strength $T_0 = 0.2$ MPa is assumed for all cases; yet several works report lower T_0 values.^{31,32,45,89} The values of shape-Poisson numbers χ have been calculated by Eq. (12), which allows placing the corresponding state points into the tensile-stress diagram (χ, ν) in Fig. 16a. Values of χ and ν also allow calculating breakage function $\eta = g(\chi, \nu)$ for the state points and determine their position in the tensile-shear diagram (χ, η) (Fig. 16b). Here the state points are located on breakage regime curves $\eta = g(\chi, \nu)$ that correspond to different Poisson's ratios. Breakage function $g(\chi, \nu) = 2$ for spheroidal and long cylindrical cases. For all cases, like in papers by Gao et al. (2014), Guo et al. (2018), and Horabik and Jozefaciuk (2021), the strength ratio η is assumed to be equal to one.^{100–102} As discussed earlier, for values of η lower than or equal to one, breakage occurs by tensile failure (Fig. 10).

The breakage velocities are presented in the seventh column of Table 3. The breakage occurs if the fluid velocity at wellbore exceeds the breakage velocity. Comparison between 6th and 7th columns of Table 3 shows that fines detachment by breakage is likely to occur in 4 cases from 6. Fig. 16 presents all 6 cases for three particle shapes (18 dots in

Fig. 16). Fines breakage occurs only in 12 cases.

Fig. 16a shows that for spheroidal and long cylindrical particles, all 12 cases belong to domain 0, where both tensile stresses κT_m^0 and κT_m^I are equal to two, while for short cylindrical particles some points belong to domain I, III, IV. For both cases of maximum tensile stress in the middle and the boundary of the beam base, Eqs. (40) and (41) show that the strength-drag numbers are equal, i.e. $\kappa = 2$. It allows calculating minimum breakage velocities using Eq. (44). Points in Fig. 16b correspond to different Poisson's ratios and, therefore, are located on different breakage regime curves, $\eta = g(\chi, \nu)$. However, the overall curve has the same general tendency as those presented in Fig. 10a, d, and g.

To evaluate possible fines breakage cases, we estimate minimum breakage velocity, so the bond ratio in Table 3 was assumed to be minimal. Spherical form of the particles is assumed. The breakage velocities for heavy oil production, polymer injection, and hydraulic fracturing by water and by fracturing fluid are lower than corresponding wellbore velocities, so fines detachment by breakage occurs. The calculated breakage velocities for dewatering in coal bed methane reservoirs and CO₂ injection in aquifers are higher than corresponding wellbore velocities, so breakage is unlikely. However, the CO₂ breakage injection velocity can decrease down to any arbitrarily low value during mineral dissolution of particle-rock bond in carbonic acid. The same corresponds to waterflooding of carbonate reservoirs during rock dissolution in water. The above demonstrates high likelihood of particle breakage near to injection and production wells.

8. Discussion

Let us discuss the validity of the breakage-model assumptions and limitations.

The distinguished features of the analytical detachment model for authigenic particles are separation of hydrodynamics from deformation and failure, graphical determination of the breakage regime from two geometric diagrams, and the explicit formulae for breakage velocity. Those features are determined by the model assumptions (section 2.1).

The Navier-Stokes assumptions are valid for water, volatile oil, and low-velocity gas. During heavy oil production, polymer injection, or fracturing by highly-viscous fluid (Lines 2, 3, and 6 in Table 3), the non-Newtonian fluid rheology must be considered. Gas compressibility at high pressure gradients can affect the Couette's flow away from the attached fine. Near to wellbore at high rates, gas turbulent flow can occur, yielding the quadratic velocity dependency for drag.

The model consider single-parameter particle forms for spheres and

bi-parametric forms for spheroids and cylinders. Those cover kaolinite booklets and platelets, silica fines, and illite' "hair". For the chlorite shells and more complex particle shapes, the shape equations can contain three and more parameters. For the breakage prediction, a particle is approximated by the beam, i.e., stresses in the particle body outside the beam are ignored (Fig. 1d and 2a). This assumption is fulfilled automatically for cylindrical fines; for spheroids, it is fulfilled with high accuracy if the radius of particle-substrate contact has the order of magnitude of the particle size. This assumption is questionable for shells and stars.

The attached particles are assumed to be significantly smaller than pores, so the pore wall near to the attached fine particle can be considered as a plane substrate. More complex domain around the attached particles in CFD model (section 2.2) must be created for large particles attached in pore throats. The assumption of non-deformable substrate in solid rocks does not create any restrictions for the model application.

The model discusses only solid particles, which covers almost all mineral fines in natural rocks; they are assumed to be low-deformable. This supports the assumption of elastic deformation. However, more complex rheology can be valid even for small particle deformations. Steady-state fluid flow with immobile particle-fluid and substrate-fluid interfaces is assumed to be around the attached particles, so the model is not applicable for abrupt alterations of pore geometry during straining and size exclusion of the migration fines. This excludes massive fines mobilisation at the beginning of production or injection in rocks with highly detachable fines, like geothermal or coal-bed methane reservoirs.

The model considers brittle particles and tensile/shear strength as the failure criteria. At this stage, it is difficult to define how limited are those assumptions. Currently, those assumptions are highly investigated for rocks. However, the fine particles are not part of rock-forming skeleton, so rheologic properties of rock and individual mineral particles can be completely different.

The breakage model applicability is limited by the absence of a strict mathematical upscaling. The present particle-breakage model, given by formulae (40-44), is developed at the microscale by merging CFD, beam theory, and strength failure criteria. We also use macroscale model (B1-B7) for fines transport at the core level. In this work, we use the breakage velocity given by Eq. (44) as an average of the ensemble. In this work, we use the breakage velocity given by Eq. (44) as an average of the ensemble of particles. From its interval of variation, we determine the variation of a single parameter – bond number. Determining MRF at the core scale from statistical properties of the particles and rock (upscaling) and determining some microscale parameters from MRF (downscaling) is a topic of forthcoming research.

9. Conclusions

Integration of Timoshenko's beam theory with breakage criteria for particle-substrate bonds and CFD flow modelling allows concluding the following.

Breakage conditions where either of the tensile or shear stresses reaches the strength value, is determined by three dimensionless groups: the strength-drag number κ , the shape-Poisson number χ , strength ratio η , as well as the Poisson's ratio ν . Stress maxima are reached either at the

central axis or boundary of the base of the beam.

Equality of tensile stress maxima at the beam base axes and boundary separates the plane (χ, ν) , which is called the tensile stress diagram, into 5 domains, where one tensile maximum exceeds the other. This allows calculating maximum tensile stress in the beam. The comparison between the maximum tensile and shear stresses is determined by their ratio $g(\chi, \nu)$, which defines the breakage curve in the tensile-shear diagram in the plane (χ, η) . The breakage occurs by tensile failure if $g(\chi, \nu) > \eta$; otherwise it is shear failure that causes the breakage.

If the strength ratio exceeds 2, particles are detached by shear stress for all values of χ and ν . For strength ratios below two and above one, the particles are detached by shear stress for shape-Poisson numbers χ such that η exceeds $g(\chi, \nu)$; for lower shape-Poisson numbers, particles are detached by tensile stress. For strength ratios below one, the particles are detached by tensile stress for all Poisson's ratios.

The definition of the breakage regime – by either tensile or shear stress, in the base middle or at the boundary – is independent of flow velocity. For an identified breakage regime, the breakage flow velocity is determined by the strength-drag number $\kappa(\chi, \nu)$ alone. For a given particle shape, the critical breakage velocity is proportional to the strength and particle size and is inversely proportional to viscosity. These conclusions are the consequence of the assumptions of a Newtonian fluid, elastic beam deformation, and the strength failure criteria.

A mathematical model for colloidal detachment by breakage is a maximum retention function (MRF). This function closes the governing equations for migration of authigenic clays. 1D problem for fines detachment, migration, and straining allows for an exact solution. This allows determining MRF from the breakthrough particle concentrations during a coreflood with piecewise constant and increasing velocity. High match of 7 coreflood test data along with belonging of tuned parameters to commonly reported intervals validates the mathematical model for authigenic fines migration with breakage.

Calculations of breakage velocity for 6 field cases show high likelihood of authigenic particle breakage near to injection and production wells with consequent formation damage.

Declaration of competing interest

The authors declare that they have no known competing financial interests or personal relationships that could have appeared to influence the work reported in this paper.

Data availability

No data was used for the research described in the article.

Acknowledgements

The authors are deeply grateful for fruitful discussions and support to A/Profs Murat Karakus, Giang D. Nguyen and Abbas Zeinijahromi, Drs Noun Melkounian, Zhao Feng Tian, Themis Carageorgos and Heng Zheng Ting (University of Adelaide), Prof Leslie Banks-Sills (Tel-Aviv University), Dr. Reza Reisabadi (University of Queensland), and A/Prof Hamid Roshan (University of New South Wales).

Appendix A. Stresses in elastic beam by Timoshenko's model

Under the model assumptions formulated in section 2.1, Timoshenko's 3D solution for elastic deformation of a cylindrical beam (Fig. 2) shows that the normal stress σ_z reaches a maximum at the beam bottom, $z = 0$, and the two shear stresses τ_{xz} and τ_{yz} are independent of z . The normal and shear stresses at the beam base with applied external load F_d are³³:

$$\sigma_z = \frac{F_d b f_{MX}}{I}, \sigma_x = \sigma_y = \tau_{xy} = 0 \quad (A1)$$

$$\tau_{xz} = \frac{(3 + 2\nu) F_d}{8(1 + \nu) I} \left(r_b^2 - x^2 - \frac{(1 - 2\nu)}{(3 + 2\nu)} y^2 \right) \tag{A2}$$

$$\tau_{yz} = - \frac{(1 + 2\nu) F_d xy}{4(1 + \nu) I} \tag{A3}$$

where, σ_z is the normal bending stress at contact area, τ_{xz} is the shear stress acting on the z plane and towards the x direction, τ_{yz} is the shear stress acting on the z plane and towards the y direction, ν the is Poisson's ratio, and I is the moment of inertia, which for circular cross-section is equal to $\pi r_b^4/4$.

As expressed by Eq. (A1), the normal bending stress expands the matter at $x < 0$ reaching a minimum in the advance point $x = -r_b, y = 0$ (Fig. 2a) and contracts at $x > 0$ reaching a maximum at the receding point $x = r_b, y = 0$. Fig. 2b illustrates Eq. (A2) and corresponds to shear stress that opposes the external load F_d and is equal zero only in advance and receded points. Eq. (A3) is illustrated by Fig. 2c, showing the transversal shear stress.

The stress tensor, as per solution (A1-A3) is:

$$\begin{bmatrix} 0 & 0 & \tau_{xz} \\ 0 & 0 & \tau_{yz} \\ \tau_{xz} & \tau_{yz} & \sigma_z \end{bmatrix} \tag{A4}$$

The principal stresses are eigen values of the stress tensor (A4):

$$\sigma_1 = \frac{\sigma_z + \sqrt{\sigma_z^2 + 4(\tau_{xz}^2 + \tau_{yz}^2)}}{2}, \sigma_2 = 0, \sigma_3 = \frac{\sigma_z - \sqrt{\sigma_z^2 + 4(\tau_{xz}^2 + \tau_{yz}^2)}}{2} \tag{A5}$$

where, $\sigma_1, \sigma_2, \sigma_3$ are the principal stresses in decreasing order of magnitude, and

$$\sigma_1 > \sigma_2 = 0 > \sigma_3. \tag{A6}$$

The equation for largest Mohr circle for the case of $\sigma_2 = 0$ is

$$\left[\sigma - \left(\frac{\sigma_1 + \sigma_3}{2} \right) \right]^2 + \tau^2 = \left[\frac{(\sigma_1 - \sigma_3)}{2} \right]^2 \tag{A7}$$

where σ and τ are tensile and shear stresses acting on unitary planes with different orientations.

Maximum tensile and shear stresses in Eqs. (8, 9) correspond to points $(\sigma_3, 0)$ and $(\sigma_1 + \sigma_3)/2, (\sigma_1 - \sigma_3)/2$ in plane (σ, τ) . Consequently, the maximum tensile and shear stresses are

$$\max \sigma = \sigma_3, \max \tau = \frac{\sigma_1 - \sigma_3}{2}, \tag{A8}$$

respectively.

Appendix B. Two-population balance model for colloidal-suspension transport

We discuss deep bed filtration of two particle populations for detrital and authigenic fines. Mass balance and capture rate equations and Darcy's law for both populations are:^{12,13,103}

$$\frac{\partial}{\partial t} (\phi c_k + \sigma_k) + \frac{\partial}{\partial x} (c_k \alpha_k U_n) = 0 \tag{B1}$$

$$\frac{\partial \sigma_k}{\partial t} = \lambda_k c_k \alpha_k U_n, k = 1, 2, n = 0, 1, 2, \dots \tag{B2}$$

$$U_n = - \frac{k_0}{1 + \beta_1 \sigma_1 + \beta_2 \sigma_2} \frac{\partial p}{\partial x} \tag{B3}$$

where ϕ is the porosity, c_k and σ_k are the suspended and retained concentrations for both populations, $k = 1, 2, \lambda_k$ are the filtration coefficients, α_k are the drift-delay factors, U_n is the flow velocity, k_0 is the initial permeability, p is the pressure, and β_k are the formation damage coefficients. Index k corresponds to the two populations; index n is attributed to the injection velocity at the n -th step of the test, corresponding to the switch from U_{n-1} to U_n . The filtration coefficient for the first population is constant. The filtration coefficient for the second population is a blocking (Langmuir) function of retained second-population concentration¹⁰³

$$\lambda_1 = const$$

$$\lambda_2(\sigma_2) = \begin{cases} \lambda_{2,0} \left(1 - \frac{\sigma_2}{\sigma_m} \right), & \sigma_2 < \sigma_m \\ 0, & \sigma_2 > \sigma_m \end{cases} \tag{B4}$$

Retained concentration is defined per unit volume of the rock, because it is determined by the difference in rock weights. Suspended concentration is defined per unit volume of the carrier fluid that fills in the pore space. Therefore, initial suspended concentrations for both populations are equal to the concentrations of mobilised fines after a velocity increase, divided by porosity

$$t = 0 : c_{k0} = \frac{\sigma_{cr}^k(U_n) - \sigma_{cr}^k(U_{n-1})}{\phi} = \frac{\Delta\sigma_{cr}^k(U_n)}{\phi}, k = 1, 2, \quad (B5)$$

i.e., the detached concentration for either of populations after changing the flow velocity from U_{n-1} to U_n is equal to the difference between the MRF values in those two velocities.

Inlet boundary condition corresponds to the injection of particle-free water

$$x = 0 : c_k = 0, k = 1, 2 \quad (B6)$$

Breakthrough concentration is a total of those for both populations. The exact solution is^{88,89}

$$c^n(x, t) = c_1^n(x, t) + c_2^n(x, t)$$

$$c_1^n = \begin{cases} \frac{\Delta\sigma_1^n(U_n)}{\phi} \exp\left(-\frac{\lambda_1 \alpha_1 U_n}{\phi} t\right), & x > \frac{\alpha_1 U_n}{\phi} t \\ 0, & x < \frac{\alpha_1 U_n}{\phi} t \end{cases}$$

$$c_2^n = \begin{cases} 0, & x > \frac{\alpha_2 U_n}{\phi} t \\ \frac{\sigma_m \left(\Delta\sigma_2^n(U_n) / \sigma_m - 1 \right)}{\phi \left\{ 1 - \frac{\sigma_m}{\Delta\sigma_2^n(U_n)} \exp\left[\frac{\lambda_2 \alpha_2 U_n}{\phi} t \left(1 - \frac{\Delta\sigma_2^n}{\sigma_m} \right) \right] \right\}}, & x < \frac{\alpha_2 U_n}{\phi} t \end{cases} \quad (B7)$$

References

- Hashemi S, Melkoumian N. A strain energy criterion based on grain dislodgment at borehole wall in poorly cemented sands. *Int J Rock Mech Min Sci.* 2016;87:90–103.
- De Silva G, Ranjith P, Perera M, Dai Z, Yang S. An experimental evaluation of unique CO₂ flow behaviour in loosely held fine particles rich sandstone under deep reservoir conditions and influencing factors. *Energy.* 2017;119:121–137.
- Jayasekara D, Ranjith P, Wanniarachchi W, Rathnaweera T. Understanding the chemico-mineralogical changes of caprock sealing in deep saline CO₂ sequestration environments: a review study. *J Supercrit Fluids.* 2020;161, 104819.
- Kong L, Ranjith PG, Li BQ. Fluid-driven micro-cracking behaviour of crystalline rock using a coupled hydro-grain-based discrete element method. *Int J Rock Mech Min Sci.* 2021;144, 104766.
- Kamel KEM, Gerard P, Colliat J-B, Massart TJ. Modelling stress-induced permeability alterations in sandstones using CT scan-based representations of the pore space morphology. *Int J Rock Mech Min Sci.* 2022;150, 104998.
- Song J, Xiang D, Hu D, Zhou H, Guo D, Zhang G. Creep characteristics of a fracturing fluid-softened shale investigated by microindentation. *Int J Rock Mech Min Sci.* 2022;152, 105067.
- Appelo CAJ, Postma D. *Geochemistry, Groundwater and Pollution.* CRC press; 2004.
- Bandara K, Ranjith P, Haque A, Wanniarachchi W, Zheng W, Rathnaweera T. An experimental investigation of the effect of long-term, time-dependent proppant embedment on fracture permeability and fracture aperture reduction. *Int J Rock Mech Min Sci.* 2021;144, 104813.
- Castro R, Arancibia L, Gómez R. Quantifying fines migration in block caving through 3D experiments. *Int J Rock Mech Min Sci.* 2022;151, 105033.
- Sharp reductions in high-productivity well due to formation damage: case study in tarim basin, China. In: Liu J, Yuan X, Zhang J, Xi W, Feng J, Wu H, eds. *Proceedings of the International Field Exploration and Development Conference.* vol. 2019. Springer; 2017.
- Song Y, Ranjith P, Wu B. A study of ellipsoidal and spherical particle flow, clogging and unclogging dynamics. *Powder Technol.* 2021;392:424–437.
- Bradford SA, Simunek J, Bettahar M, Van Genuchten MT, Yates SR. Modeling colloid attachment, straining, and exclusion in saturated porous media. *Environ Sci Technol.* 2003;37(10):2242–2250.
- Bradford SA, Torzabani S, Shapiro A. A theoretical analysis of colloid attachment and straining in chemically heterogeneous porous media. *Langmuir.* 2013;29(23):6944–6952.
- Johnson WP. Quantitative linking of nanoscale interactions to continuum-scale nanoparticle and microplastic transport in environmental granular media. *Environ Sci Technol.* 2020;54(13):8032–8042.
- Wilson MD, Pittman ED. Authigenic clays in sandstones: recognition and influence on reservoir properties and paleoenvironmental analysis. *J Sediment Res.* 1977;47(1):3–31.
- Burley S, Kantorowicz J, Waugh B. Clastic diagenesis. *Geol Soc, London, Special Publicat.* 1985;18(1):189–226.
- Kar R, Baruah H, Phukan S. Signatures of marine influences in the gondwana sandstones of Kalijhora, Darjeeling District, West Bengal, India. *Earth Sci India.* 2019;12(1).
- Obermayr M, Dressler K, Vrettos C, Eberhard P. A bonded-particle model for cemented sand. *Comput Geotech.* 2013;49:299–313.
- Bergendahl J, Grasso D. Prediction of colloid detachment in a model porous media: hydrodynamics. *Chem Eng Sci.* 2000;55(9):1523–1532.
- Chen C, Packman AI, Gaillard JF. Pore-scale analysis of permeability reduction resulting from colloid deposition. *Geophys Res Lett.* 2008;35(7).
- Israelachvili JN. *Intermolecular and Surface Forces.* Academic press; 2011.
- Bedrikovetsky P, Siqueira FD, Furtado CA, Souza ALS. Modified particle detachment model for colloidal transport in porous media. *Transport Porous Media.* 2011;86(2):353–383.
- Bedrikovetsky P, Zeinijahromi A, Siqueira FD, Furtado CA, de Souza ALS. Particle detachment under velocity alternation during suspension transport in porous media. *Transport Porous Media.* 2012;91(1):173–197.
- A novel chemical composition to consolidate the loose sand formation in the oil field. In: Mishra S, Ojha K, eds. *International Petroleum Technology Conference.* OnePetro; 2016.
- Turner LG, Steel KM. A study into the effect of cleat demineralisation by hydrochloric acid on the permeability of coal. *J Nat Gas Sci Eng.* 2016;36:931–942.
- Wang J, Huang Y, Zhou F, Song Z, Liang X. Study on reservoir damage during acidizing for high-temperature and ultra-deep tight sandstone. *J Petrol Sci Eng.* 2020;191, 107231.
- Tang Y, Lv C, Wang R, Cui M. Mineral dissolution and mobilization during CO₂ injection into the water-flooded layer of the Pucheng Oilfield, China. *J Nat Gas Sci Eng.* 2016;33:1364–1373.
- Othman F, Yu M, Kamali F, Hussain F. Fines migration during supercritical CO₂ injection in sandstone. *J Nat Gas Sci Eng.* 2018;56:344–357.
- Low salinity water flooding in carbonate reservoirs—dissolution effect. In: Hadi Y, Hussain F, Othman F, eds. *IOP Conference Series: Materials Science and Engineering.* IOP Publishing; 2019.
- Guo Z, Hussain F, Cinar Y. Physical and analytical modelling of permeability damage in bituminous coal caused by fines migration during water production. *J Nat Gas Sci Eng.* 2016;35:331–346.
- Bai T, Chen Z, Aminossadati SM, Pan Z, Liu J, Li L. Characterization of coal fines generation: a micro-scale investigation. *J Nat Gas Sci Eng.* 2015;27:862–875.
- Bai T, Chen Z, Aminossadati SM, Li L, Liu J, Lu H. Dimensional analysis and prediction of coal fines generation under two-phase flow conditions. *Fuel.* 2017; 194:460–479.
- Timoshenko S, Goodier JN. *Theory of Elasticity.* McGraw-Hill; 1951.
- Robinson ES. Mechanical disintegration of the Navajo sandstone in zion canyon, Utah. *Geol Soc Am Bull.* 1970;81(9):2799–2806.
- Young AP, Ashford SA. Instability investigation of cantilevered seacliffs. *Earth Surf Process Landforms: J British Geomorphol Res Group.* 2008;33(11):1661–1677.
- Potyondy DO, Cundall P. A bonded-particle model for rock. *Int J Rock Mech Min Sci.* 2004;41(8):1329–1364.
- Abousleiman Y, Hull K, Han Y, et al. The granular and polymer composite nature of kerogen-rich shale. *Acta Geotechnica.* 2016;11(3):573–594.
- Allison PG, Moser RD, Schirer JP, Martens RL, Jordon JB, Chandler MQ. In-situ nanomechanical studies of deformation and damage mechanisms in nanocomposites monitored using scanning electron microscopy. *Mater Lett.* 2014; 131:313–316.
- Khoo HS, Liu K-K, Tseng F-G. Mechanical strength and interfacial failure analysis of cantilevered SU-8 microposts. *J Micromech Microeng.* 2003;13(6):822.
- Liu H-K, Pan C, Liu P-P. Dimension effect on mechanical behavior of silicon micro-cantilever beams. *Measurement.* 2008;41(8):885–895.

- 41 Darnbrough J, Liu D, Flewitt P. Micro-scale testing of ductile and brittle cantilever beam specimens in situ with a dual beam workstation. *Meas Sci Technol*. 2013;24(5), 055010.
- 42 Matoy K, Schönherr H, Detzel T, et al. A comparative micro-cantilever study of the mechanical behavior of silicon based passivation films. *Thin Solid Films*. 2009;518(1):247–256.
- 43 Stephens LS, Kelly KW, Simhadri S, McCandless AB, Meletis E. Mechanical property evaluation and failure analysis of cantilevered LIGA nickel microposts. *J Microelectromech Syst*. 2001;10(3):347–359.
- 44 Vallejo LE. Fissure parameters in stiff clays under compression. *J Geotech Eng*. 1989;115(9):1303–1317.
- 45 Akin ID, Likos W. Brazilian tensile strength testing of compacted clay. *Geotech Test J*. 2017;40(4):608–617.
- 46 Maltman AJ. Shear zones in argillaceous sediments—an experimental study. *Geol Soc, London, Special Publicat*. 1987;29(1):77–87.
- 47 Vallejo L, Shettima M, Alaasmi A. Unconfined compressive strength of brittle material containing multiple cracks. *Int J Geotech Eng*. 2013;7(3):318–321.
- 48 Zhang B-y, Li Q-m, Yuan H-n, Sun X. Tensile fracture characteristics of compacted soils under uniaxial tension. *J Mater Civ Eng*. 2015;27(10), 04014274.
- 49 Tschebatoroff F. The tensile strength of disturbed and recompacted soils. *Proc 3rd ICSMFE*. 1953;1(1953):207–210.
- 50 Kalhor A, Mirabi K. Experimental investigation of the geotextile effect on the strength of kaolinite clay. *Am J Scientific Res*. 2013;(89):47–59.
- 51 Maher M, Ho Y. Mechanical properties of kaolinite/fiber soil composite. *J Geotech Eng*. 1994;120(8):1381–1393.
- 52 Abdi MR, Mirzaeifar H. Effects of discrete short polypropylene fibers on behavior of artificially cemented kaolinite. *Int J Civ Eng*. 2016;14(4):253–262.
- 53 Feng R, Zhang Y, Rezagholi A, Roshan H, Sarmadivaleh M. Brittleness Index: from conventional to hydraulic fracturing energy model. *Rock Mech Rock Eng*. 2020;53(2):739–753.
- 54 Ren J, He H, Senetakis K. A Micromechanical-based investigation on the frictional behaviour of artificially bonded analogue sedimentary rock with calcium carbonate. *Pure Appl Geophys*. 2021;178(11):4461–4486.
- 55 Corkum A, Martin C. The mechanical behaviour of weak mudstone (Opalinus Clay) at low stresses. *Int J Rock Mech Min Sci*. 2007;44(2):196–209.
- 56 Mamen B, Kolli M, Ouedraogo E, Hamidouche M, Djoudi H, Fantozzi G. Experimental characterisation and numerical simulation of the thermomechanical damage behaviour of kaolinitic refractory materials. *J Australian Ceram Soc*. 2019;55(2):555–565.
- 57 Josh M, Esteban L, Delle Piane C, Sarout J, Dewhurst D, Clennell M. Laboratory characterisation of shale properties. *J Petrol Sci Eng*. 2012;88:107–124.
- 58 Huang T, Cao L, Cai J, Xu P. Experimental investigation on rock structure and chemical properties of hard brittle shale under different drilling fluids. *J Petrol Sci Eng*. 2019;181, 106185.
- 59 Zhao J, Cao Y, Wang L, Zhang H-J, He M-C. Investigation on atomic structure and mechanical property of Na- and Mg-montmorillonite under high pressure by first-principles calculations. *Minerals*. 2021;11(6):613.
- 60 Ding C, Hu D, Zhou H, Lu J, Lv T. Investigations of P-Wave velocity, mechanical behavior and thermal properties of anisotropic slate. *Int J Rock Mech Min Sci*. 2020;127, 104176.
- 61 Ranjith P, Viète DR, Chen BJ, Perera MSA. Transformation plasticity and the effect of temperature on the mechanical behaviour of Hawkesbury sandstone at atmospheric pressure. *Eng Geol*. 2012;151:120–127.
- 62 Choens R, Bauer S, Shalev E, Lyakhovskiy V. Modelling yield cap evolution in sandstone based on brittle creep experiments. *Int J Rock Mech Min Sci*. 2021;141, 104706.
- 63 Wang S, Xu W, Yang L. Experimental and elastoplastic model investigation on brittle-ductile transition and hydro-mechanical behaviors of cement mortar. *Construct Build Mater*. 2019;224:19–28.
- 64 Zhang X, Ranjith P, Ranathunga A, Li D. Variation of mechanical properties of bituminous coal under CO₂ and H₂O saturation. *J Nat Gas Sci Eng*. 2019;61: 158–168.
- 65 Zhang G, Ranjith P, Li Z, Gao M, Ma Z. Long-term effects of CO₂-water-coal interactions on structural and mechanical changes of bituminous coal. *J Petrol Sci Eng*. 2021;207, 109093.
- 66 Kim B-H, Larson MK. Laboratory investigation of the anisotropic confinement-dependent brittle-ductile transition of a Utah coal. *Int J Min Sci Technol*. 2021;31(1): 51–57.
- 67 Han Z, Yang H, He M. A molecular dynamics study on the structural and mechanical properties of hydrated kaolinite system under tension. *Mater Res Express*. 2019;6(8), 0850c3.
- 68 Yang H, He M, Lu C, Gong W. Deformation and failure processes of kaolinite under tension: insights from molecular dynamics simulations. *Sci China Phys Mech Astron*. 2019;62(6):1–9.
- 69 Yang H, Han Z, Hu J, He M. Defect and temperature effects on the mechanical properties of kaolinite: a molecular dynamics study. *Clay Miner*. 2019;54(2): 153–159.
- 70 Zhang L-L, Zheng Y-Y, Wei P-C, Diao Q-F, Yin Z-Y. Nanoscale mechanical behavior of kaolinite under uniaxial strain conditions. *Appl Clay Sci*. 2021;201, 105961.
- 71 Fjaer E, Holt RM, Horsrud P, Raaen AM. *Petroleum Related Rock Mechanics*. Elsevier; 2008.
- 72 Jaeger JC, Cook NG, Zimmerman R. *Fundamentals of Rock Mechanics*. John Wiley & Sons; 2009.
- 73 Huang F, Kang Y, You Z, You L, Xu C. Critical conditions for massive fines detachment induced by single-phase flow in coalbed methane reservoirs: modeling and experiments. *Energy Fuels*. 2017;31(7):6782–6793.
- 74 Wagner TJ, James TD, Murray T, Vella D. On the role of buoyant flexure in glacier calving. *Geophys Res Lett*. 2016;43(1):232, 40A.
- 75 Chen X, Peng D, Morrissey JP, Ooi JY. A comparative assessment and unification of bond models in DEM simulations. *Granul Matter*. 2022;24(1):1–20.
- 76 O’neill M. A sphere in contact with a plane wall in a slow linear shear flow. *Chem Eng Sci*. 1968;23(11):1293–1298.
- 77 Ting HZ, Bedrikovetsky P, Tian ZF, Carageorgos T. Impact of shape on particle detachment in linear shear flows. *Chem Eng Sci*. 2021;241, 116658.
- 78 Derjaguin B, Landau L. The theory of stability of highly charged lyophobic sols and coalescence of highly charged particles in electrolyte solutions. *Acta Physicochim URSS*. 1941;14(633-52):58.
- 79 Verwey E, Overbeek JTG, Nes Kv. *Theory of the Stability of Lyophobic Colloids: The Interaction of Sol Particles Having an Electric Double Layer*. 1948.
- 80 Landau LD, Lifshitz EM. *Fluid Mechanics: Landau and Lifshitz: Course of Theoretical Physics*. um 6. Elsevier; 2013.
- 81 Yuan B, Moghanloo RG. Analytical modeling nanoparticles-fines reactive transport in porous media saturated with mobile immiscible fluids. *AIChE J*. 2019;65(10), e16702.
- 82 Yuan H, Shapiro AA. Induced migration of fines during waterflooding in communicating layer-cake reservoirs. *J Petrol Sci Eng*. 2011;78(3-4):618–626.
- 83 Ting HZ, Yang Y, Tian ZF, Carageorgos T, Bedrikovetsky P. Image interpretation for kaolinite detachment from solid substrate: type curves, stochastic model. *Colloids Surf A Physicochem Eng Asp*. 2022;650, 129451.
- 84 You Z, Bedrikovetsky P, Badalyan A, Hand M. Particle mobilization in porous media: temperature effects on competing electrostatic and drag forces. *Geophys Res Lett*. 2015;42(8):2852–2860.
- 85 Zhang H, Malgaresi G, Bedrikovetsky P. Exact solutions for suspension-colloidal transport with multiple capture mechanisms. *Int J Non Lin Mech*. 2018;105:27–42.
- 86 Teitelbaum Y, Shimony T, Saavedra Cifuentes E, et al. A novel framework for simulating particle deposition with moving bedforms. *Geophys Res Lett*. 2022;49(4), e2021GL097223.
- 87 Polyanin AD. *Linear Partial Differential Equations for Engineers and Scientists*. Chapman and Hall/CRC; 2002.
- 88 Polyanin AD, Zaitsev VF. *Nonlinear Partial Differential Equations*. New York: Chapman and Hall/CRC; 2004.
- 89 Zoback MD. *Reservoir Geomechanics*. Cambridge university press; 2010.
- 90 Cai W, Dou L, Ju Y, Cao W, Yuan S, Si G. A plastic strain-based damage model for heterogeneous coal using cohesion and dilation angle. *Int J Rock Mech Min Sci*. 2018;110:151–160.
- 91 Yuan B, Moghanloo RG. Nanofluid pre-coating: an effective method to reduce fines migration in radial systems saturated with two mobile immiscible fluids. *SPE J*. 2018;23:998–1018, 03.
- 92 Huang F, Dong C, You Z, Shang X. Detachment of coal fines deposited in proppant packs induced by single-phase water flow: theoretical and experimental analyses. *Int J Coal Geol*. 2021;239, 103728.
- 93 Ochi J, Vernoux J-F. Permeability decrease in sandstone reservoirs by fluid injection: hydrodynamic and chemical effects. *J Hydrol*. 1998;208(3-4):237–248.
- 94 Torkezaban S, Bradford SA, Vanderzalm JL, Patterson BM, Harris B, Prommer H. Colloid release and clogging in porous media: effects of solution ionic strength and flow velocity. *J Contam Hydrol*. 2015;181:161–171.
- 95 Ado MR. Improving heavy oil production rates in Thai process using wells configured in a staggered line drive (SLD) instead of in a direct line drive (DLD) configuration: detailed simulation investigations. *J Pet Explor Prod Technol*. 2021;11(11):4117–4130.
- 96 Gao CH. Scientific research and field applications of polymer flooding in heavy oil recovery. *J Pet Explor Prod Technol*. 2011;1(2):65–70.
- 97 Shi J-Q, Durucan S, Fujioka M. A reservoir simulation study of CO₂ injection and N₂ flooding at the Ishikari coalfield CO₂ storage pilot project. *Japan. Int J Greenhouse Gas Control*. 2008;2(1):47–57.
- 98 Simulation of immiscible CO₂ injection in a fractured carbonate reservoir, Bati Raman Field. In: Spivak A, Karaoguz D, Issever K, Nolen J, eds. *SPE California Regional Meeting*. Turkey: OnePetro; 1989.
- 99 Success story of optimizing hydraulic fracturing Design at alpha low-permeability reservoir. In: Prasetyo MH, Anggraini H, Tjahjono H, et al., eds. *SPE/IATMI Asia Pacific Oil & Gas Conference and Exhibition*. OnePetro; 2021.
- 100 Gao F, Stead D, Kang H. Numerical investigation of the scale effect and anisotropy in the strength and deformability of coal. *Int J Coal Geol*. 2014;136:25–37.
- 101 Guo W-Y, Tan Y-L, Yu F-H, et al. Mechanical behavior of rock-coal-rock specimens with different coal thicknesses. *Geomech. Eng*. 2018;15(4):1017–1027.
- 102 Horabik J, Jozefaciuk G. Structure and strength of kaolinite–soil silt aggregates: measurements and modeling. *Geoderma*. 2021;382, 114687.
- 103 Bedrikovetsky P. *Mathematical Theory of Oil and Gas Recovery*. Springer Science & Business Media; 2013.
- 104 Hashemi A, Borazjani S, Dang-Le B, et al. Formation damage by fines breakage and migration. February. In: *SPE International Conference and Exhibition on Formation Damage Control*. SPE; 2022. D011S002R006.
- 105 Hashemi A, Borazjani S, Nguyen C, et al. Fines migration and production in CSG reservoirs: laboratory & modelling study. In: *SPE Asia Pacific Oil & Gas Conference and Exhibition*. OnePetro; 2022. October.
- 106 Othman F, Naufaliansyah MA, Hussain F. Effect of water salinity on permeability alteration during CO₂ sequestration. *Adv Water Resour*. 2019 May 1;127:237–251.
- 107 Wang Y, Almutairi ALZ, Timms WA, Privat KL, Bhattacharyya SK, Le-Hussain F. In-situ fines migration and grains redistribution induced by mineral reactions—Implications for clogging during water injection in carbonate aquifers. *J Hydrol*. 2022;614, 128533.

7. Rock fines breakage by flow-induced stresses against drag: geo-energy applications

Sara Borazjani, **Abolfazl Hashemi**, Cuong Nguyen, Grace Loi, Thomas Russell,
Nastaran Khazali, Yutong Yang, Bryant Dang-Le, Pavel Bedrikovetsky

Geomechanics and Geophysics for Geo-Energy and Geo-Resources

Statement of Authorship

Title of Paper	Rock fines breakage by flow-induced stresses against drag: geo-energy applications
Publication Status	<input type="checkbox"/> Published <input checked="" type="checkbox"/> Submitted for Publication <input type="checkbox"/> Accepted for Publication <input type="checkbox"/> Unpublished and Unsubmitted work written in manuscript style
Publication Details	Sara Borazjani, Abolfazl Hashemi, Cuong Nguyen, Grace Loi, Thomas Russell, Nastaran Khazali, Yutong Yang, Bryant Dang-Le, Pavel Bedrikovetsky, Rock fines breakage by flow-induced stresses against drag: geo-energy applications, Submitted to Geomechanics and Geophysics for Geo-Energy and Geo-Resources

Principal Author

Name of Principal Author (Candidate)	Sara Borazjani		
Contribution to the Paper	Co-supervising, performing the derivations of equations and checking the results, and writing the manuscript.		
Certification:	This paper reports on original research I conducted during the period of my Higher Degree by Research candidature and is not subject to any obligations or contractual agreements with a third part that would constrain its inclusion in this thesis. I am the primary author of this paper.		
Signature		Date	15/11/2023

Co-Author Contributions

By signing the Statement of Authorship, each author certifies that:

- I. The candidate's stated contribution to the publication is accurate (as detailed above);
- II. Permission is granted to the candidate to include the publication in the thesis; and
- III. The sum of all co-author contributions is equal to 100% less the candidate's stated contribution

Name of Co-Author	Abolfazl Hashemi		
Contribution to the Paper	Deriving the equations, preparing the final results, writing part of the manuscript.		
Overall percentage (%)	45%		
Signature		Date	15/11/2023

Name of Co-Author	Cuong Cao Nguyen		
Contribution to the Paper	Collecting literature data, writing code, and analysing detrital particle detachment		
Signature		Date	15/11/2023

Name of Co-Author	Grace Loi		
Contribution to the Paper	Collecting literature data, writing code, and analysing detrital particle detachment		
Signature		Date	15/11/2023

Name of Co-Author	Thomas Russell		
Contribution to the Paper	Co-supervising, aiding in the derivations of DLVO equations and checking the DLVO results, giving consultation on the total MRF, giving advice, and proofreading the manuscript.		
Signature		Date	15/11/2023

Name of Co-Author	Nastaran Khazali		
Contribution to the Paper	Deriving equations and matching lab data using two-population particle detachment mechanism.		
Signature		Date	15/11/2023

Name of Co-Author	Yutong Yang		
Contribution to the Paper	Performing sensitivity on MRF, collecting field data for fluid velocity through fracture and fault, and preparing cross plots.		
Signature		Date	15/11/2023

Name of Co-Author	Bryant Dang-Le		
Contribution to the Paper	Collecting and analysing lab data, collecting field data.		
Signature	Bryant Dang-Le	Date	15/11/2023

Name of Co-Author	Pavel Bedrikovetsky		
Contribution to the Paper	Methodology and supervision.		
Signature		Date	15/11/2023

1 Rock fines breakage by flow-induced stresses against drag: geo-energy applications

2 Sara Borazjani, Abolfazl Hashemi, Cuong Nguyen, Grace Loi, Thomas Russell, Nastaran Khazali, Yutong Yang,
3 Bryant Dang-Le, Pavel Bedrikovetsky

4 *School of Chemical Engineering, The University of Adelaide 5000, SA, Australia*

5 **Abstract** The paper presents a strength-failure mechanism for colloidal detachment by breakage and
6 permeability decline in reservoir rocks. The current theory for permeability decline due to colloidal detachment,
7 including microscale mobilisation mechanisms, mathematical and laboratory modelling, and upscaling to natural
8 reservoirs, is developed only for *detrital particles* with detachment that occurs against electrostatic attraction. We
9 establish a theory for detachment of widely spread *authigenic particles* due to breakage of the particle-rock bonds,
10 by integrating beam theory of particle deformation, failure criteria, and creeping flow. Explicit expressions for
11 stress maxima in the beam yield a graphical technique to determine the failure regime. The core-scale model for
12 fines detachment by breakage has a form of maximum retention concentration of the fines, expressing rock
13 capacity to produce breakable fines. This closes the governing system for authigenic fines transport in rocks.
14 Matching of the lab coreflood data by the analytical model for 1D flow exhibit two-population particle behaviour,
15 attributed to simultaneous detachment and migration of authigenic and detrital fines. High agreement between the
16 laboratory and modelling data for 16 corefloods validates the theory. The work is concluded by geo-energy
17 applications to (i) clay breakage in geological faults, (ii) typical reservoir conditions for kaolinite breakage, (iii)
18 well productivity damage due to authigenic fines migration, and (iv) feasibility of fines breakage in various geo-
19 energy extraction technologies.

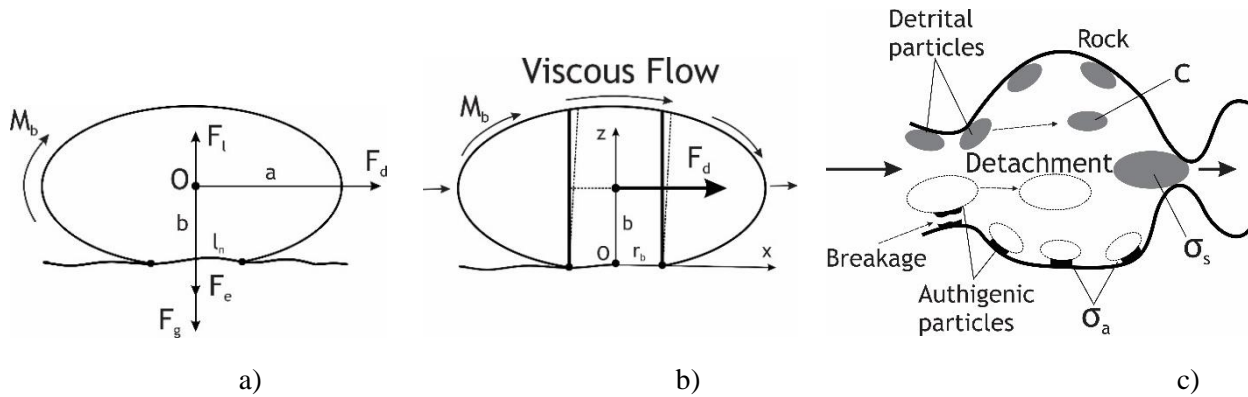
20 1. Introduction

21 The geomechanics of rock failure under high stress with consequent permeability alteration is a wide and long-
22 studied topic in geo-energy engineering. An incomplete list includes mining operation studies in gas-bearing coals
23 (Wang et al. 2022a, Xu et al. 2022), geo-engineering applications in granites (Kumari et al. 2019), loading of
24 lamellar continental shales (Duan et al. 2022), cyclic hydraulic fracturing for geothermal reservoir stimulation (Li
25 et al. 2022), drainage technology of CBM fields (Xue et al. 2022), mechanical failure of hydrate-bearing sediments
26 (Hou et al. 2022), and wellbore stability during drilling (Wang et al. 2022b). Yet, the studies of detachment of a
27 single reservoir fines by breakage and the migration-induced permeability decline are not available.

28 However, transport in porous and fractured media strongly depend on colloidal detachment, migration, straining,
29 and consequent permeability decline (Chen et al. 2008, Teitelbaum et al. 2022, Cao et al. 2023). The permeability
30 decrease yields well productivity and injectivity decline, while preferential permeability decline in high-
31 conductivity layers and patterns of natural reservoirs uniformises the flux and increases sweep efficiency
32 (Bedrikovetsky 2013). Mineral dissolution and precipitation reactions during injection of CO₂ or hydrogen into
33 underground gas storages, cause fines mobilisation and migration; the resulting sweep enhancement leads to the
34 storage capacity increase (Iglauer et al. 2015, 2021, 2022, Alzate-Espinosa 2023). Detachment of colloidal and
35 nano particles highly affects oil and gas production under migration of natural reservoir fines, water injection into
36 aquifers and petroleum reservoirs, geothermal energy recovery, coal bed methane production, storage of fresh and
37 hot water in aquifers, propagation of contaminants, bacteria and viruses, invasion of ocean into aquifers, soil
38 erosion and construction collapse, and analysis of seismic earthquake events (Zhao et al. 2014, Fox et al. 2018,
39 Drummond et al. 2019, Hu et al. 2021, Lehman et al. 2021, Liao et al. 2021, Lu et al. 2021, Sun and Xiang 2021,
40 Wurgaft et al. 2021).

41 Typical migrating fines comprise clays, while silt, silica, and coal particles can be mobilised too (Fox et al. 2018,
42 Farrell et al. 2021, Cao et al. 2023). Two types of natural fines are distinguished in the rocks: *authigenic fines*, that
43 have been grown up on the grain surfaces during geological times and are bonded to the surface, and the *detrital*
44 *fines* that have been carried by subterranean waters to a given reservoir point and attached to the rock surface
45 (Wilson et al. 1977, Appelo and Postma 2004, Farrell et al. 2021). Detrital kaolinite is attached to the grain surface
46 by electrostatic attraction (Fig. 1a), while the authigenic kaolinite bond the grain surface (Fig. 1b). The detachment

47 of detrital particles against electrostatic attraction and authigenic particles by breakage, under high velocities in
 48 pore throat is presented in Fig. 1c.



49

50

51 Figure 1. Detachment for detrital and authigenic clay particles: a) force (torque) balance at attached detrital fine; b)
 52 representation of attached authigenic particle by deformable beam (Obermayr et al. 2013); c) schematic for detachment against
 53 electrostatic attraction and by breakage at the pore scale.

54 Current mathematical and lab modelling for *detachment of detrital fines* is based on the mechanical equilibrium
 55 of a particle situated on the solid substrate; Fig. 1a shows drag, electrostatic, lift, and gravity forces exerting on an
 56 isolated particle. Presence of a second phase adds capillary force, which is wettability dependent (Roshan et al.
 57 2016, Siddiqui et al. 2019). The linear-kinetics model for fines detachment assumes that detachment rate is
 58 proportional to the difference between current and equilibrium retention concentrations, with an empirical
 59 proportionality coefficient that is equal to the inverse of detachment time (Bradford et al. 2013, Johnson and
 60 Pazmino 2023). In the alternative theory, the maximum retention concentration of the attached fines, as a function
 61 of velocity, salinity, temperature, and pH, defines fines detachment (Bedrikovetsky et al. 2011, 2012). This
 62 maximum retention function (MRF) closes the system of governing equations for colloidal transport in porous
 63 media and yields several exact solutions for 1D flows (Polyanin 2002, Polyanin and Zaitsev 2012). The MRF
 64 model has been validated by extensive laboratory studies and is widely used for prediction of colloidal transport
 65 (Yuan and Shapiro 2011, Guo et al. 2016, Yuan and Moghanloo 2018, 2019, Zhai and Atefi-Monfared 2021).

66 *Detachment of authigenic fines* by breakage under flows in porous media has been observed by Turner et al. 2016
 67 and Wang et al. 2020 during well acidizing, by Tang et al. 2016 and Othman et al. 2018 for cement dissolution in
 68 sandstones, by Hadi et al. 2019 for carbonate rock dissolution in water, by Mishra et al. 2016 during sand
 69 production, and by Liu et al. 2019 for hydraulic fracturing. Yet, a geo-mechanical analysis and mathematical model
 70 for authigenic particle detachment and migration is not available.

71 The current paper fills the gap. A novel micro-scale model for authigenic particle detachment is derived by
 72 integration of beam theory of elastic particle deformation and strength failure with viscous flow model around the
 73 attached fines. Introduction of tensile-stress and tensile-shear diagrams allows determining the regime of particle-
 74 rock-bond failure. The breakage condition has a form of breakage velocity versus micro-scale geo-mechanical
 75 parameters, which yields maximum concentration of authigenic particles versus velocity, that closes the system of
 76 governing equations. We successfully match 16 coreflood tests under piecewise-constant increasing rate by the
 77 analytical model for colloidal flow with breakage. The laboratory-based analytical model for particle detachment
 78 by breakage (i) shows feasibility of authigenic fines mobilisation in geological faults, (ii) allows calculating the
 79 fraction of detachable authigenic fines in natural rocks and estimation the range of breaking velocities, (iii) permits
 80 predicting of well productivity decline, and (iv) claims that fines breakage is feasible in major geo-energy
 81 technologies.

82 The structure of the paper is as follows. Section 2 derives the microscale mechanical conditions of attached fines
 83 mobilisation by breakage. Section 3 defines maximum retention concentration (MRF) for authigenic fines as a
 84 rock-scale model for fines mobilisation by breakage and the analytical model for 1D flows. Section 4 matches the
 85 laboratory coreflood data by the analytical model and validates the breakage-detachment model. Section 5

86 investigates breakage of authigenic clays in geological faults. Section 6 determines the fractions of detachable
 87 fines and of authigenic particles using the analytical model. Section 7 recalculates lab results into the well-
 88 productivity data. Section 8 investigates the feasibility of fines breakage in various technological geo-energy
 89 processes. Section 9 discusses the limitations of the developed breakage-detachment model. Section 10 concludes
 90 the paper.

91 **2. Model for beam deformation under creeping flow**

92 Derivation of the microscale model for fines detachment by breakage during viscous flow encompasses mechanical
 93 equilibrium of attached particle (section 2.1 and Appendix A), expressions for stress maxima (section 2.2 and
 94 Appendix B), and graphical classification of the breakage regimes (section 2.3).

95 **2.1. Definition of mechanical equilibria of detaching particles**

96 The microscale model of a single fine detachment by breakage, presented in this section, integrates beam theory
 97 for elastic cylinder deformation (Timoshenko and Goodier 1970) with strength failure criteria for particle-rock
 98 bond (Fjaer et al. 2008, Jaeger et al. 2009) and creeping flow around the particle (Tu et al. 2018). The model
 99 assumes negligible lift exerting the particle from the flux and low beam deformations under slow Darcy's flows
 100 in porous media. We discuss spheroidal and thin-cylinder shapes for kaolinite, chlorite, and silica fines, and long
 101 cylinders for illite fines (Appelo and Postma 2004). A circular particle-rock contact area is assumed. The rock
 102 deformation outside the beam stem is significantly lower than beam deformation; this supports the assumption that
 103 maximum stress in the contact particle-substrate area due to drag is fully determined by the deformation of the
 104 cylindric beam with the base on substrate (Obermayer et al. 2013, Wagner et al. 2016, Chen et al. 2022) (Fig. 1b).
 105 Following the lab data by Abousleiman 2016, Han et al. 2019, Yang et al. 2019, Feng et al. 2020, Ren et al. 2021,
 106 brittle breakage of the particle-substrate bond is assumed.

107 Drag F_d and its moment M_b for oblate spheroidal and cylindric particles are extensions of the Stokes formula that
 108 is valid for spheres (Ting et al. 2021, 2022). The dimensionless shape factors are calculated from numerical
 109 solution of Navier-Stokes flow around the particle:

$$110 \quad F_d = 6\pi\mu_f r_s V f_d(\alpha_s), \quad M_b = F_d b f_M(\alpha_s) = 6\pi\mu_f r_s V f_d(\alpha_s) b f_M(\alpha_s), \quad \alpha_s = b/a \quad (1)$$

111 where a and b are the semi-major and semi-minor of spheroid, respectively, and α_s is the aspect ratio. We derive
 112 the empirical formulae for drag and torque factors for long cylinders, given by Eqs (A1) and (A2), based on
 113 numerous runs of CFD software ANSYS/CFX.

114 The drag and torque (1) determine an external load in Timoshenko's solution for elastic beam, given by Eqs. (B1-
 115 B4). More detailed formulation of 3D elasticity problem is available from Hashemi et al. 2023. The principal
 116 stresses σ_1 , σ_2 , and σ_3 are calculated as eigen values of the stress tensor (B5); their maxima are determined using
 117 the Mohr circles and are determined by Eq. (B6). Finally, maximum tensile and shear stresses are:

$$118 \quad \max \sigma = \sigma_3, \quad \max \tau = \frac{\sigma_1 - \sigma_3}{2}, \quad (2)$$

119 The expressions for tensile and shear stresses over the beam base follow from the solution of elastic beam
 120 deformation (B1-B4); here axi are shown in Fig. 1b:

$$121 \quad \frac{\sigma_3}{T_0} = \frac{1}{\kappa} \left(X - \sqrt{X^2 + \chi \left(1 - X^2 - \frac{(1-2\nu)}{(3+2\nu)} Y^2 \right)^2} + \chi \frac{4(1+2\nu)^2}{(3+2\nu)^2} (XY)^2 \right) \quad (3)$$

122

$$\frac{\sigma_1 - \sigma_3}{2S_0} = \frac{\eta}{\kappa} \sqrt{X^2 + \chi \left(1 - X^2 - \frac{(1-2\nu)}{(3+2\nu)} Y^2 \right)^2 + \chi \frac{4(1+2\nu)^2}{(3+2\nu)^2} (XY)^2} \quad (4)$$

123

124

125

where T_0 and S_0 are the tensile and shear strengths, respectively. Here the dimensionless groups reflecting the interaction between the creeping flow around an attached particle and elastic deformation inside the particle - *strength-drag number* κ , *shape-Poisson number* χ , and *strength number* η - are defined as

126

$$\frac{1}{\kappa} = \frac{F_d}{2T_0} \frac{r_b b f_M}{I} = \frac{F_d}{2T_0} \frac{\delta \alpha_s f_M}{I}, \quad \chi = \left[\frac{r_b}{b f_M} \frac{3+2\nu}{4(1+\nu)} \right]^2, \quad \eta = \frac{T_0}{S_0}, \quad \delta = \frac{r_b}{a}, \quad X = \frac{x}{r_b}, \quad Y = \frac{y}{r_b} \quad (5)$$

127

128

129

The *strength-drag number* κ is proportional to the ratio between the tensile strength T_0 and the average pressure imposed by drag and incorporates the bond δ and aspect α_s ratios. The *shape-Poisson number* χ includes the bond δ and aspect α_s ratios along with the Poisson's ratio ν .

130

131

132

Breakage of particle-rock bond is defined by the strength failure criterium, where either tensile or shear stress reaches the corresponding strength value; this maximum normalised stress becomes equal to one, while another normalised stress remains less than one upon the breakage (Jaeger et al. 2009):

133

$$\max_{X^2+Y^2 \leq 1} \frac{-\sigma_3(X,Y)}{T_0} \leq 1, \quad \max_{X^2+Y^2 \leq 1} \frac{\sigma_1(X,Y) - \sigma_3(X,Y)}{2S_0} \leq 1 \quad (6)$$

134

2.2. Derivation of stress maxima

135

136

137

138

139

140

Consider maxima of both tensile and shear stresses, which are given by Eqs. (3, 4). The detailed derivations are presented in Hashemi et al. 2023. If maxima points (X_m, Y_m) are located inside the base circle, $X_m^2 + Y_m^2 < 1$, partial derivatives of both expressions (3, 4) over Y must be zero. It is possible to show that only along the middle of the beam base $Y=0$, partial derivatives over Y are equal zero and second partial derivatives over Y are negative. Therefore, all maxima inside the base circle $X_m^2 + Y_m^2 < 1$ are reached along the middle of the base, i.e., axis $Y=0$. Otherwise, tensile or shear stresses reaches maxima at the beam base over the boundary $X_m^2 + Y_m^2 = 1$.

141

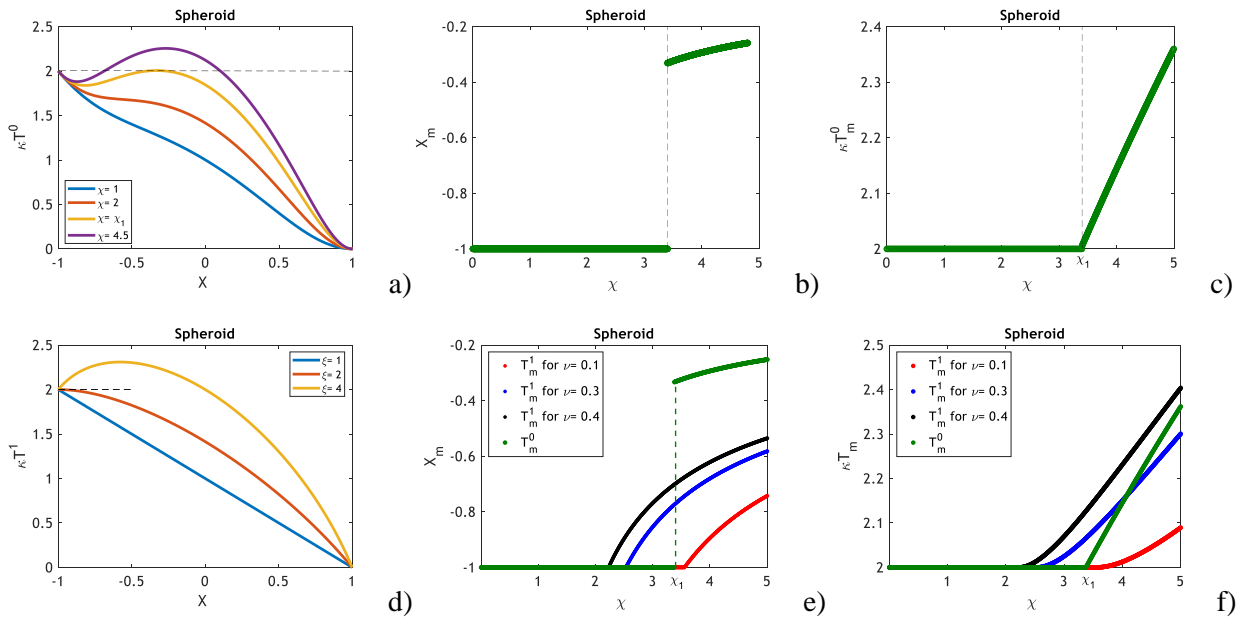
142

143

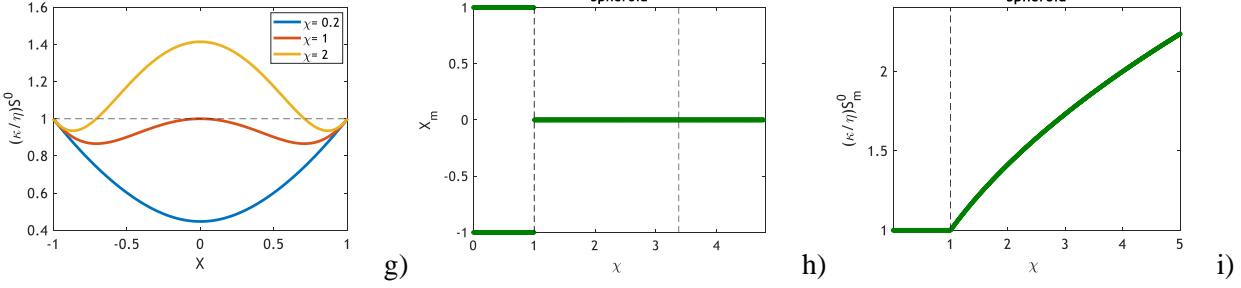
144

The stresses along the beam middle and its boundary are functions of variable X alone. The profiles for tensile stress in the middle of the beam, tensile stress at the beam boundary, and shear stress at the boundary are shown in Figs. 2a, 2d, and 2g, respectively. Figs. 2b, 2e, and 2h show the point X_m where maximum is reached, for those 3 cases. Figs. 2c, 2f, and 2i present the maxima values.

145



146



147

148 Figure 2. Maximum dimensionless stresses at the beam base versus shape-Poisson number χ : a) Maximum tensile stress along
 149 the axes $Y=0$; b) Maximum tensile stress at the beam boundary; c) Maximum shear stress along the axes $Y=0$; d) Maximum
 150 shear stress along the beam boundary.

151 Tensile stress $T^0(X, \chi)$ reaches maximum in the advanced point $X_m = -1$ and then monotonically decreases for small
 152 shape-Poisson numbers. At the bifurcation value $\chi_1 = 3.38$ the profile reaches second maximum at $X_{m1} = -0.33$. For χ
 153 $> \chi_1$, maximum point moves to the right, and maximum increases. Maximum point X_m and corresponding tensile
 154 stress maximum T_m^0 depend on shape-Poisson number alone. The maximum point and its value are calculated
 155 from the conditions of zero first derivative and negative second derivative in X :

$$156 \quad T_m^0(\chi) = \frac{1}{\kappa} \begin{cases} 2, & \chi \leq \chi_1 \\ -X_m(\chi) + \sqrt{X_m^2 + \chi(1 - X_m^2)^2}, & \chi > \chi_1 \end{cases}; \quad X_m = \begin{cases} -1, & \chi \leq \chi_1 \\ -\sqrt{\frac{\sqrt{(4\chi-1)(4\chi-9)} - 4\chi + 3}{8\chi}}, & \chi > \chi_1 \end{cases} \quad (7)$$

157 Profile of tensile stress over the beam boundary also depends on parameter ξ alone that incorporates χ and ν :

$$158 \quad T_m^1(\chi, \nu) = \frac{1}{\kappa} \begin{cases} 2, & \xi \leq 2 \\ \xi(\xi-1)^{-0.5}, & \xi > 2 \end{cases}; \quad X_m = \begin{cases} -1, & \xi \leq 2 \\ -(\xi-1)^{-0.5}, & \xi > 2 \end{cases}; \quad \xi = \chi \frac{4(1+2\nu)^2}{(3+2\nu)^2} \quad (8)$$

159 The profile for $T^l(X, \xi)$ reaches maximum at advanced point $X_m = -1$ and monotonically decreases for $X > -1$ from
 160 advanced point $X_m = -1$ for small ξ . From bifurcation value $\xi = 2$ on, $T^l(X, \xi)$ loses monotonicity, maximum point X_m
 161 moves from advanced point $X_m = -1$ to the right.

162 At low χ , maximum for shear in the base middle is reached at advanced and receded points. This occurs until
 163 bifurcation value $\chi = 1$, where X_m jumps into the origin $X_m = 0$. For $\chi > 1$, the maximum point for shear stress in the
 164 base middle remains in origin and monotonically increases:

$$165 \quad S_m^0(\chi) = \frac{\eta}{\kappa} \begin{cases} 1, & \chi < 1 \\ \sqrt{\chi}, & \chi > 1 \end{cases}; \quad X_m = \begin{cases} \pm 1, & \chi < 1 \\ 0, & \chi > 1 \end{cases}; \quad \eta = \frac{T_0}{S_0} \quad (9)$$

166 Maximum of shear over the boundary is lower than the shear maximum in the base middle for all values of shape-
 167 Poisson numbers and Poisson's ratio – $S_m^l(\chi, \nu) < S_m^0(\chi, \nu)$ – and is not considered to fulfil failure criteria.

168 Eqs. (7-9) show that stress maxima along the axis $Y=0$ are determined by aspect-Poisson number χ alone, while
 169 the maxima at the beam boundary are determined by both aspect-Poisson number χ and Poisson's ratio ν .

170 2.3. Classification of breakage regimes

171 Depending on shape-Poisson number and Poisson's ratio, either of three stresses (7), (8), or (9) can exceed the
 172 other two and fulfil the strength failure criteria (6). Let us first define the largest from the two tensile stress maxima,
 173 (7) or (8). Their equality $T_m^0(\chi, \nu) = T_m^l(\chi, \nu)$ divides plane (χ, ν) , which further in the text we call tensile stress
 174 diagram, into 5 regions. Black curve corresponds to $\xi = 2$. Blue and red curves are calculated from Eqs. (7) and (8)
 175 for $\xi > 2$:

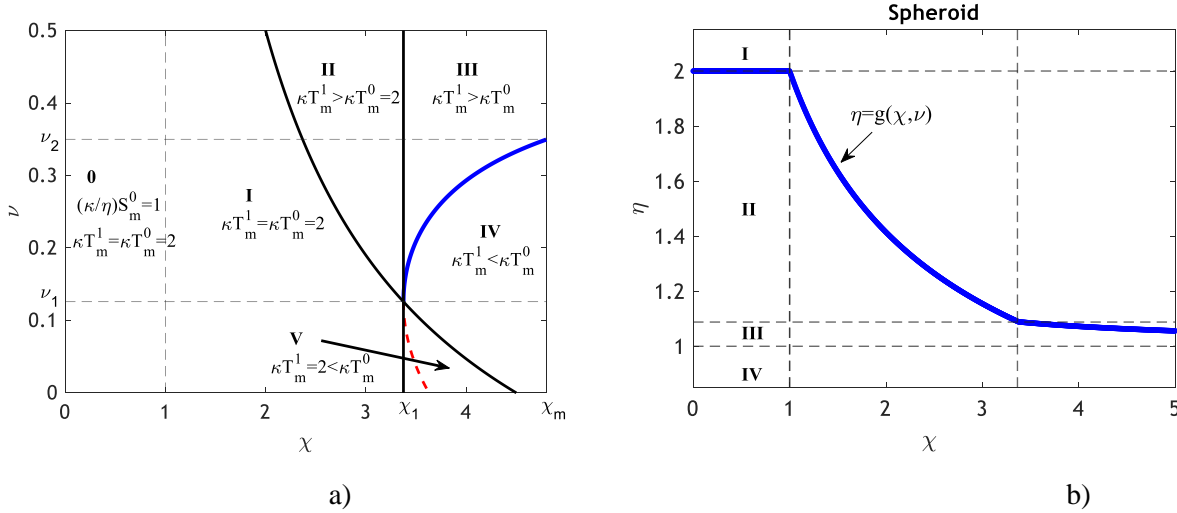
$$v_m(\chi) = \frac{3\sqrt{(\kappa T_m^0(\chi))^2 \pm \kappa T_m^0(\chi)\sqrt{(\kappa T_m^0(\chi))^2 - 4} - \sqrt{8\chi}}}{4\sqrt{2\chi} - 2\sqrt{(\kappa T_m^0(\chi))^2 \pm \kappa T_m^0(\chi)\sqrt{(\kappa T_m^0(\chi))^2 - 4}}} \quad (10)$$

176

177

178

and correspond to positive and negative values of the root in Eq. (10). Along the red curve, inequality $\xi > 2$ holds, while domain V is located below black curve, so the red curve must be ignored.



179

180

181

182

Figure 3. Classification of bond breakage regimes by tensile and shear stresses: a) tensile stress diagram; b) shear-tensile diagram.

183

184

185

The black curve, the vertical straight line $\chi = \chi_I$, and the blue curve divide (χ, ν) plane into 5 domains, depending on superiority of either of the two tensile stress maxima (Fig. 3a). The three lines cross in one point ($\chi = \chi_I, \nu = \nu_I$) where $\nu_I = 0.125$ is obtained from Eq. 10.

186

187

Now let us determine whether shear S_m^0 exceeds maximum of two tensile stresses. Define the breakage regime function

188

$$g(\chi, \nu) = \frac{T_m(\chi, \nu)}{S_m^0(\chi)} > \frac{T_0}{S_0} = \eta; \quad T_m(\chi, \nu) = \max\{T_m^0(\chi), T_m^1(\chi, \nu)\} \quad (11)$$

189

190

191

At breakage, maximum normalised stress is equal one. Therefore, as it follows from Eqs. (6), the breakage occurs due to tensile stress if $g(\chi, \nu) > \eta$. Otherwise, the breakage occurs due to shear stress. Further in the text, (χ, η) -plane with the curve $\eta = g(\chi, \nu)$ is called the shear-tensile diagram (Fig. 3b).

192

193

For all χ and ν values, breakage regime function exceeds one and does not exceed two. Depending on stress η and shape-Poisson numbers, and Poisson's ratio, the breakage curve exhibits 4 cases presented in plane (χ, η) :

194

I - For strength ratios exceeding 2, particles are detached by shear stress for all values of χ and ν ;

195

196

II - For strength ratios below two and above one, the particles are detached by shear stress for shape-Poisson number χ that does not exceed the value determined by $g(\chi, \nu) = \eta$;

197

198

III - For strength ratios below two and above one, the particles are detached by tensile stress for shape-Poisson number χ that exceeds the value determined by $g(\chi, \nu) = \eta$;

199

IV - For strength ratios lower than one, particles are detached by tensile stress for all values of χ and ν .

200

201

So, either of the 5 domains in tensile-stress diagram determines maximum tensile stress, and then either of the 4 cases in tensile-shear diagram determines which stress causes the breakage. For either of three stress cases (7), (8),

202 or (9), the normalised stress is equal one, allowing calculating stress-drag number κ . For the cases of domination
 203 of normalised tensile stress in the middle, tensile stress on the boundary, and shear stress in the middle, the
 204 formulae for strength-drag numbers κ are:

$$205 \quad \kappa = \begin{cases} 2, & \chi \leq \chi_1 \\ \sqrt{-\frac{\sqrt{(4\chi-1)(4\chi-9)}-4\chi+3}{8\chi}} + \sqrt{\left(\sqrt{-\frac{\sqrt{(4\chi-1)(4\chi-9)}-4\chi+3}{8\chi}}\right)^2} + \chi \left(1 - \left(\sqrt{-\frac{\sqrt{(4\chi-1)(4\chi-9)}-4\chi+3}{8\chi}}\right)^2\right), & \chi > \chi_1 \end{cases} \quad (12)$$

$$206 \quad \kappa = \begin{cases} 2, & \xi \leq 2 \\ \xi(\xi-1)^{-0.5}, & \xi > 2 \end{cases}; \quad \xi = \chi \frac{4(1+2\nu)^2}{(3+2\nu)^2} \quad (13)$$

$$207 \quad \kappa = \frac{T_0}{S_0} \begin{cases} 1, & \chi < 1 \\ \sqrt{\chi}, & \chi > 1 \end{cases}, \quad (14)$$

208 3. Macroscale model for fines migration with detachment by breakage

209 This section defines rock-scale model for detachment of authigenic fines by breakage (section 3.1) and its
 210 implementation into transport equations for the authigenic particles (section 3.2).

211 3.1. Maximum retention function as a rock-scale detachment model

212 Substitution of drag from Eq. (1) into the expression for strength-drag number (5) allows for exact expression for
 213 the breakage velocity:

$$214 \quad U_{cr}^b = \frac{\delta\phi T_0 r_b^2}{12\alpha_s f_M f_d \mu_f r_s} \kappa^{-1} \quad (15)$$

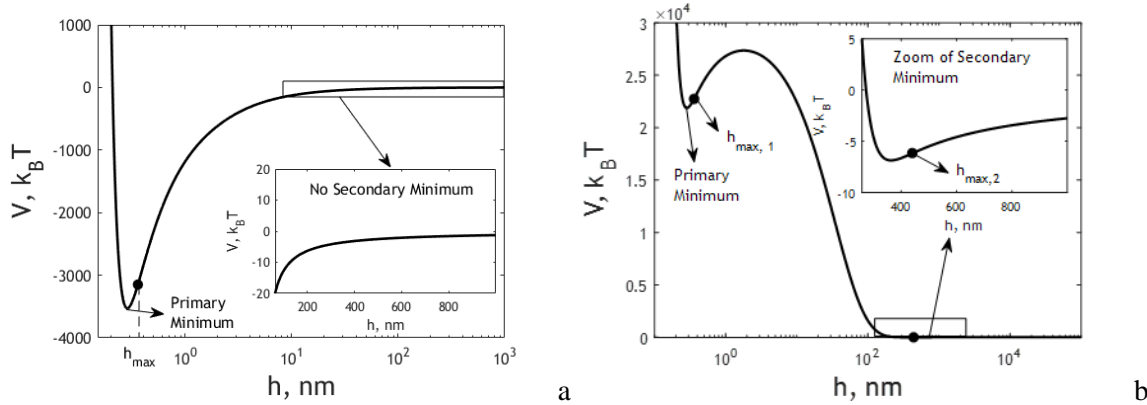
215 where κ is given by either of Eqs. (12-14). Consider the manifold of the particles attached to rock surface. The
 216 particles are stochastically distributed by fluid velocity around them near to asperous rock surface in pores of
 217 different forms and sizes, aspect, Poisson's, and bond ratios, sizes, strength, and bond radii. However, Eq. (15)
 218 determines the critical breakage velocity for each particle, defining whether the particle remains attached or breaks
 219 off the rock at a given flow velocity U . The concentration of the particles attached to rock at a given velocity is
 220 called the breakage maximum retention function (MRF) $\sigma_{cr}^b(U)$. MRF can be obtained by upscaling of Eq. (15)
 221 accounting for probabilistic distributions of coefficients δ , r_b , α_s , and r_s .

222 The maximum retention function for detachment against electrostatic DLVO attraction for detrital particles is
 223 determined by the torque balance between drag and electrostatic DLVO forces (Bradford et al. 2013):

$$224 \quad M_b = 6\pi\mu_f r_s V f_d(\alpha_s) b f_M(\alpha_s) = F_e(h) l_n, \quad F_d = 6\pi\mu_f r_s V f_d(\alpha_s) = v_C F_e(h), \quad (16)$$

225 where h is the distance between the particle and substrate.

226 Fig. 4 presents the energy profile for the DLVO forces (Israelashvili 2015). Fig. 4a shows the potential for coal
 227 fines and substrate with one energy minimum, while Fig. 4b shows two minima of the energy profile. During
 228 favourable attachment, the particle moves to the left from zero energy state to a single primary minimum. During
 229 unfavourable attachment, the particle moves to the left from zero energy to shallow secondary energy minimum
 230 and needs to overcome the energy barrier to get into primary energy minimum (Fig. 4b).



231
232 Fig. 4. DLVO energy profiles: a) coal fines and coal substrate; b) kaolinite fines and silica substrate.

233 Assuming that authigenic and detrital fines detach independently, the overall MRF is the total of individual ones:

$$234 \quad \sigma_{cr}(U) = \sigma_{cr}^e(U) + \sigma_{cr}^b(U), \quad \Delta\sigma_n = \sigma_{cr}(U_{n-1}) - \sigma_{cr}(U_n) \quad (17)$$

235 The total MRF defines the mobilised concentration by velocity increase from U_{n-1} to U_n . After mobilisation, the
236 detached fines migration is described by system of population balance accounting for particle capture by the rock.
237 MRF defines initial concentration of detached particles after abrupt change of flow rate.

238 3.2. Macroscale analytical model for colloidal transport in porous media

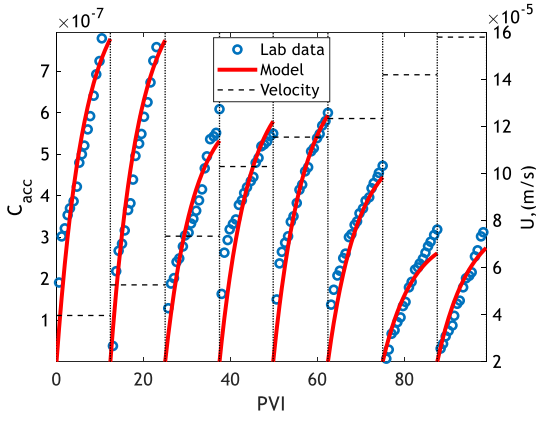
239 1D problems for fines migration with any arbitrary particle capture (filtration) function $\lambda(\sigma_s)$ and suspension
240 function $f(c)$ allow for exact solutions (Polyanin and Manzhirov 2006, Polyanin and Zaitsev 2012). In the case of
241 continuous rate increase, MRF determines the sources term in mass balance, closing the governing system for
242 colloidal-suspension transport (fines migration) in porous media (Bedrikovetsky et al. 2019). Here, for the sake of
243 simplicity, we discuss the model with constant filtration coefficient $\lambda = \text{const}$ and $f(c) = c$, in order to treat the limited
244 literature information on the corefloods with piecewise-constant increasing velocity.

245 Appendix C presents system of governing equations, which consists of the mass balance of suspended and strained
246 particles (C1), straining rate (C2), and Darcy's law accounting for permeability decline due to particle straining
247 (C3). For the case the corefloods with piecewise-constant increasing velocity $U_0=0, U_1, U_2, \dots$, fines detachment
248 occurs at moments of switching from velocity U_{n-1} to $U_n, n=1, 2, 3, \dots$, which is expressed by initial condition (C4).
249 The exact solution for 1D flow problem is expressed by Eqs. (C6) and (C7). The exact solution allows for explicit
250 expression of impedance (C9). Next section uses Eqs. (C-6) and (C9) to treat the lab data on breakthrough
251 concentration $c(l, t)$ and dimensionless pressure drop (impedance) $J(t)$ measured during the multi-rate corefloods.

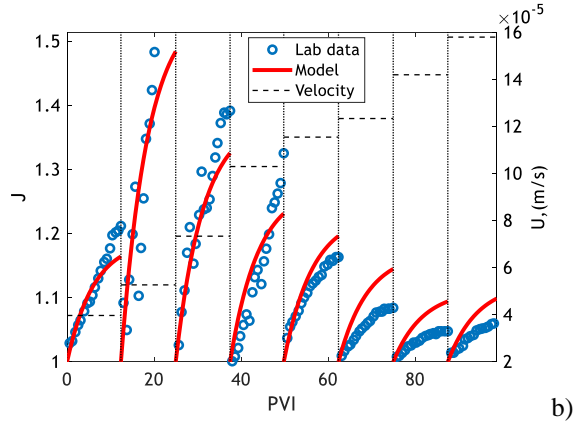
252 4. Laboratory study and model validation

253 Huang et al. 2017 used core sample from a coal seam reservoir located in the southern part of the Qinshui Basin
254 (China) for coreflooding. The laboratory study was comprised of water injection with 2% (weight percent) of KCl
255 into the anthracite coal core with permeability 21 mD and porosity 0.08. Core length was 5.16 cm. Fig. 5 shows
256 lab data during application of eight injection rates. The breakthrough concentration and pressure drop across the
257 core, have been measured during the overall test. Fig. 5a shows breakthrough concentration data and their matching
258 by the model. Fig. 5b presents the history of impedance.

259

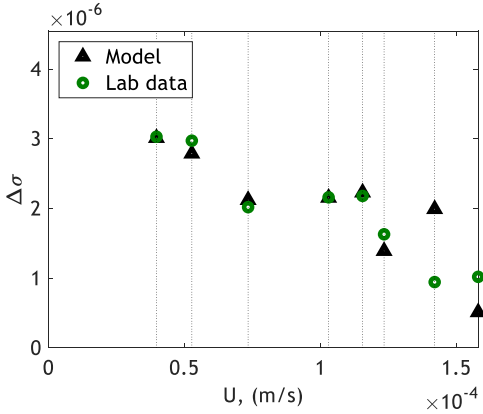


a)

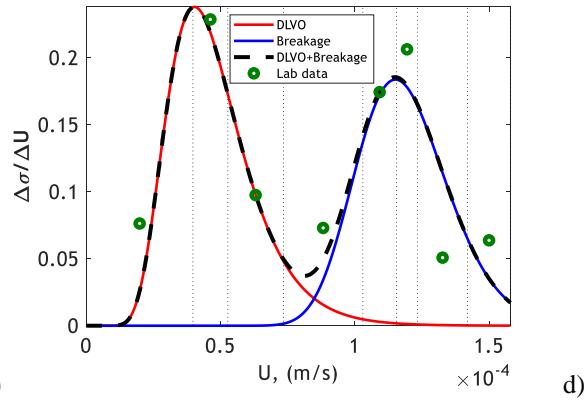


b)

260

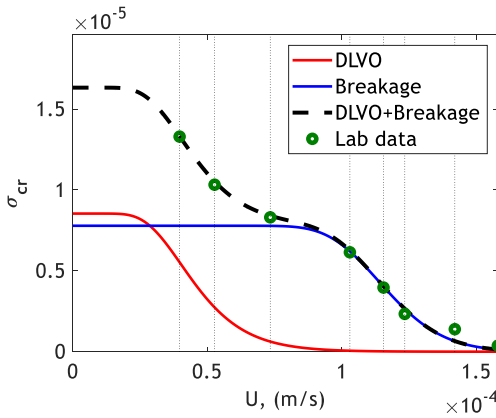


c)



d)

261



e)

262 Fig. 5. Matching lab data on authigenic and detrital fines migration in coal cores: a) accumulated breakthrough concentrations
 263 for 8 flow rates; b) impedance; c) detached particle concentration under each of 8 rates; d) approximation of detached density
 264 function by the total of two log-normal distributions; e) maximum retention functions (MRFs) for detrital and authigenic fines,
 265 and the total MRF

266 Fig. 5a shows exponential growth of the accumulated breakthrough concentrations, which corresponds to
 267 exponential decrease of the momentum breakthrough concentrations $c_n(x=l, t)$. This behaviour is typical for deep
 268 bed filtration of low-concentration colloids with constant filtration coefficient (Chen et al. 2008, You et al. 2015).

269 The mathematical model (C1-C5) contains four dimensionless parameters – α , β , λ , and $\Delta\sigma_n$ – which must be tuned
 270 for each flow rate U_n , $n=1,2,\dots,8$. Table 1 presents the tuning results. Fig. 5c shows the tuned and measured values
 271 of detached particle concentrations. The probabilistic density of velocity distribution of the detached fines are
 272 presented in Fig. 5d. The PDF is bimodal, which is attributed to fines detachment by breakage and against
 273 electrostatic forces, where the particles are authigenic and detrital, respectively. The PDF allows the approximation
 274 by the total of two log-normal distributions with high accuracy. Fig. 5e shows two individual MRFs and their total,

275 which is MRF for the overall colloid. Eight experimental points for the total detached concentrations match well
 276 with the accumulated MRF curve.

277 Table 1: The tuning result of matching accumulated concentration and impedance.

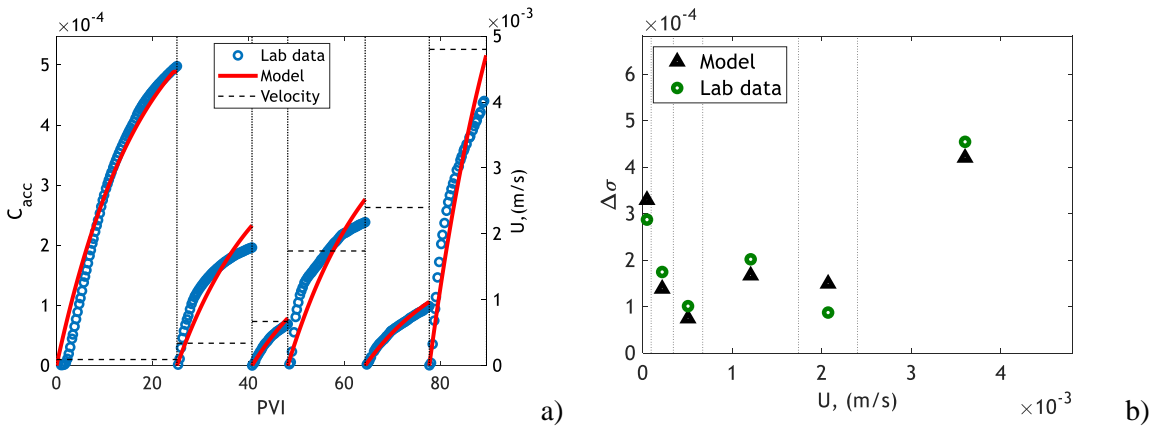
U (m/s)	3.97×10^{-5}	5.27×10^{-5}	7.34×10^{-5}	1.03×10^{-4}	1.16×10^{-4}	1.23×10^{-4}	1.42×10^{-4}	1.58×10^{-4}
α	4.7×10^{-3}	4.7×10^{-3}	4.7×10^{-3}	4.7×10^{-3}	4.7×10^{-3}	4.7×10^{-3}	4.7×10^{-3}	4.7×10^{-3}
β	0.71×10^5	1.94×10^5	1.94×10^5	1.28×10^5	0.92×10^5	0.65×10^5	0.65×10^5	0.78×10^5
λ (1/m)	647.87	639.15	625.5	606.49	598.64	593.73	582.32	572.69
$\Delta\sigma$	3.03×10^{-6}	2.97×10^{-6}	2.02×10^{-6}	2.16×10^{-6}	2.18×10^{-6}	1.62×10^{-6}	9.45×10^{-7}	1.02×10^{-6}
$R^2(C_{acc})$	0.92	0.95	0.93	0.78	0.94	0.91	0.92	0.92
$R^2(J)$	0.92	0.55	0.87	0.80	0.98	0.98	0.99	0.98

278 Tensile strength T_0 along with the bond radius r_b can be calculated from Eq. (15) and the histogram for detachment
 279 velocity (Fig. 5d). Assume the typical value of coefficient of variation of the bond radius as $C_v=0.03$ (Tian et al.
 280 2022). Eq. (15) can be used for mean detachment velocity, which is taken from the breakage-velocity histogram
 281 in Fig. 5d – $U^b_{mean}=1.21 \times 10^{-4}$ m/s. Minimum value of detachment velocity – $U^b_{min}=0.63 \times 10^{-4}$ m/s – corresponds to
 282 minimum value of bond radius, which can be estimated as $r_b(1-3C_v r_b)$. Applying Eq. (15) to mean and minimum
 283 breakage velocities allows calculating two unknowns $T_0=0.03$ MPa and $rb=3.0 \times 10^{-7}$ m. Stability of calculations of
 284 tensile strength and bond radius from mean and minimum breakage velocities is determined by high difference in
 285 their values – U^b_{mean} is 1.92 times higher than U^b_{min} .

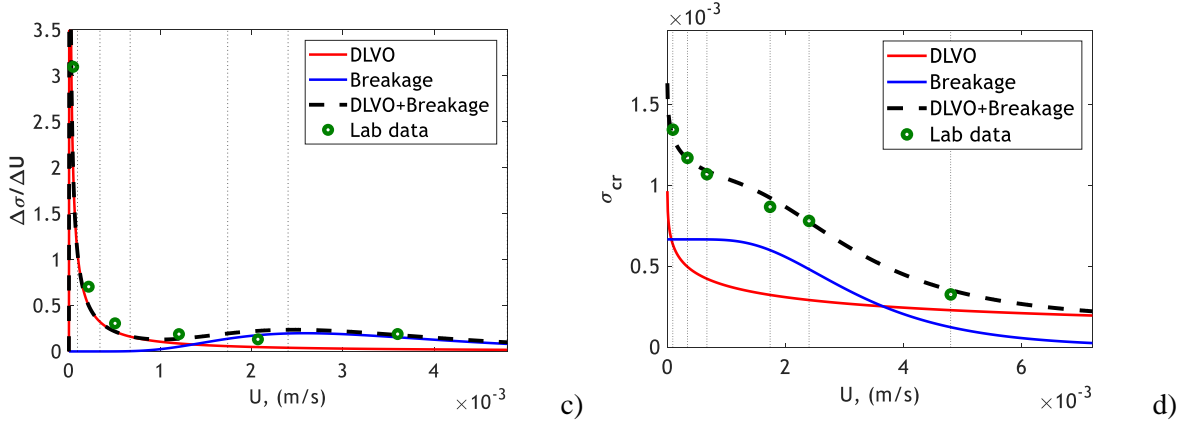
286 Torkzaban et al. 2017 conducted lab tests on consolidated (sandstone) core sample from the Yarragadee Formation
 287 (Perth Basin, Western Australia). The laboratory study was comprised of water injection with concentrations 47
 288 mg/L of sodium chlorite and 9mg/L of calcium chlorite into the sandstone core with permeability 2697 mD and
 289 porosity 0.32. Core length was 7 cm. Fig. 6 shows lab data during application of six injection rates. Table 2 presents
 290 the results of tuning the model coefficients. The breakthrough concentration has been measured during the overall
 291 test. The data on pressure drop across the core are not available from the original paper.

292 Fig. 6 shows lab data and their matching by the model (C1-C5) during application of six injection rates:
 293 breakthrough concentration data (Fig. 6a), detached concentrations at each rate (Fig. 6b), density distributions for
 294 detachment velocity for authigenic and detrital fines (Fig. 6c), and individual MRFs for authigenic and detrital
 295 fines along with overall MRF.

296 Like in the previous test, the detachment velocity distribution has a clear bimodal structure, which also supports
 297 the two-population hypothesis.



298



299

300 Fig. 6. Matching lab data on authigenic and detrital fines migration in sandstone cores: a) accumulated breakthrough
 301 concentrations for 6 flow rates; b) detached particle concentration under each of 6 rates; c) approximation of detached density
 302 function by the total of two log-normal distributions; d) maximum retention functions (MRFs) for detrital and authigenic
 303 fines, and the total MRF

304 Table 2 presents the tuning results for dimensionless parameters – α , β , λ , and $\Delta\sigma_k$ – which have been determined
 305 for each flow rate U_k , $k=1,2,\dots,8$.

306 Table 2: The tuning result of matching accumulated concentration

U , (m/s)	9.26×10^{-5}	3.4×10^{-4}	6.7×10^{-4}	1.74×10^{-3}	2.4×10^{-3}	4.8×10^{-3}
α	4.1×10^{-2}	4.11×10^{-2}	4.11×10^{-2}	4.13×10^{-2}	4.15×10^{-2}	4.2×10^{-2}
β	0	0	0	0	0	0
λ , (1/m)	19.52	19.5	19.46	19.36	19.3	19.3
$\Delta\sigma$	2.87×10^{-4}	1.74×10^{-4}	1.01×10^{-4}	2.02×10^{-4}	0.87×10^{-4}	4.54×10^{-4}
$R^2(C_{acc})$	0.97	0.78	0.96	0.77	0.97	0.90

307 Applying Eq. (15) for mean and minimum detachment velocities, which are taken from the histogram in Fig. 6c –
 308 $U_{mean}^b = 2.75 \times 10^{-3}$ m/s and $U_{min}^b = 1.22 \times 10^{-3}$ m/s, respectively – we obtain $T_0 = 0.56$ MPa and $r_b = 1.35 \times 10^{-7}$ m.

309 For both tests, the tuned parameters vary within common intervals, earlier presented in the literature (Chen et al.
 310 2008, Bradford et al. 2013, You et al. 2015, Guo et al. 2016). The obtained tensile strength for kaolinite is also
 311 typical (Han et al. 2019, Yang et al. 2019). The detached concentrations $\Delta\sigma_{cr}(U)$ versus velocity for both kinds of
 312 particles increases at small rates from zero and declines at high velocities, which complies with typical form of the
 313 maximum retention curve (Bedrikovetsky et al. 2011, 2012). High values of the coefficient of determination show
 314 high match between the experimental and modelling data, which validates the model.

315 Close match by single-population model has been achieved for lab data of 16 corefloods with piecewise-constant
 316 increasing rates (Table 3). The tuned parameters have the same order of magnitude as those presented in Tables 1
 317 and 2.

318 5. Breakage of authigenic clays in geological faults

319 Mobilization and migration of authigenic clays cause the permeability decrease in geological faults and faulted
 320 zones, which is important for sealing capacities of CO₂ and hydrogen storage, and for interpretation of various
 321 seismic events (Farrell 2021). Let us discuss whether authigenic clay detachment by breakage due to viscous water
 322 flux under fault conditions is feasible.

323 Table 3. Flow velocities in faults in different basins

No	Refs	Basin	Velocity, m/s
1	Matthai and Roberts 1996	Gulf of Mexico Basin, USA	$3.2 \times 10^{-6} - 3.2 \times 10^{-4}$
2	Liu et al. 2018	Anju Coal Mine, China	$0.5 \times 10^{-4} - 4 \times 10^{-4}$
3	Yu et al. 2020	Dongtan Coal Mine, China	$1 \times 10^{-3} - 1.2 \times 10^{-2}$

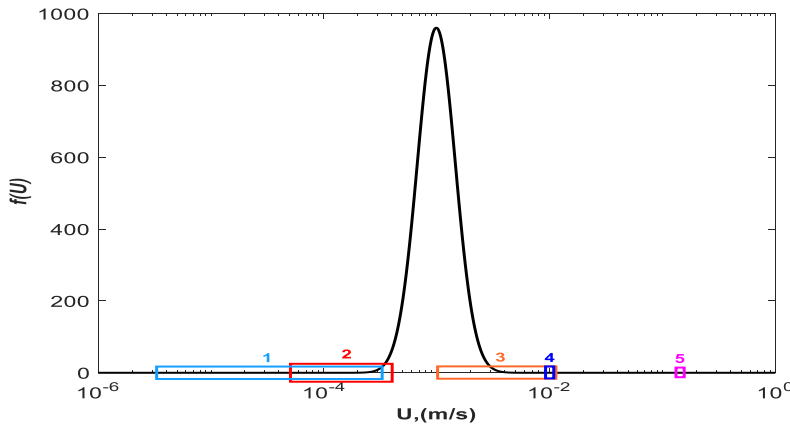
4	Eichhubl and Boles 2000	Monterey Formation,	0.01
5	Maloszewski et al. 1999	Lange Bramke Basin,	0.15

324 Table 3 presents water velocities in faults in different basins as reported in papers the referred papers. Papers by
325 Matthai and Roberts 1996, Lui et al. 2018, and Yu et al. 2020 took the velocity values from the basin data to use
326 in simulation, via paper by Eichhubl and Boles 2000 retrieved the velocity directly from tracer test, and paper by
327 Maloszewski et al. 1999 inferred it by the size of entrained rock fragments. Maloszewski et al. 1999 present the
328 probability distribution function (PDF) for velocity detachment by breakage and the velocities of water in faults
329 as presented all 5 papers. The data for calculations are presented in Table 4 and taken from publications Ting et
330 al. 2021 and Farrell et al. 2021. Ting et al. 2021 shows that particle radius, aspect ratio, bond radius and their
331 variation coefficients, presented in Table 4, are the most influential parameters on PDF.

332 Table 4. Particle parameters to calculate PDF for breakage velocity

Parameter	Mean value	Coefficient of Variation (Cv)
Particle radius r_s , (μm)	2	0.17
Aspect ratio α_s	0.65	0.17
Tensile strength T_0 , (Mpa)	0.2	-
Bond radius r_b , (μm)	0.16	0.02

333 Fig. 7 shows that breakage of kaolinite in the case 1 almost does not occur; some authigenic fines are broken in
334 the case 2. Significant part of authigenic fines is broken in the case 3. In the cases 4 and 5, all authigenic particles
335 are detached by breakage.



336
337 Fig. 7. Probability distribution function (PDF) for breakage velocity and flow velocities in the geological faults

338 6. Determining the fractions of detachable clays and authigenic fines in rocks

339 Tuning the model coefficients by matching the lab coreflood data by the analytical model for 1D deep bed filtration
340 with constant filtration coefficient λ , given by Eqs. (C5-C9) allows calculating the fraction of detachable fines with
341 respect to initial clay content in the rock (column 9 in Table 3), fraction of detached fines produced during
342 corefloods (column 10), and fraction of authigenic fines in the overall detachable fines (11th column). Table 3
343 presents the results of 16 coreflood data matching. Tests 1-3 have been performed by Ochi and Vergough 1998,
344 test 4 – by Torkzaban et al. 2015, tests 5 and 6 – by Shang et al. 2008, tests 7, 8 – by Huang et al. 2017, tests 9, 10
345 – by Huang et al. 2022, test 11 – by Guo et al. 2016, tests 12-14 – by Huang 2021, tests 15, 16 – by Hashemi et al.
346 2022, 2023.

347 The fraction of detachable fines in consolidated rocks and high-salinity water injection varies from 0.01 to 0.19%
348 (Lines 1-3, 6-11, 15, and 16), which agrees with the previously published data (Russell et al. 2017). This percentage
349 is so low due to small fraction of clay particles located at the rock surface, where they are accessible to water flux;
350 vast majority of clays are located inside the rock skeleton and matrix. In grinded rocks and high-salinity water
351 injection, the fraction increases up to 19-75% (Lines 12-14) due to high accessibility of grain surfaces to the water

352 flux in porous space. In high porosity sandstone and packed sediment, the fraction increases to 18 and 90% under
 353 low-salinity and deionized water injection (Lines 4 and 5, respectively) due to disappearance of DLVO particle-
 354 rock attraction at low salinities.

355 Table 3. The fraction of detachable kaolinite rocks, fraction of detached fines produced during corefloods, and fraction of
 356 authigenic fines in the produced particle concentration

No	Rock type	Salinity	Clay fraction, C_c	Porosity, ϕ	Produced fines, $\sum C_a$	Detachab- le fines, σ_0	$\frac{\sum C_a}{\phi} / \sigma_0$	$\sigma_0/[C_c(1-\phi)]*100$	Authi- genic fraction, σ_0^b / σ_0	U_{max}^b / U_{min}^b
1	Berea core	0.5M	0.08	0.2	-	1.08×10^{-4}	-	0.17	0.36	2.46
2		0.1M	0.08	0.2	-	7.5×10^{-5}	-	0.12	0.5	3.78
3		0.01M	0.08	0.2	-	1.02×10^{-4}	-	0.16	0.35	1.99
4	Sandstone core	8×10^{-4} M	0.013	0.32	1.55×10^{-3}	1.65×10^{-3}	0.3	18	0.41	3.98
5	Packed sediment	DI	0.03	0.45	6.53×10^{-3}	1.5×10^{-2}	0.19	90	0	-
6		0.5M	0.03	0.45	4.57×10^{-6}	9.9×10^{-6}	0.21	0.06	0	-
7	Anthracite coal core	0.27M	4.64×10^{-2}	0.1	4.62×10^{-6}	1.63×10^{-5}	0.03	0.04	0.48	2.51
8		0.27M	4.64×10^{-2}	0.1	4.58×10^{-6}	1.86×10^{-5}	0.02	0.04	0.5	1.19
9		0.27M	4.64×10^{-2}	0.24	3.62×10^{-6}	4.04×10^{-6}	0.21	0.01	0	-
10		0.27M	4.64×10^{-2}	0.24	5.92×10^{-6}	7.35×10^{-6}	0.19	0.02	0	-
11	Bituminous coal core	0.01M	6.8×10^{-2}	2.4×10^{-2}	6.2×10^{-7}	7.61×10^{-7}	0.02	1.1×10^{-3}	0.56	1.57
12	Grinded bituminous coal	0.27M	0.13	0.38	1.5×10^{-2}	6.1×10^{-2}	0.09	75	0.68	2.22
13		0.27M	0.13	0.36	4.45×10^{-2}	1.63×10^{-2}	0.98	19	0.83	2.00
14		0.27M	0.13	0.33	1.92×10^{-2}	1.88×10^{-2}	0.34	21	0.59	2.22
15	Castle gate core	0.6M	6.6×10^{-2}	0.24	2.8×10^{-5}	5.9×10^{-5}	0.09	0.15	0.77	2.22
16		0.6M	6.6×10^{-2}	0.24	8.04×10^{-5}	9.72×10^{-5}	0.17	0.22	0.51	4.45

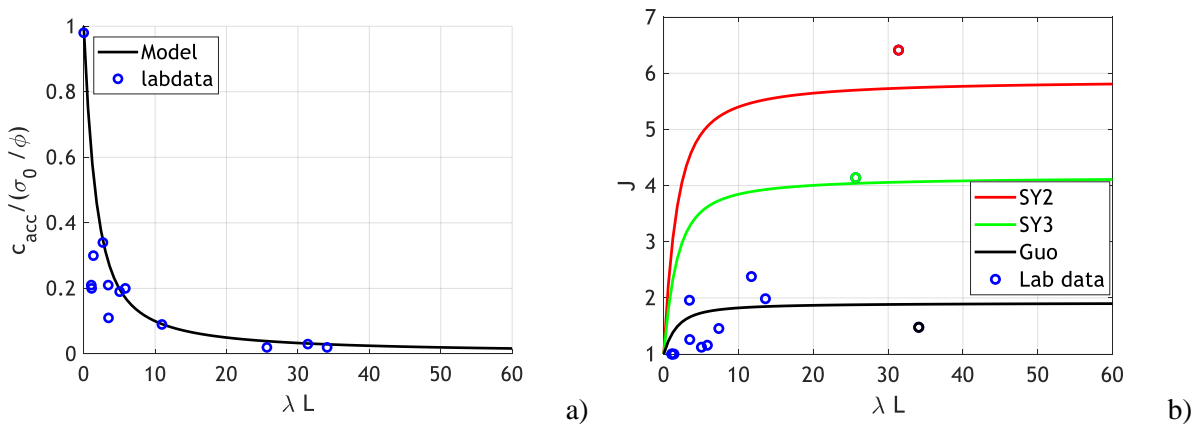
357 The fraction of authigenic fines of the overall concentration of detached fines varies from 0.36 to 0.83. For those
 358 rocks, the ratio between the maximum rate at the coreflood and minimum breakage velocity exceeds one,
 359 indicating fines b) breakage (11th column in Table 3). Authigenic particles haven't been observed in packed
 360 sediments and in artificial packed sediment cores (Lines 5,6 and 9, 10, respectively). In other 12 cases, the
 361 minimum breakage velocity is below the maximum velocity applied in the corresponding test, so authigenic fines
 362 have been observed in the production.

363 The breakage velocity of authigenic fines is widely distributed – 11th column of Table 3 shows that the ratio of
 364 maximum and minimum breakage velocities varies from 1.2 to 4.5, i.e., the calculation method for tensile strength
 365 T_0 and bond radius r_b using Eq. (15) is stable.

366 The analytical model for 1D fines migration with constant particle capture (filtration) coefficient λ , given by Eq.
 367 (C6) for $c(x,t)$, allows calculating the ratio between the stabilised accumulated concentration of produced fines and
 368 the detached overall detached concentration (8th column in Table 3):

$$369 \frac{\phi c_{acc}}{\sigma_0} = \frac{1 - \exp(-\lambda L)}{\lambda L}, \quad (18)$$

370 so the ratio depends on the dimensionless filtration coefficient λL only. Plot of curve (18) and the points from 6th
 371 column are placed in Fig. 8a. The curve and the 16-test data show the clear tendency that the higher is the filtration
 372 coefficient the faster is the particle capture and the lower fraction of the mobilised fines is produced. The fraction
 373 varies from one for zero filtration coefficient, to zero where the filtration coefficient tends to infinity. Some point
 374 scattering and mismatch with the curve is explained by heterogeneous colloid, including varying particle properties
 375 and different forms and capture probabilities for detrital and authigenic fines.



376 Fig. 8. Effects of particle capture by the rock on fines migration: a) fraction of produced fines in the detached concentration
 377 versus dimensionless filtration coefficient; b) impedance (reciprocal to normalised average permeability) versus filtration
 378 coefficient.
 379

380 The stabilised impedance is also calculated from the analytical model (C6-C9) for

$$381 J(t \rightarrow \infty) = J_{st} = 1 + \beta \Delta \sigma \left[1 - \frac{1 - e^{-\lambda L}}{\lambda L} \right] \quad (19)$$

382 Besides the dimensionless filtration coefficient, the stabilised impedance (19) depends on formation damage
 383 coefficient β and the detached fines concentration $\Delta \sigma$, which explained the scattering of the points in Fig. 8b. The
 384 curve $J_{st}(\lambda L)$ increases from 1 at zero filtration coefficient to $1 + \beta \Delta \sigma$ where filtration coefficient tends to infinity.
 385 Fig. 8b presents three curves corresponds to tuning of three lab cases; the curves correspond to points with the
 386 same colour.

387 The above plots show how the number of produced fines and permeability decline vary with filtration coefficient
 388 – increase of filtration coefficient yields decrease of produced fines and growth of permeability damage. Several
 389 papers claim insignificant fines migration based on the data of low produced concentrations. Yet, low produced
 390 concentration could be due to high filtration coefficient, so fines migration must be indicated by the impedance
 391 increase along with the number of produced fines.

392 Mineral dissolution chemical reactions weaken the rocks, decreasing strength in Eq. (15) and resulting in additional
 393 fines liberation in situ the reservoir yielding the additional sweep enhancement. Those increase the fraction of
 394 authigenic fines. The dissolution reactions make CO₂ and hydrogen storages susceptible to fines breakage.

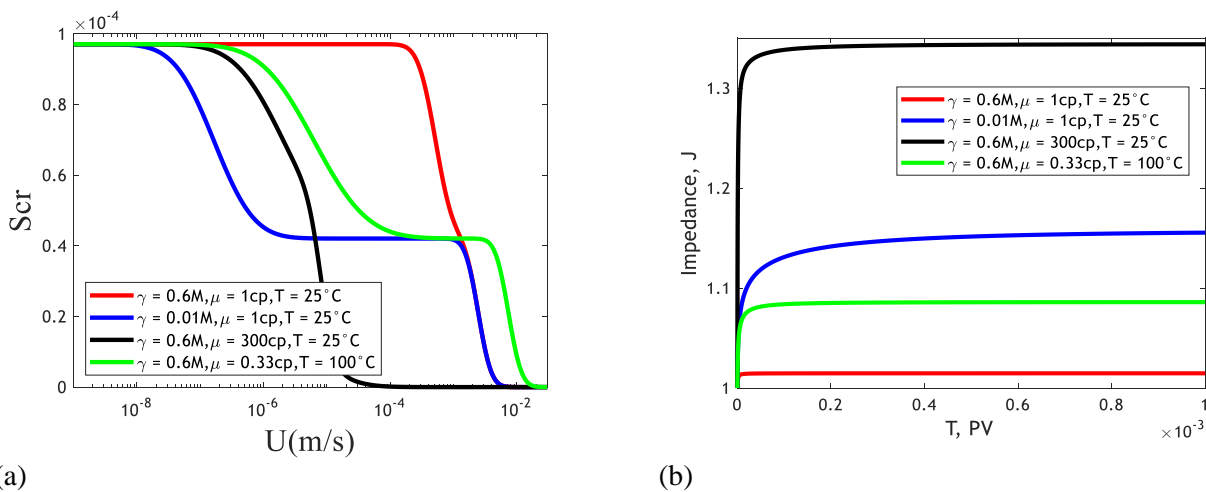
395

396 **7. Effects of colloidal breakage detachment on reservoir and well behaviour**

397 1D radial problem for fines detachment and flow toward well allows for exact solution under constant production
 398 rate (You et al. 2015, 2019). Detached fines straining results in permeability decline and increase of the pressure
 399 drop between the well and the reservoir. Treatment of 16 coreflood tests, presented in Table 3, yields calculation
 400 of filtration and formation damage coefficients along with maximum retention functions for detachment against
 401 electrostatic forces and by breakage, like it was performed in section 4. Implementing these values into the solution
 402 for fines migration in radial flow permits the estimation of wellbore impedance as well as the relative impacts of
 403 authigenic and detrital fines on well injectivity. For the parameter values of case 16 in Table 3 the critical retention
 404 function and impedance are presented in Fig. 9a and 7b respectively. The red curves in this plot correspond to the
 405 experimental conditions of the test by Hashemi et al. 2023 (salinity, $\gamma=0.6$ M, viscosity, $\mu = 1$ cp, and temperature
 406 $T = 25^\circ\text{C}$). The critical retention function shows a clear distinction between the detachment of detrital particles at
 407 low velocity and detachment of authigenic particles for higher velocities. For this $\sigma_{cr}(U)$ curve, the corresponding
 408 impedance in Fig. 9b is close to one, indicating negligible formation damage. This is a result of the high velocities
 409 required for particle detachment.

410 The conditions of the experimental test are not indicative of those in most field injection scenarios. Due to explicit
 411 calculation of the critical retention function based on physical considerations, the effect of changing environmental
 412 conditions can be examined by changing relevant parameters. In this way the results of experiments can be
 413 extended beyond the conditions they were performed under. Here we consider three different scenarios covering
 414 a range of applications.

415 The three cases considered are low salinity (corresponding to freshwater recharge wells), high viscosity
 416 (corresponding to the injection of fracturing fluid), and high temperature (corresponding to geothermal or deep
 417 petroleum wells). Changing salinity to 0.01 M decreases the velocities required to detach detrital particles but has
 418 no effect on authigenic particles, as illustrated by the critical retention function in Fig. 9a. Increasing viscosity
 419 increases drag and lift, increasing detachment of all particles. Lastly increasing temperature mostly affects detrital
 420 particles, as it decreases the electrostatic force, but it also results in a decrease in the viscosity, slightly affecting
 421 authigenic particles. All three cases result in larger values of impedance as shown in Fig. 9b. This demonstrates
 422 the importance of fines migration across a range of applications.

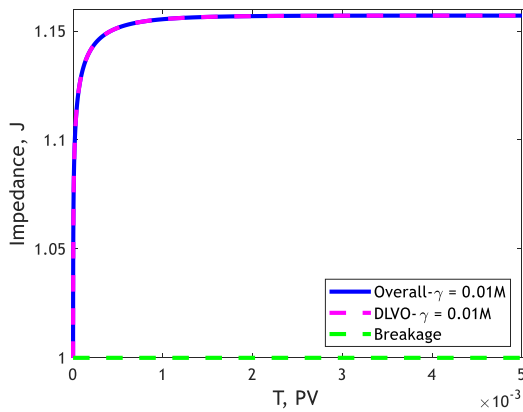


423
 424 Fig. 9. Formation damage during injection of water under different conditions: a) critical retention functions, b) impedance

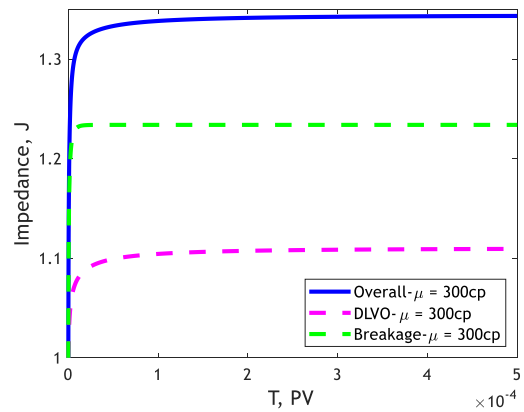
425 Changes of these system parameters clearly do not affect authigenic and detrital detachment uniformly. Thus, we
 426 consider the relative importance of each kind of detachment under the three reservoir conditions. Impedance curves
 427 showing the predicted impedance if particles detached only by DLVO (detrital) or breakage (authigenic) are shown
 428 in Fig. 10. At low salinity, breakage is negligible, and all formation damage occurs due to detrital particles which
 429 are weakly held to the rock's surface at low γ . For high viscosity, both detrital and authigenic particles contribute

430 to formation damage, with more than half of the damage caused by breakage. Lastly, Fig. 8c shows that the
 431 formation damage at high temperatures results almost entirely from the weakening of electrostatic forces.

432

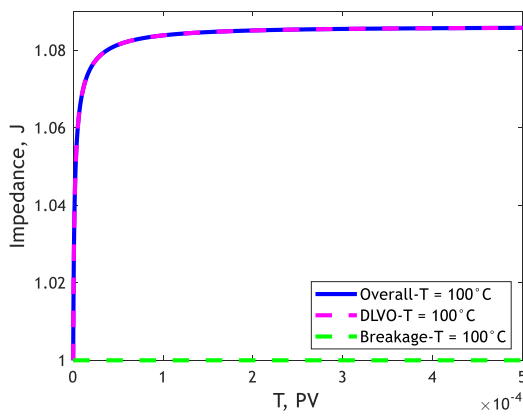


a)



b)

433



c)

434 Fig. 10. Impact on injectivity of detachment via two mechanisms: DLVO (detrital particles) and breakage (authigenic
 435 particles) under different conditions, a) low salinity water injection, b) injection of high viscosity fluid, c) injection under high
 436 temperatures

437 Geological site selection for CO₂ and hydrogen storage highly depends on well performance and storage capacity.
 438 Authigenic fines breakage along with detrital particle detachment can cause significant permeability reduction
 439 with detrimental well productivity and injectivity decline, but to storage capacity increase. High velocity in highly
 440 permeable layers and patterns yields higher fines detachment and permeability reduction, resulting in
 441 homogenisation of injectivity and productivity profiles and, finally, in enhanced sweep (Bedrikovetsky 2013). In
 442 the case of CO₂ injection, sweep increase leads to enhancement of the pore volume where capillary, stratigraphic
 443 and chemical CO₂ capture occurs, increasing the storage capacity. In the case of cyclic hydrogen injection and
 444 production, sweep enhancement results in increase of water-free hydrogen production.

445 The competitive effects of well index decline and sweep enhancement with CO₂ and hydrogen storage are in odds
 446 with each other: the higher is the injection rate, the higher is the sweep and storage capacity, but the higher is the
 447 well index decrease. The optimal injection and production rates can be determined using the mathematical
 448 modelling that includes Eqs. (12-15).

449 8. Breakage of authigenic fines during well exploitation

450 In this section we investigate whether fines breakage can occur in the vicinity of production and injection wells
 451 for different reservoir conditions. Table 4 presents the data for heavy oil production (Ado 2021), polymer injection
 452 (Gao 2021), dewatering of coal bed methane (CBM) reservoir (Shi et al. 2008), injection of supercritical CO₂ into
 453 carbonate reservoir (Spivak et al. 1989), hydraulic fracturing using water as a fracturing fluid (HFW) (Presetio et
 454 al. 2021), hydraulic fracturing using high-viscosity fracturing fluid (HF) (Prasetio et al. 2021), natural gas

455 production (NG) (Peischl et al. 2015), water production from geothermal reservoirs (GWP) (Ishido et al. 1992),
 456 water injection into aquifers (WI) (De Lino 2005), and water production from aquifers (WP) at low and high rates
 457 (Kulakov and Berdnikov 2020). The data for calculations are taken from those literature sources. For all cases,
 458 spherical particle shape ($\alpha_s=1$) corresponds to kaolinite booklet; typical fine size is taken as $r_s=2\mu\text{m}$.

459 The breakage velocity is calculated using Eq. (12-15) and is given in nineths column. The well rates are taken
 460 from the corresponding papers. Column nine shows the velocity on well walls for well radius $r_w=0.1$ m.

461 Table 4. Occurrence of fines breakage in well vicinity

No	Well type	α_s	δ	ν	χ	μ , (Pa.s)	T_0 ,(Mpa)	U_{\min}^b , (m/s)	U_w , (m/s)
1	Heavy oil	1	0.05	0.25 [29]	6.54×10^{-4}	0.30	0.2	1.01×10^{-6}	5.67×10^{-6}
2	Polymer	1	0.05	0.24 [30]	6.57×10^{-4}	0.04	0.2	6.69×10^{-6}	8.8×10^{-5}
3	CBM	1	0.05	0.35 [22]	6.27×10^{-4}	1×10^{-3}	0.2	3.57×10^{-4}	1.14×10^{-5}
4	CO ₂	1	0.05	0.21 [31]	6.67×10^{-4}	1.49×10^{-4}	0.2	8.51×10^{-4}	4.74×10^{-5}
5	HFW	1	0.05	0.33 [24]	6.32×10^{-4}	1×10^{-3}	0.2	8.93×10^{-4}	1.38×10^{-2}
6	HF	1	0.05	0.33 [14]	6.32×10^{-4}	1	0.2	8.93×10^{-7}	1.38×10^{-2}
7	NG	1	0.05	0.23 [32]	6.6×10^{-4}	1.21×10^{-4}	0.2	2.72×10^{-4}	1.33×10^{-3}
8	GWP	1	0.05	0.25 [33]	6.54×10^{-4}	1.2×10^{-4}	0.2	1.49×10^{-4}	4.44×10^{-4}
9	WI	1	0.05	0.286[34]	6.44×10^{-4}	1×10^{-3}	0.2	1.96×10^{-4}	7.02×10^{-4}
10	WP _{min}	1	0.05	0.34 [35]	6.29×10^{-4}	1×10^{-3}	0.2	1.34×10^{-4}	3.68×10^{-5}
11	WP _{max}	1	0.05	0.34 [35]	6.29×10^{-4}	1×10^{-3}	0.2	1.34×10^{-4}	3.32×10^{-4}

462 The velocity on the well wall exceeds minimum breakage velocity for heavy oil production, polymer injection,
 463 both cases of hydraulic fracturing, production of natural gas and geothermal water, water injection into aquifers
 464 and water production from artesian well with high rate, so fines breakage can occur under those conditions. The
 465 velocity on well wall is lower than minimum breakage velocity for dewatering in CBM, CO₂ injection, and water
 466 production with low rates.

467 Similar effects of well injectivity and productivity as well as in situ bond strength decline by chemical reactions
 468 occur during geothermal exploitation, where fines detachment occurs due to DLVO forces decrease at high
 469 temperature, and in fractured reservoirs that are highly susceptible to fines breakage due to high flow velocity
 470 (Altree et al. 2019, Wang et al. 2022c). During water and CO₂ injection in carbonate reservoirs, where rock
 471 dissolution yields massive release of various size particles, the effects of particle mobilisation by breakage is
 472 expected to be significantly more pronounced.

473 9. Discussions

474 The current version of the breakage-detachment model assumes single-phase flow. Adding the capillary force
475 exerting by menisci on the attached fines into torque balance (16) would cover the detachment by breakage during
476 gas flow in shale rocks and CO₂ and hydrogen storage (Roshan et al. 2016, Siddiqui et al. 2019). The appropriate
477 two-phase flow model accounts for moving interface (Shapiro 2015, 2018).

478 The model assumes brittle behaviour of the particle-substrate bond during breakage; the study of ductile bonds
479 would complicate the failure criteria (6) and phase diagrams. Accounting for non-elasticity of the rock and non-
480 Newtonian fluid, the rheology yields in more complex expressions for stress maxima than (12-15); in this case the
481 breakage regime will be velocity-dependent.

482 This paper assumes single-population colloidal transport, given by Eqs. (C1-C3) with further separation of MRF
483 into those by authigenic and detrital fines, while Hashemi et al. 2023 apply two-population balance model with
484 two different filtration functions for authigenic and detrital populations. A more general approach would
485 encompass multicomponent colloidal transport with non-linear fines straining (Bedrikovetsky et al. 2019).

486 The analytical model for well inflow performance under fines migration using the model constants obtained from
487 12 corefloods, where the authigenic fines mobilisation have been observed (Table 3), yields well index decrease
488 up to 1.4 times. We expect significantly higher effects based on more representative corefloods. Besides, all 16
489 tests have been performed in sandstones. Significantly higher formation damage is expected during waterflooding
490 or CO₂ injection in carbonates, where rock dissolution yields reduction of particle-rock bond radius with
491 consequent bond breakage and massive fines release.

492 Numerous geomechanics studies determine the strength and other failure parameters of the rocks, while the bond-
493 breakage criteria in Eq. (12-15) contain those for a single particle and substrate. Those measurements require
494 significantly more sophisticated equipment (Su et al. 2022, Roshan et al. 2023). Currently, those parameters for
495 mineral particles are unavailable. Derivation of the fine-breakage model may stimulate those experimental studies.

496 The breakage-detachment models (11-15) and (17, C4) correspond to particle- and rock scales, respectively.
497 Establishing a functional relationship between them would solve the problems of upscaling and downscaling with
498 numerous experimental and industrial applications.

499 10. Conclusions

500 The model derivations for particle detachment by breakage, integrating the Timoshenko's beam theory with CFD
501 flow modelling and strength criteria, and applying the model to different geo-energy topics allow concluding as
502 follows.

503 Maximum stresses are reached either at the beam base middle $Y=0$ or at its boundary. Breakage conditions, where
504 either of tensile or shear stresses reaches the strength value, are determined by three dimensionless parameters:
505 strength-drag number κ , aspect-Poisson number χ , and strength ratio η . The tensile-stress diagram in plane (χ, v)
506 determines which of tensile stresses is higher. The shear-stress diagram in plane (χ, η) determines 4 breakage
507 regimes depending on aspect-Poisson number χ , Poisson's ratio v , and strength ratios η .

508 The definition of breakage regime – by either tensile or shear stress - is independent of flow velocity. For an
509 identified breakage regime, breakage velocity is determined by the strength-drag number $\kappa(\chi, v)$ alone. For a given
510 particle shape, the critical breakage velocity is proportional to strength and particle size, and it is inversely
511 proportional to viscosity.

512 The expression for critical breakage velocity allows determining the breakage maximum retention function MRF,
513 which is a mathematical model for particle detachment by breakage of particle-rock surface bond. MRF closes the
514 governing system for colloidal transport with breakage detachment.

515 The lab-based analytical model for fines breakage shows that under strong subterranean water fluxes, the
 516 authigenic fines mobilisation by breakage can occur in geological faults, resulting in permeability decline and
 517 affecting sealing capacities during CO₂ and hydrogen injection for storage.

518 Matching of 16 coreflood tests exhibits high agreement between the laboratory and modelling data. Besides, the
 519 model coefficient values as obtained by tuning, belong to their common intervals of variation. This validates the
 520 developed model for migration of authigenic and detrital fines in rocks.

521 The matching allows determining the detachable fines fraction in the overall clay content, and the authigenic fines
 522 fraction in the detachable fines. The detachable fines fraction in consolidated rocks and high-salinity water
 523 injection varies from 0.01 to 0.19%. It increases up to 19-90% in grinded rocks or by deionised water injection.
 524 The authigenic fines fraction of the detachable clay particles varies in the interval 0.4-0.8.

525 In 12 corefloods from 16, where authigenic fines have been found, the breakthrough curves during corefloods
 526 exhibit two-population behaviour, which is attributed to commingled production of the authigenic and detrital
 527 particles. Besides, size distributions of produced fines are bimodal.

528 Analytical 1D model for axi symmetric flow allows recalculating coreflood tests with migration of authigenic and
 529 detrital fines into the well productivity curve, permitting estimating the formation damage due to fines migration.

530 Calculations of minimum breakage velocities / well rates using Eq. (15) for typical values of the breakage-model
 531 parameters show high feasibility of rock fines breakage during heavy oil production, polymer injection, both cases
 532 of hydraulic fracturing, production of natural gas and geothermal water, water injection into aquifers and water
 533 production from artesian well with high rate.

534 **Appendix A. CFD calculations for drag and its torque**

535 The formulae for drag and torque factors in Eq. (1) for spheroidal and thin cylindrical particles are available from
 536 Ting et al. 2021. In this work, those factors for long thin cylinders, which model illite clay particles, are calculated
 537 for $\alpha_s > 1$:

$$538 \quad f_d = (0.9014\alpha_s^2 + 1.599\alpha_s + 2.265)(\alpha_s + 1.752)^{-1} \quad (A1)$$

$$539 \quad f_M = (0.0002161\alpha_s^3 + 1.34\alpha_s^2 + 44.18\alpha_s + 21.27)(\alpha_s^2 + 31.34\alpha_s + 10.38)^{-1} \quad (A2)$$

540 **Appendix B. Stresses in elastic beam by Timoshenko's model**

541 Stress distributions in cylindric elastic beam (Timoshenko and Goodier, 1970) are

$$542 \quad \sigma_z = \frac{F_d b f_M x}{I} \quad (B1)$$

$$543 \quad \tau_{xz} = \frac{(3+2\nu)}{8(1+\nu)} \frac{F_d}{I} \left(r_b^2 - x^2 - \frac{(1-2\nu)}{(3+2\nu)} y^2 \right) \quad (B2)$$

$$544 \quad \tau_{yz} = -\frac{(1+2\nu)}{4(1+\nu)} \frac{F_d xy}{I} \quad (B3)$$

$$545 \quad \sigma_x = \sigma_y = \tau_{xy} = 0 \quad (B4)$$

546 The stress tensor, as per solution (12-15) is:

$$\begin{bmatrix} 0 & 0 & \tau_{xz} \\ 0 & 0 & \tau_{yz} \\ \tau_{xz} & \tau_{yz} & \sigma_z \end{bmatrix} \quad (B5)$$

The principal stresses are eigen values of the stress tensor (B5):

$$\sigma_1 = \frac{\sigma_z + \sqrt{\sigma_z^2 + 4(\tau_{xz}^2 + \tau_{yz}^2)}}{2}, \quad \sigma_2 = 0, \quad \sigma_3 = \frac{\sigma_z - \sqrt{\sigma_z^2 + 4(\tau_{xz}^2 + \tau_{yz}^2)}}{2} \quad (B6)$$

where, $\sigma_1, \sigma_2, \sigma_3$ are principal stresses in order of decreasing of their values, and

$$\sigma_1 > \sigma_2 = 0 > \sigma_3 \quad (B7)$$

The equation for largest Mohr circle for the case of $\sigma_2=0$ is

$$\left[\sigma - \left(\frac{\sigma_1 + \sigma_3}{2} \right) \right]^2 + \tau^2 = \left[\frac{(\sigma_1 - \sigma_3)}{2} \right]^2 \quad (B8)$$

where σ and τ are tensile and shear stresses acting on unitary planes with different orientations.

Appendix C. Population balance model for colloidal-suspension transport in porous media

We discuss deep bed filtration of the total particle population for detrital and authigenic fines. The state variables are the volumetric concentrations of suspended, attached and strained particle, c , σ_{cr} , and σ_s , respectively, and the pore pressure p . Mass balance and capture rate equations and Darcy's law for the colloidal flux are:

$$\frac{\partial}{\partial t}(\phi c + \sigma_s) + \frac{\partial}{\partial x}(c\alpha U_n) = 0 \quad (C1)$$

$$\frac{\partial \sigma_s}{\partial t} = \lambda c \alpha U_n, \quad n = 0, 1, 2, \dots \quad (C2)$$

$$U_n = -\frac{k_0}{(1 + \beta \sigma_s) \mu} \frac{\partial p}{\partial x} \quad (C3)$$

where ϕ is the porosity, λ is the constant filtration coefficient, α is the drift-delay factor, U_n is the flow velocity at n -th injection, k is the initial undamaged permeability, p is the pressure, and β is the formation damage coefficient. Index n is attributed to injection velocity, and $U_0=0$. The filtration coefficient for the low-concentration fines population is constant.

Initial suspended concentration is equal to concentrations of mobilised fines after velocity increase. It is posed at each moment $\phi L / \alpha U_{n-1}$ of the velocity switch from U_{n-1} to U_n

$$t = t_n : c_{n0} = \frac{\sigma_{cr}(U_{n-1}) - \sigma_{cr}(U_n)}{\phi} = \frac{\Delta \sigma_{cr}(U_n)}{\phi} \quad (C4)$$

Here the overall MRF is a total of two individuals MRFs by Eq. (17).

Inlet boundary condition corresponds to injection of particle-free water

$$x = 0, \quad t_n < t < t_{n+1} : c_n = 0 \quad (C5)$$

572 The exact solution of the problem (C1-C5) can be found in handbooks Polyanin and Manzhirov 2006, or Polyanin
 573 and Zaitsev 2012. Breakthrough concentration is obtained by the method of characteristics:

$$574 \quad c_n(x, t) = \begin{cases} \frac{\Delta\sigma_{cr}(U_n)}{\phi} \exp\left(-\frac{\lambda\alpha U_n}{\phi}(t-t_n)\right), & x > \frac{\alpha U_n}{\phi}(t-t_n) \\ 0, & x < \frac{\alpha U_n}{\phi}(t-t_n) \end{cases} \quad (C6)$$

575 Breakthrough concentration becomes zero at the moment of the concentration front arrival at the moment $\phi L/\alpha U_n$.
 576 At this moment, all concentrations and pressure drop stabilise. Yet, even where the switch times $t_{n+1}-t_n$ are lower
 577 than the arrival times, we neglect suspension concentration which was formed before the switch.

578 Strained concentration is obtained integration of Eq. (C2) in t accounting for expression (C6):

$$579 \quad \sigma_{s,n}(x, t) = \begin{cases} \sigma_{s,n-1}(x, t_n) + \Delta\sigma_{cr}(U_n) \left(1 - \exp\left(-\frac{\lambda\alpha U_n}{\phi}(t-t_n)\right)\right), & x > \frac{\alpha U_n}{\phi}(t-t_n) \\ \sigma_{s,n-1}(x, t_n) + \Delta\sigma_{cr}(U_n) (1 - \exp(-\lambda x)), & x < \frac{\alpha U_n}{\phi}(t-t_n) \end{cases} \quad (C7)$$

580 The dimensionless pressure drop (impedance) J is defined as:

$$581 \quad J(t) = \frac{\Delta p(t) U(0)}{\Delta p(0) U(t)} \quad (C8)$$

582 Th expression for impedance is derived from Eq. (C3) by integrating pressure gradient in x from $x=0$ to core length
 583 $x=L$:

$$584 \quad J_n(t) = \begin{cases} J_{n-1}(t_n) + \beta\Delta\sigma_{cr}(U_n) I_n(t), & t-t_n < \frac{L\phi}{\alpha U_n} \\ J_{n-1}(t_n) + \beta\Delta\sigma_k \left(\left(1 + \frac{1}{\lambda L} \exp(-\lambda L) - \frac{1}{\lambda L}\right) \right), & t-t_n > \frac{L\phi}{\alpha U_n} \end{cases} \quad (C9)$$

$$I_n(t) = \frac{\alpha U_n}{\phi L} (t-t_n) + \frac{1}{\lambda L} \exp\left(-\lambda \frac{\alpha U_n}{\phi} (t-t_n)\right) - \frac{1}{\lambda L} + \left(1 - \frac{\alpha U_n}{\phi L} (t-t_n)\right) \left[1 - \exp\left(-\frac{\lambda\alpha U_n}{\phi} (t-t_n)\right)\right]$$

585

586

587

588 References

589 Abousleiman, Y. N., Hull, K. L., Han, Y., Al-Muntasheri, G., Hosemann, P., Parker, S., & Howard, C. B. (2016).
 590 The granular and polymer composite nature of kerogen-rich shale. *Acta Geotechnica*, 11(3), 573-594.

591 Ado, M.R., 2021. Improving heavy oil production rates in THAI process using wells configured in a staggered
592 line drive (SLD) instead of in a direct line drive (DLD) configuration: detailed simulation investigations. *Journal*
593 *of Petroleum Exploration and Production Technology*, 11(11), pp.4117-4130.

594 Alzate-Espinosa, G.A., Araujo-Guerrero, E.F., Torres-Hernandez, C.A., Benítez-Peláez, C.A., Herrera-
595 Schlesinger, M.C., Higueta-Carvajal, E. and Naranjo-Agudelo, A., 2023. Impact assessment of strain-dependent
596 permeability on reservoir productivity in CSS. *Geomechanics and Geophysics for Geo-Energy and Geo-*
597 *Resources*, 9(1), p.67.

598 Appelo, C. A. J., & Postma, D. (2004). *Geochemistry, groundwater and pollution*. CRC press.

599 Bedrikovetsky, P., Siqueira, F.D., Furtado, C.A. and Souza, A.L.S. (2011). Modified particle detachment model
600 for colloidal transport in porous media. *Transport in porous media*, 86(2), pp.353-383.

601 Bedrikovetsky, P., Zeinijahromi, A., Siqueira, F.D., Furtado, C.A. and de Souza, A.L.S. (2012). Particle
602 detachment under velocity alternation during suspension transport in porous media. *Transport in Porous Media*,
603 91(1), pp.173-197.

604 Bedrikovetsky, P., 2013. Mathematical theory of oil and gas recovery: with applications to ex-USSR oil and gas
605 fields (Vol. 4). Springer Science & Business Media.

606 Bedrikovetsky, P., Osipov, Y., Kuzmina, L. and Malgaresi, G., 2019. Exact upscaling for transport of size-
607 distributed colloids. *Water Resources Research*, 55(2), pp.1011-1039.

608 Bradford, S. A., Torkzaban, S., & Shapiro, A. (2013). A theoretical analysis of colloid attachment and straining in
609 chemically heterogeneous porous media. *Langmuir*, 29(23), 6944-6952.

610 Cao, Z., Xie, Q., Xu, X., Sun, W., Fumagalli, A. and Fu, X., 2023. Mass-loss effects on the non-Darcy seepage
611 characteristics of broken rock mass with different clay contents. *Geomechanics and Geophysics for Geo-Energy*
612 *and Geo-Resources*, 9(1), p.32.

613 Chen, C., Packman, A. I., & Gaillard, J. F. (2008). Pore-scale analysis of permeability reduction resulting from
614 colloid deposition. *Geophysical Research Letters*, 35(7).

615 Chen, X., Peng, D., Morrissey, J. P., & Ooi, J. Y. (2022). A comparative assessment and unification of bond
616 models in DEM simulations. *Granular Matter*, 24(1), 1-20.

617 Cushman, J.H. and Tartakovsky, D.M. eds., 2016. The handbook of groundwater engineering. CRC Press.

618 De RA Lino, U., 2005, June. Case history of breaking a paradigm: Improvement of an immiscible gas-injection
619 project in Buracica field by water injection at the gas/oil contact. In SPE Latin American and Caribbean Petroleum
620 Engineering Conference. OnePetro.

621 Drummond, J., Schmadel, N., Kelleher, C., Packman, A., & Ward, A. (2019). Improving predictions of fine particle
622 immobilization in streams. *Geophysical Research Letters*, 46(23), 13853-13861.

623 Duan, Y., Feng, X.T., Li, X., Ranjith, P.G., Yang, B., Gu, L. and Li, Y., 2022. Investigation of the effect of initial
624 structure and loading condition on the deformation, strength, and failure characteristics of continental shale.
625 *Geomechanics and Geophysics for Geo-Energy and Geo-Resources*, 8(6), p.207.

626 Eichhubl, P. and Boles, J.R., 2000. Rates of fluid flow in fault systems; evidence for episodic rapid fluid flow in
627 the Miocene Monterey Formation, coastal California. *American Journal of Science*, 300(7), pp.571-600.

628 Farrell, N.J.C., Debenham, N., Wilson, L., Wilson, M.J., Healy, D., King, R.C., Holford, S.P. and Taylor, C.W.,
629 2021. The effect of authigenic clays on fault zone permeability. *Journal of Geophysical Research: Solid Earth*,
630 126(10), p.e2021JB022615.

- 631 Feng, R., Zhang, Y., Rezagholilou, A., Roshan, H., & Sarmadivaleh, M. (2020). Brittleness Index: from
632 conventional to hydraulic fracturing energy model. *Rock Mechanics and Rock Engineering*, 53(2), 739-753.
- 633 Fjaer, E., Holt, R. M., Horsrud, P., & Raaen, A. M. (2008). *Petroleum related rock mechanics*. Elsevier.
- 634 Fox, A., Packman, A. I., Boano, F., Phillips, C. B., & Arnon, S. (2018). Interactions between suspended kaolinite
635 deposition and hyporheic exchange flux under losing and gaining flow conditions. *Geophysical Research
636 Letters*, 45(9), 4077-4085.
- 637 Gao, C.H., 2011. Scientific research and field applications of polymer flooding in heavy oil recovery. *Journal of
638 Petroleum Exploration and Production Technology*, 1(2), pp.65-70.
- 639 Guo, Z., Hussain, F., & Cinar, Y. (2016). Physical and analytical modelling of permeability damage in bituminous
640 coal caused by fines migration during water production. *Journal of Natural Gas Science and Engineering*, 35, 331-
641 346.
- 642 Hadi, Y. A., Hussain, F., & Othman, F. (2019, July). Low salinity water flooding in carbonate reservoirs–
643 dissolution effect. In *IOP Conference Series: Materials Science and Engineering* (Vol. 579, No. 1, p. 012029).
644 IOP Publishing.
- 645 Han, Z., Yang, H., & He, M. (2019). A molecular dynamics study on the structural and mechanical properties of
646 hydrated kaolinite system under tension. *Materials Research Express*, 6(8), 0850c3.
- 647 Hashemi, A., Borazjani, S., Nguyen, C., Loi, G., Badalyan, A., Dang-Le, B. and Bedrikovetsky, P., 2022, October.
648 Fines Migration and Production in CSG Reservoirs: Laboratory & Modelling Study. In SPE Asia Pacific Oil &
649 Gas Conference and Exhibition. OnePetro.
- 650 Hashemi, A., Borazjani, S., Nguyen, C., Loi, G., Khazali, N., Badalyan, A., Yang, Y., Tian, Z.F., Ting, H.Z.,
651 Dang-Le, B. and Russell, T., 2023. Geo-mechanical aspects for breakage detachment of rock fines by Darcy's
652 flow. *arXiv preprint arXiv:2301.01422*.
- 653 Hou, X., Qi, S., Huang, X., Guo, S., Zou, Y., Ma, L. and Zhang, L., 2022. Hydrate morphology and mechanical
654 behavior of hydrate-bearing sediments: a critical review. *Geomechanics and Geophysics for Geo-Energy and Geo-
655 Resources*, 8(5), p.161.
- 656 Hu, K., Liu, D., Tian, P., Wu, Y., Deng, Z., Wu, Y., ... & Wu, Y. (2021). Measurements of the diversity of shape
657 and mixing state for ambient black carbon particles. *Geophysical Research Letters*, 48(17), e2021GL094522.
- 658 Huang, F., Kang, Y., You, Z., You, L., & Xu, C. (2017). Critical conditions for massive fines detachment induced
659 by single-phase flow in coalbed methane reservoirs: modeling and experiments. *Energy & Fuels*, 31(7), 6782-
660 6793.
- 661 Huang F, Kang Y, You L, Li X, You Z. Massive fines detachment induced by moving gas-water interfaces during
662 early stage two-phase flow in coalbed methane reservoirs. *Fuel*. 2018 Jun 15; 222:193-206.
- 663 Huang, F., Dong, C., You, Z., & Shang, X. (2021). Detachment of coal fines deposited in proppant packs induced
664 by single-phase water flow: Theoretical and experimental analyses. *International Journal of Coal Geology*, 239,
665 103728.
- 666 Iglauer, S., Akhondzadeh, H., Abid, H., Paluszny, A., Keshavarz, A., Ali, M., ... & Lebedev, M. (2022). Hydrogen
667 flooding of a coal core: effect on coal swelling. *Geophysical Research Letters*, 49(6), e2021GL096873.
- 668 Iglauer, S., Ali, M., & Keshavarz, A. (2021). Hydrogen wettability of sandstone reservoirs: implications for
669 hydrogen geo-storage. *Geophysical Research Letters*, 48(3), e2020GL090814.
- 670 Iglauer, S., Pentland, C. H., & Busch, A. (2015). CO₂ wettability of seal and reservoir rocks and the implications
671 for carbon geo-sequestration. *Water Resources Research*, 51(1), 729-774.

672 Ishido, T., Kikuchi, T., Miyazaki, Y., Nakao, S. and Hatakeyama, K., 1992. Analysis of pressure transient data
673 from the Sumikawa geothermal field (No. SGP-TR-141-26). Geological Survey of Japan, Tsukuba, Ibaraki, JP;
674 Mitsubishi Materials Corporation, Kazuno, Akita, JP.

675 Israelachvili, J.N., 2015. Intermolecular and Surface Forces. Third. ISBN: 9780123919274. DOI, 10, pp.1-676.

676 Jaeger, J. C., Cook, N. G., & Zimmerman, R. (2009). *Fundamentals of rock mechanics*. John Wiley & Sons.

677 Johnson, W.P., Pazmino, E., Colloid (Nano- and Micro-Particle) Transport and Surface Interaction in Groundwater
678 The Groundwater project, Guelph, Ontario, Canada, 2023.

679 Kulakov, V.V. and Berdnikov, N.V., 2020. Hydrogeochemical processes in the Tunguska reservoir during in situ
680 treatment of drinking water supplies. *Applied Geochemistry*, 120, p.104683.

681 Kumari, W.G.P., Beaumont, D.M., Ranjith, P.G., Perera, M.S.A., Avanthi Isaka, B.L. and Khandelwal, M., 2019.
682 An experimental study on tensile characteristics of granite rocks exposed to different high-temperature treatments.
683 *Geomechanics and Geophysics for Geo-Energy and Geo-Resources*, 5, pp.47-64.

684 Lehmann, P., Leshchinsky, B., Gupta, S., Mirus, B.B., Bickel, S., Lu, N. and Or, D., 2021. Clays are not created
685 equal: How clay mineral type affects soil parameterization. *Geophysical Research Letters*, 48(20),
686 p.e2021GL095311.

687 Li, N., Xie, H., Hu, J. and Li, C., 2022. A critical review of the experimental and theoretical research on cyclic
688 hydraulic fracturing for geothermal reservoir stimulation. *Geomechanics and Geophysics for Geo-Energy and
689 Geo-Resources*, 8, pp.1-19.

690 Liao, X., Shi, Y., Liu, C. P., & Wang, G. (2021). Sensitivity of permeability changes to different earthquakes in a
691 fault zone: Possible evidence of dependence on the frequency of seismic waves. *Geophysical Research
692 Letters*, 48(9), e2021GL092553.

693 Liu, W., Zhao, J., Nie, R., Liu, Y. and Du, Y., 2018. A coupled thermal-hydraulic-mechanical nonlinear model for
694 fault water inrush. *Processes*, 6(8), p.120.

695 Liu, J., Yuan, X., Zhang, J., Xi, W., Feng, J., & Wu, H. (2019). Sharp Reductions in High-Productivity Well Due
696 to Formation Damage: Case Study in Tarim Basin, China. In *Proceedings of the International Field Exploration
697 and Development Conference 2017* (pp. 843-857). Springer, Singapore.

698 Lu, Y., Moernaut, J., Bookman, R., Waldmann, N., Wetzler, N., Agnon, A., ... & Hubert-Ferrari, A. (2021). A new
699 approach to constrain the seismic origin for prehistoric turbidites as applied to the Dead Sea Basin. *Geophysical
700 Research Letters*, 48(3), e2020GL090947.

701 Maloszewski, P., Herrmann, A. and Zuber, A., 1999. Interpretation of tracer tests performed in fractured rock of
702 the Lange Bramke basin, Germany. *Hydrogeology Journal*, 7, pp.209-218.

703 Matthäi, S.K. and Roberts, S.G., 1996. The influence of fault permeability on single-phase fluid flow near fault-
704 sand intersections: Results from steady-state high-resolution models of pressure-driven fluid flow. *AAPG bulletin*,
705 80(11), pp.1763-1779.

706 Mishra, S., & Ojha, K. (2016, November). A Novel Chemical Composition to Consolidate the Loose Sand
707 Formation in the Oil Field. In *International Petroleum Technology Conference*. OnePetro.

708 Obermayr, M., Dressler, K., Vrettos, C., & Eberhard, P. (2013). A bonded-particle model for cemented
709 sand. *Computers and Geotechnics*, 49, 299-313.

710 Ochi, J., & Vernoux, J. F. (1998). Permeability decrease in sandstone reservoirs by fluid injection: hydrodynamic
711 and chemical effects. *Journal of hydrology*, 208(3-4), 237-248.

- 712 Othman, F., Yu, M., Kamali, F., & Hussain, F. (2018). Fines migration during supercritical CO₂ injection in
713 sandstone. *Journal of Natural Gas Science and Engineering*, 56, 344-357.
- 714 Peischl, J., Ryerson, T.B., Aikin, K.C., De Gouw, J.A., Gilman, J.B., Holloway, J.S., Lerner, B.M., Nadkarni, R.,
715 Neuman, J.A., Nowak, J.B. and Trainer, M., 2015. Quantifying atmospheric methane emissions from the
716 Haynesville, Fayetteville, and northeastern Marcellus shale gas production regions. *Journal of Geophysical*
717 *Research: Atmospheres*, 120(5), pp.2119-2139.
- 718 Polyanin, A. D. (2002). Linear partial differential equations for Engineers and Scientists. *Chapman and Hall/CRC*.
- 719 Polyanin, A. D., & Manzhirov, A. V. (2006). *Handbook of mathematics for engineers and scientists*. Chapman
720 and Hall/CRC.
- 721 Polyanin, A. D., & Zaitsev, V. F. (2012). Handbook of nonlinear partial differential equations. Chapman &
722 Hall/CRC Press, Boca Raton.
- 723 Prasetyo, M.H., Anggraini, H., Tjahjono, H., Pramadana, A.B., Akbari, A., Madyanova, M., Mekarsari, R.,
724 Akbarizal, A. and Setiawan, P., 2021, October. Success Story of Optimizing Hydraulic Fracturing Design at Alpha
725 Low-Permeability Reservoir. In SPE/IATMI Asia Pacific Oil & Gas Conference and Exhibition. OnePetro.
- 726 Ren, J., He, H., & Senetakis, K. (2021). A Micromechanical-based investigation on the frictional behaviour of
727 artificially bonded analogue sedimentary rock with calcium carbonate. *Pure and Applied Geophysics*, 178(11),
728 4461-4486.
- 729 Roshan, H., Al-Yaseri, A.Z., Sarmadivaleh, M. and Iglauer, S., 2016. On wettability of shale rocks. *Journal of*
730 *colloid and interface science*, 475, pp.104-111.
- 731 Roshan, H., Li, D., Canbulat, I. and Regenauer-Lieb, K., 2023. Borehole deformation based in situ stress estimation
732 using televiewer data. *Journal of Rock Mechanics and Geotechnical Engineering*.
- 733 Russell, T., Pham, D., Neishaboor, M.T., Badalyan, A., Behr, A., Genolet, L., Kowollik, P., Zeinjahromi, A. and
734 Bedrikovetsky, P., 2017. Effects of kaolinite in rocks on fines migration. *Journal of Natural Gas Science and*
735 *Engineering*, 45, pp.243-255.
- 736 Shang J, Flury M, Chen G, Zhuang J. Impact of flow rate, water content, and capillary forces on in situ colloid
737 mobilization during infiltration in unsaturated sediments. *Water Resources Research*. 2008 Jun;44(6).
- 738 Shi, J.Q., Durucan, S. and Fujioka, M., 2008. A reservoir simulation study of CO₂ injection and N₂ flooding at
739 the Ishikari coalfield CO₂ storage pilot project, Japan. *International Journal of Greenhouse Gas Control*, 2(1),
740 pp.47-57.
- 741 Siddiqui, M.A.Q., Chen, X., Iglauer, S. and Roshan, H., 2019. A multiscale study on shale wettability: Spontaneous
742 imbibition versus contact angle. *Water Resources Research*, 55(6), pp.5012-5032.
- 743 Shapiro, A.A., 2015. Two-phase immiscible flows in porous media: The Mesoscopic Maxwell–Stefan approach.
744 *Transport in Porous Media*, 107, pp.335-363.
- 745 Shapiro, A.A., 2018. A three-dimensional model of two-phase flows in a porous medium accounting for motion
746 of the liquid–liquid interface. *Transport in Porous Media*, 122(3), pp.713-744.
- 747 Spivak, A., Karaoguz, D., Issever, K. and Nolen, J.S., 1989, April. Simulation of immiscible CO₂ injection in a
748 fractured carbonate reservoir, Bati Raman Field, Turkey. In SPE California regional meeting. OnePetro.
- 749 Su, L., Lv, A., Aghighi, M.A. and Roshan, H., 2022. A theoretical and experimental investigation of gas
750 adsorption-dependent bulk modulus of fractured coal. *International Journal of Coal Geology*, 257, p.104013.

- 751 Sun, X. and Xiang, Y. (2021). Aquifer permeability decreases before local earthquakes inferred from water level
752 response to period loading. *Geophysical Research Letters*, 48(15), p.e2021GL093856.
- 753 Tang, Y., Lv, C., Wang, R., & Cui, M. (2016). Mineral dissolution and mobilization during CO₂ injection into the
754 water-flooded layer of the Pucheng Oilfield, China. *Journal of Natural Gas Science and Engineering*, 33, 1364-
755 1373.
- 756 Teitelbaum, Y., Shimony, T., Saavedra Cifuentes, E., Dallmann, J., Phillips, C. B., Packman, A. I., ... & Arnon, S.
757 (2022). A Novel Framework for Simulating Particle Deposition with Moving Bedforms. *Geophysical Research*
758 *Letters*, 49(4), e2021GL097223.
- 759 Timoshenko, S. P., & Goodier, J. N. (1970). Theory of Elasticity. *McGraw-Hill International Editions: New*
760 *York*, 341, 342.
- 761 Ting, H.Z., Bedrikovetsky, P., Tian, Z.F. and Carageorgos, T., 2021. Impact of shape on particle detachment in
762 linear shear flows. *Chemical Engineering Science*, 241, p.116658.
- 763 Ting, H.Z., Yang, Y., Tian, Z.F., Carageorgos, T. and Bedrikovetsky, P., 2022. Image interpretation for kaolinite
764 detachment from solid substrate: Type curves, stochastic model. *Colloids and Surfaces A: Physicochemical and*
765 *Engineering Aspects*, 650, p.129451.
- 766 Torkezaban, S., Bradford, S. A., Vanderzalm, J. L., Patterson, B. M., Harris, B., & Prommer, H. (2015). Colloid
767 release and clogging in porous media: Effects of solution ionic strength and flow velocity. *Journal of contaminant*
768 *hydrology*, 181, 161-171.
- 769 Tu, J., Yeoh, G. H., & Liu, C. (2018). *Computational fluid dynamics: a practical approach*. Butterworth-
770 Heinemann.
- 771 Turner, L. G., & Steel, K. M. (2016). A study into the effect of cleat demineralisation by hydrochloric acid on the
772 permeability of coal. *Journal of Natural Gas Science and Engineering*, 36, 931-942.
- 773 Wagner, T. J., James, T. D., Murray, T., & Vella, D. (2016). On the role of buoyant flexure in glacier
774 calving. *Geophysical Research Letters*, 43(1), 232-240A.
- 775 Wang, J., Huang, Y., Zhou, F., Song, Z., & Liang, X. (2020). Study on reservoir damage during acidizing for high-
776 temperature and ultra-deep tight sandstone. *Journal of Petroleum Science and Engineering*, 191, 107231.
- 777 Wang, C., Xu, X., Zhang, Y., Arif, M., Wang, Q. and Iglauer, S., 2022a. Experimental and numerical investigation
778 on the dynamic damage behavior of gas-bearing coal. *Geomechanics and Geophysics for Geo-Energy and Geo-*
779 *Resources*, 8(2), p.49.
- 780 Wang, T., Liu, Y., Cai, M., Zhao, W., Ranjith, P.G. and Liu, M., 2022b. Optimization of rock failure criteria under
781 different fault mechanisms and borehole trajectories. *Geomechanics and Geophysics for Geo-Energy and Geo-*
782 *Resources*, 8(4), p.127.
- 783 Wang, Y., Yin, H., Othman, F., Zeinijahromi, A. and Hussain, F., 2022c. Analytical model for fines migration due
784 to mineral dissolution during CO₂ injection. *Journal of Natural Gas Science and Engineering*, 100, p.104472.
- 785 Wilson, M. D., & Pittman, E. D. (1977). Authigenic clays in sandstones; recognition and influence on reservoir
786 properties and paleoenvironmental analysis. *Journal of Sedimentary Research*, 47(1), 3-31.
- 787 Wurgaft, E., Wang, Z. A., Churchill, J. H., Dellapenna, T., Song, S., Du, J., ... & Lazar, B. (2021). Particle triggered
788 reactions as an important mechanism of alkalinity and inorganic carbon removal in river plumes. *Geophysical*
789 *Research Letters*, 48(11), e2021GL093178.

- 790 Xu, X., Liu, J., Jin, X., Zhang, Y., Arif, M., Wang, C. and Iglauer, S., 2022. Dynamic mechanical response
791 characteristics of coal upon exposure to KCl brine. *Geomechanics and geophysics for geo-energy and geo-*
792 *resources*, 8(6), p.174.
- 793 Xue, Y., Liu, J., Ranjith, P.G., Gao, F., Zhang, Z. and Wang, S., 2022. Experimental investigation of mechanical
794 properties, impact tendency, and brittleness characteristics of coal mass under different gas adsorption pressures.
795 *Geomechanics and Geophysics for Geo-Energy and Geo-Resources*, 8(5), p.131.
- 796 Yang, H., Han, Z. F., Hu, J., & He, M. C. (2019). Defect and temperature effects on the mechanical properties of
797 kaolinite: a molecular dynamics study. *Clay Minerals*, 54(2), 153-159.
- 798 You, Z., Badalyan, A., & Hand, M. (2015). Particle mobilization in porous media: temperature effects on
799 competing electrostatic and drag forces. *Geophysical Research Letters*, 42(8), 2852-2860.
- 800 You, Z., Badalyan, A., Yang, Y. & Hand, M., 2019. Fines migration in geothermal reservoirs: Laboratory and
801 mathematical modelling. *Geothermics*, 77, pp.344-367.
- 802 Yu, H., Zhu, S., Xie, H. and Hou, J., 2020. Numerical simulation of water inrush in fault zone considering seepage
803 paths. *Natural Hazards*, 104, pp.1763-1779.
- 804 Yuan, B., & Moghanloo, R. G. (2018). Nanofluid pre-coating: an effective method to reduce fines migration in
805 radial systems saturated with two mobile immiscible fluids. *SPE Journal*, 23(03), 998-1018.
- 806 Yuan, B., & Moghanloo, R. G. (2019). Analytical modeling nanoparticles-fines reactive transport in porous media
807 saturated with mobile immiscible fluids. *AIChE Journal*, 65(10), e16702.
- 808 Yuan, H., & Shapiro, A. A. (2011). Induced migration of fines during waterflooding in communicating layer-cake
809 reservoirs. *Journal of Petroleum Science and Engineering*, 78(3-4), 618-626.
- 810 Zhai, X. and Atefi-Monfared, K., 2021. Production versus injection induced poroelasticity in porous media
811 incorporating fines migration. *Journal of Petroleum Science and Engineering*, 205, p.108953.
- 812 Zhao, Y., Liu, S., Zhao, G. F., Elsworth, D., Jiang, Y., & Han, J. (2014). Failure mechanisms in coal: Dependence
813 on strain rate and microstructure. *Journal of Geophysical Research: Solid Earth*, 119(9), 6924-6935.

8. Fines migration and production in CSG reservoirs: laboratory & modelling study detailed coreflood treatment coal cases

Hashemi, A., Borazjani, S., Nguyen, C., Loi, G., Badalyan, A., Dang-Le, B. and Bedrikovetsky, P., 2022, October.

In SPE Asia Pacific Oil & Gas Conference and Exhibition. OnePetro.

Statement of Authorship

Title of Paper	Fines migration and production in CSG reservoirs: laboratory & modelling study detailed coreflood treatment coal cases
Publication Status	<input checked="" type="checkbox"/> Published <input type="checkbox"/> Submitted for Publication <input type="checkbox"/> Accepted for Publication <input type="checkbox"/> Unpublished and Unsubmitted work written in manuscript style
Publication Details	Hashemi, A., Borazjani, S., Nguyen, C., Loi, G., Badalyan, A., Dang-Le, B. and Bedrikovetsky, P., 2022, October. Fines Migration and Production in CSG Reservoirs: Laboratory & Modelling Study. In SPE Asia Pacific Oil & Gas Conference and Exhibition. OnePetro.

Principal Author

Name of Principal Author (Candidate)	Abolfazl Hashemi		
Contribution to the Paper	Derived the equations, prepared the graphs, wrote part of the manuscript, presented at the conference.		
Overall percentage (%)	85%		
Certification:	This paper reports on original research I conducted during the period of my Higher Degree by Research candidature and is not subject to any obligations or contractual agreements with a third part that would constrain its inclusion in this thesis. I am the primary author of this paper.		
Signature		Date	15/11/2023

Co-Author Contributions

By signing the Statement of Authorship, each author certifies that:

- I. The candidate's stated contribution to the publication is accurate (as detailed above);
- II. Permission is granted to the candidate to include the publication in the thesis; and
- III. The sum of all co-author contributions is equal to 100% less the candidate's stated contribution

Name of Co-Author	Sara Borazjani		
Contribution to the Paper	Co-supervising, aiding in the derivations of breakage equations and checking the results		
Signature		Date	15/11/2023

Name of Co-Author	Cuong Cao Nguyen		
Contribution to the Paper	Collecting literature data, writing code, and analysing detrital particle detachment		
Signature		Date	15/11/2023

Name of Co-Author	Grace Loi		
Contribution to the Paper	Collecting literature data, writing code, and analysing detrital particle detachment		
Signature		Date	15/11/2023

Name of Co-Author	Alex Badalyan		
Contribution to the Paper	Supervising lab design and data collection		
Signature		Date	15/11/2023

Name of Co-Author	Bryant Dang-Le		
Contribution to the Paper	Collecting and analysing lab data, collecting field data.		
Signature	Bryant Dang-Le	Date	15/11/2023

Name of Co-Author	Pavel Bedrikovetsky		
Contribution to the Paper	Methodology and supervision.		
Signature		Date	15/11/2023

SPE-210764-MS

Fines Migration and Production in CSG Reservoirs: Laboratory & Modelling Study

Abolfazl Hashemi, Sara Borazjani, Cuong Nguyen, Grace Loi, Alexander Badalyan, Bryant Dang-Le, and Pavel Bedrikovetsky, University of Adelaide

Copyright 2022, Society of Petroleum Engineers DOI [10.2118/210764-MS](https://doi.org/10.2118/210764-MS)

This paper was prepared for presentation at the SPE Asia Pacific Oil & Gas Conference and Exhibition held in Adelaide, Australia on 17 - 19 October, 2022.

This paper was selected for presentation by an SPE program committee following review of information contained in an abstract submitted by the author(s). Contents of the paper have not been reviewed by the Society of Petroleum Engineers and are subject to correction by the author(s). The material does not necessarily reflect any position of the Society of Petroleum Engineers, its officers, or members. Electronic reproduction, distribution, or storage of any part of this paper without the written consent of the Society of Petroleum Engineers is prohibited. Permission to reproduce in print is restricted to an abstract of not more than 300 words; illustrations may not be copied. The abstract must contain conspicuous acknowledgment of SPE copyright.

Abstract

Fines detachment is an important component of methane production from Coal Bed Methane reservoirs. Production of coal fines is widely observed during dewatering and simultaneous gas-water production. The theory for fines detachment by drag against electrostatic attraction, model of the transport of those detrital fines, and their validation by laboratory test is widely used for planning and design of Coal Seam Gas developments. However, clay particles that naturally grow on coal grains and asperous parts of coal surfaces (authigenic and potential coal fines) are detached by breakage. To the best of our knowledge, the analytical theory for detachment of authigenic and potential coal fines is not available. The present paper fills the gap. Based on Timoshenko's beam theory, we derive failure conditions for breakage of authigenic and potential coal fines of the rock surface. It allows defining maximum retention function for fines breakage. The maximum retention is incorporated into transport equation of mobilized fines, allowing developing analytical models for linear flow of core flooding and radial flow of well inflow performance. Matching of laboratory coreflood data from four laboratory studies show high agreement. The model coefficients obtained by treatment of laboratory data allow predicting skin growth in production wells under fines migration.

Introduction

Fines migration in CSG fields comprises a serious environmental and gas-production challenge. The literature widely reports of two kinds of fines: so-called potential coal fines, which are a part of the coal body and can be detached by breakage under a significant drag force exerted by the inflowing water, and detrital coal fines, that are attached to the coal body by electrostatic forces. The potential coal fines include coal particles and authigenic clays that break off from the rock skeleton by drag exerted by the water flow.

Figure 1 shows Scanning Electron Microscope (SEM) images of the detrital coal particles at the cleat surfaces of coal rocks. The SEM images of authigenic coal fines are shown in **Figure 2**. It includes kaolinite booklets, crystals of illite and iron sulphate minerals. It is assumed that authigenic coal particles have been broken off the surface and transported in the rock, until an attachment site on the rock surface was met. This is how an authigenic particle becomes detrital. **Figure 3** shows SEM images of hairy illite particles broken

by drag exerted by the flow of highly viscous fracturing fluid. Figure 4 shows authigenic kaolinite particles in the Berea core, and the breakage after a critical fluid velocity.

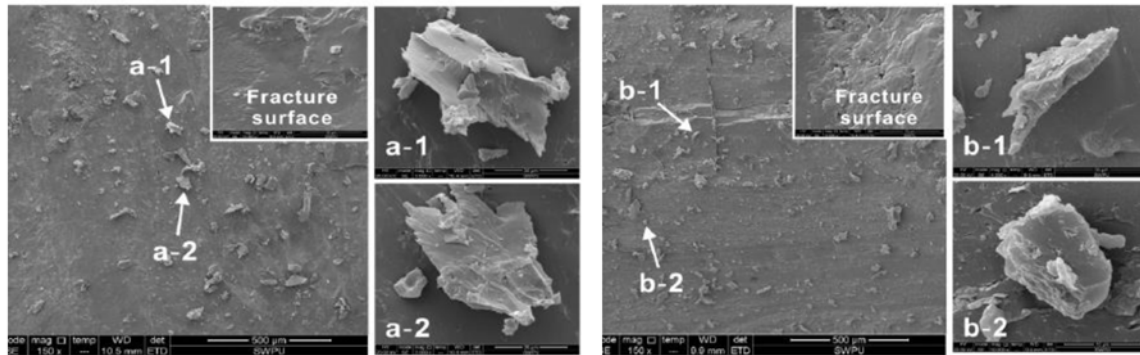


Figure 1—SEM images of detrital coal fines and fracture surfaces (Huang et al. 2018)

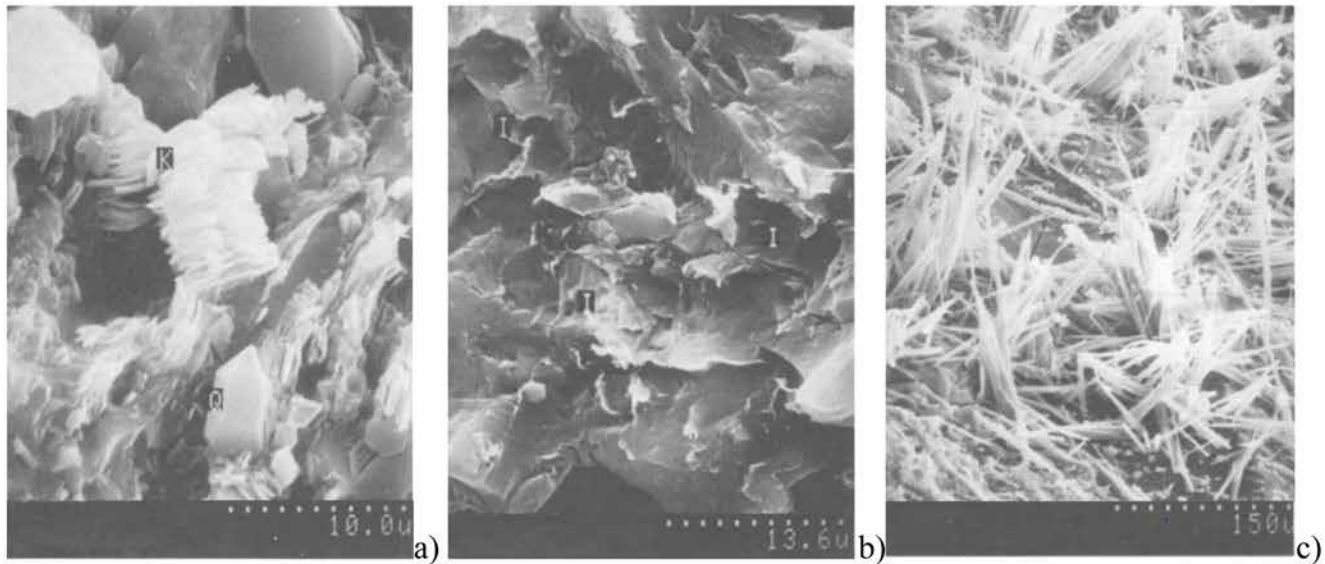


Figure 2—SEM images of authigenic coal fines (a) booklets of kaolinite, (b) flaky illite crystal, and (c) iron sulphate minerals growing from a coal fracture surface. (Nick et al. 1995)

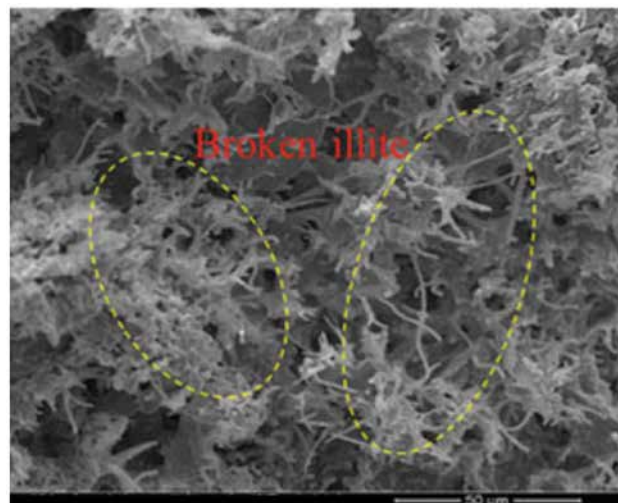


Figure 3—SEM images of hairy illite broken after treatment with fracturing fluid. (Liu et al., 2019)

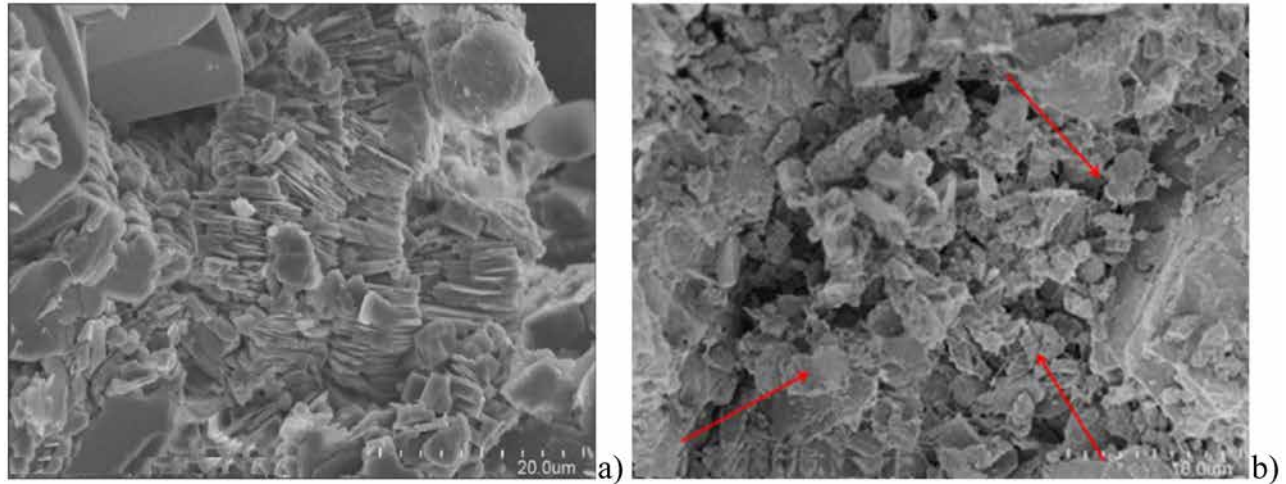


Figure 4—SEM images of a) non-damaged kaolinite structure of Berea core, b) broken kaolinite sheets of damaged Berea core that have undergone critical velocity test. (Shafian et al., 2021)

The detachment by breakage can be modelled on the pore scale by contact modelling of flow in coal cleats and stress in the rock matrix. In Figure 5a, SEM images of the cleats with significantly non-uniform borders are presented. Figure 5b show the digitalized solid and liquid domains for 2D modelling. Figures 5c,d show large scale stress distribution, and its zoom near to the bond between the particle and coal rock surface. This is the schematic of breakage modelling on the pore scale. Very similar study by the same team of authors is shown in Figure 6. Figure 6a presents SEM image of sharp asperity in the cleat. Figure 6b shows stress distribution in the rock along the cleat, and Figure 6c gives zoom of failure zones near to potential particles.

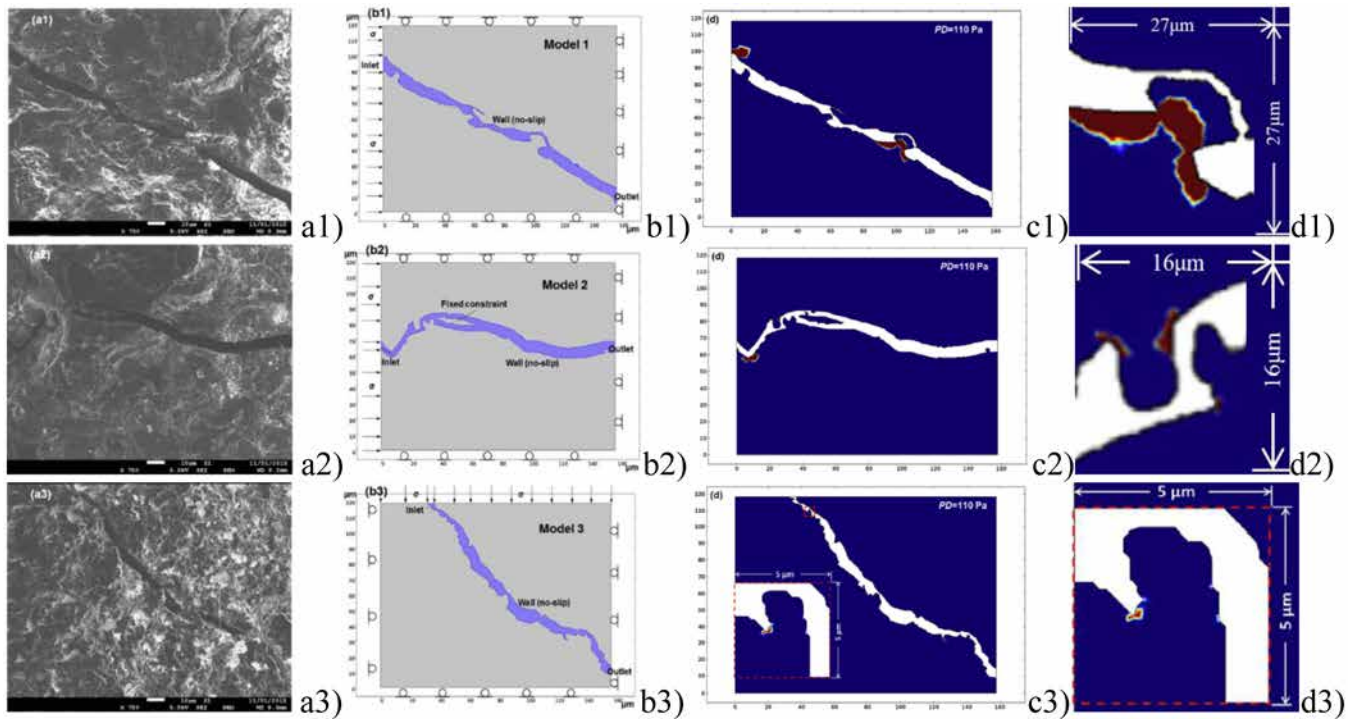


Figure 5—SEM photos potential fine generation at different coal cleats (a1,a2,a3), cleat and asperity geometries used in numerical simulations (b1,b2,b3) and failure zones (in red) for each case as a result of numerical simulation (c1,c2,c3), and zoom for failure zones (d1,d2,d3). (Bai et al. 2015)

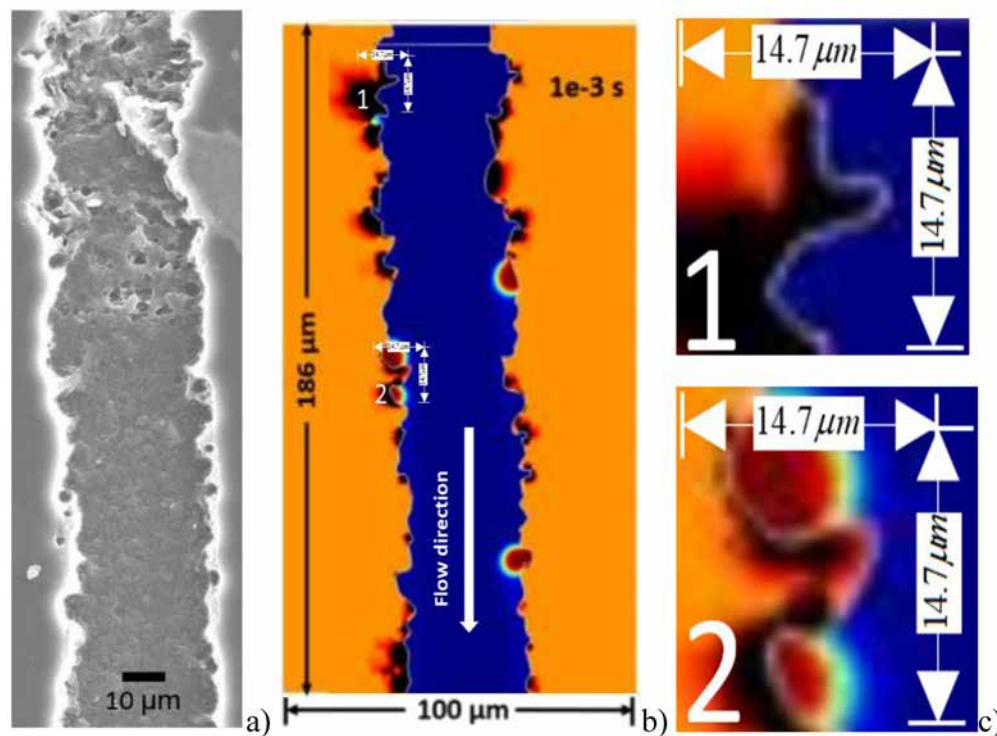


Figure 6—SEM photos potential fine generation at a coal cleat (a), cleat and asperity geometries used in numerical simulations (in orange) and water is flowed through the cleat in blue (b), zoom for potential fine particles and failure zones (in black) for each case as a result of numerical simulation (c). (Bai et al. 2016)

However, to predict water flow during CBM production, the microscale breakage model must be upscaled to the core scale and incorporated into the flow equation. The traditional theory for coal fines migration, where the detachment occurs by the drag exceeding the electrostatic attraction, is well developed. A theory for potential coal fines, where the drag deforms the coal asperities and attached clays and detaches fines by rock failure, is not available.

The *objectives* of this study are:

- derivation of microscale equations for fines generation by breakage using failure criteria;
- using analytical 1D linear fines-migration model to treat the lab data of coreflows with increasing flow rate and measurements of produced fines and permeability decline; and
- laboratory-based modelling prediction of well productivity decline during dewatering of CBM wells.

The *methodology* comprises microscale break-off modelling, equations for core-scale transport and fines migration, used to determine the model parameters from lab data and to predict well behaviour. The micro-model developed is based on beam theory and comprises static rock deformation by the flow-through water, construction of the Mohr's circles, and calculating the failure criteria by maximum tensile and shear stresses, limited by the strength values. The failure condition determines the number of fines that detach after application of each flow rate U , allowing determination of the Maximum Retention Function (MRF) of potential coal fines.

The breakage micro-model is incorporated into transport equations that account for fines mobilisation, migration, straining, and consequent permeability decline. Nonlinear 1D flows in linear (x,t) and radial (r,t) geometries allow for analytical modelling.

We performed the corefloods with piecewise-constant increasing flow rate with measurements of the pressure drop across the core and breakthrough concentration of fines. The goal is the validation of the breakage theory developed. The analytical linear flow model is used for tuning three model parameters. In particular, we determine the ratio between the potential coal fines and coal detrital fines in the produced suspension. The analytical radial flow model is used for lab-based prediction of well rate, water-cut, produced fines, and pressure drawdown under dewatering and gas production in CBM reservoirs.

The *experimental data treatment* by the analytical model comprises eight series of the lab flooding data with coal cores has been treated. Six tests exhibit detachment by both mechanisms, one - by breakage alone, and one - against the electrostatic attraction. Close match between lab and model has been observed.

The present paper closes the gap in the theory of breakage, migration and formation damage of authigenic coal particles and clays. The failure criteria derived are based on beam theory [18, 24, 37] and an analytical solution for beam under stress, developed by S. Timoshenko [30], and Computational Fluid Dynamics (CFD) solution of Navier-Stokes equations for flow around the attached fines. We derived an analytical expression for maxima of tensile and shear stresses and present the classification of breakage regimes.

The novelty of this work encompasses the multiscale model for fines detachment by breakage, their migration and consequent permeability impairment. This includes explicit formulae for fines production and pressure drop increase in coal cores. Explicit formulae for CBM well productivity and fines production during fines migration have also been developed.

The structure of the text is as follows. After section one of introduction, follows section two with description of drag force and its moment in the moving viscous fluid. Section three presents Timoshenko's 3D solution, and introduction of three dimensionless numbers for beam loading. Section four calculated maximum stresses. Section five, presents breakage criteria and classification of the breakage regimes. Section six defines MRF. A brief description of the transport equation and analytical models for coreflood and inflow well performance are given in section seven. Section eight presents laboratory methodology. The results of laboratory data treatment are given in section nine. Section ten exhibits the results of well behaviour prediction under migration of potential and authigenic coal fines. Section 11 discusses and concludes the paper.

Fluid-particle interaction by drag and its moment.

Coal fines detachment by breakage is an important occurrence during methane production from Coal Beds. Another event of the detachment in CBM production is mobilization of kaolinite/illite particles from the coal surfaces. The detaching force is the drag exerting from the creeping viscous flow around the particle (Fig. 7). The expression for drag force is a modification of Stokes formula, which is valid for particles immersed in the flux moving with velocity V far away from liquid-solid boundaries:

$$F_d = 6\pi\mu_f r_s V f_d \quad (1)$$

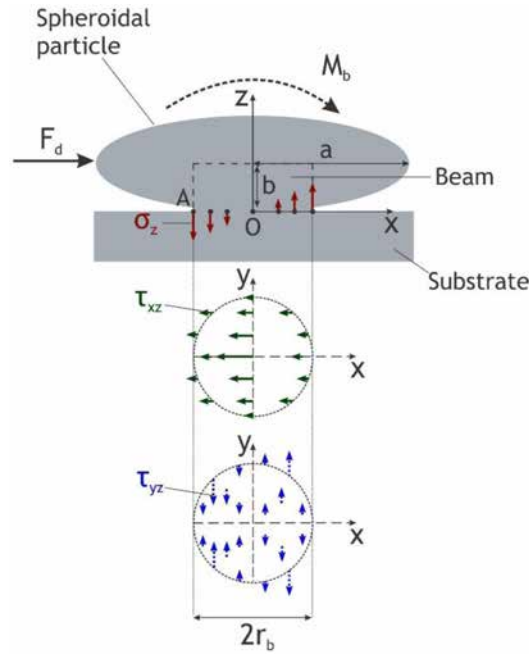


Figure 7—Schematic of equivalent beam for attached spheroidal particle

Here f_d is the shape factor that accounts for irregular form particles and for attaching substrate. This force is applied in the centre of mass of the particle. For irregular form particles, the shape factor f_M is introduced for the moment of the drag:

$$M_b = F_d b f_M \quad (2)$$

Here r_s is an equivalent radius of the spherical particle with the same volume, b is small semi-axis of the spheroidal particle, μ_f is the viscosity of fluid. Darcy's velocity for flow in porous media is determined with:

$$U = \phi V \quad (3)$$

where, ϕ is the effective porosity.

For no-slip flow condition, the shape factors for drag force and moment for oblate spheroids, which model kaolinite fines, are as follows [31]:

$$f_d = (0.8707\alpha_s^2 + 0.7908\alpha_s + 0.05844)(\alpha_s + 0.008453)^{-1} \quad (4)$$

$$f_M = (1.296\alpha_s^2 + 0.1509\alpha_s + 0.03718)(\alpha_s^2 + 0.0843\alpha_s + 0.0002284)^{-1}$$

respectively. Here α_s is the aspect ratio between the small and large axes of spheroid:

$$\alpha_s = \frac{b}{a} \quad (5)$$

3D stress distribution in beam

Figure 7 shows the beam equivalent to spheroidal particle [18, 21]. Drag force which is applied to the centre of spheroid becomes applied to the upper edge of the beam. It is assumed that the particle matter outside the beam does not affect stress distribution inside the beam. The base of the particle and beam coincide, so the conditions for detachment of the base are the same for the particle and the beam. Timoshenko's solution for the beam deformation loaded by force F_d and applied to the upper edge of the beam assumes independence of stresses of z , and exhibits maximum tensile stress in z at the cylinder base, i.e. at $z=0$,

$$\sigma_z = \frac{F_d b f_M x}{I} \quad (6)$$

$$\tau_{xz} = \frac{(3+2\nu) F_d}{8(1+\nu) I} \left(r_b^2 - x^2 - \frac{(1-2\nu)}{(3+2\nu)} y^2 \right) \quad (7)$$

$$\tau_{yz} = -\frac{(1+2\nu) F_d xy}{4(1+\nu) I} \quad (8)$$

$$\sigma_x = \sigma_y = \tau_{xy} = 0 \quad (9)$$

Here, σ_x , σ_y , σ_z are diagonal terms of 3x3 stress tensor, and τ_{xz} , τ_{yz} are non-diagonal terms.

Calculation of eigen values of the stress tensor provide the principal stresses, σ_1 , σ_2 , σ_3 for the equations (6-9). The maximum tensile and shear stresses are determined from the Mohr's circles:

$$\frac{\sigma_3}{T_0} = \frac{1}{\kappa} \left(X - \sqrt{X^2 + \chi \left(1 - X^2 - \frac{(1-2\nu)}{(3+2\nu)} Y^2 \right)^2} + \chi \frac{4(1+2\nu)^2}{(3+2\nu)^2} (XY)^2 \right) \quad (10)$$

$$\frac{\sigma_1 - \sigma_3}{2S_0} = \frac{\eta}{\kappa} \sqrt{X^2 + \chi \left(1 - X^2 - \frac{(1-2\nu)}{(3+2\nu)} Y^2 \right)^2} + \chi \frac{4(1+2\nu)^2}{(3+2\nu)^2} (XY)^2 \quad (11)$$

where the dimensionless drag-strength- number κ and shape-Poisson number χ are defined as

$$\frac{1}{\kappa} = \frac{1}{2T_0} \frac{F_d}{I} r_b^2 \frac{bf_M}{r_b}, \quad \chi = \left(\frac{bf_M}{r_b} \right)^{-2} \frac{(3+2\nu)^2}{16(1+\nu)^2}, \quad \eta = \frac{T_0}{S_0}, \quad X = \frac{x}{r_b}, \quad Y = \frac{y}{r_b} \quad (12)$$

From now on, κ is called the drag-strength number, and χ is the shape-Poisson number. The drag-strength number is a function of tensile strength T_0 , the moment of inertia I , drag F_d , and radius of bond r_b . The ratio r_b/a is called the bond ratio. The shape-Poisson number depends on bond ratio, aspect ratio, and Poisson's ratio.

Analytical expressions for tensile and shear stresses in the middle and at the boundary of the beam base

We prove that maximum stresses inside the circle are reached along the middle $Y=0$. Therefore, we discuss stresses just in the middle at $Y=0$, and at the bond boundary $Y^2=1-X^2$. Maxima of tensile and shear stresses in the middle and at the bond boundary can be calculated explicitly. Maxima are calculated by zero first derivative in X and negative second derivative. Maximum of tensile stress in the middle is determined by the conditions of

$$T_m^0(\chi) = \frac{1}{\kappa} \begin{cases} 2, & \chi \leq \chi_1 \\ -X_m(\chi) + \sqrt{X_m^2 + \chi(1-X_m^2)^2}, & \chi > \chi_1 \end{cases}; \quad X_m = \begin{cases} -1, & \chi \leq \chi_1 \\ -\sqrt{-\frac{\sqrt{(4\chi-1)(4\chi-9)}-4\chi+3}{8\chi}}, & \chi > \chi_1 \end{cases} \quad (13)$$

where, χ_1 is determined by the condition where maximum point $X=X_m$ jumps from $X_m=-1$ to X_{m1} . These values were found numerically $\chi_1=3.4$, $X_{m1}=-0.33$.

Maximum of tensile stress over the bond boundary is:

$$T_m^1(\chi, \nu) = \frac{1}{\kappa} \begin{cases} 2, & \zeta \leq 2 \\ \zeta(\zeta-1)^{-0.5}, & \zeta > 2 \end{cases}; \quad X_m = \begin{cases} -1, & \zeta \leq 2 \\ -(\zeta-1)^{-0.5}, & \zeta > 2 \end{cases} \quad (14)$$

where,

$$\zeta = \chi \frac{4(1+2\nu)^2}{(3+2\nu)^2} \quad (15)$$

To meet the failure criteria with respect to tensile stresses, we need to compare T_m^0 and T_m^1 . The blue curve in Figure 8a corresponds to their equality:

$$T_m^0(\chi) = T_m^1(\chi, \nu) \quad (16)$$

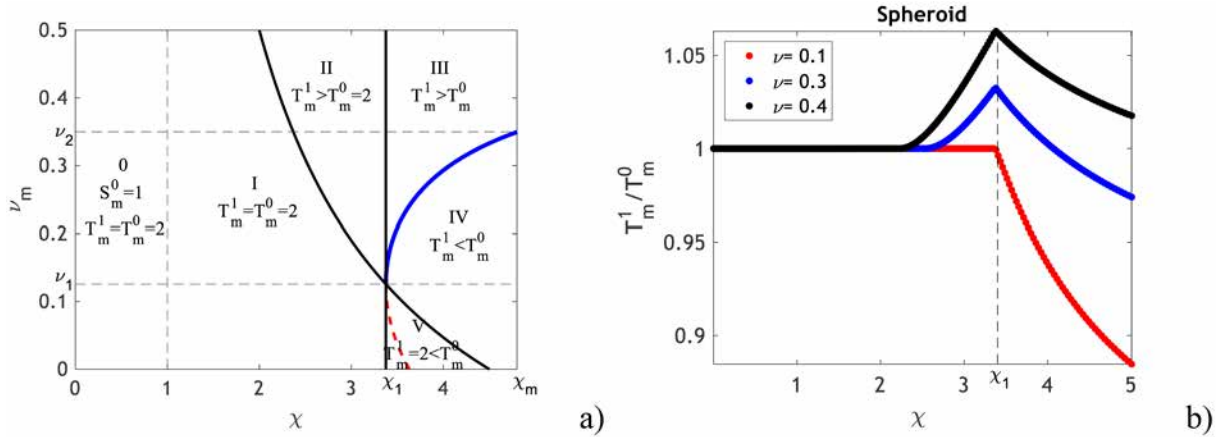


Figure 8—Comparison between dimensionless tensile stresses in the middle and on the beam boundary: a) determination of the critical Poisson's ratio whether the tensile stresses are equal; b) the ratio between tensile stresses on the boundary and in the middle

Formulae (13-15) allow distinguishing six zones 0 to V in the plane (χ, ν) . Figure 8a shows the relationship between T_m^0 and T_m^1 in each zone.

Figure 8b shows profiles for the ratio between two tensile stresses over χ for three typical values of Poisson's ratio ν from three intervals $[0, \nu_1]$, $[\nu_1, \nu_2]$, $[\nu_2, 0.5]$. In this work, we assume that for rock minerals ν does not exceed 0.5.

Explicit expression shear stress maxima are:

$$S_m^0(\chi) = \frac{T_0}{S_0 \kappa} \begin{cases} 1, & \chi < 1 \\ \sqrt{\chi}, & \chi > 1 \end{cases}; \quad X_m = \begin{cases} \pm 1, & \chi < 1 \\ 0, & \chi > 1 \end{cases} \quad (17)$$

$$S_m^1(\chi_1) = \frac{T_0}{S_0 \kappa} \begin{cases} \sqrt{\xi}, & \xi \geq 1 \\ 1, & \xi < 1 \end{cases}; \quad X_m = \begin{cases} 0, & \xi \geq 1 \\ \pm 1, & \xi < 1 \end{cases} \quad (18)$$

We prove that always S_m^0 is higher than S_m^1 . Therefore, further in the analysis of particle failure we compare two tensile stresses with shear stress in the middle. Shear stress in the middle is constant at $\chi < 1$, so we introduce zone zero in plane (χ, ν) .

Let us introduce dimensionless stresses in equation for Mohr circles:

$$\left[\frac{\kappa \sigma}{T_0} - \left(\frac{\kappa \sigma_1}{2T_0} + \frac{\kappa \sigma_3}{2T_0} \right) \right]^2 + \left(\frac{\kappa \tau}{\eta S_0} \right)^2 = \left[\frac{\kappa \sigma_1}{2T_0} - \frac{\kappa \sigma_3}{2T_0} \right]^2 \quad (19)$$

Figure 9 shows Mohr circles that correspond to zone 0 and five points in the middle $(X, 0)$ where abscissa X changes from -1 to 1 . Figure 9a shows profiles for dimensionless tensile stresses that monotonically decrease from 2 at $X=-1$ to zero at $X=1$. This corresponds to change of position of maximum tensile stress in Figure 9b, which corresponds to left edge point of circles $(-\sigma_3, 0)$ from -2 to zero. Maximum shear stress that is equal to circle radius, decreases from 1 to min at $X=0$ and then increases back to one (Figure 9a). This corresponds to movement of the top point of circles from maximum at $X=-1$ to min at $X=0$ and then to max in the receded point. Abscissa of the circle centre is obtained from Eq. (19) and is proportional to σ_z , which in turn is equal to X . This corresponds to movement of the circle centre from -1 at advanced point to zero at the base beam centre and to one in receded point.

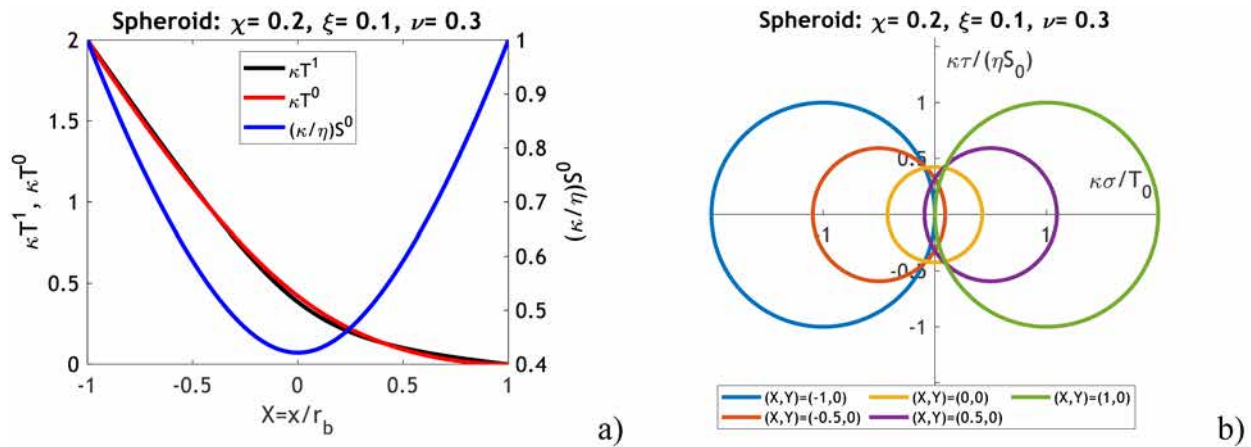


Figure 9—Mohr circles for particles from zone 0 taken in five points in the middle of the beam base

Failure criteria

Let us discuss the case of breakage by tensile stress:

$$\frac{\max(-\sigma_3)}{T_0} \geq \frac{\max(\sigma_1 - \sigma_3)}{2S_0} \tag{20}$$

where T^0 and S^0 are tensile and shear strengths, respectively.

For tensile stress in the middle, the ratio is called the breakage regime function:

$$g(\chi) = \frac{\max\left(-X + \sqrt{X^2 + \chi(1 - X^2)^2}\right)}{\max\left(\sqrt{X^2 + \chi(1 - X^2)^2}\right)} = \frac{T_m(\chi)}{S_m(\chi)} > \frac{T_0}{S_0} = \eta \tag{21}$$

This is the condition of breakage by tensile stress. Figure 10 presents three types of $g(\chi)$ function that corresponds to different intervals in ν in Figure 8a. Depending on which stress is higher the forms of function $g(\chi)$ are different. Figures 10a,b,c correspond to Poisson's ratio varying from 0 to ν_1 . Consequently, $g=2$ in zones zero and one. Figures 10d,e,f correspond to ν varying between ν_1 and ν_2 . Figures 10g,h,i correspond to Poisson's ratio varying from ν_2 to 0.5.

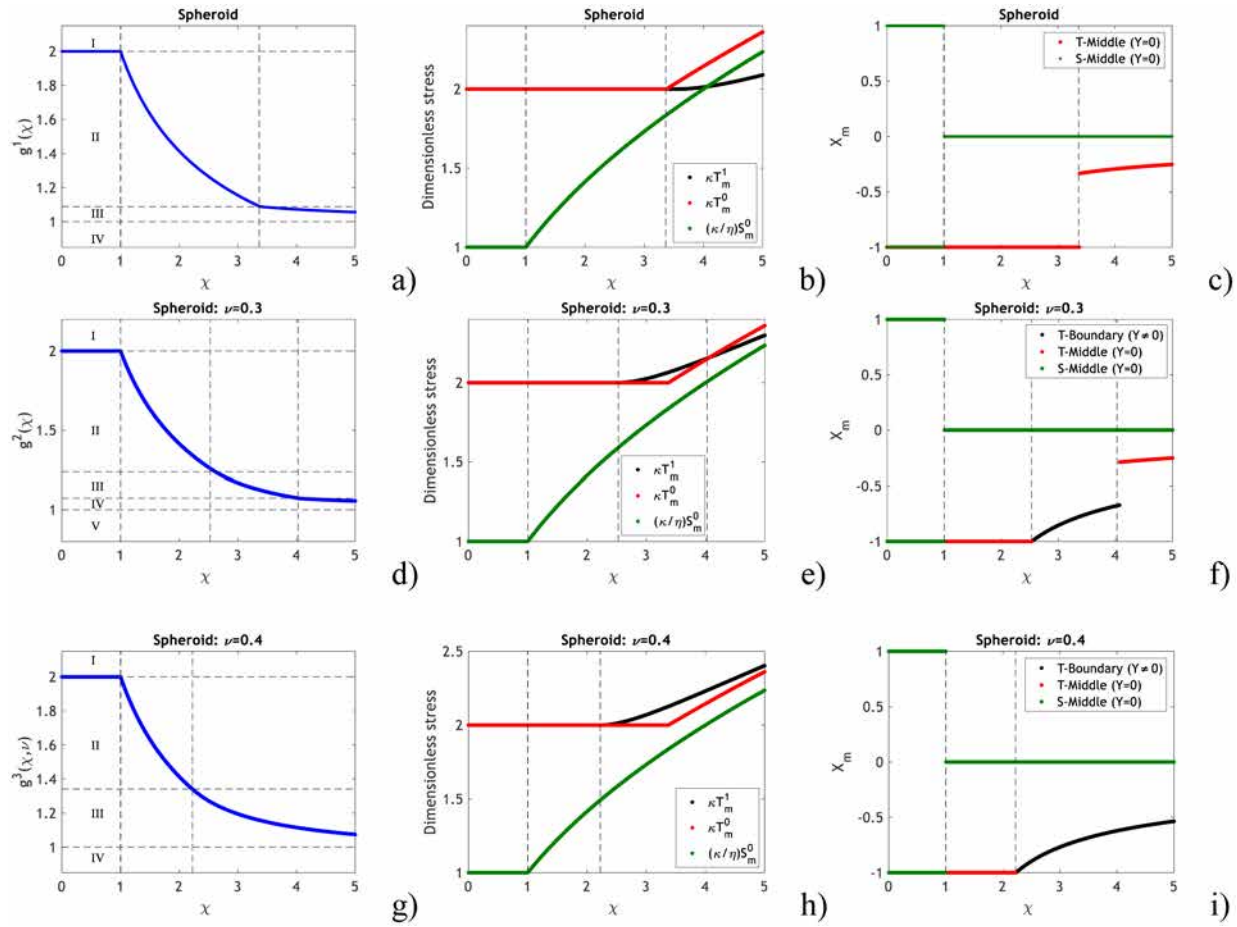


Figure 10—Breakage regime function $g(x)$ for different ν : a, b, c correspond to ν varying from zero to ν_1 ; d, e, f – to interval from ν_1 to ν_2 ; g, h, i– to interval from ν_2 to 0.5. Breakage regime function for three cases is presented in Figures a, d, and g. Three dimensionless stresses versus χ are shown in Figures. b, e, and h. Figures. c, f, and i show the points X_m where stresses reach maximum.

For all χ , if strength ratio exceeds 2, failure occurs due to shear stress. For all χ , if strength ratio is below 1, failure occurs due to tensile stress. If strength ratio varies from 1 to 2, failure is due to shear for lower values of χ , while for large value of χ the breakage is due to tensile stress. The boundary value for χ is determined by

$$g(\chi) = \eta = \frac{T_0}{S_0} \quad (22)$$

Let us express the drag-strength number via Darcy velocity $V\phi$:

$$\kappa = \frac{1}{2T_0} \frac{F_d}{I} r_b^2 \frac{bf_M}{r_b} = \frac{1}{T_0} \frac{2F_d}{\pi r_b^2} \frac{\alpha_s f_M}{\delta} = \frac{12\alpha_s f_M f_d \mu_f r_s (V\phi)}{\delta \phi T_0 r_b^2} \quad (23)$$

The above analysis determines maximum breaking stress allowing selecting equation (13), (14), or (17) to calculate the drag-strength number. From here we calculate Darcy's velocity, which breaks a particle with above mentioned parameters

$$U = (V\phi) = \frac{\delta \phi T_0 r_b^2}{12\alpha_s f_M f_d \mu_f r_s} \kappa \quad (24)$$

Maximum retention function as a model for fines breakage

Following papers [3, 4, 31], we introduce maximum retention function for particle breakage along with particle detachment against electrostatic forces. Introduced vector x consisting of parameters from the

equation of mechanical equilibrium of a particle on the rock surface. As it follows from analysis presented in sections 4 and 5, vector x has components of aspect ratio, bond ratio, tensile and shear strengths, viscosity, and Poisson's ratio.

Consider uniform particle on an ideal substrate. It defines a unique value of critical velocity. So, for velocities lower than critical, no particle is detached, and concentration of attached particle is equal to its initial value. For any velocity above critical, all particles are detached. However, all laboratory tests for injection of particle-free water exhibit gradual particle detachment. Usually, the detachment starts at some low velocity, and finishes at some high velocity. Gradual particle detachment is explained by the probabilistic distribution of particle properties. Consider mutual distribution of all components $f(x)$.

Equation (24) show how to calculate critical Darcy velocity for a particle with all known parameters. Let us determine the domain of parameters x , where velocity is lower than critical:

$$\Omega_U = \{\bar{x} \in R^n : U_{cr}(\bar{x}) < U\} \quad (25)$$

The concentration of remaining particles that are attached after flow with velocity U is

$$\sigma_{cr}^e(U) = \sigma_0 \iiint_{\Omega_U} f(x) dx^n \quad (26)$$

where σ_0 is the concentration of removable particles. This function is called Maximum Retention Function (MRF) and is a mathematical model for fines detachment. Concentration of attached particles by the flow with velocity U is:

$$\sigma_{cr}(U) = \sigma_0 \left(\int_0^{U_{cr}} f(U) dU \right) \quad (27)$$

By this formula in the further laboratory test treatment we determine the concentration of detached particles.

We assume that detrital and authigenic (potential) fines are detached independently. In this case, overall maximum retention function is a total of those for authigenic and detrital particles:

$$\sigma_{cr}(U) = \sigma_e^0 \int_U^\infty f_e(U) du + \sigma_f^0 \int_U^\infty f_f(U) du \quad (28)$$

Consequently, the concentration of detached particles while velocity regime changes from U_{n-1} to U_n is:

$$\Delta\sigma_n = \sigma_e^0 \int_{U_{n-1}}^{U_n} f_e(U) du + \sigma_f^0 \int_{U_{n-1}}^{U_n} f_f(U) du \quad (29)$$

Linear and radial transport of detached fines

MRF (26) is substituted into equation of mass balance of attached, suspended, and strained particles for colloidal-suspension-nano transport in porous media. This 3D system of equations is presented by [Bedrikovetsky et al. 2011, 2012](#), [Chequer et al. 2021](#), [Russell et al. 2018](#), and [Yang et al. 2018](#). The exact solution for 1D laboratory coreflood is obtained by [Bedrikovetsky et al. 2011](#), [Russell et al. 2018](#), and [Yang et al. 2017](#). This solution is used to treat the laboratory data on fines mobilisation in section 9. In [Chequer et al. 2021](#), the exact solution for 1D radial well inflow performance is obtained. This solution is used to predict skin growth during oil production with fines migration in section 9.

Laboratory study

In this section, we describe characteristics of fluid and rock used, laboratory setup, characterisation of effluents, and methodology of experimental study.

Materials

Sodium chloride solution with concentration 0.6 M was prepared from analytical grade NaCl with purity 99.7% (w/w) and degassed deionised water.

The core sample with the following dimensions was used in the present study: $L_{\text{half-core}} = 2.500$ cm; $L_{\text{overall-core}} = 5.072$ cm; $D_{\text{core}} = 3.797$ cm. This core was dried in the atmospheric oven at 60 °C for 24 hours for dehydration. Then, it was placed in a vacuum desiccator and vacuumed to the residual pressure of 1 Pa. After that, 0.6 M NaCl solution was introduced into the desiccator for core imbibition. Measured imbibition porosity was = 24.4% and resulting pore volumes $PV_{\text{half-core}} = 6.913$ cm³ and $PV_{\text{overall-core}} = 13.749$ cm³.

Laboratory setup

A schematic view and photo of an experimental apparatus for real-time permeability measurements with all key elements are shown in Figures 11a, b, respectively.

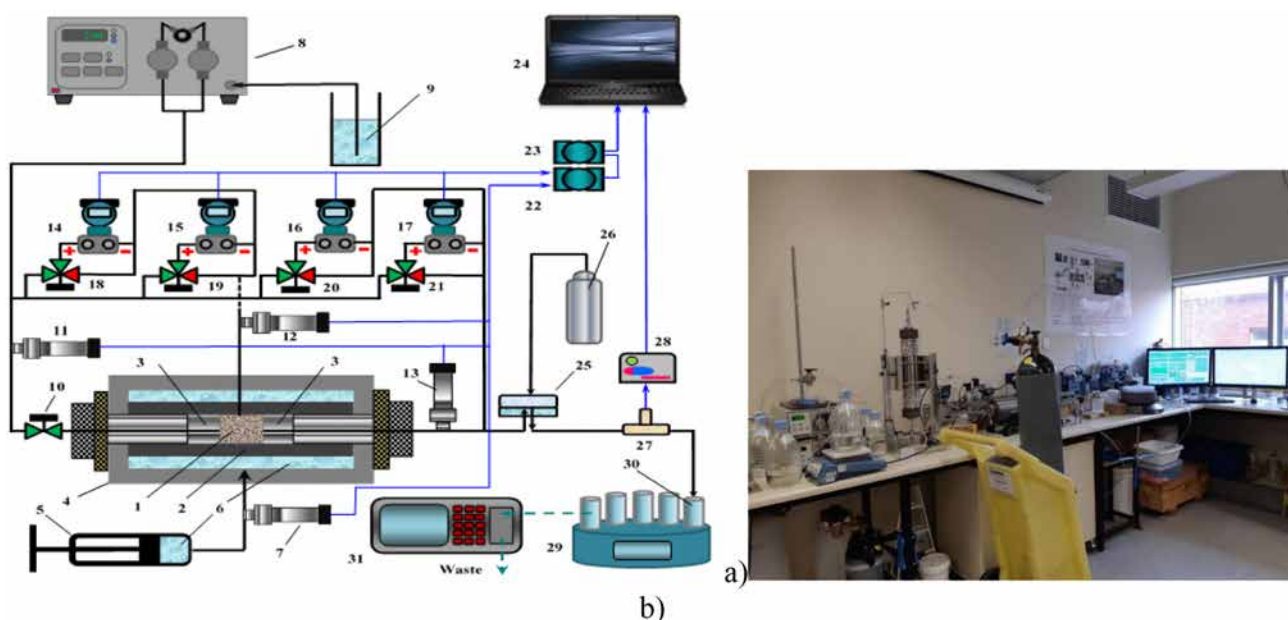


Figure 11—(a) Schematic and (b) photo of laboratory set-up for the detachment of authigenic (potential) and detrital particles.

The core 1 was placed in a Viton sleeve 2, fixed there by two flow distributors 3 and placed inside a high-pressure coreholder 4. Overburden pressure of 1000 psi was created by a manual pressure generator 5 by compressing distilled water 6, this pressure was measured by an absolute pressure transmitter 7. High-performance liquid chromatography pump 8 delivered 0.6 M NaCl solution and suspensions 9 to the core via an inlet valve 10. Inlet, middle and outlet pressures at the core were measured by two absolute pressure transmitters 11, 12 and 13, respectively. Differential pressures across the half-core and the overall-core were measured by differential pressure transmitters 14-17 via multiport valves 18-21. Data acquisition 22 and signal conditioning modules 23 delivered experimental parameters to a computer 24. Back-pressure regulator 25 was setup at 300 psi from compressed air cylinder 26. Electrolytic conductivity sensor 27 with a dedicated signal-conditioner 28 measured electrolytic conductivity of effluent suspensions. Effluent auto-sampler 29 was used to collect effluents in plastic tubes 30. Suspended particle concentrations (in ppm) sampling tubes were measured by portable particle counter 31.

Characterisation of effluents

Effluent particle number and size distribution was measured by a portable POLA-2000 particle counter/sizer. This instrument delivers the number of particles in effluent streams in the 0.5-to-15.0 μm particle size

range with 15 equally spaced size intervals. For each particle size interval the total number of particles are multiplied by the volume of one particle, and the sum of the respective volumes of particles was converted to particle concentration expressed in parts-per-million (*ppm*).

Methodology of experimental study

The experimental program consisted of four sub-programs.

In the first sub-program, the core was saturated by 0.6 M NaCl solution at flowrate 0.2 mL/min, and undamaged core permeability was measured. We carried out removal of fines by high-velocity corefloods with the following flowrates – 0.2, 2, 20, 70 and 100 mL/min. The system was returned to initial low flowrate (0.2 mL/min) after each elevated flowrate to check the effect of particle removal on core permeability. During this procedure, effluents were collected and particle concentrations were measured. After that, all effluent samples were mixed together (3,374 mL) and particle concentration of the overall effluent suspension was measured (this gives the total volume of fines to be injected into the core during the second sub-program).

The second sub-program dealt with re-injection of the effluent particles collected during the first sub-program. We collected effluent particles and measured their concentrations which is known as breakthrough concentration. Also, we monitored in real-time the variation of half-core and overall-core impedance with pore volumes injected (PVI). As a result, an external filter cake was formed on the core inlet face. To remove this filter cake, the core was immersed with its inlet face by approximately 2 mm deep in 0.6 M NaCl solution located in ultrasound bath for about 2 minutes. Suspension with thus removed particles was added to the remaining suspension left particle re-injection. The resulting suspension was diluted to make 5,000 mL by addition of 0.6 M NaCl solution. The final particle concentration in the resultant suspension was measured.

In the third sub-program, we injected 0.6 M NaCl solution into the core to check if we have restored initial core permeability by external cake removal. After that we re-injected suspension prepared in the second sub-program. We monitored in real-time the variation of half-core and overall-core impedance with PVI. This procedure has stopped after impedances 1.4 and 1.8 for the half-core and the overall-core, respectively, were reached.

Removal of newly deposited fines was carried out in the fourth sub-program similar to that in the first sub-program with three additional flowrates: 120, 170, and 200 mL/min. The last step in this sub-program was injection of degassed deionised water to achieve appreciable fines removal with associated formation damage. Effluents were collected and particle concentrations were measured.

Treatment of the laboratory data

This section presents the results of treatment of laboratory data on coal cores flooding from four papers [9, 11, 12, 13]. The mean value of the required parameters collected from literature. These parameters include Poisson's ratio [6, 7, 22, 23, 28, 32, 38, 40], Young's modulus [8, 15, 19, 38, 39, 40], Shear strength [1, 2, 8, 23, 32], Tensile strength [1, 2, 14, 20, 22, 32, 38, 40], aspect ratio [16, 33, 36], pore size distribution [25], particle size distribution [10, 29] and zeta potential [12,13]. The mean value for Poisson's ratio is 0.29, for Young's modulus is 3 Gpa, for Shear and tensile strengths is 21 Kpa, and aspect ratio is 0.63.

Huang et al. 2017, 2018. We consider detachment of fines by two different mechanisms against electrostatic attraction and by breakage. However, often two mechanisms against electrostatic attraction occurs in porous media - for detrital particles attaching primary and secondary minimum. [Figure 12](#) show Derjaguin, Landau, Verwey and Overbeek (DLVO) energy profile for the system coal-coal for the condition of laboratory tests. The system has only primary energy minimum, attachment of coal particle to coal substrate is favourable. The same corresponds to tests by [Guo et al. 2016](#) and [Huang et al. 2021](#). [Figure 13a](#) presents the dimensionless pressure drop across the core divided by velocity (impedance J). [Figure 13b](#) presents cumulative breakthrough concentrations for each velocity. The figure presents the results for four

core flooding SY2, SY3, SY4, and SY5 as performed under piece-wise constant increasing velocities. The quality of match is very high for all tests.

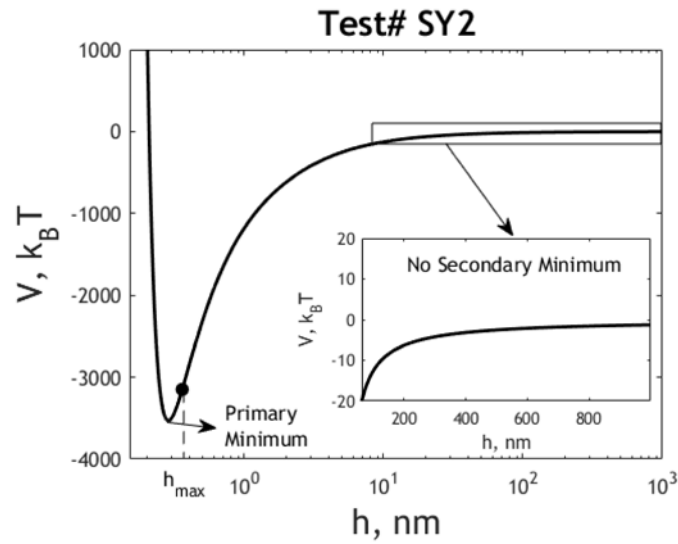
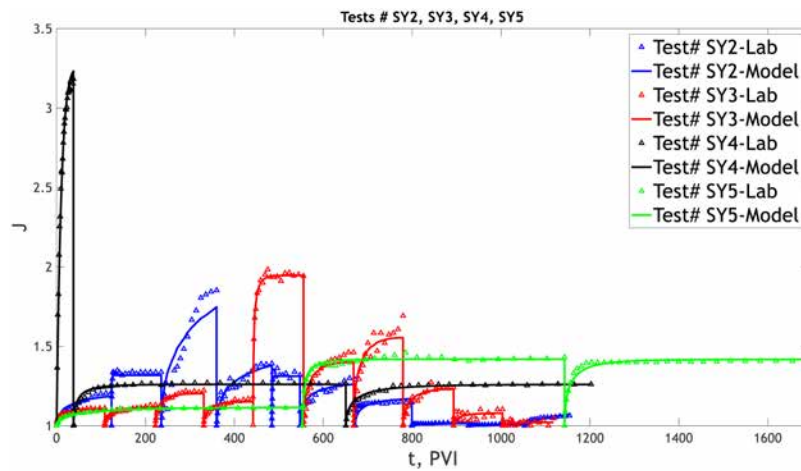
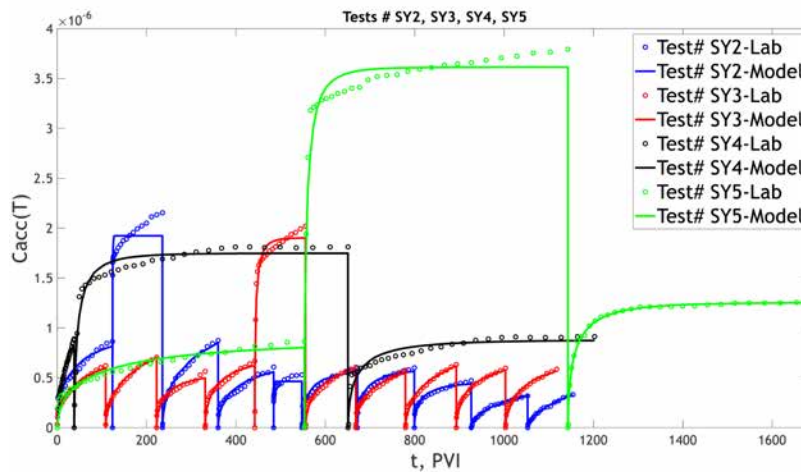


Figure 12—DLVO energy profile (Data from Test# SY2 by Huang et al. 2017).



a)



b)

Figure 13—Tuning for Test# SY2, SY3, SY4, SY5

Figures 14 and 15 present calculation of maximum retention function. In figures 14a and c are calculated concentration of detached particle by formula 29 for tests SY2 and SY3. Figures 15a, 15c present calculation of detached particles for tests SY4 and SY5. Figures 14b and d present maximum retention function by DLVO (red), by breakage (blue) and the overall maximum retention function (black dashed).

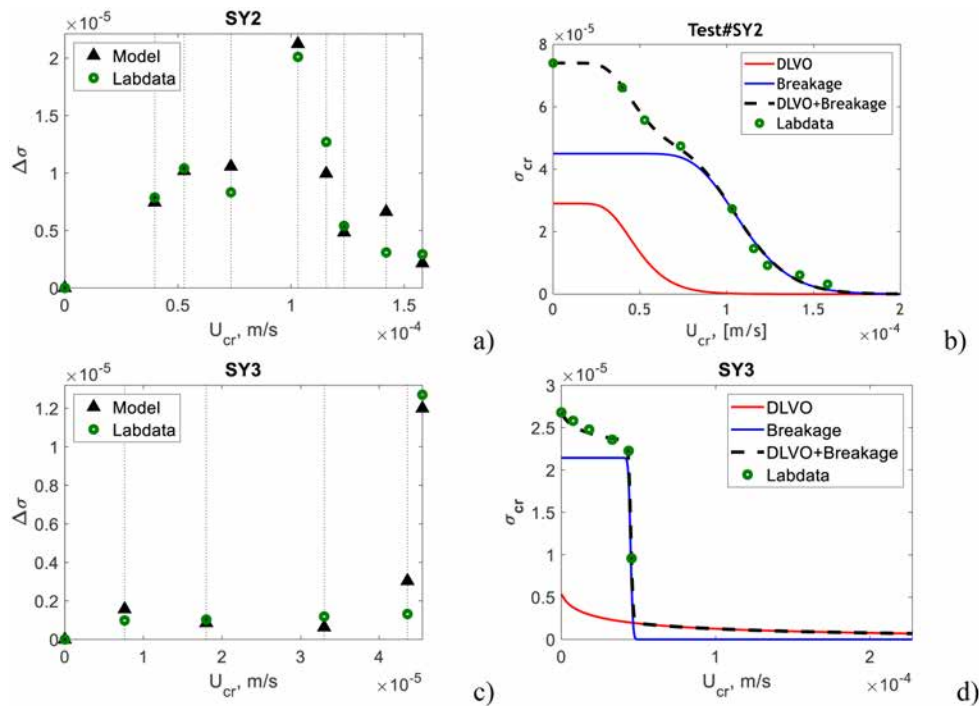


Figure 14—Results for Test# SY2, SY3 (Data by Huang et al. 2017)

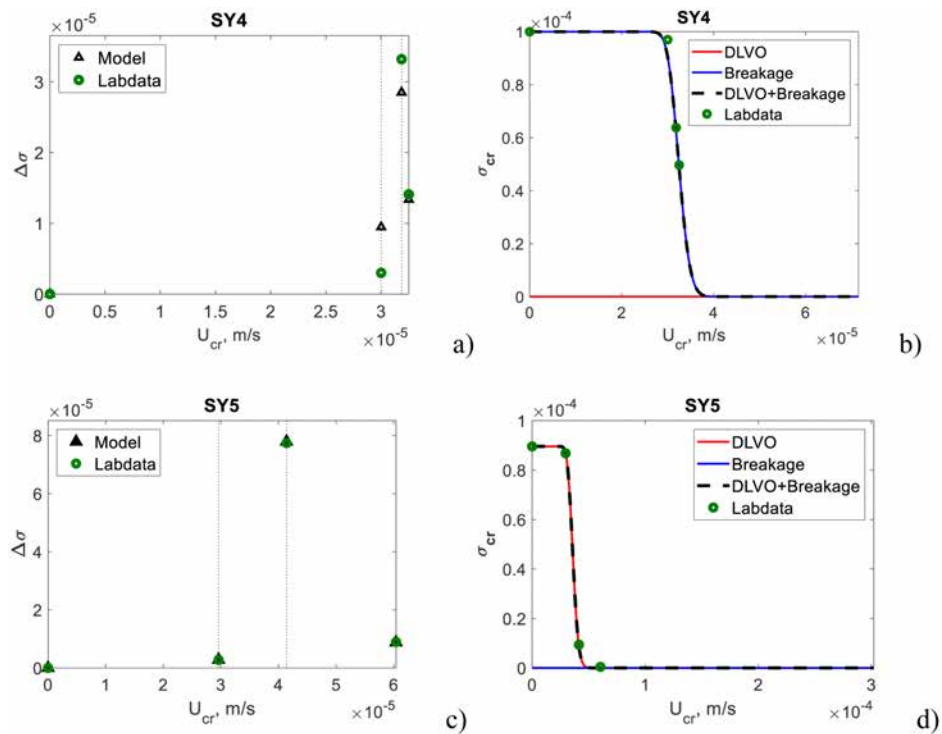
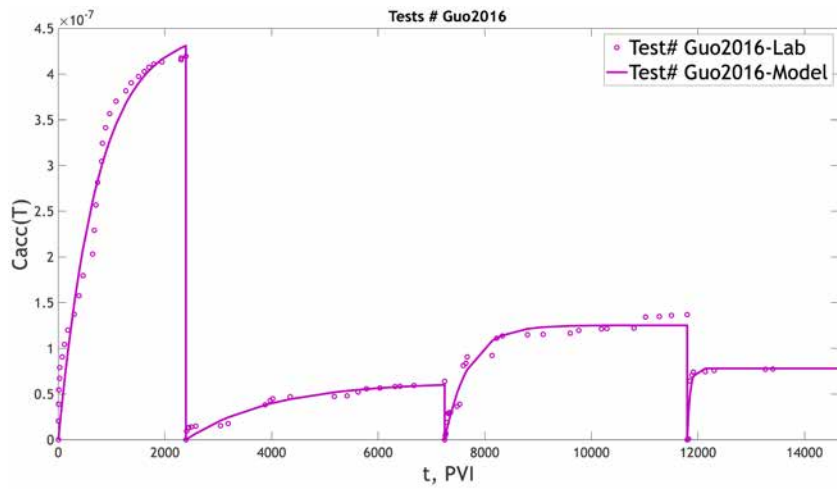
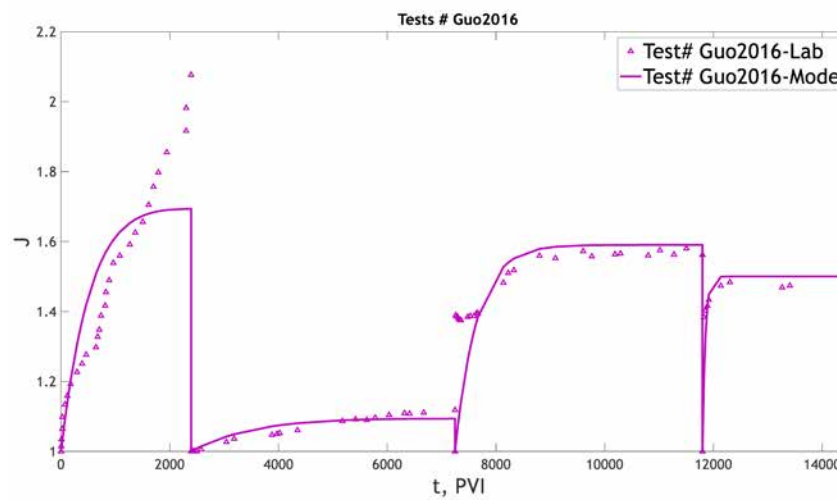


Figure 15—Results for Test# SY4, SY5. First one matched only with breakage and it was not possible to match with DLVO, second one matched with both and it is hard to decide which one is acceptable.

Guo *et al.* 2016. The results of coreflood under four different velocities are presented in Figure 16a and b. High quality of match can be observed. Figure 17a shows calculations of concentration of detached particle due to velocity alternations, and maximum retention functions in Figure 17b.

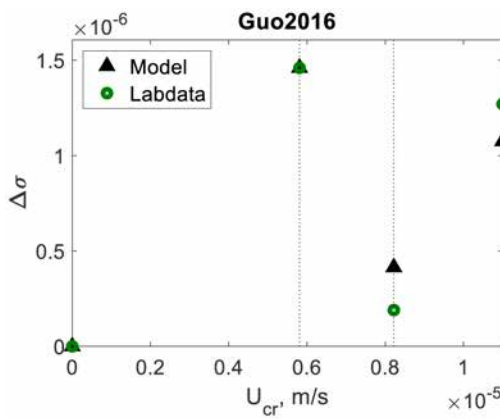


a)

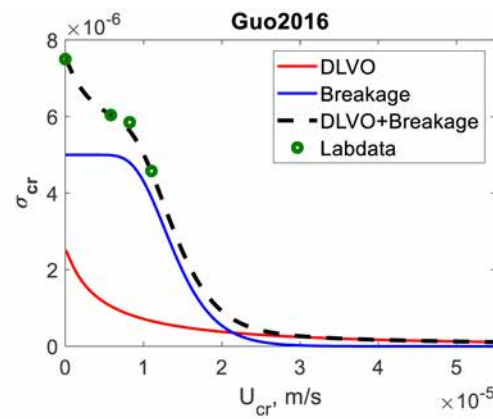


b)

Figure 16—Tuning for paper Guo2016.



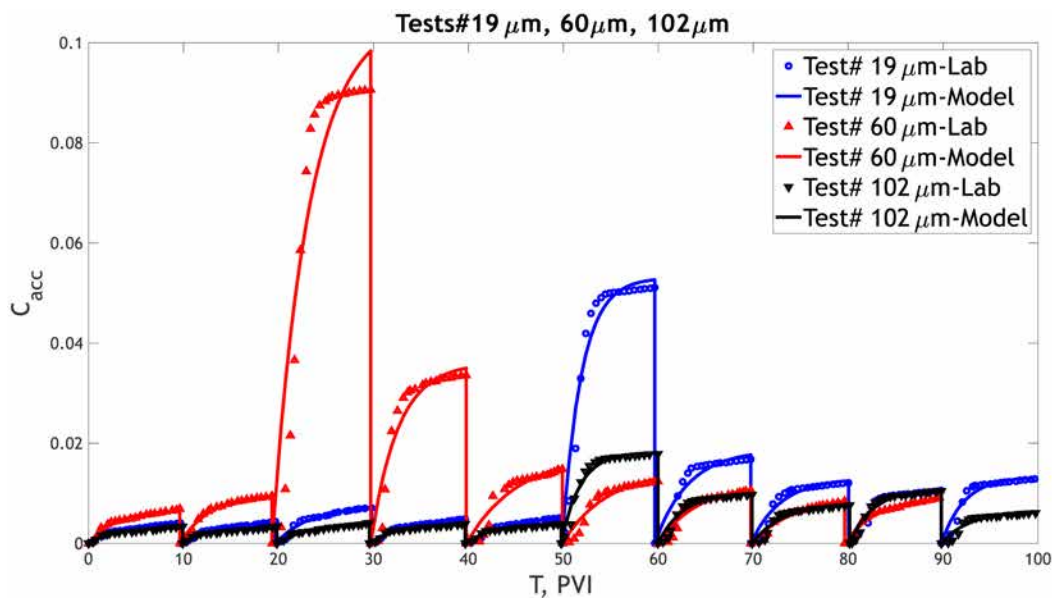
a)



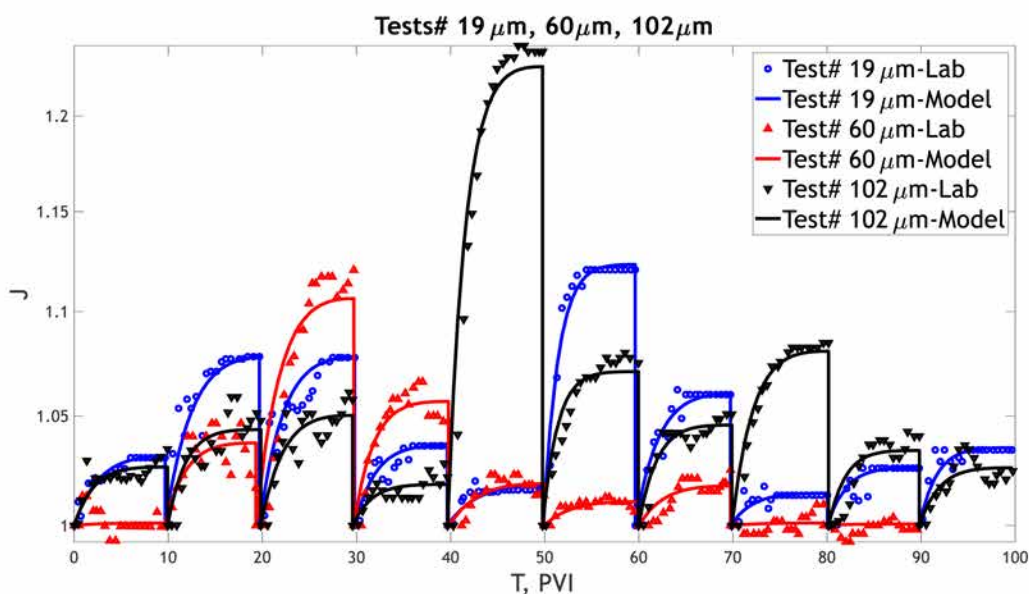
b)

Figure 17—Results for Guo2016.

Huang et al. 2021. The breakthrough concentrations and impedance under ten different velocities are shown in figure 18 for three artificial porous media with different size grains. Three porous media have been engineered from coal particles with 19, 60, 102 μm by sieving. High quality match has been observed. Figures 19b, d, and f show plots of maximum retention function by DLVO, breakage and overall detachment.



a)



b)

Figure 18—Tuning for Test# 19 μm, 60 μm, 102 μm.

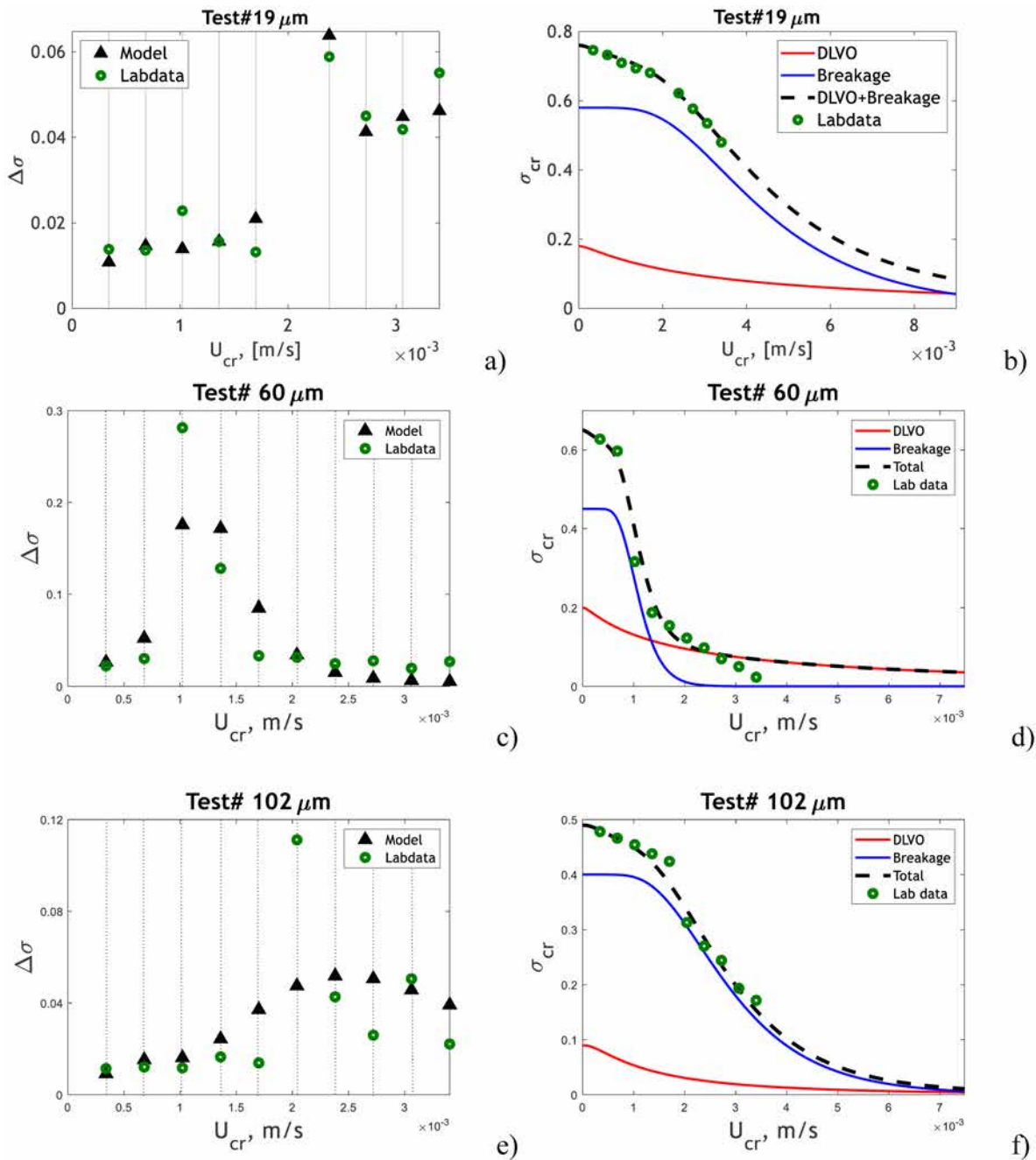


Figure 19—Results for Test# 19µm, 60µm, 102µm.

In all above-mentioned tests besides high quality of matching, variation of tuned parameters varies in common intervals of their values, obtained from the literature. For all processes two stage fines detachment has been observed.

Laboratory-based analytical-model predictions of skin growth in production wells due to fines migration

In this section, we predict skin factor growth in production wells due to fines detachment, migration, and straining accounting for both detrital and authigenic fines.

The analytical solution for radial oil flow towards the well under fines migration is presented in work [5]. First, we use the model parameters obtained in coreflood tests by Huang et al. 2017, presented in Figures 13

and 14. Tuning of lab data by the model revealed the percentage of detrital (40%) and authigenic (60%) of fines particles. Figure 20a skin factor for detrital fines only (red curve) and authigenic particles only (blue curve). The black curve corresponds to independent detachment of fines against electrostatic attraction and by breakage. Lab data shows that the critical detachment velocity for breakage is two times higher than for detachment against electrostatic attraction. So, if lab tests were finished at low rates, where fines haven't broken off yet, only 40% of the overall skin would be predicted.

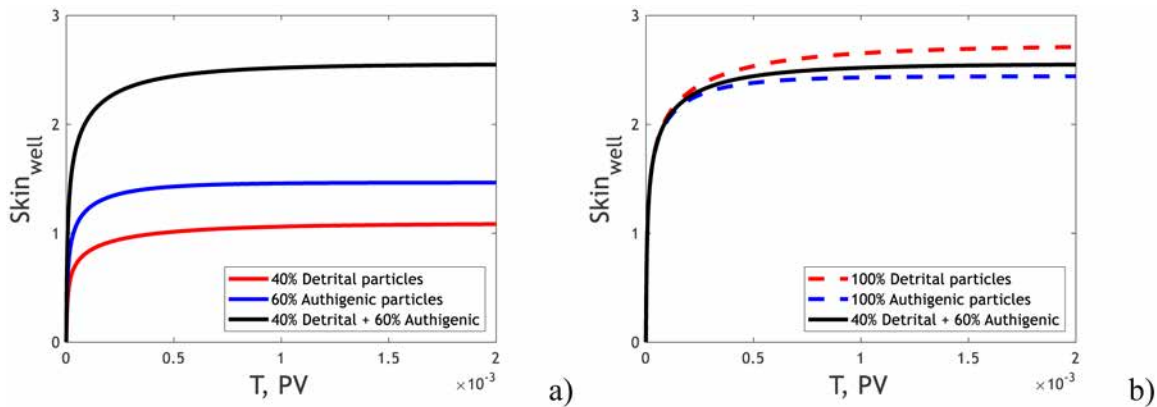


Figure 20—Prediction of well performance. Parameters used are: $\beta = 20000, \lambda = 20$
 $1/m, \alpha = 1 \times 10^{-2}, \sigma_0^e = 3 \times 10^{-5}, \sigma_0^f = 4.5 \times 10^{-5}, \mu_{U_{Cr}}(DLVO) = -9.934, \sigma_{U_{Cr}}(DLVO) = 0.306,$
 $\mu_{U_{Cr}}(Breakage) = -9.130, \sigma_{U_{Cr}}(Breakage) = 0.2004.$ (Data from Test# SY2 by Huang et al. 2017)

Figure 20b compares skin growth by detrital and authigenic fines. The critical breakage velocity is significantly higher, than the mobilisation velocity for detrital fines. Therefore, authigenic fines are mobilised in smaller well vicinity than the detrital ones, so the skin due to detrital fines is higher. However, the bulk of the damage is localised in thin well vicinity, so the difference is not high.

Figure 21 presents the skin based on lab tests by Huang et al. 2021. The overall skin is the total of two individual skins due to detachment of detrital and authigenic fines. In this case, the bulk of skin is reached by authigenic fines due their large initial concentration if compared with detrital particles (Figure 21a). Figure 21b show higher impact of detrital fines into the overall skin, because they detach in a larger zone around the well.

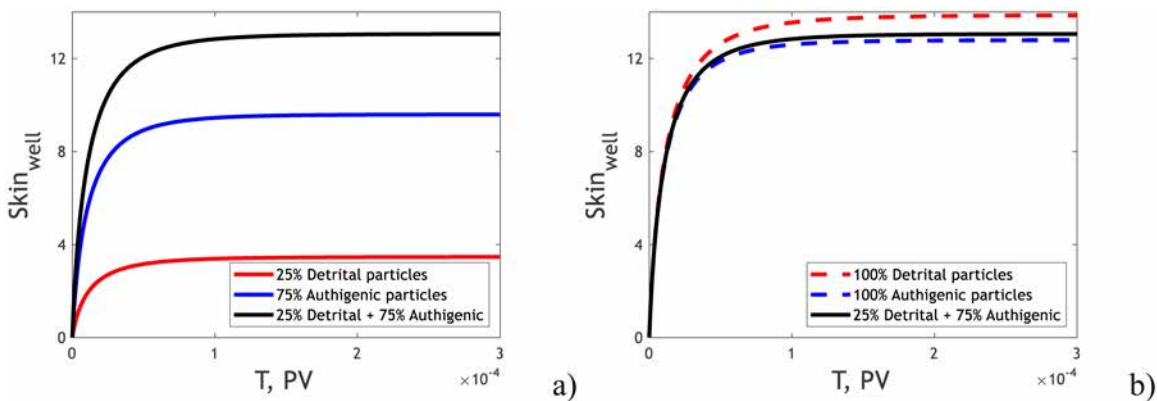


Figure 21—Prediction of well performance. Parameters used are: $\beta = 10, \lambda = 2$
 $1/m, \alpha = 1 \times 10^{-1}, \sigma_0^e = 0.2, \sigma_0^f = 0.6, \mu_{U_{Cr}}(DLVO) = -5.74, \sigma_{U_{Cr}}(DLVO) = 1.45,$
 $\mu_{U_{Cr}}(Breakage) = -5.44, \sigma_{U_{Cr}}(Breakage) = 0.46.$ (Data from Test# 19 μ m by Huang et al. 2021)

Conclusions

Transformation of the theory of authigenic and potential fines in coal beds, treatment of the laboratory data and analytical-model and lab-based well behaviour prediction allows drawing the following conclusions.

1. Mathematical analysis of the analytical solution for stresses in beam theory allows concluding that particle breakage can occur due to tensile stress either in the middle or at the boundary of the beam base, or by shear stress in the middle.
2. Timoshenko's solution for the beam depends on two dimensionless numbers: drag-strength number κ , Poisson's ratio ν , and shape-Poisson number χ . Analytical expression for maximum stresses at the beam base are derived. Five areas I, II, III, IV, V distinguish different formulae for maximum tensile stress in the middle of the beam and on its boundary and allow determining maximum tensile stress.
3. The determined maximum tensile stress can be compared with maximum shear stress using the breakage regime function, allowing calculating the failure criterion. Here, four breakage regimes can be distinguished: if tensile-shear ratio exceeds two, breakage is going on by shear stress; if tensile-shear ratio is lower than one, breakage is going on by tensile stress. Two different regimes can be distinguished when the tensile-shear ratio is between one and two. The above methodology allows for applying of maximum tensile and shear strength criterion for an attached particle, which is represented by an equivalent beam.
4. The critical detachment velocity that breaks a particle of the coal surface is determined by the value κ of the drag-strength number. The explicit formula determines critical velocity via particle aspect ratio and bond ratio.
5. Explicit integral formulae express probabilistic distribution of critical detachment velocity via distribution of the particle properties. The accumulated velocity distribution determines particle concentration which remain attached for any given velocity. This function reflects the fines generation capacity of rocks and it is called maximum retention function.
6. Breakage velocities for authigenic/potential fines in coal beds are two times higher than those for detrital particle detachment.
7. The model coefficients obtained from coreflood data are used for well behaviour prediction. Ignoring breakage of authigenic fines can lead to significant underestimation of skin factor in production wells. This error is large at high concentration of attached authigenic particles.

References

1. Bai T, Chen Z, Aminossadati SM, Li L, Liu J, Lu H. Dimensional analysis and prediction of coal fines generation under two-phase flow conditions. *Fuel*. 2017 Apr 15;194:460–79.
2. Bai T, Chen Z, Aminossadati SM, Pan Z, Liu J, Li L. Characterization of coal fines generation: A micro-scale investigation. *Journal of Natural Gas Science and Engineering*. 2015 Nov 1;27:862–75.
3. Bedrikovetsky, P., Siqueira, F. D., Furtado, C., de Souza, A. L. S., 2011, Modified particle detachment model for colloidal transport in porous media, *Journal of Transport in Porous Media*, **86**:353–383.
4. Bedrikovetsky, P., Zeinijahromi, A., Siqueira, F. D., Furtado, C., de Souza, A. L. S., 2012, Particle detachment under velocity alternation during suspension transport in porous media, *Journal of Transport in Porous Media*, v. **91** (1), p. 173–197.
5. Chequer, L., Nguyen, C., Loi, G., Zeinijahromi, A. and Bedrikovetsky, P., 2021. Fines migration in aquifers: Production history treatment and well behaviour prediction. *Journal of Hydrology*, **602**,p.126660.

6. Deisman N, Ivars DM, Darcel C, Chalaturnyk RJ. Empirical and numerical approaches for geomechanical characterization of coal seam reservoirs. *International Journal of Coal Geology*. 2010 Jun 1;**82** (3-4):204–12.
7. Gao F, Stead D, Kang H. Numerical investigation of the scale effect and anisotropy in the strength and deformability of coal. *International Journal of Coal Geology*. 2014 Dec 15;**136**:25–37.
8. Guo WY, Tan YL, Yu FH, Zhao TB, Hu SC, Huang DM, Qin Z. Mechanical behavior of rock-coal-rock specimens with different coal thicknesses. *Geomechanics and Engineering*. 2018 Jan 1;**15** (4):1017–27.
9. Guo Z, Hussain F, Cinar Y. Physical and analytical modelling of permeability damage in bituminous coal caused by fines migration during water production. *Journal of Natural Gas Science and Engineering*. 2016 Sep 1;**35**:331–46.
10. Han G, Ling K, Wu H, Gao F, Zhu F, Zhang M. An experimental study of coal-fines migration in Coalbed-methane production wells. *Journal of Natural Gas Science and Engineering*. 2015 Sep 1;**26**:1542–8.
11. Huang F, Dong C, You Z, Shang X. Detachment of coal fines deposited in proppant packs induced by single-phase water flow: Theoretical and experimental analyses. *International Journal of Coal Geology*. 2021 Apr 15;**239**:103728.
12. Huang F, Kang Y, You L, Li X, You Z. Massive fines detachment induced by moving gas-water interfaces during early stage two-phase flow in coalbed methane reservoirs. *Fuel*. 2018 Jun 15;**222**:193–206.
13. Huang F, Kang Y, You Z, You L, Xu C. Critical conditions for massive fines detachment induced by single-phase flow in coalbed methane reservoirs: modeling and experiments. *Energy & Fuels*. 2017 Jul 20;**31** (7):6782–93.
14. Liu H, Lin Y, Marrero TR. Effect of ζ potential on the strength of compacted coal logs. *Industrial & engineering chemistry research*. 1996 Jan 8;**35** (1):263–8.
15. Liu J, Yuan X, Zhang J, Xi W, Feng J, Wu H. Sharp Reductions in High-Productivity Well Due to Formation Damage: Case Study in Tarim Basin, China. In *Proceedings of the International Field Exploration and Development Conference 2017 2019* (pp. 843-857). Springer, Singapore.
16. Mathews JP, Eser S, Hatcher PG, Scaroni AW. The shape of pulverized bituminous vitrinite coal particles. *KONA Powder and Particle Journal*. 2007;**25**:145–52.
17. Nick KE, Conway MW, Fowler KS. The relation of diagenetic clays and sulfates to the treatment of coalbed methane reservoirs. In *SPE Annual Technical Conference and Exhibition 1995 Oct 22*. OnePetro.
18. Obermayr M, Dressler K, Vrettos C, Eberhard P. A bonded-particle model for cemented sand. *Computers and Geotechnics*. 2013 Apr 1;**49**:299–313.
19. Okubo S, Fukui K, Qingxin Q. Uniaxial compression and tension tests of anthracite and loading rate dependence of peak strength. *International Journal of Coal Geology*. 2006 Oct 2;**68** (3-4):196–204.
20. Pomeroy CD, Morgans WT. The tensile strength of coal. *British Journal of Applied Physics*. 1956 Jul 1;**7** (7):243.
21. Potyondy DO, Cundall PA. A bonded-particle model for rock. *International journal of rock mechanics and mining sciences*. 2004 Dec 1;**41** (8):1329–64.
22. Poulsen BA, Adhikary DP. A numerical study of the scale effect in coal strength. *International Journal of Rock Mechanics and Mining Sciences*. 2013 Oct 1;**63**:62–71.

23. Poulsen BA, Shen B, Williams DJ, Huddleston-Holmes C, Erarslan N, Qin J. Strength reduction on saturation of coal and coal measures rocks with implications for coal pillar strength. *International Journal of Rock Mechanics and Mining Sciences*. 2014 Oct 1;**71**:41–52.
24. Robinson ES. Mechanical disintegration of the Navajo sandstone in Zion Canyon, Utah. *Geological Society of America Bulletin*. 1970 Sep 1;**81** (9):2799–806.
25. Roslin A, Pokrajac D, Wu K, Zhou Y. 3D pore system reconstruction using nano-scale 2D SEM images and pore size distribution analysis for intermediate rank coal matrix. *Fuel*. 2020 Sep 1;**275**:117934.
26. Russell T, Chequer L, Borazjani S, You Z, Zeinijahromi A, Bedrikovetsky P. Formation damage by fines migration: Mathematical and laboratory modeling, field cases. In *Formation Damage During Improved Oil Recovery* 2018 Jan 1 (pp. 69–175). Gulf Professional Publishing.
27. Shafian SR, Saaid IM, Razali N, Salleh IK, Irawan S. Experimental investigation of colloidal silica nanoparticles (C-SNPs) for fines migration control application. *Applied Nanoscience*. 2021 Jul;**11** (7):1993–2008.
28. Shovkun I, Espinoza DN. Coupled fluid flow-geomechanics simulation in stress-sensitive coal and shale reservoirs: Impact of desorption-induced stresses, shear failure, and fines migration. *Fuel*. 2017 May 1;**195**:260–72.
29. Tao S, Tang D, Xu H, Li S, Geng Y, Zhao J, Wu S, Meng Q, Kou X, Yang S, Yi C. Fluid velocity sensitivity of coal reservoir and its effect on coalbed methane well productivity: a case of Baode Block, northeastern Ordos Basin, China. *Journal of Petroleum Science and Engineering*. 2017 Apr 1;**152**:229–37.
30. Timoshenko S, Goodier JN. *Theory of Elasticity*: by S. Timoshenko and JN Goodier. McGraw-Hill; 1951.
31. Ting HZ, Yang Y, Tian ZF, Carageorgos T, Bedrikovetsky P. Image interpretation for kaolinite detachment from solid substrate: Type curves, stochastic model. *Colloids and Surfaces A: Physicochemical and Engineering Aspects*. 2022 Oct 5;**650**:129451.
32. Tolooiyan A, Mackay R, Xue J. Measurement of the tensile strength of organic soft rock. *Geotechnical Testing Journal*. 2014 Sep 19;**37** (6):991–1001.
33. Ulusoy U, Iğathinathane C. Dynamic image based shape analysis of hard and lignite coal particles ground by laboratory ball and gyro mills. *Fuel processing technology*. 2014 Oct 1;**126**:350–8.
34. Yang, Y. and Bedrikovetsky, P., 2017. Exact Solutions for Nonlinear High Retention-Concentration Fines Migration. *Transport in Porous Media*, pp.1–22.
35. Yang, Y, Siqueira, F. D, Vaz, A., Badalyan, A., You, Z., Zeinijahromi, A., Carageorgos T., Bedrikovetsky, P. (2018). Fines migration in aquifers and oilfields: laboratory and mathematical modelling. In: Narayanan, N., Mohanadhas, B. and Mangottiri, V. eds., *Flow and Transport in Subsurface Environment*. Springer, pp. 3–67.
36. Yin W, Zhu Z, Yang B, Fu Y, Yao J. Contribution of particle shape and surface roughness on the flotation behavior of low-ash coking coal. *Energy Sources, Part A: Recovery, Utilization, and Environmental Effects*. 2019 Mar 4;**41** (5):636–44.
37. Young AP, Ashford SA. Instability investigation of cantilevered seacliffs. *Earth Surface Processes and Landforms: The Journal of the British Geomorphological Research Group*. 2008 Oct 15;**33** (11):1661–77.
38. Yue J, Yue G, Wang Z, Li M, Wang B, An F. Freezing method for rock cross-cut coal uncovering I: Mechanical properties of a frozen coal seam for preventing outburst. *Scientific Reports*. 2019 Nov 8;**9** (1):1–7.

39. Zhang S, Liu Q, Yang Y, Wang D, He J, Sun L. Preparation, morphology, and structure of kaolinites with various aspect ratios. *Applied Clay Science*. 2017 Oct 1;**147**:117–22.
40. Zhao Y, Liu S, Zhao GF, Elsworth D, Jiang Y, Han J. Failure mechanisms in coal: Dependence on strain rate and microstructure. *Journal of Geophysical Research: Solid Earth*. 2014 Sep;**119** (9):6924–35.

9. Fines migration during Coal Bed Methane production: mathematical and laboratory modelling, field cases

Hashemi, A., Dang-Le, B., Nguyen, C., Loi, G. and Khazali, N., 2023.

The APPEA Journal, 63(2), pp.S177-S182.

Statement of Authorship

Title of Paper	Fines migration during Coal Bed Methane production: mathematical and laboratory modelling, field cases
Publication Status	<input checked="" type="checkbox"/> Published <input type="checkbox"/> Submitted for Publication <input type="checkbox"/> Accepted for Publication <input type="checkbox"/> Unpublished and Unsubmitted work written in manuscript style
Publication Details	Hashemi, A., Dang-Le, B., Nguyen, C., Loi, G. and Khazali, N., 2023. Fines migration during coal bed methane production: mathematical and laboratory modelling, field cases. The APPEA Journal, 63(2), pp.S177-S182.

Principal Author

Name of Principal Author (Candidate)	Abolfazl Hashemi		
Contribution to the Paper	Collecting data, performing lab data analysis, deriving the equations, writing code for the authigenic particle detachment, preparing the graphs, writing the manuscript.		
Overall percentage (%)	85%		
Certification:	This paper reports on original research I conducted during the period of my Higher Degree by Research candidature and is not subject to any obligations or contractual agreements with a third part that would constrain its inclusion in this thesis. I am the primary author of this paper.		
Signature		Date	15/11/2023

Co-Author Contributions

By signing the Statement of Authorship, each author certifies that:

- I. The candidate's stated contribution to the publication is accurate (as detailed above);
- II. Permission is granted to the candidate to include the publication in the thesis; and
- III. The sum of all co-author contributions is equal to 100% less the candidate's stated contribution

Name of Co-Author	Bryant Dang-Le		
Contribution to the Paper	Collecting and analysing lab data, collecting field data.		
Signature	Bryant Dang-Le	Date	15/11/2023

Name of Co-Author	Cuong Cao Nguyen		
Contribution to the Paper	Collecting literature data, writing code, and analysing detrital particle detachment		
Signature		Date	15/11/2023

Name of Co-Author	Grace Loi		
Contribution to the Paper	Collecting literature data, writing code, and analysing detrital particle detachment		
Signature		Date	15/11/2023

Name of Co-Author	Nastaran Khazali		
Contribution to the Paper	Deriving equations and matching lab data using two-population particle detachment mechanism.		
Signature		Date	15/11/2023

Fines migration during coal bed methane production: mathematical and laboratory modelling, field cases

Abolfazl Hashemi^{A,*}, Bryant Dang-Le^A, Cuong Nguyen^A, Grace Loi^A and Nastaran Khazali^A

For full list of author affiliations and declarations see end of paper

***Correspondence to:**

Abolfazl Hashemi
University of Adelaide, Level 2, Santos
Petroleum Engineering Bldg., Frome Road,
North Terrace Campus, Adelaide, SA 5005,
Australia
Email: Abolfazl.hashemi@adelaide.edu.au

ABSTRACT

Fines migration in coalbed methane (CBM) fields comprises a serious environmental and gas-production challenge. The literature widely reports two kinds of fines: potential coal fines, which are a part of the coal body and can be detached by breakage under a significant drag force exerted from the inflowing water, and detrital coal fines, which are attached to the coal body by electrostatic forces. The theory for detrital coal fines migration is well developed. A theory for potential coal fines, where the drag deforms the coal asperities and detaches fines by rock failure, is not available. The objectives of this study are (1) to derive the governing equations for fines generation by breakage using failure criteria, and (2) to predict well productivity during dewatering and gas production using laboratory-based modelling. The micro-model developed is based on beam theory and comprises static rock deformation by the flow-through water and calculating failure criteria by tensile and shear stresses. The failure condition determines the number of fines that detach after the application of each flow rate, allowing determining the maximum retention function of potential coal fines. The breakage micro-model is incorporated into filtration equations that account for fines mobilisation, migration, straining and consequent permeability decline. Eight series of lab flooding data with coal cores have been treated. The close match between the lab and model validates the model developed. The model allows predicting productivity decline due to permeability reduction by fines breakage and straining.

Keywords: authigenic particles, breakage, coal fines, clay, detachment, fines migration, impedance, maximum retention function, porous media, skin factor, stress.

Introduction

There are two types of particle fines attached to porous media surface. The first type is detrital particles which are already broken off their growing environment and transported and then attached to a substrate by an electrostatic force (Fig. 1a). The second type is called authigenic or potential fines, which have grown and have physical bond to a substrate. Fig. 1b–d are scanning electron microscope (SEM) photos of kaolinite booklets, flaky illite and iron sulfate minerals growing from a coal fracture surface (Nick *et al.* 1995). The authigenic coal fines are in the form of asperities in the coal cleat. In Fig. 1e, the SEM photo of one coal cleat is numerically simulated (Bai *et al.* 2015). The white colour is the cleat and the rest is the coal body. After fluid flow through the cleat, the created stress inside the body of the coal has been indicated using different colours. The red colour indicates that the stress is higher than a critical value, thus failure happens. As can be seen in the figure, the base of the asperity has failed and the particle can be detached. Although it is difficult to observe the detachment of the authigenic particles in lab, there are some images indicating the breakage of authigenic particles. Fig. 1f reports the breakage of hairy illite particles after the injection of fracturing fluid (Liu *et al.* 2019).

There are numerous studies on modelling of the detachment of detrital particles from a substrate by drag force against the electrostatic attraction (Bedrikovetsky *et al.* 2011, 2012; Bradford *et al.* 2013). However, there is no model for the fluid velocity required to

Accepted: 6 March 2023

Published: 11 May 2023

Cite this:

Hashemi A *et al.* (2023)
The APPEA Journal
63(S1), S177–S182. doi:10.1071/AJ22147

© 2023 The Author(s) (or their employer(s)). Published by CSIRO Publishing on behalf of APPEA.

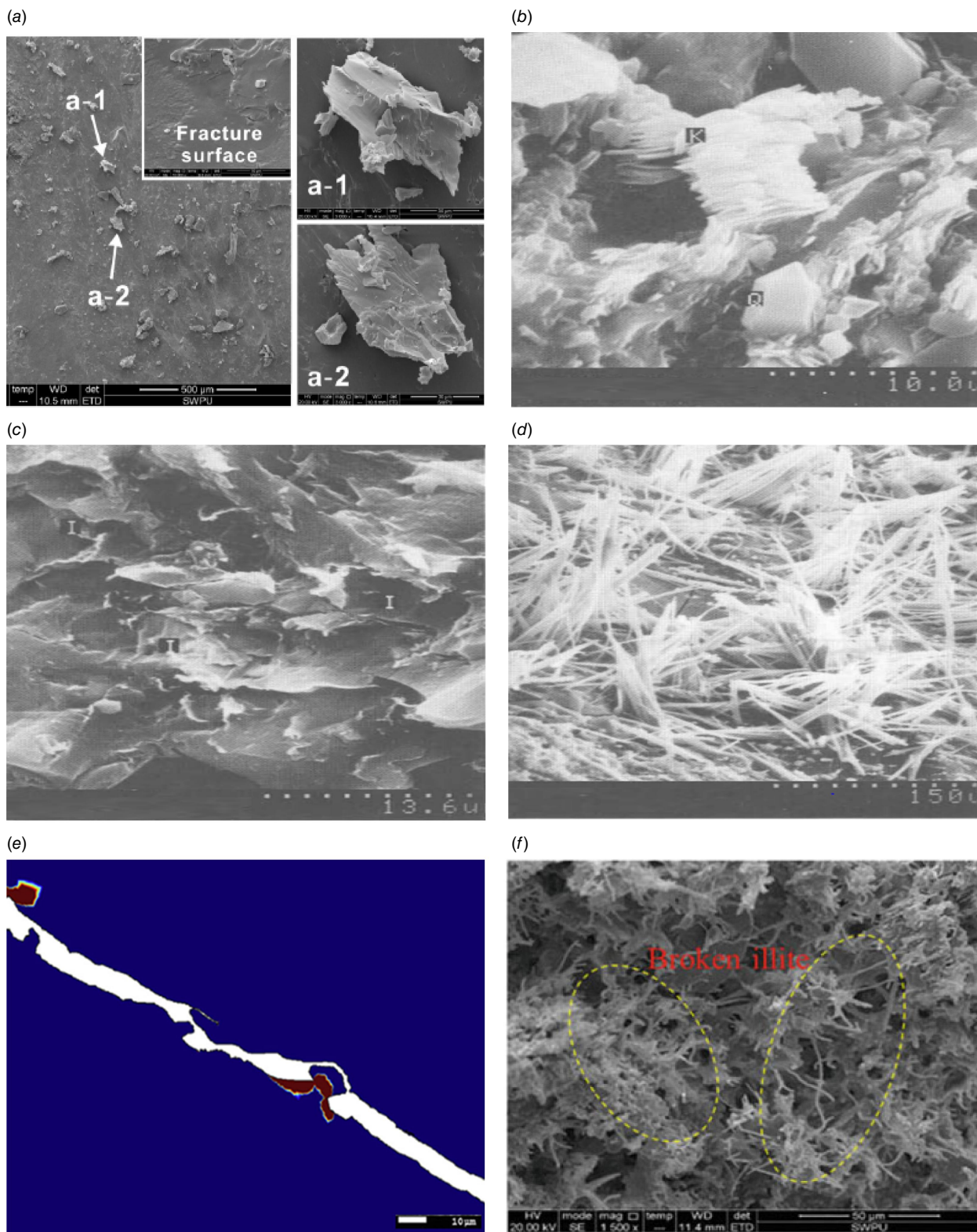


Fig. 1. SEM images of (a) detrital coal fines on a fracture surface (Huang et al. 2018), (b) booklets of kaolinite, (c) flaky illite crystal, (d) iron sulfate minerals (Nick et al. 1995), (e) coal cleat used in numerical simulation (Bai et al. 2015), and (f) hairy illite broken after treatment by fracturing fluid (Liu et al. 2019).

detach an authigenic particle by breakage from a substrate. This paper fills the gap by presenting a novel mechanism of detachment of authigenic particles in porous media. The theory for breakage detachment includes a novel mathematical model, laboratory procedure compatible with mathematical model and upscaling from pore to core. This theory integrates elastic beam theory (Timoshenko and Goodier 1951) with failure criteria and interaction between viscous flow and particle deformation. In the following section, we present the methodology to calculate detachment velocity for detrital and authigenic particles and the concept of maximum retention function (MRF) is developed. The complete derivation of the equations can be found in Hashemi *et al.* (2023).

Methodology

Detachment velocities

The detachment of detrital particle is described by a well-developed theory. Detrital particles are attached to a substrate by a vertical electrostatic force (F_e). The electrostatic force is obtained using the Derjaguin, Landau, Verwey and Overbeek (DLVO) theory (Israelachvili 2011). The creeping viscous flow creates a horizontal drag force, F_d . Applying torque balance for the horizontal drag force and the vertical electrostatic force leads to the following equation to calculate the injection velocity for detachment of detrital particle (see Hashemi *et al.* 2023):

$$U^e = \frac{\phi F_e l_n}{6\pi\mu_f r_s f_d b f_M} \quad (1)$$

Here ϕ is porosity, l_n is the lever arm for the electrostatic force, μ_f is the viscosity of the fluid, r_s is an equivalent radius of the spherical particle with the same volume, f_d and f_M are the shape factors for drag force and moment, b is the lever arm for drag force and equals to the semi-axis dimension of the particle vertical to flow direction. We assume the particle has a spheroidal shape and the equations for the shape factors can be found in Ting *et al.* (2021).

Fig. 2 shows a spheroidal authigenic particle bonded to a substrate. The detachment happens when the bond breaks. So to study the detachment, we should know the stresses created by the fluid drag force in the bond plane. The material of the particle is brittle and shows linear elastic behaviour. We assume a cylindrical beam with a base at the substrate that extends to the centre of the particle. It is further assumed that the fluid drag force is applied at the top of the beam in the form of a shear force. The stresses for this type of beam are presented by Timoshenko and Goodier (1951). The detachment of the particle is obtained from the analysis of stresses at the base of the beam (i.e. σ_z , τ_{xz} , τ_{yz} at $z = 0$) and applying maximum possible tensile and shear stresses as the failure criteria. So the injection

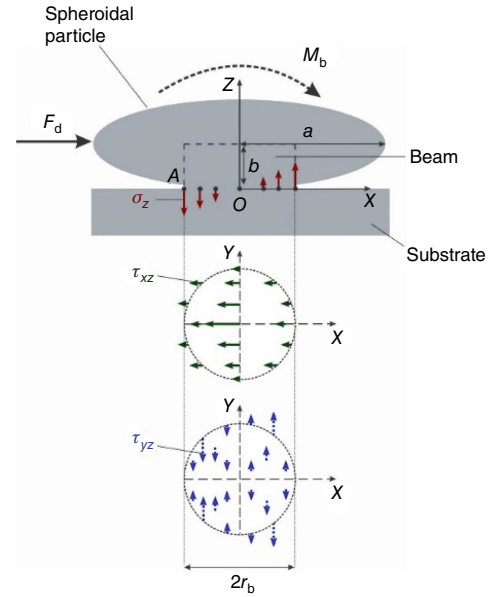


Fig. 2. Schematic of equivalent beam for attached spheroidal particle.

fluid velocity to detach authigenic particles is calculated as follows:

$$U^b = \frac{\delta\phi T_0 r_b^2}{12\alpha_s f_M f_d \mu_f r_s} \kappa \quad (2)$$

Here, δ is the ratio of the bond radius and horizontal semi-axis dimension (i.e. r_b/a), T_0 is the tensile strength of the material, α_s is the aspect ratio (i.e. b/a) and κ is the strength-drag number defined in Hashemi *et al.* (2023).

Maximum retention function

Considering a single value for each parameter in Eqns 1 or 2, one value for each detachment velocity (critical velocity) is obtained. If we consider a normal distribution for each parameter, a distribution for each velocity is obtained. Fitting a probability distribution to the velocity distributions, one function is created for detrital particles i.e. $f_e(U)$ and one for authigenic particles i.e. $f_b(U)$. Following Bedrikovetsky *et al.* (2011, 2012), we introduce the maximum retention function (MRF). Having the distributions for critical velocities, it is possible to obtain at each velocity (U) how many particles remained attached to the substrate. The amount of attached particles is called MRF and is defined as:

$$\sigma_{cr}(U) = \sigma_e^0 \int_U^\infty f(U^e) du + \sigma_b^0 \int_U^\infty f(U^b) du \quad (3)$$

Here σ_e^0 and σ_b^0 are the initial concentration of detrital and authigenic particles, respectively. The amount of detached particles ($\Delta\sigma_n$) can be calculated using Eqn 3 after replacing the bounds of the integrals with two consecutive velocities U_{n-1} and U_n . Here, n is the number of injection rates and $U_0 = 0$.

Results and discussion

To treat lab data, the detachment velocity is incorporated into the filtration equations. In Russell et al. (2018), the filtration equations have been solved to obtain fines mobilisation, migration and straining and the consequent permeability decline. The coreflood tests with piecewise-constant increasing flow rate were collected from the literature. In total, eight core flood tests on coal rock were analysed. In this text, we only present the results of test#SY2 from Huang et al. (2017). The cumulative particle concentration

at the outlet and normalised pressure drop across the core divided by velocity (impedance J) are plotted for each injection rate. The cumulative particle concentration and impedance are matched with the related equations (Fig. 3a, b). Consequently, for each flow rate, four tuning parameters are obtained; i.e. the concentration of detached particles $\Delta\sigma_n$, the drift delay factor α , the filtration coefficient λ and the formation damage coefficient β .

The obtained $\Delta\sigma_n$ from laboratory data are matched with $\Delta\sigma_n$ obtained from Eqn 3 and six tuning parameters are obtained. The tuning parameters are the initial concentration,

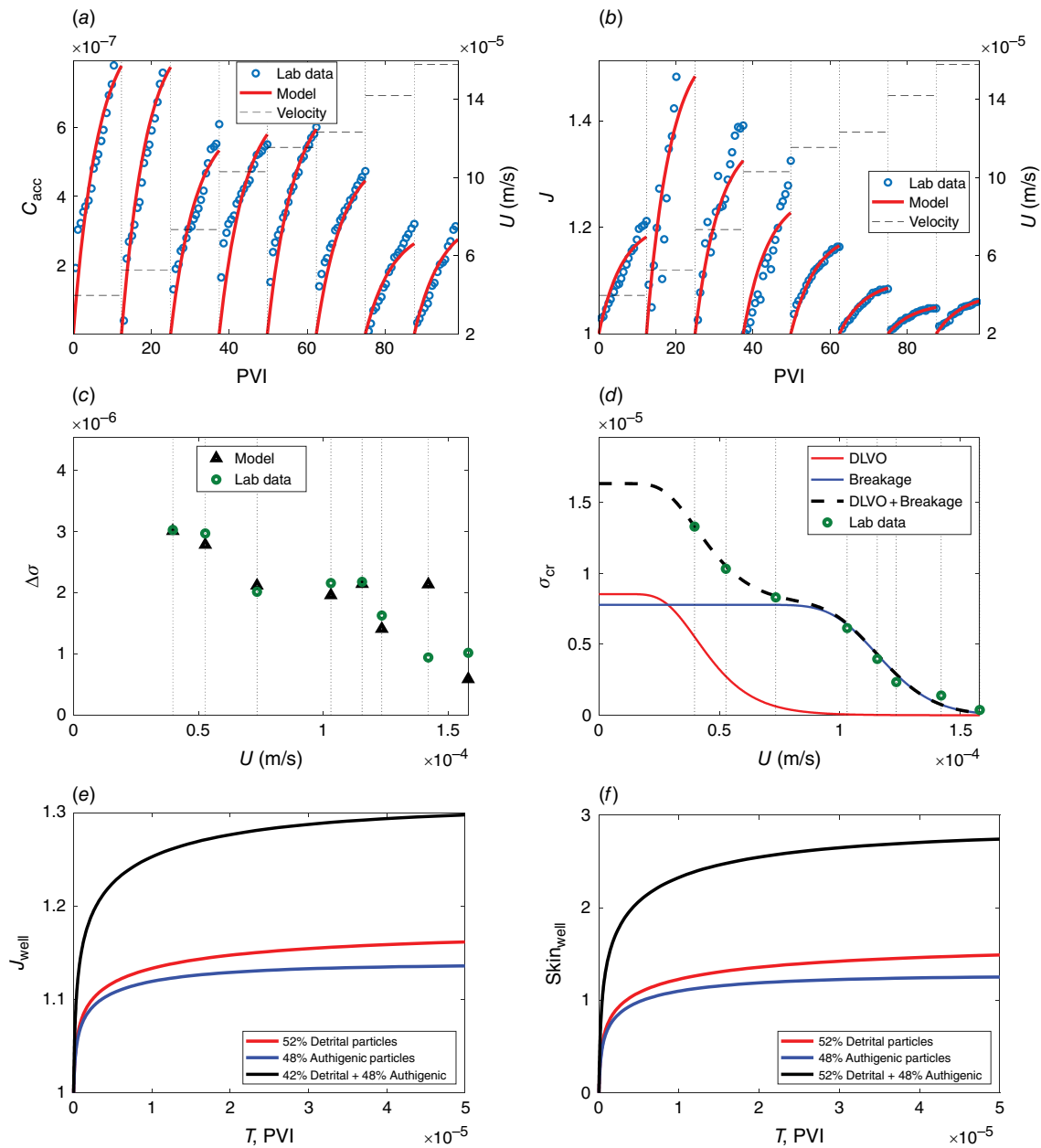


Fig. 3. Tuning of (a) accumulated concentration, $R^2 = 0.91$ and (b) well impedance, $R^2 = 0.88$. Matching of (c) the concentration of detached particles, $R^2 = 0.7$ and (d) MRF, $R^2 = 0.99$. Prediction of (e) the impedance and (f) the skin factor for radial flow around the wellbore.

the mean value and the standard deviation of the probability distribution function for detachment velocities of both detrital and authigenic particles. The best tuning parameters should give us a good match of both $\Delta\sigma$ and MRF. Fig. 3c, d present matching of $\Delta\sigma$ and MRF. It is expected to detect the detachment of detrital particles at low injection rates and authigenic particles at higher rates. So, we first try to match all the lab data with just the first part of Eqn 3. If it is not possible to match the last points, we apply the second term in Eqn 3.

Having obtained the formation damage coefficient (β) and following the equations derived by Russell *et al.* (2018) for radial flow around a wellbore, the skin growth can be predicted. For this test, the percentage of initial concentration of detrital and authigenic particles are 52% and 48%, respectively. Consequently, the well impedance and skin factor due to the detrital particle is slightly higher than the authigenic particles (Fig. 3e, f). The total well impedance or skin factor is the summation of impedance or skin factor created by two mechanisms. Moreover, because the detachment velocity for authigenic particles is higher, the related skin happens close to the wellbore where the velocity is higher. While for detrital particles the skin growth can happen deeper into the formation.

Conclusion

Development of the theory for the detachment of authigenic or potential fines in coalbed methane (CBMs), treatment of the experimental data and prediction of well skin factor allows drawing the following conclusions:

1. The developed theory takes into account the shape of the particle and the mechanical properties of the material. Assuming a distribution of parameters allows obtaining the distribution of detachment velocities for both types of particles.
2. Using the concept of maximum retention function (MRF) enables us to upscale the detachment model from pore to core and well scales.
3. Analysing eight coreflood tests shows that the detachment velocities for authigenic/potential fines in coal beds are usually two times higher than those for detrital particles.
4. Detachment of authigenic fines can have significant effect on skin factor in wells. The effect depends on the

initial concentration and the velocity range achievable in well production or injection. Moreover, the skin growth due to authigenic particles happens mostly close to the wellbore where the fluid velocity is higher but detrital particles can create skin deeper into the formation.

References

- Bai T, Chen Z, Aminossadati SM, Pan Z, Liu J, Li L (2015) Characterization of coal fines generation: a micro-scale investigation. *Journal of Natural Gas Science and Engineering* **27**, 862–875. doi:10.1016/j.jngse.2015.09.043
- Bedrikovetsky P, Siqueira FD, Furtado CA, Souza ALS (2011) Modified particle detachment model for colloidal transport in porous media. *Transport in Porous Media* **86**(2), 353–383. doi:10.1007/s11242-010-9626-4
- Bedrikovetsky P, Zeinijahromi A, Siqueira FD, Furtado CA, de Souza ALS (2012) Particle detachment under velocity alternation during suspension transport in porous media. *Transport in Porous Media* **91**(1), 173–197. doi:10.1007/s11242-011-9839-1
- Bradford SA, Torkzaban S, Shapiro A (2013) A theoretical analysis of colloid attachment and straining in chemically heterogeneous porous media. *Langmuir* **29**(23), 6944–6952. doi:10.1021/la4011357
- Hashemi A, Borazjani S, Nguyen C, Loi G, Khazali N, Badalyan A, Yang Y, Tian ZF, Ting HZ, Dang-Le B, Russell T, Bedrikovetsky P (2023) Geo-mechanical aspects for breakage detachment of rock fines by Darcy's flow. *arXiv Preprint arXiv:2301.01422*. doi:10.48550/arxiv.2301.01422
- Huang FS, Kang YL, You ZJ, You LJ, Xu CY (2017) Critical conditions for massive fines detachment induced by single-phase flow in coalbed methane reservoirs: modelling and experiments. *Energy & Fuels* **31**(7), 6782–6793. doi:10.1021/acs.energyfuels.7b00623 [In English]
- Huang F, Kang Y, You L, Li X, You Z (2018) Massive fines detachment induced by moving gas-water interfaces during early stage two-phase flow in coalbed methane reservoirs. *Fuel* **222**(6), 193–206. doi:10.1016/j.fuel.2018.02.142
- Israelachvili JN (2011) 'Intermolecular and Surface Forces.' (Academic press)
- Liu J, Yuan X, Zhang J, Xi W, Feng J, Wu H (2019) Sharp reductions in high-productivity well due to formation damage: a case study in Tarim Basin, China. In 'Proceedings of the International Field Exploration and Development Conference 2017'. pp. 843–857. (Springer)
- Nick KE, Conway MW, Fowler KS (1995) The relation of diagenetic clays and sulfates to the treatment of coalbed methane reservoirs. In 'SPE Annual Technical Conference and Exhibition, Dallas, Texas, October 1995'. (Society of Petroleum Engineers; OnePetro)
- Russell T, Chequer L, Borazjani S, You Z, Zeinijahromi A, Bedrikovetsky P (2018) Formation damage by fines migration: mathematical and laboratory modelling, field cases. In 'Formation damage during improved oil recovery'. (Eds B Yuan, DA Wood) pp. 69–175. (Gulf Professional Publishing)
- Timoshenko S, Goodier JN (1951) 'Theory of Elasticity', 2nd edn. (McGraw-Hill)
- Ting HZ, Bedrikovetsky P, Tian ZF, Carageorgos T (2021) Impact of shape on particle detachment in linear shear flows. *Chemical Engineering Science* **241**, 116658. doi:10.1016/j.ces.2021.116658

Data availability. The data that support this study are available on the University of Adelaide website at <https://doi.org/10.25909/21981059.v3>.

Conflicts of interest. The authors confirm that there are no conflicts of interest.

Declaration of funding. No funding from external organisations was received for this research.

Author affiliation

^AAustralian School of Petroleum and Energy Resources (ASPER), University of Adelaide, SA, Australia.

The authors



Abolfazl Hashemi is currently a PhD student at the University of Adelaide (UoA). He studied Chemical Engineering: Exploitation of Hydrocarbon Resources at the Petroleum University of Technology in Iran between 1998 and 2002. In 2003, he was accepted to the Technical University of Delft as a Master of Science student in Petroleum Engineering. After completing his MSc in 2005, he worked for 12 years at the National Iranian Oil Company as a Petroleum Engineer. In 2019, he was accepted as a PhD student at the University of Adelaide, where he is currently enrolled in his final year of study.



Bryant Dang-Le is currently a PhD student at the UoA. He gained his Bachelor's degree in Engineering (Petroleum) from the University of Adelaide.



Cuong Nguyen is currently a PhD student at the UoA. He received his Bachelor's degree in Petroleum Engineering from the University of Adelaide.



Grace Loi is currently a PhD student at the UoA. She received her Bachelor's degree in Petroleum Engineering from the University of Adelaide.



Nastaran Khazali is currently a PhD student at the UoA. She received her Bachelor's degree and Master of Science degree in Petroleum Engineering from the Amirkabir University of Technology (Tehran Polytechnique).

10. Discussion

The expansion of the theory of fines detachment in porous media to include authigenic particles marks a significant advancement in the field. Prior to this development, literature primarily focused on detrital particle detachment, referring to particles attached to a substrate solely through electrostatic forces. However, authigenic particles, which are chemically bonded to a surface through geological processes such as growth or cementation, were not thoroughly addressed in existing literature. A comprehensive review revealed a lack of analytical solutions for these particles. Thus, the primary objective of this study is to address this gap by providing analytical insights into the detachment behavior of authigenic particles.

Inspired by the Bonded-Particle Model, we assume that a small cylindrical beam links the surface to the midpoint of the particle, with the fluid drag force acting solely upon this beam. Employing a linear elastic material model, stress at the beam's cross-section is determined using Timoshenko and Goodier's solution. Additionally, we propose a simple failure criterion where points break when subjected to certain limits of tensile or shear stress. By employing this criterion, we analytically solve the problem, determining both the fluid velocity required to break the first point and the corresponding location of this initial failure. We hypothesize that once the first point breaks, the bond weakens, leading to instantaneous failure of adjacent points and subsequent detachment of the particle.

By establishing the relationship between breakage velocity and particle properties, we can employ this equation across a spectrum of particle distributions, thereby deriving a distribution for breakage velocity. Utilizing this velocity distribution, we can integrate successive velocities to quantify the extent of particle detachment. Our research team

has pioneered this methodology for detrital particles, denoting it as the Maximum Retention Function. Extending the application of this approach, the current study incorporates authigenic particles into the Maximum Retention Function (MRF) theory. This framework facilitates the assessment of fines detachment following fluid injection up to specific velocities for each rock sample. Furthermore, through mathematical analysis, we align the data to estimate the total detachable fines.

In this study, Chapter 3 delves into the Maximum Retention Function (MRF) theory and its extensive application in modeling fluid flow within porous media. Chapter 4 marks our inaugural publication on the detachment of authigenic particles, employing a 2D beam theory approach. Chapter 5 provides a comprehensive derivation of the analytical solution for the 3D beam theory. In Chapter 6, we merge our theoretical framework with field data, demonstrating its applicability in enhancing our understanding of fines migration phenomena. Chapters 7, 8, and 9 explore various real-life applications of this theory in geophysics/geo-energy reservoirs, Coal Seam Gas (CSG) extraction, and Coalbed Methane (CBM) extraction, respectively.

The developed theory provides a dependable means of estimating the fluid drag necessary for particle detachment, yet it exhibits considerable sensitivity to two key parameters: the tensile strength of the bond and the distribution of bond radius. Obtaining accurate values for these parameters through experimentation is crucial for refining the model's predictive accuracy. For instance, employing high-resolution scanning techniques may allow for the precise examination of fine particles, enabling the determination of breakage surface and radius, thereby facilitating the calculation of the bond's tensile strength. Conversely, laboratory tests can provide data on the tensile

strength of the bond, which in turn can inform calculations regarding the distribution of bond radius.

Moreover, a significant insight from this study pertains to the impact of fluid velocity on particle detachment. Elevated fluid velocities within porous media amplify the significance of authigenic particle detachment, highlighting the dynamic interplay between fluid dynamics and particle behavior.

11. Future works

This study lays the groundwork for further exploration into the detachment of authigenic particles in porous media, presenting numerous avenues for future research expansion. Several potential areas of investigation include:

- We assumed that the bond comprises a linear elastic material. Expanding this research to incorporate elastic-plastic bond materials would offer a broader understanding of particle detachment behavior. Additionally, the torque balance applied in this study should be extended to encompass the plasticity characteristics of the material, providing a more comprehensive analysis of particle detachment mechanisms.
- We take beam cross-section as a cylindrical beam. This may not always be the case. This study can be easily extended to square cross section of the beam and the results can be compared.
- To date, there have been no laboratory studies that visually document the mechanical detachment of authigenic particles under the influence of fluid drag forces. A potential avenue for future research involves conducting experiments using specialized cameras capable of capturing the detachment of particles due to fluid drag forces.

- We applied the maximum tensile and shear failure criteria in our analysis. However, there is potential to explore alternative failure criteria, which may offer a deeper understanding of the underlying physics of the problem. While incorporating different failure criteria could result in more complex solutions, it could also lead to a more comprehensive model that better captures the intricacies of the problem at hand.
- The findings of this study have potential applications on larger scales, such as cylindrical columns in buildings. Given the concerns surrounding column failure, our analytical solution offers precise predictions for both the failure force and the initial failure point. Therefore, it would be advisable to conduct large-scale laboratory tests to validate our findings and ensure their applicability in real-world scenarios.

11. Conclusions

Derivation of mechanical equilibrium breakage condition on microscale for authigenic particles, development of upscaling procedure for any colloidal-suspension-nano detachment of authigenic and detrital fines, and treatment the laboratory data by analytical models for 1D transport problems allow drawing the following conclusions.

1. For *detrital fines*, where drag and lift detach fines against electrostatic and capillary forces, probability distribution for physical constants contained by the particle-scale mechanical equilibrium of attached particles explains gradual fines detachment during corefloods with flow rate increase. The upscaled procedure developed consists of derivation of PDF for detachment velocity from individual PDFs of mechanical-equilibrium coefficients, and defining MRF as a product of Cumulative Distribution Function (CDF) for detachment velocity and the detachable concentration. The resulting stochastic model allows for direct calculation of maximum retention function that fully determines the detachment rate, from PDFs of the physical mechanical-equilibrium constants. The stochastic model encompasses detachment by rolling, sliding, and lifted particles. The stochastic model is represented by MRF of velocity, salinity, pH, and temperature.

2. The stochastic model is based on observation that constant coefficients in mechanical equilibrium conditions for attached particles yield stepwise MRF. The model reflecting observed in laboratory gradual fines detachment and continuous MRF, assumes probabilistic distribution for all micro scale parameters. We discuss normal distribution for all parameters, with the minimum value set to zero for each parameter. The parameters include particle radius,

pore size, aspect ratio, zeta potentials for particle and rock, lever arm ratio, and their standard deviations.

PDF detachment velocity can be approximated by log-normal distribution with high accuracy. Therefore, MRF has the form of CDF for log-normal distribution. So, MRF is three-parametric, which includes the mean and standard deviation of CDF for log-normal distribution, and the detachable concentration.

3. The sensitivity analysis shows that the most influential parameters for the mean and standard deviation of detachment velocity are the aspect ratio and pore radius. The less influential are variation of lever-arm ratio and particle radius.

An increase in particle radius, pore size, aspect ratio, and lever arm ratio leads to a decrease in mean detachment velocity, whereas higher zeta potentials for both particles and rock result in its increase. Variations of those 5 parameters result in increase of mean detachment velocity. Increase in all five parameters decreases standard deviation of detachment velocity, while increase in their standard deviations results in increase of standard deviation of detachment velocity.

4. For four coreflood tests on detrital fines detachment, high accuracy of the agreement between the lab data and predictions by the stochastic model have been observed. The micro-scale tuning parameters (lever-arm ratio and its standard deviation) as well as macroscale filtration and formation damage coefficients, drift-delay number and detachable concentration vary in the common intervals. This validates the stochastic model for fines detachment.

5. For *authigenic fines*, where the detachment occurs due to breakage, the micro-scale release conditions are achieved by integration of 3D elastic beam theory, failure maximum stress criteria given by tensile/shear strength, and CFD-based modelling of viscous creeping flow, that in reality does detach the particles.

Breakage conditions, where either the tensile or shear stresses reach the strength value, are determined by three dimensionless groups: the strength-drag number (κ), the aspect-Poisson number (χ), the strength ratio (η), as well as Poisson's ratio (ν).

6. Stress maxima are reached at the base of the particle, either at the central axis, $Y=0$ or at the base boundary, $X^2+Y^2=1$.

Stress maxima along the axis $Y=0$ are determined by the aspect-Poisson number χ alone, while the maxima at the beam boundary are determined by both the aspect-Poisson number χ and Poisson's ratio ν . Equality of tensile stress maxima at the beam base axes and boundary separates the plane (χ,ν) , which is called the tensile stress diagram, into five domains, where one tensile maximum exceeds the other.

Shear stress maximum at the central axis of the particle base is always higher than that at the boundary.

7. Employing Timoshenko and Goodier's stress equations, a novel breakage regime for a circular bond at the base of the beam is analytically derived. The breakage regime – by either tensile or shear stress – is determined by breakage function $g(\chi,\nu)$, which is the ratio of stress

maximum of two tensile maxima and maximum shear. The breakage regime depends on the shape-Poisson number, Poisson's ratio, and the ratio η between tensile and shear strengths. The breakage occurs by tensile failure if $g(\chi, \nu) > \eta$, i.e., where the point (χ, η) is located below the curve $g(\chi, \nu)$ in the shear-tensile diagram (χ, η) . If the strength ratio exceeds 2, particles are detached by shear stress for all values of χ and ν . For strength ratios below two and above one, the particles are detached by shear stress for shape-Poisson numbers χ such that η exceeds $g(\chi, \nu)$; for lower aspect-Poisson ratios, particles are detached by tensile stress. For strength ratios below one, the particles are detached by tensile stress for all Poisson's ratios.

8. The definition of the breakage regime – by either tensile or shear stress, in the base middle or at the boundary - is independent of flow velocity. For an identified breakage regime, the breakage flow velocity is determined by the strength-drag number $\kappa(\chi, \nu)$ alone. For a given particle shape, the critical breakage velocity is proportional to the strength and particle size and is inversely proportional to viscosity. These conclusions are the consequence of the assumptions of a Newtonian fluid, elastic beam deformation, and the strength failure criteria.

9. During bond breakage under increasing velocity, the particles of all shapes detach in order of decreasing of their radii, i.e., the large particles break first. For particles of the same volume, the breakage velocity versus aspect ratio is non-monotonic for spherical particles – very flat or almost spherical particles are detached at low flow velocities while the highest flux detaches particles with intermediate aspect ratio. However, for long cylinders, the product of drag and moment factors by the aspect ratio versus aspect ratio is a monotonically decreasing function, and the lower the aspect ratio the higher the breakage velocity.

10. A mathematical model for colloidal detachment by breakage is a Maximum Retention Function (MRF), derived from the formula for breakage flow velocity.

The breakage MRF allows closing the governing equations for migration of authigenic clays with bond failure. The total MRF for authigenic and detrital fines can be determined from breakthrough particle concentration during a coreflood with piecewise constant and increasing velocity. The determination of the MRF is based on the analytical model for fines mobilisation, migration, and straining (size exclusion). Matching the breakthrough curve allows determining the MRF along with the filtration coefficient for straining and drift-delay factor.

11. With simultaneous detachment of authigenic and detrital fines, the MRF is the total of those obtained from mechanical equilibrium conditions for detachment against electrostatic attraction, and by breakage. For weak DLVO particle-rock attraction and high bond strength, the total MRF has a velocity plateau, where all detrital particles are already detached and authigenic particle breakage hasn't started yet. For high electrostatic attraction and low bond strength, the velocity intervals for detachment by both causes overlap, and the plateau disappears.

For MRF with a plateau, the initial percentage of authigenic and detrital fines is calculated directly from the plateau height. For MRF without plateau, the percentage of authigenic and detrital fines is calculated by tuning the MRF coefficients.

12. The model for fines detachment by breakage is validated by the coreflood with 7 constant-rate injections by the two-population feature of produced particle concentrations. High match

of the breakthrough concentrations and pressure drop using the two-population model, tuned coefficients within commonly reported intervals, as well as bimodal size distributions of produced fines all support the validity of the proposed formulation.

13. Calculations of breakage velocity and its comparison with field data indicates that breakage of authigenic particles can occur during CO₂ injection for storage, polymer injection into oilfields, leak-off of highly viscous fracturing fluids during well fracturing, and waterflooding in carbonate oilfields. Fines detachment by breakage during heavy oil production, dewatering of coal seams, and well fracturing by water is unlikely.